



UNIVERSIDADE FEDERAL DE MINAS GERAIS  
INSTITUTO DE GEOCIÊNCIAS  
PROGRAMA DE PÓS-GRADUAÇÃO EM GEOLOGIA



**TESE DE DOUTORADO**

Geodynamic evolution of the Southern Brasília orogen (SE  
Brazil): New petrochronological insights from UHT and HP  
metamorphic rocks

**AUTORA:** Mahyra Tedeschi

**ORIENTAÇÃO:** Prof. Antônio Carlos Pedrosa-Soares

**ORIENTAÇÃO NA UNIVERSIDADE DE BERNA, SUIÇA:** Prof. Daniela Rubatto

Nº38

**BELO HORIZONTE**  
**DATA (12/01/2018)**

Tese de Doutorado



# Geodynamic evolution of the Southern Brasília orogen (SE Brazil): New petrochronological insights from UHT and HP metamorphic rocks

Tese de doutoramento apresentada ao Programa de Pós-Graduação em Geologia do Instituto de Geociências da Universidade Federal de Minas Gerais.

Autora:  
Mahyra Tedeschi

Orientador:  
Prof. Antônio Carlos Pedrosa-Soares

Co-Orientadores:  
Prof. Ivo Antônio Dussin  
Prof. Tiago Amâncio Novo

Orientadora na Universidade de Berna, Suíça  
(Estágio-sanduiche, CNPq, Ciência sem Fronteiras):  
Prof. Daniela Rubatto

Co-Orientadores na Universidade de Berna, Suíça:  
Dr. Pierre Lanari  
Prof. Jörg Hermann

Belo Horizonte, Janeiro de 2018





T256g  
2018

Tedeschi, Mahyra Ferreira.

Geodynamic evolution of the Southern Brasília orogen (SE Brazil) [manuscrito] : new petrochronological insights from UHT and HP metamorphic rocks / Mahyra Tedeschi – 2018.

224 f., enc. (principalmente color.)

Orientador: Antônio Carlos Pedrosa-Soares.

Coorientadora: Daniela Rubatto.

Tese (doutorado) – Universidade Federal de Minas Gerais, Instituto de Geociências, 2018.

Área de concentração: Geologia Regional.

Bibliografia: f. 155-157.

Inclui anexos.

1. Petrologia – Teses. 2. Rochas metamórficas – Teses. 3. Geoquímica – Teses. I. Pedrosa-Soares, Antônio Carlos. II. Rubatto, Daniela. III. Universidade Federal de Minas Gerais. Instituto de Geociências. IV. Título.

CDU: 552.4





UNIVERSIDADE FEDERAL DE MINAS GERAIS

PROGRAMA DE PÓS-GRADUAÇÃO EM GEOLOGIA



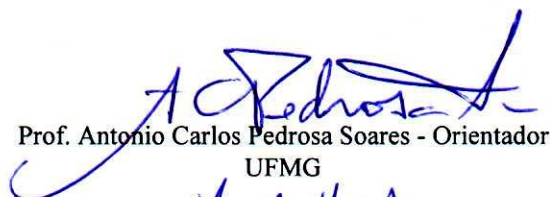
## FOLHA DE APROVAÇÃO

**Geodynamic evolution of the Southern Brasília orogen (SE Brazil): New petrochronological insights from UHT and HP metamorphic rocks**

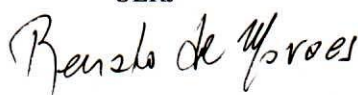
**MAHYRA FERREIRA TEDESCHI**


Tese submetida à Banca Examinadora designada pelo Colegiado do Programa de Pós-Graduação em GEOLOGIA, como requisito para obtenção do grau de Doutora em GEOLOGIA, área de concentração GEOLOGIA REGIONAL.


Aprovada em 12 de janeiro de 2018, pela banca constituída pelos membros:

  
Prof. Antonio Carlos Pedrosa Soares - Orientador  
UFMG

  
Prof. Claudio de Morisson Valeriano  
UERJ

  
Prof. Renato de Moraes  
USP

  
Prof. Carlos Eduardo Ganade de Araújo  
CPRM

  
Prof. Pierre Lanari  
Universidade de Berna, Suíça

Belo Horizonte, 12 de janeiro de 2018.

## Dedications

*Aos meus pais, Sun e Walter, minhas maiores inspirações.*

*To my parentes, Sun and Walter, my greatest inspirations.*

## Agradecimentos

Depois desses (incríveis) quatro anos e meio de pesquisa, é hora de agradecer àquelas pessoas que me acompanharam e às instituições que me apoiaram nessa jornada. Ao meu orientador, Prof. Dr. Antônio Carlos Pedrosa-Soares por ter me incentivado ao longo desses sete anos de parceria. Seu apoio e sua luta para realização dessa tese foram essenciais. Ao Prof. Dr. Tiago Novo por “descobrir” comigo a nappe Guaxupé. Ao Prof. Dr. Ivo Dussin pela ajuda cuidadosa com os dados de geocronologia. Ao Dr. Marco Aurélio Piacentini Pinheiro por compartilhar o entusiasmo na investigação e pelas frutíferas discussões sobre Orógeno Brasília Meridional.

Aos orientadores de Berna por me introduzirem no fascinante mundo da Petrocronologia. Ao Dr. Pierre Lanari por me permitir novas visões da microsonda e modelagem metamórfica. A Profa. Dra. Daniela Rubatto por dividir comigo seu entusiasmo pela geocronologia - com significado. Ao Prof. Dr. Jörg Hermann pelas instigantes discussões e por me apresentar, junto com o Prof. Dr. Thomas Pettke, eclogitos e xistos-azuis. Ao Dr. Daniel Peters por me encorajar e revisar a minha tese. Ao Thomas Aebi pelas preciosas dicas na preparação das amostras. Aos professores Thomas Pettke and Alfons Berger, Universität Bern, pelo apoio analítico com LA-ICP-MS e SEM. A Dra. Anne-Sophie Bouvier pelo suporte na utilização da SwissSIMS. Aos funcionários e colegas dos grupos de petrologia e geoquímica isotópica da Universidade de Berna que me receberam de braços abertos: Alice Vho, Barbara Grose, Jisuk Kang, Jonas Pape, Elias Kemp, Fumiko Higashino, Marco Burn, Peter Tollan, Sarah Antenen, Sigrid Zimmermann e Thomas Bovay. Aos amigos de Berna, Alice Vho, Camille Lopez, Jisuk Kang, Karin Roth, Lola Camesi, Luciana Assis e Pierre Lanari por tonarem essa experiência incrível, muito além das expectativas.

Ao Dr. Luiz Carlos pelo seu total apoio para realização do doutorado junto à CPRM. A Joana Magalhães por dividir a doce-complexa experiência UFMG-CPRM-SUIÇA. Francisco Vilela e Márcio Silva por compreenderem as necessidades e me apoiarem para realização desse trabalho. Ao Dr. Carlos (Caê) Ganade por me apresentar os (retro)eclogitos. A Mayara Pinheiro por ser minha guia de editoração. Aos companheiros de campo e de pós-graduação pelos bons momentos, frutíferas discussões, ajuda na coleta e preparação das amostras: Carol Deluca, Cristina Araújo, Lorena Martins, Eliane Voll, Humberto Broz, Leonardo Alkmim, Luiz Salim, Pedro Leonardo Rossi, Renata Azevedo, Lucas Lana e Tobias Fonte-Boa. Agradeço ao Dr. Luís Garcia e Marcos Flores, do Laboratório de Microanálises (UFMG), pela assistência com as análises de microsonda e a Ana Alkmim, Universidade Federal de Ouro Preto, pela assistência com as análises LA-ICP-MS. As Melris, Bob Salim, Amanda Almeida, Marco Couto Jr., Mariana Leite, Larissa Paraguassu, Lourdinha Fernandes, Paulo Amorim, Humberto Reis, Marcela Zanon, Caio Alencar, amigos que torceram e me apoiaram nessa caminhada. A William Campos por sua assistência junto ao Programa de Pós-graduação. Aos colegas da CPRM pelo apoio.

A Companhia de Pesquisa de Recursos Minerais - Serviço Geológico do Brasil por permitir e apoiar a realização deste trabalho. Ao programa Ciências sem Fronteiras pela concessão da bolsa de estágio “sanduíche” (CNPq 202054/2015-2). Ao Projeto Fronteiras de Minas (UFMG-CODEMIG) por financiar os campos e as análises no Brasil.

Agradeço a Deus, pois sem Ele nada seria possível. Aos meus pais, agradeço por me ensinarem os principais valores da vida. Com eles aprendo, todos os dias, independentemente de qualquer distância física, o significado de trabalho com entrega e a buscar os meus sonhos com coragem. Ao Deco, agradeço por ter tomado conta dos nossos pais em mais essa jornada. Continuo achando: juntos, somos um time e tanto! A tia Fá e tia Elza, agradeço pelas orações e pela torcida.



## Acknowledgements

After four and half exciting years of research, it is time to thank everybody who accompanied and more importantly supported me during this time. I would like to thank my supervisor, Prof. Dr. A.C. Pedrosa-Soares for encouraging me during these seven years partnership. His support and fight to allow me to work on this thesis were crucial. To Prof. Dr. Tiago Novo for “discovering” the Guaxupé nappe with me. Prof. Dr. Ivo Dussin for his careful help with the geochronological data. To Dr. Marco Aurélio Piacentini Pinheiro for sharing the enthusiasm of the research and great discussions about the Southern Brasília orogen.

To my supervisors in Bern, who I would like to thank for having me introduced me to the fascinating world of petrochronology. To Dr. Pierre Lanari for showing me the microprobe with a different view and introducing me into thermodynamic modelling. Prof. Dr. Daniela Rubatto for sharing her enthusiasm for geochronology – with a meaning. Prof. Dr. Jörg Hermann for intriguing discussions and for unfolding, together with Prof. Dr. Thomas Pettke, the world of eclogites and blue schists to me. To Dr. Daniel Peters for encouraging me and reviewing my thesis. Dr. Thomas Pettke and Dr. Alfons Berger, Universität Bern, are thanked for analytical assistance with the LA-ICP-MS and SEM. To Thomas Aebi for teaching me precious hints about sample preparation. To my colleagues from the Petrology and Geochemistry research groups and secretaries from the Universität Bern who have warmly received me: Alice Vho, Barbara Grose, Jisuk Kang, Jonas Pape, Elias Kemp, Fumiko Higashino, Marco Burn, Peter Tollan, Sarah Antenen, Sigrid Zimmermann and Thomas Bovay. To my friends from Bern Alice Vho, Camille Lopez, Jisuk Kang, Karin Roth, Lola Camesi, Luciana Assis and Pierre Lanari who have made this experience much more incredible than I had ever dreamed.

To Dr. Luiz Carlos for his full support during the completion of this doctorate at CPRM. To Joana Magalhães for sharing the sweet-complex UFMG-CPRM-SWITZERLAND experience. Francisco Vilela and Márcio Silva for understanding the needs and having supported this work. To Dr. Carlos (Caê) Ganade for introducing me to the (retro) eclogites. I am thankful to Dr. Luís Garcia and Márcio Flores for assistance with EPMA analysis in Federal University of Minas Gerais (LMA-UFMG). Ana Alkmim, Universidade Federal de Ouro Preto, is thanked for analytical assistance with the LA-ICP-MS. To Mayara Pinheiro for being my editorial counselor. To my field work and post-graduation fellows for the good moments, fruitful discussions, assistance during sampling and sample preparation: Carol Delucca, Cristina Araújo, Lorena Martins, Eliane Voll, Humberto Reis, Leonardo Alkmim, Luiz Salim, Pedro Leonardo Rossi, Renata Azevedo, Lucas Lana and Tobias Fonte-Boa. To my friends who supported me during this journey: Melris, Bob Salim, Amanda Almeida, Marco Couto Jr., Mariana Leite, Larissa Paraguassu, Lourdinha Fernandes, Paulo Amorim, Humberto Reis, Marcela Zanon and Caio Alencar. To William Campos for his assistance in the post-graduation program. To my colleagues from CPRM for their support.

I am very grateful to the Geological Survey of Brazil (CPRM) for supporting me to do this work. To the Science without Borders program (CNPq 202054/2015-2) for the scholarship. To the Fronteiras de Minas project (UFMG-CODEMIG) for funding field work and analyses in Brazil.

I thank God, that made everything possible. To my parents, who I thank for teaching me the main values of life. With them I learn every day, no matter the physical distance between us, the meaning of working hard and bravely fight for my dreams. To Deco my acknowledgments for taking care of our parents along this way. I keep thinking: We are a great team! To my aunts Fá and Elza I thank for praying and cheering for me.





## Abstract

The Southern Brasília orogen is one of the orogens formed around the São Francisco paleocontinent during the West Gondwana amalgamation. Its formation is interpreted to have been the result of the subduction of the passive margin of the São Francisco plate under the Paranapanema plate, which subsequently evolved into a collisional orogeny that formed nappe systems verging to the east. Certain tectonic domains play a key role towards understanding the subduction to collision evolution of the southernmost portion of the Southern Brasília orogen, including the ultra-high temperature metamorphosed magmatic arc rocks of the Guaxupé nappe, of which ages and isotopic signatures of magmatism and metamorphism are poorly constrained and for which the heat source for metamorphism remained a matter of debate, as well as the “retro-eclogites” (e.g., from Pouso Alegre), which as (ultra)-high pressure mafic rocks can provide insights into subduction, collision and exhumation processes.

As a general characteristic of the rocks from the Guaxupé nappe, zircon data spread in a Concordia diagram. Textural analyses were thus coupled to U-Pb zircon chronology and Lu-Hf ratios to determine the crystallization age of their protoliths. It was thereby revealed that this nappe hosts, besides magmatic arc rocks, a so far undescribed basement rock and a ca. 790 Ma opdalite of uncertain origin. A banded mafic granulite displays a crystallization age of  $2559 \pm 66$  Ma for a juvenile protolith ( $\epsilon\text{Hf}_{(2550)} = +2.7$  to  $+10.0$ ). Most of its zircon rims record the Brasiliano Event at ca. 600–700 Ma and 15 % of all grains register an unusual event at ca. 2.4 Ga. The same approach applied to the opdalite revealed the first  $786 \pm 10$  Ma-igneous rock in the Guaxupé nappe ( $\epsilon\text{Hf}_{(786)} = -12.6$  to  $-13.4$ ). Younger magmatic activity, which is ascribed to continental arc activity, is recorded by a banded mafic granulite at  $691 \pm 3$  Ma ( $\epsilon\text{Hf}_{(690)} = -8.2$  to  $-12.6$ ) and by mafic granulite enclaves, synchronous to anatexis, at  $664 \pm 9$  Ma ( $\epsilon\text{Hf}_{(660)} = -5.9$  to  $-11.4$ ).

Comparison of the relative distribution of metamorphic zircon data from different samples permitted the identification of an 80 m.y. long-lived metamorphism with three main zircon crystallization stages: (i) 670–650 Ma, (ii) 640–630 Ma, and (iii) 615–590 Ma. The first stage is interpreted as subduction-related, with basic magma emplacement that triggered ultra-high temperature metamorphism. The two following stages were linked to collision and exhumation. Thus, the ultra-high temperature ( $998 \pm 23$  °C obtained by orthopyroxene-clinopyroxene thermometry) is interpreted to have taken place in an arc-related setting.

Peak metamorphic conditions of  $690 \pm 35$  °C and  $13.5 \pm 2.8$  kbar for the “retro-eclogite” were obtained by phase equilibria modelling, and compositions of the garnet and omphacite ( $\text{Jd}_{20}$ , reconstructed composition). Monazite and metamorphic zircon from the host rocks were dated at ca. 630 Ma and their growth was linked to peak metamorphic conditions similar to the ones recorded in the “retro-eclogite”. Local retrogression into symplectite and corona proceeded coevally at  $595 \pm 25$  °C and  $4.8 \pm 1.5$  kbar. A zircon age of  $603 \pm 7$  Ma obtained for metamorphic zircons rims was linked to retrogression. The low maximum pressure of 14 kbar and the high geothermal gradient do not necessarily support subduction process-related metamorphism but rather favor a continental collision setting. The calculated exhumation rate of  $1 \text{ mm.y}^{-1}$  for the clinopyroxene-garnet amphibolite, and high geothermal gradient for the symplectite and corona formation stage indicate that exhumation was tectonically driven. The combined investigation on rocks from the Guaxupé nappe and Pouso Alegre permitted constraining a subduction-related metamorphism from 670–640 Ma, which was followed by peak-collisional metamorphism at ca. 630 Ma and decompression accompanied by widespread migmatization until ca. 600 Ma.



## Resumo

O Orógeno Brasília Meridional é um dos orógenos edificadas em volta do paleocontinente do São Francisco durante a amalgamação do Gondwana Oeste. Sua evolução é descrita como resultado da subducção da margem passiva da placa do São Francisco sobre a placa do Paranapanema, com evolução para uma orogenia colisional, durante a qual formou-se uma pilha de nappes vergentes para leste. Neste cenário, alguns compartimentos tectônicos têm papel fundamental na compreensão da evolução subducção-colisão na área: as rochas do arco magmático da Nappe Guaxupé metamorfizadas em temperatura ultra-alta, cujas idades e assinaturas isotópicas do magmatismo e metamorfismo, bem como a fonte do calor do metamorfismo, são debatidas; e os “retro-eclogitos”, uma vez que, rochas de pressão (ultra)-alta podem fornecer informações sobre os processos de subducção, colisão e exumação.

Como uma característica comum às rochas da Nappe Guaxupé, os dados U-Pb em zircão formam um espalhamento na Concórdia. Por isso, análises de textura (imagens CL), Lu-Hf e U-Pb foram realizadas em zircão para determinação das idades de cristalização dos protólitos. A nappe revelou abrigar, além de rochas do arco magmático, as primeiras ocorrências do embasamento e de opdalito de ca. 790 Ma, cuja origem é incerta. Um granulito máfico bandado forneceu uma idade de cristalização de  $2559 \pm 66$  Ma para um protólito juvenil ( $\epsilon\text{Hf}_{(2550)} = +2,7$  a  $+10,0$ ). A maioria das bordas de zircão marca o evento Brasileiro (ca. 600–700 Ma), enquanto 15% das análises registra um evento incomum em ca. 2,4 Ga. A mesma abordagem foi aplicada para opdalito e revelou a primeira rocha com idade de cristalização em  $786 \pm 10$  Ma ( $\epsilon\text{Hf}_{(786)} = -12,6$  a  $-13,4$ ) na nappe. Atividade magmática mais jovem, interpretada como originada em ambiente de arco continental, é registrada pelo granulito máfico bandado em  $691 \pm 3$  Ma ( $\epsilon\text{Hf}_{(690)} = -8,2$  a  $-12,6$ ) e pelo enclave máfico granulítico, sincrônico à anatexia, em  $664 \pm 9$  Ma ( $\epsilon\text{Hf}_{(660)} = -5,9$  a  $-11,4$ ). A comparação entre as distribuições relativas de dados de zircões metamórficos em diferentes amostras permitiu a identificação de um evento metamórfico de longa duração (80 m.y.), com três estágios principais de cristalização de zircão: (i) 670–650 Ma, (ii) 640–630 Ma, e (iii) 615–590 Ma. O primeiro é relacionado à subducção, com a colocação de magmas máficos responsáveis pela instalação do metamorfismo de temperatura ultra-alta, e os outros dois, à colisão e à exumação, respectivamente. Portanto, o evento de ultra-alta temperatura ( $T = 998 \pm 23$  °C) teve lugar no ambiente relacionado ao arco magmático.

As condições de pico metamórfico do clinopiroxênio-granada anfíbolito (“retro-eclogito”) tiveram lugar em ca. 630 Ma e são  $690 \pm 35$  °C e  $13,5 \pm 2,8$  kbar, obtidas a partir de modelagem termodinâmica e composições de granada e onfacita ( $\text{Jd}_{20}$ , composição reconstruída). Zircão metamórfico e monazita das encaixantes foram datados em ca. 630 Ma e ligadas às condições de pico metamórfico, similares às registradas pelo clinopiroxênio-granada anfíbolito. Retrogressão local para simplectita e corona registra condições de  $595 \pm 25$  °C e  $4,8 \pm 1,5$  kbar. Uma idade em zircão de  $603 \pm 7$  Ma foi obtida a partir de bordas metamórficas e é ligada a este estágio. A baixa máxima pressão de ca. 14 kbar e o alto gradiente geotermal, mais provavelmente sustentam um metamorfismo relacionado à colisão continental do que à subducção. O baixo valor calculado para a taxa de exumação máxima de 1 mm por ano, e o alto gradiente termal para o estágio de retrogressão indicam que a exumação foi comandada por tectônica. A investigação combinada nas rochas da Nappe Guaxupé e de Pouso Alegre permitiram identificar um estágio de metamorfismo pré-colisional entre 670–640 Ma, seguido pelo pico metamórfico colisional em ca. 630 Ma e decompressão acompanhada por ampla migmatização até ca. 600 Ma.



## Summary

1	General introduction .....	1
1.1	Structure of the Thesis .....	1
1.2	Preface .....	2
1.3	Nature of the problem .....	3
1.4	Aim of this study .....	4
1.4.1	The Guaxupé nappe rocks: .....	5
1.4.2	The clinopyroxene-garnet amphibolite (“retro-eclogite”) of Pouso Alegre and its host rocks	5
1.5	Studied area and field work .....	7
1.6	References .....	8
2	Geological setting: The Southern Brasília orogen .....	10
2.1	The Basement of the southern portion of the Brasília orogen .....	12
2.1.1	The Socorro-Guaxupé nappe basement .....	12
2.1.2	The São Francisco craton basement .....	14
2.2	The Socorro-Guaxupé nappe .....	15
2.2.1	Nappe units .....	15
2.2.2	Arc magmatism .....	18
2.2.3	Metamorphism .....	18
2.3	The Andrelândia nappe system .....	19
2.3.1	General structure .....	19
2.3.2	The retro-eclogites .....	20
2.4	Tectonic evolution models .....	21
2.4.1	Orogen migration .....	21
2.4.2	Interference of orogens .....	21
2.5	References .....	21
3	Constraining the petrochronological evolution of garnet-free UHT granulites in the Guaxupé nappe (SE Brazil): from subduction to collision.....	28
3.1	Abstract .....	29

3.2	Introduction.....	30
3.3	Geological Setting .....	32
3.3.1	General Framework .....	32
3.3.2	The Guaxupé nappe .....	34
3.4	Sampling and Field relationship.....	36
3.5	Petrography and mineral composition .....	39
3.5.1	Banded mafic granulite (C-833-A) .....	39
3.5.2	Banded mafic granulite (C-838-A) .....	39
3.5.3	Opdalite (C-838-2) .....	43
3.5.4	Granitic (hornblende)-biotite-bearing leucosome (C-838-B).....	44
3.5.5	Mafic granulite enclave (C-716-B) .....	44
3.6	Zircon U-Pb geochronology and Lu-Hf isotopes .....	45
3.6.1	Banded mafic granulite (C-833-A) .....	47
3.6.2	Opdalite (C-838-2) .....	48
3.6.3	Banded mafic granulite (C-838-A) .....	50
3.6.4	Granitic (hornblende)-biotite-bearing leucosome (C-838-B).....	50
3.6.5	Mafic granulite enclave (C-716-B) .....	51
3.7	Zircon inclusions, geochemistry and thermometry.....	52
3.7.1	Types of inclusion in zircon.....	52
3.7.2	Geochemistry.....	52
3.7.3	Ti-in-zircon thermometry.....	54
3.8	Bulk rock chemistry.....	55
3.9	P-T estimates for the banded mafic granulite (C-838-A).....	58
3.9.1	Mineral thermobarometry.....	58
3.10	Discussion.....	59
3.10.1	Crystallization timing and petrogenesis of protoliths .....	59
3.10.2	Petrochronological metamorphic evolution .....	62
3.10.3	UHT metamorphism in the Southern Brasília orogen .....	68
3.10.4	Regional implications for the Southern Brasília orogeny .....	69
3.11	Conclusions.....	73

3.12	Acknowledgments .....	74
3.13	References .....	74
3.14	Appendix 3.A - Analytical Methods .....	84
3.14.1	Sample preparation, imaging and qualitative analyses.....	84
3.14.2	Bulk rock analysis .....	85
3.14.3	Electron probe micro-analysis .....	85
3.14.4	Trace elements LA-ICP-MS.....	85
3.14.5	LA-ICP-MS U-Pb zircon dating.....	86
3.14.6	Lu-Hf in zircon analyses .....	87
3.15	Appendix 3.B - U-Pb Geochronology: zircon description.....	87
3.15.1	Banded mafic granulite (C-833-A).....	87
3.15.2	Opdalite (C-838-2) .....	88
3.15.3	Banded mafic granulite (C-838-A).....	88
3.15.4	Granitic (hornblende)-biotite-bearing leucosome (C-838-B).....	88
3.15.5	Mafic granulite enclave (C-716-B).....	89
4	Reconstruction of multiple P-T-t stages from retrogressed mafic rocks: subduction versus collision in the Southern Brasilia Orogen (SE Brazil).....	90
4.1	Abstract .....	91
4.2	Introduction.....	92
4.3	Geological setting.....	95
4.4	Sample description.....	96
4.4.1	Petrography.....	99
4.4.2	Petrographic interpretation .....	100
4.5	Results.....	100
4.5.1	Bulk Rock Chemistry.....	100
4.5.2	Mineral Compositions .....	101
4.5.3	Thermobarometry .....	103
4.5.4	U-Th-Pb geochronology and trace elements of zircon and monazite.....	108
4.5.5	Garnet trace element composition.....	116
4.6	Discussion.....	116

4.6.1	Petrochronological evolution of clinopyroxene-garnet amphibolite MT-13.....	116
4.6.2	Magmatic and metamorphic history of the Pouso Alegre rock assemblage.....	121
4.6.3	P-T-t record of a common metamorphic history.....	123
4.6.4	Collision versus subduction setting .....	125
4.7	Conclusions.....	127
4.8	Acknowledgments .....	128
4.9	Appendix 4.A – Analytical methods .....	128
4.9.1	Sample preparation, imaging and qualitative analyses.....	128
4.9.2	Bulk rock analysis .....	128
4.9.3	Electron probe micro-analysis .....	128
4.9.4	Trace elements LA-ICP-MS.....	129
4.9.5	Accessory mineral thermometry.....	130
4.9.6	LA-ICP-MS U-Pb zircon dating.....	130
4.9.7	SIMS U-Th-Pb dating.....	131
4.10	Supplementary Figures .....	132
4.11	References.....	139
5	Regional discussions.....	149
5.1	The basement of the southern portion of the Brasília orogen.....	149
5.2	Timing and source of the arc magmatism in the Guaxupé nappe .....	150
5.3	Metamorphic evolution of the banded mafic granulites from the Guaxupé nappe .....	151
5.4	Origin and evolution of the “retro-eclogites” from Pouso Alegre.....	152
5.5	Other regional implications .....	153
5.5.1	Arc magmatism in the Southern Brasília orogen.....	153
5.5.2	The 790 Ma source for the metasedimentary rocks.....	154
5.5.3	Metamorphic evolution of the Southern Brasília orogen .....	154
5.6	References.....	155
6	General conclusions and outlook .....	158
7	Conference abstracts.....	161



7.1	Mapeamento geológico 1:100.000 das folhas Caldas e Poços de Caldas (SF-23-V-DIV) e Poços de Caldas (SF-23-V-C-VI), Sudoeste de Minas Gerais. In: 47º Congresso Brasileiro de Geologia, 2014, Salvador. 47º Congresso Brasileiro de Geologia. ....	161
7.2	Reconstruction of high-pressure metamorphic conditions from symplectites: insights from Pouso Alegre mafic rocks (Brasília Belt, Brazil) In: 14th Swiss Geoscience Meeting, 2016, Geneva. Abstract Volume 14th Swiss Geoscience Meeting. ....	163
7.3	Reconstruction of P-T-t metamorphic conditions from symplectites: insights from Pouso Alegre mafic rocks (Brasília Belt, Brazil) In: European Geoscience Union 2017, 2017, Vienna. European Geoscience Union 2017. ....	165
7.4	Reconstrução dos múltiplos estágios P-T-t de rochas máficas retrometamorfisadas: subducção versus colisão no orógeno Brasília Meridional (SE Brasil) In: Geosudeste 2017, 2017, Diamantina. Anais Geosudeste 2017. ....	167
7.5	Crosta juvenil arqueana no embasamento (Paranapanema) do orógeno Brasília Meridional: primeiros dados U-Pb e Lu-Hf (LA-ICPMS) em zircão de ortogranulito In: Geosudeste 2017, 2017, Diamantina. Anais Geosudeste 2017. ....	168
8	Appendices .....	169

## List of illustrations

- Figure 1.1:** Map of Brazil with the indicated location of the regional cut-out, which displays the main access roads into the studied area (red polygon). ..... 7
- Figure 2.1:** Geotectonic context of the São Francisco craton and Southern Brasília orogen within Western Gondwana. (A) Distribution of cratonic blocks in Western Gondwana (red rectangle marks location of the studied region illustrated in B): Distribution of Ediacaran orogens formed around the São Francisco craton with the southern portion of the Brasília orogen in the red rectangle. .... 10
- Figure 2.2:** Tectonic map of the Southern Brasília orogen (modified after Campos Neto et al., 2011; Westin et al., 2016; Cioffi et al., 2016 a, b). Red rectangle delimits the studied area, and stars indicate the location of the studied “retro-eclogite” outcrop of Pouso Alegre (yellow) and mafic migmatitic granulites (blue). ..... 12
- Figure 2.3:** Proposed delimitations of the basement of the Paraná Basin and their relationships with the surrounding orogenic systems. (A) Outline of the Paranapanema block obtained from gravimetric studies (modified from Quincas, 1995 in Mantovani and Brito-Neves, 2009). (B) Tectonic sketch map of the basement of the Paraná Basin as proposed by Milani (1997) based on deep wells data. .... 13
- Figure 2.4:** Geological map and cross-section showing the main occurrences of the Archean and Paleoproterozoic basement of the Southern Brasília orogen in the Ouro Fino shear zone. Map and cross-section from Cioffi et al. (2016b) compiled and modified from Perrota (1991), Morais (1999a,b), Peternel (2005), Trouw et al. (2008) and Cioffi et al. (2016a). ..... 15
- Figure 2.5:** Geological Map of the studied area with the location of the studied samples from the Guaxupé nappe (compiled and simplified from Degler et al., 2015; Fava et al., 2015; Peixoto et al., 2015; Ribeiro et al., 2010a, b, c; and Tedeschi et al., 2015; with inputs from Cioffi et al., 2016; Westin et al., 2016). Dashed red line indicates the limit between Minas Gerais (east) and São Paulo (west) states. .... 17
- Figure 3.1:** (A) Distribution of cratonic blocks and orogenic belts in Western Gondwana (red rectangle: location of the studied region illustrated in B): WAC, West African craton; AC, Amazonian craton; SF, São Francisco craton; CC, Congo craton; PP, Paranapanema block; KC, Kahalari craton. (B) Sketch map of the Southern Brasília orogen (modified from Campos Neto et al., 2011; Cioffi et al., 2016a; Westin et al., 2016). (C) Dashed rectangle shows the location of the geological map showed in Figure 3.2. .... 33
- Figure 3.2:** Regional geological map of the studied area with location of analyzed samples (compiled and simplified from Degler et al., 2015; Fava et al., 2015; Peixoto et al., 2015; Ribeiro et al., 2010a, b, c; and Tedeschi et al., 2015; with inputs from Cioffi et al., 2016a, and Westin et al., 2016). Dashed red line indicates the limit between Minas Gerais (east) and São Paulo (west) states, and red labels refer to the cities mentioned in the text. .... 35

**Figure 3.3:** Field relationships of the studied rocks of the Granulitic - Elói Mendes unit (1) Mafic granulite (restite), (2) Banded mafic granulite, (3) light-green enderbitic to charnockitic leucosome, and (4) pinkish granitic (hornblende)-biotite-bearing leucosome and (5) mafic granulite enclave of gabbroic composition. (A) Schöllén diatexite from the northern part of the section. (B) Light-green opdalitic rock bearing enclaves of banded mafic granulite. Mesoscopic aspects of each sample: (C) Banded mafic granulite cut by concordant light-green charnockitic leucosome (C-838-A); (D) mafic Schöllén (restites) in charnockitic leucosome with peritectic orthopyroxene and clinopyroxene (C-838-2); (E) Schlieren of biotite and Scholle of stromatic metatexite in the pinkish granitic (hornblende)-biotite-bearing leucosome (C-838-B); (F) Banded mafic granulite (C-833-A); (G) Agmatic texture formed by the mafic granulite enclaves (gabbroic composition; sample C-716-B) in the diatexite; and (H) euhedral peritectic hornblende in the nebulitic diatexite. .... 37

**Figure 3.4:** Transmitted light microphotographs of the studied samples. (A-B) Transition between the granulitic and green charnockitic leucosome in the different banded mafic granulite - the limits between the leucosome and melanosome bands are indicated by dashed pink lines, (A) leucosome with few orthopyroxene and clinopyroxene such as in C-833-A, (B) leucosome hosting peritectic orthopyroxene and clinopyroxene (C-838-A); (C) opdalite C-838-2 and (D) mafic granulite enclave with hornblende porphyroblasts (crystals have 2-4 mm)..... 40

**Figure 3.5:** (A) Microphotograph showing the texture of the banded mafic granulite (C-838-A) with the selected rectangle area mapped shown in: (B) Map with discriminated phases and (C) Al<sub>2</sub>O<sub>3</sub> (wt%) compositional map. Compositional maps for clinopyroxene and orthopyroxenes (D) Al<sub>2</sub>O<sub>3</sub> (a.p.f.u) (E) FeO (a.p.f.u) and (F) CaO (a.p.f. .... 42

**Figure 3.6:** Cathodoluminescence (CL) images of representative zircon grains. Location of the spot analyses and corresponding <sup>206</sup>Pb/<sup>238</sup>U or <sup>207</sup>Pb/<sup>206</sup>Pb dates in Ma marked with yellow circles (spot size ~30 microns), blue dashed circles for trace elements (spot size ~20 microns), and dashed red circles for Lu-Hf (spot size ~50 microns)..... 46

**Figure 3.7:** U-Pb, Lu-Hf and trace elements zircon data for the banded mafic granulites C-833-A. Data interpreted as magmatic (see text) are plotted in (A) Concordia diagram (ellipses: 2σ uncertainty), the brown filled ellipse represents the older grain containing <sup>176</sup>Hf/<sup>177</sup>Hf within the cogenetic range from (B) initial <sup>176</sup>Hf/<sup>177</sup>Hf ratio against age using <sup>207</sup>Pb/<sup>206</sup>Pb dates and (C) Weighted average age from the oldest 10 grains. (D) Concordia diagram (ellipses: 2σ uncertainty) for rims and single phases, (E) normalized zircon/chondrite rare-earth elements diagrams for cores and rims and (F) data that yielded a concordant age. .... 48

**Figure 3.8:** Geochronological results for Neoproterozoic rocks. U-Pb (Concordia and Probability density diagrams), <sup>176</sup>Hf/<sup>177</sup>Hf ratio versus age using <sup>206</sup>Pb/<sup>238</sup>U dates and normalized zircon/chondrite rare-earth elements diagrams for: (A-D) Opdalite C-838-2, cores are blue and rims in yellow, (E-H) Banded mafic granulite C-838-A, cores in green and rims in orange, and (K-M)

Pinkish granitic (hornblende)-biotite-bearing leucosome C-838-B, core in dark-blue and rims in pink and (N-Q) Mafic granulite enclave C-716-B. In the Concordia diagrams ellipses are  $2\sigma$  errors..... 49

**Figure 3.9:** Zircon crystallization temperatures from Ti-in-zircon thermometry using the calibration of Watson et al. (2006). ..... 54

**Figure 3.10:** Bulk rock chemistry of the studied rocks. (A)  $\text{Na}_2\text{O}+\text{K}_2\text{O}(\text{wt}\%)$  versus  $\text{SiO}_2(\text{wt}\%)$  classification plot (Middlemost, 1989); (B) chondrite-normalized (McDonough and Sun, 1995); (C) spider diagram normalized to chondrite (McDonough and Sun, 1995). Frost et al. (2001) classification (D)  $\text{FeO}^{\text{tot}}/(\text{FeO}^{\text{tot}}+\text{MgO})$  versus  $\text{SiO}_2$  with composition field of cordilleran granites (E)  $\text{Na}_2\text{O} + \text{K}_2\text{O} - \text{CaO}$  (MALI index) vs.  $\text{SiO}_2$  diagram (F)  $\text{Al}_2\text{O}_3/(\text{Na}_2\text{O} + \text{K}_2\text{O})(\text{molar})$  vs.  $\text{Al}_2\text{O}_3/(\text{CaO} + \text{Na}_2\text{O} + \text{K}_2\text{O})$  (molar) diagram (Shand's index; Shand, 1974) and I-type boundary according to Chappel and White (1974). Tectonic settings discrimination for granites according to Pearce et al. (1984) (G)  $\log \text{Rb}(\text{ppm})$  versus  $\text{Y}+\text{Nb}(\text{ppm})$  with addition of 'post-collisional granites' field after Pearce (1986) and (H)  $\log \text{Rb}(\text{ppm})$  versus  $\text{Ta}+\text{Yb}(\text{ppm})$ ..... 58

**Figure 3.11:** Zircon Hf isotope data of the Socorro-Guaxupé nappe plotted as (A) initial  $^{176}\text{Hf}/^{177}\text{Hf}$  (t) ratio versus individual dates (t), using  $^{207}\text{Pb}/^{206}\text{Pb}$  dates for grains older than 1 Ga and  $^{206}\text{Pb}/^{238}\text{U}$ , for younger grains, (B) Detail of the Neoproterozoic rocks showing the Hf signature fields characteristic of each sample spreading along an approximately horizontal line and indicating different degrees of Pb loss, and (C) Hf-isotope evolution diagram with magmatic data being plotted as  $\epsilon\text{Hf}$  recalculated for their crystallization ages (obtained from the oldest grain) and metamorphic data being plotted for recalculated for their individual dates (t). Reference lines are: depleted mantle according to Blichert-Toft and Albarède (1997), chondrite of Griffin et al. (2000) and "New Crust" evolution line from Dhuime et al. (2011). ..... 61

**Figure 3.12:** Probability density diagram for the zircon U/Pb ages of the rims and single phases from the banded mafic granulites (C-833-A and C-838-A), opdalite (C-838-2), and the (hornblende)-biotite-bearing leucosome and the magmatic grains of the mafic granulite enclave (C-716-B) for comparison. .... 66

**Figure 3.13:** Summary of the geological evolution of the Guaxupé nappe with emphasis on the temporal distribution, Hf signatures and *P-T* constraints of igneous and metamorphic events of the studied samples. Data from (1) Tedeschi et al. (2017); (2 and 3) Rocha et al. (2017). Transparency applied to elements that constitute previous events, bright colors correspond to new events. Colors follow those used in the data presentation (Figs. 3.7, 3.8, 3.9, 3.10 and 3.12). The distribution of zircon grains represented along the metamorphism bars indicate relative amount of zircon crystallization. SGN – Socorro-Guaxupé nappe; OFSZ – Ouro Fino Shear Zone. .... 72

**Figure 4.1:** (A) Distribution of cratonic blocks and orogenic belts in Western Gondwana (red rectangle: location of the studied region illustrated in B): WAC, West African craton; SC, Sahara meta-craton; AC, Amazonian craton; SF, São Francisco craton; CC, Congo craton; PP, Paranapanema block; KC, Kahalari craton; West Gondwana orogen (in blue), including the Brasília

orogen (1), Borborema province (2), Dahomide (3) and Oubanguide (4) belts (modified from De Wit et al., 2008; Ganade de Araujo, 2014). (B) Sketch map of the Southern Brasília orogen (modified from Campos Neto et al., 2011; Westin et al., 2016). Red star (1): location of the studied “retro-eclogite” occurrence of Pouso Alegre. Yellow stars: other occurrences of “retro-eclogites” (2-Varginha nappe, 3-Airuoca klippe, 4- Liberdade nappe, 5-Carmo do Cachoeira nappe and 6-São Sebastião do Paraíso). (C) Location of the studied samples in the geological map (Ribeiro et al., 2011) on the terrain image (Google Earth®). (D) Outcrop photo showing the clinopyroxene-garnet amphibolite flanked by sapprolites of gneisses..... 94

**Figure 4.2:** Hand specimen and transmitted light photomicrographs of: (A-B) clinopyroxene-garnet amphibolite MT-13, (C-D) migmatitic sillimanite-garnet gneiss MT-22A, with the yellow narrow indicating the biotite rotated shadow, and (E-F) migmatitic amphibole-garnet augen gneiss MT-17. .... 97

**Figure 4.3:** Photomicrograph (A) showing the texture of clinopyroxene-garnet amphibolite MT-13 with the selected rectangle area mapped showed in: (B) Backscattered image; (C) Al<sub>2</sub>O<sub>3</sub> (wt%) compositional map from XMapTools; (D) Phases maps and (E) Distinct assemblages identified from texture and compositional map. .... 102

**Figure 4.4:** Na<sub>2</sub>O vs Al<sub>2</sub>O<sub>3</sub> diagram for amphibole (A) and clinopyroxene (B) compositions from the clinopyroxene-garnet amphibolite (MT-13). (C) Al (M1)-X<sub>cats</sub> vs Na (M2)-X<sub>acm</sub> diagram with the distribution of stoichiometric clinopyroxene compositions, Jadeite composition obtained with the model and reconstructed symplectite composition (see text for details). .... 104

**Figure 4.5:** Pressure-temperature (*P-T*) diagram calculated with Theriak-Domino (de Capitani and Petrakakis, 2010) showing the estimated *P-T* conditions for the clinopyroxene-garnet amphibolite MT-13 obtained with (1) GrtMod (Lanari et al., 2017) and in accordance with the Jd fraction estimated from the reconstruction of the symplectite (§ 4.5.1.1). Zr-in-rutile thermometry with 1 $\sigma$  results are shown in the blue field. Numbers for the fields: 1-Grt (2)Amp Zo Ttn Qz, 2-Grt Omp (2)Amp Zo Ttn Qz, 3-Grt Omp (2)Amp Ttn Qz 4-Grt Amp Zo Ttn Qz, 5-Grt Omp Amp Zo Ttn Qz, 6-Grt Omp Amp Zo Ttn Qz, 7-Grt Omp Amp Zo Ttn Qz, 8-Fsp Grt Omp Amp Ttn Qz Rt, 9-Fsp Ilm Grt Omp Opx Amp Qz, 10-Fsp Ilm Grt Omp Amp Qz and 11-Fsp Ilm Grt Omp Opx (2)Amp Qz..... 106

**Figure 4.6:** Pressure-temperature (*P-T*) diagram calculated for retrieved local compositions from the domains (A) symplectite and (B) for the amphibole+plagioclase corona. Dashed lines in (A) indicate Jd fraction and the blue ellipse represents the *P-T* conditions obtained from the semi-empirical thermobarometry applying the calibration of Holland and Blundy (1994). Numbered reactions are available on Appendix VII. .... 107

**Figure 4.7:** U-Pb zircon data from clinopyroxene-garnet amphibolite MT-13. (A) Concordia diagram (2 $\sigma$  error ellipses) with CL-images of representative grains analyzed (yellow circle for LA-ICP-MS, blue circles for SIMS analyses and dashed red circles for trace elements, spot size ~25 microns); Filled ellipses for cores analyses LA-ICP-MS (black) and rims (grey) and empty ellipses

for SIMS analyses of cores (black) and rims (grey). (B) Kernel density diagram for data considered for age calculation; core data in black and rim data in grey. (C) Data defining the metamorphic age from the weighted average of the rims. (D) Data defining the protolith age. .... 109

**Figure 4.8:** Chondrite normalized diagrams of the REE composition of: (A) Different dated domains in zircon and garnet from the clinopyroxene-garnet amphibolite MT-13 with location of the analyzed spots in representative grains (spot size ~25 microns); (B) Dated monazite and garnet from the migmatitic sillimanite-garnet gneiss MT-22A. Chondrite normalizing values from McDonough and Sun (1995). .... 111

**Figure 4.9:** Geochronological results for migmatitic sillimanite-garnet gneiss MT-22A. (C) Probability density diagrams showing the distribution of the zircon data of the migmatitic sillimanite-garnet gneiss MT-22A and CL-images of representative grains analyzed (spot size ~25 microns). The light blue bars indicate the data with low Th/U ratios, used for calculating the metamorphic age from the Concordia diagram in A. (B) The Concordia diagram for the grains with Th/U ratios higher than 0.1, from which the main data peak defines the maximal depositional age. (D) Weighted average  $^{206}\text{Pb}/^{238}\text{U}$  ages diagram for monazite, and (E) backscattered electron images of representative grains analyzed on the Concordia diagrams (ellipses are  $1\sigma$  error). .... 113

**Figure 4.10:** Geochronological results (LA-ICP-MS analyses,  $1\sigma$  error ellipses) for migmatitic amphibole-garnet augen gneiss MT-17, allanite-bearing biotite granite MT-19 and biotite gneiss MT-20 with CL-images of representative analyzed grains. In the Concordia diagrams younger analyses discarded are represented by dashed lines (see text for explanation). .... 115

**Figure 4.11:**  $\text{Al}_2\text{O}_3$  vs  $\text{Na}_2\text{O}$  binary diagram showing the stable phases and their relationship with the bulk-rock (A) at peak conditions and at (B) the retrogression stage. The diagrams show the possible element exchanges occurring between the symplectite and corona domains during retrogression. See text for details. .... 119

**Figure 4.12:**  $P$ - $T$ - $t$  trajectories for the clinopyroxene-garnet amphibolite MT-13 (red), migmatitic amphibole-garnet gneiss MT-17 (green) and migmatitic sillimanite-garnet gneisses MT-22A (blue); stars represent the  $P$ - $T$  condition and rectangles their uncertainties. The ellipse filled with stripes represents the symplectite conditions of formation, which are the same as for corona. Zircon age of 630 Ma is from Coelho et al. (2017) which investigated a similar sample. The 670 Ma from zircon grains of the migmatitic sillimanite-garnet gneiss MT-22A cannot be strictly correlated to a  $P$ - $T$  condition (thus indicated by "?"). See text for discussion of the ages. Metamorphic facies grid for metabasaltic rocks and geothermal gradients from Bucher and Frey (2002); CM – Contact metamorphism, Grn – Granulite, Amp – Amphibolite, Gsc – Greenschist, Sgsc – Subgreenschist, Bsc - Blueschist. .... 124

**Figure 6.1:** Summary of the geological evolution of the Guaxupé nappe and Pouso Alegre section with emphasis on the temporal distribution, Hf signatures and  $P$ - $T$  constraints of igneous and metamorphic events of the studied samples. Data from (1) Tedeschi et al. (2017); (2 and 3) Rocha

et al. (2017). Transparency applied to elements that constitute previous events, bright colors correspond to new events. The distribution of zircon grains represented along the metamorphism bars indicate relative amount of zircon crystallization. SGN – Socorro-Guaxupé nappe; OFSZ – Ouro Fino Shear Zone ..... 160

## List of tables

<b>Table 3.1:</b> Summary details for the Guaxupé nappe samples. UTM coordinates are relative to the WGS84 datum. T - crystallization ages (see text for explanation); 1-temperature outliers; 2-Concordia age; * Ambiguous source age, see text for details; $\epsilon_{\text{Hf}}$ calculated for grain individual $^{207}\text{Pb}/^{206}\text{Pb}$ dates. ....	38
<b>Table 4.1</b> Summary details for the Pouso Alegre samples. UTM coordinates are relative to the WGS84 datum. Data indexes: 1-Thermodynamic modelling; 2- Zr-in-rutile thermometry. ....	98
<b>Table 4.2</b> Correlations between the main occurrences of retro-eclogites from the Southern Brasília orogen. Data from: 1) This study; 2) Coelho et al. (2017); 3) Campos Neto et al. (2011); 4) Reno et al. (2009); 5) Campos Neto and Caby (1999); 6) Trouw (2008); 7) Hoppe (1985); 8) Luvizotto (2003); 9) Hoppe (1989); 10) Garcia and Campos Neto (2003); 11) Campos Neto and Caby (2000). ....	126



# 1 General introduction

## 1.1 Structure of the Thesis

This thesis is presented in the compiled form of thesis chapters and scientific articles as follows:

*Chapter 1 (General introduction)* – A general introduction into the research topic, its main goals, the location of the studied area and a brief summary of the field work.

*Chapter 2 (Geological setting: The Southern Brasília orogen)* – A geological introduction into the Southern Brasília orogen with a focus on the studied geotectonic domains.

*Chapter 3 (Constraining the petrochronological evolution of garnet-free UHT granulites in the Guaxupé nappe (SE Brazil): From subduction to collision)*, by M. Tedeschi et al. (2017), a manuscript submitted to Precambrian Research. This manuscript comprises the investigation of magmatic and metamorphic zircon ages, petrogenetic processes and *T-t* evolution recorded by the mafic to intermediate rocks from the Guaxupé nappe.

*Chapter 4 (Reconstruction of multiple *P-T-t* stages from retrogressed mafic rocks: subduction versus collision in the Southern Brasília Orogen (SE Brazil))* – The paper “Reconstruction of multiple *P-T-t* stages from retrogressed mafic rocks: subduction versus collision in the Southern Brasília orogen (SE Brazil)” is published in *Lithos* (Tedeschi et al., 2017). In this article, the mafic rocks from Pouso Alegre, commonly referred to in the literature as “retro-eclogites”, were investigated applying a petrochronological approach in order to reconstruct their *P-T-t* histories.

*Chapter 5 (Regional discussions)* – Summarizes the data obtained in this thesis and discusses it in the light of the prevailing literature of the Southern Brasília orogen.

*Chapter 6 (General conclusions and outlook)* – This chapter is dedicated to the general conclusions of this work, discusses geological problems that remain unsolved and gives an outlook for future studies.

Conferences abstracts – The abstracts presented in conferences are attached at the end of this thesis.

Appendices – The supplementary tables of both manuscripts (chapter 3 and 4) are presented.

## 1.2 Preface

With the advent of in-situ dating techniques and especially with the wide spread employment of Laser Ablation Inductively Coupled Plasma Mass Spectrometry (LA-ICP-MS) in the last 20 years an outstanding collection of geological age data has been produced. These data played a crucial role in confirming the existence and/or developing novel geodynamic models, but evidently further revealed new geological questions and problems. As a result, novel analytical techniques and approaches have emerged in Earth Sciences to meet this demand. Within this context, the term “Petrochronology” emerged from the necessity that petrologists and chronologists have to understand geological processes and their rates. It is necessary to integrate numerous ages with the petrologic evolution of a rock towards obtaining “significant ages” (Engi et al., 2017). Kylander-Clark et al. (2013) defined petrochronology as “the interpretation of isotopic dates in the light of complementary elemental or isotopic information from the same mineral(s)”. This interpretation however, emphasizes the dates and does not contemplate the investigated processes. Thus, a more practical and appropriate definition, connecting processes and their timing, was provided by Engi et al. (2017): “Petrochronology is the branch of Earth Science that is based on the study of rock samples and that links time (i.e., ages or duration) with specific rock-forming processes and their physical conditions. Petrochronology is founded in petrology and geochemistry, which define a petrogenetic context or delimit a specific process, to which chronometric data are then linked.” This branch of Earth Sciences has expanded rapidly in recent years with several combinations of employed methods (e.g., in-situ major and trace elements, Hf and U-Pb isotopes in zircon; trace elements, U-Th-Pb and Nd isotopes in monazite; trace elements and Hf isotopes in rutile).

Petrochronology can be applied to magmatic, sedimentary, metamorphic and hydrothermal systems to address a variety of geological problems. Notably, reconstructing the tectonic evolution of metamorphosed areas constitutes an important task and challenge because it comprises not only the recognition of the different metamorphosed domains and the understanding of the rock-forming processes, but likewise the estimation of rates at which these processes occur (Rubatto et al., 2011; Engi et al., 2017). In this respect, metamorphism can be a double-edged sword providing hints about the  $P$ - $T$  path that a rock underwent (e.g., preserved mineral assemblages, mineral inclusions in accessory minerals), but also erasing signatures of the pre-metamorphic history (e.g., overprinting of previous mineral assemblages, resetting and/or decoupling of isotopic systems).

For robust decay systems with low diffusion rates such as U-Pb, Th-Pb, Lu-Hf and Sm-Nd, minerals remain closed systems for most of the cases and may retain their radiogenic signatures even at high temperature. Isotopic dating of these minerals is hence considered to usually provide the formation ages. Accordingly, in an igneous rock such mineral formation ages would resemble

the magmatic crystallization age, and in a metamorphic rock these ages correspond to either a particular mineral reaction, a fluid infiltration event, or deformation-induced recrystallization. The reliability of such apparent closed systems has been challenged for rocks that experienced fluid interaction and high-grade metamorphism (e.g., Taylor et al., 2016; Kelsey and Hand, 2015; Rubatto, 2017). Nonetheless, complex isotopic data can provide and sometimes constitute the only alternative to get insights into the pre-metamorphic evolution of a rock (Taylor et al., 2016). Coupling of geochemical systems with detailed petrography has been the key to interpreting such altered isotopic systems. Once a resolved age is obtained it can be used as a tool when combined with compositional data of accessory minerals and/or major phases to recover *P-T-t* trajectories (Engi et al., 2017).

### 1.3 Nature of the problem

The Southern Brasília orogen (SBO) is one of several orogens that formed during the Western Gondwana amalgamation around the São Francisco paleocontinent in the Neoproterozoic (Brito-Neves et al., 1999; Cordani et al., 2003). Its Southern part hosts many tectonic pieces needed to reconstruct its overall geodynamic evolution, including the basement of the São Francisco block, the passive margin, the magmatic arc, syn-collisional sedimentary and magmatic rocks, all of which were intensely metamorphosed during the Neoproterozoic (Campos Neto et al., 2011; Trouw et al., 2013; Coelho et al., 2017). Despite numerous recent studies (Coelho et al., 2017; Reno et al., 2009, 2012; Rocha et al., 2017), some key pieces are still missing, and others remained only superficially constrained. Among those, the (U)HP-UHT metamorphic rocks of the SBO constitute an intriguing target for detailed research to further constrain its metamorphic evolution. The occurrence of (U)HP-UHT together itself is alluring. Thus, the geological setting and processes required to obtain such extreme conditions together, which at first glance appear unusual and discrepant, have been the subject of several works in the world (e.g., Santosh and Kusky, 2009; Harley et al., 2016).

In this thesis, the high pressure and ultra-high temperature (HP-UHT) rocks of the Guaxupé nappe and Ouro Fino Shear Zone from the southern portion of the Brasília orogen were investigated. These rocks bear potential to provide better insights into the prevalent protolithic and the metamorphic processes that occurred during the Brasília orogeny. Despite recent advances, the duration and conditions of the continental arc and continental collision magmatism and metamorphism are not clearly distinguished.

The migmatites of the Socorro-Guaxupé nappe were first interpreted by Campos Neto and Figueiredo (1995) to resemble deeper parts of a magmatic arc. Its active magmatism has been

assigned to a time interval between 730 and 640 Ma (Hackspacher et al., 2003; Mora et al., 2014; Vinagre et al., 2014; Rocha, 2016). Basic to intermediate rocks with crustal isotopic signatures for Nd (Nascimento, 2010; Rocha, 2016) and Hf (Mora et al., 2014) were produced. The migmatites record peak-metamorphic conditions at ultra-high temperatures of ca. 1000 °C during a period from 630 to 625 Ma. This event has been related to the collision and is associated with the occurrence of mafic rocks (Rocha, 2016). The origin of the older, inherited zircon dates (> 670 Ma) in the nappe has not been identified. Furthermore, the basement rocks that contributed to the crustal isotopic signatures, as well as the ages, sources and origin of the basic magmatism that induced the ultra-high temperature metamorphism, and the existence and duration of a pre-collisional metamorphism remain unclear.

The high-pressure counterpart of the UHT rocks, the clinopyroxene-garnet-bearing mafic rocks displaying decompression features (i.e., corona and symplectite), have been described as retro-eclogites that formed during subduction-related metamorphism (Reno et al., 2009; Campos Neto et al., 2011) or to collision related eclogitization (Coelho et al., 2017). These rocks have variable protolith ages between 1.5 Ga and 670 Ma, and metamorphic ages between 670 and 630 Ma. The significance of some of these metamorphic data has been challenged however, due to reduced number of analyses (e.g., Coelho et al., 2017). Therefore, these age-intervals do not clearly support a subduction context. Furthermore, the pressure conditions obtained by conventional thermobarometry on the retro-eclogites have been interpreted to reflect retrogression conditions. The peak mineral assemblage, which would have recorded higher pressures, is considered to be completely overprinted (e.g. Campos Neto and Caby, 1999; Coelho et al., 2017).

## **1.4 Aim of this study**

The main goal of this thesis is to improve and contribute to the understanding of the geodynamic evolution of the southern portion of the Brasília orogen. The workflow applied included 100,000 scale geological mapping of the studied region (Caldas and Poços de Caldas sheets; UFMG-CODEMIG) and detailed geological cross sections comprising the tectonic systems identified as hosts of the metamorphosed magmatic arc and the basement-passive margin interface of this orogenic system. A petrochronological approach focusing on intensely metamorphosed and deformed geotectonic key domains was then combined with the field information (basement, mafic rocks interpreted as subduction-related retro-eclogites and remnants of the magmatic arc) to understand the magmatic or sedimentary rock-forming and metamorphic processes, and estimate their rates by linking the processes to their ages.

#### **1.4.1 The Guaxupé nappe rocks:**

A detailed investigation focused on the timing and processes involved in the generation and evolution of UHT-metamorphosed mafic to intermediate rocks of the Guaxupé nappe. The aims and the approaches applied in each case can be detailed as follows:

- Identification and characterization of the basement rocks of the Guaxupé nappe, and delineation of the arc magmatism duration by combined in-situ U-Pb zircon dating, Lu-Hf isotopes and trace element geochemistry in zircon.
- Investigation of the magmatic petrogenetic processes involved in the generation of the nappe rocks using lithochemistry, Lu-Hf isotope geochemistry as petrogenetic parameters, trace element geochemistry in zircon and Ti-in-zircon thermometry.
- Investigation of the metamorphic evolution of the nappe rocks applying petrography, lithochemistry, quantitative compositional maps, conventional thermometry, Lu-Hf isotope in zircon, trace element geochemistry in zircon and Ti-in-zircon thermometry.
- Constraining the timing of metamorphism by textural cathodoluminescence-based domain in-situ U-Pb zircon dating, comparison of probability density plots and linking age information to the metamorphic conditions.
- Identification and characterization of possible causes for the ultra-high temperature metamorphism.

#### **1.4.2 The clinopyroxene-garnet amphibolite (“retro-eclogite”) of Pouso Alegre and its host rocks**

A detailed petrochronological investigation focused on the reconstruction of the *P-T-t* trajectories of the retrogressed clinopyroxene-garnet amphibolite (“retro-eclogite”), which is interpreted to be a subduction marker, and their country rocks. The aims and the approaches applied can be detailed as follows:

- Determination of protolith and metamorphic ages of the clinopyroxene-garnet amphibolites and their country rocks, migmatitic sillimanite-garnet and basement gneisses by in situ zircon and monazite dating (LA-ICP-MS and SIMS).
- Estimation of *P-T* conditions by reconstruction of local domains through quantitative compositional maps, corresponding thermodynamic modelling of local equilibria, conventional thermobarometry, Ti-in-zircon and Zr-in-rutile thermometry, and quantitative chemical analyses of inclusions in zircon, rutile and garnet.

- Constraining the timing of the successive metamorphic stages by linking zircon domain ages with the corresponding the  $P$ - $T$  conditions based on trace elements abundances in zircon, monazite and garnet, and mineral compositions of inclusions hosted by specific cathodoluminescent domains in zircon;
- Investigation of reactions, timing and conditions of symplectite and corona formation.
- Constraining of the geological setting and processes involved in the formation of these rocks through their  $P$ - $T$ - $t$  evolution and their respective paleogeothermal gradients.

Ultimately, data obtained in this study will be linked with literature data in order to refine the subduction to collisional evolution in the southernmost portion of the Brasília orogen.

## 1.5 Studied area and field work

The Southern Brasília orogen is located between 21°S and 23°S and its southernmost portion is situated within Minas Gerais state, Brazil. The studied area, hereinafter referred to solely as Guaxupé nappe, encompasses the northern lobe of the Socorro-Guaxupé nappe from the proximity of Guaxupé to the Ouro Fino Shear Zone, close to the Pouso Alegre city (Fig. 1.1).

The first part of the work was dedicated to the geological mapping of the Caldas (SF.23-V-D-IV) and Poços de Caldas (SF.23-V-C-VI) 100,000 sheets in Minas Gerais state within the scope of the UFMG-CODEMIG project “Fronteiras de Minas”. During the ninety days of field work, around 700 outcrops were investigated and described in detail, and the resulting geological map and report (Tedeschi et al., 2015) were the basis for further sample collection. Moreover, a geological profile along an ca. 80 km traverse from the northern portion of the nappe to the Pouso Alegre mafic rocks was constructed employing a detailed scale (1:25) within the 3 km-proximities of the occurrence of the mafic rocks.

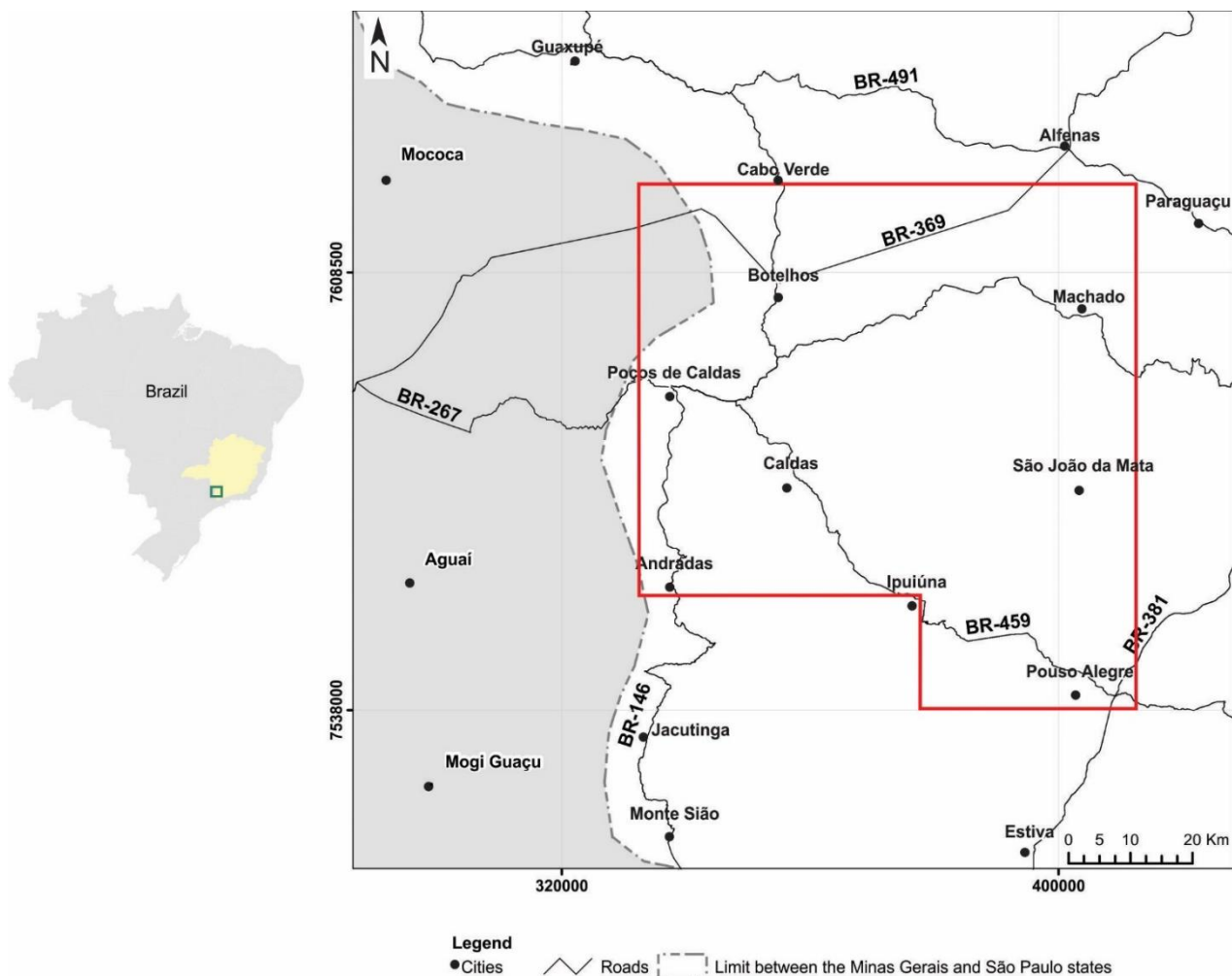


**Figure 1.1:** Map of Brazil with the indicated location of the regional cut-out, which displays the main access roads into the studied area (red polygon).

## 1.6 References

- Brito Neves, B.B., Campos Neto, M.C., Fuck, R.A., 1999. From Rodinia to Western Gondwana: an approach to the Brasiliano-Pan African cycle and orogenic collage. *Episodes* 22, 155-166.
- Campos Neto, M.C.; Figueiredo, M.C.H., 1995. The Rio Doce orogeny, southeastern Brazil. *Journal South American Earth Sciences* 8(2), 143-162.
- Campos Neto, M.C., Basei, M.A.S., Assis Janasi, V.d., Moraes, R., 2011. Orogen migration and tectonic setting of the Andrelândia Nappe system: An Ediacaran western Gondwana collage, south of São Francisco craton. *Journal of South American Earth Sciences* 32, 393-406.
- Coelho, M.B., Trouw, R.A.J., Ganade, C.E., Vinagre, R., Mendes, J.C., Sato, K., 2017. Constraining timing and P-T conditions of continental collision and late overprinting in the Southern Brasília Orogen (SE-Brazil): U-Pb zircon ages and geothermobarometry of the Andrelândia Nappe System. *Precambrian Research* 292, 194-215.
- Cordani, U. G., Brito-Neves, B. B., D'Agrella-Filho, M. S., 2003. From Rodinia to Gondwana: a review of the Available Evidence from South America. *Gondwana Research* 6(2), 275-283.
- Engi, M., Lanari, P., Kohn, M., 2017. Significant Ages - An Introduction to Petrochronology. In: Kohn, M.J., Lanari, P., Engi, M. (Eds.), *Petrochronology. Reviews in Mineralogy and Geochemistry* 83, pp. 55-102.
- Hackspacher, P.C., Fetter, A.H., Ebert, H.D., Janasi, V.A., Dantas, E.L., Oliveira, M.A.F., Braga, I.F., Negri, F.A. 2003. Magmatismo há ca. 660-640 Ma no Domínio Socorro: registros de convergência pré-colisional na aglutinação do Gondwana Ocidental. *Geologia USP, Série Científica* 3, 85-96.
- Harley, S.L., 2016. A matter of time: The importance of the duration of UHT metamorphism. *Journal of Mineralogical and Petrological Sciences* 111, 50-72.
- Kelsey, D.E., Hand, M., 2015. On ultrahigh temperature crustal metamorphism: phase equilibria, trace element thermometry, bulk composition, heat sources, timescales and tectonic settings. *Geoscience Frontiers* 6, 311-356.
- Kylander-Clark, A., Hacker, B. R., Cottle, J. M., 2013. Laser-ablation split-stream ICP petrochronology. *Chemical Geology* 345, 99-112.
- Mora, C.A.S., Campos Neto, M.C., Basei, M.A.S., 2014. Syn-collisional lower continental crust anatexis in the Neoproterozoic Socorro–Guaxupé Nappe System, southern Brasília Orogen, Brazil: constraints from zircon U-Pb dating, Sr-Nd-Hf signatures and whole-rock geochemistry. *Precambrian Research* 255, 847-864.



Nascimento, M.B. 2010. Evolução Metamórfica P-T-t da Porção Norte do Complexo Guaxupé na Região de Arceburgo-Santa Cruz da Prata, MG. PhD thesis, Universidade Estadual Paulista “Júlio de Mesquita Filho”, p. 162.

Rocha, B. C., Moraes, R., Möller, A., Cioffi, C. R., Jercinovic, M.J., 2017. Timing of anatexis and melt crystallization in the Socorro-Guaxupé Nappe, SE Brazil: insights from trace element composition of zircon, monazite and garnet coupled to U-Pb geochronology. *Lithos* 277, 337-355.

Rubatto, D., Regis, D., Hermann, J., Boston, K., Engi, M., Beltrando, M., McAlpine, S.R.B., 2011. Yo-Yo subduction recorded by accessory minerals in the Sesia Zone, Western Alps. *Nature Geoscience* 4, 338-342.

Santosh, M., Kusky, T., 2009. Origin of paired high pressure–ultrahigh-temperature orogens: a ridge subduction and slab window model. *Terra Nova* 22, 35-40.

Taylor, R.J.M., Kirkland, C.L., Clark, C., 2016. Accessories after the facts: Constraining the timing, duration and conditions of high-temperature metamorphic processes. *Lithos* 264, 239-257.

Tedeschi, M., Novo, T., Azevedo, R., Amaral, L.F.S., Degler, R., Viera, P.L.N.C.R., 2015. Geologia das Folha Caldas (SF.23-V-D-IV) e Poços de Caldas (SF.23-V-C-VI) 1:100.000. Projeto Fronteiras de Minas, CODEMIG-UFMG, Belo Horizonte, Brazil.

Trouw, R.A.J., Peternel, R., Ribeiro, A., Heilbron, M., Vinagre, R., Duffles, P., Trouw, C.C., Fontainha, M., Kussama, H.H., 2013. A new interpretation for the interference zone between the southern Brasília belt and the central Ribeira belt, SE Brazil. *Journal of South American Earth Sciences* 48, 43-57.

Vinagre R., Trouw R.A.J., Mendes J.C., Duffles P., Peternel R., Matos, G., 2014. New Evidence of a Magmatic Arc in the Southern Brasília Belt, Brazil: The Serra da Água Limpa Batholith (Socorro-Guaxupé Nappe). *Journal of South American Earth Science* 54, 120-139.

## 2 Geological setting: The Southern Brasília orogen

The Brasília orogen is an 1800 km-long nearly N-S trending orogen, extending roughly between the 10° and 26° S from central to southeast Brazil (Fig. 2.1A). It is one of the orogenic systems that formed around the São Francisco paleocontinent during the Western Gondwana amalgamation in the Neoproterozoic, known as the Brasiliano event (Fig. 2.1B; Brito-Neves et al., 1999; Alkmim et al., 2001; Cordani et al., 2003). The northern and southern segments of the Brasília orogenic system evolved separately during the Brasiliano event, representing distinct convergences against the northwest and southwest margins of the São Francisco craton (Valeriano et al., 2017). The Amazonian paleocontinent was thereby involved in the formation of the northern sector (Fuck et al., 2017), while the southern sector resulted from the collision of the passive continental margin of the São Francisco paleocontinent with the active continental margin of the Paranapanema block (Campos Neto, 2000; Mantovani and Brito-Neves, 2005, 2009; Trouw et al., 2000, 2013). The collisional stage of the Southern Brasília orogen formed a complex set of nappe systems verging to the east, in which each nappe system comprises specific domains with distinctive tectono-metamorphic features (Campos Neto and Caby, 1999, 2000; Campos Neto et al., 2011; Valeriano et al., 2017; Trouw et al., 2000, 2013). The overthrusting distances of the East-verging nappes were estimated to be between 150 and 300 km (Campos Neto and Caby, 1999, 2000; Campos Neto et al., 2007).

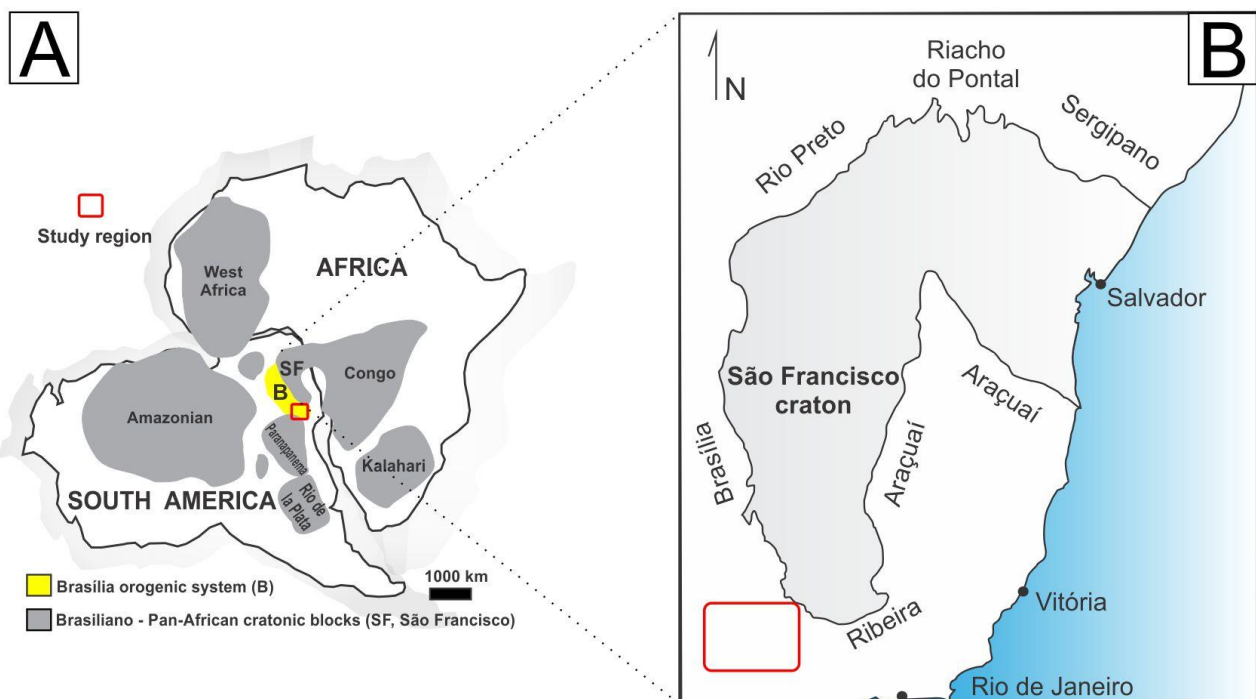


**Figure 2.1:** Geotectonic context of the São Francisco craton and Southern Brasília orogen within Western Gondwana. (A) Distribution of cratonic blocks in Western Gondwana (red rectangle marks location of the studied region illustrated in B): Distribution of Ediacaran orogens formed around the São Francisco craton with the southern portion of the Brasília orogen in the red rectangle.

The main tectonic domains identified within the nappe system, from west to east, are (Fig. 2.2):

1. The Socorro-Guaxupé nappe (SGN) – The SGN mainly contains highly metamorphosed igneous rocks that were interpreted to represent the magmatic arc unit of the active margin of the Paranapanema plate (Figueiredo and Campos Neto, 1995; Campos Neto et al., 2011), and minor paragneisses and schists (Campos Neto and Caby, 2000; Rocha et al., 2016);
2. The Andrelândia nappe system (ANS) – The ANS is mainly composed of metasedimentary rocks exhibiting an inverted metamorphic gradient with high-pressure granulite and eclogite facies in the upper parts, and amphibolite to greenschist facies at the base (Campos Neto et al., 2011; Trouw et al., 2013). Studies on the ANS described mixtures of sediments derived from both active and passive margins (Belém et al., 2011; Trouw et al., 2013). Trouw et al. (2013) consider the Carrancas and Lima Duarte nappes as part of the ANS. Campos Neto et al. (2010, 2011), however, separate the nappes into two systems. The ANS thereby represents subduction-related metasedimentary sequences (forearc basin) as part of the former accretionary prism. The Carrancas and Lima Duarte nappes are composed of metasedimentary rocks and form, together with the São Francisco basement and associated basins, the passive margin (Campos Neto et al., 2011; Cioffi et al., 2016; Westin et al., 2016).

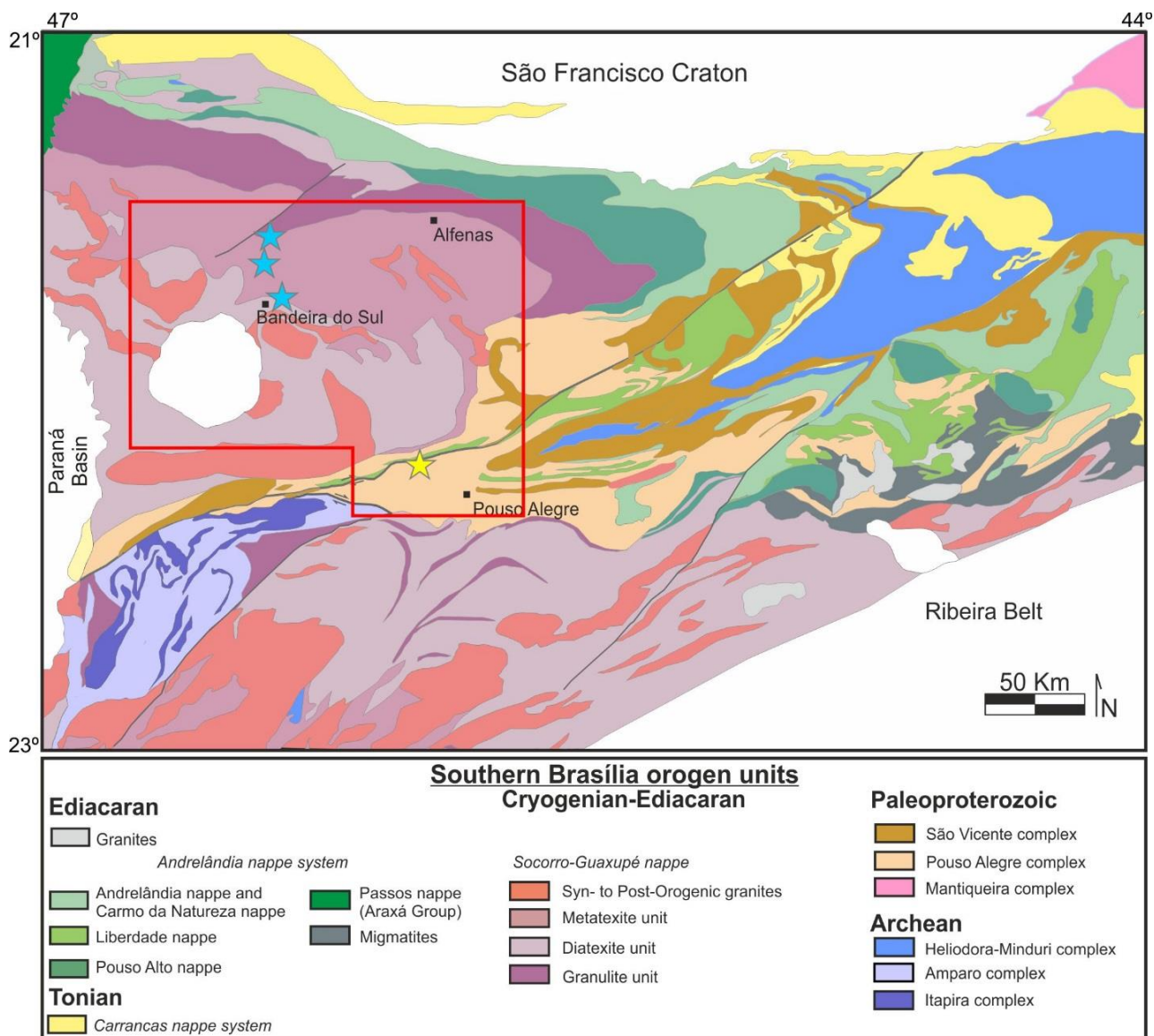


**Figure 2.2:** Tectonic map of the Southern Brasília orogen (modified after Campos Neto et al., 2011; Westin et al., 2016; Cioffi et al., 2016 a, b). Red rectangle delimits the studied area, and stars indicate the location of the studied “retro-eclogite” outcrop of Pouso Alegre (yellow) and mafic migmatitic granulites (blue).

## 2.1 The Basement of the southern portion of the Brasília orogen

### 2.1.1 The Socorro-Guaxupé nappe basement

In current geotectonic models, the Paranapanema block is the basement of the Socorro-Guaxupé nappe (Campos Neto et al., 2011; Mantovani and Brito-Neves, 2005; Trouw et al., 2013). The basement, however, was extensively covered by volcanic and sedimentary rocks of the Paraná basin during the Gondwana break-up in the Cretaceous (Renne et al., 1992). Its existence and delimitation have thus been mainly inferred from geophysics, lithochemical and isotopic compositions of basalts in the basin, and borehole data indicating ancient granitic rocks beneath

the Paraná basin (Cordani et al., 1984; Mantovani and Brito-Neves, 2005; Mantovani and Brito-Neves, 2009). Mantovani and Brito-Neves (2009) deduced from the few direct geologic and many indirect (geologic, geochemical and isotopic) available data, that the Paranapanema block must predominantly be of granitic nature (orthogneisses). These authors constrained the age of the Paranapanema block to be Paleoproterozoic to Mesoproterozoic, i.e., pre-Brasiliano, based on Rb-Sr and K-Ar data. U-Pb dating revealed Paleoproterozoic gneiss fragments (2.1 Ga) within the Neoproterozoic gneisses in the southern part of the Socorro-Guaxupé nappe, the Socorro Lobe (Trouw, 2008).

Geophysical observations show a lateral extent of  $10^5$  km<sup>2</sup> of the Paranapanema Block, i.e., an intermediate-sized plate (Fig. 2.3A; Mantovani and Brito-Neves, 2009). Due to the absence of robust data regarding its evolution, the use of the term “block” is preferred over “craton”. The possibility that the Paranapanema block is composed of smaller minor blocks (microplates or microcontinents) that are separated by the orogenic belts was indicated by deep well studies (Fig. 2.3B; Milani 1997, unpublished PhD thesis; published in Mantovani and Brito-Neves, 2009). Mantovani and Brito-Neves (2009) argue, however, that these data are inconclusive and that the interpreted orogenic structures between the apparent sub-blocks rather represent graben structures (Fig. 2.3B). They further note in support of a single stable segment, that other Gondwanan basins, especially the very large ones, are always located in lithospheric cratonic areas.

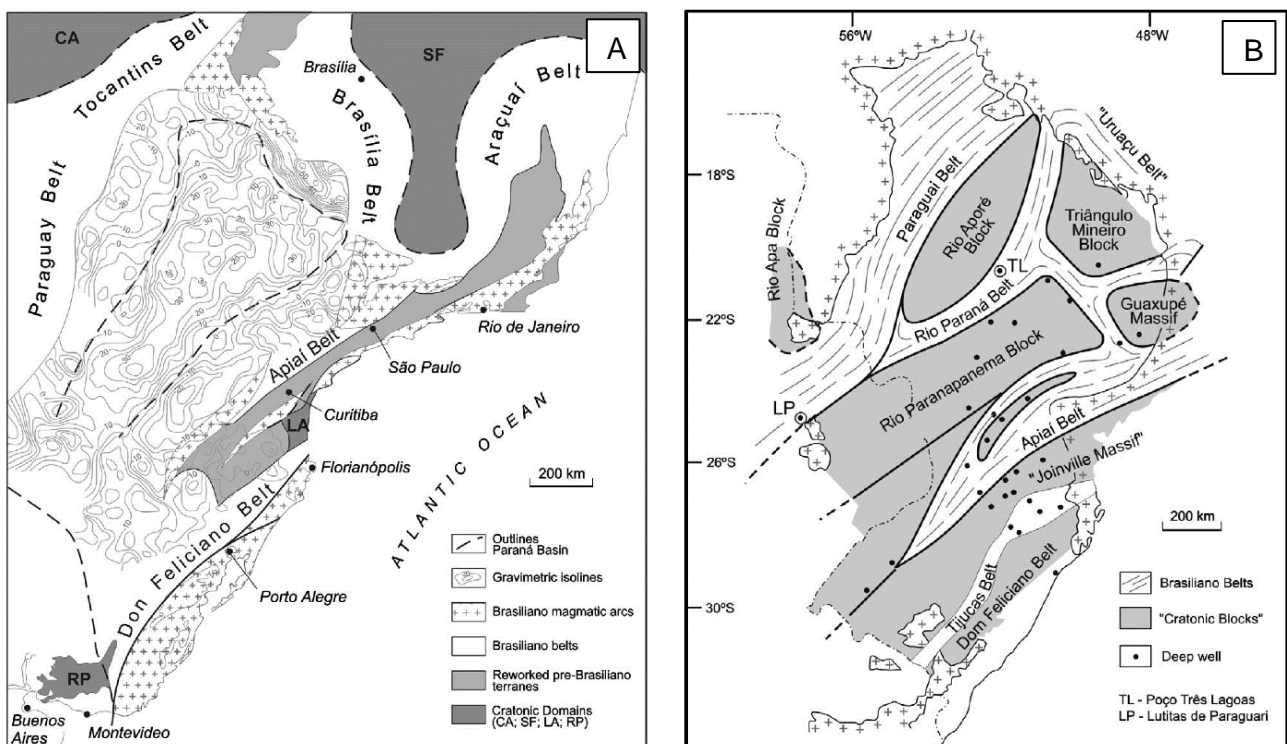


**Figure 2.3:** Proposed delimitations of the basement of the Paraná Basin and their relationships with the surrounding orogenic systems. (A) Outline of the Paranapanema block obtained from gravimetric studies (modified from Quincas, 1995 in Mantovani and Brito-Neves, 2009). (B) Tectonic sketch map of the basement of the Paraná Basin as proposed by Milani (1997) based on deep wells data.

### 2.1.2 The São Francisco craton basement

The basement of the southern part of the SBO comprises Paleoproterozoic and Archean rocks interpreted to represent part of the reworked São Francisco craton. They mainly occur in a corridor that crosscuts the nappes, the Ouro Fino Shear Zone (Fig. 2.4). The Paleoproterozoic rocks are also frequently interspersed as tectonic slivers in the Andrelândia nappe system (Campos Neto et al., 2011; Cioffi et al., 2016a).

The Paleoproterozoic basement is represented by the Pouso Alegre and São Vicente complexes (Cioffi et al., 2016; Westin et al., 2016). In the Pouso Alegre complex, two suites of ca. 2.15 Ga and 2.08 Ga juvenile rocks are interpreted as the reworked sector of the Mineiro Belt, an accretionary event proceeded between ca. 2.4 Ga and 2.1 Ga (Cioffi et al., 2016; Teixeira and Alkmim, 2017). The São Vicente complex is composed of metasedimentary rocks and amphibolites deposited in a convergent margin basin environment, in which the Pouso Alegre complex acted as main sediment source (Westin et al., 2016).

The Archean basement comprises juvenile Mesoarchean TTG-type rocks dated at ca. 3.00 Ga and 2.76 Ga Neoproterozoic crustal granites (Amparo, Serra Negra and Heliodora-Minduri complexes; Cioffi et al., 2016b). The formers are interpreted as products of partial melting of mafic rock that were extracted from the mantle at ca. 3.4–3.2 Ga. Crustal granitic magmatism records the transition from TTG-type to high-K granitic magmatism. It is interpreted to have formed by reworking of the Mesoarchean TTG crust, most likely in a collisional setting.

Because the Eoarchean rocks have no chronocorrelate in the São Francisco craton, they are considered as an exotic terrane. Two different timings have been proposed for the accretion of these rocks with the São Francisco craton. A Neoproterozoic accretion is supported by the timing of granitic magmatism in both segments (Mamona event at ca. 2760 – 2680 Ma; Farina et al., 2015). The other hypothesis points towards a Paleoproterozoic accretion based on the interpretation that the Pouso Alegre complex represents the extension of the Mineiro Belt (Cioffi et al., 2016b). Time constraints in this case are provided by the youngest, ca. 2.0 Ga rocks in the Pouso Alegre complex. Cioffi et al. (2016b) however emphasized that both interpretations are uncertain due to the occurrence of similar late-Archean high-K magmatism in other cratons and the intense level of reworking in the Southern Brasília orogen, especially for the Archean rocks.



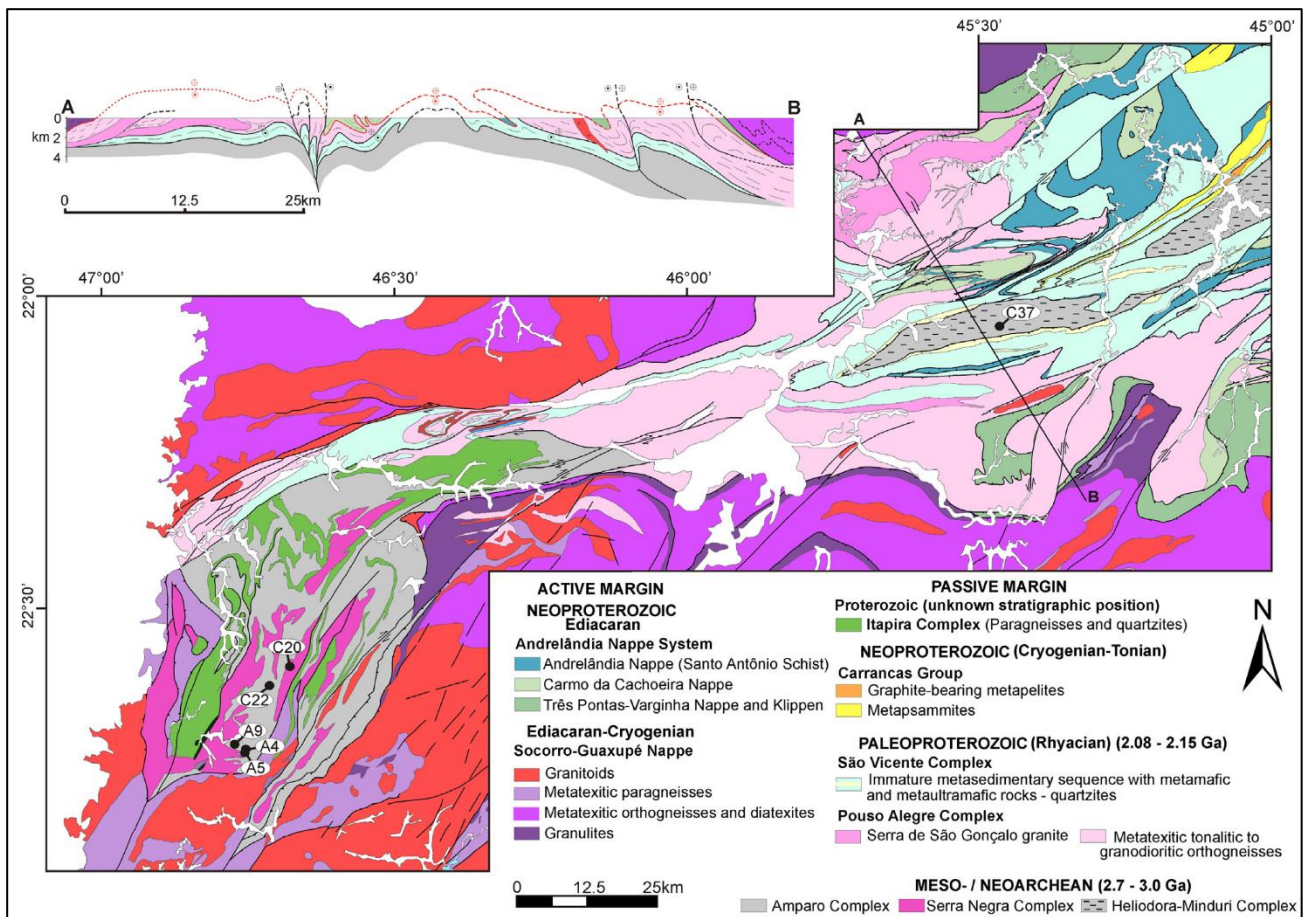


**Figure 2.4:** Geological map and cross-section showing the main occurrences of the Archean and Paleoproterozoic basement of the Southern Brasília orogen in the Ouro Fino shear zone. Map and cross-section from Cioffi et al. (2016b) compiled and modified from Perrota (1991), Morais (1999a,b), Peternel (2005), Trouw et al. (2008) and Cioffi et al. (2016a).

## 2.2 The Socorro-Guaxupé nappe

The Socorro-Guaxupé nappe (SGN) is a 10 km-thick crustal segment composed of migmatized gneisses. It is interpreted as the metamorphosed root of an Andean-type magmatic arc formed along the active margin of the Parapanema Block (Fig. 2.2; Campo Neto and Figueiredo, 1995; Campos Neto and Caby, 2000; Campos Neto et al., 2011). Some authors concluded that it represents the southeastward extension of the Goiás Magmatic Arc (Pimentel and Fuck, 1992; Pimentel et al., 2000; Laux et al., 2004, 2005). The Goiás arc however comprises older juvenile magmatic rocks that have not been reported in the SGN (Campos Neto et al., 2011).

### 2.2.1 Nappe units

The Socorro-Guaxupé nappe is subdivided into a northern (Guaxupé) and southern lobe (Socorro). They are separated by a structural window in the Ouro Fino shear zone, where Archean

and Paleoproterozoic rocks from the basement and minor Neoproterozoic metasedimentary rocks outcrop (Figs. 2.2 and 2.4; Campos Neto et al., 2011; Cioffi et al., 2016 a, b; Ribeiro et al., 2011; Westin et al., 2016).

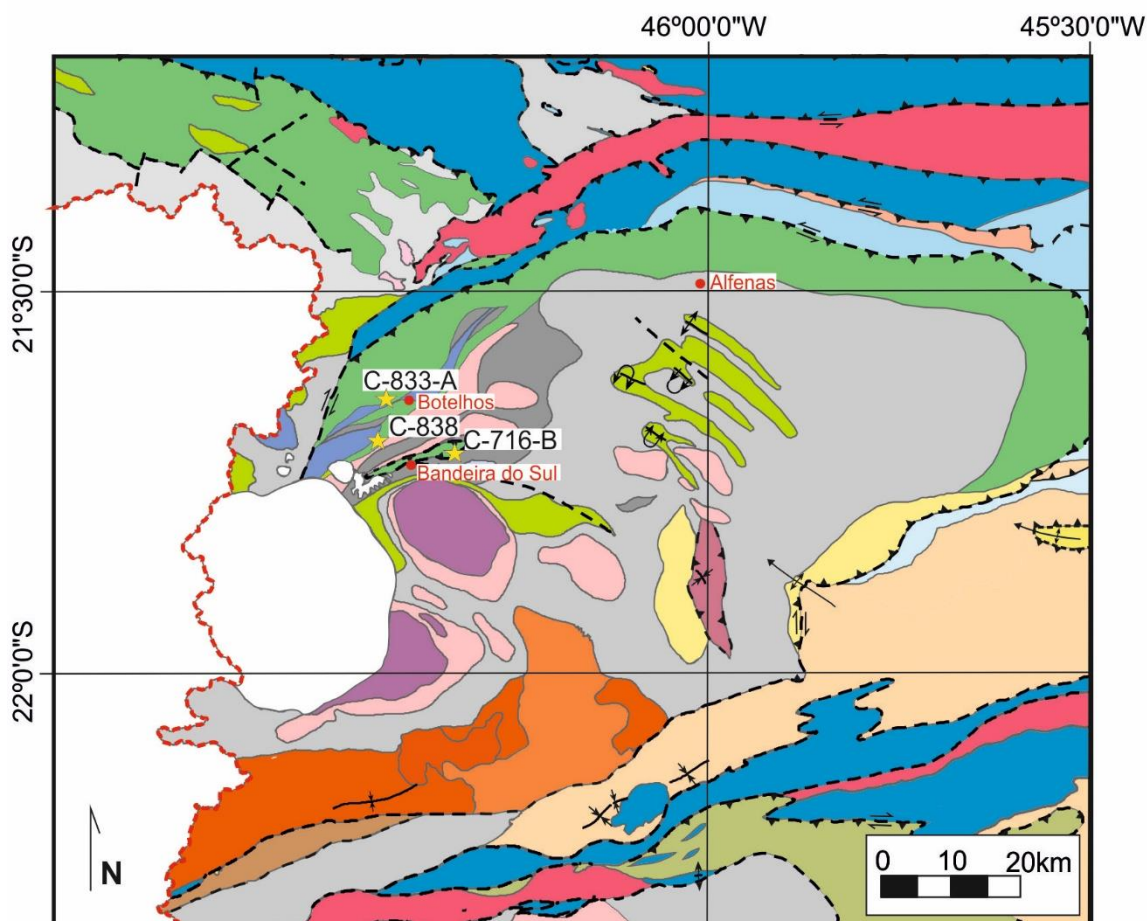
The Socorro-Guaxupé nappe has a wedge shape in which the units are asymmetrically distributed. A slight increase in the degree of partial melting in the migmatites is observed from north to south. The northern sector hosts the base of the structure that is represented by the Basal Granulitic Unit (GU). The GU there is superposed by the Upper Metatexite unit (MU) and to the south, the Diatexitic unit (DU) (Campos Neto and Caby, 2000; Campos Neto et al., 2011). In geological maps, the Basal Granulitic Unit is mainly associated with the Elói Mendes Orthogneisses, while the Metatexitic and Diatexitic units comprise the rocks of São João da Mata complex and Serra da Água Limpa granites. A gradual transition is observed between the Elói Mendes and the São João da Mata units (Fig. 2.5; Degler et al., 2015; Fernandes et al., 1987; Ribeiro et al., 2011b; Tedeschi et al., 2015).

The Granulitic unit is ~ 3 km thick and mainly composed of metamorphosed magmatic rocks. The most common lithotype of the granulitic unit is a green (garnet)-(clinopyroxene)-orthopyroxene granulite of enderbitic composition. At the base of the unit, stromatic gneisses containing green enderbitic leucosomes are the prevalent lithology. Towards the top, metatexites and diatexites are abundant, and pink granitic leucosomes are associated with the green opdalite. Interspersed decimeter-thick gabbro-noritic and amphibolitic layers are considered syn-metamorphic (Campos Neto and Caby, 2000; Tedeschi et al., 2015).

The Metatexitic unit mainly contains metasedimentary gneisses and migmatitic (sillimanite)-garnet gneisses, in which the degree of anatexis decreases towards the top/upper units (southwestward; Campos Neto and Caby, 2000). Besides, (sillimanite)-muscovite schists, (orthopyroxene)-garnet gneisses, quartzites, calc-silicate gneisses, marbles, (hornblende)-biotite gneisses and mafic meta-intrusives are locally abundant (Campos Neto and Caby, 2000; Rocha et al., 2017; Tedeschi et al., 2015).

The most common lithotypes in the Diatexitic unit are pinkish to greyish anatectic granitic gneisses that comprise nebulitic gneisses and granitoids encompassing portions of stromatic gneiss. The stromatic gneiss is a (clinopyroxene)-(hornblende)-biotite-bearing gneiss of dioritic-tonalitic composition, corresponding to the mesosoma within the biotite leucosome. Accumulations of leucosomes locally form igneous bodies that can be mapped at a 1:100,000 scale as labeled the Serra da Água Limpa granite (Fig.2.5; Martins, 2016; Peixoto et al., 2015; Tedeschi et al., 2015) are correlated to the Pinhal-type granites from Wernick and Penalva (1984). Diverse enclaves are found within this unit: dioritic-monzodioritic gneisses, garnet-diopside-scapolite calc-silicate rocks, sillimanite-cordierite metapelites (kinzigites).





### Cretaceous

□ Poços de Caldas Alkaline Intrusion

### Cryogenian-Ediacaran

#### Socorro-Guaxupé nappe

- Late and Post-orogenic syenites
- Pinhal Ipuíuna Batholith - (Hbl)-Bt granitoid
- Botelhos Leucogranite - Anatectic leucogranite
- Serra da Água Limpa Granite  
Anatectic (Hbl)-Bt and (Grt)-Bt granites
- Charnockite suit - Opx-bearing rocks
- Paiolino Orthogneiss  
Hbl-Bt (augen) gneiss, locally Opx-bearing
- Cachoeira de Minas complex  
Cpx-Grt-Hbl orthogneiss, locally quartzites
- Paraderived São João da Mata unit  
Migmatitic (Hbl)-Bt gneisses, locally Sil-bearing
- São João da Mata unit  
Migmatitic (Opx)-(Hbl)-Bt orthogneisses
- Elói Mendes unit  
Migmatitic Opx-Cpx-(Hbl)-(Grt) and (Cpx)-Grt granulites
- Bela Vista Schist  
Grt-Sil schist, quartzite and amphibolitic lens

### Tonian-Ediacaran

#### Andrelândia nappe system

- Granites
- Arantina unit  
Ky-Kfs gneiss and mafic granulites;  
Ky-Grt-Bt-Ms schist and amphibolites
- São Vicente unit  
Paragneisses, quartzite, Ms Schist,  
amphibolites and metaultramafic

### Paleoproterozoic

- São Vicente complex
- Pouso Alegre complex
- Gaspar Lopes orthogneiss

### Archean

- Archean gneisses complexes  
Orthogneisses and  
metaultramafic rocks

**Figure 2.5:** Geological Map of the studied area with the location of the studied samples from the Guaxupé nappe (compiled and simplified from Degler et al., 2015; Fava et al., 2015; Peixoto et al., 2015; Ribeiro et al., 2010a, b, c; and Tedeschi et al., 2015; with inputs from Cioffi et al., 2016; Westin et al., 2016). Dashed red line indicates the limit between Minas Gerais (east) and São Paulo (west) states.

### 2.2.2 Arc magmatism

The formation of the magmatic arc in the Guaxupé nappe is mainly recorded by the Granulitic unit. Campos Neto and Figueiredo (1995) and Campos Neto et al. (1996) first proposed that the enderbitic granulites of the Granulitic unit derive from magmatic arc igneous protoliths. The magmatism has been constrained to a time interval between 670 and 640 Ma (e.g. Basei et al., 1995; Hackspacher et al., 2003; Mora et al., 2014; Vinagre et al., 2014). Zircon age clusters around 655-650 Ma are interpreted to indicate the main period of arc magmatism (Rocha, 2016). Older dates up to 800 Ma have been interpreted as to represent inherited grains from a previous magmatism (Rocha, 2016; Rocha et al., 2017).

Isotopic signatures of  $\epsilon\text{Nd}$  from 0 to -23 and  $\epsilon\text{Hf}$  from -5 to -10 of the Granulitic unit suggest a crustal protolith. These signatures have been associated to an active continental margin related magmatism (Mora et al., 2014; Nascimento, 2010; Rocha, 2016). The absence of juvenile rocks has been attributed to the formation of the arc magmatic from metasomatized mantle rather than by crustal contamination of basement, especially since zircon inheritance from the basement has not been reported in the Guaxupé lobe (Rocha, 2016).

### 2.2.3 Metamorphism

Conventional thermobarometry applied to the granulitic rocks of the Granulitic unit (based on orthopyroxene-garnet mineral pairs) provided peak metamorphic conditions of 900–1040 °C and 12–14 kbar. Retrograde conditions were estimated to 740–980 °C and 5–8 kbar by amphibole-plagioclase thermobarometry (Campos Neto and Caby, 2000; Del Lama et al., 2010; Rocha, 2016). Close to the contact with the Granulitic unit, the Metatexitic unit, records peak conditions of ca. 1030 °C and 12 kbar, and retrogression at 865 °C and 9 kbar in paraderived orthopyroxene-garnet-bearing rocks (Opx-Grt and Amp-Pl pairs, respectively; Rocha et al., 2017).

The green leucosomes in the gneisses of the Granulitic unit have been interpreted, together with charnockites and veins and mangeritic bodies, to represent anhydrous anatexis in the root of the magmatic arc (Campos Neto et al., 2017). Accretionary metamorphism, around 635–625 Ma, is suspected to have triggered the dry anatexis (Campos Neto et al., 2011 and references therein). Rocha et al. (2017) proposed an overall long-lived metamorphic cycle of ca. 30 m.y. based on dating and trace element geochemistry in monazite and zircon, and trace element geochemistry in garnet. Their work presents five generations of monazite:  $631 \pm 4$  Ma prior to the partial melting;  $628 \pm 4$  Ma recording the prograde decompression, and multiple monazite growth episodes recording melt crystallization events at  $624 \pm 3$  Ma,  $612 \pm 5$  Ma and  $608 \pm 6$  Ma. The UHT event

has been constrained between 630 and 625 Ma, and associated to syn-collisional magmatism, possibly induced by the underplating of mafic magmas.

## **2.3 The Andrelândia nappe system**

The Andrelândia nappe system is located below the Socorro-Guaxupé nappe. It is composed of highly metamorphosed rocks and displays an inverse metamorphic gradient. It has been displaced for at least 85 km during nappe stacking (Campos Neto et al., 2011). These authors subdivide the nappe system, from the top to the bottom, into the Três Pontas-Varginha (and Pouso Alto) nappe (TPVN), the Liberdade nappe (LN) and the Andrelândia (and Carmo da Cachoeira) nappe (AN). The Carrancas nappe system and the Lima Duarte nappe are listed separately here due to on-going discussions about their geodynamic context (Campos Neto et al., 2011; Trouw, 2013).

### **2.3.1 General structure**

The upper Três Pontas-Varginha nappe is located below the Socorro-Guaxupé nappe and as Klippen in the eastern part of the Southern Brasília orogen (Fig.2.2). The rocks of the Três Pontas-Varginha nappe comprise high-pressure granulitic pelites, wackes, subordinate psammites and mafic igneous rocks. Felsic (biotite)-garnet-kyanite-K-feldspar migmatitic granulites recorded around 850 °C and 16 kbar (Cioffi et al., 2012; Garcia and Campos Neto, 2003). The upper felsic sillimanite-bearing rocks record 880 °C and 13 kbar (Garcia and Campos Neto, 2003).

The intermediate Liberdade nappe, is mainly composed of garnet and kyanite-bearing schists containing quartzite lenses, amphibolites, metawackes and calc-silicate rocks. Metabasites with quartz-rutile-garnet-omphacite assemblages exhibit decompression features such as plagioclase corona around garnet and diopside-quartz-plagioclase intergrowths. They are referred to as retro-eclogites (Campos Neto et al., 2011). These features are attributed to fast exhumation. Fragments of Paleoproterozoic gneisses and ultramafic rocks are also abundant within this nappe (Campos Neto et al., 2011). The lower Andrelândia nappe is composed of flysch-type wackes, pelitic, psammitic metasediments. The Carmo da Cachoeira nappe also comprises high-pressure garnet amphibolites also considered as retrogressed eclogites (Garcia and Campos Neto, 2003).

The Carrancas nappe system and the Lima Duarte nappe are overlying the border between the São Francisco craton and the Southern Brasília orogen. The former is mainly composed of quartzites and graphite schists, and the latter consists of psamo-pelitic sediments metamorphosed. The suture zone position has been subject to two different interpretations. Some authors argue,

based on age, isotopic and lithochemical provenance studies (Campos Neto et al. 2004, 2010, 2011) that the Andrelândia nappe system are metasedimentary rocks that were deposited in an forearc basin related to the active margin of the Southern Brasília orogen. In this interpretation, the Carracas and Lima Duarte correspond to the passive margin of the São Francisco Craton. Therefore, the suture is located between the ANS and the Carracas and Lima Duarte. Other authors, such as Ribeiro et al. (1995) and Trouw et al. (2000, 2013) interpret that the majority of rocks of the ANS were deposited in the passive margin of the São Francisco Craton, with the exception of the Santo Antônio Schist which represents an active margin setting (Belém et al., 2011). Thus, they locate the suture on the top of the ANS in contact with the SGN.

### **2.3.2 The retro-eclogites**

In the Southern Brasilia orogen, garnet-clinopyroxene-bearing rocks containing disequilibrium features from decompression (i.e., corona and symplectite) are referred as retro-eclogites (Trouw, 1992; Campos Neto et al., 1999). Such rocks are found in several locations such as the Pouso Alegre (PA), Liberdade (L), Varginha (V), Andrelândia (Carmo da Cachoeira-CC) and Passos (São Sebastião do Paraíso-SSP) nappes. The PA is hosted by the basement (Coelho et al., 2017) while the others are hosted by metasediments (e.g. Campos Neto and Caby, 1999; Garcia and Campos Neto, 2003).

Choudhuri et al. (1978) first classified mafic rocks of the ANS as retro-eclogites. These authors studied garnet + clinopyroxene assemblages associated with symplectites and coronas in metabasites from the Pouso Alegre region. Coelho et al. (2017) determined metamorphic conditions of 12 to 16 kbar at 700 to 800 °C on the same rocks. These authors, however, argue that higher pressure assemblages have been completely overprinted. Campos Neto and Caby (1999) reported retro-eclogites in the Liberdade nappe that record maximum pressures of 17.5 kbar at  $T \sim 660$  °C. Garcia and Campos Neto (2003) report the highest pressures observed for SBO rocks so far, of 18.5 kbar at 820 °C. Trouw (2008) proposed that rocks from Virgínia, SE of Pouso Alegre, reached eclogitic facies based on their clinopyroxene-garnet composition and that plagioclase is secondary, occurring only in the corona. Parkinson et al. (2001) reported coesite as inclusion in zircon in kyanite-garnet-hypersthene granulites from the Varginha nappe NW of Pouso Alegre. However, no spectroscopic details were provided to support this finding.

Protolith ages of the retro-eclogite vary between ca. 1.5 Ga and 670 Ma (Campos Neto et al., 2011; Coelho et al., 2017; Trouw, 2008). Metamorphic ages obtained by U-Pb dating on zircon of ca. 670 Ma are associated to subduction (Reno et al., 2009). This data, however, has been

challenged by Coelho et al., (2017), who provided an age of 625 Ma for eclogitization related to continental collision.

## **2.4 Tectonic evolution models**

The orogenic evolution of the southern portion of the SBO has been explained by two different tectonic models: the orogen migration and interference of orogens.

### **2.4.1 Orogen migration**

In the studies from Campos Neto et al., (2010; 2011), the evolution of the area is related to a single orogeny, the Brasília orogeny. The formation of the collision nappe pile thereby was diachronic and resulted from a continuous outward migration of the orogen towards the São Francisco craton. This is based on the distribution of progressively younger metamorphic ages (monazite) towards the east. Therefore, lower nappes register younger metamorphic ages (590–575 Ma) than upper ones (618–595 Ma) within the Andrelândia nappe system. The evolution proceeded over 40 m.y. and was mainly controlled by a process similar to channel flow suggested by Beaumont et al. (2001, 2004) for the orogenic middle and lower crust of the Himalayan-Tibetan Orogen.

### **2.4.2 Interference of orogens**

A second model ascribes contrasting directions of tectonic transport and metamorphic polarities to an interference zone formed by the collision between the Brasília and Ribeira (younger) orogens, in which the superposition of structures and metamorphism are delimited (Heilbron et al., 2008; Peternel et al., 2005; Trouw et al., 2000, 2013). According to these authors sillimanite growth is related to the collision event with the Ribeira orogen at around 590–550 Ma, while Campos Neto et al. (2011) interpret it as a result of decompression.

## **2.5 References**

Alkmim, F.F., Marshak, S., Fonseca, M.A., 2001. Assembling West Gondwana in the Neoproterozoic; clues from the Sao Francisco Craton region, Brazil. *Geology* 29, 319–322.

Alkmim, F.F., Teixeira, W. 2017. The Paleoproterozoic Mineiro Belt and the Quadrilátero Ferrífero. Southern Brasília Belt. In: Helibron, M., Cordani, U.G., Alkmim, F.F. (Eds), *São Francisco Craton, Eastern Brazil*. Springer International Publishing, Switzerland, pp. 71–97.

- Basei, M.A.S., Siga Jr., O., Sato, K., Sproesser, W.M., 1995. A metodologia urânio-chumbo na Universidade de São Paulo: princípios metodológicos, aplicações e resultados obtidos. *Anais da Academia Brasileira de Ciências* 67 (2), 221–237.
- Belém, J., Pedrosa-Soares, A.C., Noce, C.M., da Silva, L.C., Armstrong, R., Fleck, A., Gradim, C.T., Queiroga, G.N., 2011. Bacia precursora versus bacias orogênicas: exemplos do Grupo Andrelândia com base em datações U-Pb (LA-ICP-MS) em zircão e análises litoquímicas. *Geonomos* 19, 224–243.
- Brito Neves, B.B., Campos Neto, M.C., Fuck, R.A., 1999. From Rodinia to Western Gondwana: an approach to the Brasiliano-Pan African cycle and orogenic collage. *Episodes* 22, 155–166.
- Campos Neto, M.C., 2000. Orogenic systems from SW-Gondwana: an approach to Brazilian-Pan African cycle and orogenic collage in SE-Brazil. In: Cordani, U., Thomaz Filho, A., Milani, E.J. (Eds.), *Tectonic Evolution of South America*, CPRM1, pp. 335–365.
- Campos Neto, M.C.; Figueiredo, M.C.H., 1995. The Rio Doce orogeny, southeastern Brazil. *Journal South American Earth Sciences* 8(2), 143–162.
- Campos Neto, M.C., Janasi, V.A., Caby, R., 1996. Ocorrência de granulitos empobrecidos nas porções basais a Nappe de Empurrão Socorro–Guaxupé. *Boletim do IG-USP* 18, 11–14.
- Campos Neto, M.C., Caby, R., 1999. Neoproterozoic high-pressure metamorphism and tectonic constraint from the nappe system south of the São Francisco Craton, southeast Brazil. *Precambrian Research* 97 (1–2), 3–26.
- Campos Neto, M.C., Caby, R., 2000. Lower crust extrusion and terrane accretion in the Neoproterozoic nappes of southeast Brazil. *Tectonics* 19, 669–687.
- Campos Neto, M.C., Basei, M.A.S., Vlach, S.R.F., Caby, R., Szabó, G.A.J., Vasconcelos, P., 2004. Migração de orógenos e superposição de orogêneses: um esboço da colagem Brasileira no sul do Cráton do São Francisco, SE e Brasil. *Geologia USP Série Científica* 4 (1), 13–40.
- Campos Neto, M.C., Janasi, V.A., Basei, M.A.S., Siga Junior, O., 2007. Sistema de Nappes Andrelândia, setor oriental: Litoestratigrafia e posição estratigráfica. *Revista Brasileira de Geociências* 37 (4), 47–60.
- Campos Neto, M.C., Cioffi, C.R., Moraes, R., Motta, R.G., Siga Jr., O., Basei, M.A.S., 2010. Structural and metamorphic control on the exhumation of high-P granulites: the Carvalhos Klippe example, from the oriental Andrelândia Nappe system, southern portion of the Brasília Orogen, Brazil. *Precambrian Research* 180, 125–142.
- Campos Neto, M.C., Basei, M.A.S., Assis Janasi, V.d., Moraes, R., 2011. Orogen migration and tectonic setting of the Andrelândia Nappe system: An Ediacaran western Gondwana collage, south of São Francisco craton. *Journal of South American Earth Sciences* 32, 393–406.

- Cioffi, C.R., Campos Neto, M.C., Rocha, B.C., Moraes, R., Henrique-Pinto, R., 2012. Geochemical signatures of metasedimentary rocks of high-pressure granulite facies and their relation with partial melting: Carvalhos Klippe, Southern Brasília Belt, Brazil. *Journal of South American Earth Sciences* 40, 63-76.
- Cioffi, C.R., Campos Neto, M.C., Möller, A., Rocha, B.C., 2016a. Paleoproterozoic continental crust generation events at 2.15 and 2.08 Ga in the basement of the southern Brasília Orogen, SE Brazil. *Precambrian Research* 275, 176–196.
- Cioffi, C. R.; Campos Neto, M. C., Möller, A., Rocha, B. C. 2016b. Tectonic significance of the Meso- to Neoproterozoic complexes in the basement of the southern Brasília Orogen. *Precambrian Research* 287, 91–107.
- Coelho, M.B., Trouw, R.A.J., Ganade, C.E., Vinagre, R., Mendes, J.C., Sato, K., 2017. Constraining timing and P-T conditions of continental collision and late overprinting in the Southern Brasília Orogen (SE-Brazil): U-Pb zircon ages and geothermobarometry of the Andrelândia Nappe System. *Precambrian Research* 292, 194–215.
- Cordani, U.G., Brito Neves, B.B. de B., Fuck, R.A., Thomaz Filho, A. and Cunha, F. M. B., 1984, Estudo preliminar de integração do Pré-Cambriano com os eventos tectônicos da Bacias Sedimentares Brasileiras. *Revista Ciência-Técnica-Petróleo. Seção Exploração de Petróleo. Petrobrás/Cenpes/Sintep, Publicação*15, p. 70.
- Cordani, U. G., Brito-Neves, B. B., D'Agrella-Filho, M. S., 2003. From Rodinia to Gondwana: a review of the Available Evidence from South America. *Gondwana Research* 6(2), 275–283.
- Degler, R., Zogheib, F.F., Martins, L.C.D., Novo, T., 2015. Geologia das Folha Nova Resende (SF.23-V-D-I) 1:100.000. Projeto Fronteiras de Minas, CODEMIG-UFMG, Belo Horizonte, Brazil.
- Farina, F., Capucine, A., Lana, C., 2015. The Neoproterozoic transition between medium and high-K granitoids: Clues from the southern São Francisco Craton (Brazil). *Precambrian Research* 266, 375–394.
- Fuck, R., Pimentel, M., Alvarenga, C.J.S., Dantas, E.L., 2017. The Northern Brasília Belt. In: Helibron, M., Cordani, U.G., Alkmim, F.F. (Eds), *São Francisco Craton, Eastern Brazil*. Springer International Publishing, Switzerland, pp. 189–205.
- Garcia, M.G.M., Campos Neto, M.C., 2003. Contrasting metamorphic conditions in the Neoproterozoic collision-related Nappes south of Sao Francisco Craton, SE Brazil. *Journal of South American Earth Sciences* 15 (8), 853–870.
- Hackspacher, P.C., Fetter, A.H., Ebert, H.D., Janasi, V.A., Dantas, E.L., Oliveira, M.A.F., Braga, I.F., Negri, F.A. 2003. Magmatismo há ca. 660-640 Ma no Domínio Socorro: registros de

convergência pré-colisional na aglutinação do Gondwana Ocidental. *Geologia USP, Série Científica* 3, 85–96.

Del Lama, E.A., Zanardo, A., Oliveira, M.A.F., Morales, N., 2000. Exhumation of high pressure granulites of the Guaxupé complex, southeastern Brazil. *Geological Journal* 35, 231–249.

Laux, J.H., Pimentel, M.M., Dantas, E.L., Armstrong, R., Junges, S.L. 2005. Two Neoproterozoic crustal accretion events in the Brasília Belt, central Brazil. *Journal of South American Earth Sciences* 18, 183–198.

Mantovani, M.S.M., Brito-Neves, B.B., 2005. The Paranapanema lithospheric block: its importance for Proterozoic (Rodinia, Gondwana) supercontinent theories. *Gondwana Research* 8 (3), 303–315.

Mantovani, M. S. M., Brito-Neves, B. B., 2009. The Paranapanema Lithospheric Block: its nature and role in the Accretion of Gondwana. In: Gaucher, C.; Sial, A.; Halverson, G.; Frimmel, H. (Eds.), *Neoproterozoic-Cambrian Tectonics, Global Change and Evolution: A Focus on South Western Gondwana*. Elsevier, Amsterdam, 2009. pp. 257–272.

Martins, L.C.D., 2016. Evidências de reciclagem crustal durante a gênese do arco Socorro na zona de interferência entre as Faixas Brasília e Ribeira, SE do Brasil. MSc dissertation, Universidade Federal de Minas Gerais, p. 136.

Morais, S.N., 1999a. Programa Levantamentos Geológicos Básicos do Brasil: Integração Geológica da Folha Campinas. (Escala) 1:250.000 SF-23-Y-A. Estados de São Paulo e Minas Gerais (Nota Explicativa) – São Paulo – CPRM, p. 26.

Morais, S.N., 1999b. Programa Levantamentos Geológicos Básicos do Brasil: Integração Geológica da Folha Guaratinguetá. (Escala) 1:250.000 SF-23-Y-B. Estados de São Paulo e Minas Gerais (Nota Explicativa) – São Paulo – CPRM, p. 28.

Milani, E. J. Evolução tectono-estratigráfica da Bacia do Paraná e seu relacionamento com a geodinâmica fanerozoica do Gondwana sul-ocidental. 1997. PhD thesis, Universidade Federal do Rio Grande do Sul. In: Mantovani, M. S. M., Brito-Neves, B. B., 2009. The Paranapanema Lithospheric Block: its nature and role in the Accretion of Gondwana. In: Gaucher, C.; Sial, A.; Halverson, G.; Frimmel, H. (Eds.), *Neoproterozoic-Cambrian Tectonics, Global Change and Evolution: A Focus on South Western Gondwana*. Elsevier, Amsterdam, 2009. pp. 257–272.

Mora, C.A.S., Campos Neto, M.C., Basei, M.A.S., 2014. Syn-collisional lower continental crust anatexis in the Neoproterozoic Socorro–Guaxupé Nappe System, southern Brasília Orogen, Brazil: constraints from zircon U-Pb dating, Sr-Nd-Hf signatures and whole-rock geochemistry. *Precambrian Research* 255, 847–864.



- Nascimento, M.B. 2010. Evolução Metamórfica P-T-t da Porção Norte do Complexo Guaxupé na Região de Arceburgo-Santa Cruz da Prata, MG. PhD thesis, Universidade Estadual Paulista “Júlio de Mesquita Filho”, p. 162.
- Parkinson, C.D., Motoki, A., Onishi, C.T., Maruyama, S., 2001. Ultrahigh-pressure pyrope kyanite granulites and associated eclogites in Neoproterozoic Nappes of Southeast Brazil. UHPM Workshop. Waseda University, pp. 87–90.
- Peixoto, E.I.P., Falci, A., Noronha, R.C., Degler, R., Martins, L.C.D., Nassif, M.T., Freitas, A.R., Novo, T., 2015. Geologia das Folhas Andradas (SF.23-Y-A-III) e Ouro Fino 1:100.000 (SF.23-Y-B-I). Projeto Fronteiras de Minas, CODEMIG-UFMG, Belo Horizonte, Brazil.
- Perrota, M.M., 1991. A Faixa Alto Rio Grande na região de São Gonçalo do Sapucaí, MG. MSc dissertation, IGc-USP, p. 158.
- Peternel, R., 2005. A zona de superposição entre as Faixas Brasília e Ribeira na região entre Caxambu e Pedralva, sul de Minas Gerais. PhD Thesis. Instituto de Geociências – UFRJ, p. 257.
- Pimentel, M.M.; Fuck R.A., 1992. Neoproterozoic crustal accretion in central Brazil. *Geology* 20, 375–379.
- Pimentel, M.M., Fuck, R.A., Gioia, D.M.C.L., 2000. The Neoproterozoic Goiás Magmatic Arc, Central Brazil: A review and new Sm-Nd isotopic data. *Revista Brasileira de Geociências*, 30, 35–39.
- Renne, P.R., Ernesto, M., Pacca, I.G., Coe, R.S., Glen, J.M., Prevot, M., Perrin, M., 1992. The age of the Parana flood volcanism, rifting of Gondwanaland, and the Jurassic–Cretaceous boundary. *Science* 258, 975–979.
- Ribeiro, A., Trouw, R.A.J., Andreis, R.R., Paciullo, F.V.P., Valença, J.G., 1995. Evolução das bacias proterozóicas e o termo-tectonismo brasileiro na margem sul do cráton do São Francisco. *Revista Brasileira de Geociências* 25, 235–248.
- Ribeiro, A., Nascimento, D., Bongioiolo, E., Trouw, R., Polo, H., Tavares, F., Nepomuceno, F., 2010. Geologia da Folha Pouso Alegre (SF.23-Y-B-II) 1:100.000. Programa Geologia do Brasil, CPRM-UFRJ, Rio de Janeiro, Brazil.
- Ribeiro, A., Nascimento, D., Campos, M.T., Oliveira, F., Rocha, F., 2010. Geologia da Folha Machado (SF.23-V-D-V) 1:100.000. Programa Geologia do Brasil, CPRM-UFRJ, Rio de Janeiro, Brazil.
- Ribeiro, A., Campos, M.T., Paciullo, F.V., Carvalho, M.V., Valeriano, C.M., Nascimento, D., 2010. Geologia da Folha Alfenas (SF.23-V-D-II) 1:100.000. Programa Geologia do Brasil, CPRM-UFRJ, Rio de Janeiro, Brazil.

- Rocha, B.C. 2016. Idade, duração e condições P-T do metamorfismo de temperatura ultra-alta, anatexia e cristalização de fundido na nappe Socorro-Guaxupé. PhD thesis, Universidade de São Paulo, p. 229.
- Rocha, B. C., Moraes, R., Möller, A., Cioffi, C. R., Jercinovic, M.J., 2017. Timing of anatexis and melt crystallization in the Socorro-Guaxupé Nappe, SE Brazil: insights from trace element composition of zircon, monazite and garnet coupled to U-Pb geochronology. *Lithos* 277, 337–355.
- Tedeschi, M., Novo, T., Azevedo, R., Amaral, L.F.S., Degler, R., Viera, P.L.N.C.R., 2015. Geologia das Folha Caldas (SF.23-V-D-IV) e Poços de Caldas (SF.23-V-C-VI) 1:100.000. Projeto Fronteiras de Minas, CODEMIG-UFMG, Belo Horizonte, Brazil.
- Trouw, R.A.J., 1992. Evolução tectônica do sul do Cráton do São Francisco baseada em análise metamórfica. *Congresso Brasileiro de Geologia*, 37, pp. 327.
- Trouw, R.A.J., Heilbron, M., Ribeiro, A., Paciullo, F., Valeriano, C.M., Almeida, J.C.H., Tupinambá, M., Andreis, R.R., 2000. The central segment of Ribeira belt. In: Cordani, U.G., Milani, E.J., Thomaz Filho, A., Campos, D.A. (Eds.), *Tectonic Evolution of South America*. 31th International Geological Congress. Rio de Janeiro, Brazil, pp. 287–310.
- Trouw, C. C., 2008. Mapeamento da Folha Virgínia–MG, Geocronologia U-Pb (SHRIMP) em zircões e interpretação geotectônica. PhD Thesis, Universidade do Rio de Janeiro, p.127.
- Trouw, R.A.J., Nunes, R.P.M., Castro, E.M.O., Trouw, C.C., Matos, G.C., 2008. Nota explicativa das Folhas Varginha (SF.23-V-D-VI) e Itajubá (SF.23-Y-B-III). Programa Geologia do Brasil. Contrato CPRM-UFRJ, p. 99.
- Trouw, R.A.J., Peternel, R., Ribeiro, A., Heilbron, M., Vinagre, R., Duffles, P., Trouw, C.C., Fontainha, M., Kussama, H.H., 2013. A new interpretation for the interference zone between the southern Brasília belt and the central Ribeira belt, SE Brazil. *Journal of South American Earth Sciences* 48, 43–57.
- Valeriano, C., 2017. The Southern Brasília Belt. In: Heilbron, M., Cordani, U.G., Alkmim, F.F. (Eds), *São Francisco Craton, Eastern Brazil*. Springer International Publishing, Switzerland, pp. 189–205.
- Vinagre R., Trouw R.A.J., Mendes J.C., Duffles P., Peternel R., Matos, G., 2014. New Evidence of a Magmatic Arc in the Southern Brasília Belt, Brazil: The Serra da Água Limpa Batholith (Socorro-Guaxupé Nappe). *Journal of South American Earth Science* 54, 120–139.
- Wernick, E., Penalva F., 1980. Contribuição à geologia do Grupo Pinhal (SP e MG). *Revista Brasileira de Geociências* 10(1), 43–62.
- Westin, A., Campos Neto, M.C., Hawkesworth, C.J., Cawood, P.A., Dhuime, B., Delavault, H., 2016. A Paleoproterozoic intra-arc basin associated with a juvenile source in the southern Brasília

Orogen: application of U–Pb and Hf–Nd isotopic analyses to provenance studies of complex areas. *Precambrian Research* 276, 178–193.

Zogheib, F.F., Degler, R., Martins, L.C.D., Novo, T., 2015. Geologia das Folhas Guaxupé (SF.23-V-C-III) 1:100.000. Projeto Fronteiras de Minas, CODEMIG-UFMG, Belo Horizonte, Brazil.

### 3 Constraining the petrochronological evolution of garnet-free UHT granulites in the Guaxupé nappe (SE Brazil): from subduction to collision

Mahyra Tedeschi<sup>1,2\*</sup>, Antônio Pedrosa-Soares<sup>1#</sup>, Ivo Dussin<sup>1,3#</sup>, Pierre Lanari<sup>4</sup>, Tiago Novo<sup>1</sup>, Marco Aurélio P. Pinheiro<sup>2</sup>, Cristiano Lana<sup>5#</sup>, Daniel Peters<sup>6</sup>

<sup>1</sup> Programa de Pós-Graduação em Geologia, Universidade Federal de Minas Gerais, IGC-CPMTC, Av. Antônio Carlos 6627, Belo Horizonte, Brazil

<sup>2</sup> Geological Survey of Brazil (CPRM), Avenida Brasil 1731, Belo Horizonte, MG, Brazil

<sup>3</sup> Faculdade de Geologia, Multilab, Universidade do Estado do Rio de Janeiro, R. São Francisco Xavier 524, Rio de Janeiro, Brazil

<sup>4</sup> Institute of Geological Sciences, University of Bern, Baltzerstrasse 1-3, Bern, Switzerland

<sup>5</sup> Laboratório de Geoquímica Isotópica, Universidade Federal de Ouro Preto, Campus do Cruzeiro, Ouro Preto, Brazil

<sup>6</sup> Institut de Recherche en Astrophysique et Planétologie (IRAP), Observatoire Midi-Pyrénées (OMP), CNRS, 14 avenue Edouard Belin, 31400 Toulouse, France

\*Corresponding author: mahyra.tedeschi@cprm.gov.br

Fellow of the Brazilian Research Council (CNPq)

#### Highlights:

- Arc-related UHT-metamorphism in the Southern Brasília orogen
- Long-lived metamorphic event of ~80 m.y.
- Magmatic timing (790–640 Ma) in the Guaxupé nappe
- 2.55 Ga juvenile basement in the Southern Brasília orogen
- *In situ* low grade and allochthonous anatexis recorded by <sup>176</sup>Hf/<sup>177</sup>Hf

### 3.1 Abstract

High to ultra-high temperature metamorphic rocks can provide valuable Pressure-Temperature-time ( $P$ - $T$ - $t$ ) and protolith information despite frequently disturbed isotopic systems and the presence of retrogressed assemblages. Such information can be difficult to obtain for mafic protoliths, in which accessory chronometers and metamorphic index minerals are scarce. In this study the timing of magmatism and metamorphism of mafic to felsic protoliths has been investigated using U-Pb dating, Lu-Hf and trace element signatures of zircon, as well as the metamorphic temperature conditions from banded mafic granulites. The coupling of U-Pb and Lu-Hf analyses on zircon permitted to identify relicts of juvenile Neoproterozoic basement in the Guaxupé nappe. Igneous crystallization ages of 790 Ma, 690 Ma and 660 Ma were obtained for the mafic to felsic rocks. Metamorphic ages of the orthopyroxene-clinopyroxene and (hornblende)-biotite-bearing leucosomes, as well as metamorphic rims in protolith zircons reveal a long-lived metamorphic event (ca. 670–590 Ma) partially coeval with the intrusion of mafic magma (ca. 660 Ma). Conventional thermometry on zoned clinopyroxene and orthopyroxene yields temperatures in the range of 1000–900 °C, recording UHT peak conditions. Hornblende-plagioclase-quartz assemblage formed during the retrogression at ~740° C and ~6 kbar. Three metamorphic stages have been identified by comparing the results with those from previous studies: (i) a pre-collisional to collisional (670–640 Ma), (ii) a subduction to collision (640–630 Ma), and (iii) a decompression-related (630–590 Ma) accompanied by widespread partial melting. The UHT-metamorphism most likely proceeded from 670 Ma to 630 Ma. The short time gap (10–20 m.y.) between the magmatic and metamorphic events, the close association of UHT rocks with mafic magmas, and the age distributions suggest that the UHT metamorphism in the Southern Brasília orogen was related to the development of a magmatic arc.

**Keywords:** Petrochronology; Zircon U-Pb and Lu-Hf; UHT metamorphism; Guaxupé nappe; Southern Brasília orogen; Paranapanema block

## 3.2 Introduction

Identifying protoliths and reconstructing the metamorphic history of rocks that experienced ultrahigh-temperature (UHT) metamorphism is particularly challenging. This type of metamorphism can affect both the appearance and the composition of a rock due to major mineral reactions, overstepping of elemental and isotopic closure temperatures and open systems behavior. Melting and melt extraction are for example known to fractionate chemical components, and perturb isotopic systems (Kelsey and Hand, 2015; Taylor et al., 2016). The estimation of metamorphic conditions, rates and durations of such processes (i.e.,  $T-t$  and  $P-T-t$  paths), can provide valuable insights on the tectonic settings and the causes of UHT metamorphism (Harley, 2016; Kelsey et al., 2008; Kelsey and Hand, 2015), as it may help to unravel pre-metamorphic origins (Kemp et al., 2007; Möller et al. 2003; Stepanov et al., 2016).

Geochronometers are pivotal for the investigation of tectonometamorphic processes, as they permit to constrain both their duration and rate. Even zircon, generally considered as a robust accessory mineral, can lose its time records under UHT conditions (Cherniak and Watson, 2003). Examples of both, preserved (Drüppel et al., 2013; Ewing et al., 2013; Möller et al., 2003) and (partially-) reset, ages (Stepanov et al., 2016; Wang et al., 2017) have been described for HT to UHT terranes. The spreading of U-Pb zircon data along the concordia or along a discordia sub-parallel to the concordia is common (Rocha et al., 2017; Vervoort and Kemp, 2016; Wang et al., 2017; Whitehouse and Kemp, 2010) and has been interpreted as long duration metamorphic event or partial resetting (Rubatto, 2017; Taylor et al., 2016; Vervoort and Kemp, 2016).

The original protolith composition and subsequent melt and fluid-rock interactions affect the stable mineral assemblage used to retrieve the  $P-T-t$  information (Rubatto, 2017; Taylor et al., 2016). Partial melting, involving incongruent reactions and interaction between melts and fluids, can add further complexity to these already challenging complex local bulk systems (e.g. Lanari and Engi, 2017). Temperature – and also pressure – conditions are commonly obtained from Mg- and Al-rich rocks, which can contain unequivocal UHT mineral assemblages such as sapphirine + quartz (e.g., Baldwin et al., 2005; Kelsey et al., 2004; Santosh et al., 2007) or orthopyroxene + sillimanite ± quartz (e.g., Kelly and Harley, 2004; Moraes and Fuck, 2000). Less attention has been paid to the associated garnet-free mafic granulites as they are free of diagnostic UHT mineral. In such context, the UHT conditions are often inferred based on thermobarometry applied to the associated rocks (Kelsey, 2008; Kelsey and Hand, 2015). Mafic granulites usually contain pyroxene interpreted to have an igneous origin, preventing the use of pyroxene-thermometry (Kelsey, 2008). Recently, Yang and Wei (2017) showed that major element-based thermometers for mafic granulites may underestimate the predicted temperatures compared to REE-based thermometers (Liang et al., 2013; Sun and Liang, 2015), especially for garnet-free clinopyroxene-

orthopyroxene granulites. This was attributed to the partial resetting of Fe-Mg exchange thermometers by diffusion as previously discussed by Bègin and Pattison (1994). In addition, mafic bulk-rock composition does not favor the crystallization of accessory minerals such as monazite and allanite, which can play an important role, since can be used to derive either time or temperature constraints.

In order to solve these problems, different strategies have been developed and employed. Concerning the interpretation of complex U-Pb data, an examination and description of the full range of age data is critical if one wants to retrieve the duration and thermal intensity of metamorphism (Taylor et al., 2016). Coupling between U-Pb and Lu-Hf analyses in zircon have proven to be an efficient tool to assist understanding of the data spread in the Concordia (Vervoort and Kemp, 2016; Wang et al., 2017; Whitehouse and Kemp, 2010). Hf isotopic data also provide petrogenetic information in rocks that experienced changes during UHT metamorphism (i.e. migmatization or interaction with fluids), or in metasedimentary rocks (Belousova et al., 2002; Kemp et al., 2007). Metamorphic temperature of unfavorable assemblages obtained with Ti-in-zircon and clinopyroxene-orthopyroxene thermometry may represent at least minimum estimates (Kelsey and Hand, 2015; Taylor et al., 2016; Yang and Wei, 2017).

The complexity of such petrochronological investigations may explain why the P-T-t conditions of garnet-free granulites from the Guaxupé nappe in the Southern Brasília orogen (southeastern Brazil) remains unconstrained. The Guaxupé nappe is considered to mainly host remnants of a metamorphosed Neoproterozoic arc with associated sedimentary basins (Campos Neto and Caby, 1999, 2000; Campos Neto et al., 2011). The garnet-bearing gneisses of the nappe recorded a UHT metamorphism event with temperatures up to 1000 °C (Del Lama et al., 2000; Rocha, 2016). U-Pb zircon data obtained with different methods (e.g., TIMS, LA-ICP-MS) provided continuous concordant age data that spread over more than 100 Ma, for both, the gneisses and melting products, mostly interpreted based on the data clusters (Campos Neto and Caby, 2000; Mora et al, 2014; Rocha, 2016; Rocha et al., 2017).

In this study, the timing and processes involved in the generation and evolution of a series of mafic to intermediate rocks were investigated by combining (i) U-Pb geochronology, Lu-Hf and trace elements analyses of zircon, (ii) quantitative compositional mapping, (iii) conventional thermobarometry and (iv) Ti-in-zircon thermometry. This multi-method approach provides a strong basis to decipher the metamorphic history of the UHT mafic to intermediate granulites, and further constraints the tectonic settings and evolution of the Southern Brasília orogen.

### 3.3 Geological Setting

#### 3.3.1 General Framework

The Brasília orogenic system is a 1800 km-long nearly N-S trending belt, extending roughly between 10° and 26° S from northwestern to southeastern Brazil (Fig. 3.1A). It is one of the orogenic belts that formed during Western Gondwana amalgamation in the Neoproterozoic (Alkmim et al., 2001; Brito-Neves et al., 1999; Cordani et al., 2003; Fig. 3.1A). The northern and southern segments of the Brasília orogenic system evolved separately during the Brasiliano event, representing distinct collision zones against the northwest and southwest margins of the São Francisco craton (Valeriano et al., 2017). The Southern Brasília orogen resulted from the convergence and collision between the Paranapanema (active margin) and São Francisco (passive margin) paleocontinental blocks at around 630 Ma (Campos-Neto et al., 2011; Coelho et al., 2017; Mantovani and Brito-Neves, 2009; Trouw et al., 2013). During the collision stage, a complex framework of nappe systems verging to the east was formed (Campos Neto and Caby, 1999, 2000; Campos Neto et al., 2011; Trouw et al., 2000, 2013; Valeriano et al., 2017). Each nappe system comprises specific geotectonic domains with distinctive tectono-metamorphic features (Fig. 3.1B and C and Fig. 3.2).

The migmatized granulite and amphibolite facies rocks (Fig. 3.2) from the Guaxupé Nappe (GN) have been interpreted to represent a Neoproterozoic magmatic arc and associated sedimentary units that were thrust over the Andrelândia nappe system, which is mostly composed of metasedimentary rocks (Campos Neto and Figueiredo 1995; Campos Neto et al., 2011; Trouw et al., 2013). It has been suggested that rocks from the Guaxupé nappe constitute an extension of the Goiás magmatic arc, located in the central and northern part of the Brasília Orogen (e.g., Pimentel and Fuck, 1992; Pimentel et al., 2000). However, unlike the northern segment, older crystallization ages of around 800 Ma, as well as juvenile Lu-Hf and Sm-Nd signatures have hitherto not been recognized in the Socorro-Guaxupé nappe (Janasi, 1999; Mora et al., 2014; Rocha, 2016; Rocha et al., 2017; Vinagre et al., 2014).

Most part of the Paranapanema block (i.e., the arc basement), was covered by the volcanic and sedimentary rocks of the Paraná basin during the Cretaceous (Renne et al., 1992). This block was constrained from borehole data indicating ancient granitic rocks beneath the Paraná basin (Cordani et al., 1984), regional geophysical data and geochemical fingerprint derived of basaltic composition of volcanic rocks formed in the basin (Mantovani and Brito-Neves, 2005, 2009), and Paleoproterozoic U-Pb ages (ca. 2.1 Ga) from gneisses of the southernmost part of the Brasília orogen (Trouw, 2008).

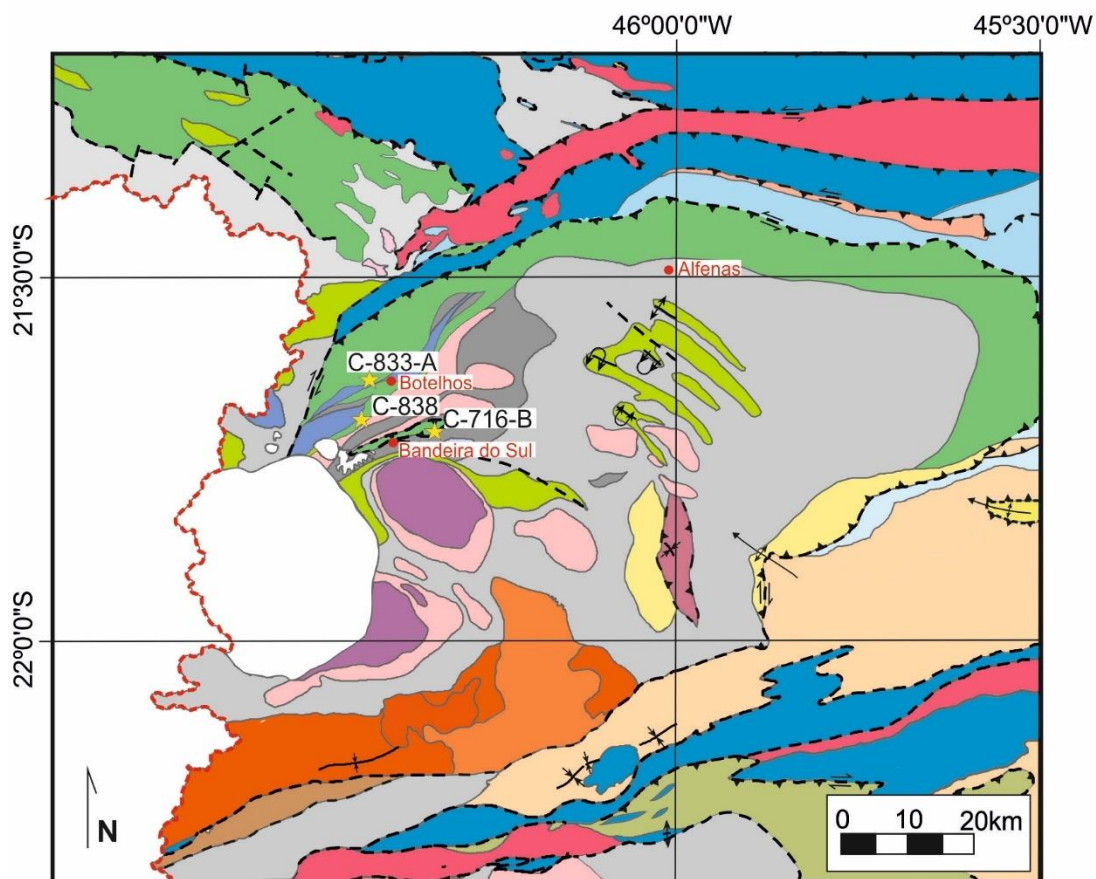




### 3.3.2 The Guaxupé nappe

The Socorro-Guaxupé nappe is divided into three main units: the granulitic, metatexitic and diatexitic units (Campos Neto and Caby, 2000; Fig. 3.1B). The granulitic unit can be roughly correlated to the Elói Mendes unit and occurs at the base of the nappe system and as tectonic lenses encompassed by the migmatites from the São João da Mata unit (Tedeschi et al., 2015). The Elói Mendes unit mainly comprises banded felsic to mafic (garnet)-orthopyroxene-clinopyroxene-bearing granulites, with concordant intercalations of charnockitic and enderbitic leucosomes interpreted as result of anhydrous anatexis, and veins and patches of pink hornblende-bearing granitic leucosome (Campos Neto et al., 2000; Mora et al., 2014; Rocha et al., 2017; Tedeschi et al., 2015). The metatexitic and diatexitic units roughly correspond to the São João da Mata unit (Fig. 3.2), which mainly consists of (orthopyroxene)-(hornblende)-biotite and (orthopyroxene)-(garnet)-biotite migmatites, and minor metasedimentary rocks (e.g., kinzigite, schist, quartzite; Campos-Neto and Caby, 2000; Ribeiro et al., 2011a; Rocha et al., 2017; Tedeschi et al., 2015). In this unit, a remarkable increase in the degree of anatexis from north (Botelhos city) to south (Bandeira do Sul; Fig. 3.2) is shown by the transition from metatexites to diatexites (Campos-Neto and Caby, 2000; Tedeschi et al., 2015).

The Guaxupé nappe has been interpreted as a former magmatic arc that formed on an active continental margin (Campos-Neto and Figueiredo, 1995; Campos-Neto and Caby, 2000; Rocha, 2016). The arc magmatism has been ascribed to a period between 730 and 640 Ma (Hackspacher et al., 2003; Mora et al., 2014; Rocha, 2016). Clusters of concordant U-Pb ages suggest a main period of pre-collisional magmatism around 655-650 Ma (Rocha, 2016). These rocks later experienced UHT metamorphism at 630-625 Ma (Rocha et al., 2017). Ages of ca. 610 Ma from soccer-ball zircons were attributed to retrograde cooling stage (Mora et al., 2014) and post-collisional emplacement of syenitic bodies (Töpfer, 1996). Conventional thermobarometry applied to orthopyroxene-garnet granulites from the granulitic unit provided peak *P-T* conditions of 900 °C and 12 kbar (Rocha, 2016) and 1040 °C at 14 kbar (Del Lama et al., 2000). These conditions were either attributed to metamorphism that took place in the deep root of the magmatic arc (Campos Neto and Caby, 2000; Campos Neto et al., 2004), or associated to thickened crust and minor mafic magma underplating during the collision (Rocha, 2016). Peak *P-T* conditions of 1030 °C and 11.7 kbar were obtained for the paraderived garnet-orthopyroxene migmatites from the metatexitic unit (Rocha et al., 2017).



### Cretaceous

- Poços de Caldas Alkaline Intrusion

### Cryogenian-Ediacaran

#### Socorro-Guaxupé nappe

- Late and Post-orogenic syenites
- Pinhal Ipuiúna Batholith - *(Hbl)-Bt* granitoid
- Botelhos Leucogranite - *Anatetic leucogranite*
- Serra da Água Limpa Granite  
*Anatetic (Hbl)-Bt and (Grt)-Bt* granites
- Charnockite suit - *Opx-bearing* rocks
- Paiolinho Orthogneiss  
*Hbl-Bt (augen) gneiss, locally Opx-bearing*
- Cachoeira de Minas complex  
*Cpx-Grt-Hbl orthogneiss, locally quartzites*
- Paraderived São João da Mata unit  
*Migmatitic (Hbl)-Bt gneisses, locally Sil-bearing*
- São João da Mata unit  
*Migmatitic (Opx)-(Hbl)-Bt orthogneisses*
- Elói Mendes unit  
*Migmatitic Opx-Cpx-(Hbl)-(Grt) and (Cpx)-Grt granulites*
- Bela Vista Schist  
*Grt-Sil schist, quartzite and amphibolitic lens*

### Tonian-Ediacaran

#### Andrelândia nappe system

- Granites
- Arantina unit  
*Ky-Kfs gneiss and mafic granulites;  
Ky-Grt-Bt-Ms schist and amphibolites*
- São Vicente unit  
*Paragneisses, quartzite, Ms Schist,  
amphibolites and metaultramafic*

### Paleoproterozoic

- São Vicente complex
- Pouso Alegre complex
- Gaspar Lopes orthogneiss

### Archean

- Archean gneisses complexes  
*Orthogneisses and metaultramafic rocks*

**Figure 3.2:** Regional geological map of the studied area with location of analyzed samples (compiled and simplified from Degler et al., 2015; Fava et al., 2015; Peixoto et al., 2015; Ribeiro et al., 2010a, b, c; and Tedeschi et al., 2015; with inputs from Cioffi et al., 2016a, and Westin et al., 2016). Dashed red line indicates the limit between Minas Gerais (east) and São Paulo (west) states, and red labels refer to the cities mentioned in the text.

### 3.4 Sampling and Field relationship

Five samples were collected in the granulitic unit along a 15 km NW-SE section, from three large and fresh outcrops along the road cuts BR-146 and BR-267 (Fig 3.2; Location details are given in Table 3.1). In the studied area, the granulites (part of the Elói Mendes unit; Fig. 3.2) crop out either in the sheared branch of the outer border of the granulitic wedge or as a tectonic slice enveloped by the diatextitic unit (the São João da Mata unit of Tedeschi et al., 2015; Fig. 3.2). The outcrops reveal a transitional migmatitic granulite in which stromatic metatexites to Schöllén diatexites prevail in the northern part of the section (Figs. 3.3A and 3.3B). In the southern part Schöllén to nebulitic diatexites are the most common migmatitic structures. The stromatic metatexite consists of mm- to cm-thick sharp-layered migmatite that contains alternating fine-grained mesocratic (green) to melanocratic (dark-green) bands (granulite) and light-green medium-grained felsic bands (leucosome). The felsic bands exhibit coarse-grained peritectic orthopyroxene, clinopyroxene and/or hornblende (samples C-833-A and C-838-A; Figs. 3.3C and D). At the mesoscopic scale, a progressive gradation of the amount of light-green medium-grained leucosome is observed, characterized by an increase of its volume fraction from the bottom to the top of the outcrop. On the top, where leucosome prevails, the Schöllén diatexite is composed of centimetric to up to 2 meters long Schöllén. Two types of leucosomes are recognized in the Schöllén diatexites, the light-green enderbitic to charnockitic leucosome, and the pink to light gray (hornblende)-biotite-bearing leucosomes. Thus, the Schöllén diatexite contains: i) fine-grained mafic granulite or amphibolite (#1 in Fig. 3.3A), locally it constitutes a melanosome (#1 in Fig. 3.3D); ii) banded mafic granulite containing light-green bands of charnockitic leucosome (#2 in Fig. 3.3A); iii) light-green enderbitic to charnockitic leucosomes (#3 in Fig. 3.3A), and iv) pink to light gray (hornblende)-biotite-bearing leucosomes (#4 in Fig. 3.3A).

Both types of migmatite display folds and a foliation often cut either concordantly by leucosome layers or cross cut by mm- to m-thick veins. The layers of leucosome are the product of *in situ* and *in source* melting. The layers are connected to metric to decametric veins or batches of light-green charnockitic leucosome. The faint transition from the stromatic metatexite and the light-green enderbitic to charnockitic leucosomes suggests a feeding relationship. Locally, the light-green charnockitic rocks are, however, observed to cut and incorporate enclaves of the banded mafic granulite and mafic granulites (i.e., breccia), indicating a more complex genesis (Fig. 3B; sample C-838-A). Such type of structure suggests that part of the light-green enderbitic to charnockitic rocks are intrusive, and not necessarily correspond to *in source* leucosomes. The pink to light gray (hornblende)-biotite leucosomes often cut the host metatexite, exhibiting either sharp or faint transitions to the green leucosome that suggest local melt mixing. Local concordant centimetric to decimetric amphibolitic (plagioclase + hornblende, with retrograde biotite) layers can be found where the gneissic structure is preserved. Further south, the stromatic metatexite is rarely



observed, and Schöllén and nebulite diatexites are the most common types of rocks. The nebulite diatexites are medium to coarse-grained white granitic neosomes, usually containing peritectic euhedral hornblende and some Schlieren and Schöllén (Fig. 3H). Fine-grained mafic granulite enclaves of gabbroic composition with coarse-grained porphyroblasts of hornblende are cut by white hornblende-bearing leucosomes dykes/veins and resemble a magmatic breccia (Fig. 3G). The leucosomes veins have a greenish-greyish color in contact with the enclaves.

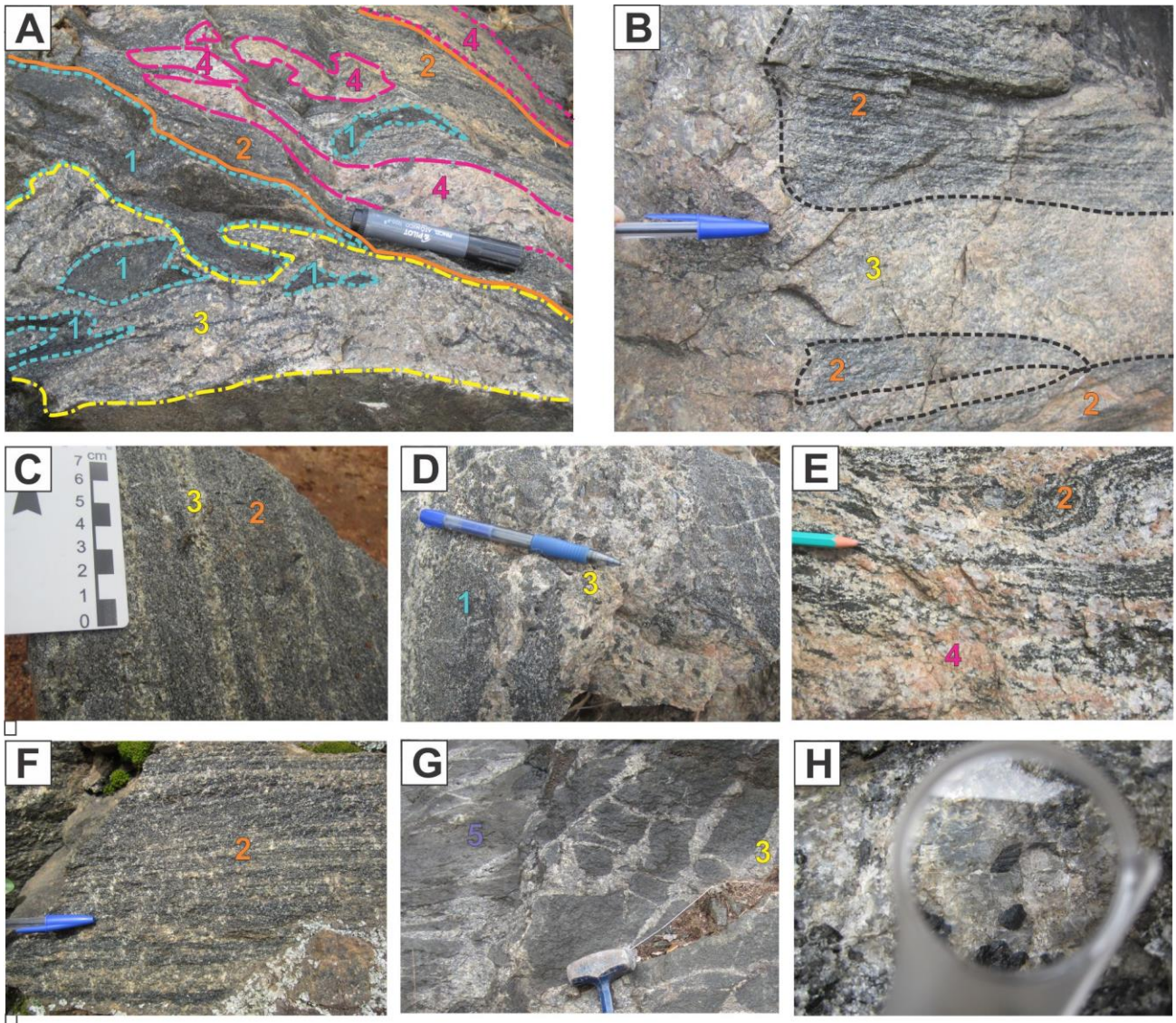


**Figure 3.3:** Field relationships of the studied rocks of the Granulitic - Elói Mendes unit (1) Mafic granulite (restite), (2) Banded mafic granulite, (3) light-green enderbitic to charnockitic leucosome, and (4) pinkish granitic (hornblende)-biotite-bearing leucosome and (5) mafic granulite enclave of gabbroic composition. (A) Schöllén diatexite from the northern part of the section. (B) Light-green opdalitic rock bearing enclaves of banded mafic granulite. Mesoscopic aspects of each sample: (C) Banded mafic granulite cut by concordant light-green charnockitic leucosome (C-838-A); (D) mafic Schöllén (restites) in charnockitic leucosome with peritectic orthopyroxene and clinopyroxene (C-838-2); (E) Schlieren of biotite and Scholle of stromatic metatexite in the pinkish granitic (hornblende)-biotite-bearing leucosome (C-838-B); (F) Banded mafic granulite (C-833-A); (G) Agmatic texture formed by the mafic granulite enclaves (gabbroic composition; sample C-716-B) in the diatexite; and (H) euhedral peritectic hornblende in the nebulitic diatexite.

**Table 3.1:** Summary details for the Guaxupé nappe samples. UTM coordinates are relative to the WGS84 datum. T - crystallization ages (see text for explanation); 1-temperature outliers; 2-Concordia age; \* Ambiguous source age, see text for details;  $\epsilon\text{Hf}$  calculated for grain individual  $^{207}\text{Pb}/^{206}\text{Pb}$  dates.

Sample	Lithology	UTM Coordinates		Mineral assemblage		Protolith			Metamorphism		T-(P) conditions			
		E	N	Major	Acces.	Minimum crystallization age (Ma)	$\epsilon\text{Hf}$	Ti-in-zircon (°C)	Data range (Ma)	$\epsilon\text{Hf}$	Ti-in-zircon T (°C)	T Peak (P) (°C)	T Retrog. (R1) (°C)	T and P Retrog. (R2) (°C and kbar)
C-833-A	Banded mafic granulite	354420	7605627	Hbl + Opx + Cpx + Pl + Kfs + Bt + Qz	Ilm + Ap + Zrn + Py	2559 ± 66	+2.7 – +10.0	~ 695–840 990; 1025 and ~1150 <sup>1</sup>	2405 ± 10 <sup>2</sup> ~590–680	n.a. -18.5 – -34.7	~590–715 ~680–740 ~878 and ~1135 <sup>1</sup>	n.a.	n.a.	n.a.
C-838-2	Opdalite	352305	7600153	Opx + Cpx + Hbl + Pl + Kfs + Bt + Qz	Zrn + Ap + Rt + Ilm	786 ± 10	-11.8 – -15.8	670–780	~630–690	-12.6 – -13.4	~690–700	998 ± 23	865 ± 38	740 ± 28 and ~6 kbar
C-838-A	Banded mafic granulite	352305	7600153	Hbl + Opx + Cpx + Pl + Kfs + Bt + Qz	Ilm + Ap + Zrn	691 ± 3	-8.2 – -12.6	~690–780 ~920 <sup>1</sup>	~570–670	-9.0 – -14.1	~700–830	n.a.	n.a.	n.a.
C-838-B	Granitic (Hbl)-Bt-bearing leucosome	352305	7600153	Bt + Pl + Kfs + Qz + Hbl	Rt + Ilm + Zrn + Py	2.7 Ga inherited grain*	-3.7*	n.a.	~580–680	-20.9 – -52.1	n.a.	n.a.	n.a.	n.a.
C-716-B	Mafic granulite enclave	361224	7597330	Opx + Cpx + Hbl + Pl + Bt	Ilm + Py + Ccp + Zrn + Qz + Ap	664 ± 9	-5.9 – -11.44	~710–810 1010 <sup>1</sup>	n.a.	n.a.	n.a.	n.a.	n.a.	n.a.

## 3.5 Petrography and mineral composition

The petrography and mineral chemistry are presented in the following section. The full dataset is provided in the Appendix II for sample C-833-A, C-838-A and C-838-B. The quantified X-ray map is provided for sample C-838-A. The analytical procedures are described in Appendix 3.A. The mineral abbreviations used follow Evans and Whitney (2010).

### 3.5.1 Banded mafic granulite (C-833-A)

The banded mafic granulite (C833-A) consists of alternating bands of fine-grained dark-green granulites (restite) and light-green charnockitic leucosomes, with faint contacts between the bands (Figs. 3.4A and 5B). The dark-green granulite exhibits a granonematoblastic texture and is composed of diopside-augite (5–8 vol%), hypersthene (5–8 %), oligoclase-andesine (50–60 %) and quartz (5 %). Retrograde hornblende (15–20 vol%) and late euhedral biotite flakes (10–15 %) partly replaced that assemblage. The granoblastic leucosome is essentially made of oligoclase (80 vol%), and quartz (10 %). The mafic minerals that constitute the granulite also make up around 10 vol% of the mineral modes in the leucosome. A regional foliation is defined by oriented mafic minerals in the mafic bands, and quartz ribbons in the leucosome. Quartz usually shows chessboard extinction. Ilmenite, apatite, zircon and pyrite are accessory minerals.

#### 3.5.1.1 *Petrographic interpretation*

In the banded mafic granulite C-833-A, the faint boundaries between the bands point towards physical interactions between leuco- and melanocratic bands. The following compositional and textural features support this interpretation: i) the mafic minerals in the leucosome and granulite (meso- to melanocratic bands) are the same; ii) the leucocratic phases in the granulite are texturally connected to the leucosome, suggesting that they were formed, at least partially, by in situ partial melting (Fig. 3.4).

### 3.5.2 Banded mafic granulite (C-838-A)

The banded mafic granulite (C-838-A) exhibits even fainter limits between the compositional bands when compared to C-833-A (Fig. 3.4B and 3.5A, B and C). Dark-green fine-grained granulitic bands composed of hornblende (25–30 vol%) and oligoclase-andesine (45–50



%), mainly display nematogranoblastic textures. Hypersthene and diopside-augite are minor phases with modal abundances of less than 5 vol% and as traces, respectively. Locally, the consumption of pyroxene by hornblende reveals the retrograde origin for the amphibole, which is overgrown by euhedral biotite (5 vol%) as the lower grade mineral. The charnockitic leucosome forms medium-grained domains. Medium-grained anhedral hypersthene (10 vol%) and diopside-augite (10–15 %), weakly aligned along the main banding, are placed in a granoblastic fabric comprising oligoclase (40–45 %) and quartz (35–40 %; Fig. 3.4B). Hornblende and biotite partially replaced pyroxene grains. Quartz exhibits chessboard extinction. Plagioclase commonly shows anti-perthitic exsolutions. Apatite, zircon and ilmenite are accessory minerals in both granulite and leucosome.

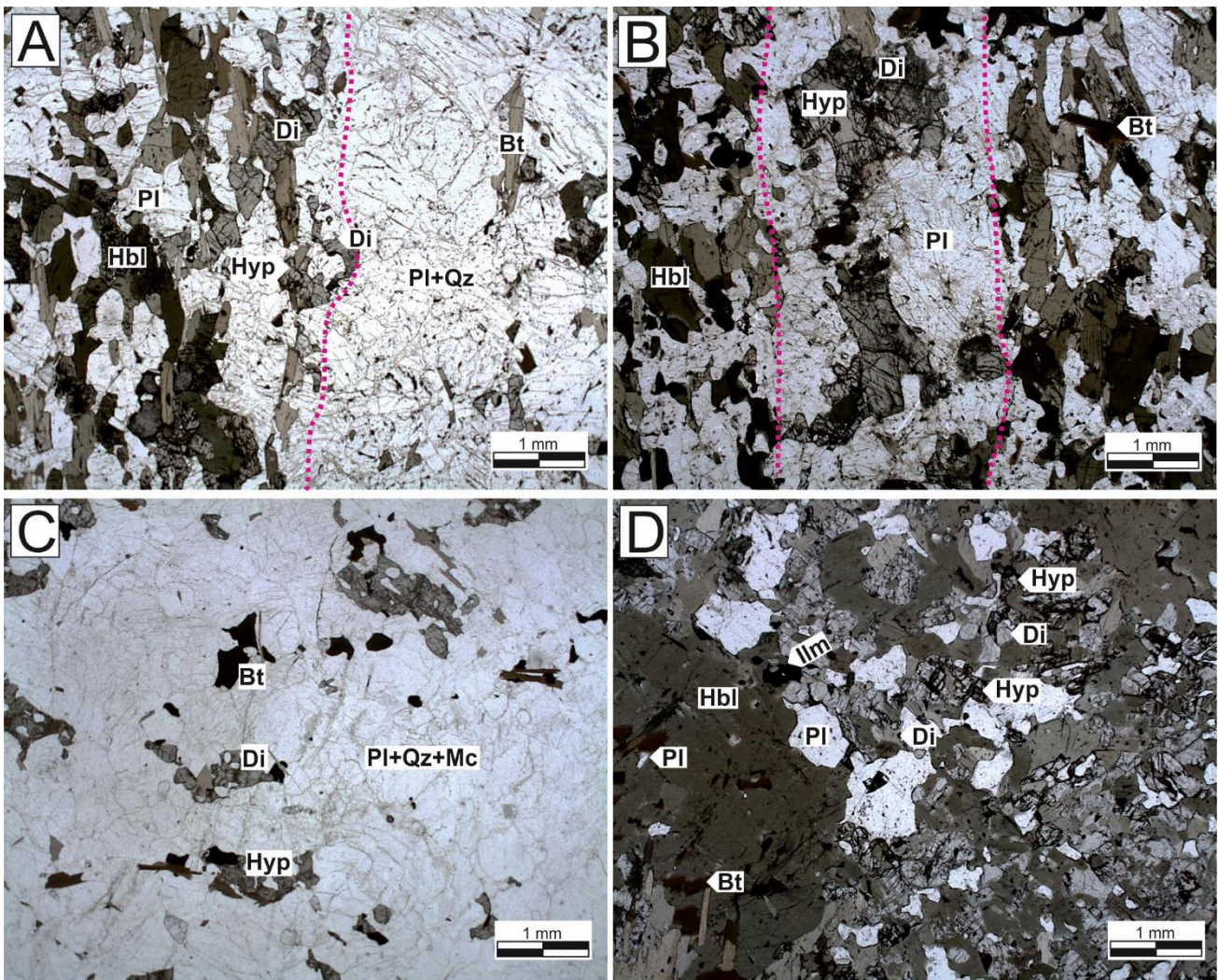


**Figure 3.4:** Transmitted light microphotographs of the studied samples. (A-B) Transition between the granulitic and green charnockitic leucosome in the different banded mafic granulite - the limits between the leucosome and melanosome bands are indicated by dashed pink lines, (A) leucosome with few orthopyroxene and clinopyroxene such as in C-833-A, (B) leucosome hosting peritectic orthopyroxene and clinopyroxene (C-838-A); (C) opdalite C-838-2 and (D) mafic granulite enclave with hornblende porphyroblasts (crystals have 2-4 mm).



### 3.5.2.1 Mineral compositions

To investigate compositional variability at the micrometer scale, X-ray compositional maps were acquired by electron probe micro-analysis (EPMA) for the banded mafic granulite C-838-A using 15 keV accelerating voltage, a specimen current of 100 nA and dwell times of 200 ms. The detailed analytical procedure is reported in Lanari et al. (2013, 2017). The semi-quantitative maps were standardized to maps of oxide weight percentage concentrations using internal standards (de Andrade et al., 2005) and the program XMAPTOOLS 2.3.1 (Lanari et al., 2014). Structural maps in atom per formula unit (a.p.f.u.) were used to investigate the local compositional variability of the mineral phases, as well as the mineral modes that were obtained from the classified map. The main compositional variations are caused by the size and microstructural position of the mineral phases in the leucosome and dark-green granulitic domains.

Hypersthene occurs mainly as medium- to coarse-grained grains in the leucosome and minor as fine-grained grains in the mafic granulitic bands. In the leucosome, hypersthene exhibits slight compositional zoning from core to rim ( $\text{En}_{56-51}\text{Fs}_{40-46}\text{MgTs}_4$ ), (Figs. 3.5D, E and F). These grains show a decrease in  $X_{\text{Mg}}$  ( $\text{Mg}^{2+}/(\text{Mg}^{2+}+\text{Fe}^{2+})$ ) from 0.58 in the core to 0.55 towards the rim. The classified image revealed that fine grains in the granulitic bands are entrapped in hornblende (Fig. 3.5B). These fine-grained inclusions also display a compositional zoning with  $X_{\text{Mg}} = 0.56$  in the core and  $X_{\text{Mg}} = 0.53$  in the rim.

Transmitted light petrography highlights medium-grained diopside in the leucosome (Fig. 3.5A). Sub-millimetric clinopyroxene occurs as rounded inclusions in big K-feldspar (Fig. 3.5B). The compositional maps show the presence of fine-grained diopside in the granulitic mafic bands included in hornblende or plagioclase. These diopside inclusions are locally found in contact with biotite (Figs. 3.5B and C). In the leucosome, diopside displays a compositional zoning from core to rim ( $\text{Di}_{62-68}\text{Hd}_{37-32}\text{Jd}_{7-4}$ ; Figs. 3.5E, F and G). Other compositional variations are  $X_{\text{Mg}}$  (from 0.63 to 0.70), Al and Na (Al = 0.10 a.p.f.u. and Na = 0.07 a.p.f.u.). In the mafic layers, diopside exhibit smaller compositional variations ( $\text{Di}_{63-65}\text{Hd}_{36-28}\text{Jd}_{6-4}$ ).

Amphibole has a very homogeneous composition close to pure hornblende (Al in the site M2 = 0.6 a.p.f.u.; Na = 0.59 a.p.f.u.; Ca = 1.8 a.p.f.u.; and  $X_{\text{Mg}} = 0.11$ ).

The classified map reveals that K-feldspar mainly occurs as clusters of medium-grained crystals forming lenses that are exclusively located in leucosome. K-feldspar also occurs as small grains included in plagioclase and in the borders of amphibole (Fig. 3.5B). At the contact with hornblende, larger K-feldspar grains usually contain fine-grained plagioclase and quartz inclusions, and occasionally clinopyroxene inclusions. The lenses are usually surrounded by plagioclase and the mafic phases from the leucosomes (Fig. 3.5B).

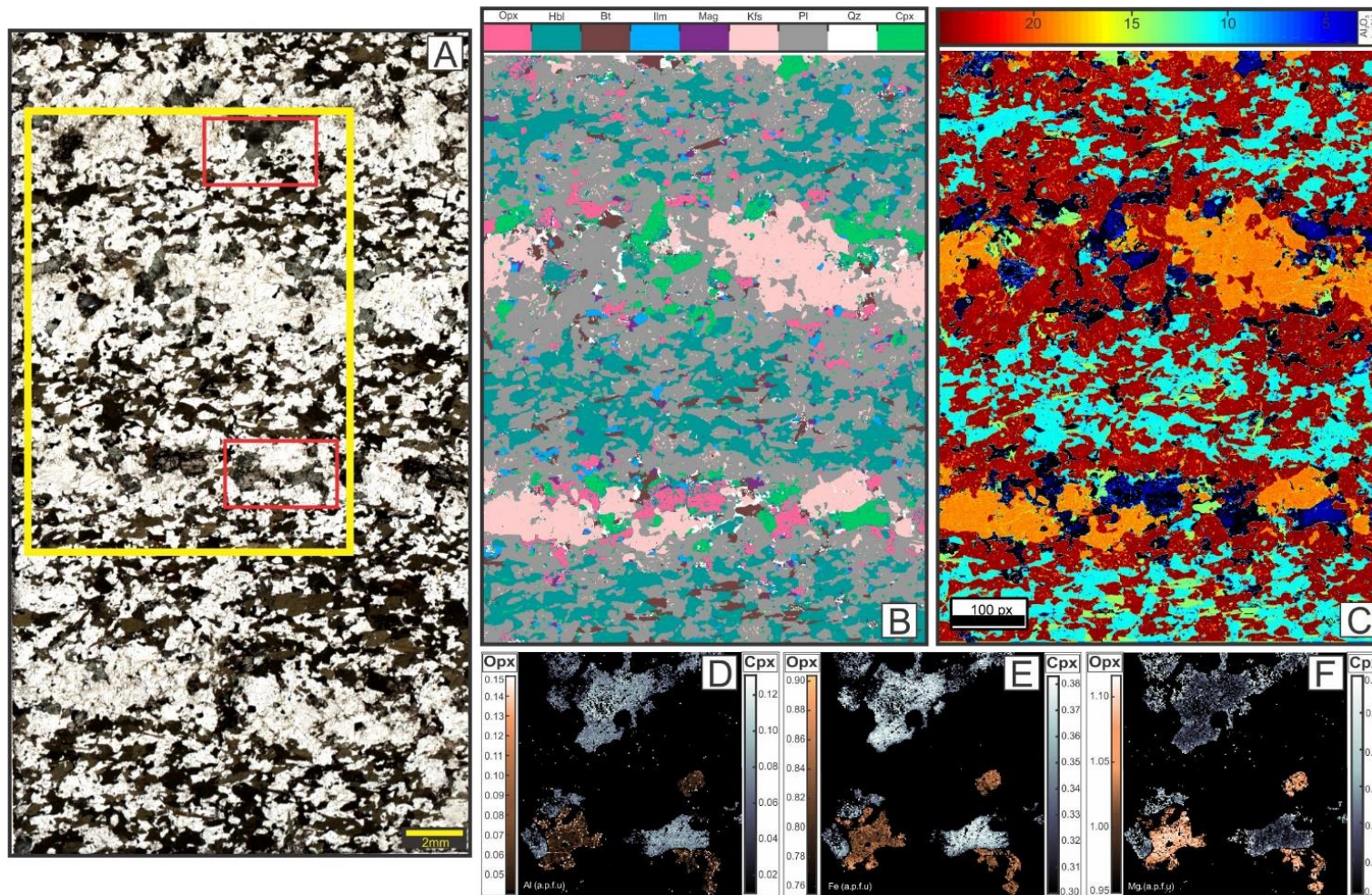


**Figure 3.5:** (A) Microphotograph showing the texture of the banded mafic granulite (C-838-A) with the selected rectangle area mapped shown in: (B) Map with discriminated phases and (C) Al<sub>2</sub>O<sub>3</sub> (wt%) compositional map. Compositional maps for clinopyroxene and orthopyroxenes (D) Al<sub>2</sub>O<sub>3</sub> (a.p.f.u) (E) FeO (a.p.f.u) and (F) CaO (a.p.f.u) .

The distance between K-feldspar and amphibole and pyroxene does not seem to control their composition as the same compositional zoning is observed from core ( $\text{Ab}_{23}\text{Mc}_{77}$ ) to rim ( $\text{Ab}_{10}\text{Mc}_{90}$ ).

Plagioclase composition varies according to the position in each domain: (i) plagioclase located in mafic bands is finer-grained and exhibits concentric zoning ( $\text{Ab}_{68-65}\text{An}_{28-32}\text{Mc}_{3.5-3}$ ); (ii) coarser-grained, zoned crystals ( $\text{Ab}_{70-66}\text{An}_{28-31}\text{Mc}_3$ ). The microcline fraction in plagioclase varies between the different domains: the inner portion of the leucosome has  $K = 0.02$  a.p.f.u. and towards the mafic band  $K = 0.04$  a.p.f.u.

Biotite compositions also change according to the position in each domain: (i) in the leucosome, biotite flakes have higher  $X_{\text{Mg}}$  (0.46–0.40 from core to rim) and lower Ti contents (0.23–0.20 a.p.f.u.) compared to biotite in the mafic band with lower  $X_{\text{Mg}}$  (0.36–0.42) and higher Ti contents (0.28–0.26 a.p.f.u.).

### 3.5.2.2 *Petrographic interpretation*

As for sample C-833-A, the banded mafic granulite C-838-A shows connections between the leucocratic phases from leucosome and granulite suggesting partial melt preservation in the residue (*cf* Sawyer, 2008). Furthermore, petrography and phase identification on compositional maps (Fig. 3.5) revealed that fine-grained K-feldspar and quartz have grown in and at the border of plagioclase, hornblende and biotite in the meso- to melanocratic bands. These features are interpreted as microfilms and pools of melt of incipient melting (Sawyer, 1999; Sawyer, 2008). The amount of these features increases towards the leucosome where K-feldspar lenses occur. The great amount of K-feldspar localized in the leucosome suggest that leucosomes have been formed also by contribution of in source melts (Fig. 3.5B).

### 3.5.3 **Opdalite (C-838-2)**

The light-green medium-grained opdalite C-838-2 displays foliated and isotropic domains. Isotropic domains have an equigranular phaneritic texture (Fig. 3.4C). This sample consists of oligoclase (40–45 vol%), quartz (30–35 %), orthoclase (8–10 %), diopside-augite (5 %) and hypersthene (5–8 %; Fig. 3.4C). Hypersthene contains rounded plagioclase inclusions. Anhedral ilmenite is usually associated with pyroxene. Symplectite of biotite, ilmenite and quartz represents local disequilibrium features. Quartz often shows undulose extinction. Antiperthitic plagioclase, zircon, apatite and rutile are present as accessory phases.

### **3.5.4 Granitic (hornblende)-biotite-bearing leucosome (C-838-B)**

The granitic (hornblende)-biotite-bearing leucosome C-838-B is a medium-grained leucocratic rock hosted in the stromatic metatexite (Fig. 3.3A). It is mainly composed of microcline, quartz and plagioclase, with modal contents varying from granitic to granodioritic. The mafic minerals biotite (5 vol%), hornblende (3–5 %) and actinolite (< 3 %) display a weak preferred orientation. Perthite and antiperthite are found in microcline and plagioclase, respectively. Myrmekite and block extinction are locally observed. Plagioclase is incipiently replaced by carbonate and sericite, and to a lesser extent by epidote and clinozoisite. Muscovite partly replaces biotite, locally forming pseudomorphs. Relicts of fine- to medium-grained Schöllén (Fig. 3.3E) have tonalitic compositions containing hornblende (15 vol%) and biotite (10 %). Ilmenite and pyrite constitute together 5 vol% of the mineral mode. Some hornblende crystals are replaced by retrograde actinolite. Rutile, zircon and apatite are accessory minerals.

### **3.5.5 Mafic granulite enclave (C-716-B)**

The isotropic mafic granulite enclave C-716-B shows a dark-green fine-grained matrix with randomly distributed coarse-grained blasts of hornblende (Fig 3.4D). The granoblastic matrix is composed of hornblende (55–60 vol%), plagioclase (15–20 %), clinopyroxene (10–15 %) and orthopyroxene (5 %). The modal proportions suggest a primary hornblende-gabbro-noritic to noritic composition. Plagioclase and rarely quartz occur as rounded inclusions in the clino- and orthopyroxene. The coarse-grained (up to 1 cm) hornblende porphyroblasts are the products of the late retrogression. Amphibole exhibits fading contacts with the matrix and contains all the matrix minerals as inclusions. The amount of matrix inclusions thereby increases towards the rim of the porphyroblasts. Furthermore, quartz inclusions are common and retrograde biotite (3–5 vol%) grows along fractures and borders of these hornblende crystals. The accessory minerals are apatite, quartz and zircon. Opaque minerals (1 vol%) are ilmenite, which locally exhibits magnetite exsolutions, and other minor pyrite and chalcopyrite.

### 3.6 Zircon U-Pb geochronology and Lu-Hf isotopes

As a noteworthy characteristic of all the analyzed samples, the zircon U-Pb spot data spread along the concordia curve in the Concordia diagram. A careful evaluation of the dates thus requires a combination of distinct analytical approaches chronometers and petrogenetic parameters. The main goals are to understand the meaning of such scattered data and constrain the ages of the magmatic and metamorphic stages. The term date(s) herewith used refers to individual (or groups of)  $^{206}\text{Pb}/^{238}\text{U}$  and  $^{206}\text{Pb}/^{207}\text{Pb}$  spot analyses, while the term age is used for groups of  $^{206}\text{Pb}/^{238}\text{U}$  and  $^{206}\text{Pb}/^{207}\text{Pb}$  dates that are regarded as geologically significant. The analytical methods are described in Appendix 3.A. In order to retrieve the protolith ages, a similar approach to the one of Whitehouse and Kemp (2010) was used for the high-grade metamorphic rocks. This approach can be summarized as follow:

- 1) A detailed investigation of the internal structure of zircon through cathodoluminescence (CL) imaging to identify the core, successive rim generation and entire grains (single grains) sharing a unique CL-response (Fig. 3.6). Detailed descriptions of zircon population are reported in Appendix 3.B.

- 2) U-Pb zircon core dates of one sample are assumed to represent a single magmatic event. The oldest grains in this data cluster are thus considered to represent the crystallization age while the younger dates are attributed to be the result of either Pb loss or resetting during metamorphism. This is especially important in rocks that were strongly affected by partial melting (Gerdes and Zeh, 2009; Rubatto, 2017; Vervoort and Kemp, 2016).

- 3) Lu-Hf analyses were carried out on zircon grains covering the respective date ranges and cathodoluminescence domains. The  $^{176}\text{Hf}/^{177}\text{Hf}_{(t)}$  ratios were then used to reveal coupling or decoupling between the U-Pb and Lu-Hf systems (Gerdes and Zeh, 2009; Vervoort and Kemp, 2016; Wang et al., 2017; Whitehouse and Kemp, 2010). The Hf signature further provides hints towards possible melt sources and processes involved in the generation of the magmatic protolith and the metamorphic products (Belousova et al., 2010; Dhuime et al., 2015; Taylor et al., 2016).

The U-Pb and Lu-Hf data of the analyzed zircons from samples (C-833-A), (C-838-2), (C-838-A), (C-838-B) and (C-716-B) are presented in the Appendices V and VI, respectively.





**Figure 3.6:** Cathodoluminescence (CL) images of representative zircon grains. Location of the spot analyses and corresponding  $^{206}\text{Pb}/^{238}\text{U}$  or  $^{207}\text{Pb}/^{206}\text{Pb}$  dates in Ma marked with yellow circles (spot size ~30 microns), blue dashed circles for trace elements (spot size ~20 microns), and dashed red circles for Lu-Hf (spot size ~50 microns).

### 3.6.1 Banded mafic granulite (C-833-A)

Cathodoluminescence (CL) images reveal that zircon from the banded mafic granulite exhibits sub-rounded habits, which is a common feature of high-grade metamorphic zircon (Whitehouse and Kemp, 2010). Their textures and habits resemble that of “truly metamorphic” zircons described in Taylor et al. (2016) as they show an equant morphology, internal sector zoning textures with planar features of bright CL responses or fir-tree zoning.

A total of 108 U-Pb analyses on 86 grains provide spreading dates in the Concordia diagram (Fig. 3.7A). Fifty-eight cores and entire grains with similar CL-responses at Th/U ratios between 0.1 and 1.3 describe a fairly continuous spread dataset in the Concordia diagram, spreading from an oldest  $^{207}\text{Pb}/^{206}\text{Pb}$  date of  $2575 \pm 66$  Ma down to  $1656 \pm 82$  Ma (Fig. 3.7A), followed by a void space and a cluster of seven cores with  $^{206}\text{Pb}/^{238}\text{U}$  dates between 700 Ma and 600 Ma. Eighteen grains from this sample were further analyzed for Lu-Hf isotopes, resulting  $^{176}\text{Hf}/^{177}\text{Hf}_{(t)}$  ratios covering a range from 0.28123 to 0.28143. Three grains are exceptions with  $^{176}\text{Hf}/^{177}\text{Hf}_{(t)} = 0.28157\text{--}0.28172$  (Fig. 3.7B). This restricted  $^{176}\text{Hf}/^{177}\text{Hf}_{(t)}$  range implies that zircon cores grew during a single magmatic event, which can be dated at  $2559 \pm 66$  Ma using the oldest dates of the cores (Fig. 3.7A). To refine this estimate, ten oldest grains were selected providing a weighted average  $^{206}\text{Pb}/^{207}\text{Pb}$  age of  $2506 \pm 24$  Ma (MSWD = 1.5; Probability = 0.14; Fig. 3.7C).  $\epsilon\text{Hf}$  recalculated for crystallization age of 2550 Ma yields values between +10.0 and +2.7.

Rims dates also spread in the concordia. Their Th/U ratios range between 0.04 and 1.75 ( $n = 48$ ). The great majority, ca. 80 %, of zircon rims yields mostly clustered  $^{206}\text{Pb}/^{238}\text{U}$  dates between 590 and 680 Ma, which are in line with the main metamorphic stage recorded in the Southern Brasília orogen (Fig. 3.7D). The youngest data cluster ( $n = 17$ ) was obtained almost exclusively from bright CL rims and yields a concordant age of  $607 \pm 2$  Ma. For the other 20 % of zircon rims ( $n = 9$ ), the  $^{207}\text{Pb}/^{206}\text{Pb}$  dates range between  $2425 \pm 88$  Ma and  $2351 \pm 46$ , with two outliers at  $1900 \pm 52$  Ma and  $2081 \pm 32$  (Fig. 3.7F). The six oldest grains of this group yield a concordant age of  $2405 \pm 10$  Ma (MSWD = 0.19; probability 0.67). This range of metamorphic ages between 2.3–2.4 Ga, together with the lack of dates between 2.3 Ga and 600 Ma (observed for the cores) corroborate the interpretation of a metamorphic event at ca. 2.4 Ga.

Lu-Hf analyses in six Neoproterozoic rims revealed  $^{176}\text{Hf}/^{177}\text{Hf}_{(t)}$  between 0.28140 and 0.28187 and  $\epsilon\text{Hf}_{(t)}$  between -18.5 and -34.7.

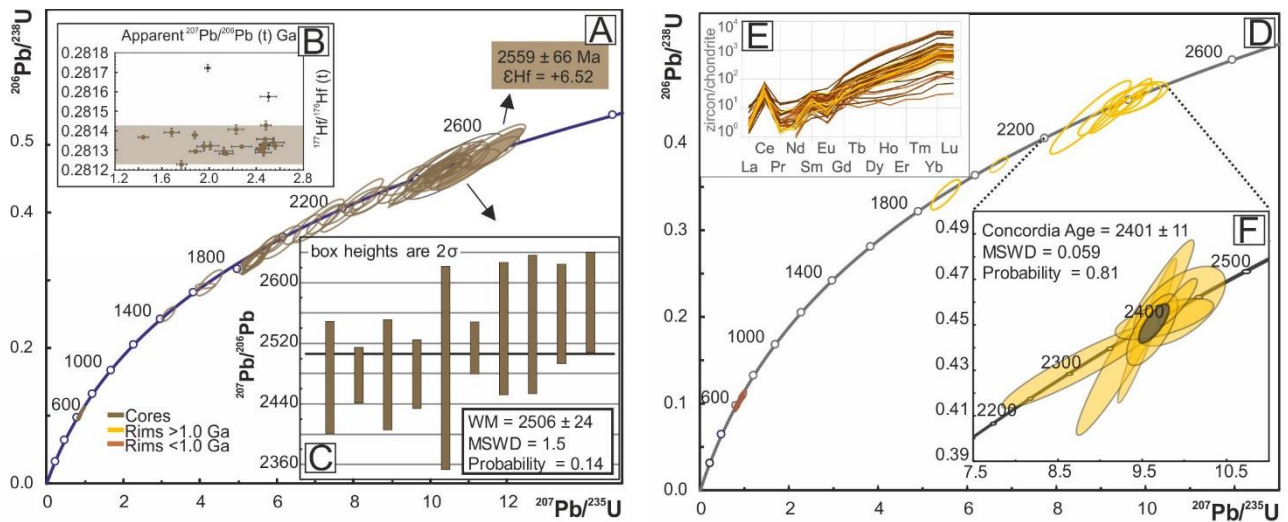


**Figure 3.7:** U-Pb, Lu-Hf and trace elements zircon data for the banded mafic granulites C-833-A. Data interpreted as magmatic (see text) are plotted in (A) Concordia diagram (ellipses:  $2\sigma$  uncertainty), the brown filled ellipse represents the older grain containing  $^{176}\text{Hf}/^{177}\text{Hf}$  within the cogenetic range from (B) initial  $^{176}\text{Hf}/^{177}\text{Hf}$  ratio against age using  $^{207}\text{Pb}/^{206}\text{Pb}$  dates and (C) Weighted average age from the oldest 10 grains. (D) Concordia diagram (ellipses:  $2\sigma$  uncertainty) for rims and single phases, (E) normalized zircon/chondrite rare-earth elements diagrams for cores and rims and (F) data that yielded a concordant age.

### 3.6.2 Opdalite (C-838-2)

The zircon population comprises grains with parallel oscillatory zoning, irregular intermediate-CL responses (different shades of gray) and zircon exhibiting intermediate-CI responses lacking internal structures or exhibiting ghost of older broad growth features. Apart from this group, thin bright-CL rim less than  $10\ \mu\text{m}$  in width (locally reaching  $30\ \mu\text{m}$ ) usually irregularly overgrow the older domain exhibiting lobate contacts (Fig. 3.6).

Eighty-one spots reveal a spreading set of concordant dates. Cores and single grains showing oscillatory zoning spread from ca. 620 Ma to ca. 790 Ma (Fig. 3.8A and C). The oldest dates  $786 \pm 10\ \text{Ma}$  ( $^{206}\text{Pb}/^{238}\text{U}$  age) and the seven oldest grains between  $786 \pm 10\ \text{Ma}$  and  $752 \pm 5\ \text{Ma}$ . Thus, the minimum age of the magmatic protolith is interpreted to be  $786 \pm 10\ \text{Ma}$ . Since rims are almost absent or too thin for analysis (Figs. 3.6 and 3.8C), only six rim dates were obtained spreading between ca. 630 Ma and 690 Ma without defining any cluster. Thus, no metamorphic age constraint can be obtained for this sample.

Lu-Hf signatures of twenty-nine grains comprising the whole age spectrum reveal very homogeneous signatures with  $^{176}\text{Hf}/^{177}\text{Hf}_{(t)} = 0.28192\text{--}0.28199$  (one grain shows  $^{176}\text{Hf}/^{177}\text{Hf}_{(t)} = 0.28210$ ), including two analyses of rims (Fig. 3.8B).  $\epsilon\text{Hf}_{(790)}$  varies between -11.8 and -15.8 for the core, and the  $\epsilon\text{Hf}_{(t)}$  between -12.6 and -13.4 for rim.



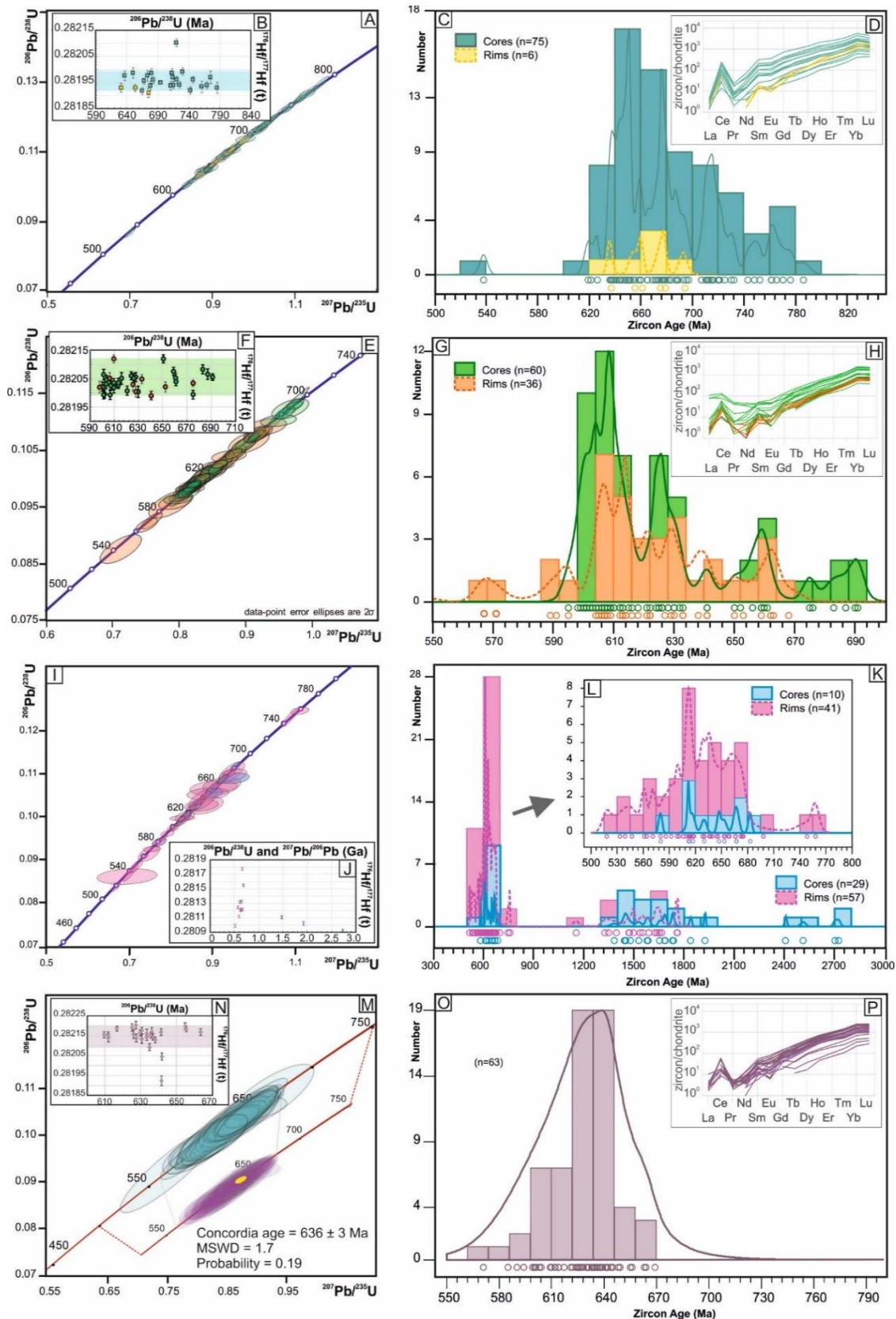


**Figure 3.8:** Geochronological results for Neoproterozoic rocks. U-Pb (Concordia and Probability density diagrams),  $^{176}\text{Hf}/^{177}\text{Hf}$  ratio versus age using  $^{206}\text{Pb}/^{238}\text{U}$  dates and normalized zircon/chondrite rare-earth elements diagrams for: (A-D) Opdalite C-838-2, cores are blue and rims in yellow, (E-H) Banded mafic granulite C-838-A, cores in green and rims in orange, and (K-M) Pinkish granitic (hornblende)-biotite-bearing leucosome C-838-B, core in dark-blue and rims in pink and (N-Q) Mafic granulite enclave C-716-B. In the Concordia diagrams ellipses are  $2\sigma$  errors.

### 3.6.3 Banded mafic granulite (C-838-A)

The main zircon type is characterized by CL-dark elongated grains that usually form bipyramidal grains. They show oscillatory to parallel zoning despite sub-rounded habits. Zircon cores are often overgrown by unzoned CL-bright rims that are mainly thinner than 20  $\mu\text{m}$  (Fig. 3.6).

LA-ICP-MS data of 101 spot analyses on 96 zircon grains spread along the Concordia between a maximum core  $^{206}\text{Pb}/^{238}\text{U}$  date of ca. 690 Ma (core dates between 690 and 595 Ma) and a minimum rim date of ca. 540 Ma (rim dates between 670 and 540 Ma; Fig. 3.8F and H). The oldest grain shows a  $^{206}\text{Pb}/^{238}\text{U}$  age of  $691 \pm 3$  Ma and the three oldest grains of  $690 \pm 3$  Ma (MSWD = 0.41; Probability = 0.66). To reveal possible inheritance, the oldest and youngest grains of this group were analyzed for Lu-Hf signatures yielding  $^{176}\text{Hf}/^{177}\text{Hf}_{(t)} = 0.28206\text{--}0.28207$ . Such  $^{176}\text{Hf}/^{177}\text{Hf}$  values were also obtained for other grains covering the full spectrum of ages for cores and single phases that display homogeneous and varied  $^{176}\text{Hf}/^{177}\text{Hf}_{(t)}$  of 0.28199–0.28208 within errors (Fig. 3.8G). Hence, the minimum age of the magmatic protolith is interpreted to be  $691 \pm 3$  Ma.

For the metamorphic stage, 36 rims (CL-bright similar to the rims or with clearly disturbed responses) record a time span of 100 m.y. (U-Pb ages of 670–570 Ma). The dates define asymmetric data population from 660 Ma to 590 Ma with a peak at 620–600 Ma in a probability density plot (Fig. 3.8H). Two rim analyses define another minor date peak around 565 Ma (Fig. 3.8H). A group of nine analyses has a weighted average  $^{206}\text{Pb}/^{238}\text{U}$  age of  $611 \pm 2$  Ma (MSWD = 1.9; Probability = 0.052). Younger ages – concordant but poorly distributed – can be related to post-600 Ma disturbance or to the formation of cracks. No significant age can be assigned for a late event.

Interestingly, the  $^{176}\text{Hf}/^{177}\text{Hf}_{(t)}$  ratios of the rim are the same (0.28199–0.28212) than for the core (Fig. 3.8G). The  $\epsilon\text{Hf}_{(690)}$  values for the core range from -8.2 to -12.6, with one grain dated to ca. 1333 Ma yielding  $\epsilon\text{Hf}_{(t)} = +3.12$ . Rims have similar  $\epsilon\text{Hf}_{(t)}$  ranging from -9.0 to -14.1 (outlier #146 = -37.9).

### 3.6.4 Granitic (hornblende)-biotite-bearing leucosome (C-838-B)

The zircon population of the leucosome C-838-B is homogeneous regarding grain size and habit, but texturally different as revealed by the cathodoluminescence images (Fig. 3.6).

U-Pb data reveal a large range of concordant dates (Fig. 3.8K and L). Core dates spread from ca. 580 Ma to 2720 Ma, while rims date to ca. 520 Ma to ca. 1761 Ma. A more detailed

evaluation of each domain reveals that core  $^{207}\text{Pb}/^{206}\text{Pb}$  dates mainly spread from ca. 2.7 Ga to 1.3 Ga with Th/U ratios between 0.04 and 0.72 (n=29). A subgroup of ten grains displays a range of ca. 680 Ma to 580 Ma dates. Such bimodal distribution is also observed for the rims (n=57). Older rims cover an interval between 1.7 Ga and 1.4 Ga, while younger rims date between ca. 770 Ma and 530 Ma.

Lu-Hf data for older cores from this sample do not define a cluster.  $^{176}\text{Hf}/^{177}\text{Hf}_{(t)}$  ratios of three old cores are 0.28093, 0.28102 and 0.28111 for  $^{207}\text{Pb}/^{206}\text{Pb}$  dates of 2725 Ma, 1925 Ma and 1479 Ma, respectively. Four younger cores yield  $^{176}\text{Hf}/^{177}\text{Hf}_{(t)}$  ratios of 0.28120 to 0.28155 for  $^{206}\text{Pb}/^{238}\text{U}$  ages between ca. 680 and 580 Ma. Because  $^{176}\text{Hf}/^{177}\text{Hf}_{(t)}$  ratios do not define a narrow range, two possibilities can be considered (Fig. 3.8J): (i) the oldest grains record the crystallization age and dates lower than 2725 Ma are the result of later disturbances. In this case, the oldest grain with a  $^{207}\text{Pb}/^{206}\text{Pb}$  date of  $2725 \pm 19$  Ma would represent the magmatic crystallization age of the rock. Grains yielding younger ages record the effects of metamorphism, more likely to be partially reset during anatexis. (ii) The leucosome is a product of partial melting from a sedimentary rock source. In this case, crystallization could have happened at any time between the magmatic stage (2.7 Ga) and the onset of the Neoproterozoic metamorphism (ca. 680 Ma). The option of inheritance of zircon preserving ages older than 1 Ga, in a 680 Ma rock that melted to generate the C-838-B leucosome is unlikely. Preservation of many grains during two partial melting events, including a UHT-related metamorphism, and distribution in a continuum spectrum of its contribution make it unlikely.

Around 40 % of the analyses of core provide U-Pb dates between ca. 580–680 Ma without defining any clear cluster. This distribution and the fact that they have CL-responses similar to the young rims and distinct  $^{176}\text{Hf}/^{177}\text{Hf}_{(t)}$  ratios from the older group (0.28120–0.28155) suggest that these grains have formed during the Neoproterozoic. Rims show highly crustal  $\epsilon\text{Hf}_{(t)}$  between -20.9 and -52.1 ( $^{176}\text{Hf}/^{177}\text{Hf}_{(t)}$  between 0.28099 and 0.28177; Fig. 3.8J). A main metamorphic crystallization stage can be assigned to the time interval 600–620 Ma.

### 3.6.5 Mafic granulite enclave (C-716-B)

The majority of the grains show sector zoning with CL-medium-bright responses, and a faint, broad oscillatory zoning (Fig. 3.6; Corfu et al., 2003). Some grains have a CL-brighter (grey shade) rim around embayed core. These rims are usually less than 5  $\mu\text{m}$  wide and likely related to annealing (Corfu et al., 2003).

Sixty-three analyses on sector-zoned domains yield Th/U ratios between 0.35 and 2.02. Most analyses (87 %) form a Concordia age of  $636 \pm 2$  Ma (Figs. 3.8O and P). However,

$^{176}\text{Hf}/^{177}\text{Hf}_{(t)}$  form a narrow range between 0.28205 and 0.28220 (Fig. 3.8N) and the oldest among those grains of  $664 \pm 9$  Ma is thus interpreted as the crystallization age of the protolith. Grain # 5.1 with a U-Pb date of  $642 \pm 8$  Ma is an outlier with  $^{176}\text{Hf}/^{177}\text{Hf}_{(t)} = 0.28192$ , i.e., the same value as recorded by the opdalite (C-838-2). The low  $^{176}\text{Hf}/^{177}\text{Hf}_{(t)}$  in this zircon could be inherited from the opdalite. The  $\epsilon\text{Hf}_{(t)}$  values vary from -5.9 and -11.44 ( $n = 23$ ).

## 3.7 Zircon inclusions, geochemistry and thermometry

### 3.7.1 Types of inclusion in zircon

The abundance and types of inclusion in zircon were investigated in the banded mafic granulites, C-833-A (Neoproterozoic) and C-838-A (Neoproterozoic).

Apatite, quartz and feldspar are the most common inclusions in both samples. Biotite is often found in the Neoproterozoic grains. Polyphase inclusions containing two or three of the aforementioned phases (including two types of feldspar) are locally found, while no Ti-rich phases are observed as inclusions.

For sample C-833-A, the following variation in the type of inclusions can be noted. Whereas the grains of CL-domains recording Archean dates (including grain #100, the oldest grain of ca. 2575 Ma) include apatite and quartz, and one grain has amphibole, the Neoproterozoic CL-domains mainly contain feldspar, biotite and apatite.

In sample C-838-A, quartz and apatite are found as inclusion in ~30 % of the grains, covering ages from ca. 690 to 600 Ma. These inclusions are abundant in pristine as well as in fractured grains. One feldspar inclusion appears to be zoned. Biotite is associated to fractures.

### 3.7.2 Geochemistry

As a general characteristic cores and rims from both, protolith and metamorphic grains, show  $\text{Th}/\text{U} > 0.1$ . The zircon grains from the intermediate to mafic samples C-716-B, C-838-A, C-833-A and C-838-2 display  $\text{Th}/\text{U}$  around unity (core and rim). Less common are the higher  $\text{Th}/\text{U}$  ratios approaching 2 for the core (except for sample C-833-A). The intermediate to mafic samples were further analyzed for trace element contents. The REE and Ti systematics are discussed in detail in the following.

*Banded mafic granulite C-833-A* – Trace element analyses of 49 zircon grains from sample 833-4 do not reveal differences in REE compositions between cores, Paleoproterozoic rims and Neoproterozoic rims (Fig 3.7E). HREE patterns vary from steep to flat ( $Gd_N/Lu_N$  between 1 and 152) with most of the data showing intermediate  $Gd_N/Lu_N$  between 10 and 50. Only Paleoproterozoic rims display a narrower range with  $Gd_N/Lu_N$  between 18 and 27 ( $n=6$ ). The magnitudes of the Eu anomaly ( $Eu/Eu^*$ ) vary between 0.15 and 1.40 and cannot be correlated to specific CL-domains or age range. Positive Ce anomalies ( $Ce/Ce^*$ ) range between 2 and 32. In general, no correlation was observed between the REE distribution and the CL-domains or age domains.

*Opdalite C-838-2* – Zircon from opdalite C-838-2 ( $n=18$ ) has homogeneous REE patterns. They exhibit moderate HREE slopes with  $Gd_N/Lu_N$  between 6 and 17, moderate to discrete negative Eu anomalies ( $Eu/Eu^* = 0.60 - 0.76$ ), and prominent positive Ce anomalies between 4 and 24 (average=18;  $\sigma=9$ ). Although this sample has only few metamorphic grains and rims, two analyses indicate slightly steeper REE slopes for these domains (Fig. 3.8D). They display steeper HREE slopes with  $Gd_N/Lu_N = 62$  (rim) and 19 (dark-CL disturbed grain) and more pronounced negative Eu anomalies ( $Eu/Eu^* 0.41$  and 0.48).

*Banded mafic granulite C-838-A* – The banded mafic granulite C-838-A ( $n=22$ ) exhibits the highest variations of LREEs in zircon of all samples, while HREEs display similar steep patterns with  $Gd_N/Lu_N$  between 13 and 40 (average 25,  $\sigma=7$ ). Cores, rims and newly-formed grains appear compositionally similar, with the newly-formed grains having narrower REE distribution than the cores (Fig. 3.8I). An inherited grain with a  $^{207}Pb/^{206}Pb$  age of ca. 1393 Ma and a positive  $\epsilon Hf$  displays a negative anomaly for Nd. Negative Eu anomalies are found in both, cores ( $Eu/Eu^* = 0.22 - 0.78$ ) and grains with only one CL-response ( $Eu/Eu^* = 0.27 - 0.81$ ). LREE patterns spread with positive Ce anomalies between 1 and 14.

*Mafic granulite enclave C-716-B* – Zircon from the mafic granulite C-716-B ( $n=27$ ) have homogenous REE distribution patterns with the exception of Eu anomalies, which vary between slightly positive to highly negative values ( $Eu/Eu^* = 0.12 - 1.12$ ; Fig. 3.8Q). They exhibit moderate HREE slope with  $Gd_N/Lu_N = 14 - 48$  (average=22;  $\sigma=10$ ). Negative Nd and Pr anomalies are visible although they can be an effect from positive Ce ( $Ce/Ce^* = 3.22 - 27.14$ ) and Eu anomalies. Few samples show a slightly negative Tb anomaly.

### 3.7.3 Ti-in-zircon thermometry

Titanium concentrations in zircon were measured as part of the trace elements analyses by LA-ICP-MS for samples C-833-A, C-838-2, C-838-A and C-716-B. The corresponding temperatures were calculated using the calibration of Watson et al. (2006). Only one sample, C-838-2, contains rutile and quartz. In the other samples ilmenite is the Ti-rich phase, which means that  $\text{TiO}_2$  activity can have been lower than one. For those samples a  $\text{TiO}_2$  activity of 0.6 for metabasalts is assumed following Ghent and Stout (1984). Thus, temperatures obtained with lower  $\text{TiO}_2$  activities represent minimum values. The results for each sample are reported in figure 3.9.

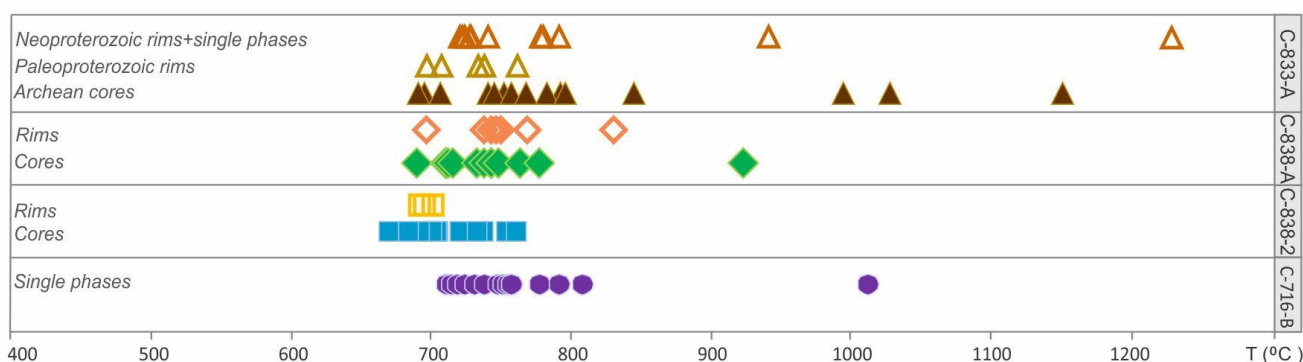


**Figure 3.9:** Zircon crystallization temperatures from Ti-in-zircon thermometry using the calibration of Watson et al. (2006).

*Banded mafic granulite C-833-A* – Zircon in the banded mafic granulite 833-A displays variable Ti contents. Approximately 35 % of the grains have Ti concentrations below the limit of detection. The group of Archean zircon cores exhibits Ti contents varying from 5 to 15 ppm that yield temperatures of ~695–840 °C (average =  $757 \pm 45$  °C;  $1\sigma$ ;  $n=12$ ), two grains have Ti = 125 ppm (#27) and Ti = 100 ppm (#102) and  $T = 1025$  °C and  $T = 990$  °C, respectively; one zircon contains 270 ppm of Ti (#75) corresponding to  $T \sim 1150$  °C. The old rims (1680 and 2480 Ma) are relatively homogeneous with Ti = 6–13 ppm and resulting temperatures of ~700–760 °C (average =  $730 \pm 26$  °C;  $1\sigma$ ;  $n=5$ ). The Neoproterozoic rims have Ti contents in the range of 8–17 ppm corresponding to temperatures of ~720–790 °C (average =  $727 \pm 27$  °C;  $1\sigma$ ;  $n=9$ ). Two rims contain Ti = 66 ppm (#81) and Ti = 418 ppm (#101) yield temperatures of ~940 °C and ~1226 °C, respectively.

*Opdalite C-838-2* – Titanium concentrations in zircon from the opdalite C-838-2 range from 4 to 12 ppm in cores and are more homogeneous in the rims (5–6 ppm). Corresponding temperatures are 670–780 °C (average =  $704 \pm 29$  °C;  $1\sigma$ ;  $n=11$ ) for the cores and 690–700 °C (average =  $694 \pm 5$  °C;  $1\sigma$ ;  $n=3$ ) for the rims.

*Banded mafic granulite C-838-A* – Zircon cores in sample C-838-A have Ti concentrations ranging from 5–15 ppm, except the grain #55 that contains 57 ppm Ti. Rims range from 6–11 ppm

Ti with one exception containing 25 ppm of Ti. The temperatures obtained for the cores are ~690–780 °C (average =  $732 \pm 26$  °C;  $1\sigma$ ;  $n=12$ ) as well as ~922 °C for grain #55, and ~700–830 °C for the rims (average =  $743 \pm 40$  °C;  $1\sigma$ ;  $n=7$ ).

*Mafic granulite enclave C-716-B* – Zircons from the mafic granulite enclave C-716-contain 7–20 ppm of Ti, with an exception of 113 ppm Ti (grain #8), yielding temperatures of ~710–810 °C ( $T \sim 1010$  °C for grain #8).

### 3.8 Bulk rock chemistry

The set of samples selected for bulk rock analysis comprises the main rock types outcropping in the granulitic unit of the studied area. Thus, SiO<sub>2</sub> contents vary over a wide range from 47 wt% in amphibolite layer C-833-B to 75 wt% in the white (hornblende)-biotite-bearing leucosome C-838-4 (bulk-rock chemistry data are available in Appendix I and the diagrams in Fig. 3.10). The banded mafic granulite (SiO<sub>2</sub> = 57–69 wt%) requires a careful evaluation, since the effects of anatexis and melt migration can both significantly modify the rock composition (Sawyer, 2008). The mafic rocks have a gabbroic composition while the leucosomes have a granitic to quartz-monzonite composition. The banded granulites vary between the monzogabbroic to granodioritic compositions, and the opdalite is quartz monzonitic.

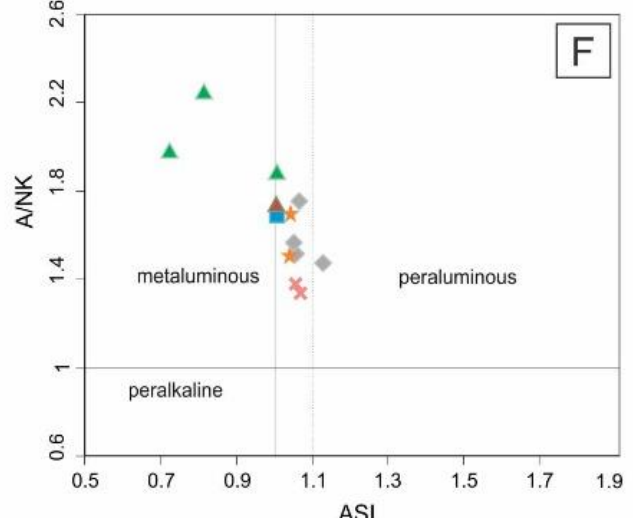
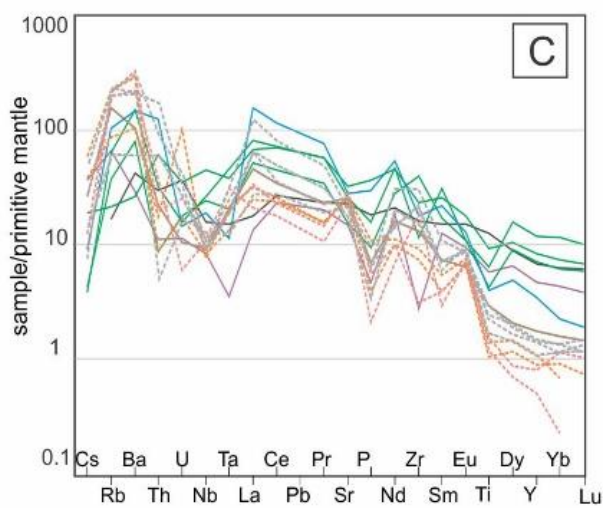
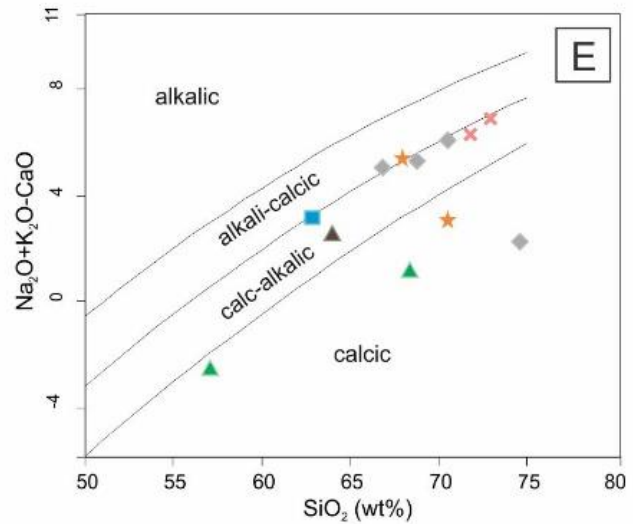
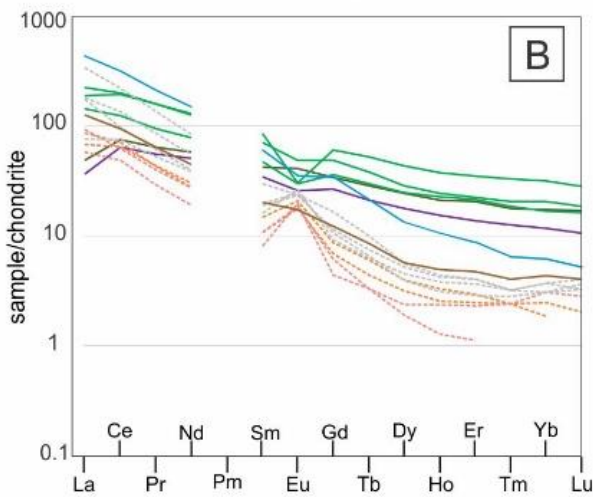
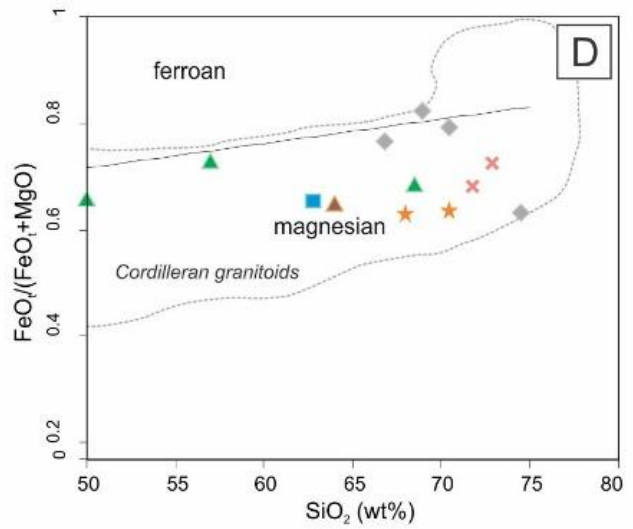
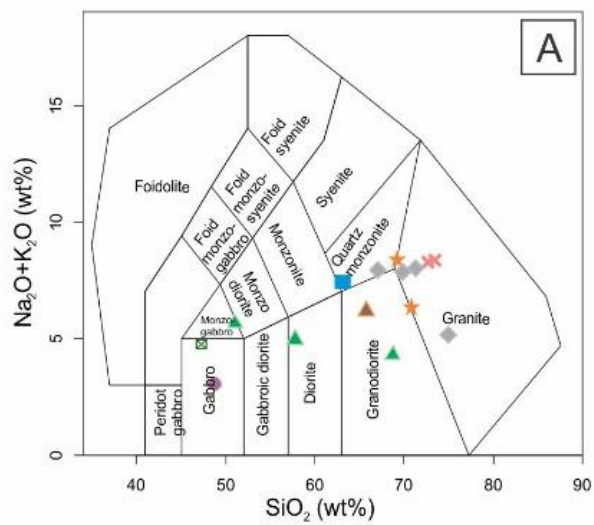
The classification of Frost et al. (2001) for the intermediate to felsic rocks has been applied (Figs. 3.10D–F). The majority of samples are magnesian and only the white muscovite-biotite-bearing leucosome plots in the ferroan field. All of them fit within the cordilleran field. In the Na<sub>2</sub>O+K<sub>2</sub>O-CaO (MALI) versus SiO<sub>2</sub> diagram, gneisses are calc-alkalic and calcic, while leucosomes and the opdalite are alkali-calcic (Fig. 3.10E). This discrepancy is again observed in the A/NK vs. A/CNK diagram (Shand, 1943), in which the banded granulites are metaluminous and the leucosomes are peraluminous (Fig. 3.10F). Although slightly peraluminous, they still are mainly I-type granites (Chappell, 2001; Chappell and White, 1974). Using the geotectonic discrimination diagrams of Pearce et al. (1984), the samples display a volcanic-arc distribution (Figs. 3.10G-H). In the log(Rb) vs. log(Nb+Y) diagram (including the post-collisional field from Pearce, 1996), most samples plot in the volcanic-arc field, except for a banded mafic granulite and the opdalite that display post-collisional signatures.

In chondrite-normalized REE diagrams, leucosomes and mafic samples (mafic granulite enclave, amphibolitic layer, banded granulite) define two distinct groups (Fig. 3.10B). However, the Neoarchean banded mafic granulite (C-833-A) and the opdalite (C-838-2) are exceptions. The leucosome exhibits HREE-depletion, resulting in concave REE patterns with enrichments from Tm

to Lu ( $Gd/Yb_N$  1–4, and C-838-B; Fig. 3.10B). Mafic rocks display flatter patterns ( $Gd/Yb_N$  2–4). For LREEs in mafic samples the pattern is even slightly flatter ( $La/Sm_N = 1–3$ ) than the leucosome ( $La/Sm_N = 5–11$ ) but similar in terms of absolute chondrites-enrichments. Furthermore, leucosomes have conspicuous positive Eu anomalies with  $Eu/Eu^*$  between 0.99 and 3.45, while the mafic samples display slightly positive to negative  $Eu/Eu^*$  between 0.44 and 1.17. The Neoproterozoic banded mafic granulite C-833-A has a REE pattern similar to the leucosome ( $La/Sm_N = 6$ ;  $Gd/Yb_N = 3$  and  $Eu/Eu^* = 1.20$ ). The opdalite C-838-2 displays a singular steep REE pattern ( $La/Sm_N = 7$  and  $Gd/Yb_N = 6$ ) with a slightly negative Eu anomaly ( $Eu/Eu^* = 0.87$ ).

Primitive-mantle-normalized trace element systematics reveal that leucosomes are LREE-enriched while the mafic enclave and layer and banded mafic granulite are enriched in HREEs (Fig. 3.10C). However, groups rarely show common behaviors regarding single elements. The exceptions are negative Nb and Sm anomalies, depletion from Ti to Lu in the spidergram (Fig. 3.10C) and positive Ba and Rb anomalies in the leucosomes. A negative P anomaly is observed for almost all the samples.





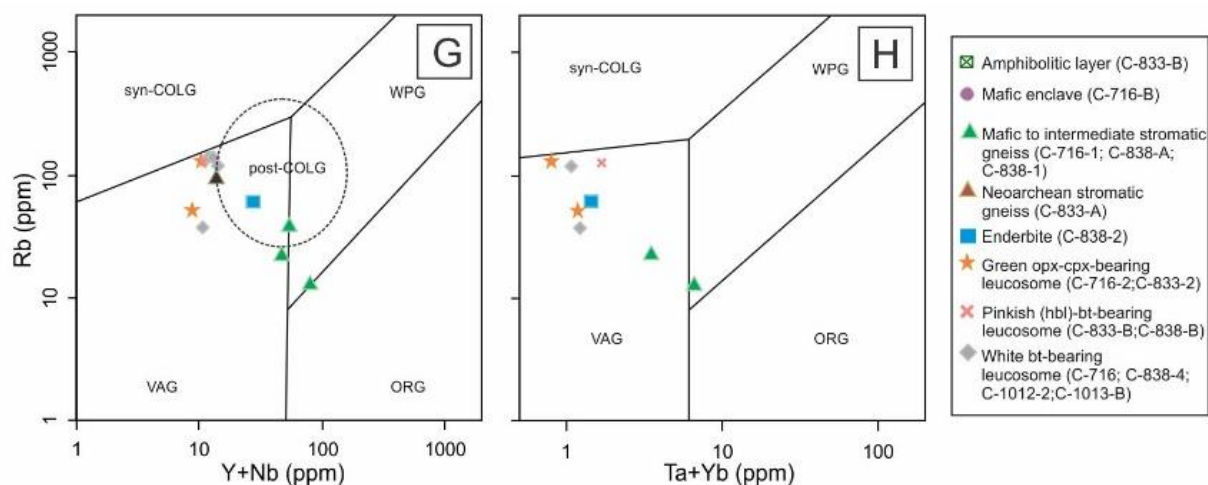


**Figure 3.10:** Bulk rock chemistry of the studied rocks. (A)  $\text{Na}_2\text{O}+\text{K}_2\text{O}$ (wt%) versus  $\text{SiO}_2$ (wt%) classification plot (Middlemost, 1989); (B) chondrite-normalized (McDonough and Sun, 1995); (C) spider diagram normalized to chondrite (McDonough and Sun, 1995). Frost et al. (2001) classification (D)  $\text{FeO}^{\text{tot}}/(\text{FeO}^{\text{tot}}+\text{MgO})$  versus  $\text{SiO}_2$  with composition field of cordilleran granites (E)  $\text{Na}_2\text{O} + \text{K}_2\text{O} - \text{CaO}$  (MALI index) vs.  $\text{SiO}_2$  diagram (F)  $\text{Al}_2\text{O}_3/(\text{Na}_2\text{O} + \text{K}_2\text{O})$ (molar) vs.  $\text{Al}_2\text{O}_3/(\text{CaO} + \text{Na}_2\text{O} + \text{K}_2\text{O})$  (molar) diagram (Shand's index; Shand, 1974) and I-type boundary according to Chappel and White (1974). Tectonic settings discrimination for granites according to Pearce et al. (1984) (G) log Rb(ppm) versus Y+Nb(ppm) with addition of 'post-collisional granites' field after Pearce (1986) and (H) log Rb(ppm) versus Ta+Yb(ppm).

### 3.9 P-T estimates for the banded mafic granulite (C-838-A)

#### 3.9.1 Mineral thermobarometry

Clinopyroxene and orthopyroxene are the only relicts of the pre-retrogression assemblage. The orthopyroxene-clinopyroxene thermometer was applied to the composition zoning shown by medium-grained orthopyroxene and clinopyroxene (Fig. 3.5D–F). The calibration of Kretz (1982), based on the equilibrium exchange of Ca, Mg and Fe between clinopyroxene and orthopyroxene, yielded temperatures of  $998 \pm 23$  °C (1  $\sigma$ ) for the cores and  $916 \pm 19$  °C for the rims.

Retrograde conditions were estimated via amphibole crystallization from the equilibrium distribution of Na and Ca between plagioclase rims and hornblende applying the edenite-tremolite calibration of Holland and Blundy (1994). Amphibole-plagioclase pairs yield a temperature of  $740 \pm 28$  °C (1 $\sigma$ ). Pressures were estimated on the same mineral pairs based on the Al content in amphibole (Hammarstrom and Zen, 1986; Hollister et al., 1987; Johnson and Rutherford, 1989), a method previously applied by Del Lama et al. (2010) for similar rocks positioned in the northern sector of SGN. Calculated pressures range between 4 kbar and 7 kbar, with an average of  $5.7 \pm 0.9$  kbar. The average  $T$  and  $P$  given here are reported together with a standard deviation value (1 $\sigma$ ) obtained from the variability from the  $P$  and  $T$  maps (see Lanari et al., 2014, 2017 for an in-

depth discussion). This number reflects the relative uncertainties of the estimates that are related to the analytical precision of the EPMA measurements (Lanari et al., 2013).

The Ti-in-biotite thermometer (Henry et al., 2005) yields different temperatures related to the domain in which the flakes are. Biotite records slightly higher temperatures ( $750 \pm 12$  °C,  $1\sigma$ ) in the paleosome than in the leucosome ( $740$  to  $660 \pm 57$  °C).

## 3.10 Discussion

### 3.10.1 Crystallization timing and petrogenesis of protoliths

#### 3.10.1.1 *U-Pb disturbed systems (all samples)*

The spreading of U-Pb zircon dates in the Concordia for zircon cores (Figs. 3.7 and 3.8) is attributed to Pb loss with partial resetting during the UHT metamorphic event (section 9.2). The results suggest a partial decoupling of the U-Pb and Lu-Hf systems with preservation of the original Hf isotopic signatures (*cf* Vervoort and Kemp, 2016; Whitehouse and Kemp, 2010). In this context, crystallization ages only represent minimum ages because Pb could have been lost prior to the thermal UHT metamorphism event. As  $\epsilon_{\text{Hf}}$  is age dependent, it can be underestimated for rocks that experienced Pb loss, especially for older rocks as discussed by Vervoort and Kemp (2016).

The interpretation that the older grains may have experienced partial Pb loss does not corroborate previous interpretations of 800–700 Ma grains that have been considered as inherited (e.g., Hackspacher et al., 2003; Rocha, 2016). In fact, they represent minimum crystallization ages. Therefore, crystallization ages for the Guaxupé nappe might have been older than previously considered. Furthermore, significant zircon inheritance is unlikely expected in mafic to intermediate magmas as Zr solubility is high at high temperatures (Boehnke et al., 2013; Watson and Harrison, 1983).

#### 3.10.1.2 *Neoproterozoic rocks*

*Banded mafic granulite C-833-A* – Coupled U-Pb and Lu-Hf analyses of zircon indicate a minimum crystallization age of  $2559 \pm 65$  Ma for the protolith. Zircon cores have a juvenile signature with  $\epsilon_{\text{Hf}(2550)}$  between +10 and +2.7. The higher values are similar to  $\epsilon_{\text{Hf}}$  of depleted mantle (Fig. 3.11C; Blichert-Toft and Albarède, 1997). Most  $\epsilon_{\text{Hf}(2550)}$  signatures are mixtures

between depleted mantle and the 'new crust' that may have formed in intra-oceanic arc setting involving recycling of crustal material (Dhuime et al., 2011; Wang et al., 2017).

The hypotheses that the 2.5 Ga zircon grains are inherited is highly discarded, based on: (i) the amount of grains dating > 1 Ga (ca. 60 %); (ii) the unlikely preservation of such amount of zircon grains in a rock of this composition at such high temperatures; (iii) the difference between the  $^{176}\text{Hf}/^{177}\text{Hf}_{(t)}$  from rocks crystallized at ca. 600 Ma and the older grains (2.5–1 Ga) and (iv) furthermore, no other rock in the Guaxupé nappe records Paleoproterozoic to Archean inheritances. A metasedimentary rock origin for the protolith of this rock is ruled out due to its steady  $^{176}\text{Hf}/^{177}\text{Hf}_{(t)}$  signature, which indicates a homogeneous juvenile source.

Three zircon cores in this sample recorded crystallization temperatures higher than 900 °C. Such high temperatures are in line with a possible gabbroic composition as described for similar compositions (e.g., Grimes et al., 2009; Larsen, 1929).

*Granitic (hornblende)-biotite-bearing leucosome C-838-B* – The signature of the melted source that gave rise to this leucosome is ambiguous. Three data points in the Hf evolution diagram (Fig. 3.11), calculated from their respective individual  $^{207}\text{Pb}/^{206}\text{Pb}$  dates (grains > 1 Ga), follow the average crustal evolution. Such signatures could indicate melts deriving either from a sedimentary source or from inhomogeneous igneous rocks that experienced Pb-loss with  $\epsilon\text{Hf}_{(2700)}$  between -4 and +4. Hence, the only conclusion that can be drawn is that 2.7 Ga-old crustal material contributed to form the granitic (hornblende)-biotite-bearing leucosome instead of the juvenile 2.55 Ga basement.

### 3.10.1.3 *Neoproterozoic rocks*

Hosted in the Neoproterozoic basement, three different magmatic rocks have been identified based on their bulk rock compositions and zircon U-Pb and Lu-Hf signatures (Figs. 3.11A and B):

*Opdalite C-838-2* – This quartz monzonitic opdalite registers a magmatic event at  $786 \pm 10$  Ma. The low  $\epsilon\text{Hf}$  values (-12.6 to -13.4) suggest a crustal origin for the melt. In the Hf evolution diagram (Fig. 3.11) the line of average crustal evolution is parallel to a line linking the Neoproterozoic juvenile basement (C-833-A) and the opdalite, indicating that the composition of the latter can result from melting of the former. Anatexis in the lower crust was likely the main source of the opdalite. Crystallization temperatures between 670 and 780 °C retrieved from Ti-in-zircon thermometry are in line with this scenario.

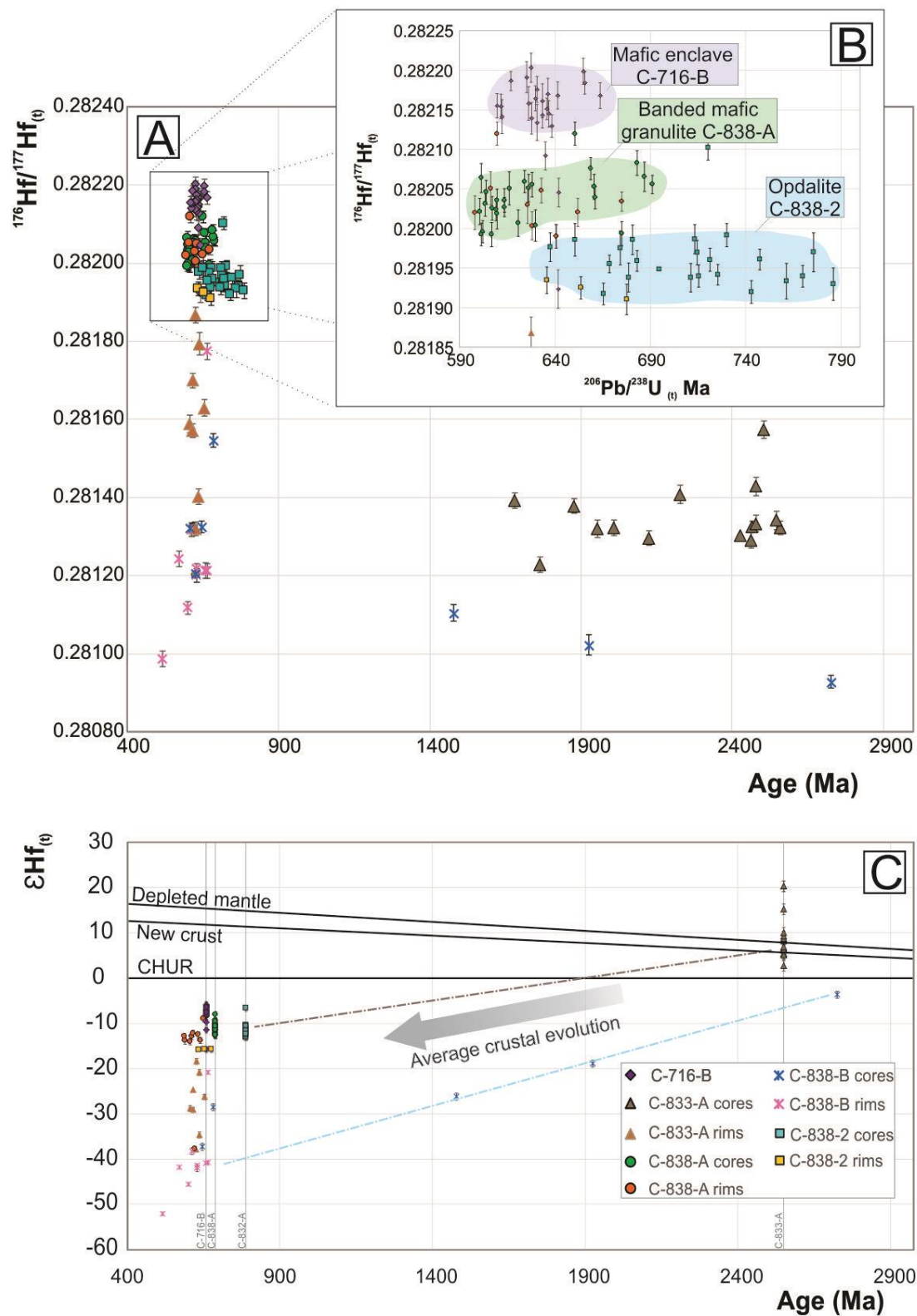


**Figure 3.11:** Zircon Hf isotope data of the Socorro-Guaxupé nappe plotted as (A) initial  $^{176}\text{Hf}/^{177}\text{Hf}(t)$  ratio versus individual dates ( $t$ ), using  $^{207}\text{Pb}/^{206}\text{Pb}$  dates for grains older than 1 Ga and  $^{206}\text{Pb}/^{238}\text{U}$ , for younger grains, (B) Detail of the Neoproterozoic rocks showing the Hf signature fields characteristic of each sample spreading along an approximately horizontal line and indicating different degrees of Pb loss, and (C) Hf-isotope evolution diagram with magmatic data being plotted as  $\epsilon\text{Hf}$  recalculated for their crystallization ages (obtained from the oldest grain) and metamorphic data being plotted for recalculated for their individual dates ( $t$ ). Reference lines are: depleted mantle according to Blichert-Toft and Albarède (1997), chondrite of Griffin et al. (2000) and “New Crust” evolution line from Dhuime et al. (2011).

*Banded mafic granulite C-838-A* – The igneous cores of zircon yielded a magmatic crystallization age of  $691 \pm 3$  Ma. The variable bulk rock composition from monzogabbro to granodiorite can represent magmatic differentiation of the original rocks, as well as a residuum after melt extraction during the anatexis. Like the opdalite, this sample exhibits a crustal  $\epsilon_{\text{Hf}}$  signature (-8.2 to -12.6), which could also reflect partial melting of the basement. A mantle source contributed to the melt forming the gabbroic rocks. The highest temperature of  $\sim 922$  °C recorded in one zircon igneous core most likely represents the crystallization temperature during UHT conditions, while temperatures of 690–780 °C recorded in all other cores are interpreted as underestimated crystallization temperatures due to lower  $\text{TiO}_2$  activity. It could likewise record cooling temperatures.

*Mafic granulite enclave C-716-B* – The mafic granulite enclave is the youngest magmatic rock in this area and zircon crystallization was dated at  $664 \pm 9$  Ma. It has a gabbroic composition and the less radiogenic signature ( $\epsilon_{\text{Hf}} = -5.9$  to -11.4) among the Neoproterozoic rocks (Fig. 3.11C). The bulk rock composition and Hf signature indicate mixing between melt products from mantle and juvenile basement. The crustal Hf signature of the gabbroic enclave furthermore suggests that a metasomatic mantle was involved. Field relationship with the enclaves discordantly disposed as fragments in the felsic leucosome (i.e., magma mixing breccia), suggest a synchronous origin with migmatization. The absence of significant presence of metamorphic rims in zircon and the spreading of zircon dates in the Concordia diagram corroborate a late magmatic origin. Ti-in-zircon thermometry provided temperatures between 710 and 810 °C, up to 1010 °C for a single grain. Ti-in-zircon usually records lower temperatures than major phases-based thermometers (Taylor et al., 2016), although, similar temperatures have been reported for gabbroic magma crystallization as well as high Th/U in zircon (Grimes et al., 2009). It should be noted, that the temperatures from Ti-in-zircon are probably underestimated as  $\text{TiO}_2$  activity was likely lower than one.

To conclude, the Neoproterozoic rock features and signatures are compatible with a volcanic-arc environment (Frost et al., 2001; Pearce et al., 1984). The  $\epsilon_{\text{Hf}}$  signature and lithochemistry, with the opdalite as oldest rock and the gabbroic rock as the youngest, reveal a magmatic activity progressively becoming more juvenile in composition.

### **3.10.2 Petrochronological metamorphic evolution**

The integration of the petrological evolution in an age context permits a better understanding of the rock-forming processes, including the timing and the rates at which these

processes occur (Engi et al., 2017). In the following section,  $P$ - $T$  conditions are coupled to trace elements, Lu-Hf isotopes and U-Pb ages in zircon to reconstruct the ( $P$ )- $T$ - $t$  path.

### 3.10.2.1 Conventional thermobarometric constraints

A robust determination of the peak conditions of the Opx-Cpx granulites is not possible due to the lack of appropriate barometers. However, temperature estimates obtained for this unit can provide valuable insights when combined with  $P$  or  $P$ - $T$  estimates available in the literature.

The cores of clinopyroxene and orthopyroxene are assumed to record the peak metamorphic conditions (M1) with a temperature of  $998 \pm 23$  °C. Though pyroxene of mafic granulites could potentially resemble igneous relicts, two observations are in favor of UHT metamorphic conditions, in addition to the recrystallized texture presented by the ortho- and clinopyroxenes: (i) orthopyroxene-clinopyroxene thermometry yielded temperatures compatible with peak- $P$ - $T$  estimates obtained for a metasedimentary-derived orthopyroxene-garnet leucosome ( $1030 \pm 110$  °C and  $11.7 \pm 1.4$  kbar; Rocha et al., 2017) and a garnet-bearing mafic granulite (ca. 1050 °C and 14 kbar; Del Lama et al., 2000); (ii) UHT metamorphism postdates (see section 9.2.4) the magmatic age of the protolith of the banded mafic granulite analyzed for thermometry (C-838-A) at ca. 690 Ma.

Post-peak temperatures ( $916 \pm 19$  °C) obtained from the pyroxenes rims (R1) are comparable with the peak conditions recorded in a garnet-bearing granulite ( $894 \pm 4$  °C and  $11.9 \pm 0.3$  kbar; Rocha, 2016) and the post-peak conditions ( $865 \pm 38$  °C,  $8.9 \pm 0.8$  kbar) obtained from garnet and orthopyroxene rims in orthopyroxene-garnet leucosome (Rocha et al., 2017).

A second retrograde stage (R2) corresponds to amphibole recrystallization occurred at  $\sim 740$  °C, according to amphibole-plagioclase thermometry. Biotite thermometry reveals similar temperatures of  $\sim 740$  °C. The  $T$  conditions of R2 overlap within uncertainty with the retrograde temperatures of ca. 770 °C recorded in a garnet-bearing granulite (Rocha, 2016). Whereas  $T$  conditions are similar, the pressure estimates are different. Rocha (2016) obtained  $P = 9$  kbar for R1, in line with the results of Del Lama et al. (2000) attained on similar rocks. The pressure conditions obtained in this study (around 6 kbar) are lower, despite using the same geobarometers used by Del Lama et al. (2000). Such differences might possibly represent two different crustal levels that are now exposed in the nappe framework.

### 3.10.2.2 *Temperature insights through zircon*

High Th/U ratios of rims and newly-formed zircon grains can be linked to high and ultra-high temperature rocks, especially for the samples showing Th/U up to 2 (Rubatto, 2017; Whitehouse and Kemp, 2010). Mafic to intermediate composition of the protolith influences, e.g., inhibiting monazite crystallization (Rubatto, 2017).

Only two zircon rims among the studied samples reveal ultra-high temperatures by Ti-in-zircon thermometry. These grains are associated with 650 Ma-old rims from the Neoproterozoic basement and record  $T > 900$  °C (see Fig. 3.8). The Ti-in-zircon thermometer commonly yields lower temperatures than the thermometers based on mineral equilibrium (e.g. Ewing et al., 2012; Kohn et al., 2015). Such differences have been attributed to post-crystallization modification by diffusion or post peak crystallization (Baldwin et al., 2007; Korhonen et al., 2014; Taylor et al., 2016). For the studied rocks, most of the metamorphic zircon rims record retrograde temperatures of 700 °C that likely represent post-peak temperatures since zircon records the cooling history rather than peak conditions in high grade rocks (Harley et al., 2007).

### 3.10.2.3 *Constraints of anatexis*

Trace element bulk rock analyses of leucosomes exhibit positive Eu anomalies and depletions in HREE, regardless of whether they are orthopyroxene-clinopyroxene- or (hornblende)-biotite-bearing. Such patterns are usual for feldspathic cumulates leucosomes produced by low-degree of partial melting (Sawyer, 1987). A similar origin can be constrained from REE in zircon (Figs. 3.6 and 3.7). In garnet-absent rocks, clinopyroxene is expected to have flat REE patterns, while orthopyroxene commonly fractionates the HREE (e.g., Yang and Wei, 2017). In the studied rocks, the REE patterns of zircon cores are retained in the younger rims. This indicates that there was no release or consumption of REE from other, e.g., mafic, phases that are the main HREE hosts. A limited interaction between melt and peritectic phases, e.g., due to a low degree of partial melting, is possibly the reason.

Distinct  $^{176}\text{Hf}/^{177}\text{Hf}$  signatures are expected, if zircon domains formed during different episodes of a rock's evolution (Gerdes and Zeh, 2009; Rubatto, 2017). In the Guaxupé nappe, there is no difference between  $^{176}\text{Hf}/^{177}\text{Hf}$  of zircon cores and rims of the banded mafic granulite (C-838-A) and the opdalite (C-838-2) (Figs. 3.6 and 3.10). The preservation of primary  $^{176}\text{Hf}/^{177}\text{Hf}$  compositions in metamorphic zircons is usually attributed to subsolidus recrystallization (Zeh et al., 2010). This can be an explanation for the absence of melting texture in the opdalite (C-838-2), in which there are fewer zircon rims with a smaller thickness (Figs. 3.6 and 3.12). In contrast, the



preservation of similar  $^{176}\text{Hf}/^{177}\text{Hf}$  ratios in zircon cores and rims of the banded mafic granulite C-838-A, despite strong evidence for anatexis and interaction between melt and restite, with crystallization of newly formed zircon grains, requires a distinct explanation. The clues are: (i) diffuse contact between leucosome and melanosome, (ii) films of melt along mineral boundaries in the melanosome, (iii) peritectic hypersthene and diopside in the leucosome, and (iv) quartz-feldspatic inclusions in zircon rims (Figs. 3.4B and 3.10). The isotopic signatures thus rather suggest that zircon crystallized from a small-volume of melt, likely related to *in situ* melting (Taylor et al., 2016). Due to the presence of K-feldspar only in the leucosome bands, the melt can be also a result of *in source* melting. The fluid or melt that interacted with the growing zircon must have had a low  $^{176}\text{Hf}/^{177}\text{Hf}$  ratio, i.e., without significant contributions from the breakdown of Lu-host phases such as of garnet or other ferromagnesian minerals (Melo et al., 2017; Taylor et al., 2016).

Another mechanism is required for the zircons rims of the banded mafic granulite (C-833-A) and the pinkish granitic (hornblende)-biotite-bearing leucosome (C-838-B) that show newly formed zircon grains with an increase of  $^{176}\text{Hf}/^{177}\text{Hf}$  ratios compared to their protoliths. Such variation implies an input of Hf with high  $^{176}\text{Hf}/^{177}\text{Hf}$  ratios, which also has to account for the 20  $\epsilon\text{Hf}$  units variation between rim and core for the samples C-833-A and C-838-B. Zircon domains and grains with high  $^{176}\text{Hf}/^{177}\text{Hf}$  compared to relict cores are generally interpreted to have crystallized in the presence of Hf-enriched melt and/or fluid (Chen et al., 2011). Release of radiogenic Hf into melts is thereby usually attributed to garnet breakdown (Zheng et al., 2005; Rubatto, 2017), apatite dissolution (Valley et al., 2010) or partial melting reactions involving breakdown of biotite (Melo et al., 2017). In the granitic (hornblende)-biotite-bearing leucosome (C-838-B) variable Hf ratios could be inherited, based on the assumption that the leucosome originated from melting of metasedimentary rocks (section 9.1.2). Since the source of the (hornblende)-biotite-bearing leucosome C-838-B appears to have been an ancient crust (2.7 Ga), in contrast to its Schöllen diatexite host, such melt might have been allochthonous. Interactions between the (hornblende)-biotite-bearing leucosome and green orthopyroxene-clinopyroxene-bearing melts are suggested by field observations, indicating physical mixture and further supporting an allochthonous melt origin (Fig. 3.4A). Melt-rock interactions are more likely to be the cause of the  $^{176}\text{Hf}/^{177}\text{Hf}$  variability in sample C-833-A.

#### 3.10.2.4 Age constraints and link to P-T conditions

Dating of zircon rims provide scattered  $^{206}\text{Pb}/^{238}\text{U}$  dates showing complex distributions. Similar age probability peaks can be retrieved for different samples in an attempt to constrain the age of the successive metamorphic stages (Fig. 3.12). Zircon is particularly important as the

orthopyroxene-bearing leucosomes do not contain any other geochronometers such as monazite or titanite.

Growth, dissolution and re-precipitation of zircon can generally occur at any time during high temperature metamorphism and long periods of melting (Rubatto et al., 2013) and can explain the long-lived metamorphic event registered by zircon ages. Several processes such as metamictization, Pb-redistribution or diffusion can cause zircon resetting depending on the duration of the UHT stage (Harley, 2016). Multiple zircon ages and cluster of ages are further expected as a result of the evolution of (ultra) high-temperature terranes because of dynamic zircon crystallization in the presence of melt. The resulting zircon compositional variability thereby commonly reflects zircon crystallization from segregated melts or interaction between different melts with the respective zircon grains not necessarily exhibiting distinct growth zones (Harley, 2016; Harley and Nandakumar, 2014). Thus, different domains are likely to record different ages. However, because analyses were performed on zircon separates the influence of the domain in which the zircon is hosted cannot be retrieved.

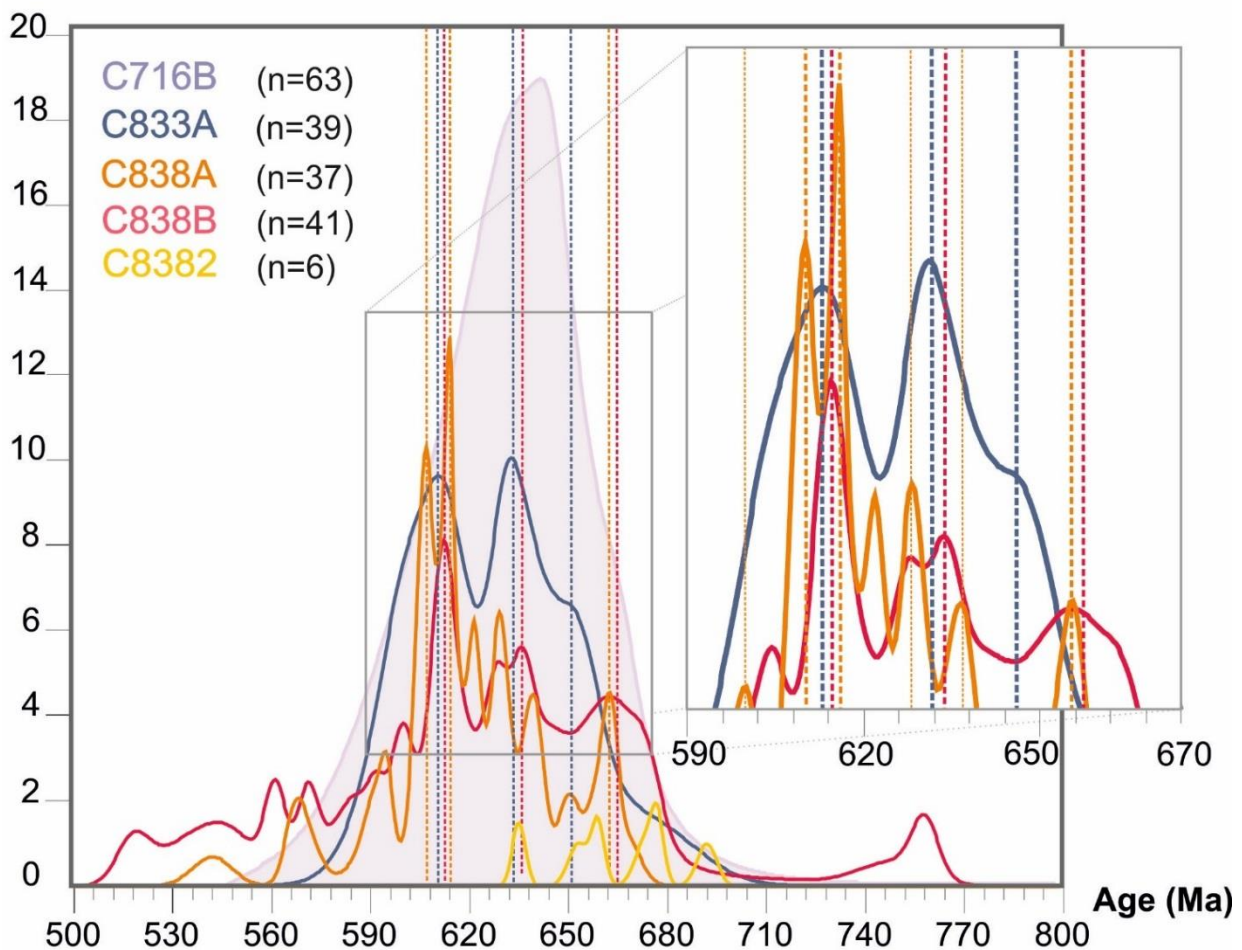


**Figure 3.12:** Probability density diagram for the zircon U/Pb ages of the rims and single phases from the banded mafic granulites (C-833-A and C-838-A), opdalite (C-838-2), and the (hornblende)-biotite-bearing leucosome and the magmatic grains of the mafic granulite enclave (C-716-B) for comparison.

The oldest metamorphic zircon age suggests that the Neoproterozoic metamorphism starts at ca. 680 Ma (Figs. 3.7 and 3.12). The first and most discrete date peak is at ~660 Ma, recorded by zircon from both, the leucosome from the banded mafic granulite (C-838-A) and the pinkish granitic (hornblende)-biotite-bearing leucosome (C-838-B). Zircon data from the newly formed zircon grains and rims of the leucosome from the banded mafic granulite (C-833-A) define the next dates peak at ca. 650 Ma. The three leucosomes show an intermediate around 640–630 Ma that is succeeded by the most prominent age peak at 615–605 Ma, recorded by the same samples. This stage corresponds to the most extensive zircon crystallization record. Zircon growth continued afterwards as indicated by a few zircon ages in the range of 590–550 Ma. The green charnockitic (C-838-A) and the pinkish (hornblende)-biotite-bearing (C-838-B) leucosomes share a common zircon growth history with a progressive increase of the crystallization rate of zircon around 615–600 Ma.

In summary, zircon age data suggest a long-lasting metamorphic event of at least 80 m.y., including three main episodes of zircon growth at (i) 670–650 Ma, (ii) 640–630 Ma, and (iii) 615–590 Ma.

The main arguments of coeval migmatization and emplacement of mafic rocks are: (i) the field relationship between the gabbroic enclaves and their host leucosome; (ii) their chronological relationship, with the mafic enclave being younger than the protolith of its host rock, thus the mafic enclave cannot be a residuum; (iii) the mafic magma emplacement age (ca. 660 Ma) corresponds to the oldest peak of metamorphic zircon crystallization (Fig. 3.12); and (iv) two ca. 655 Ma zircon rims record  $T > 900$  °C for the banded mafic granulite (C-833-A). Therefore, it seems that temperature increased during the early metamorphic event, related to the emplacement of mafic magma.

Zircon crystallization is strongly controlled by the composition and supply of melt (Rubatto, 2017; Rubatto et al., 2001) and is thought to proceed from late melts or along retrograde paths (Kohn et al., 2015; Tedeschi et al., 2017). Many younger zircon grains crystallized at ca. 630–600 Ma under temperatures between 830–690 °C. The great amount of zircon crystallization during that period can be explained by widespread anatexis triggered by elevated temperatures after the UHT metamorphism, together with potential fluid input, during a regional decompression.

UHT peak conditions (~1030 °C at 12 kbar) were dated at 630–625 Ma, from EPMA monazite dating of resorbed Y-rich monazite cores preserved in garnet (Rocha et al., 2017). Those authors presented semi-quantitative maps and quantitative profiles on garnet crystals showing zoned garnet with cores that yield the peak conditions and are enriched in Ca and Mg compared to the rims. The monazite grains exhibiting Y-rich cores, interpreted as prograde and attributed to pre-garnet growth, are inclusions in Ca-poorer rims of garnets, and probably record retrograde

conditions estimated to ca. 860 °C and 9 kbar (Rocha et al., 2017). Taylor et al. (2016) discuss that in some cases Y zoning in monazite may not reflect prograde conditions, resulting in misleading geological complex evolutions (e.g., Kelly et al., 2012; Spear and Pyle, 2010). That Y-enrichment could be explained by local dissolution of peritectic garnet during decompression or beginning of melt production, providing local Y supply. Because those monazites are Th-poor (Rocha et al., 2017), decompression before melting was more likely the driving process. A similar mechanism has been suggested for HREE-enrichment in zircon, which were related to garnet dissolution in HP amphibolites by Tedeschi et al. (2017). Yakymchuk (2017) considered that local variations in melt compositions around apatite could cause monazite crystallization. This process known as pileup, is due to slow diffusion and can generate heterogeneities in the melt compositions (Harrison and Watson, 1984). The Y-rich domains around apatite with ages around 630 Ma, assigned to prograde decompression by Rocha et al. (2017), could thus represent the retrograde decompression in the Guaxupé nappe. The 630 Ma age peak from zircon (this study) and monazite (Rocha et al., 2017) can mark the onset of a retrograde *P-T-t* path (Figs. 3.12 and 3.13). We suggest that retrograde decompression between ca. 625 Ma to 600 Ma triggered widespread migmatization with overwhelming recrystallization of zircon (Fig. 3.12) and Y-poor and Th-rich monazite (*cf* Rocha et al., 2017).

In summary, ultra-high temperature metamorphism in the SGN is estimated to have started at ca. 660 Ma. It was probably triggered by the emplacement of mafic melts; similar processes have been described in other regions (e.g. Ivrea Zone, Ewing et al, 2013; Val Malenco, Hermann et al., 1997).

### **3.10.3 UHT metamorphism in the Southern Brasília orogen**

The tectonic settings in which ultra-high temperature granulite metamorphism takes place are still intensely debated in literature (Harley, 2016; Kelsey and Hand, 2015 and references therein). According to Harley (2016), a key characteristic of G–UHT metamorphism in arc–back arc settings is the strong chronological link between magmatism, accretionary crustal growth and granulite development, as the accretion of juvenile crustal material can enhance conditions for granulite-UHT metamorphism. A key characteristic of arc-related setting for UHT metamorphism is the strong temporal link with major sedimentation, magmatism and metamorphism taking place within a short interval (5–20 m.y.).

The UHT metamorphism lasted for 40 m.y. at a maximum in the Guaxupé nappe (see section 3.10.2.4). An interval of ca. 30 m.y. marks the transition from “fast” to “slow” granulite-UHT

metamorphism (Harley, 2016). Some key features indicate that the studied UHT rocks were metamorphosed within an arc-related system:

- i) The banded mafic granulite (C-838-A) has a crystallization age of  $691 \pm 3$  Ma and the first neo-formed zircon grains and rims yielded dates around  $668 \pm 7$  Ma. This indicates a short interval (ca.10–20 m.y.) between magmatic and metamorphic stages.
- ii) There is an overlapping between the metamorphic zircon ages of the leucosomes (section 3.10.2.3) and the magmatic ages of the mafic magma (C-716-B) suggesting an input of mantle magma during a pre-collisional stage, inducing or increasing a migmatization process.
- iii) The two metamorphic zircon rims that yielded  $T > 900$  °C present  $^{206}\text{Pb}/^{238}\text{U}$  dates at ca. 655 Ma. This is overlapping the emplacement age of the gabbroic mafic enclaves.
- iv) In the southernmost part of the Southern Brasília orogen, metamorphic age from 670 Ma to 630 Ma and the ultra-high temperatures are only recorded in the Guaxupé (this study) and Varginha nappes, which is located directly below the first (see Coelho et al., 2017 for a review). The Varginha nappe is interpreted to represent the metasedimentary rocks of the active margin (Campos Neto et al., 2011) or of passive margin (Trouw et al., 2013).

A thickened crust is required to explain some high pressures recorded (~12–10 kbar) in the Guaxupé nappe and can also explain the crustal Hf isotopic signatures of gabbroic rocks. Indeed, crustal thickening by magmatic addition and intra-arc thrust tectonics is expected for long-lived arc systems on continental margins (Ducea, 2001; Thorpe et al., 1981). The crustal thickening could contribute with additional radioactive decay heat (Clark et al., 2011; Harley, 2016).

### **3.10.4 Regional implications for the Southern Brasília orogeny**

#### **3.10.4.1 *Disclosing the Guaxupé basement***

It has been shown in this study that the Guaxupé nappe hosts a fragment of Neoproterozoic juvenile basement ( $2559 \pm 65$  Ma). This is the first report of a juvenile Archean segment in this nappe. The Neoproterozoic banded mafic granulite (C-833-A) has the same mineral assemblages and similar lithochemical signatures as the Neoproterozoic gneisses (C-838-A). Additional fragments of Neoproterozoic basements can be assumed to have been involved in the formation of the granulitic unit.

The age of the Neoproterozoic basement differs from the other basements close to the Guaxupé nappe, such as the Pouso Alegre (2.1 Ga; Cioffi et al., 2016a; Tedeschi et al., 2017) and Amparo and Serra Negra complexes (3.0–2.7 Ga; Cioffi et al., 2016b), while  $\epsilon_{\text{Hf}}$  signatures are similar (+2.3 to +5.3). In the Socorro nappe further south, a Paleoproterozoic granitic gneiss has been reported (2.1 Ga; Trouw, 2008).

Nonetheless, the Neoproterozoic component in the Socorro-Guaxupé nappe has a metamorphic age of  $2041 \pm 11$  Ma, which is not recorded for any of the aforementioned rocks, as well as in the São Francisco craton. This together with its allochthonous character – as it is part of the Guaxupé nappe – suggest that the Neoproterozoic gneiss could constitute a fragment of an exotic block apart of the São Francisco Craton, probably from the Paranapanema block.

#### 3.10.4.2 *Neoproterozoic magmatism in the Guaxupé nappe*

The first identification of an igneous rock of ~800 Ma (opdalite C-838-2), constrains the chronological history between the Guaxupé nappe in the southernmost portion and the northern part of the Brasília Orogen. Igneous rocks of ca. 800 Ma have been described in the northern portion of the Brasília orogen for arc rocks with juvenile to slightly negative  $\epsilon_{\text{Nd}}$  (Pimentel and Fuck 1992; Pimentel et al., 2016). The youngest magmatic event in the Northern Brasília orogen took place between 670 and 630 Ma, but also presents juvenile  $\epsilon_{\text{Nd}}$  signatures (Laux et al., 2005; Pimentel et al., 2016). In the Guaxupé nappe however, crustal isotopic signatures are dominant.

No clear definition of a magmatic-arc setting for the opdalite (C-838-2) can be made. Zircon from ca. 730–800 Ma have been reported and interpreted as inheritance or xenocrystals in many rocks of the nappe. Such zircon may potentially reflect older protoliths than the one previously invoked (e.g. Rocha, 2016). The  $\epsilon_{\text{Hf}}$  and lithochemical signatures point out to the partial melting of a Neoproterozoic basement acting as a significant source for the magmatic arc.

#### 3.10.4.3 *Evolution of the Guaxupé nappe*

The evolution of the nappe can be divided into the following stages (Fig. 3.13):

- (i) Onset of magmatism at ca. 790 Ma with the intrusion of magma with intermediate composition, mainly derived from lower crust with juvenile signature ( $\epsilon_{\text{Hf}}(2550)$  between +10 and +2.7).

- (ii) Continuation or onset of intermediate to basic arc magmatism at ca. 690 Ma and beginning of arc-related metamorphism at ca. 680–670 Ma. This metamorphism is registered in the metasedimentary rocks from the nappe below the Guaxupé nappe. Monazite dating in the Três-Pontas-Varginha nappe show crystallization ages of 630–660 Ma (Reno et al., 2012) and zircon dating in the Ouro Fino Shear Zone,  $672 \pm 4$  Ma (Tedeschi et al., 2017).
- (iii) Intrusion of mafic magmas having the most juvenile Hf signatures. This magmatic activity triggered UHT metamorphism at ca. 660 Ma.
- (iv) End of arc magmatism marked by the presence of mangerites emplaced at ca. 640 Ma with crustal  $\epsilon_{\text{Hf}}$  (-5 to -10; Mora et al., 2014).
- (v) Transition from subduction to collision at ca. 640–630 Ma;
- (vi) Collision and decompression with extensive partial melting. This stage is marked by continuous monazite and zircon crystallization in the nappe from 630 to 600 Ma. The peak conditions of the collisional stage were 720 °C and 14 kbar achieved at ca. 630 Ma recorded by the high-pressure amphibolite and migmatite of Pouso Alegre close to the nappe. This stage was dated using zircon in the HP amphibolite, monazite in a sillimanite-garnet gneiss and zircon in the orthogneiss from the basement. A slow decompression is recorded ( $1\text{mm.y}^{-1}$ ; Tedeschi et al., 2017).
- (vii) Interference from the Ribeira orogeny (Trouw et al., 2013), the orogen migration or the onset of nappe faulting (Campos Neto et al., 2011) may have been partially recorded and can explain the ages younger than 600 Ma.

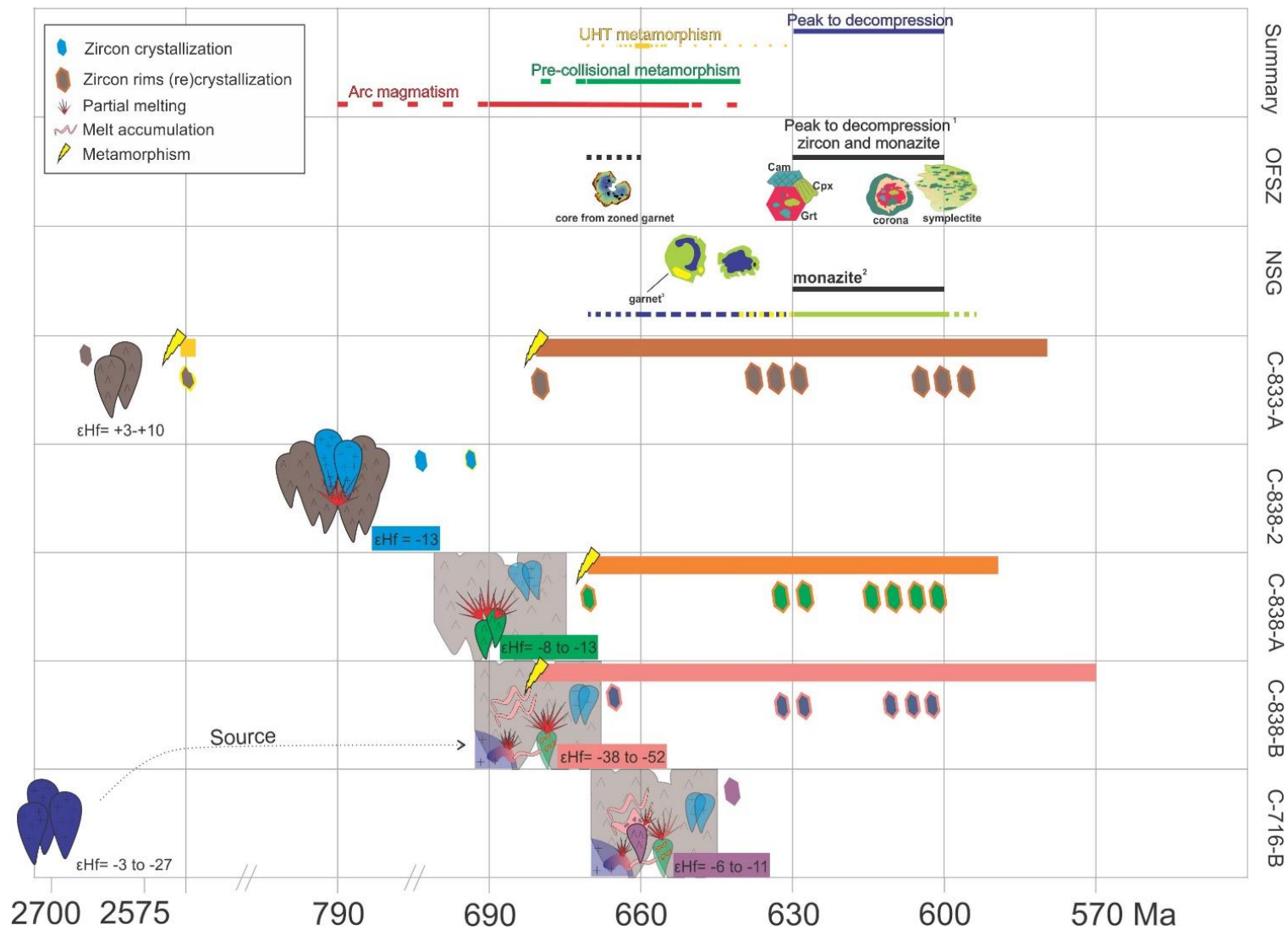


**Figure 3.13:** Summary of the geological evolution of the Guaxupé nappe with emphasis on the temporal distribution, Hf signatures and *P-T* constraints of igneous and metamorphic events of the studied samples. Data from (1) Tedeschi et al. (2017); (2 and 3) Rocha et al. (2017). Transparency applied to elements that constitute previous events, bright colors correspond to new events. Colors follow those used in the data presentation (Figs. 3.7, 3.8, 3.9, 3.10 and 3.12). The distribution of zircon grains represented along the metamorphism bars indicate relative amount of zircon crystallization. SGN – Socorro-Guaxupé nappe; OFSZ – Ouro Fino Shear Zone.



### 3.11 Conclusions

In this study, a new petrochronological dataset was presented for retrogressed UHT granulites. The following aspects of basement evolution through subduction and collisional stage in the southernmost portion of the Brasília orogen were unraveled:

- The basement of the Guaxupé nappe contains a juvenile ( $\epsilon_{\text{Hf}} = +2.7$  to  $+10$ ) Neoproterozoic (2559  $\pm$  65 Ma) fragment, probably from the Paranapanema block. Unlike the other basements in the region it registers an old metamorphic stage at ca. 2.4 Ga.
- The combination of coupled U-Pb and Lu-Hf analyses in zircon permitted the identification of older rocks in the Guaxupé nappe. Such conclusions were previously only inferred from inherited zircon. The arc magmatism lasted at least from 690 to 640 Ma. The first occurrence of magmatic rock at 786  $\pm$  10 Ma in the nappe indicates that magmatic activity started before, lasting for at least ca. 150 m.y.
- The Neoproterozoic juvenile basement acted as the main source for the Neoproterozoic magmatism. A mantle source is also required, especially to form the gabbroic rocks.
- The nappe rocks experienced a long-lived metamorphic event of ca. 80–100 m.y. The 680–640 Ma interval is attributed to subduction-related metamorphism, followed by the collision-related metamorphism between 640 and 630 Ma. A third stage between 630 and 600 Ma is linked to decompression and amphibolite facies metamorphism.
- Field evidence, petrography and  $^{176}\text{Hf}/^{177}\text{Hf}$  ratios indicate that anatexis was driven by different processes: (i) incongruent *in situ* partial melting without external melt contribution was the main anatexis process for the Neoproterozoic banded mafic granulite C-838-A, and (ii) partial melting associated with inputs of allochthonous melt/fluid possibly involving a crustal metasedimentary source was dominant for the granitic (hornblende)-biotite-bearing leucosome C-838-B.
- Peak temperatures of 998  $\pm$  23° C obtained in the mafic to intermediate granulites can be linked to the arc-related UHT metamorphism.

The present study highlights the need for detailed investigations of other metamorphosed magmatic rocks in the Southern Brasília orogen. They could record similar disturbed U-Pb ages that can help to constrain the duration of UHT metamorphism and identify relicts of pre-UHT metamorphism.

## 3.12 Acknowledgments

This research was supported by the Brazilian “Science Without Borders Program” with a scholarship and grant to M. Tedeschi (CNPq 202054/2015-2), and CODEMIG and CNPq projects coordinated by A. Pedrosa Soares. We are grateful to all those institutions. D. Rubatto and J. Hermann are greatly thanked for fruitful discussion. We also thank A. Alkmim, Universidade Federal de Ouro Preto, for analytical assistance with the LA-ICP-MS. A. Pedrosa Soares and I. Dussin are grateful to the CNPq for their productivity grants.

## 3.13 References

- Alkmim, F.F., Marshak, S., Fonseca, M.A., 2001. Assembling West Gondwana in the Neoproterozoic; clues from the Sao Francisco Craton region, Brazil. *Geology* 29, 319–322.
- Baldwin, J.A., Brown, M., Schmitz, M.D., 2007. First application of titanium-in-zircon thermometry to ultra-high temperature metamorphism. *Geology* 35, 295–298.
- Baldwin, J.A., Powell, R., Brown, M., Moraes, R., Fuck, R.A., 2005. Modelling of mineral equilibria in ultrahigh-temperature metamorphic rocks from the Anápolis–Itaúçu Complex, central Brazil. *Journal of Metamorphic Geology* 23 (7), 511–531.
- Bégin, N. J., Pattison, D. R. M., 1994. Metamorphic evolution of granulites in the Minto Block, northern Québec: extraction of peak P-T conditions taking account of late Fe-Mg exchange. *Journal of Metamorphic Geology* 12, 411–428.
- Belousova, E., Griffin, W., O’Reilly, S.Y., Fisher, N., 2002. Igneous zircon: trace element composition as an indicator of source rock type. *Contributions to Mineralogy and Petrology* 143, 602–622.
- Belousova, E.A., Kostitsyn, Y.A., Griffin, W.L., Begg, G.C., O’Reilly, S.Y., Pearson, N.J., 2010. The growth of the continental crust: constraints from zircon Hf-isotope data. *Lithos* 119, 457–466.
- Blichert-Toft, J., Albarède, F., 1997. The Lu-Hf geochemistry of chondrites and the evolution of the mantle-crust system. *Earth and Planetary Sciences Letters* 148, 243–258.
- Boehnke, P., Watson, E.B.B., Trail, D., Harrison, T.M.M., Schmitt, A.K.K., 2013. Zircon Saturation Re-Revisited. *Chemical Geology* 351, 324–334.
- Brito Neves, B.B., Campos Neto, M.C., Fuck, R.A., 1999. From Rodinia to Western Gondwana: an approach to the Brasiliano-Pan African cycle and orogenic collage. *Episodes* 22, 155–166.

- Campos Neto, M.C., Basei, M.A.S., Janasi, V., Moraes, R., 2011. Orogen migration and tectonic setting of the Andrelândia Nappe system: An Ediacaran western Gondwana collage, south of São Francisco craton. *Journal of South American Earth Sciences* 32, 393–406.
- Campos Neto, M.C., Basei, M.A.S., Vlach, S.R.F., Caby, R., Szabó, G.A.J., Vasconcelos, P., 2004. Migração de orógenos e superposição de orogêneses: um esboço da colagem Brasileira no sul do Cráton do São Francisco, SE e Brasil. *Geologia USP Série Científica* 4 (1), 13–40.
- Campos Neto, M.C., Caby, R., 1999. Neoproterozoic high-pressure metamorphism and tectonic constraint from the nappe system south of the São Francisco Craton, southeast Brazil. *Precambrian Research* 97 (1–2), 3–26.
- Campos Neto, M.C., Caby, R., 2000. Lower crust extrusion and terrane accretion in the Neoproterozoic nappes of southeast Brazil. *Tectonics* 19, 669–687.
- Campos Neto, M.C.; Figueiredo, M.C.H., 1995. The Rio Doce orogeny, southeastern Brazil. *Journal South American Earth Sciences* 8(2), 143–162.
- Chappell, B.W., White, A.J.R., 1974. Two contrasting granite types. *Pacific Geology* 7, 173–174.
- Chappell, B.W., White, A.J.R., 2001. Two contrasting granite types: 25 years later. *Australian Journal of Earth Sciences*, 48: 489–499.
- Chen, Y.-X., Zheng, Y.-F., Chen, R.-X., Zhang, S.-B., Li, Q., Dai, M., Chen, L., 2011. Metamorphic growth and recrystallization of zircons in extremely  $^{18}\text{O}$ -depleted rocks during eclogite-facies metamorphism: Evidence from U–Pb ages, trace elements, and O–Hf isotopes. *Geochimica Cosmochimica Acta* 75, 4877–4898.
- Cherniak, D.J., Watson, B.E., 2003. Diffusion in zircon. *Reviews in Mineralogy and Geochemistry* 53, 113–143.
- Cioffi, C.R., Campos Neto, M. C., Möller, A., Rocha, B.C., 2016a. Paleoproterozoic continental crust generation events at 2.15 and 2.08 Ga in the basement of the southern Brasília Orogen, SE Brazil. *Precambrian Research* 275, 176–196.
- Cioffi, C. R.; Campos Neto, M. C., Möller, A., Rocha, B. C. 2016b. Tectonic significance of the Meso- to Neoarchean complexes in the basement of the southern Brasília Orogen. *Precambrian Research* 287, 91–107.
- Clark, C., Fitzsimons, I.C. W, Healy, D, Harley, S.L, 2011. How does the continental crust get really hot? *Elements* 7, 235–240.
- Coelho, M.B., Trouw, R.A.J., Ganade, C.E., Vinagre, R., Mendes, J.C., Sato, K., 2017. Constraining timing and P-T conditions of continental collision and late overprinting in the Southern Brasília Orogen (SE-Brazil): U-Pb zircon ages and geothermobarometry of the Andrelândia Nappe System. *Precambrian Research* 292, 194–215.

- Cordani, U. G., Brito-Neves, B. B., D'Agrella-Filho, M. S., 2003. From Rodinia to Gondwana: a review of the Available Evidence from South America. *Gondwana Research* 6(2), 275–283.
- Cordani, U.G., Brito Neves, B.B. de B., Fuck, R.A., Thomaz Filho, A., Cunha, F. M. B., 1984, Estudo preliminar de integração do Pré-Cambriano com os eventos tectônicos da Bacias Sedimentares Brasileiras. *Revista Ciência-Técnica-Petróleo. Secção Exploração de Petróleo. Petrobrás/Cenpes/Sintep, Publicação*15, p. 70.
- Corfu, F., Hanchar, J.M., Hoskin, P.W.O, Kinny, P., 2003. Atlas of zircon textures, in: Hanchar, J.M., Hoskin, P.W.O. (Eds.), *Zircon. Reviews in Mineralogy and Geochemistry*, 53, pp. 469-500.
- De Andrade, V., Vidal, O., Lewin, E., O'Brien, P., Agard, P., 2006. Quantification of electron microprobe compositional maps of rock thin sections: An optimized method and examples. *Journal of Metamorphic Geology* 24, 655-668.
- Del Lama, E.A., Zanardo, A., Oliveira, M.A.F., Morales, N., 2000. Exhumation of high pressure granulites of the Guaxupé complex, southeastern Brazil. *Geological Journal* 35, 231–249.
- Degler, R., Zogheib, F.F., Martins, L.C.D., Novo, T., 2015. *Geologia das Folha Nova Resende (SF.23-V-D-I) 1:100.000. Projeto Fronteiras de Minas, CODEMIG-UFMG, Belo Horizonte, Brazil.*
- Dhuime, B., Hawkesworth, C., Cawood, P., 2011. When continents formed. *Science* 331, 154–155.
- Dhuime, B., Wuestefeld, A., Hawkesworth, C.J., 2015. Emergence of modern continental crust about 3 billion years ago. *Nature Geosciences* 8, 552–555.
- Drüppel, K., Elsässer, L., Brandt, S., Gerdes, A., 2013. Sveconorwegian mid-crustal ultrahigh-temperature metamorphism in Rogaland, Norway: U–Pb LA-ICP-MS geochronology and pseudosections of sapphirine granulites and associated paragneisses. *Journal of Petrology* 54, 305–350.
- Ducea, M., 2001. The California arc: Thick granitic batholiths, eclogitic residues, lithospheric-scale thrusting, and magmatic flare-ups. *GSA Today*, 11(11), 4-10.
- Engi, M., Lanari, P., Kohn, M., 2017. Significant Ages - An Introduction to Petrochronology. In: Kohn, M.J., Engi, M., Lanari, P. (Eds.), *Petrochronology. Reviews in Mineralogy and Geochemistry* 83, pp. 55-102.
- Ewing, T., Hermann, J., Rubatto, D., 2013. The robustness of the Zr-in-rutile and Ti-in-zircon thermometers during high-temperature metamorphism (Ivrea-Verbano Zone, northern Italy). *Contributions to Mineralogy and Petrology* 165, 757–779.
- Ferry, J.M., Watson, E.B., 2007. New thermodynamic models and revised calibrations for the Ti-in-zircon and Zr-in-rutile thermometers. *Contributions to Mineralogy and Petrology* 154 (4), 429–437.

- Frost, B.R., Barnes, C.G., Collins, W.J., Arculus, R.J., Ellis, D.J., Frost, C.D., 2001. A geochemical classification for granitic rocks. *Journal of Petrology* 42, 2033–2048.
- Fuck, R., Pimentel, M., Alvarenga, C.J.S., Dantas, E.L., 2017. The Northern Brasília Belt. In: Helibron, M., Cordani, U.G., Alkmim, F.F. (Eds), *São Francisco Craton, Eastern Brazil*. Springer International Publishing, Switzerland, pp. 189–205.
- Garcia, M.G.M., Campos Neto, M.C., 2003. Contrasting metamorphic conditions in the Neoproterozoic collision-related Nappes south of Sao Francisco Craton, SE Brazil. *Journal of South American Earth Sciences* 15 (8), 853–870.
- Gerdes, A., Zeh, A., 2009. Zircon formation versus zircon alteration-New insights from combined U–Pb and Lu–Hf in-situ LA-ICP-MS analyses, and consequences for the interpretation of Archean zircon from the Central Zone of the Limpopo Belt. *Chemical Geology* 261, 230–243.
- Ghent, E.D., Stout, M.Z., 1984. TiO<sub>2</sub> activity in metamorphosed pelitic and basic rocks-principles and applications to metamorphism in southeastern Canadian cordillera. *Contributions to Mineralogy and Petrology* 86, 248–255.
- Griffin, W.L., Pearson, N.J., Belousova, E., Jackson, S.E., van Acherbergh, E., O'Reilly, S.Y., Shee, S.R., 2000. The Hf isotope composition of cratonic mantle: LAM-MC-ICPMS analysis of zircon megacrysts in kimberlites. *Geochimica et Cosmochimica Acta* 64, 133–147.
- Grimes, C.B., John, B.E., Cheadle, M.J., Mazdab, F.K., Wooden, J.L., Swapp, S., Schwartz, J.J., 2009. On the occurrence, trace element geochemistry, and crystallization history of zircon from in situ ocean lithosphere. *Contributions to Mineralogy and Petrology* 158, 757–783.
- Hackspacher, P.C., Fetter, A.H., Ebert, H.D., Janasi, V.A., Dantas, E.L., Oliveira, M.A.F., Braga, I.F., Negri, F.A. 2003. Magmatismo há ca. 660-640 Ma no Domínio Socorro: registros de convergência pré-colisional na aglutinação do Gondwana Ocidental. *Geologia USP, Série Científica* 3, 85–96.
- Hammarstrom, J.M., Zen, E.-An., 1986. Aluminium in hornblende: an empirical igneous geobarometer. *American Mineralogist* 71, 1297-1313.
- Henry, D.J., Guidotti, C.V., Thomson, J.A., 2005. The Ti-saturation surface for low-to-medium pressure metapelitic biotites: implications for geothermometry and Ti-substitution mechanisms. *American Mineralogist* 90, 316–328.
- Harley, S.L., 2016. A matter of time: The importance of the duration of UHT metamorphism. *Journal of Mineralogical and Petrological Sciences* 111, 50-72.
- Harley, S.L., Kelly, N.M., Möller, A., 2007. Zircon and the thermal histories of hot mountain belts. *Elements* 3, 25–30.

- Harley, S.L., Nandakumar, V., 2014. Accessory mineral behavior in granulite migmatites: A case study from the Kerala Khondalite Belt, India. *Journal of Petrology* 55, 1965–2002.
- Harrison, T.M., Watson, E.B., 1984. The behavior of apatite during crustal anatexis: equilibrium and kinetic considerations. *Geochimica et Cosmochimica Acta* 48, 1467–1477.
- Hermann, J., Müntener, O., Trommsdorff, V., Hansmann, W., Piccardo, G. B., 1997. Fossil crust-to-mantle transition, Val Malenco (Italian Alps). *Journal of Geophysical Research* 102, 20123–20132.
- Holland, T., Blundy, J., 1994. Non-ideal interactions in calcic amphiboles and their bearing on amphibole-plagioclase thermometry: *Contributions to Mineralogy and Petrology* 116, 433–447.
- Hollister, L.S., Grissom, G.C., Peters, E.K., Stowell, H.H., Sisson, V.B., 1987. Confirmation of the empirical correlation of Al in hornblende with pressure of solidification of calc-alkaline plutons. *American Mineralogist* 72, 231–239.
- Janasi, V.A., 1999. Petrogênese de granitos crustais da Nappe de Empurrão Socorro- Guaxupé (SP-MG): uma contribuição da geoquímica elemental e isotópica. Thesis (Livre-Docência)—IGC-USP, 304 p.
- Janasi, V.A., 2002. Elemental and Sr-Nd isotope geochemistry of two Neoproterozoic mangerite suites in SE Brazil: implications for the origin of the mangerite–charnockite–granite series. *Precambrian Research* 119, 301–327.
- Johnson, M.C., Rutherford, M.J., 1989. Experimental calibration of the aluminium-in-hornblende geobarometer with application to Long Valley Caldera (California) volcanic rocks. *Geology* 17, 837–841.
- Kelly, N.M., Harley, S.L., 2004. Orthopyroxene–corundum in Mg–Al-rich granulites from the Oygarden Islands, East Antarctica. *Journal of Petrology* 45 (7), 1481–1512.
- Kelly, N.M., Harley, S.L., Möller, A., 2012. Complexity in the behavior and recrystallization of monazite during high-T metamorphism and fluid infiltration. *Chemical Geology* 322–323, 192–208.
- Kelsey, D.E., 2008, On ultrahigh-temperature crustal metamorphism. *Gondwana Research* 13, 1–29.
- Kelsey, D.E., White, R. W., Holland, T.J.B., Powell, R., 2004. Calculated phase equilibria in K<sub>2</sub>O-FeO-MgO-Al<sub>2</sub>O<sub>3</sub>-SiO<sub>2</sub>-H<sub>2</sub>O for sapphirine-quartz-bearing mineral assemblages. *Journal of Metamorphic Geology* 22, 559–578.
- Kelsey, D.E., Hand, M., 2015. On ultrahigh temperature crustal metamorphism: phase equilibria, trace element thermometry, bulk composition, heat sources, timescales and tectonic settings. *Geoscience Frontiers* 6, 311–356.

- Kemp, A.L.S., Slmura, T., Hawkesworth, C.J., 2007. Linking granulites, silicic magmatism, and crustal growth in arcs: Ion microprobe (zircon) U-Pb ages from the Hidaka metamorphic belt, Japan. *Geology* 35, 807-810.
- Kohn, M.J., Corrie, S.L., Markley, C., 2015. The fall and rise of metamorphic zircon. *American Mineralogist* 100, 897-908.
- Korhonen, F.J., Clark, C., Brown, M., Taylor, R.J.M., 2014. Taking the temperature of Earth's hottest crust. *Earth and Planetary Science Letters* 408, 341–354.
- Kretz, R., 1982. Transfer and exchange equilibria in a portion of the pyroxene quadrilateral as deduced from natural and experimental data. *Geochimica et Cosmochimica Acta* 46, 411-21.
- Lanari, P., Engi, M., 2017. Local bulk composition effects on mineral assemblages, in: Kohn, M.J., Engi, M., Lanari, P. (Eds.) *Petrochronology. Reviews in Mineralogy and Geochemistry* 83, pp. 55-102.
- Lanari, P., Giuntoli, F., Loury, C., Burn, M., Engi, M., 2017. An inverse modeling approach to obtain P-T conditions of metamorphic stages involving garnet growth and resorption. *European Journal of Mineralogy* 29, 181–199.
- Lanari, P., Riel, N., Guillot, S., Vidal, O., Schwartz, S., Pcher, A., Hattori, K.H., 2013. Deciphering high-pressure metamorphism in collisional context using microprobe mapping methods: application to the Stak eclogitic massif (northwest Himalaya). *Geology* 41(2), 111–114.
- Lanari, P., Vidal, O., De Andrade, V., Dubacq, B., Lewin, E., Grosch, E. G., Schwartz, S., 2014. XMapTools: a MATLAB-based program for electron microprobe X-ray image processing and geothermobarometry. *Computers & Geosciences* 62, 227-240.
- Larsen, E.S., 1929. The temperature of magmas. *American Mineralogist* 14, 81-94.
- Laux J.H., Pimentel M.M., Dantas E.L., Armstrong R., Junges S.L. 2005. Two Neoproterozoic crustal accretion events in the Braslia Belt, central Brazil. *Journal of South American Earth Sciences*, 18:183-198.
- Liang, Y., Sun, C.G., Yao, L.J., 2013. A REE-in-two-pyroxene thermometer for mafic and ultramafic rocks. *Geochimica et Cosmochimica Acta* 102, 246–260.
- Mantovani, M.S.M., Brito-Neves, B.B., 2005. The Paranapanema lithospheric block: its importance for Proterozoic (Rodinia, Gondwana) supercontinent theories. *Gondwana Research* 8 (3), 303–315.
- Mantovani, M. S. M., Brito-Neves, B. B., 2009. The Paranapanema Lithospheric Block: its nature and role in the Accretion of Gondwana. In: Gaucher, C.; Sial, A.; Halverson, G.; Frimmel, H. (Eds.), *Neoproterozoic-Cambrian Tectonics, Global Change and Evolution: A Focus on South Western Gondwana*. Elsevier, Amsterdam, 2009. pp. 257–272.

- Martins, L., Vlach, S.R.F., Janasi, V.d.A., 2009. Reaction microtextures of monazite: correlation between chemical and age domains in the Nazaré Paulista migmatite, SE Brazil. *Chemical Geology* 261 (3–4), 271–285.
- McDonough, W.F., Sun, S.S., 1995. The composition of the earth. *Chemical Geology* 120, 223–254.
- Melo, M., Lana, C., Stevens, G., Pedrosa-Soares, A., Gerdes, A., Alkmin, A., Nalini Jr., H., Alkmim, F., 2017. Assessing the isotopic evolution of S-type granites of the Carlos Chagas Batholith, SE Brazil: Clues from U–Pb, Hf isotopes, Ti geothermometry and trace element composition of zircon. *Lithos* 284–285, 730–750.
- Middlemost, E.A.K., 1989. Iron Oxidation Ratios, Norms and the Classification of Volcanic Rocks. *Chemical Geology* 77, 19–26.
- Möller, A., O’ Brien, P.J., Kennedy, A., Kröner, A., 2003. Linking growth episodes of zircon and metamorphic textures to zircon chemistry: an example from the ultrahigh-temperature granulites of Rogaland (SW Norway). In: Vance, D., Müller, W., I.M, Villa (Eds.), *Geochronology: Linking the Isotopic Record with Petrology and Textures—Geological Society, London, Special Publications* 220, pp. 65–81.
- Mora, C.A.S., Campos Neto, M.C., Basei, M.A.S., 2014. Syn-collisional lower continental crust anatexis in the Neoproterozoic Socorro–Guaxupé Nappe System, southern Brasília Orogen, Brazil: constraints from zircon U–Pb dating, Sr–Nd–Hf signatures and whole-rock geochemistry. *Precambrian Research* 255, 847–864.
- Moraes, R., Fuck, R.A., 2000. Ultra-high-temperature metamorphism in Central Brazil: the Barro Alto complex. *Journal of Metamorphic Geology* 18, 345–358.
- Pearce, J.A., 1996. Sources and settings of granitic rocks. *Episodes* 19, 120–125.
- Pearce, J.A., Harris, N.B.W., Tindle, A.G., 1984. Trace element discrimination diagrams for the tectonic interpretation of granitic rocks. *Journal of Petrology* 25, 956–983.
- Peixoto, E.I.P., Falci, A., Noronha, R.C., Degler, R., Martins, L.C.D., Nassif, M.T., Freitas, A.R., Novo, T., 2015. *Geologia das Folhas Andradas (SF.23-Y-A-III) e Ouro Fino 1:100.000 (SF.23-Y-B-I)*. Projeto Fronteiras de Minas, CODEMIG-UFMG, Belo Horizonte, Brazil.
- Pimentel, M.M., 2016. The tectonic evolution of the Neoproterozoic Brasília Belt, central Brazil: a geochronological and isotopic approach. *Brazilian Journal of Geology* 46 (1), 67–82.
- Pimentel, M.M., Fuck R.A., 1992. Neoproterozoic crustal accretion in central Brazil. *Geology* 20, 375–379.



- Pimentel, M.M., Fuck, R.A., Gioia, D.M.C.L., 2000. The Neoproterozoic Goiás Magmatic Arc, Central Brazil: A review and new Sm-Nd isotopic data. *Revista Brasileira de Geociências*, 30(1):35–39.
- Renne, P.R., Ernesto, M., Pacca, I.G., Coe, R.S., Glen, J.M., Prevot, M., Perrin, M., 1992. The age of the Parana flood volcanism, rifting of Gondwanaland, and the Jurassic–Cretaceous boundary. *Science* 258, 975–979.
- Reno, B.L., Piccoli, P.M., Brown, M., Trouw, R.A.J., 2012. In situ monazite (U–Th)–Pb ages from the Southern Brasília Belt, Brazil: constraints on the high temperature retrograde evolution of HP granulites. *Journal of Metamorphic Geology* 30 (1), 81–112.
- Ribeiro, A., Nascimento, D., Bongioiolo, E., Trouw, R., Polo, H., Tavares, F., Nepomuceno, F., 2010. *Geologia da Folha Pouso Alegre (SF.23-Y-B-II) 1:100.000*. Programa Geologia do Brasil, CPRM-UFRJ, Rio de Janeiro, Brazil.
- Ribeiro, A., Nascimento, D., Campos, M.T., Oliveira, F., Rocha, F., 2010. *Geologia da Folha Machado (SF.23-V-D-V) 1:100.000*. Programa Geologia do Brasil, CPRM-UFRJ, Rio de Janeiro, Brazil.
- Ribeiro, A., Campos, M.T., Paciullo, F.V., Carvalho, M.V., Valeriano, C.M., Nascimento, D., 2010. *Geologia da Folha Alfenas (SF.23-V-D-II) 1:100.000*. Programa Geologia do Brasil, CPRM-UFRJ, Rio de Janeiro, Brazil.
- Rocha, B.C. 2016. Idade, duração e condições P-T do metamorfismo de temperatura ultra-alta, anatexia e cristalização de fundido na nappe Socorro-Guaxupé. PhD thesis, Universidade de São Paulo, p. 229.
- Rocha, B. C., Moraes, R., Möller, A., Cioffi, C. R., Jercinovic, M.J., 2017. Timing of anatexis and melt crystallization in the Socorro-Guaxupé Nappe, SE Brazil: insights from trace element composition of zircon, monazite and garnet coupled to U-Pb geochronology. *Lithos* 277, 337–355.
- Rubatto, D., 2017. Zircon: The Metamorphic Mineral, In: Kohn, M.J., Engi, M., Lanari, P. (Eds.) *Petrochronology. Reviews in Mineralogy and Geochemistry* 83, pp. 261-289.
- Rubatto, D., Williams, I.S., Buick, I.S., 2001. Zircon and monazite response to prograde metamorphism in the Reynolds Range, central Australia. *Contributions to Mineralogy and Petrology* 140, 458–468.
- Rubatto, D., Hermann, J., Buick, I.S., 2006. Temperature and bulk composition control on the growth of monazite and zircon during low-pressure anatexis (Mount Stafford, central Australia). *Journal of Petrology* 47, 1973–1996.
- Santosh, M., Kusky, T., 2009. Origin of paired high pressure–ultrahigh-temperature orogens: a ridge subduction and slab window model. *Terra Nova* 22, 35-40.

- Santosh, M., Tsunogae, T., Li, J.H., Liu, S.J., 2007. Discovery of sapphirine-bearing Mg-Al granulites in the North China Craton: implications for Palaeoproterozoic ultrahigh temperature metamorphism. *Gondwana Research* 11, 263-285.
- Sawyer, E. W., 1987. The role of partial melting and fractional crystallization in determining discordant migmatite leucosome compositions. *Journal of Petrology* 32, 701–738.
- Sawyer, E.W., 1999. Criteria for the Recognition of Partial Melting. *Physics and Chemistry of the Earth, Part A: Solid Earth and Geodesy* 24(3), 269-279.
- Sawyer, E.W., 2008. The Atlas of migmatites. *The Canadian Mineralogist, Special Publication* 9. NRC Research Press, Ottawa, p. 371.
- Shand, S.J., 1943. *Eruptive rocks*. D. Van Nostrand Company, New York, p. 360.
- Spear, F.S., Pyle, J.M., 2010. Theoretical modeling of monazite growth in a low-Ca metapelite. *Chemical Geology* 273 (1–2), 111–119.
- Stepanov, A., Rubatto, D., Hermann, J., Korsakov, A.V., 2016. Contrasting P–T paths within the Barchi-Kol UHP terrain (Kokchetav Complex): Implications for subduction and exhumation of continental crust. *American Mineralogist* 101(4), 788-807.
- Sun, C.G., Liang, Y., 2015. A REE-in-garnet–clinopyroxene thermobarometer for eclogites, granulites and garnet peridotites. *Chemical Geology* 393–394, 79–92.
- Taylor, R.J.M., Kirkland, C.L., Clark, C., 2016. Accessories after the facts: Constraining the timing, duration and conditions of high-temperature metamorphic processes. *Lithos* 264, 239-257.
- Tedeschi, M., Lanari, P., Rubatto, D., Pedrosa-Soares, A., Hermann, J., Dussin, I., Pinheiro, M. A. P., Bouvier, A.-S., Baumgartner, L., 2017. Reconstruction of multiple P-T-t stages from retrogressed mafic rocks: Subduction versus collision in the Southern Brasília orogen (SE Brazil). *Lithos* 294-295, 283-303.
- Tedeschi, M., Novo, T., Azevedo, R., Amaral, L.F.S., Degler, R., Viera, P.L.N.C.R., 2015. *Geologia das Folhas Caldas (SF.23-V-D-IV) e Poços de Caldas (SF.23-V-C-VI) 1:100.000*. Projeto Fronteiras de Minas, CODEMIG-UFMG, Belo Horizonte, Brazil.
- Thorpe, R.S., Francis, P.W., Harmon, R.S., 1981. Andean andesites and crustal growth. *Philosophical Transactions of the Royal Society of London* 301, 305-320.
- Töpfer, C., 1996. *Brasiliano-granitoide in den Bundesstaaten São Paulo und Minas Gerais, Brasilien - eine Vergleichende studie*. Münchner Geologische Hefte A17, 258.
- Trouw, C. C., 2008. Mapeamento da Folha Virgínia–MG, Geocronologia U-Pb (SHRIMP) em zircões e interpretação geotectônica. PhD Thesis, Universidade do Rio de Janeiro, p.127.

- Trouw, R.A.J., Heilbron, M., Ribeiro, A., Paciullo, F., Valeriano, C.M., Almeida, J.C.H., Tupinambá, M., Andreis, R.R., 2000. The central segment of Ribeira belt. In: Cordani, U.G., Milani, E.J., Thomaz Filho, A., Campos, D.A. (Eds.), *Tectonic Evolution of South America*. 31th International Geological Congress. Rio de Janeiro, Brazil, pp. 287–310.
- Trouw, R.A.J., Nunes, R.P.M., Castro, E.M.O., Trouw, C.C., Matos, G.C., 2008. Nota explicativa das Folhas Varginha (SF.23-V-D-VI) e Itajubá (SF.23-Y-B-III). Programa Geologia do Brasil. Contrato CPRM-UFRJ, p. 99.
- Trouw, R.A.J., Peternel, R., Ribeiro, A., Heilbron, M., Vinagre, R., Duffles, P., Trouw, C.C., Fontainha, M., Kussama, H.H., 2013. A new interpretation for the interference zone between the southern Brasília belt and the central Ribeira belt, SE Brazil. *Journal of South American Earth Sciences* 48, 43–57.
- Valeriano, C., 2017. The Southern Brasília Belt. In: Heilbron, M., Cordani, U.G., Alkmim, F.F. (Eds.), *São Francisco Craton, Eastern Brazil*. Springer International Publishing, Switzerland, pp. 189–205.
- Valley, P.M., Fisher, C.M., Hanchar, J.M., Lam, R., Tubrett, M., 2010. Hafnium isotopes in zircon: A tracer of fluid-rock interaction during magnetite–apatite (“Kiruna-type”) mineralization. *Chemical Geology* 275, 208–220.
- Vervoort, J.D., Kemp, A.I.S., 2016. Clarifying the zircon Hf isotope record of crust–mantle evolution. *Chemical Geology* 425, 65–75.
- Vinagre R., Trouw R.A.J., Mendes J.C., Duffles P., Peternel R., Matos, G., 2014. New Evidence of a Magmatic Arc in the Southern Brasília Belt, Brazil: The Serra da Água Limpa Batholith (Socorro-Guaxupé Nappe). *Journal of South American Earth Science* 54, 120–139.
- Wang, W., Liu, S., Cawood, P. A., Guo, Rongrong, Bai, X., Guo, B., 2017. Late Neoproterozoic crust–mantle geodynamics: Evidence from Pingquan Complex of the Northern Hebei Province, North China Craton. *Precambrian Research* 303, 473–493.
- Watson, E.B., Harrison, T.M., 1983. Zircon saturation revisited: temperature and composition effects in a variety of crustal magma types. *Earth and Planetary Sciences Letters* 64, 295–304.
- Watson, E.B., Wark, D.A., Thomas, J.B., 2006. Crystallization thermometers for zircon and rutile. *Contributions to Mineralogy Petrology* 151, 413–433.
- Westin, A., Campos Neto, M.C., Hawkesworth, C.J., Cawood, P.A., Dhuime, B., Delavault, H., 2016. A Paleoproterozoic intra-arc basin associated with a juvenile source in the Southern Brasília Orogen: Application of U–Pb and Hf–Nd isotopic analyses to provenance studies of complex areas. *Precambrian Research* 276, 178–193.

- Whalen, J. B., McNicoll, V. J., van Staal, C.R., Lissenberg, C. J., Longstaffe, F.J., Jenner, G. A., van Breeman, O., 2006. Spatial, temporal and geochemical characteristics of Silurian collision-zone magmatism, Newfoundland Appalachians: An example of a rapidly evolving magmatic system related to slab break-off. *Lithos* 89, 377-404.
- Whitehouse, M., Kemp, A.I.S., 2010. On the difficulty of assigning crustal residence, magmatic protolith and metamorphic ages to Lewisian granulites: constraints from combined in situ U–Pb and Lu–Hf isotopes. *Geological Society, London, Special Publications* 335, 81–101.
- Whitney, D.L., Evans, B.W., 2010. Abbreviations for names of rock-forming minerals. *American Mineralogist* 95, 185–187.
- Yakymchuk, C., 2017. Behaviour of apatite during partial melting of metapelites and consequences for prograde suprasolidus monazite growth. *Lithos* 274-275, 412-426.
- Yang, C., Wei, C. Ultrahigh temperature (UHT) mafic granulites in the East Hebei, North China Craton: Constraints from a comparison between temperatures derived from REE-based thermometers and major element-based thermometers. *Gondwana Research* 46, 156-169.
- Zeh, A., Gerdes, A., Will, T.M., Frimmel, H.E., 2010. Hafnium isotope homogenization during metamorphic zircon growth in amphibolite-facies rocks: examples from the Shackleton Range (Antarctica). *Geochimica et Cosmochimica Acta* 74 (16), 4740–4758.
- Zheng, Y.F., Wu, Y.-B., Zhao, Z.-F., Zhang, S.-B., Xu, P., Wu, F.-Y., 2005. Metamorphic effect on zircon Lu–Hf and U–Pb isotope systems in ultrahigh-pressure eclogite-facies metagranite and metabasalt. *Earth and Planetary Sciences Letters* 240, 378–400.
- Zogheib, F.F., Degler, R., Martins, L.C.D., Novo, T., 2015. Geologia das Folha Guaxupé (SF.23-V-C-III) 1:100.000. Projeto Fronteiras de Minas, CODEMIG-UFMG, Belo Horizonte, Brazil.

## **3.14 Appendix 3.A - Analytical Methods**

### **3.14.1 Sample preparation, imaging and qualitative analyses**

Zircon was separated using standard rock crushing and heavy mineral separation techniques. Grains were individually selected, picked and mounted in epoxy resin. Grain mounts were polished to expose the grain centres. Zircons were imaged in cathodoluminescence (CL) for domain identification using a Quanta-250-FEI SEM fitted with a CL detector at the Multilab from Universidade do Estado do Rio de Janeiro (UERJ). For petrography, carbon-coated zircon mounts were investigated with a ZEISS EVO50 scanning electron microscope (SEM) at the Institute of

Geological Sciences (University of Bern) with 20 keV acceleration voltage and beam current from 500 pA to 2000 nA at high vacuum conditions.

### **3.14.2 Bulk rock analysis**

Major and trace element bulk rock compositions of four samples were analysed at the SGS GEOSOL laboratories (Brazil). Major element oxides were determined by XRF and trace elements by ICP-MS. Results are reported in Appendix I.

### **3.14.3 Electron probe micro-analysis**

The banded mafic granulite (C-838-A) was analysed by electron probe micro-analyser (EPMA) using both quantitative spot analyses and X-ray compositional mapping in wavelength-dispersive mode. EPMA analyses were carried out with a JEOL JXA-8200 superprobe at the Institute of Geological Sciences (University of Bern). Operating conditions for spot analyses were 15 keV accelerating voltage, 10 nA beam current and 40 s dwell times (including 2×10 s of background measurement). The following standards were used: wollastonite (Si), almandine (Fe), forsterite (Mg), orthoclase (K), anorthite (Ca), albite (Na) and ilmenite (Ti). Compositional maps were acquired following the procedure described in Lanari et al. (2012; 2013) using 15 KeV accelerating voltage, 100 nA beam current and dwell times of 200 ms. A map of 700,000 pixels over an area of 700 × 1000 µm<sup>2</sup> with a spot size of 20 µm x 20 µm was acquired. Spot measurements were also carried out in the same area to be used as internal standards (de Andrade et al., 2005).

The compositional maps were classified and converted into concentration maps of oxide weight percentage using the software XMAPTOOLS 2.3.1 (Lanari et al., 2014). Results are presented in Appendix II.

### **3.14.4 Trace elements LA-ICP-MS**

Trace elements compositions were obtained using a Thermo-Scientific Finnigan Element 2 SF-ICP-MS coupled to a CETAC213 ultraviolet laser system at the Isotope Geochemistry Laboratory of the Universidade Federal de Ouro Preto, Brazil. Conditions for laser fluency, frequency and spot size were 3 J/cm<sup>2</sup>, 6 Hz and 20 µm. Both the acquisition and reduction data were performed in blocks of 120 analyses using NIST SRM 612 as primary standard and NIST

SRM 610, USGS BCR-1 and USGS BHVO-2G as secondary reference materials. The software Glitter (van Achterbergh et al., 2001) was used for processing the time-resolved signal data. The internal standard value for zircon was  $\text{SiO}_2 = 32.78$  wt%. Spots were placed near or comprising one third of the position of the U-Pb dating spots and in the same CL-domains. The results are also within error of recommended values. The results from trace elements in zircon analyses are available in the Appendix III for C-833-A, C-838-2, C-838-A, C-838-B and C-716-B.

### 3.14.5 LA-ICP-MS U-Pb zircon dating

U-Pb isotopic analyses were performed with two LA-ICP-MS systems: (1) Samples C-838-A, C-838-2 and C-838-B were analysed with a Thermo-Finnigan Neptune multicollector ICP-MS (Thermo-Finnigan Neptune multicollector) coupled to a Photon-Machines 193 nm G2 laser system at Universidade Federal de Ouro Preto (UFOP) following the procedure described in Santos et al. (2017). Instrument set up parameters were a spot size of 20  $\mu\text{m}$ , a frequency of 6 Hz, 10 % energy with an intensity of 0.3 mJ. U-Pb data were standardized using the zircon GJ-1 (reference 609 Ma, Jackson et al., 2004) as primary standard and tested using the zircon Pleisovice (reference 337 Ma, Slama et al., 2008) as secondary standard. External errors were propagated considering the internal reproducibility of the individual ratios, external reproducibility of GJ-1, long-term uncertainty of the validation material, ratio uncertainties of the reference material and Pb-common ratio uncertainty (Lana et al., 2017). (2) Samples C-833-A and C-716-B were analysed with the microprobe ArF Excimer Laser 193  $\mu\text{m}$  da Photon (Machines Inc. Model ATLEX SI) coupled to the high-resolution Neptune-Plus multicollector (Thermo Fisher Scientific, USA), at the MULTILAB, Universidade do Estado do Rio de Janeiro (UERJ). Instrument set up parameters were 6-7 mJ/cm<sup>2</sup> laser fluency, 10 Hz, 25  $\mu\text{m}$  and Laser energy spot between 60 and 70 %. U-Pb data were standardized using GJ-1 zircon (reference 609 Ma, Jackson et al., 2004) as primary standard and tested using the zircon 91500 (reference 1065 Ma, Wiedenbeck et al., 1995) as secondary standard. External errors were calculated with the error propagation of individual measurements of GJ-1 and the individual measurements of each spot. Data reduction was done using an Excel program developed by Chemale et al. (2012).

Data evaluation for each spot was filtered considering outliers values of common Pb contents, errors of isotopic ratios and high percentages of discordance and Th/U ratios. The Concordia diagrams were obtained using the software Isoplot/Ex (Ludwig, 2003) and the histograms and probability density plots with Density Plotter (Vermeesch, 2012). Individual uncertainties are presented at 2 $\sigma$  level. The confidence level for the weighted averages is 95 %. The results from U-Pb LA-ICP-MS analyses are available in the Appendix V for C-833-A, C-838-2, C-838-A, C-838-B and C-716-B.

### 3.14.6 Lu-Hf in zircon analyses

Data were obtained using a Thermo-Finnigan Neptune multicollector ICP-MS coupled to a Photon-Machines 193 nm laser system (LA-MC-ICP-MS, Photon machines 193/Neptune Thermo Scientific), at Universidade Federal de Ouro Preto, Brazil. Data were collected as described in Santos et al. (2017). Spots were placed near or comprising partially the position of the U-Pb dating spots or in the same CL-domains. The laser was operated with a spot of 50  $\mu\text{m}$  in diameter (60 % power), fluence of 4.54 J/cm, and a pulse rate of 6 Hz. Both the acquisition and reduction data were performed in blocks of 160 analyses interspersed with the following reference materials: BB ( $^{176}\text{Hf}/^{177}\text{Hf} = 0.281674 \pm 0.000018$ ; Santos et al., 2017), GJ1 ( $^{176}\text{Hf}/^{177}\text{Hf} = 0.282000 \pm 0.000005$ ; Morel et al. 2008) and Plešovice ( $^{176}\text{Hf}/^{177}\text{Hf} = 0.282481 \pm 0.000014$ ; Slama et al., 2008). The results are also within error of recommended values. The results from Lu-Hf LA-ICP-MS analyses are available in the Appendix VI for C-833-A, C-838-2, C-838-A, C-838-B and C-716-B.

## 3.15 Appendix 3.B - U-Pb Geochronology: zircon description

### 3.15.1 Banded mafic granulite (C-833-A)

Cathodoluminescence (CL) images reveal that zircons from the banded mafic granulite C-833-A range from 100 to 300  $\mu\text{m}$  in size and are equant to elongated with width:length ratios of 1:1 to 1:4. They typically exhibit sub-rounded habits, a common feature of high-grade metamorphic grains (Whitehouse and Kemp, 2010). Their textures and habits resemble that of “truly metamorphic” zircons described in Taylor et al. (2016), i.e., having an equant morphology and internal sector zoning textures, with planar features of bright CL responses or fir-tree zoning. Some grains exhibit thin CL-bright planes that resemble spaced oscillatory zoning. Most of the grains, however display intermediate CL responses in light-grey shades over whole crystals or occur on either cores, or rims (usually wrapping dark CL cores). Bright CL rims represent 60 % of the number of rims, with usually some weak zoning texture. Less commonly, cores, rims, or sometimes even entire grains (grains with only one CL response) exhibit dark CL responses. There are some zircon grains with several successive rims are observed; however, they do not follow any pattern that allow to related CL responses or textures (Fig. 3.6). The decision whether CL-homogeneous phases would be considered as rims or cores were based on comparisons of textures and individual ages, as well on Lu-Hf isotope ratios.

### **3.15.2 Opdalite (C-838-2)**

Zircon grains from the opdalite C-838-2 are yellow and mainly comprise elongated prismatic crystals with width:lengths ratios of 1:2 to 1:7 and rounded habits. The main population comprises parallel oscillatory zoned grains, in which zonation are either thin and well defined, or broad and faint. It is often the case that irregular recrystallization domains grow over oscillatory domains, not forming regular rims, but with indentation annealed domains (Fig. 3.6). The second most common zircon type has irregular intermediate-CL responses (different shades of gray), sometimes presenting convolute structures. These grains contain recrystallization domains similar to the zircons of the first group, but the occurrence/distribution of these domains is more common. The third and least common group of zircons exhibits intermediate-CL responses lacking internal structures or showing some ghosts of older broad growth features. Apart from the group, thin bright-CL rims less than 10  $\mu\text{m}$  in width (locally reaching 30  $\mu\text{m}$ ) usually irregularly overgrow older domains and exhibit lobate contacts with the cores.

### **3.15.3 Banded mafic granulite (C-838-A)**

Zircon grains separated from the banded mafic granulite C-838-A are yellow and range from 100 to 250  $\mu\text{m}$  in size. They are approximately equant to elongated with width:length ratios varying mainly around 3:4, 3:7 and around 1:4 (Fig. 3.6). Cathodoluminescence imaging reveals a slightly heterogeneous zircon population. The most common zircon type is characterized by CL-dark elongated grains that usually form bipyramidal grains as shown by oscillatory to parallel zoning despite sub-rounded habits. A variation of this group exhibits the bipyramidal habit with an irregular texture overprinting previous zoning. These grains usually show irregular interlobate rims. Less frequently they are equant, short bipyramidal CL-dark grains with fine oscillatory to faint sector zoning. Zircon cores are often overgrown by unzoned CL-bright rims that are often thinner than 20  $\mu\text{m}$ . Single phases (i.e. grains without rims) are difficult to assign the protolith or the metamorphic zircon populations.

### **3.15.4 Granitic (hornblende)-biotite-bearing leucosome (C-838-B)**

Zircon population of the leucosome C-838-B is homogeneous regarding their habits and sizes, but texturally different as revealed by the cathodoluminescence images (Fig. 3.6). Grains are mainly bipyramidal with width:length = 2:7, 1:3, and 3:8 to 3:10. Two texturally contrasting groups can be identified. The first and most common group comprises CL-intermediate response (dark to



medium gray shades) cores or entire grains showing one texture, exhibiting faint space sector or oscillatory zoning. They are usually enveloped in a light gray-CL domain with oscillatory zoning and prismatic habits. Besides, grains are surrounded by another outer bright-CL rim that lack an internal structure and exhibit prismatic to rounded shapes. The second group comprises CL-dark cores or single phases mainly lacking internal structures, but locally some relic portions show zoning. This group usually displays irregular shaped intermediate-CL rims without internal structures or exhibits sector divisions and/or tiny (<10 µm thick) CL-bright rims. Locally, aforementioned rims show embayed contacts with the cores.

### **3.15.5 Mafic granulite enclave (C-716-B)**

The zircon grains of the mafic granulite enclave C-716-B comprises clear pinkish grains of 150 µm to 300 µm length. The most common width:length ratios are between 1:2 to 1:3, and the whole grain population appears heterogeneous in cathodoluminescence images. The majority of the grains show sector zoning with CL-medium-bright responses, and a faint, broad oscillatory zoning (Corfu et al., 2003). Some grains exhibit CL-brighter (grey shade) rims around embayed cores. These rims are usually less than 5µm wide and likely related to annealing (Corfu et al., 2003). Around 10 % of the grains are composed of equant CL-dark grains, in which some sectoring is visible (Fig. 3.6).

## 4 Reconstruction of multiple P-T-t stages from retrogressed mafic rocks: subduction versus collision in the Southern Brasília Orogen (SE Brazil)

Mahyra Tedeschi<sup>1,2,3\*</sup>, Pierre Lanari<sup>2</sup>, Daniela Rubatto<sup>2,4</sup>, Antônio Pedrosa-Soares<sup>1#</sup>, Jörg Hermann<sup>2</sup>, Ivo Dussin<sup>1,5#</sup>, Marco Aurélio P. Pinheiro<sup>3</sup>, Anne-Sophie Bouvier<sup>4</sup>, Lukas Baumgartner<sup>4</sup>

<sup>1</sup>Universidade Federal de Minas Gerais, Programa de Pos-Graduação em Geologia, CPMTC-IGC, Av. Antônio Carlos 6627, Belo Horizonte, Brazil (#Fellow of the Brazilian Research Council-CNPq)

<sup>2</sup>Institute of Geological Sciences, University of Bern, Baltzerstrasse 1-3, Bern, Switzerland

<sup>3</sup>Geological Survey of Brazil (CPRM), Avenida Brasil 1731, Belo Horizonte, MG, Brazil

<sup>4</sup>Institute of Earth Sciences, University of Lausanne, Geopolis, Lausanne, Switzerland

<sup>5</sup>Universidade do Estado do Rio de Janeiro, Multilab, Faculdade de Geologia, R. São Francisco Xavier 524, Rio de Janeiro, Brazil

\*Corresponding author: mahyratedeschi@gmail.com

### Highlights:

- The crustal section reached peak conditions of c. 14 kbar and 700 °C at 630 Ma
- Only garnet relicts recorded the peak pressure conditions in the mafic rocks
- Corona and symplectite are coupled reactions forming at 5 kbar and 600 °C at 600 Ma
- The mafic rocks recorded a high geothermal gradient typical of collisional settings
- Continental collision is likely the favoured process instead of oceanic subduction

**Keywords:** Petrochronology, Phase equilibrium, U-Th-Pb geochronology, Symplectite, XMapTools, Brasília orogen

## 4.1 Abstract

The identification of markers of subduction zones in orogenic belts requires the estimation of paleo-geothermal gradients through pressure-temperature-time (P-T-t) estimates in mafic rocks that potentially derive from former oceanic units. However, such markers are rare in supracrustal sequences specially in deeply eroded and weathered Precambrian orogens, and reconstructing their metamorphic history is challenging because they are commonly retrogressed and only preserve a few mineral relicts of high-pressure metamorphism. Metamorphosed mafic rocks from Pouso Alegre region of the Neoproterozoic Southern Brasília Orogen outcrop as rare lenses within continental gneisses. They have previously been classified as retrograde eclogites, based on the presence of garnet and the characteristic symplectitic texture replacing omphacite. These rocks were interpreted to mark the suture zone between the Paranapanema and São Francisco cratons. To test the possible record of eclogitic conditions in the Pouso Alegre mafic rocks, samples including the surrounding felsic rocks have been investigated using quantitative compositional mapping, forward thermodynamic modeling and in-situ dating of accessory minerals to refine their P-T-t history. In the metamorphosed mafic rocks, the peak pressure assemblage of garnet and omphacite ( $Jd_{20}$ , reconstructed composition) formed at  $690 \pm 35$  °C and  $13.5 \pm 3.0$  kbar, whereas local retrogression into symplectite or corona occurred at  $595 \pm 25$  °C and  $4.8 \pm 1.5$  kbar. The two reactions were coupled and thus took place at the same time. A zircon U-Pb age of  $603 \pm 7$  Ma was obtained for metamorphic rims and linked to the retrogression stage. Monazite and metamorphic zircon U-Th-Pb ages for the surrounding rocks are at ca. 630 Ma and linked to peak pressure conditions similar to the one recorded by the mafic rocks. The low maximal pressure of 14 kbar and the high geothermal gradient do not necessarily support subduction process-related metamorphism but, more likely, metamorphism related to continental collision.

## 4.2 Introduction

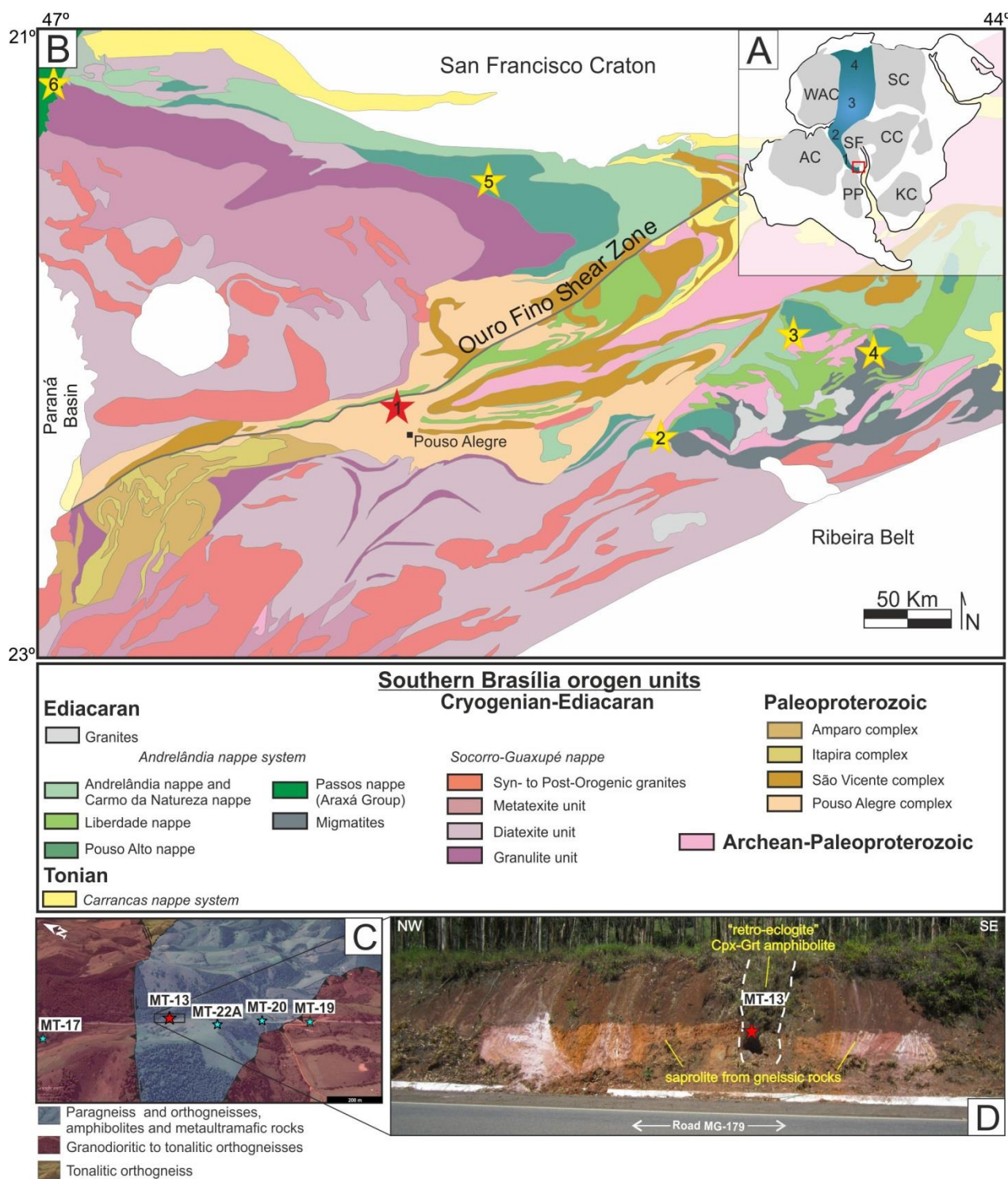
Mafic rocks within collisional orogens may be used as markers for oceanic subduction zones, particularly if they preserve relicts of eclogite facies metamorphism (Evans et al., 1979; Ganade de Araújo et al., 2014; Gilotti, 2013; Heinrich, 1986; Singh et al., 2013; Weller and St-Onge, 2017). Lenses of mafic rocks metamorphosed at high-pressure (HP) within felsic crustal sequences that lack evidence for HP metamorphism are common in numerous orogenic belts from the Paleoproterozoic (e.g. Belemorian province, Liu et al., 2017; Trans-Hudson orogeny, Weller and St-Onge, 2017) to the Cenozoic (e.g. Tso Moriri in Himalaya, Guillot et al., 2007; Adula Nappe in the Alps, Heinrich, 1986). Relict HP (20-30 kbar) mineral assemblages in such mafic boudins have been attributed to subduction-related metamorphic processes and thus used as markers of suture zones. However, the P-T trajectories of such rocks should be carefully determined in order to indicate in which geodynamic scenario (subduction or collision) they have formed. This is particularly important for rocks whose P-T conditions are located below the coesite stability field and thus cannot be directly related to subduction (Brown, 2009). Because such rocks play an important role in informing geodynamic models (Godard, 2001; McClelland and Lapen, 2013) determining the correct, maximal P-T conditions they reached is crucial.

Reconstructing the pressure-temperature-time (P-T-t) history of polymetamorphic mafic rocks within felsic units is challenging. Firstly, mafic lenses are scarce in deeply eroded terranes rich in orthogneisses and paragneisses, where they are commonly retrogressed because of late amphibolite to granulite facies metamorphism and/or strong interaction with fluids during exhumation (Lanari et al., 2013). Thermobarometric investigations are complicated as only a few relicts of the HP mineral assemblage are preserved. In Precambrian belts, it can be even more difficult to recognize high-pressure relicts because of long lasting surface weathering.

Metamorphosed mafic rocks from Pouso Alegre in the Neoproterozoic Southern Brasília orogen, in SE-Brazil (Fig. 4.1A; Campos-Neto and Caby, 1999; Coelho et al., 2017; Trouw et al., 2013) are a typical example of such complex rocks. They crop out as scarce lenses within migmatitic sillimanite-garnet gneiss, migmatitic amphibole-garnet orthogneiss, biotite gneiss, granite and mafic rocks (Fig. 4.1C). They have been previously classified as “retro-eclogites” (Choudhuri et al., 1978; Hoppe et al., 1985; Trouw et al., 2013), based on the presence of garnet, considered as the only remnant of the HP assemblage, (assumed omphacite + garnet, Coelho et al., 2017) and typical retrogression products such as symplectite and coronitic textures. However, no quantitative estimate of the peak pressure is available to support this interpretation. Nevertheless, these metamorphosed mafic rocks have been quoted as markers of a suture zone formed after oceanic subduction between the Paranapanema and São Francisco cratons (Campos-Neto et al., 2011; Coelho et al., 2017; Trouw et al., 2013).

Since reconstructing the metamorphic pressure-temperature-time evolution of retrogressed mafic samples is challenging, it requires a detailed petrochronological approach. It is necessary to clearly identify the mineral relicts formed during the HP stages, and to analyze their chemical and isotopic compositions. It has been shown that the use of quantitative compositional mapping (Lanari et al., 2013; Loury et al., 2016) and the study of mineral inclusions in accessory minerals (Hart et al., 2016; Hermann et al., 2001) are efficient techniques to identify HP relicts that are no longer preserved in the mineral matrix and to reconstruct P-T-t conditions. Thermobarometric estimates can be obtained from thermodynamic forward models such as equilibrium phase diagrams (e.g. Powell and Holland, 2008) and this technique can be enhanced by restricting the investigations to local domains, i.e., to retrieve the physical and chemical conditions (P-T-X) of a specific reaction (Lanari and Engi, 2017, and references therein). Accessory phases can be dated and linked to the growth or breakdown of major phases to constrain specific P-T-t stages (e.g., Rubatto and Hermann, 2001).

In this study, we combine quantitative compositional mapping (Lanari et al., 2012, 2014), with forward thermodynamics modelling to retrieve the maximal P conditions recorded by a mafic rock of Pouso Alegre. A comprehensive approach, that uses the local density corrected composition of the symplectite domain and compares it to the omphacite composition obtained by the model, was applied to retrieve the former omphacite composition. Subsequent retrogression stages are examined from modelling local domains and their chemical and chronological relationships are evaluated by mass balance (Centrella et al., 2015). U-Th-Pb ages from zircon and monazite provide time constraints for two distinct metamorphic events. They are correlated to P-T estimates using inclusion compositions, trace elements on zircon, monazite, garnet and rutile, with Zr-in-rutile and Ti-in-zircon thermometry. The evolution of the mafic rock is related to that of the country rocks for which additional P-T estimates, as well as zircon and monazite ages were obtained. Appendix 3.A presents the descriptions of the analytical methods applied in the following sections.



### 4.3 Geological setting

The Brasília orogenic system is a 1800 km-long, nearly N-S trending belt, extending roughly between the 10° and 26° S parallels. It is one of the orogenic belts formed during West Gondwana amalgamation in Neoproterozoic time (Cordani et al., 2003; Fig. 4.1A). The northern and southern segments of that orogenic system evolved separately in relation to distinct paleocontinental blocks (Fuck et al., 2017; Valeriano, 2017). The Southern Brasília belt has been related to the convergence of the Paranapanema and São Francisco paleocontinental blocks (Fig. 4.1B), involving oceanic subduction and collisional orogeny, which resulted in stacked nappe systems verging to east (Campos Neto et al., 2011; Mantovani et al., 2005; Trouw et al., 2000, 2013).

Each nappe system represents a specific compartment with distinctive tectono-metamorphic features (Fig. 4.1B). The Socorro-Guaxupé nappe (SGN) is mainly composed of meta-igneous rocks from a Neoproterozoic magmatic arc, with minor paragneisses and schists (Campos Neto and Caby, 2000; Rocha et al., 2016), and is placed over the metasedimentary rocks of the Andrelândia nappe system (ANS). Those ANS metasedimentary rocks show an inverted metamorphic pattern, with high-pressure granulite and eclogite facies on top, and amphibolite to greenschist facies at the base (Campos Neto et al., 2011; Trouw et al., 2013). Studies on ANS described mixtures of sediments derived from both active and passive margins (Belém et al., 2011; Trouw et al., 2013). Campos Neto et al. (2011) suggested that they represent subduction-related metasedimentary sequences, forming an accretionary prism. The continental margin of the lower plate is then related to São Francisco Craton and represented by the Carrancas nappe system (Fig. 4.1B; Campos Neto et al., 2011; Trouw et al., 2000). Depending on the interpretation, the suture zone is located above (Trouw et al., 2013) or below the ANS (Campos Neto et al., 2011).

The investigated samples are from the tectonic boundary between the SGN and ANS, located 20 km to the northeast of Pouso Alegre city, along the Ouro Fino shear zone (Table 1; Fig. 4.1B and 4.1C). This shear zone is 300 km long and cuts a wide tectonic window disclosing Archean and Paleoproterozoic migmatitic orthogneisses of the Pouso Alegre complex (Cioffi et al., 2016). It has been interpreted as the reworked margin of the São Francisco Craton, tectonically interleaved with orthogneisses and metasedimentary rocks of the SGN and ANS (Ribeiro et al., 2011).

The recently proposed Neoproterozoic West Gondwana orogen (WGO; Ganade de Araujo et al., 2014) is a roughly linear belt that extended for more than 4000 km from the present-day Northeast Africa to Central Brazil (Fig. 4.1A). The reconstruction of this paleo-subduction zone was mostly based on chrono-correlations of HP to UHP rocks from Mali, Togo and NE-Brazil. As one of the oldest known deep continental subduction zones in geological history, the existence of this long

suture has implications for life sustainability in the Ediacaran (Ganade de Araujo et al., 2014) and for the geotectonic evolution of Central Brazil. The extension of this suture further to the south is solely based on the possible presence of HP rocks of Ediacaran age in the Southern Brasília orogen (Campos Neto and Caby, 1999, 2000; Campos-Neto et al., 2011; Trouw et al., 2000, 2013; Parkinson et al., 2001). Such HP rocks are mainly garnet amphibolites, with plagioclase being interpreted as retrograde, labeled as “retro-eclogites” (e.g., Choudhuri et al., 1978; Hoppe et al., 1985). They are found in several places, like Pouso Alegre, Liberdade, Varginha and Passos (São Sebastião do Paraíso) nappes (Fig. 4.1B).

Those “retro-eclogites” were firstly classified by Choudhuri et al. (1978), after studies on rocks from the Pouso Alegre region that show the garnet + clinopyroxene assemblage in the presence of symplectite and corona. Coelho et al. (2017) determined metamorphic conditions of 12 to 16 kbar at 700 to 800 °C for the same rocks, suggesting that the higher pressure assemblages were completely overprinted. Hoppe et al. (1985) reported that the eclogitic rocks from northern Pouso Alegre (PA) and São Sebastião do Paraíso (SSP) contain symplectites and coronitic textures only at PA, where migmatitic paragneisses and orthogneisses constitute the associated rocks. Using the composition of pyroxene (Jd<sub>30</sub> from SSP, but not PA) Hoppe et al. (1985) estimated 630 °C and 7-8 kbar as minimum conditions for the eclogite and 490 ± 50 °C for the retrograde stage corresponding to amphibole formation. Campos Neto and Caby (1999) indicated maximum pressures of 17.5 kbar (for a T = 660 °C) in the Liberdade nappe, located northeast of Pouso Alegre. Parkinson et al. (2001) described coesite as inclusion in zircon hosted by kyanite-garnet-hypersthene granulites from the Varginha nappe in the NW of Pouso Alegre, but no spectroscopy details were provided to support this finding. Trouw (2008) proposed that rocks from Virgínia, to the SE of Pouso Alegre, reached eclogitic facies based on their clinopyroxene-garnet composition and plagioclase corona.

#### **4.4 Sample description**

Five samples were collected along a 2 km NW-SE transect at 20 km to the northeast of Pouso Alegre (Road MG-19; Fig. 4.1B and 4.1C). The main rock for this study, the clinopyroxene-garnet amphibolite (sample MT-13), crops out as a meter-thick lens of fresh metamorphic mafic rock enveloped by a steep-dipping assemblage of saprolitic to well-preserved rocks (Fig. 4.1D). Samples from the host rocks are a migmatitic amphibole-garnet gneiss with augen structure (MT-17), a deformed allanite-bearing biotite granite (MT-19), and a biotite gneiss (MT-20). By comparison with the country rocks in the region, the host rocks of the mafic lens can be correlated to the Pouso Alegre Complex (Cioffi et al., 2016). Interleaved migmatitic sillimanite-garnet gneiss (MT-22A) shows sharp to mylonitic contact with the aforementioned rocks. After field mapping, the



migmatitic sillimanite-garnet gneiss was correlated to the Andrelândia Group, a unit mapped in the area (Ribeiro et al., 2011; Fig 4.1C). The clinopyroxene-garnet amphibolite is better preserved in its inner part, where it is weakly to non-foliated, while at the borders it shows a mylonitic foliation. The country rocks show the same steep-dipping tectonic foliation imprinted in the lens of clinopyroxene-garnet amphibolite, corresponding to the mylonitic foliation related to the Ouro Fino shear zone.

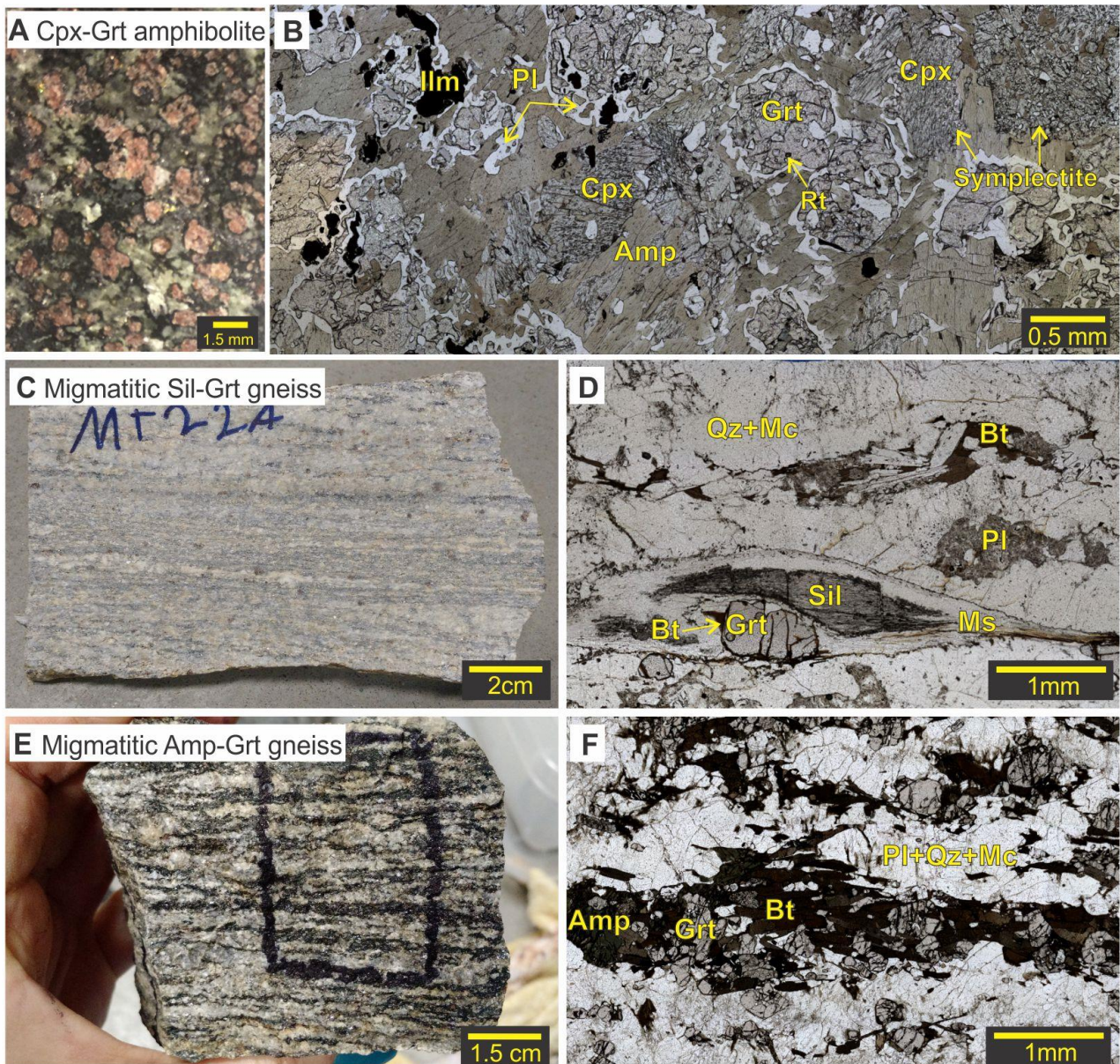


**Figure 4.2:** Hand specimen and transmitted light photomicrographs of: (A-B) clinopyroxene-garnet amphibolite MT-13, (C-D) migmatitic sillimanite-garnet gneiss MT-22A, with the yellow narrow indicating the biotite rotated shadow, and (E-F) migmatitic amphibole-garnet augen gneiss MT-17.

**Table 4.1** Summary details for the Pouso Alegre samples. UTM coordinates are relative to the WGS84 datum. Data indexes: 1-Thermodynamic modelling; 2- Zr-in-rutile thermometry.

Sample	Lithology	UTM Coordinates		Mineral assemblage		Protolith age (Ma)		Metamorphism age (Ma)		P-T conditions	
		E	N	Major	Minor/ Acces.	LA-ICP-MS	+SIMS	LA-ICP-MS	+SIMS	T (°C)	P (kbar)
MT-13	Cpx-Grt amphibolite	409623	7560455	Grt + Cpx + Amp + Pl + Qz	Rt + Ilm + Ttn + Zrn	n.a.	1513 ± 17	n.a.	603±7	690 ± 35 <sup>1</sup> 701 ± 16 <sup>2</sup>	13.4 ± 2.8
MT-17	Migmatitic Grt-Amp gneiss	408216	7561674	Grt + Amp + Pl + Kfs + Bt + Qz	Ep + Ttn + Zrn	2066 ± 2	n.a.	n.a.	n.a.	~700	~13.5
MT-19	Aln-bearing Bt granite	409525	7560729	Bt + Pl + Kfs + Qz	Aln + Zrn	2076 ± 3	n.a.	626 ± 5	n.a.	n.a.	n.a.
MT-20	Bt gneiss	408714	7560425	Bt + Pl + Kfs + Qz	Grt + Zrn	2076 ± 4	n.a.	632 ± 2	n.a.	n.a.	n.a.
MT-22A	Migmatitic Sil-Grt gneiss	409473	7560974	Sil + Grt + Kfs + Ms + Qz + Bt	Mnz + Zrn	794 ± 4	n.a.	672 ± 4 (Zrn)	637 ± 7 (Mnz)	n.a.	n.a.

#### 4.4.1 Petrography

The clinopyroxene-garnet amphibolite MT-13 comes from an inner and less deformed portion of the mafic lens. This sample contains mm- to cm-sized pinkish poikiloblastic garnet. Each crystal exhibits an irregular shape with lobate edges (Figs. 4.2A and B) being systematically surrounded by a composite corona made of inner plagioclase and outer amphibole. Garnet in contact with clinopyroxene is rare. The garnet porphyroblasts show several inclusions, including rutile, zircon, clinopyroxene and quartz. Clinopyroxene in contact with amphibole forms subhedral crystals, or is developed within a symplectite, together with plagioclase, amphibole and quartz (Figs. 4.2A and B, Fig. 4.3). Ilmenite, rutile, apatite, zircon and titanite are minor phases in this sample. Rutile grains are present as inclusions in garnet, amphibole, clinopyroxene (symplectite and subeuhedral crystals) and in the plagioclase corona. As well as ilmenite, rutile is often surrounded by a titanite corona. Twenty per cent of rutile crystals (530 have been investigated) contain inclusions of zircon and ilmenite, and only 4 % have silicate inclusions such as clinopyroxene, amphibole, garnet, feldspar, quartz, titanite and biotite (Supplementary Figure S.1). SiO<sub>2</sub> inclusions were checked by Raman spectroscopy and they all resulted made of quartz and no higher pressure polymorphs were found.

The felsic and intermediate country rocks include a migmatitic gneiss (samples MT-17, Figs. 4.2E and F), a granite (MT-19), an orthogneiss (MT-20) and a migmatitic sillimanite-garnet gneiss (sample MT-22A, Figs. 4.2C and D). Sample MT-22A is a greyish, fine-grained stromatic gneiss exhibiting millimetric bands of leucosome and melanosome (Fig. 4.2C). The leucosome bands are composed of K-feldspar and quartz ribbons, whilst the melanosome bands consist of fibrous sillimanite (mostly replaced by white mica), feldspar (highly weathered to clay minerals) and millimetric red garnet porphyroblasts. Garnet crystals, exhibiting a pseudo-automorphic shape with only few lobate edges, have quartz inclusions and are locally replaced by biotite, which also grew in rotated pressure shadows (Fig. 4.2D). Owing to the weathering alteration, it is impossible to determine the original bulk chemical composition of sample MT-22A.

Sample MT-17 (Fig. 4.2E) is a stromatic amphibole-garnet gneiss, showing alternating melanocratic and leucocratic bands, and augen structure. The melanosome consists of millimetric red garnet, dark-green amphibole, biotite and oligoclase. The leucosome consists of medium- to coarse-grained oligoclase, microcline and quartz (Fig. 4.2F). Titanite, ilmenite, epidote, zircon and apatite are accessory phases. The melanocratic bands show clusters of titanite and epidote. Sample MT-19 is a deformed, fine-grained allanite-bearing biotite metagranite. Allanite and zircon are the minor phases. Sample MT-20 is a biotite orthogneiss with minor garnet (1–2 vol%), showing incipient mylonitization, with millimetric plagioclase and quartz porphyroclasts surrounded by biotite. White mica locally replaces biotite. Zircon and apatite are accessory phases.

#### 4.4.2 Petrographic interpretation

The clinopyroxene-garnet amphibolite MT-13 is highly retrogressed as shown by the presence of symplectite, corona and titanite overgrowth over rutile. The symplectite observed in this sample is typical of retrogressed mafic eclogites and formed through the reaction omphacite + H<sub>2</sub>O → clinopyroxene + plagioclase + amphibole ± quartz (Lanari et al., 2013; Waters, 2003). The general shape of garnet crystals showing lobate edges suggests garnet resorption (Lanari et al., 2017; Robyr et al., 2014) that may have occurred during the formation of the corona. Plagioclase and amphibole systematically appear in sequence of zones in the corona around garnet (Fig. 4.3). Chemical potential gradients are interpreted to control the mineral sequence observed in the corona (Carlson and Johnson, 1991; White et al., 2008). The spatial distribution of minerals is thus due to limited intergranular diffusion of some species, such as Al<sub>2</sub>O<sub>3</sub>. Rutile is interpreted to have formed early during the metamorphic history, as it has been trapped as inclusion by most of the major phases.

Both the migmatitic sillimanite-garnet gneiss MT-22A and the migmatitic amphibole-garnet gneiss MT-17 can be interpreted as highly deformed stromatic migmatites, since microcline and quartz make up the major part of the felsic layers. Features like discordant leucosome veins, Schöllén and Schlieren textures, which can be evidence of melt migration (cf. Sawyer, 2008), are absent. The distribution of the weathering products (clay-minerals) and the preservation of twinning suggest that former plagioclase has been strongly weathered in sample MT-22A. The idiomorphic shape of the garnet crystals suggests little or no resorption. In MT-17, secondary biotite locally replaces amphibole and garnet. The fine-grained allanite-bearing biotite granite (MT-19) and biotite gneiss (MT-20) are closely located to each other and have similar mineralogical composition.

### 4.5 Results

#### 4.5.1 Bulk Rock Chemistry

Bulk rock chemistry data are available in Appendix I and the diagrams in Supplementary Figure S.2.

*Clinopyroxene-garnet amphibolite MT-13* has a basaltic composition with tholeiitic affinity. Chondrite-normalized trace element spider and REE diagrams show a pattern between N-MORB and E-MORB.



*Amphibole-garnet migmatitic gneiss MT-17* shows a composition between diorite and granodiorite ( $\text{SiO}_2 = 62.5 \text{ wt}\%$ ). It exhibits the highest enrichment in REE among the sample set, with  $(\text{La}/\text{Sm})_N = 3.0$  and  $(\text{Tb}/\text{Yb})_N = 1.66$  and an approximately flat distribution for the HREE. Both the allanite-bearing biotite granite MT-19 and biotite gneiss MT-20 are calc-alkaline, with granitic and granodioritic compositions, respectively. The first exhibits high LREE contents and  $(\text{La}/\text{Sm})_N = 5$ , with a slight negative slope for the HREE distribution with  $(\text{Tb}/\text{Yb})_N = 2.9$  and a positive Eu anomaly ( $\text{Eu}/\text{Eu}^* = 1.3$ ). The positive Eu anomaly suggests accumulation of plagioclase. Sample MT-20 shows enrichment in LREE and  $(\text{La}/\text{Sm})_N = 4.27$ , but is extremely depleted in HREE with  $(\text{Tb}/\text{Yb})_N = 1.96$ , and shows a negative Eu anomaly ( $\text{Eu}/\text{Eu}^* = 0.52$ ). The spider diagram shows negative anomalies for P and Ti for samples MT-17, MT-19 and MT-20 and of Nb for sample MT-19.

#### 4.5.2 Mineral Compositions

X-ray compositional maps were acquired by electron probe micro-analyser (EPMA) and standardized in concentration maps of oxide weight percentage using the internal standard technique (de Andrade et al., 2005) and the program XMAPTOOLS 2.3.1 (Lanari et al., 2014). Structural formula maps in atom per formula unit (a.p.f.u.) were used to investigate the compositional variability of the mineral phases at the thin section scale. Representative mineral compositions are available in the Appendix II for samples MT-13, MT-22A and MT-17, and the compositional maps in Supplementary figures S.3, S.4, S.5 and S.6.

Garnet in clinopyroxene-garnet amphibolite MT-13 shows a relatively homogeneous chemical composition for the core of the grains (Figs. 4.3C and S.3) with an average structural formula of  $\text{Alm}_{53}\text{Prp}_{19}\text{Grs}_{26}\text{Sps}_{1.5}$ . Slight compositional zoning is observed within this core, especially in Ca ( $\text{Grs}_{24-28}$ ) and Fe ( $\text{Alm}_{51-54}$ ). A thin rim of  $\sim 25 \mu\text{m}$  thickness systematically occurs at the contact with the corona. The average structural formula of the rim is  $\text{Alm}_{58}\text{Prp}_{18}\text{Grs}_{22}\text{Sps}_{2.3}$ . Mn-content increases from 0.05 a.p.f.u. in the core to 0.07 a.p.f.u. in the near-rim zone.

Similarly to garnet, clinopyroxene in sample MT-13 shows slight compositional variations between the grains located in different domains (Figs. 4.4 and S.4). Clinopyroxene has low Na-content ( $\text{Jd}_{3-5}$ ) and XMg ( $\text{Mg}^{2+}/(\text{Mg}^{2+}+\text{Fe}^{2+})$ ) ranging from 0.70 to 0.74. The highest jadeite content ( $\text{Jd}_5$ ) is observed in grains located in both garnet and symplectite. It is important to note that some of the clinopyroxene grains present as “pseudo-inclusions” in garnet could also be linked to the corona or to an early symplectitic stage and appear as “inclusions” because of 3D sectioning effects. As the clinopyroxene composition does not significantly change between the different domains, it is labelled Cpx2 and related to the growth of the corona and symplectite. No relict of

HP clinopyroxene (Cpx1) with omphacite composition is preserved in the investigated domain. Several spot analyses of clinopyroxene inclusions in garnet, rutile and garnet were measured and the highest jadeite content observed is Jd<sub>8</sub>.

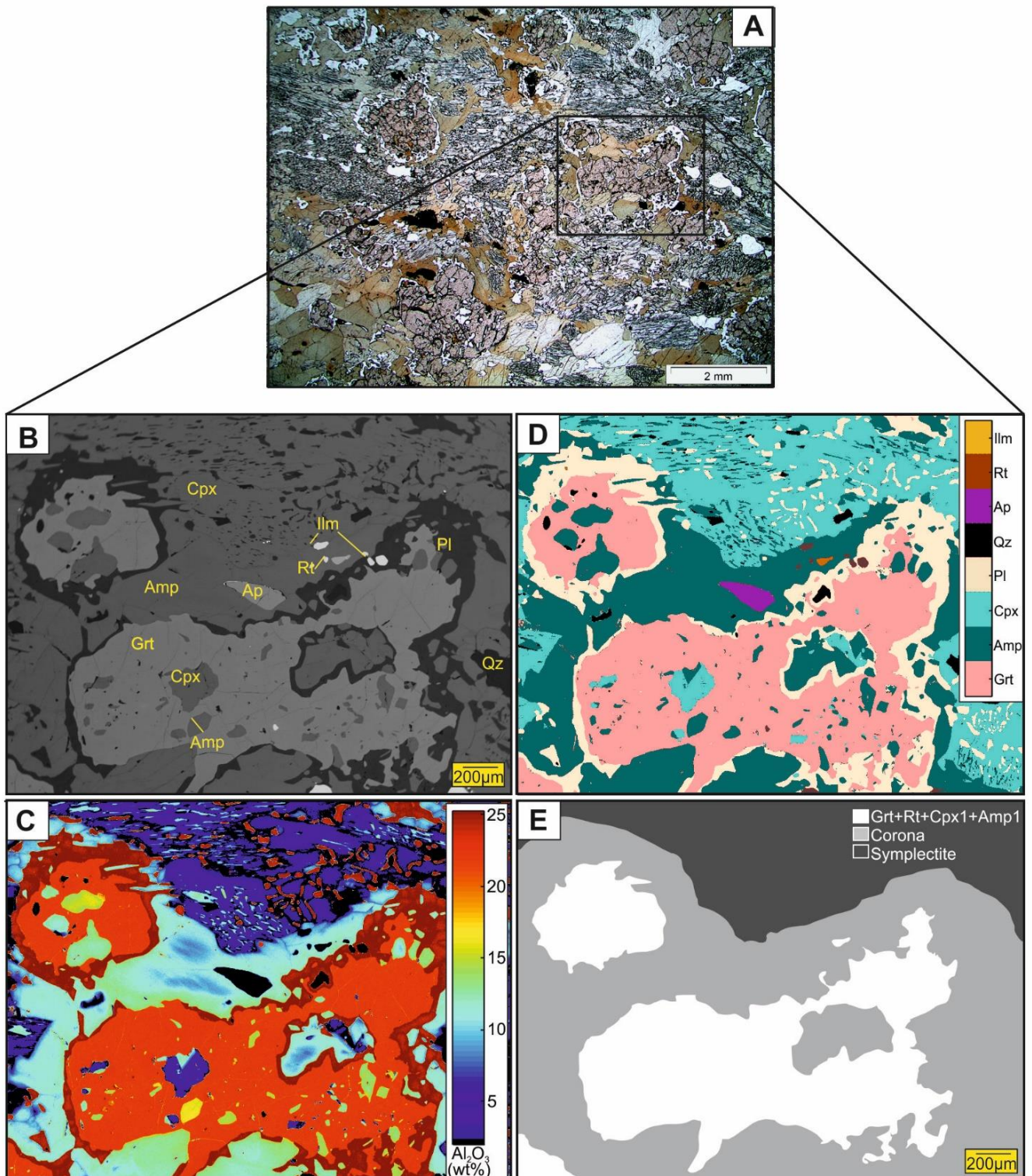


**Figure 4.3:** Photomicrograph (A) showing the texture of clinopyroxene-garnet amphibolite MT-13 with the selected rectangle area mapped showed in: (B) Backscattered image; (C) Al<sub>2</sub>O<sub>3</sub> (wt%) compositional map from XMapTools; (D) Phases maps and (E) Distinct assemblages identified from texture and compositional map.

Amphibole in sample MT-13 has a composition varying from ferroan-hornblende to hornblende (cf. Tindle and Webb, 1994). Amphibole occurs as: (a) coarse grains in the corona, (b) fine grains in the symplectite and (c) inclusions in garnet. (a) The coarse-grained amphibole surrounding the plagioclase in the corona is compositionally zoned, with a core depleted in Al (1.4 a.p.f.u.), Na (0.4 a.p.f.u.), Ca (1.74 a.p.f.u.) and high XMg (0.64). The chemical zoning of the amphibole rim is asymmetric with slightly different compositions observed in the direction of garnet (Al = 2.3 a.p.f.u.; Na = 0.6 a.p.f.u., Ca = 1.84 a.p.f.u.; XMg = 0.58) or toward the symplectite (Al = 1.7 a.p.f.u.; Na = 0.55 a.p.f.u., Ca = 1.84 a.p.f.u.; XMg = 0.62). (b) The fine-grained amphibole in the symplectite shows similar composition to the amphibole in the outer part of the corona, located close to the symplectite. (c) Amphibole inclusions in garnet show variable chemical compositions. Those associated to plagioclase show the same composition/zoning pattern as those from the outer-garnet corona (Fig. 4.4 and S.5). Other inclusions are more homogeneous in composition with higher Al (2.5–3.0 a.p.f.u.), Na (0.65 a.p.f.u.), Ca (1.86 a.p.f.u.), and lower XMg (0.50–0.55). Plagioclase is present in the corona and in the symplectite (Fig. 4.3). In the corona, plagioclase composition varies from An<sub>40</sub> at the contact with garnet to An<sub>35-28</sub> at the contact with amphibole. In the symplectite, plagioclase shows homogeneous composition of An<sub>27</sub>.

Garnet poikiloblasts in the migmatitic sillimanite-garnet gneiss MT-22A show compositional zoning features similar to MT-13 (Fig. S.6) with an increase of Fe and Mn from core (Alm<sub>82</sub>Prp<sub>8.5</sub>Grs<sub>6</sub>Sps<sub>1</sub>) to rim (Alm<sub>85</sub>Prp<sub>6.5</sub>Grs<sub>4</sub>Sps<sub>4</sub>). From the zoning pattern, it appears that several small crystals constitute each poikiloblast. There is no apparent change in garnet composition associated to fractures or inclusions. EPMA spot analyses were also performed on the weathered phase that constitutes around 15 vol% of the rock. The results show a low oxide weight percentage sum (74–80 wt%), explained by the presence of clay minerals. The augen gneiss MT-17 exhibits almandine-rich garnet with an average composition of Alm<sub>60-67</sub>Grs<sub>27-33</sub>Prp<sub>2-5</sub>Sps<sub>1-3</sub>. Amphibole from its mafic bands constitutes potassium pargasite to potassium hornblende compositions (XMg = 0.19–0.22).

### 4.5.3 Thermobarometry

#### 4.5.3.1 *Phase equilibria*

In order to reconstruct the P-T evolution of sample MT-13, isochemical phase diagrams were produced for different bulk compositions using THERIAK-DOMINO (de Capitani and Brown, 1987; de Capitani and Petrakakis, 2010), the internally consistent thermodynamic dataset TC55 (Holland and Powell, 1998 and subsequent updates), together with the following solid solution

models: garnet (Holland and Powell, 1998); clinopyroxene (Holland and Powell, 1996); amphibole (Diener et al., 2007); plagioclase (Baldwin et al., 2005); and an ideal model for ilmenite.

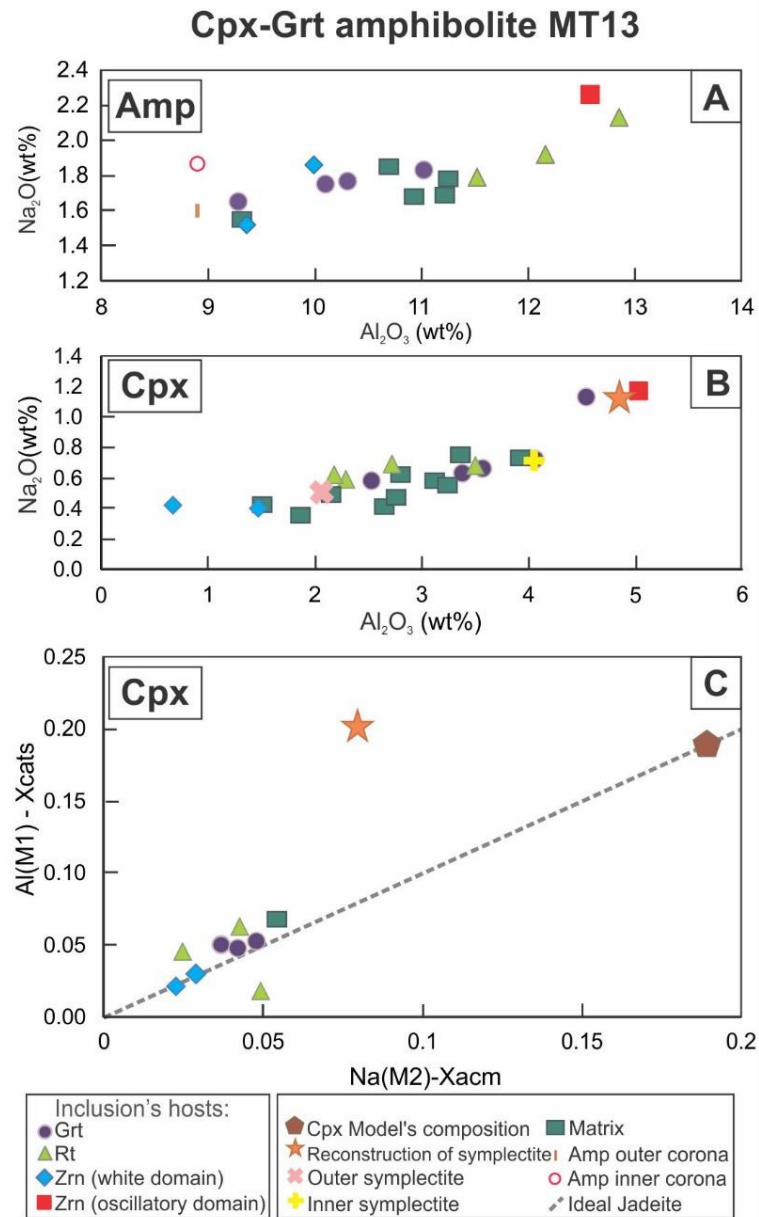


**Figure 4.4:** Na<sub>2</sub>O vs Al<sub>2</sub>O<sub>3</sub> diagram for amphibole (A) and clinopyroxene (B) compositions from the clinopyroxene-garnet amphibolite (MT-13). (C) Al (M1)-X<sub>cats</sub> vs Na (M2)-X<sub>acm</sub> diagram with the distribution of stoichiometric clinopyroxene compositions, Jadeite composition obtained with the model and reconstructed symplectite composition (see text for details).

The chemical system was simplified to Na<sub>2</sub>O–CaO–FeO–MgO–Al<sub>2</sub>O<sub>3</sub>–SiO<sub>2</sub>–H<sub>2</sub>O–TiO<sub>2</sub> because of the absence of K- and Mn-bearing phases. Whereas the presence of Mn in the model affects the size of the stability field of garnet (Tinkham et al., 2001), the effect on the position of garnet isopleths is limited for low-spessartine contents garnets (< 2 %) as those observed in this sample. The computations were carried out assuming a saturating pure H<sub>2</sub>O fluid (a<sub>H<sub>2</sub>O</sub> = 1). Due to the presence of ilmenite, Fe is assumed to be all Fe<sup>+2</sup>. The program GRTMOD (Lanari et al., 2017),



which applies an automated strategy to minimize an objective function that represents the difference between the observed and modeled garnet composition, was used for the determination of the optimal P-T conditions from garnet composition.

In the clinopyroxene-garnet amphibolite, at least two metamorphic stages have been identified and defined by different phases: i) garnet and rutile for the prograde to HP stage (Fig. 4.5); ii) symplectite and corona for the retrogression (Fig. 4.6). Owing to the strong retrogression, only few relics of the HP stage are observed, and the HP assemblage is unknown. As no weathering is observed in this sample, the unmodified bulk rock composition was used to model the stable assemblage, mineral phase proportions and compositions conditions of the HP stage. This assumption strongly relies on the preservation of the original bulk rock composition in a closed system and on the absence of significant compositional changes during retrogression (this hypothesis is tested in §4.5.1.2).

According to the P-T isochemical phase diagram for the bulk rock composition of sample MT-13 (Fig. 4.5), optimal P-T conditions of  $690 \pm 35$  °C and  $13.4 \pm 2.8$  kbar ( $\text{Alm}_{56} \text{Prp}_{18} \text{Grs}_{26}$ ) for the average garnet core composition were modelled using the program GRTMOD. The mineral assemblage predicted to be stable at these conditions is garnet (34 vol%), clinopyroxene (39 %), amphibole (16 %), quartz (10 %) and rutile (1 %). The modelled clinopyroxene composition at 690°C and 14 kbar has a relatively high Na-content ( $\text{Jd}_{20}$ ).

The bulk rock composition cannot be used to model the reactions that lead to the formation of the symplectite and corona because the evolution of these domains involved local equilibria (Brouwer and Engi, 2005). One way to address this problem is to restrict the analysis to local domains, i.e., to use a local bulk composition as an approximation of the reactive bulk composition. The integration of pixel compositions in specific domains (shown in Fig. 4.6) after a density correction (Lanari and Engi, 2017) was used to approximate local bulk compositions of the symplectite and the corona. An attempt to reconstruct the composition of  $\text{Cpx}_1$  from the symplectite local bulk composition returned  $\text{Si}(2)\text{Al}(0.20)\text{Mg}(0.63)\text{Fe}(0.26)\text{Ca}(0.76)\text{Na}(0.08)$  in a.p.f.u. calculated on a basis of 6 oxygen (see § 4.5.1.1). Since in a simple ternary clinopyroxene model, Al must be equal to Na and therefore to the jadeite content, Al contours were used to constrain pressure conditions around 14 kbar (Fig. 4.5). The mineral assemblage composed of clinopyroxene, amphibole, plagioclase and quartz, observed in the symplectite, is predicted to be stable between 500 and 730 °C, 1 and 7 kbar in the corresponding P-T isochemical phase diagram calculated from local bulk rock (Fig. 4.6A). In this stability field, the modelled clinopyroxene shows low Na-contents ( $\text{Jd}_{3-5}$ ). The range of measured jadeite content in clinopyroxene in this sample allows the pressure estimate to be refined for the symplectite formation to  $6 \pm 1$  kbar. The mineral

assemblage observed in the corona is predicted to be stable between 500 and 700 °C, 2 and 7 kbar (Fig. 4.6B). The modelled plagioclase composition matches the observations.

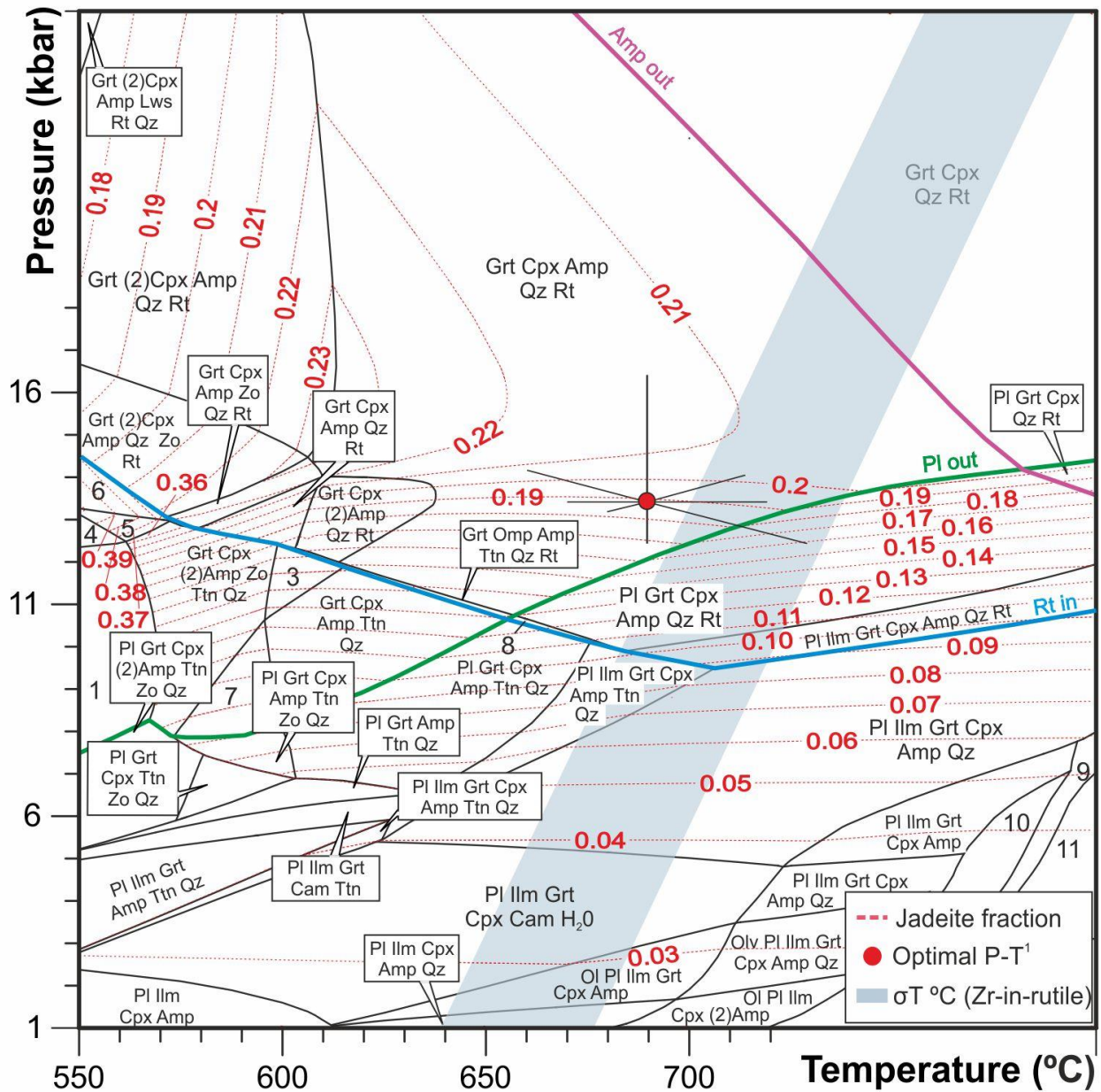


**Figure 4.5:** Pressure-temperature ( $P$ - $T$ ) diagram calculated with Theriak-Domino (de Capitani and Petrakakis, 2010) showing the estimated  $P$ - $T$  conditions for the clinopyroxene-garnet amphibolite MT-13 obtained with (1) GrtMod (Lanari et al., 2017) and in accordance with the Jd fraction estimated from the reconstruction of the symplectite (§ 4.5.1.1). Zr-in-rutile thermometry with  $1\sigma$  results are shown in the blue field. Numbers for the fields: 1-Grt (2)Amp Zo Ttn Qz, 2-Grt Omp (2)Amp Zo Ttn Qz, 3-Grt Omp (2)Amp Ttn Qz, 4-Grt Amp Zo Ttn Qz, 5-Grt Omp Amp Zo Ttn Qz, 6-Grt Omp Amp Zo Ttn Qz, 7-Grt Omp Amp Zo Ttn Qz, 8-Fsp Grt Omp Amp Ttn Qz Rt, 9-Fsp Ilm Grt Omp Opx Amp Qz, 10-Fsp Ilm Grt Omp Amp Qz and 11-Fsp Ilm Grt Omp Opx (2)Amp Qz.

For the migmatitic amphibole-garnet gneiss (MT-17) THERIAK-DOMINO was used to model the stable mineral assemblage and phases composition at specific  $P$  and  $T$  conditions. The chemical system applied was  $\text{Na}_2\text{O}-\text{K}_2\text{O}-\text{CaO}-\text{FeO}-\text{Fe}_2\text{O}_3-\text{MgO}-\text{Al}_2\text{O}_3-\text{SiO}_2-\text{H}_2\text{O}-\text{TiO}_2$

simplified because of the low Mn content in garnet, the main Mn-bearing phase. The internally consistent database applied was TC55, together with the following solid solution models: garnet, biotite and liquid (modified after White et al., 2007); amphibole (Diener et al., 2007); plagioclase (Holland and Powell, 2003); and magnetite (White et al., 2002). The results showed conditions of around 14 kbar and 700°C.

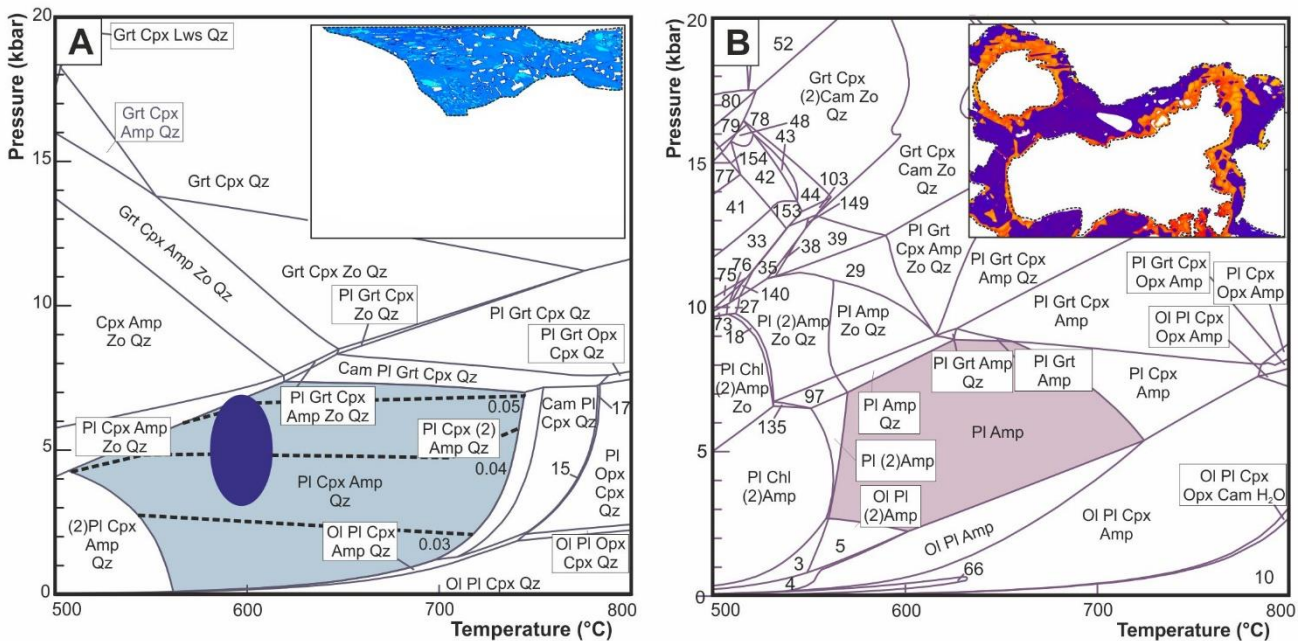


**Figure 4.6:** Pressure-temperature ( $P$ - $T$ ) diagram calculated for retrieved local compositions from the domains (A) symplectite and (B) for the amphibole+plagioclase corona. Dashed lines in (A) indicate  $Jd$  fraction and the blue ellipse represents the  $P$ - $T$  conditions obtained from the semi-empirical thermobarometry applying the calibration of Holland and Blundy (1994). Numbered reactions are available on Appendix VII.

#### 4.5.3.2 Mineral thermobarometry

The temperature of amphibole crystallization in sample MT-13 was estimated from the distribution of Na and Ca between plagioclase and hornblende using the edenite-tremolite calibration of Holland and Blundy (1994). The Na-rich amphibole inclusions in garnet yield temperature of  $620 \pm 47$  °C ( $1\sigma$ ). Amphibole in the symplectite and corona yields temperatures of  $595 \pm 26$  °C and  $600 \pm 16$  °C, respectively. Following the strategy of Lanari et al. (2013), we determined the pressure of clinopyroxene pixels within the symplectite based on the reaction: jadeite + tremolite = albite + edenite (Waters, 2003). Activities of end members were calculated for amphibole and clinopyroxene following the models of Dale et al. (2000) and Holland (1990), respectively. The pressure estimates range between 3 and 7 kbar with an average of  $4.8 \pm 1.5$  kbar (Fig. 4.6). The average T and P given here are reported together with a standard deviation value ( $1\sigma$ ) obtained from the variability of the P and T maps (see Lanari et al., 2014 for a

discussion). This number reflects the relative uncertainty in the estimates that is related to the analytical precision of the EPMA measurements (Lanari et al., 2013).

#### 4.5.3.3 *Rutile thermometry and trace element compositions*

Temperature of rutile formation can be determined using Zr-in-rutile thermometry (Tomkins et al., 2007; Watson et al., 2006; Zack et al., 2004). Zr concentration in rutile is dependent on both Si and Zr activities so that thermometry can be only applied in the presence of the appropriate buffering assemblage zircon and quartz. Those phases must have coexisted along in equilibrium with the growing rutile. Rutile LA-ICP-MS trace element analyses were performed to estimate the formation temperature of rutile.

In sample MT-13, metamorphic zircon and quartz are observed in the rock and as inclusions in rutile, suggesting that the activities were buffered. Seventeen analyses on different morphologically grains reveal Zr contents in rutile ranging from 440 to 770 ppm. The input pressures were fixed to 5, 10 and 15 kbar. The corresponding Zr-in-rutile temperatures calculated with the calibration of Tomkins et al. (2007) are  $675 \pm 16$  °C,  $701 \pm 16$  °C and  $724 \pm 17$  °C ( $1\sigma$ ) (Fig. 4.5). Using the calibration of Watson et al. (2006) the Zr-in-rutile temperatures range between 675 and  $725 \pm 30$  °C, with an average of  $696 \pm 16$  °C ( $1\sigma$ ).

Most of the analyzed trace elements (22 elements) do not show any correlation with the Zr content and consequently with temperature (e.g., Si, Al, Nb, W, U, Pb). The best positive correlation is observed for Hf (14 to 28 ppm), whereas other elements such as Fe (345 to 13,200 ppm) show a more scattered signal. Nb has concentrations between 322 and 701 ppm, and Cr between 461 and 929 ppm; both elements do not show correlations with temperature.

#### 4.5.4 **U-Th-Pb geochronology and trace elements of zircon and monazite**

Isotopic (Appendices IV and V), trace element (Appendix III) and inclusion compositional (Appendix II) data are reported on MT-13, MT-22A, MT-17, MT-19 and MT-20.

##### 4.5.4.1 *Clinopyroxene-garnet amphibolite MT-13*

Zircons are mainly prismatic, between 120 and 200  $\mu\text{m}$  in length, with length:width ratios of 2:1 and 3:1. Cathodoluminescence imaging reveals parallel oscillatory zoning cores that are surrounded by high luminescent rims, which are variable in thickness and shape. A considerably

part of the population exhibits crystals with small remnants of irregularly shaped cores and thick rims. The core-rim boundary is commonly embayed (Fig. 4.7 and Supplementary Figure S.7).

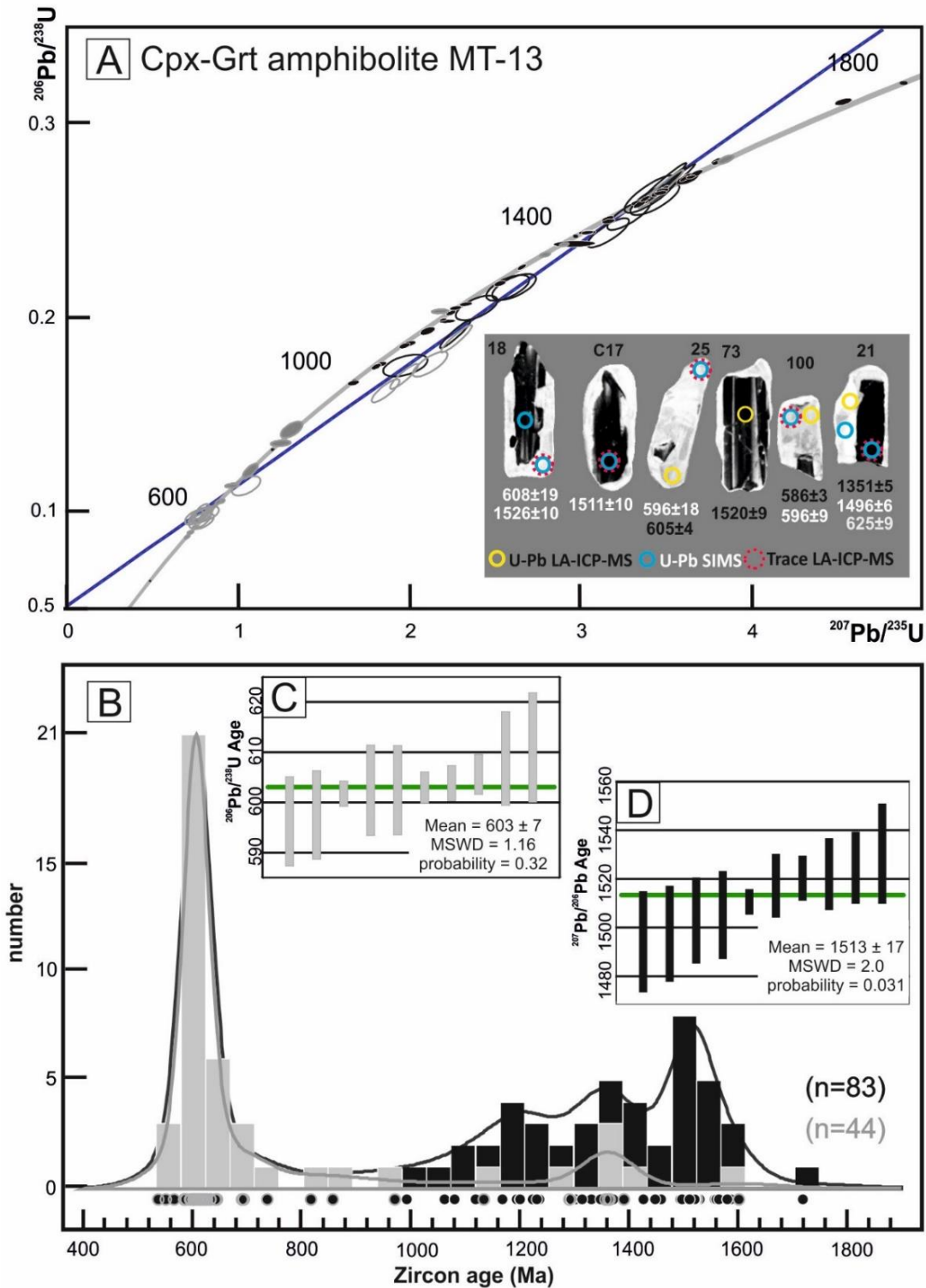


**Figure 4.7:** U-Pb zircon data from clinopyroxene-garnet amphibolite MT-13. (A) Concordia diagram (2 $\sigma$  error ellipses) with CL-images of representative grains analyzed (yellow circle for LA-ICP-MS, blue circles for SIMS analyses and dashed red circles for trace elements, spot size ~25 microns); Filled ellipses for cores analyses LA-ICP-MS (black) and rims (grey) and empty ellipses for SIMS analyses of cores (black) and rims (grey). (B) Kernel density diagram for data considered for age calculation; core data in black and rim data in grey. (C) Data defining the metamorphic age from the weighted average of the rims. (D) Data defining the protolith age.



Zircon grains were analyzed for U-Th-Pb by SIMS and LA-ICP-MS (141 spots on 87 grains) using the same zircon standard (91500, reference 1065 Ma, Wiedenbeck et al., 1995). Both methods provided similar results. LA-ICP-MS data were filtered based on common lead content and reproducibility of isotopic ratios within analysis. Th/U ranges from 0.01–1.4 in cores, and 0.01–0.05 in rims and single phase grains (entire crystals which show the same CL-bright response as rims). The data spread along Concordia between a maximal core  $^{207}\text{Pb}/^{206}\text{Pb}$  age of c. 1590 Ma and an age of c. 550 Ma defined by rim analyses (Fig. 4.7A). The data scatter for both core and rim dates require caution in the interpretation of ages, which are obtained only for the main cluster of dates corresponding to each domain (Fig. 4.7B). The oldest concordant group of core dates yield an average age of  $1513.3 \pm 17.1$  (MSWD = 2, N = 10; Fig. 4.10D). Nonetheless, there are cores dates that spread between this age and c. 1600 Ma, with similar CL-responses to the older cores.

Chondrite-normalized (McDonough and Sun, 1995) pattern of core domains (N=11) have a steep HREE pattern (Fig. 4.8A), with  $\text{Lu}_N/\text{Gd}_N$  mainly between 16 and 34 and slight to moderate negative Eu anomaly ( $\text{Eu}/\text{Eu}^*$  0.45–0.91). This signature is compatible with a mafic protolith containing little plagioclase. Both cores and rims show a disperse results for LREE, especially for La, Ce and Pr, that may indicate the presence of micro-inclusions. Ti was analyzed in the different CL-domains and temperatures were calculated using the Watson et al. (2006) calibration. The eleven cores, with Ti contents between 1.6 and 41.7 ppm, provided temperatures in between ca. 600 and 890°C. The age of the oldest cluster of core analyses is thus interpreted to date the protolith based on oscillatory zoning, relatively high Th/U, Ti-in-zircon temperatures and high REE content.

The vast majority (c. 80 % of a total 46 grains) of zircon rims yield dates between 550 Ma and 700 Ma. The youngest cluster of concordant analyses yield an average age of  $603.1 \pm 6.8$  Ma (MSWD = 1.16, N = 10; Fig. 4.7B). The intermediate dates that scatter between protolith age and the youngest cluster either describe a Discordia with lower intercept at c. 670 Ma (mainly SIMS analyses), or scatter along Concordia. These intermediate dates are possibly due to partial Pb loss in the cores, incomplete resetting of the U-Pb system in the rims, or physical mixing of core and rim domains during analysis and no geological meaning is attributed to them.

Trace element compositions of zircon rims indicate two patterns for domains that are similar in CL zoning: a) the majority of analyses (N = 13) show a flat HREE pattern, with  $\text{Lu}_N/\text{Gd}_N$  of 0.86–3.75 and moderate negative to slightly positive Eu anomaly ( $\text{Eu}/\text{Eu}^*$  0.65–1.17), b) a few zircon rims (N = 6) have higher  $\text{Lu}_N/\text{Gd}_N$  (20 to 300) and moderate Eu anomaly ( $\text{Eu}/\text{Eu}^*$  0.58–0.75) or low MREE content below the limit of detection (Fig. 4.8A). For the nineteen zircon rims, the Ti content is in between 1.5 and 21 ppm, with some values under the limit of detection. The resulting Ti-in-

zircon temperatures ranges from 590 to 810 °C for rim type 2 (steep HREE), and from 610 to 790 °C for rim type 1 (flat HREE).

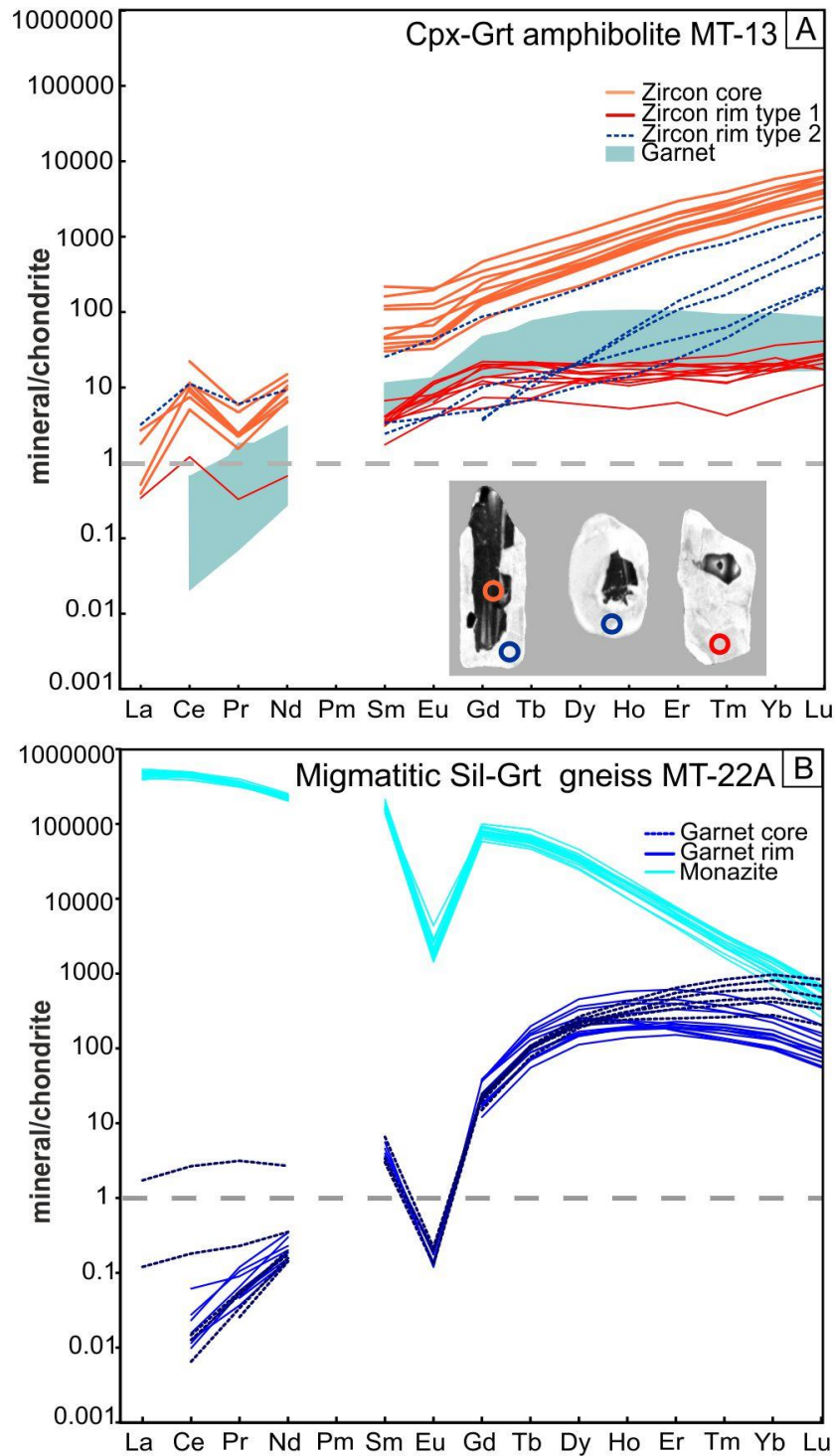


**Figure 4.8:** Chondrite normalized diagrams of the REE composition of: (A) Different dated domains in zircon and garnet from the clinopyroxene-garnet amphibolite MT-13 with location of the analyzed spots in representative grains (spot size ~25 microns); (B) Dated monazite and garnet from the migmatitic sillimanite-garnet gneiss MT-22A. Chondrite normalizing values from McDonough and Sun (1995).

Inclusions in zircon have showed to be a valuable tool in connecting P-T conditions to age information (Gilotti, 2013; Hermman et al., 2001; Katayama and Maruyama, 2009), especially in (U)HP rocks in which prograde to peak assemblages are easily replaced during decompression. Oscillatory cores contain numerous sub- $\mu\text{m}$  inclusions of amphibole, clinopyroxene and quartz. Clinopyroxene and amphibole found in the core have high  $\text{Al}_2\text{O}_3$  and  $\text{Na}_2\text{O}$ , comparable to the values for the reconstructed symplectite composition (see § 4.5.1.1) and inclusions in rutile, respectively (Fig. 4.4). The data from amphibole inclusions in an oscillatory core show a composition of edenitic hornblende (Tindle and Webb, 1994 and references therein). Given the altered nature of the cores (disturbed CL zoning, fractures and disturbed U-Pb ages) the mineral inclusions are interpreted as secondary: they are suspected to have formed in the zircon cores along fractures and zoned of alteration due to fluid infiltration during metamorphism (grains #24 and #47 in Supplementary Figure S.1).

The zircon rims contain a few 1 and 10  $\mu\text{m}$  sized inclusions of clinopyroxene, amphibole, quartz, garnet and biotite (Supplementary Figure S.1). Clinopyroxene inclusions in zircon rims show the lowest values of  $\text{Al}_2\text{O}_3$  and  $\text{Na}_2\text{O}$  among Cpx analyses (including matrix, symplectite, inclusions in rutile and garnet; Fig. 4.4). Hornblende inclusions have a similar composition to the amphiboles in corona, inclusions in garnet and some of the matrix crystals (Fig. 4.4). One garnet inclusion has the composition  $\text{Alm}_{54}\text{Grs}_{25}\text{Prp}_{18}$  (considering  $\text{MnO} = 1\%$ ), the same found for crystals in the matrix.

#### 4.5.4.2 *Gneisses*

The migmatitic sillimanite-garnet gneiss MT-22A has zircon grains that are prismatic and elongated (50 to 300  $\mu\text{m}$ ). Around 80 % of the grains have a CL-dark response, with some oscillatory zoning preserved mainly in the cores (Fig. 4.9). Similar, mottled, CL-dark zoning has been attributed to metamictization and/or alteration (Corfu et al., 2003; Nasdala et al., 2003). Concordant zircon dates spread between c. 1470–620 Ma with two main clusters at around 670 Ma and 800 Ma. Because of the poor CL zoning, Th/U ratio was the main criteria to distinguish between domains. The eleven younger analyses with Th/U ratios higher than 0.1, and with recognizable oscillatory zoning are interpreted as magmatic and provide a concordia age of  $793.8 \pm 3.9$  Ma (Fig. 4.9). Zircon euhedral morphology and the cluster of ages for preserved magmatic zircons suggest that this rock had mainly one zircon source. Zircon domains with low Th/U ratios yield dates ranging mainly from 940–550 Ma with a major cluster of nine analyses constraining a concordia age of  $671.8 \pm 3.8$  Ma. Such analyses were mostly located in the external portion of the crystal.



Monazite grains in the gneiss are clear, light yellow, anhedral and smaller than 150  $\mu\text{m}$  (Fig. 4.9). The crystals do not display any internal structure in BSE imaging. Twenty grains analyzed by SIMS have an average  $^{206}\text{Pb}/^{238}\text{U}$  age of  $636.5 \pm 7.2$  Ma (MSWD = 0.65; 95 % c.i.; Fig. 4.9). Chondrite-normalized REE patterns on sixteen monazite grains show homogeneous compositions. Crystals have the expected signature for monazite with strong enrichment in LREE (La  $\sim$  500,000), a progressive depletion in HREE (Gd/Lu 111–245) and strong negative Eu anomaly ( $\text{Eu}/\text{Eu}^*$  0.01–0.04), as described in previous works (Hermann and Rubatto, 2003; Rubatto et al., 2006) (Fig. 4.8B).

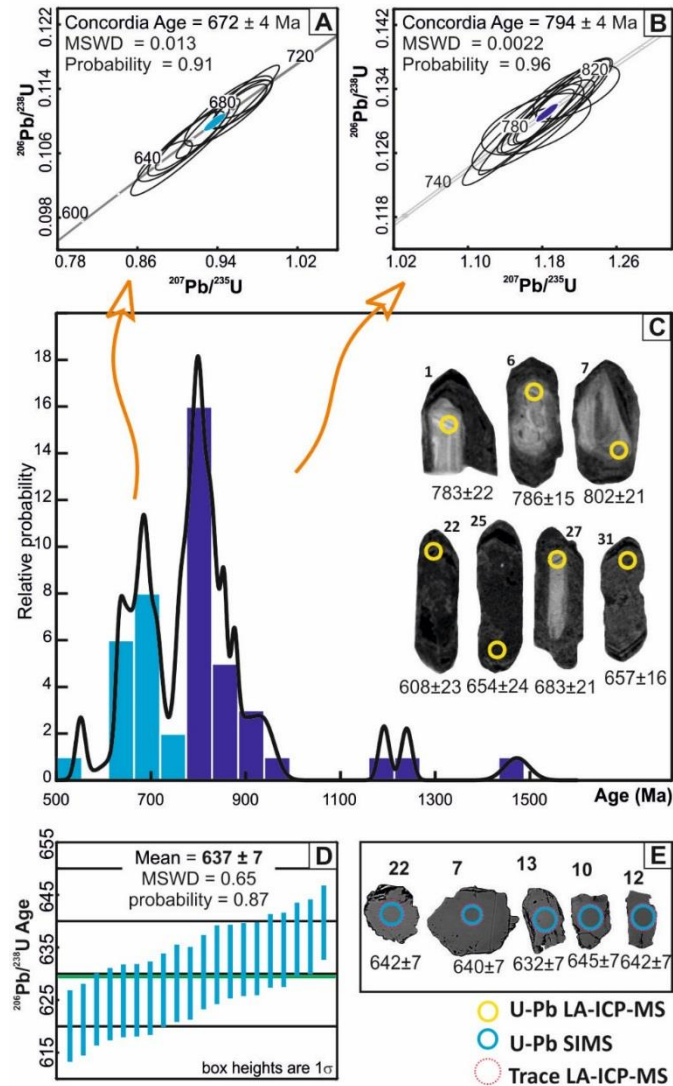


**Figure 4.9:** Geochronological results for migmatitic sillimanite-garnet gneiss MT-22A. (C) Probability density diagrams showing the distribution of the zircon data of the migmatitic sillimanite-garnet gneiss MT-22A and CL-images of representative grains analyzed (spot size  $\sim$ 25 microns). The light blue bars indicate the data with low Th/U ratios, used for calculating the metamorphic age from the Concordia diagram in A. (B) The Concordia diagram for the grains with Th/U ratios higher than 0.1, from which the main data peak defines the maximal depositional age. (D) Weighted average  $^{206}\text{Pb}/^{238}\text{U}$  ages diagram for monazite, and (E) backscattered electron images of representative grains analyzed on the Concordia diagrams (ellipses are  $1\sigma$  error).

In the migmatitic amphibolite-garnet gneiss MT-17 zircon grains range in size from 100  $\mu\text{m}$  to 400  $\mu\text{m}$ . Most grains show oscillatory zoning with CL-medium-bright responses. Irregularly shaped CL-dark cores, as well as discrete few  $\mu\text{m}$  thick CL-dark rims, are found in some of the grains (Fig. 4.10A). Forty-seven LA-ICP-MS analyses on oscillatory domains yield Th/U ratios between 0.31 and 0.74. Most analyses (87 %) define a concordia age of  $2065.6 \pm 2.3$  Ma (Fig. 4.10A), interpreted as the crystallization age of the protolith.

In the allanite-bearing biotite granite MT-19 zircon grains are elongated prismatic, up to 400  $\mu\text{m}$  in length with oscillatory zoning in the majority of the grains. A subset of grains has CL-dark domains combined with poorly zoned rims brighter in CL images (Fig. 4.10C). Seventy-two analyses were obtained by LA-ICP-MS. Oscillatory cores have Th/U mostly in the range 0.10–0.35 and 0.01–0.18 for the rims. On a Concordia diagram the data separate in two well-defined groups, with 90 % of the data around 2 Ga. We adopt the approach used by Whitehouse and Kemp (2010), and consider the largest group of older dates to be significant. In this group, the oscillatory domains provide a concordia age of  $2076.1 \pm 3.2$  Ma (Fig. 4.10C) with some scattering data down to c. 2.0 Ga. Based on the zoning of the crystals, this age is interpreted as dating the crystallization of the protolith. A discrete group of analyses on rims with low Th/U yield a concordia age of  $626 \pm 5$  Ma that is interpreted to be related to a metamorphic event (Fig. 4.10D).

Biotite gneiss MT-20 has a heterogeneous zircon population, with most grains showing multiple domains in CL. Generally, complex cores have various CL zoning that in most crystals is truncated by rims with weak or no regular zoning and variable CL-emission (Fig. 4.10E). Seventy-three analyses in fifty-six grains were carried out with LA-ICP-MS. Th/U ratios range mainly between 0.15 and 0.84 for the cores, and  $<0.01$  for the rims. Similarly, to MT-19, the analyses define two major clusters in the Concordia diagram, but with a most representative cluster for younger ages (c. 600 Ma). With a similar approach as described for MT-19, the fifteen older analyses corresponding to zircon cores define a concordia age of  $2076.2 \pm 4.4$  Ma (Fig. 4.10E). A coherent group of twenty-eight overgrowths with Th/U  $< 0.1$  yielded a concordia age of  $632.2 \pm 2.4$  Ma (Fig. 4.10F). Ages are interpreted, based on internal zoning and Th/U composition, to constrain the Paleoproterozoic age of the protolith and a Neoproterozoic metamorphism.

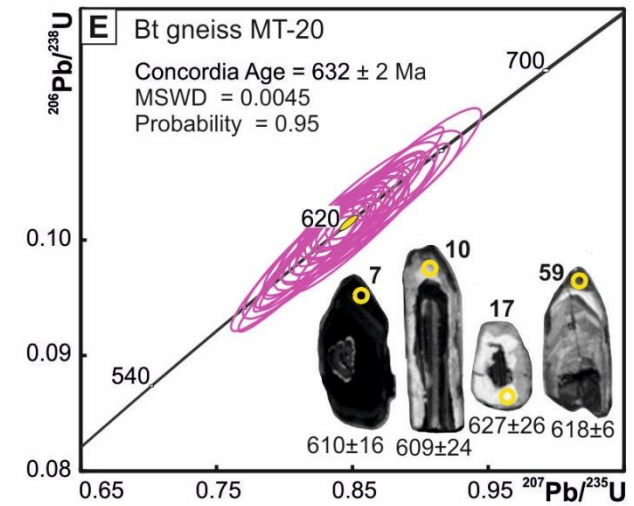
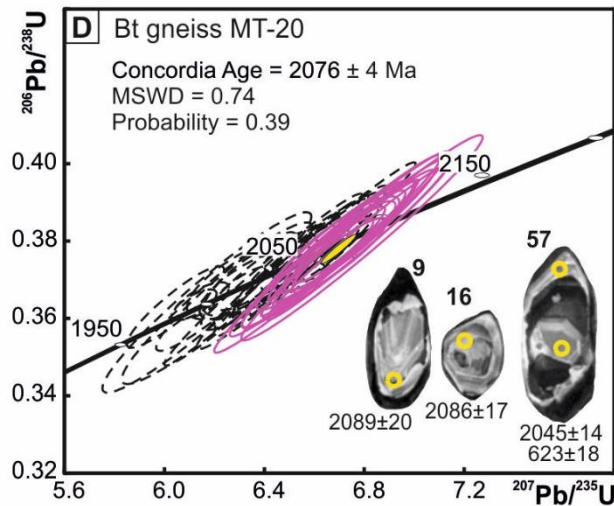
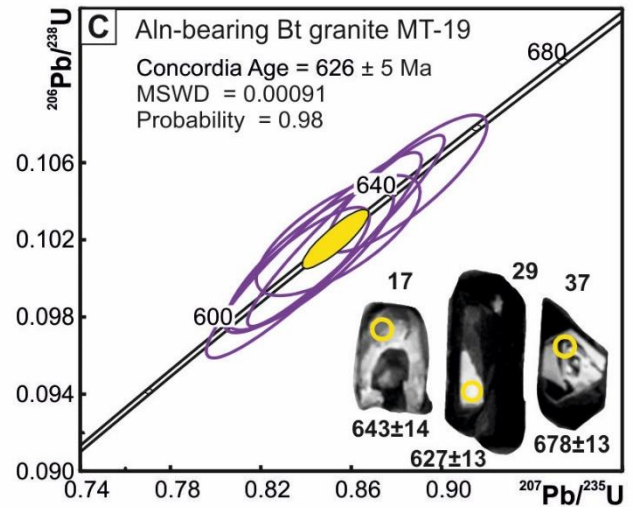
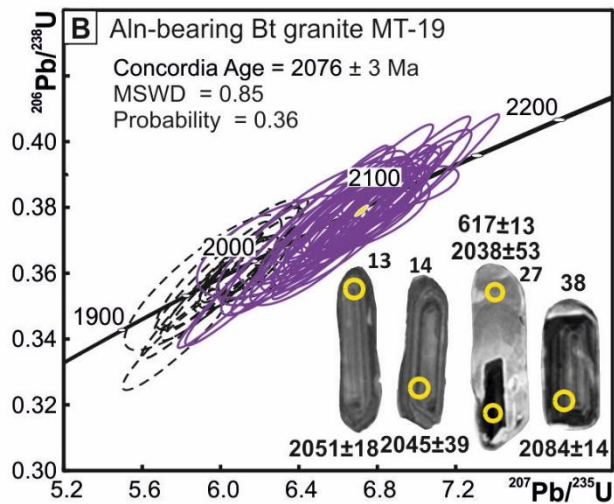
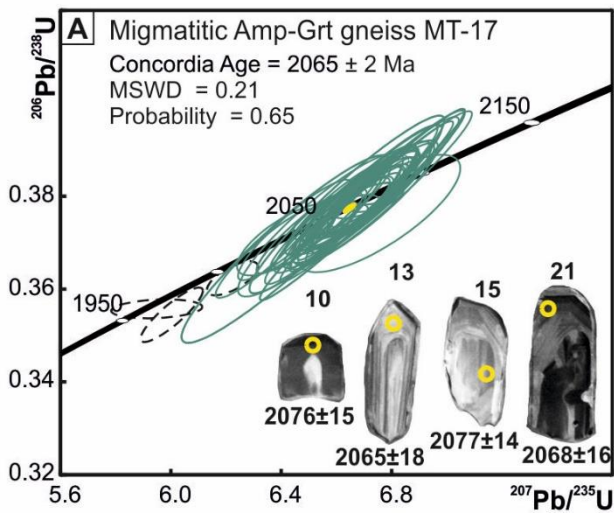


**Figure 4.10:** Geochronological results (LA-ICP-MS analyses,  $1\sigma$  error ellipses) for migmatitic amphibole-garnet augen gneiss MT-17, allanite-bearing biotite granite MT-19 and biotite gneiss MT-20 with CL-images of representative analyzed grains. In the Concordia diagrams younger analyses discarded are represented by dashed lines (see text for explanation).

## 4.5.5 Garnet trace element composition

*Clinopyroxene-garnet amphibolite MT-13.* Corroborating the major element compositional maps, eighteen trace elements spot analyses reveal a homogeneous composition for garnet crystals. Chondrite-normalized (McDonough and Sun, 1995) garnet patterns show LREE depletion (La–Sm<sub>N</sub> 0.01–0.53; Some La, Ce and Pr concentrations are under detection limit), slight to moderate negative Eu anomaly (Eu/Eu\* 0.54–0.84) and relative flat HREE enrichment (Lu/Gd<sub>N</sub> 0.73–2.34; Fig. 4.8A).

*Migmatitic sillimanite-garnet gneiss MT-22A.* Twenty garnet analyses (Fig. 4.8B) reveal a significant variation between core and rim. The cores are enriched in heavier elements (e.g., Ho, Er, Tm, Yb and Lu; Lu/Gd<sub>N</sub> 1.43–37.07), while the rims display a convex shape with depletion in these elements (Lu/Gd<sub>N</sub> 2.66–14.53). The analyses show a discrete spread in LREE (Ce 0.006–0.18) and a marked negative Eu anomaly (Eu/Eu\* 0.005–0.015, only 30 % of Eu analyses are above detection limit). LREE depletion below chondrite values, strong negative Eu anomaly and relative HREE enrichment are typical for high-grade metamorphic garnet from granulites or migmatites (Hermann and Rubatto, 2003; Kelly and Harley, 2005; Rubatto et al., 2006).

## 4.6 Discussion

### 4.6.1 Petrochronological evolution of clinopyroxene-garnet amphibolite MT-13

#### 4.6.1.1 Pressure peak conditions

Garnet thermobarometry indicates growth conditions of  $690 \pm 35$  °C and  $13.4 \pm 2.8$  kbar for the average garnet core composition. The absence of strong major element compositional zoning in garnet might be interpreted as a direct consequence of intragranular diffusion that enhanced re-equilibration of the small crystals in equilibrium with the omphacitic matrix near the peak conditions. Theoretical models show that the time required to produce unzoned crystals of 2–3 mm size is in the order of 10–50 Ma (Caddick et al., 2010) for metamorphic temperatures around 690 °C. Age dating results (see below) suggest that this sample might have experienced more than 20 Ma at conditions hotter than 600 °C (Coelho et al., 2017; and results from this study). In this case any prograde growth zoning would be significantly affected by diffusion and the final garnet composition may eventually reflect (partial) equilibrium conditions at HT conditions. Alternatively, the garnet completely recrystallized at peak metamorphic conditions, also equilibrating any zoning in trace elements. At these conditions, the metamorphic assemblage predicted to be stable in a rock of this composition consists of garnet, clinopyroxene, amphibole, rutile and quartz. This HP

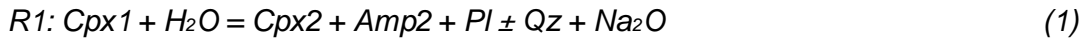
assemblage has been strongly retrogressed into symplectite and coronas and the comparison between modelled and measured clinopyroxene composition shows that the former omphacite (Cpx1) was completely re-equilibrated after the HP stage (Fig. 4.4). Comparing the integrated composition of Cpx1 from the symplectite domain using the average composition determined from the compositional maps (see § 4.4.3.1) returned Si(2)Al(0.20)Mg(0.63)Fe(0.26)Ca(0.76)Na(0.08) in a.p.f.u. and, the composition of Cpx1 predicted by the model at 690 °C and 13.4 kbar is Si(2)Al(0.19)Mg(0.59)Fe(0.22)Ca(0.81)Na(0.19). The two compositions are fairly similar with the exception of Na that appears to be significantly lower in the symplectite. In a simple ternary clinopyroxene model, Al must be equal to Na and therefore, to the jadeite content. As  $(1-Ca) \approx Al$  in the symplectite composition, we can assume that the symplectite formed from a HP omphacite with a Jd<sub>20-21</sub> composition. In this scenario, Na was lost during the symplectite formation, whereas Si, Al, Fe and Mg were kept unchanged.

A Zr-in-rutile temperature of  $701 \pm 16$  °C ( $1\sigma$ ) was determined at a pressure of 10 kbar using the calibration of Tomkins et al. (2007). The temperature range is in agreement with the conditions derived for the garnet core. The homogeneous distribution of Zr in rutile suggests that rutile grew in a narrow range of temperature. The P-T diagram indicated that rutile occurs above 9 kbar. The inclusions in rutile, such as amphibole, plagioclase, titanite and clinopyroxene (Jd<sub>9-4</sub>), suggest a lower pressure around 5–9 kbar (Fig. 4.5). Amphibole and clinopyroxene inclusions in rutile have a different composition compared to the grains preserved in the mineral matrix. Clinopyroxene shows higher XMg (~0.76) and amphibole higher Na<sub>2</sub>O and Al<sub>2</sub>O<sub>3</sub> contents (Fig. 4.4), reflecting a different coexisting metamorphic assemblage. Based on these observations, rutile is interpreted to have grown during burial from 9 to 14 kbar at 675–720°C. The presence of rutile inclusions in garnet supports the scenario of growth before or together with garnet.

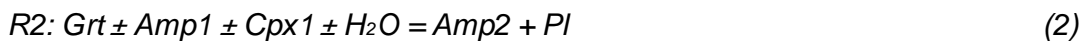
Apart from rutile, garnet is the only remnant of the higher-pressure stage in this rock and therefore the maximal estimate of  $13.4 \pm 2.8$  kbar is based on garnet thermobarometry. Omphacite (Cpx1) is no longer preserved, but reconstruction from the composition of the symplectite shows that Jd<sub>20</sub> omphacite may have coexisted with this garnet at similar pressure conditions. If the sample would have reached higher pressure, this could have been recorded by inclusions trapped in the accessory minerals. Inclusions in rutile indicate a lower grade metamorphic assemblage (prograde) as for zircon (retrograde). We conclude that there is no evidence that the mafic rock MT-13 reached pressures higher than 14 kbar. Therefore, this sample is better classified as a high-pressure (HP) amphibolite, instead of “retro-eclogite”.

#### 4.6.1.2 Formation of symplectite and corona and implications for element mobility

The HP assemblage of garnet, omphacite, amphibole and quartz was partially transformed into two retrogression products: symplectite and corona. The symplectite consists of clinopyroxene, amphibole and plagioclase, and has formed through the destabilization of a former omphacite (Cpx1), following the reaction:



Similar reactions have been observed in retrogressed mafic eclogites (Lanari et al., 2013; Waters, 2003). The corona is made of plagioclase and amphibole and has formed through the reaction:



with unconstrained proportions of amphibole (Amp1) and clinopyroxene (Cpx1). A significant fraction of garnet may have been dissolved during the formation of the corona.

The P-T conditions of formation of these two domains have been estimated by using local bulk compositions to approximate their reactive bulk compositions (Lanari and Engi, 2017). This strategy relies on the assumption of thermodynamic equilibrium, whereas the investigated domains preserve strong evidence of frozen-in chemical potential gradients. Nevertheless, the equilibrium models predict modal abundances and mineral compositions that are in line with the observation such as the average compositions of mineral phases determined in each domain. Any spatial organization or compositional zoning caused by chemical potential gradients within a single domain cannot be modelled by this technique and, therefore, requires the use of  $\mu$ - $\mu$  diagrams (White et al., 2008). However, the alternative strategy described in this study does not require any kinetic assumption such as immobile  $Al_2O_3$ , providing an estimate of the average physical and chemical conditions in each domain.

Amphibole thermometry and clinopyroxene barometry have been applied to the minerals located in the symplectite and corona. This inverse method can be used to obtain P-T conditions from retrogressed domains (Lanari et al., 2013; Loury et al., 2016; Waters, 2003). The symplectite formed at  $595 \pm 26$  °C and  $4.8 \pm 1.5$  kbar, in good agreement with the results of the forward equilibrium models (Fig. 4.6A). A temperature of  $600 \pm 16$  °C has been estimated for the corona. No pressure data could be obtained because of the absence of clinopyroxene. At this temperature, the pressure is fixed by the geometry of the stability field of plagioclase + amphibole at  $5 \pm 2.5$  kbar (Fig. 4.6B). Symplectite and corona have thus formed at similar P and T conditions along the retrogression. Titanite corona around rutile, and locally ilmenite, suggests a similar path in the P-T diagram (Fig. 4.5).

It is interesting to evaluate the possible element exchanges occurring between the two domains – symplectite and corona – during retrogression. This can be analyzed in  $\text{Al}_2\text{O}_3$  against  $\text{Na}_2\text{O}$  binary diagrams that consider bulk rock, symplectite, corona and mineral compositions for the peak and retrograde stages (Fig. 4.11). The bulk rock composition correctly lies between composition of the modelled peak minerals (Fig. 4.11A), and in between that of retrograde garnet, symplectite and corona (Fig. 4.11B). Reaction R1 is well constrained as the composition of Cpx1 can be derived from the model at 690°C and 13.4 kbar (§ 4.5.1.1). From Figure 4.11B, it can be deduced that about ~2 wt% of  $\text{Na}_2\text{O}$  is released from the reaction R1:  $\text{Cpx1} \rightarrow \text{symplectite}$ . The reaction R2 is more difficult to constrain because it is not possible to evaluate the bulk composition of the reactants. However, the texture suggests that the corona formed from garnet and amphibole1 ( $\pm \text{Cpx 1}$ ), marked by the mixing line shown in Figure 4.11B (dashed grey line). For a reacting volume made of amphibole (80 wt%) and garnet (20 wt%), the formation of the corona requires a gain of ~2 wt% of  $\text{Na}_2\text{O}$  at a fixed value of  $\text{Al}_2\text{O}_3$ . Then, the reaction R2 can be refined as:



This mass balance model shows that the two reactions were coupled. The excess of Na released from the symplectite reaction corresponding to 2.1 g of  $\text{Na}_2\text{O}$  per 100 g of the parent omphacite (assuming no volume change) is required to drive reaction R2 and develop the corona. These reactions do not require any mobility of Al, and presumably other immobile elements, such as trace elements, between the two reacting domains. The likely immobility of trace elements at this stage has implications for zircon-garnet trace element correlation (see below).

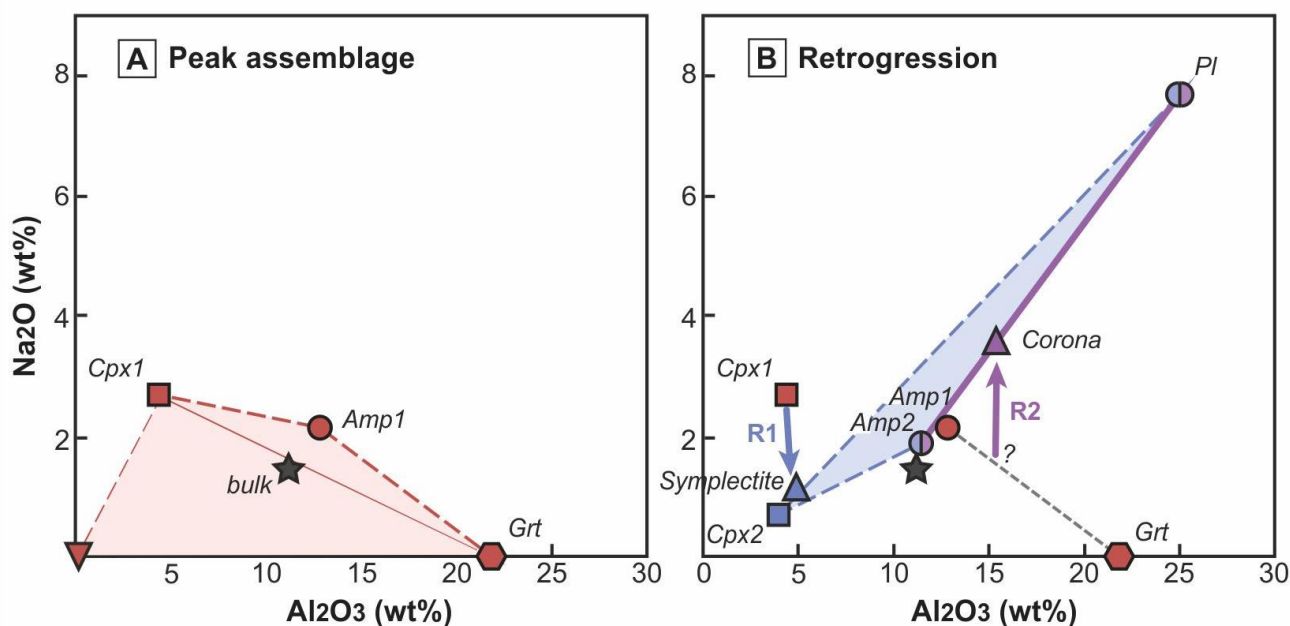


**Figure 4.11:**  $\text{Al}_2\text{O}_3$  vs  $\text{Na}_2\text{O}$  binary diagram showing the stable phases and their relationship with the bulk-rock (A) at peak conditions and at (B) the retrogression stage. The diagrams show the possible element exchanges occurring between the symplectite and corona domains during retrogression. See text for details.



#### 4.6.1.3 *Age constraints and link to P-T conditions*

The age of zircon rims in mafic sample MT13 is determined from the youngest cluster of concordant analyses at  $603 \pm 7$  Ma. It is important to link this age to a metamorphic stage.

The CL-bright zircon rims with low Th/U show trace elements patterns that are either flat (type 1) or enriched in HREE (type 2, Fig. 4.8A). The depletion of HREE and the absence of negative Eu anomaly are commonly attributed to presence of garnet and absence of plagioclase in the coexisting assemblage (Ganade de Araujo et al., 2014; Rubatto, 2002). The absence of Eu anomaly in the zircon rims can be explained by a bulk rock composition effect, as a small Eu anomaly is observed in zircon cores (Rubatto, 2017), which presumably grew in a gabbroic protolith in the presence of plagioclase. Therefore, the absence of Eu anomaly in this case is not indicative of zircon growth under plagioclase free, eclogite facies conditions.

Zircon depletion or enrichment in HREE is linked to garnet stability, as garnet is a major carrier of HREE. In this rock sample, however, where chemical equilibrium was essentially localized (see above formation of symplectite and corona) trace element equilibrium between phases in different domains cannot be expected. Garnet textures indicate that garnet has been resorbed during the formation of the corona. Only the zircon growing in a corona would thus incorporate the HREE from garnet. Zircon type 2 has a HREE enriched pattern and possibly formed within a corona while garnet was being dissolved. Retrograde titanite is a potential repository for LREE and MREE and might contribute to the steep pattern of zircon-rim type 2. Type 1 zircon has a flat HREE pattern and could thus have formed before garnet resorption, or in a different domain where garnet was not resorbed, i.e., in the symplectite domain. Zircon rim type 1 and type 2 were never observed in the same grains, and can be related to two different populations. The possibility that type 2 zircon represents mixing analyses between 1.5 Ga core and type 1 rim is excluded by the fact that type 2 analyses do not show older, thus mixed ages. Similar conclusions can be drawn from the dataset of Coelho et al. (2017) in which zircon rims show HREE enrichment but never have ages older than 625 Ma. Therefore, we propose that zircon type 1 and 2 grew in different domains with different local bulk compositions, most likely during retrogression and the formation of symplectite and corona.

This interpretation is also supported by the analyses of inclusions in zircon rims. Clinopyroxene and amphibole inclusions in zircon show similar compositions to that of minerals in the symplectite and corona (Fig. 4.4). A single inclusion of omphacite in zircon core shows similar  $Al_2O_3$  to the average composition of the reconstructed symplectite (interpreted as Cpx1). As zircon cores show typical magmatic features and have ages around 1.5 Ga, this inclusion is interpreted



as a secondary inclusion formed during metamorphism and alteration of zircon cores, as reported in other metamorphic rocks (Rubatto, 2017).

In conclusion, metamorphic zircon formation in the mafic rock occurred from c. 630 to c. 600 Ma and registers the metamorphic evolution from peak to decompression. The age of  $603 \pm 7$  Ma defined by a cluster of rim dates can be linked to the retrogression stage involving symplectite and corona growth. The results of this study are in line with the predictions by the model of Kohn et al. (2015), showing that zircon is likely to grow under retrograde conditions when garnet is dissolved.

#### **4.6.2 Magmatic and metamorphic history of the Pouso Alegre rock assemblage**

The Pouso Alegre rock assemblage is composed of three distinct rock units that were associated during Neoproterozoic tectono-metamorphic events. These units are:

1) the Paleoproterozoic migmatite, orthogneiss and granite of the regional basement (samples MT-17, MT-19 and MT-20);

2) Mesoproterozoic mafic rocks metamorphosed to clinopyroxene-garnet amphibolite (MT-13) that were previously classified as “retro-eclogite” (Fig. 4.1C and D); and,

3) a Neoproterozoic peraluminous gneiss of uncertain origin (migmatitic sillimanite-garnet gneiss, MT-22A).

##### **4.6.2.1 Formation and evolution**

1. *Paleoproterozoic rock assemblage* - The migmatitic amphibole-garnet gneiss MT-17, allanite-bearing biotite granite MT-19 and biotite gneiss MT-20 have magmatic zircon or zircon cores dates at  $2065 \pm 2$  Ma,  $2076 \pm 3$  Ma and  $2076 \pm 4$  Ma, respectively (Fig. 4.12). The three gneisses show similar ages, as well as mineralogical and major element compositions, but distinct trace element signatures for HREE (Supplementary Figure S.2 and Appendix I), suggesting that they are members of a Late Rhyacian magmatic suite. The ages of c. 2.07 Ga and field relations suggest that these rocks belong to the Pouso Alegre complex, a basement unit of the reworked margin of the São Francisco craton (Cioffi et al., 2016). The bulk rock chemistry of the migmatitic amphibole-garnet gneiss and biotite gneiss are compatible with the granodioritic and granitic samples described by Cioffi et al. (2016), as showing juvenile Hf and Nd signatures. Trace element signatures from sample MT-17 and MT-20, are in accordance to those from granites and

granodiorites of the Pouso Alegre basement, which in turn resemble subduction-related patterns of modern arcs (Cioffi et al., 2016). However, the allanite-bearing biotite granite MT-19 is depleted in HREE, suggesting that it represents a melt from a source that retained significant amount of garnet, possibly a metasedimentary rock (cf. Wilson, 1989).

2. *Clinopyroxene-garnet amphibolite MT-13* - It forms a steep-dipping concordant body hosted by sapolites from migmatitic-gneissic rocks, most probably correlated with the orthogneisses of the Rhyacian Pouso Alegre complex (see § 4.3). The bulk rock chemistry indicates a tholeiitic composition for the protolith, with a signature between N-MORB and E-MORB. REE patterns for the magmatic zircon cores (Fig. 4.8) show a small Eu anomaly, supporting a basaltic liquid composition for the protolith, with minimal plagioclase fractionation. Kaczmarek et al. (2008) reported similar trace element signatures in partly metamorphosed zircon grains from metagabbros. Ti-in-zircon temperatures are spread, but show highest values around 900 °C, compatible with crystallization of residual basaltic magmas after crystallisation of cumulus phases.

The chemistry, an age that is 900 My older than the collision event, together with its location in a continental section, argue for a continental rift origin rather than a relic oceanic crust. The significant amount of magmatic zircon grains found in this mafic rock, as well as their morphology, suggests that the protolith was a plutonic to subvolcanic rock. Zircon cores constrain a minimum crystallization age at  $1513 \pm 17$  Ma, in line with the  $1504 \pm 29$  Ma age reported by Coelho et al. (2017) for mafic rocks from Pouso Alegre. In conclusion, we suggest that the clinopyroxene-garnet amphibolite represents a tholeiitic magma that intruded the Rhyacian basement during a c. 1.5 Ga extensional episode possibly correlated to Calymmian (1.6 – 1.4 Ga) rifting events known in the region (e.g., Heilbron et al., 2017).

3. *Migmatitic sillimanite-garnet gneiss MT-22A* - The presence of garnet and sillimanite indicates an aluminous protolith that could be either sedimentary or granitic. The zircon population is homogeneous, with euhedral elongated crystals and presents narrow range with main distribution around 790 Ma. These features are in line with a magmatic protolith, but could also be compatible with a sediment. Ages around 800 Ma have been reported as detrital zircon grains from metasedimentary rocks of the Andrelândia nappe system and nearby units (Belém et al., 2011; Trouw, 2008; Westin et al., 2016). However, contrasting to the narrow zircon age distribution shown by the migmatitic sillimanite-garnet gneiss MT-22A, those samples show large age spectra, spreading from the Cambrian to the Paleoproterozoic with relatively few grains around 800 Ma, like the Santo Antônio schist (Belém et al., 2011) and the Arantina unit (Coelho et al., 2017). Those units have been interpreted as sedimentary deposits related to passive or active margins (e.g., Belém et al., 2011; Coelho et al., 2017). The period of c. 900 – 700 Ma has been associated with continental rifting to ocean opening events (Heilbron et al., 2017). However, primary magmatic

sources for the c. 800 Ma zircons remain unknown in the Southern Brasília orogen. Therefore, a first finding of such a source could be represented by the sillimanite-garnet migmatitic gneiss MT-22A dated at  $794 \pm 4$  Ma.

#### 4.6.3 P-T-t record of a common metamorphic history

Zircon rims interpreted as metamorphic (based on both texture and Th/U composition) yield identical ages for the allanite-bearing biotite granite MT-19 ( $626 \pm 5$  Ma) and the biotite gneiss MT-20 ( $632 \pm 2$  Ma; Fig. 4.10). No appreciable metamorphic zircon was found in the migmatitic amphibole-garnet gneiss MT-17. The similar protolith age for the three samples suggests that they constituted a unique basement and thus also the migmatitic amphibole-garnet gneiss underwent metamorphism around c. 630 Ma. P-T estimates for migmatitic amphibole-garnet gneiss MT-17 are 13.5 kbar and 700 °C, in line with the conditions of the clinopyroxene-garnet amphibolite MT-13.

In the migmatitic sillimanite-garnet gneiss MT-22A, zircon rim domains with low Th/U are dated at  $672 \pm 4$  Ma, whereas monazite is  $637 \pm 7$  Ma. Monazite has a trace element composition that is relatively poor in HREE and thus is consistent with growth in an assemblage containing garnet (Rubatto et al., 2006). Monazite/garnet distribution coefficients for trace elements have been calculated using the average composition of the monazite (limited compositional variation), and garnet core ( $Yb D_{Mnz/Grt} = 2.8$ ) and rim ( $Yb D_{Mnz/Grt} = 7.3$ ) compositions. Monazite-garnet partitioning for HREE is generally reported as in favour of monazite, with monazite/garnet Yb between 3.8 and 5.3 (Hermann and Rubatto, 2003; Rubatto et al., 2006). The REE zoning in garnet shows depletion from core to rim, with only the garnet rim containing less HREE, specifically Lu, than the monazite. Therefore, the growth of monazite in this sample is correlated to the garnet rim. No P-T conditions can be constrained for this sample. However, its spatial location, as well as the same metamorphic age, point to an evolution together with the other studied rocks. The peak pressure conditions for this rock would thus be in the kyanite stability field, and sillimanite would form during decompression, as described in the literature for rocks of similar composition, the high pressure granulites from the Andrelândia nappe system (Cioffi et al., 2012).

The age of the low Th/U zircon domains is not straightforward to interpret because of the quality of the material analyzed and the difference with the monazite age. This age is defined by a number of analyses on zircons that have dark and mottled CL zoning, which is commonly attributed to alteration (Corfu et al., 2003). If these zircon domains result from partial alteration of the magmatic cores, then the constrained age is a maximal age for the alteration event. Thus, this age constrain is tentatively attributed to an earlier stage of metamorphism around  $672 \pm 4$  Ma or older, maybe related to the garnet core formation.

Similar prolonged metamorphic event, between c. 630 Ma and 600 Ma, has been identified in the Socorro-Guaxupé nappe, however for distinct P-T conditions of c. 1000 °C and 12 kbar (Rocha et al., 2016). Moreover, similar P-T path, with peak conditions around 14 kbar and 700 °C followed by nearly isothermal decompression are recorded by rocks from the Andrelândia nappe system (Coelho et al., 2017; Motta and Moares, 2017) with metamorphic ages within the 630–600 Ma interval.

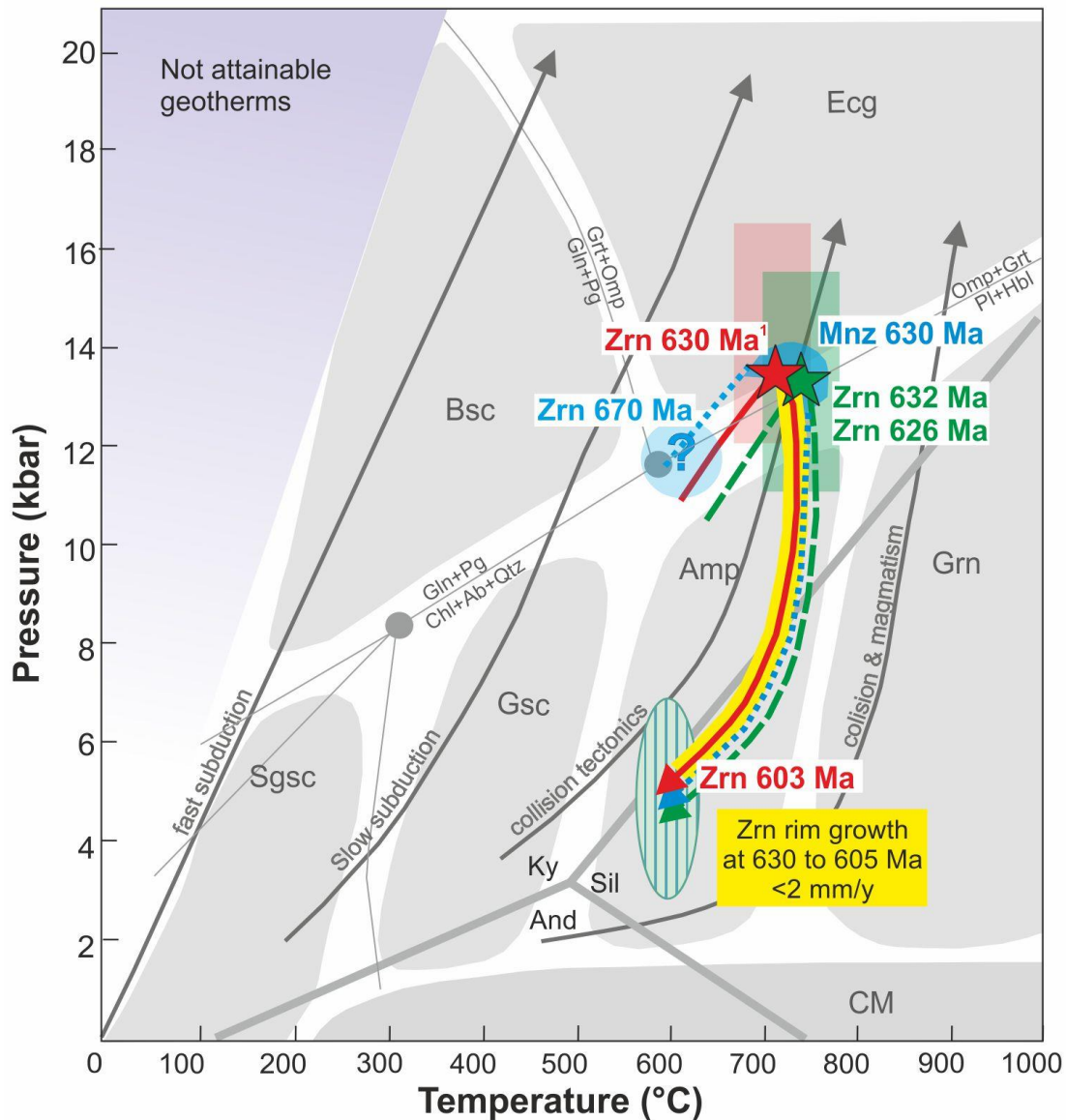


**Figure 4.12:** *P-T-t* trajectories for the clinopyroxene-garnet amphibolite MT-13 (red), migmatitic amphibole-garnet gneiss MT-17 (green) and migmatitic sillimanite-garnet gneisses MT-22A (blue); stars represent the *P-T* condition and rectangles their uncertainties. The ellipse filled with stripes represents the symplectite conditions of formation, which are the same as for corona. Zircon age of 630 Ma is from Coelho et al. (2017) which investigated a similar sample. The 670 Ma from zircon grains of the migmatitic sillimanite-garnet gneiss MT-22A cannot be strictly correlated to a *P-T* condition (thus indicated by “?”). See text for discussion of the ages. Metamorphic facies grid for metabasaltic rocks and geothermal gradients from Bucher and Frey (2002); CM – Contact metamorphism, Grn – Granulite, Amp – Amphibolite, Gsc – Greenschist, Sgsc – Subgreenschist, Bsc - Blueschist.

#### 4.6.4 Collision versus subduction setting

The reconstructed P-T-time path for the Pouso Alegre mafic rock and country gneisses (Fig. 4.12) indicate maximal pressure and temperature conditions at the amphibolite-eclogite boundary followed by near-isothermal decompression. This cooling/exhumation path provides important constraints on geothermal gradients, and metamorphic rates for the Southern Brasília orogen.

The maximal P-T correspond to a geothermal gradient of  $\sim 50$  °C/kbar and a crustal thickness of  $\sim 40$  km, using an average crustal density of  $2700 \text{ kg/m}^3$ . While this is a relatively low geotherm compared to stable cratons, this geotherm is comparable to what is observed in collisional belts (Brown, 2007; Sizova et al., 2014). HP and UHP rocks related to subduction evolve along cooler geotherms of  $< 35$  °C/kbar (Brown, 2007; Brown, 2009; Weller and St-Onge, 2017).

Decompression from  $\sim 14$  to 5 kbar over c. 30 My results in an average exhumation rate of  $1 \text{ mm.y}^{-1}$ . Such rates would be compatible with erosion-driven exhumation (Burbank, 2002; Schlunegger and Willett, 1999). However, the limited cooling during exhumation suggests a tectonic process, whereby rock units move upwards crossing different geothermal gradients. This is commonly observed in the dynamic exhumation of collisional belts, e.g., in the Himalaya (Chakraborty et al., 2017; McClelland and Lapen, 2013). The second stage ( $\sim 600$  °C and  $4.5 \pm 1.5$  kbar) is close to a typical post-collisional geotherm of  $\sim 90$ – $130$  °C/kbar (or  $\sim 25$ – $35$  °C/km; Schlunegger and Willett, 1999) and may represent the onset of a post-orogenic stabilization.

Based on these results, we conclude that the Pouso Alegre HP mafic rocks, previously called “retro-eclogites” can not be considered as evidence for the southern extension of the West Gondwana UHP belt proposed by Ganade de Araujo et al. (2014). Furthermore, the collisional event recorded by the Pouso Alegre HP of c. 630 Ma, before the one recorded by the other rocks from the West Gondwana in the northeast Brazil and in Africa of c. 610–615 Ma (Ganade de Araujo et al., 2014). However, the Pouso Alegre HP mafic rocks can represent relatively HP metamorphic products from mafic intrusions in a continental setting, metamorphosed in the deep root of the Ediacaran continent-continent collisional zone.

**Table 4.2** Correlations between the main occurrences of retro-eclogites from the Southern Brasília orogen. Data from: 1) This study; 2) Coelho et al. (2017); 3) Campos Neto et al. (2011); 4) Reno et al. (2009); 5) Campos Neto and Caby (1999); 6) Trouw (2008); 7) Hoppe (1985); 8) Luvizotto (2003); 9) Hoppe (1989); 10) Garcia and Campos Neto (2003); 11) Campos Neto and Caby (2000).

	Pouso Alegre	Liberdade nappe	Varginha nappe	São Sebastião do Paraíso	Carmo da Cachoeira
<b>Protolith Age (Ma)</b>	1520 <sup>1</sup> ; 1504 ± 29 <sup>2</sup>	-	1400 <sup>6</sup>	-	-
<b>Method</b>	SIMS and LA-ICP-MS <sup>1</sup> ; SHRIMP <sup>2</sup>	-	SHRIMP <sup>6</sup>	-	-
<b>Lithochemical signature</b>	N-MORB to T-MORB <sup>1</sup>	N-MORB <sup>3</sup>	-	Tholeiite signature <sup>7</sup>	-
<b>Isotopic signature</b>	-	Sm-Nd t <sub>DM</sub> ages 1.15-1.48 Ga epsilon Nd <sub>(610)</sub> : (-3 to +0.2) <sup>3</sup>	-	-	-
<b>Interpretation</b>	intrusion (dyke) <sup>1</sup> ; paleodykes <sup>2</sup>	oceanic crust <sup>3</sup>	-	-	-
<b>Metamorphism Age</b>	600–630 <sup>1</sup> ; 623 ± 16 (n=9) <sup>2</sup>	699 ± 25 (n=5) <sup>3</sup> ; 678 ± 29 (n=4) <sup>4</sup> ; 600–630 <sup>2</sup>	670; 620 <sup>6</sup>	-	-
<b>Method</b>	SIMS and LA-ICP-MS <sup>1</sup> ; SHRIMP <sup>2</sup>	SHRIMP <sup>3</sup> ; HR-SIMS <sup>4</sup> ; SHRIMP <sup>2</sup>	SHRIMP <sup>6</sup>	-	-
<b>Interpretation</b>	decompression <sup>1</sup> ; eclogitization at minimum pressure <sup>2</sup>	HP metamorphism <sup>3</sup> ; eclogitization at minimum pressures of 17 kbar <sup>2</sup> ; eclogitization <sup>4</sup>	pre-collisional metamorphism; collisional metamorphism <sup>6</sup>	-	-
<b>Evidence for interpretation</b>	Cpx and Cam inclusion in Zrn rim and 2 patterns for REE <sup>1</sup> ; absence of Eu anomaly in REE in the rims <sup>2</sup>	-	-	-	-
<b>Peak P-T constraints</b>	701 ± 16 °C at 14 ± 2 kbar <sup>1</sup> ; 692 ± 60 °C at 12.7 ± 2.7 kbar <sup>2</sup>	660 °C at 17.5 kbar <sup>5</sup>	eclogite facies <sup>6</sup>	711–799 °C at 12.5–13.5 kbar <sup>8</sup> ; 650–700 °C at 12–14 kbar <sup>9</sup>	Cpx(Jd <sub>20</sub> )–Grt–Pl 818°C at 18.5 kbar <sup>10</sup>
<b>Evidence</b>	P-T modelling (mineral integration, mineral inclusions in Rt and Zrn and Zr-in-rutile thermometry) <sup>1</sup> ; avPT with THERMOCALC <sup>2</sup>	lamella in Cpx with X <sub>Jd</sub> up to 0.76 included in Grt <sup>5</sup>	assemblage Cpx+Grt, with Pl overgrowth around garnet indicating decompression <sup>6</sup>	Grt-Cpx thermometer <sup>8</sup> ; X <sub>Jd</sub> in Cpx barometer <sup>9</sup>	Cpx bearing assemblage. TWEEQU equilibria and Jd content 0.20 <sup>10</sup>
<b>Retrogression P-T constraints</b>	550–700°C at <7kbar <sup>1</sup> ; 598 ± 58 °C at 5.5 ± 1.1 kbar <sup>2</sup>	650 ± 75°C at 11.6 kbar <sup>5</sup>	granulite facies <sup>6</sup>	490 ± 50°C <sup>8</sup>	Amp–Grt–Pl 665°C at 10.8 Kbar <sup>10</sup>
<b>Evidence</b>	trace elements in Zrn and inclusions in Zrn rim <sup>1</sup> ; considering garnet rim composition <sup>2</sup>	garnet-amphibole thermometry in the corona <sup>5</sup>	Opx indicator <sup>6</sup>	Hbl+Pl in symplectites around Grt <sup>8</sup>	amphibole bearing assemblage <sup>10</sup>
<b>Host rocks</b>	Paleoproterozoic basement and migmatitic Sil-Grt gneiss <sup>1</sup> ; Bt gneiss from the basement <sup>2</sup>	biotite gneisses and feldspathic schists with intercalations of muscovite schist and quartzite. (Liberdade Nappe units)	Ky-Kfs gneiss <sup>6</sup>	garnet-bearing biotite gneiss (upper Araxá Group) <sup>9</sup>	Ky- and Grt-bearing schists, gneisses and quartzites <sup>10</sup> ; active margin metasediments <sup>11</sup>
<b>Host rock age protolith</b>	2100 <sup>1</sup> , 800 <sup>2</sup> Ma	-	-	-	-
<b>Age Method</b>	LA-ICPC-MS <sup>1</sup>	-	-	-	-
<b>Host rock age metamorphism</b>	626 ± 5 Ma and 632 ± 2 Ma, 672 ± 4 (Zrn) Ma and 634 ± 3 Ma (Mnz) <sup>1</sup>	-	-	-	-
<b>Age Method</b>	LA-ICPC-MS and SIMS for Mnz <sup>1</sup>	-	-	-	-
<b>P-T constraints</b>	750 °C at 13 kbar <sup>1</sup>	-	-	-	Metapelite: muscovite- (473°C at 5.3 Kbar) and biotite- (521°C at 5.5 Kbar) bearing mineral associations <sup>10</sup>
<b>P-T method</b>	avPT THERIAK-DOMINO <sup>1</sup>	-	-	-	TWEEQU equilibria <sup>10</sup>

## 4.7 Conclusions

The Pouso Alegre rock assemblage is composed of intermediate to felsic rocks that formed at c. 2.07 Ga and were intruded by gabbros at c 1.5 Ga. This igneous complex was overlain by an aluminous volcanoclastic or igneous body at around 800 Ma. Together, those rocks experienced a roughly synchronous metamorphic event in the Brasiliano orogeny, attaining a collisional metamorphic peak around 630 Ma and retrogression conditions around 600 Ma.

The metamorphic evolution of the clinopyroxene-garnet amphibolite was reconstructed using an approach that combines compositional mapping and thermobarometry of targeted textural domains. The methodology employed for the clinopyroxene-garnet amphibolite, which displays typical textures found in decompressed eclogite, allowed reconstructing peak metamorphic conditions, of  $13.5 \pm 3.0$  kbar and  $700$  °C. The surrounding migmatitic garnet-amphibole gneiss record similar P-T conditions. This metamorphic stage was dated at c. 630 Ma by zircon rims in the country rock gneisses MT-19 and MT-20, monazite from the aluminous gneiss MT-22A, and some zircon rims in the clinopyroxene-garnet amphibolite MT-13. Reconstructions of local domain compositions were used to determine P-T conditions of formation of late stage symplectite and corona at  $4.8 \pm 1.5$  kbar and temperatures between  $595 - 600 \pm 26$  °C. The symplectite of  $\text{Cpx}_2 + \text{Amp}_2 + \text{Pl} \pm \text{Qz}$  and coronas of plagioclase and amphibole around garnet formed in coupled reactions involving Na exchange. Metamorphic zircon rims from the clinopyroxene-garnet amphibolite constrain decompression at these conditions around  $603 \pm 7$  Ma.

The high geothermal gradient from the clinopyroxene-garnet amphibolite is not compatible with a subduction gradient, but rather indicates metamorphism related to continent-continent collision tectonics. Hence, the Pouso Alegre mafic rocks cannot be used to extend the UHP belt of the West Gondwana orogen to the Southern Brasília orogen. Nevertheless, the clinopyroxene-garnet amphibolite could be related to a relatively high P metamorphism in the root of the Ediacaran continent-continent collisional zone that may link those orogens.

The calculated low maximal exhumation rate of  $1 \text{ mm.y}^{-1}$  for the clinopyroxene-garnet amphibolite, and high geothermal gradient for the symplectite and corona formation stage would indicate that exhumation was tectonic-driven.

The present study highlights the need for detailed investigations on other rocks with similar compositions and textures that have been called “retro-eclogites” in the Southern Brasília orogen (Table 2), as they possibly do not record the required PT conditions to be formed during an ocean subduction process.

## **4.8 Acknowledgments**

This research was supported by the Brazilian “Science Without Borders Program” with a scholarship and grant to M. Tedeschi (CNPq 202054/2015-2), and CODEMIG and CNPq projects coordinated by A. Pedrosa Soares. We are grateful to all those institutions. We also thank T. Pettke and A. Berger, University of Bern, for analytical assistance with the LA-ICP-MS and SEM, and L. Garcia and M. Flores for assistance with EPMA analysis in Federal University of Minas Gerais (LMA-UFMG). A. Pedrosa Soares and I. Dussin are grateful to the CNPq for their productivity grants. We thank R. Moares and an anonymous reviewer for their fruitful comments and suggestions and M. Scambelluri for his efficient editorial handling.

## **4.9 Appendix 4.A – Analytical methods**

### **4.9.1 Sample preparation, imaging and qualitative analyses**

Zircon, rutile and monazite were separated, using standard rock crushing and heavy mineral separation techniques. Grains were individually selected, picked and mounted in epoxy resin. Grain mounts were polished to expose the grain centres. Backscatter electron images (BSE) for monazite and rutile were performed with a ZEISS EVO50 scanning electron microscope (SEM) at the Institute of Geological Sciences (University of Bern). Zircons were imaged in cathodoluminescence (CL) to domain identification using a Quanta-250-FEI SEM fitted with a CL detector at the Multilab from Universidade do Estado do Rio de Janeiro (UERJ). Mineral abbreviations follow Whitney and Evans (2010).

### **4.9.2 Bulk rock analysis**

Major and trace elements of four samples (MT-13, MT-17, MT-19 and MT-20) were analysed at the SGS GEOSOL laboratories (Brazil). Major element oxides were determined using X-ray Fluorescence and trace elements by ICP-MS. Results are reported in Appendix I. Due to extensive weathering, sample MT-22A from the migmatitic Sil-Grt gneiss was not analysed for bulk-rock chemistry.

### **4.9.3 Electron probe micro-analysis**

The Cpx-Grt amphibolite (MT-13) was analysed by electron probe micro-analyser (EPMA) using both quantitative spot analyses and X-ray compositional mapping in wavelength-dispersive mode. EPMA analyses were carried out with a JEOL JXA-8200 superprobe at the Institute of



Geological Sciences (University of Bern). Operating conditions for spot analyses were 15 keV accelerating voltage, 10 nA beam current and 40 s dwell times (including 2×10 s of background measurement). Mineral inclusions in zircon and rutile were analysed with spots of 1 µm and 3 µm. The following standards were used: almandine (Si, Fe, Al), forsterite (Mg), orthoclase (K), anorthite (Ca), albite (Na), tephrite (Mn) and ilmenite (Ti) for garnet, and wollastonite (Si), orthoclase (K), anorthite (Al, Ca), albite (Na), forsterite (Mg), almandine (Fe), tephrite (Mn) and ilmenite (Ti) for pyroxene and amphibole. Compositional maps were acquired following the procedure described in Lanari et al. (2012; 2013) using 15 KeV accelerating voltage, 100 nA beam current and dwell times of 200 ms. A map of 655,500 pixels over an area of 950 × 690 µm<sup>2</sup> with a step size of 1µm was acquired on sample MT-13 (Fig. 4.3) and two maps of 324,000 and 422,500 pixels over areas of 600 × 540 µm<sup>2</sup> and 650 × 650 µm<sup>2</sup> with a step size of 3 µm were acquired on sample MT-22A (Supplementary Figure S.6). Point analyses were also measured on the same area to be used as internal standards (de Andrade et al., 2005).

The compositional maps were classified and converted into concentration maps of oxide weight percentage using the software XMAPTOOLS 2.3.1 (Lanari et al., 2014). Local bulk compositions were approximated from merged oxide weight percentage maps using the export built-in function of XMAPTOOLS by integrating the pixel compositions of specific domains after a density correction (Mészáros et al., 2017; Lanari and Engi, 2017). The density of each phase was estimated using THERIAK (de Capitani and Brown, 1987) at 700 °C and 12 kbar. This technique to obtain local bulk composition was applied to the different retrogressed domains such as the symplectite and corona areas (Fig. 4.3E).

The migmatitic Grt-Amp gneiss (MT-17) and the migmatitic Sil-Grt gneiss (MT-22A) single spot analyses were performed with a JEOL JXA-8900RL electron microprobe of the Microanalysis Laboratory of Federal University of Minas Gerais (Brazil). The operating conditions were: 15 keV acceleration voltages, 5 µm beam diameter and 20 nA beam current. Standards used were quartz (Si), Al<sub>2</sub>O<sub>3</sub> (Al), jadeite (Na), periclase (Mg), sanidine (K), almandine (Fe), anortite (Ca), rutile (Ti) and rodonite (Mn). Results are reported in the Appendix II.

#### **4.9.4 Trace elements LA-ICP-MS**

Trace elements compositions were obtained using a GeoLas-Pro 193 nm ArF Excimer laser ablation system (Lambda Physik, Germany) combined with an Elan DRC-e quadrupole mass spectrometer (Perkin Elmer, Canada) at the Institute of Geological Sciences (University of Bern). Conditions for laser fluency, frequency and spot size were 6 J/cm<sup>-2</sup>, 6Hz and 24 µm and 32 µm for zircon (MT-13); 6 J/cm<sup>-2</sup>, 8 Hz and 32, 44, 60 and 90µm for rutile (MT-13); 6 J/cm<sup>-2</sup>, 6 Hz and 24

$\mu\text{m}$  for monazite (MT-22A) and  $8 \text{ J/cm}^2$ , 10 Hz and  $90 \mu\text{m}$  for garnet (MT-13 and MT-22A). Both the acquisition and reduction data were performed in blocks of 1h using NIST SRM 612 as primary standard and USGS GSD-1G as secondary reference material. The measurement accuracy is generally within 0.7-3% ( $1\sigma$ ,  $N=6$ ). The software SILLS 132 (Guillong et al., 2008) was used for data reduction. The internal standard values were:  $\text{TiO}_2 = 99 \text{ wt\%}$  for rutile;  $\text{SiO}_2 = 32.45 \text{ wt\%}$  for zircon;  $\text{P}_2\text{O}_5 = 29.55 \text{ wt\%}$  for monazite and  $\text{SiO}_2 = 39 \text{ wt\%}$  (MT-13) and  $37 \text{ wt\%}$  (MT-22A) for garnet. For zircon and monazite spots were placed near or at the same position of the U-Pb dating spots and in the same CL-domains. Results are reported in the Appendix III.

#### **4.9.5 Accessory mineral thermometry**

Zr-in-rutile and Ti-in-zircon temperatures for the Cpx-Grt amphibolite (MT-13) were estimated using the calibrations of Tomkins et al. (2007) for  $\alpha$ -quartz and Watson et al. (2006). The uncertainty for the obtained temperatures in rutile was calculated following the procedure of Ewing et al. (2013), by summing in quadrature an estimate of the relative errors contributed to the calculated temperature (in Kelvin) by the pressure estimate ( $\pm 2 \text{ kbar}$ ), the analytical uncertainty on the measurement of Zr (2.2 % based on secondary standard GSD-1G), and the uncertainty inherent in the calibration. An uncertainty of  $\pm 3 \%$  on the calibration of Watson et al. (2006) is assumed, since Tomkins et al. (2007) do not detail the uncertainty from the calibration and the results from both calibrations are inside the uncertainty above. The propagated overall uncertainty is  $\pm 4 \%$ . For Ti-thermometry the uncertainty on Ti LA-ICP-MS measurement was estimated to 2.5 %, the uncertainty from the Watson et al. (2006) equation is less than 1 %, supplying a propagated uncertainty of  $\pm 2.6 \%$ .

#### **4.9.6 LA-ICP-MS U-Pb zircon dating**

U-Pb isotopic analyses were performed with several LA-ICP-MS systems: (1) for samples MT-17, MT-19 and MT-20 using a microprobe ArF Excimer Laser  $193 \mu\text{m}$  da Photon (Machines Inc. Model ATLEX SI) coupled to the high-resolution Neptune-Plus multicollector (Thermo Fisher Scientific, USA), at the MULTILAB, Universidade do Estado do Rio de Janeiro (UERJ). Instrument set up parameters were  $8\text{-}9 \text{ mJ/cm}^2$  laser fluency, 10 Hz,  $25 \mu\text{m}$  and Laser energy spot between 20 and 40 %. U-Pb data were standardized using GJ-1 zircon (reference 609 Ma, Jackson et al., 2004) as primary standard and tested using the zircon 91500 (reference 1065 Ma, Wiedenbeck et al., 1995) as secondary standard. External errors were calculated with the error propagation of individual measurements of GJ-1 and the individual measurements of each spot. Data reduction was done using an Excel program developed by Chemale et al. (2012). (2) Sample MT-13, was analysed with a Thermo-Finnigan Neptune multicollector ICP-MS (Thermo-Finnigan Neptune

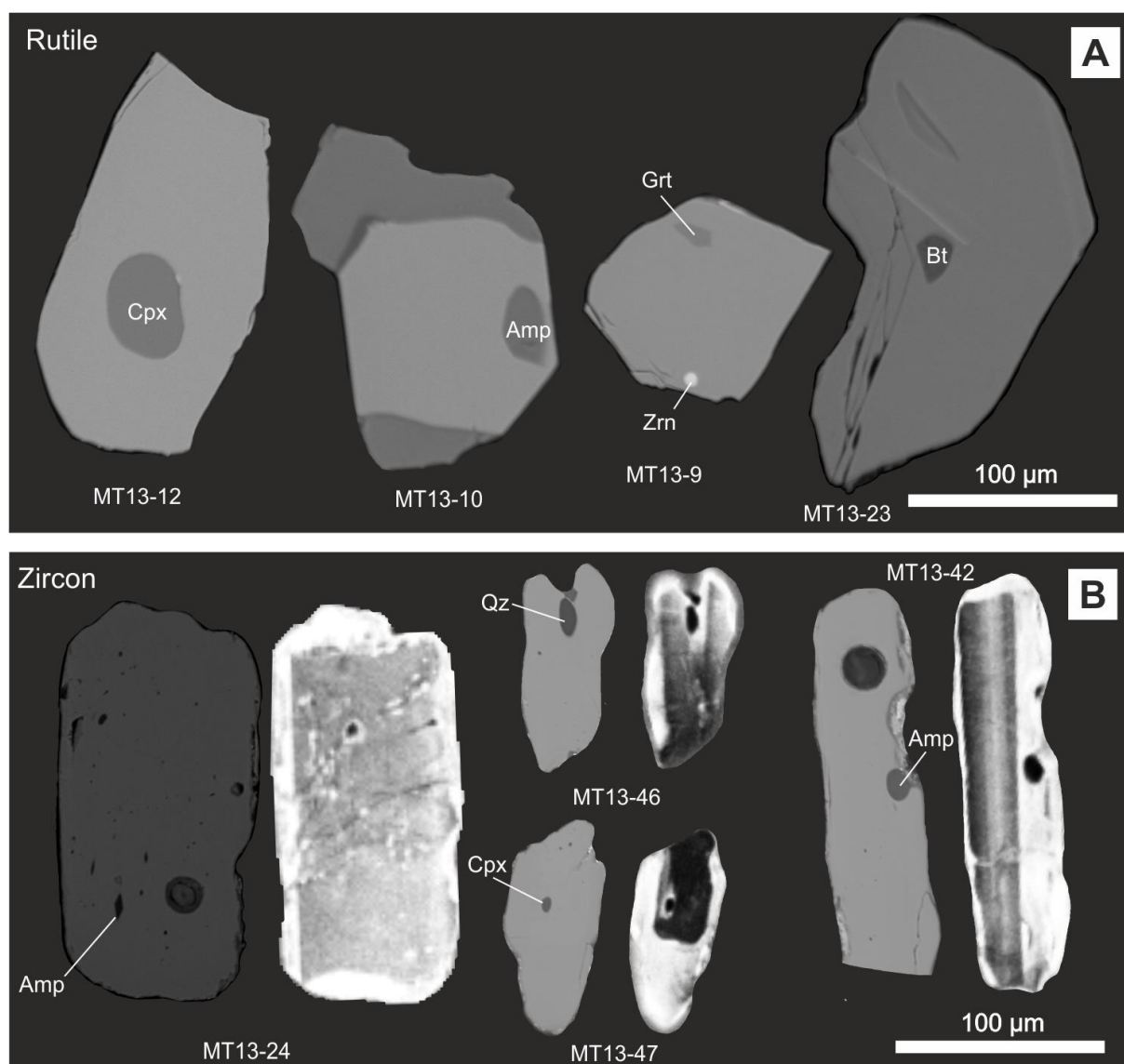
multicollector) coupled to a Photon-Machines 193 nm G2 laser system at Universidade Federal de Ouro Preto (UFOP) following the procedure described in Santos et al. (2017). Instrument set up parameters were a spot size of 20  $\mu\text{m}$ , a frequency of 6 Hz, 10 % energy, and an intensity of 0.3 mJ. U-Pb data were standardized using the zircon GJ-1 (reference 609 Ma, Jackson et al., 2004) as primary standard and tested using the zircon Pleisovice (reference 337 Ma, Slama et al., 2008) as secondary standard. External errors were propagated considering the internal reproducibility of the individual ratios, external reproducibility of GJ-1, long-term uncertainty of the validation material, the ratio uncertainties of the reference material and Pb-common ratio uncertainty (Santos et al., 2017). Data evaluation for each spot was filtered considering outliers values of common Pb contents, errors of isotopic ratios and high percentages of discordance and Th/U ratios. From the selected spots, only those with discordance lesser than 10 % were used to age calculations and plotted in Concordia diagrams. The Concordia diagram and histograms were obtained using the software Isoplot/Ex (Ludwig, 2003) and Density Plotter for sample MT-13 (Vermeesch, 2012). Individual uncertainties are quoted at  $1\sigma$  level. The confidence level for weighted average is 95 %. The results from U-Pb LA-ICP-MS analyses are available in the Appendix V for MT-13, MT-22A, MT-17, MT-19 and MT-20.

#### 4.9.7 SIMS U-Th-Pb dating

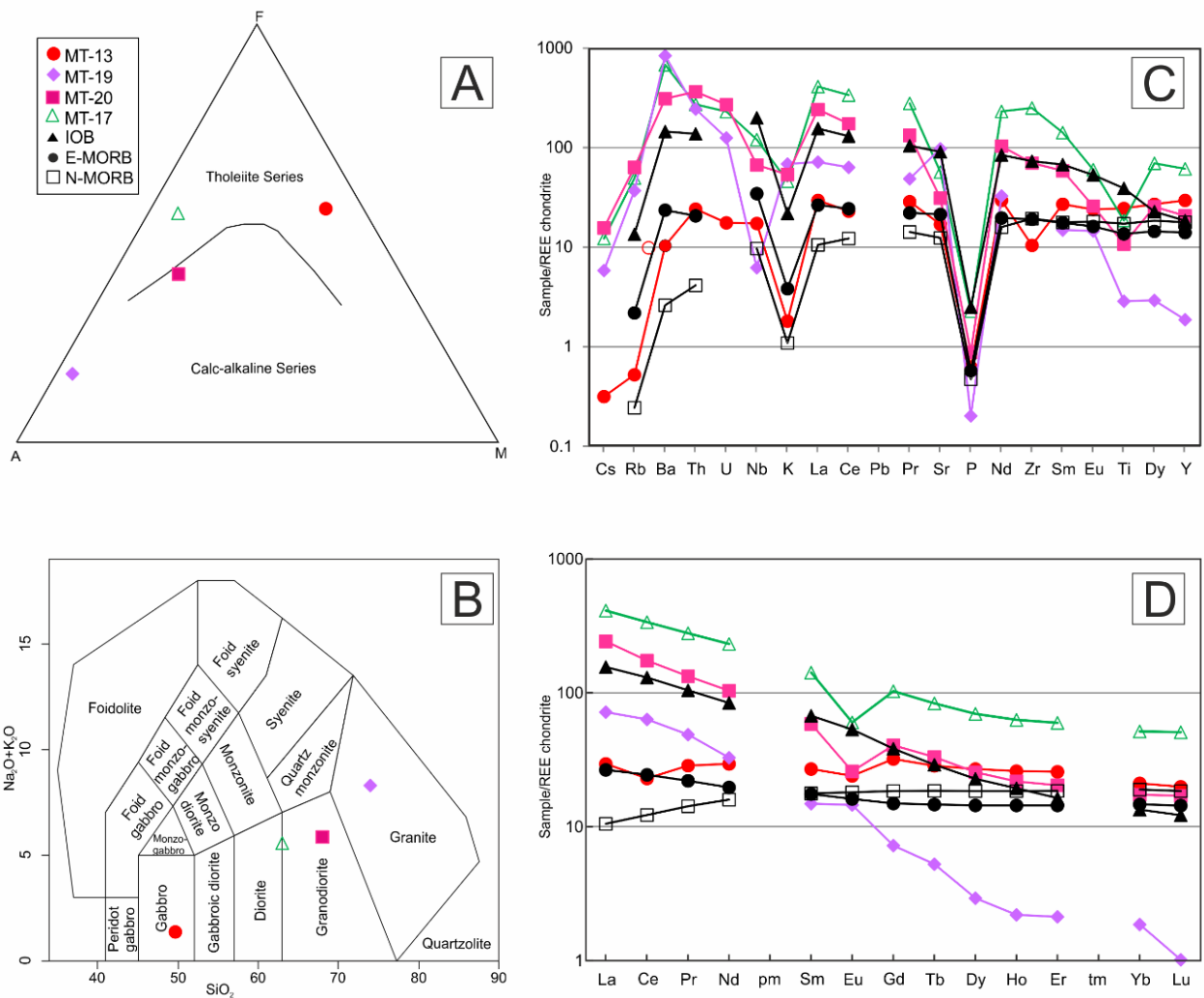
U-Th-Pb geochronology of zircon from the Cpx-Grt amphibolite MT-13 and monazite from the migmatitic Sil-Grt gneiss MT-22A were carried out using the SwissSIMS Cameca IMS 1280-HR (University of Lausanne). Basic instrument set up parameters (ca. 3-5 nA, 25  $\mu\text{m}$   $\text{O}_2^-$  primary beam, mass resolution  $M/\Delta M \sim 5000$ , energy window 40 eV) are similar to those previously described for zircon U-Th-Pb analysis by Whitehouse and Kamber (2005). The mono-collection peak-hopping routine used an automatic routine in the Cameca CIPS software to scan over the peaks and choose the peak centre for major peaks or to extrapolate the mass to B-field curve for minor peaks (e.g.  $^{204}\text{Pb}$  was calibrated by centring the  $^{94}\text{Zr}_2^{16}\text{O}$  peak,  $^{207}\text{Pb}$  and  $^{208}\text{Pb}$  by centring the  $^{206}\text{Pb}$  peak). Measured peaks include  $^{90}\text{Zr}_2^{16}\text{O}$ ,  $^{94}\text{Zr}_2^{16}\text{O}$ ,  $^{204}\text{Pb}$ ,  $^{206}\text{Pb}$ ,  $^{207}\text{Pb}$ ,  $^{208}\text{Pb}$ ,  $^{238}\text{U}$ ,  $^{232}\text{Th}^{16}\text{O}$ ,  $^{238}\text{U}^{16}\text{O}$  and  $^{238}\text{U}^{16}\text{O}_2$  for zircon and  $^{140}\text{Ce}^{31}\text{P}^{16}\text{O}_2$ ,  $^{232}\text{Th}^{143}\text{Nd}^{16}\text{O}_2$ ,  $^{141}\text{Pr}^{31}\text{P}^{16}\text{O}_2$ ,  $^{204}\text{Pb}$ ,  $^{206}\text{Pb}$ ,  $^{207}\text{Pb}$ ,  $^{208}\text{Pb}$ ,  $^{238}\text{U}$ ,  $^{232}\text{Th}$ ,  $^{232}\text{Th}^{16}\text{O}$ ,  $^{238}\text{U}^{16}\text{O}$  for monazite. U-Pb-Th data were standardised to 91500 zircon (1065 Ma, Wiedenbeck et al., 1995) and USGS44069 monazite (425 Ma, Aleinikoff et al., 2006). Secondary standards run in the same analytical session reproduced average  $^{206}\text{Pb}/^{238}\text{U}$  ages within reference values: TEM zircon  $418 \pm 6$  Ma (reference 417 Ma, Black et al., 2003), Pleisovice zircon  $340 \pm 4$  Ma (reference 337 Ma, Slama et al., 2008), Itambé monazite  $507 \pm 6$  Ma (reference 513 Ma, Gonçalves et al., 2016). Uncertainty on standard  $^{206}\text{Pb}/^{238}\text{U} - \text{UO}_2/\text{U}$  calibration were 1.4 % for zircon and 1.13 % for monazite, which were propagated to the data as external error. Common Pb correction was based on the measured  $^{204}\text{Pb}$  signal (when significant relative to

background) assuming the present day model terrestrial Pb composition of Stacey and Kramers (1975). Radiogenic ratios and single ages were calculated using the CIPS program compiled by Martin Whitehouse. Age calculations use the decay constant recommendations of Steiger and Jäger (1977). The program IsoPlot Ex 4.15 (Ludwig, 2003) was employed to plot the diagrams and calculate concordia and weighted average ages. Individual uncertainties are quoted at  $1\sigma$  level and the confidence level for weighted average is 95 %. Uncertainty on average  $^{206}\text{Pb}/^{238}\text{U}$  ages is forced to be no less than the reproducibility of the standard on the same analytical session. The results from U-Pb SIMS analyses are available in the Appendix IV for samples MT-13 and MT-22A.

#### 4.10 Supplementary Figures



**Supplementary Figure S.1:** Backscattered electron and cathodoluminescence images of inclusions in rutile and zircon from the clinopyroxene-garnet amphibolite MT-13. (A) Backscattered electron images of rutile with inclusions of clinopyroxene, amphibole, garnet, zircon and biotite (cracked grain) and (B) Backscattered electron (left) and correspondent cathodoluminescence (right) images of zircon with inclusions of amphibole, clinopyroxene and quartz.



**Supplementary Figure S.2:** Bulk rock chemistry for the clinopyroxene-garnet amphibolite MT-13 and its country rocks, amphibole-garnet migmatitic gneiss MT-17, allanite-bearing biotite granite MT-19 and biotite gneiss MT-20. (A) AFM diagram (Irvine and Baragar, 1971); (B)  $\text{Na}_2\text{O}+\text{K}_2\text{O}$  (wt%) versus  $\text{SiO}_2$  (wt%) classification plot (Middlemost, 1989); (C) spider diagram normalized to chondrite (McDonough and Sun, 1995) and (D) chondrite-normalized (McDonough and Sun, 1995). Reference values for IOB, N-MORB and E-MORB by Sun and McDonough (1989).

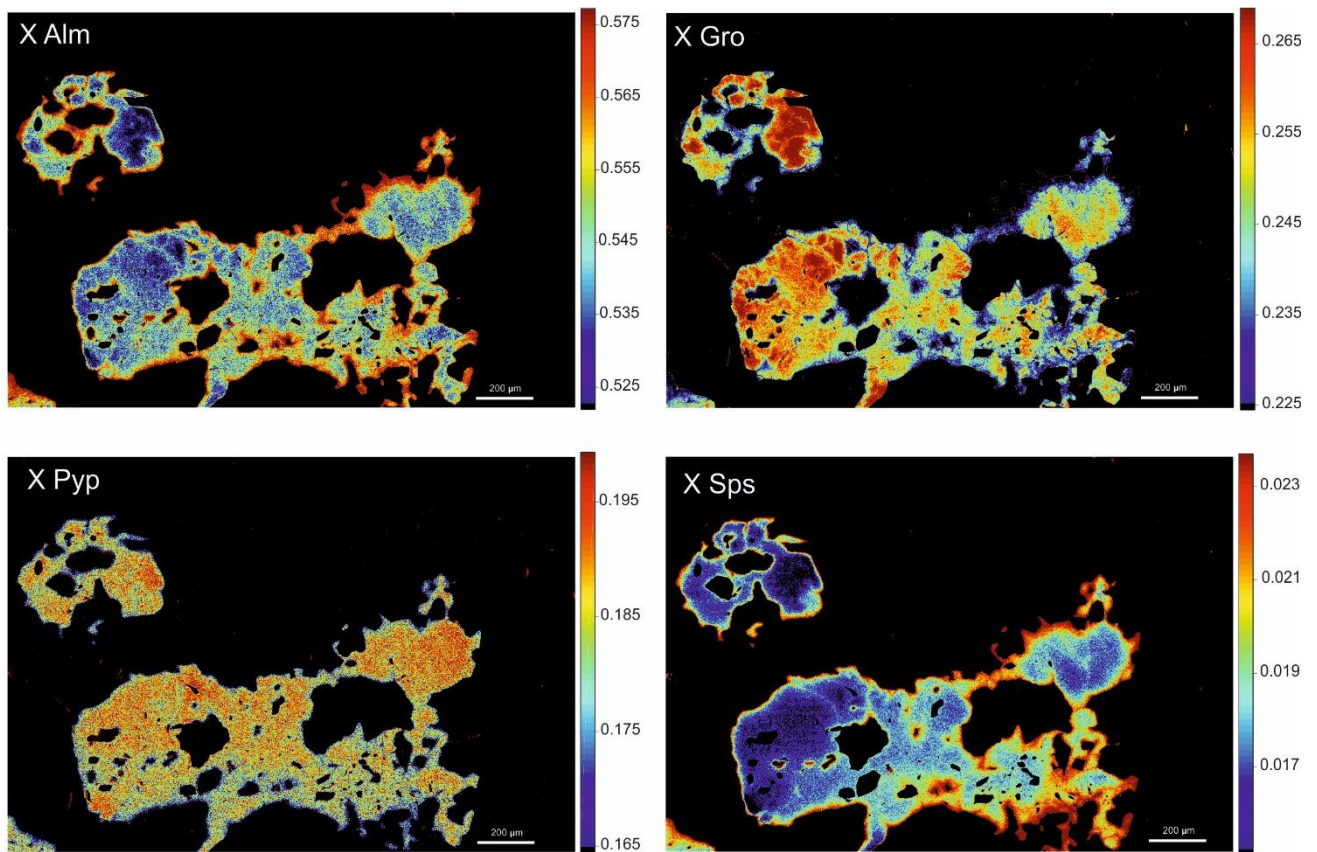
## References

Irvine, T.N., Baragar, W.R.A., 1971. A guide to the chemical classification of the common volcanic rocks. *Canadian Journal of Earth Sciences* 8, 523-548.

Middlemost, E.A.K., 1989. Iron Oxidation Ratios, Norms and the Classification of Volcanic Rocks. *Chemical Geology* 77, 19-26.

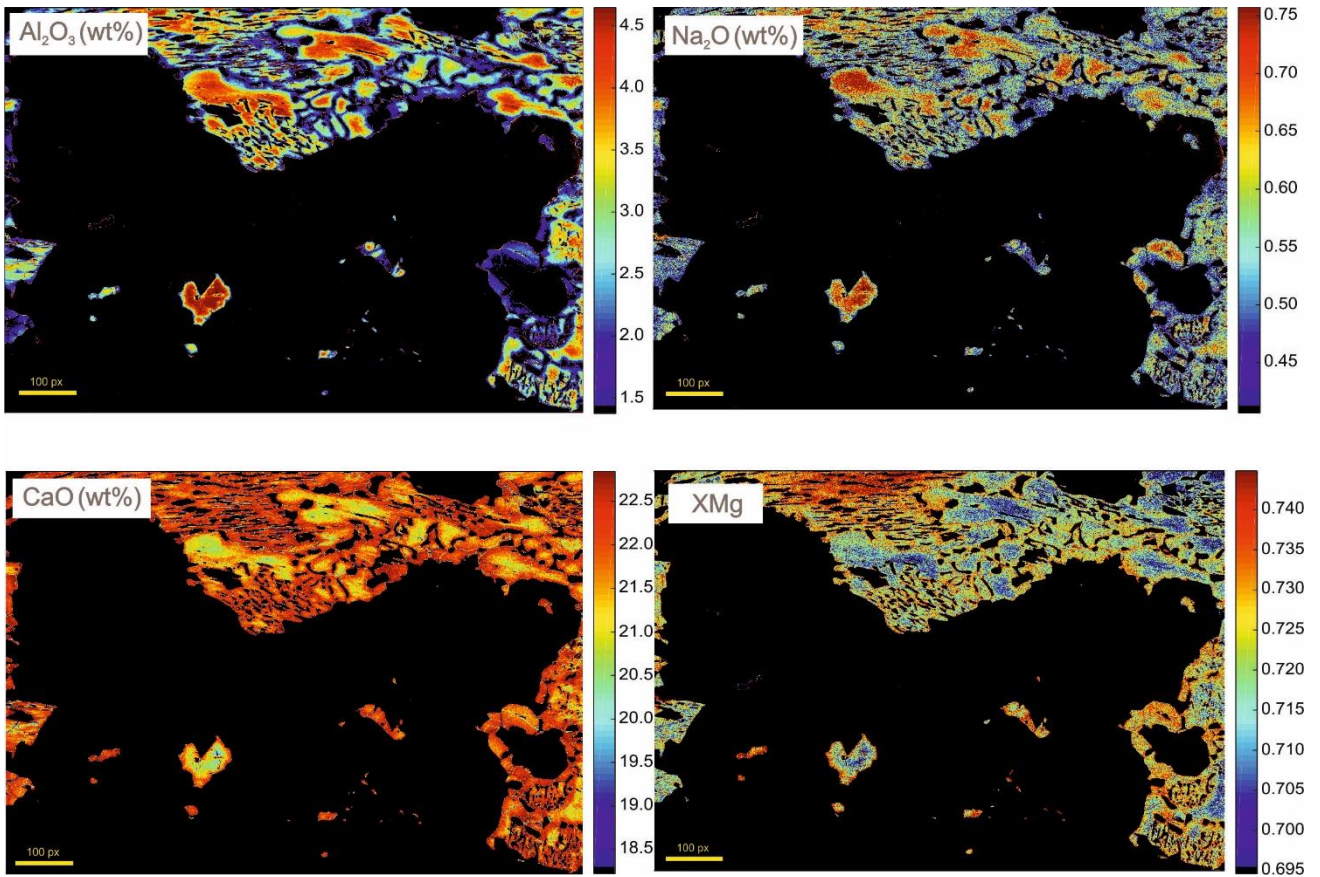
McDonough, W.F., Sun, S.S., 1995. The composition of the earth. *Chemical Geology* 120, 223-254.

Sun, S.S., McDonough, W.F., 1989. Chemical and isotopic systematics of oceanic basalts: implication for mantle composition and processes, in: Saunders, A.D., Norry, M.J. (Eds.), *Magmatism in Ocean Basins*. Geological Society, London, Special Publications 42, 313-345.

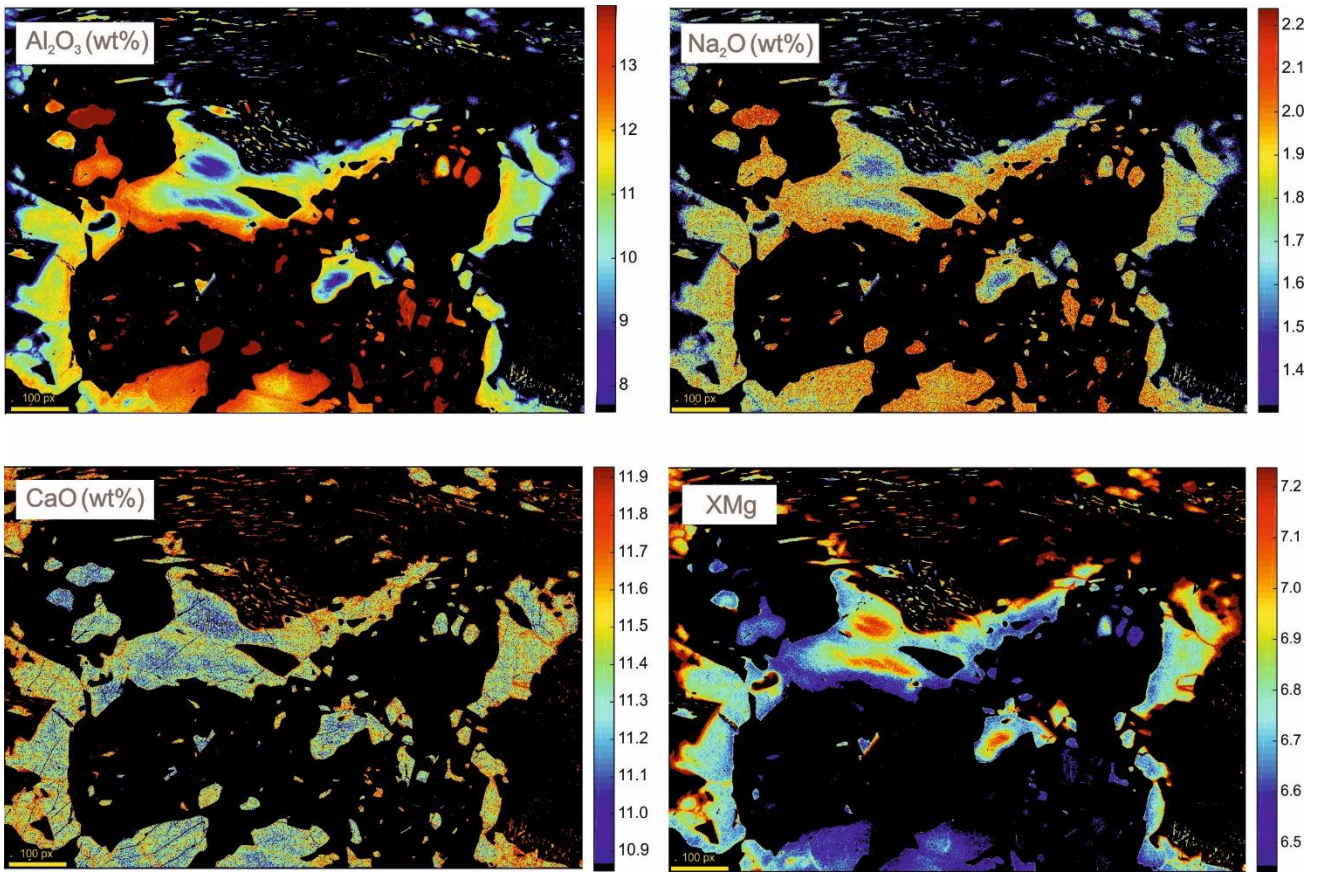


**Supplementary Figure S.3:** Garnet compositional maps for the clinopyroxene-garnet amphibolite (sample MT-13). Maps of almandine, grossular, pyrope and spessartine. The composition is mainly homogeneous with a slightly different rim, probably due to diffusion.



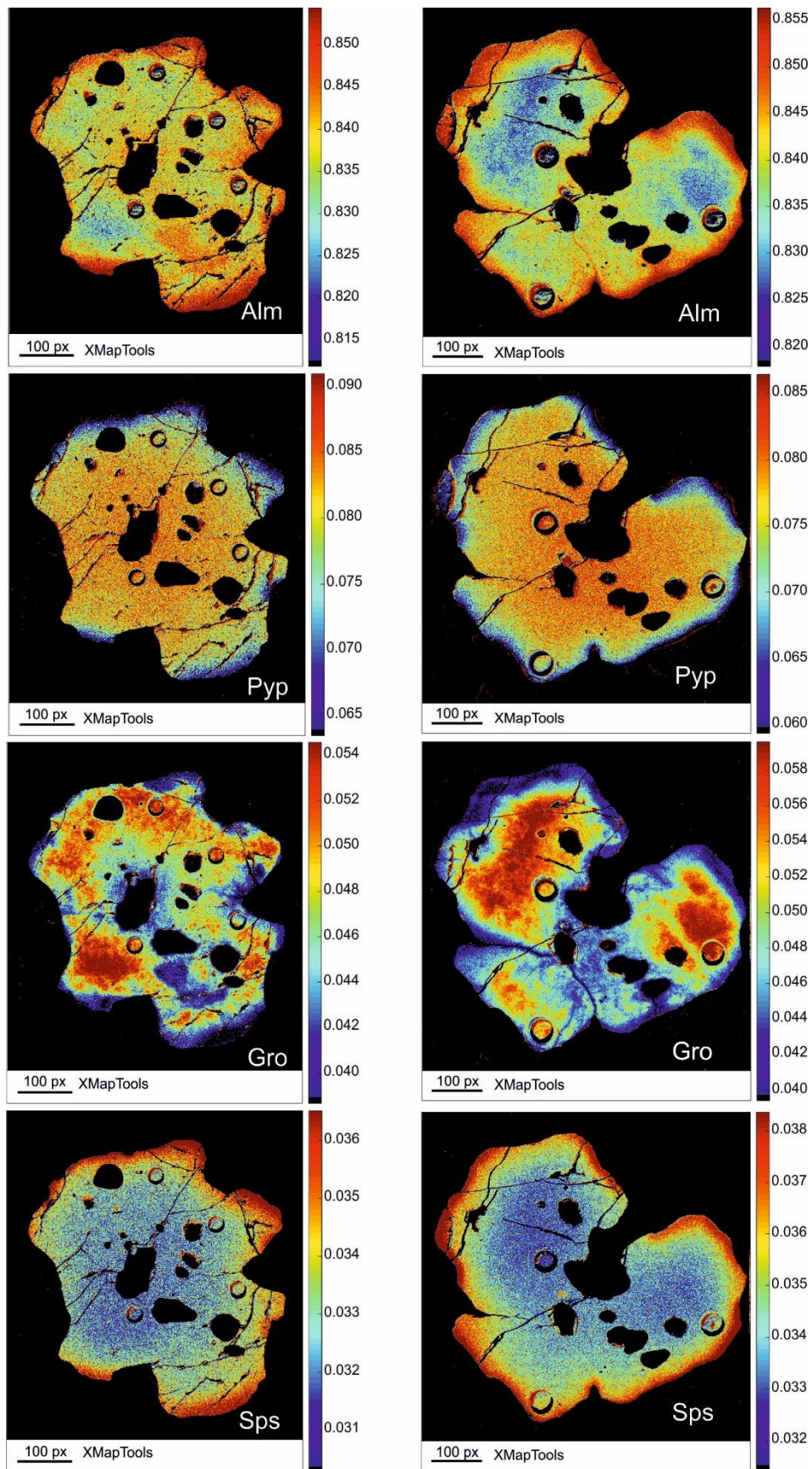


**Supplementary Figure S.4:** Clinopyroxene compositional maps for the clinopyroxene-garnet amphibolite (sample MT-13).

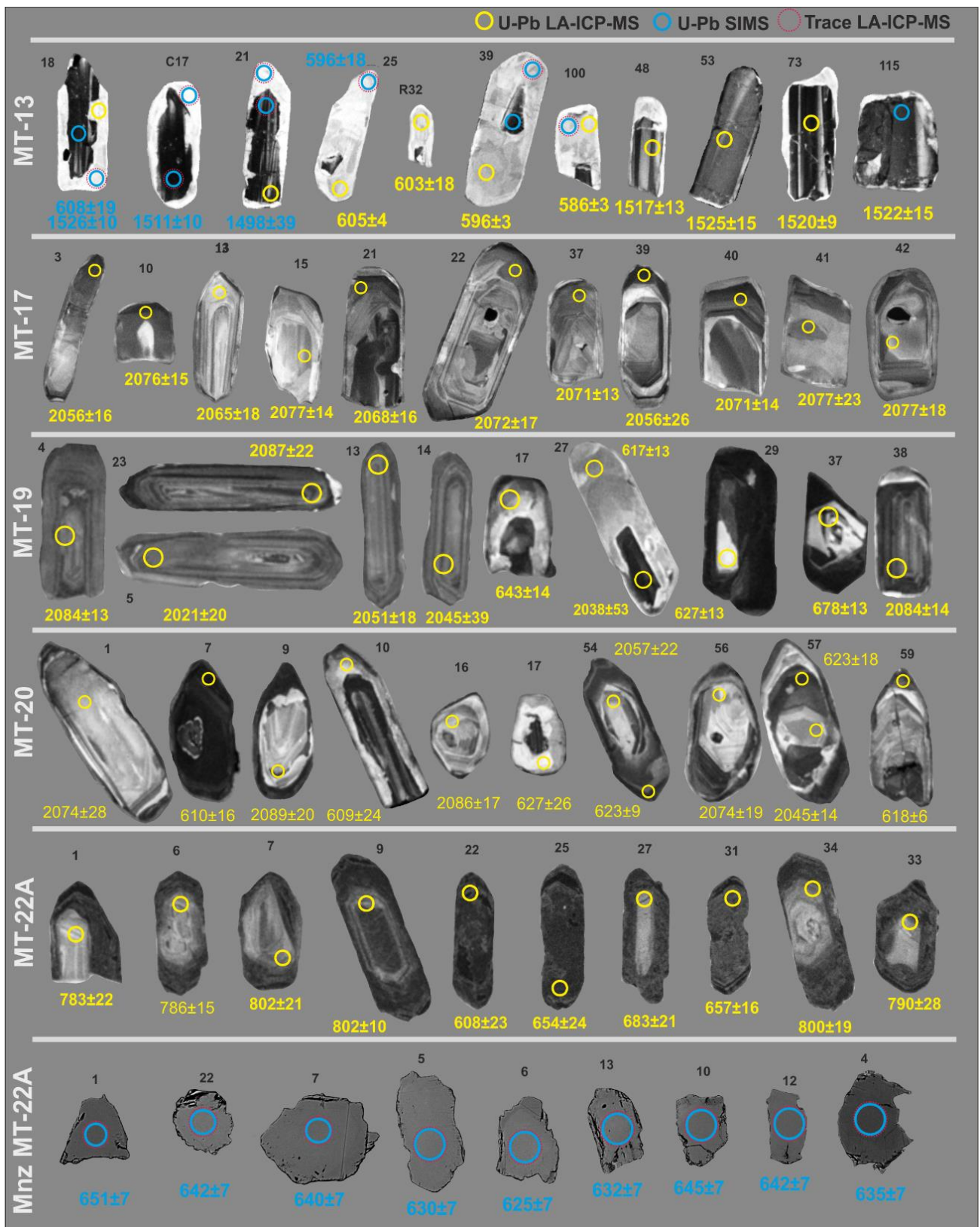


**Supplementary Figure S.5:** Amphibole compositional maps for the clinopyroxene-garnet amphibolite (sample MT-13).





**Supplementary Figure S.6:** Garnet compositional maps for the migmatitic sillimanite-garnet gneiss (sample MT-22A). Maps of almandine, grossular, pyrope and spessartine.



**Supplementary Figure S.7:** Cathodoluminescence (CL) and backscattered (BSE) images of representative zircon and monazite grains, respectively. Location of spot analyses and corresponding  $^{206}\text{Pb}/^{238}\text{U}$  or  $^{207}\text{Pb}/^{206}\text{Pb}$  ages in Ma are marked with: yellow circle for LA-ICP-MS, blue circles for SIMS analyses and dashed red circles for trace elements (spot size ~25 microns).

## 4.11 References

- Aleinikoff, J.N., Schenck, W.S., Plank, M.O., Srogi L., Fanning, C.M., Kamo, S.L., Bosbyshell, H., 2006. Deciphering igneous and metamorphic events in high-grade rocks of the Wilmington Complex, Delaware: morphology, cathodoluminescence and backscattered electron zoning and SHRIMP U–Pb geochronology of zircon and monazite. *Geological Society of America Bulletin* 118, 39-64.
- Baldwin, J. A., Powell, R., Brown, M., Moraes, R., Fuck, R. A., 2005. Modeling of mineral equilibria in ultrahigh-temperature metamorphic rocks from the Anápolis-Itaúçu Complex, central Brazil. *Journal of Metamorphic Geology* 23, 511-531.
- Belém, J., Pedrosa-Soares, A.C., Noce, C.M., da Silva, L.C., Armstrong, R., Fleck, A., Gradim, C.T., Queiroga, G.N., 2011. Precursor basin versus orogenic basins: examples from the Andrelândia Group basend on zircon U-Pb (LA-ICP-MS) and lithochemical analysis. *Geonomos* 19, 224-243.
- Black, L.P., Kamo, S.L., Allen, C.M., Aleinikoff, J.N., Davis, D.W., Korsch, R.J., Foudoulis, C., 2003. TEMORA 1: a new zircon standard for Phanerozoic U-Pb geochronology. *Chemical Geology* 200, 155-170.
- Brouwer, F.M., Engi, M., 2005. Staurolite and other high-alumina phases in Alpine eclogite: Analysis of domain evolution. *Canadian Mineralogist* 43, 105-128.
- Brown, M., 2007. Metamorphic conditions in orogenic belts: A record of secular change. *International Geology Review* 49, 193-234.
- Brown, M., 2009. Metamorphic patterns in orogenic systems and the geological record. Geological Society, London, Special Publications 318, 37-74.
- Bucher, K., Frey, M., 2002. Petrogenesis of metamorphic rocks, seventh ed. Springer, Berlim.
- Burbank, D.W., 2002. Rates of erosion and their implications for exhumation. *Mineralogical Magazine* 66, 25-52.
- Caddick, M.J., Konopasek, J., Thompson, A.B., 2010. Preservation of garnet growth zoning and the duration of prograde metamorphism. *Journal of Petrology* 51, 2327-2347.
- Campos Neto, M. C., Caby, R., 1999. Neoproterozoic high-pressure metamorphism and tectonic constraint from the nappe system south of the Sao Francisco Craton, southeast Brazil. *Precambrian Research* 97(1-2), 3-26.

- Campos Neto, M. C., Caby, R., 2000. Lower crust extrusion and terrane accretion in the Neoproterozoic nappes of southeast Brazil: petrologic and structural constraints. *Tectonics* 19(4), 669-687.
- Campos Neto, M.d.C., Basei, M.A.S., Assis Janasi, V.d., Moraes, R., 2011. Orogen migration and tectonic setting of the Andrelândia Nappe system: An Ediacaran western Gondwana collage, south of São Francisco craton. *Journal of South American Earth Sciences* 32, 393-406.
- Carlson, W., D., Johnson, C., D., 1991. Coronal reaction textures in garnet amphibolites of the Llano Uplift. *American Mineralogist* 76, 756-772.
- Centrella, S., Austrheim, H., Putnis, A., 2015. Coupled mass transfer through a fluid phase and volume preservation during the hydration of granulite: An example from the Bergen Arcs, Norway. *Lithos* 236-237, 245-255.
- Chakraborty, S., Mukhopadhyay, D., Chowdhury, P., Rubatto, D., Anczkiewicz, R., Trepmann, C., Gaidies, F., Sorcar, N., Dasgupta, S., 2017. Channel Flow and localized fault bounded slice tectonics (LFBST): Insights from petrological, structural, geochronological and geospeedometric studies in the Sikkim Himalaya, NE India. *Lithos* in press
- Chemale, F., Kawashita, K., Dussin, I.A., Avila, J.N., Justino, D., Bertotti, A., 2012. U-Pb zircon in situ dating with LA-MC-ICP-MS using a mixed detector configuration. *Anais da Academia Brasileira de Ciências* 84, 275-295.
- Choudhuri, A., Fiori, A.P., Winters, A.A.M., Bettencourt, J.S., Rodrigues, J.E., 1978. A note on small bodies of eclogite as inclusion in high grade gneisses north of Pouso Alegre, Minas Gerais. *Revista Brasileira de Geociências* 8, 63-68.
- Cioffi, C.R., Campos Neto, M.d.C., Rocha, B.C.d., Moraes, R., Henrique-Pinto, R., 2012. Geochemical signatures of metasedimentary rocks of high-pressure granulite facies and their relation with partial melting: Carvalhos Klippe, Southern Brasília Belt, Brazil. *Journal of South American Earth Sciences* 40, 63-76.
- Cioffi, C.R., Campos Neto, M.d.C., Möller, A., Rocha, B.C., 2016. Paleoproterozoic continental crust generation events at 2.15 and 2.08 Ga in the basement of the southern Brasília Orogen, SE Brazil. *Precambrian Research* 275, 176-196.
- Coelho, M.B., Trouw, R.A.J., Ganade, C.E., Vinagre, R., Mendes, J.C., Sato, K., 2017. Constraining timing and P-T conditions of continental collision and late overprinting in the Southern Brasília Orogen (SE-Brazil): U-Pb zircon ages and geothermobarometry of the Andrelândia Nappe System. *Precambrian Research* 292, 194-215.
- Cordani, U. G., Brito-Neves, B. B., D'Agrella-Filho, M. S., 2003. From Rodinia to Gondwana: a review of the Available Evidence from South America. *Gondwana Research* 6(2), 275-283.



- Corfu, F., Hanchar, J.M., Hoskin, P.W.O, Kinny, P., 2003. Atlas of zircon textures, in: Hanchar, J.M., Hoskin, P.W.O. (Eds.), *Zircon. Reviews in Mineralogy and Geochemistry*, 53, pp. 469-500.
- Dale, J., Holland, T., Powell, R., 2000. Hornblende-garnet-plagioclase thermobarometry: A natural assemblage calibration of the thermodynamics of hornblende: *Contributions to Mineralogy and Petrology* 140, 353-362.
- De Andrade, V., Vidal, O., Lewin, E., O'Brien, P., and Agard, P., 2006. Quantification of electron microprobe compositional maps of rock thin sections: An optimized method and examples. *Journal of Metamorphic Geology* 24, 655-668.
- de Capitani, C., Petrakakis, K., 2010. The computation of equilibrium assemblage diagrams with Theriak/Domino software. *American Mineralogist* 95, 1006-1016.
- de Capitani, C., Brown, T.H., 1987. The computation of chemical equilibrium in complex systems containing non-ideal solutions. *Geochimica et Cosmochimica Acta* 51, 2639-2652.
- De Wit, M.J., Brito-Neves, B.B., Trouw, R.A.J., Pankhurst, R.J., 2008. Pre-Cenozoic correlations across the South Atlantic region: the ties that bind, in: Pankhurst, R.J., Trouw, R.A.J., Brito-Neves, B.B., De Wit, M.J. (Eds.), *West Gondwana: Pre-Cenozoic Correlations Across the Atlantic Region*. Geological Society, London, Special Publications 294, 1-8.
- Diener, J.F.A., Powell, R., White, R.W., Holland, T.J.B., 2007. A new thermodynamic model for clino- and orthoamphiboles in the system  $\text{Na}_2\text{O}-\text{CaO}-\text{FeO}-\text{MgO}-\text{Al}_2\text{O}_3-\text{SiO}_2-\text{H}_2\text{O}-\text{O}$ . *Journal of Metamorphic Geology* 25, 631-656.
- Evans, B.W., Trommsdorff, V., Richter, W., 1979. Petrology of an eclogite-metarodingite suite at Cima di Gagnone, Ticino, Switzerland, *American Mineralogist* 64, 15-31.
- Ewing, T., Hermann, J., Rubatto, D., 2013. The robustness of the Zr-in-rutile and Ti-in-zircon thermometers during high-temperature metamorphism (Ivrea-Verbano Zone, northern Italy). *Contributions to Mineralogy and Petrology* 165, 757-779.
- Fuck, R., Pimentel, M., Alvarenga, C., Dantas, E., 2017. The Northern Brasília Belt, in: Helibron, M., Cordani, U.G., Alkmim, F.F. (Eds), *São Francisco Craton, Eastern Brazil*. Springer International Publishing, Switzerland, 326 p.
- Ganade de Araujo, C.E., 2014. *Evolução Tectônica da Margem ativa Neoproterozóica do Orógeno Gondwana Oeste na Província Borborema (NE-Brasil)*. PhD Thesis, Universidade de São Paulo, p. 243.
- Ganade de Araujo, C.E., Rubatto, D., Hermann, J., Cordani, U.G., Caby, R., Basei, M.A., 2014. Ediacaran 2,500-km-long synchronous deep continental subduction in the West Gondwana Orogen. *Nature Communication* 5(5198).

- Garcia, M.G.M., Campos Neto, M.C., 2003. Contrasting metamorphic conditions in the Neoproterozoic collision-related Nappes south of Sao Francisco Craton, SE Brazil. *Journal of South America Earth Sciences*, 15 (8), 853-870.
- Gilotti, J. A., 2013. The realm of ultrahigh-pressure metamorphism. *Elements* 9(4), 255-260.
- Godard, G., 2001. Eclogites and their geodynamic interpretations: a history. *Journal of Geodynamics*. Special Issue on the history of Geodynamics 32, 165-203.
- Gonçalves, G., Lana, C., Scholz, R., Buick, I.S., Gerdes, A., Kamo, S.L., Corfu, F., Marinho, M.M., Chaves, A., Valeriano, C., Nalini, H.A.Jr, 2016. An assessment of monazite from the Itambé pegmatite district for use as U–Pb isotope reference material for microanalysis and implications for the origin of the “Moacyr” monazite. *Chemical Geology* 424, 30-50.
- Guillong, M., Meier, D.L., Allan, M.M., Heinrich, C.A., Yardley, B.W.D., 2008. SILLS: A MATLAB-based program for the reduction of laser ablation ICP-MS data of homogeneous materials and inclusions, in: Sylvester P. (Eds.), *Laser ablation ICP-MS in the Earth sciences: Current practices and outstanding issues*. Mineralogical Association of Canada Short Course Series 40, pp. 328-333.
- Guillot, S., Mahéo, G., de Sigoyer, J., Hattori, K., Pêcher, A., 2007. Tethyan and Indian subduction viewed from the Himalayan high- to ultra-high pressure metamorphic rocks. *Tectonophysics* 451, 225-241.
- Hart, E., Storey, C., Bruand, E., Schertl, H.-P., Alexander, B.D., 2016. Mineral inclusions in rutile: A novel recorder of HP-UHP metamorphism. *Earth and Planetary Science Letters* 446, 137-148.
- Heilbron, M., Cordani, U., Alkmim, F., (Eds.) 2017. *São Francisco Craton, Eastern Brazil*. Springer International Publishing, Switzerland, 326 p.
- Heinrich, C., A., 1986. Eclogite facies regional metamorphism of hydrous mafic rocks in the central Alpine Adula Nappe. *Journal of Petrology* 27(1), 123-154.
- Hermann, J., Rubatto, D., Korsakov, A., Shatsky, V.S., 2001. Multiple zircon growth during fast exhumation of diamondiferous, deeply subducted continental crust (Kokchetav massif, Kazakhstan). *Contributions to Mineralogy and Petrology* 141, 66–82.
- Hermann, J., Rubatto, D., 2003. Relating zircon and monazite domains to garnet growth zones: age and duration of granulite facies metamorphism in the Val Malenco lower crust. *Journal of Metamorphic Geology* 21, 833-852.
- Holland, T.J.B., 1990. Activities of components in omphacitic solid solutions: *Contributions to Mineralogy and Petrology* 105, 446–453.
- Holland, T., Blundy, J., 1994. Non-ideal interactions in calcic amphiboles and their bearing on amphibole-plagioclase thermometry: *Contributions to Mineralogy and Petrology* 116, 433–447.

- Holland, T.J.B., Powell, R., 1996. Thermodynamics of order-disorder in minerals: I. Symmetric formalism applied to minerals of fixed composition. *American Mineralogist* 81, 1413-1424.
- Holland, T.J.B., Powell, R., 1998. An internally-consistent thermodynamic dataset for phases of petrological interest. *Journal of Metamorphic Geology* 16, 309–344.
- Holland, T.J.B., Powell, R., 2003. Activity-composition relations for phases in petrological calculations: an asymmetric multicomponent formulation. *Contributions to Mineralogy and Petrology* 145, 492–501.
- Hoppe, A., Klein, H., Choudhuri, A., Schmidt, W., 1985. Eclogites pré-cambrianos no sudoeste de Minas Gerais, Simpósio de Geologia de Minas Gerais. SBG/Núcleo Minas Gerais, Belo Horizonte, pp. 180-192.
- Hoppe, A., Choudhuri, A., Klein, H., Schmidt, W., 1989. Precambrian eclogites from Minas Gerais, Brazil, International Geological Congress, Washington, pp. 68-69.
- Jackson, S., Pearson, N.J., Griffin W.L., Belousova E.A., 2004. The application of laser ablation-inductively coupled plasma-mass spectrometry to in situ U–Pb zircon geochronology. *Chemical Geology* 211, 47-69.
- Kaczmarek, M-A, Müntener, O., Rubatto, D., 2008. Trace element chemistry and U–Pb dating of zircons from oceanic gabbros and their relationship with whole rock composition (Lanzo, Italian Alps). *Contributions to Mineralogy and Petrology* 155, 295-312.
- Katayama, I., Maruyama, S., 2009. Inclusion study in zircon from ultrahigh-pressure metamorphic rocks in the Kokchetav massif: an excellent tracer of metamorphic history. *Journal of the Geological Society* 166(4), 783-796.
- Kelly, N., Harley, S., 2005. An integrated microtextural and chemical approach to zircon geochronology: refining the Archean history of the Napier Complex, east Antarctica. *Contributions to Mineralogy and Petrology* 149, 57-84.
- Kohn, M.J., Corrie, S.L., Markley, C., 2015. The fall and rise of metamorphic zircon. *American Mineralogist* 100, 897-908.
- Lanari, P., Guillot, S., Schwartz, S., Vidal, O., Tricart, P., Riel, N., Beyssac, O., 2012. Diachronous evolution of the alpine continental subduction wedge: evidence from P-T estimates in the Briançonnais Zone houillere (France – Western Alps). *Journal of Geodynamics* 56-57, 39-54.
- Lanari, P., Riel, N., Guillot, S., Vidal, O., Schwartz, S., Pêcher, A., Hattori, K.H., 2013. Deciphering high-pressure metamorphism in collisional context using microprobe mapping methods: Application to the Stak eclogitic massif (northwest Himalaya). *Geology* 41(2), 111–114.

- Lanari, P., Vidal, O., De Andrade, V., Dubacq, B., Lewin, E., Grosch, E. G., Schwartz, S., 2014. XMapTools: a MATLAB©-based program for electron microprobe X-ray image processing and geothermobarometry. *Computers & Geosciences* 62, 227-240.
- Lanari, P., Engi, M., 2017. Local bulk composition effects on mineral assemblages, in: Kohn, M.J., Engi, M., Lanari, P. (Eds.) *Petrochronology. Reviews in Mineralogy and Geochemistry*, 83 pp. 55-102.
- Lanari, P., Giuntoli, F., Loury, C., Burn, M., Engi, M., 2017. An inverse modeling approach to obtain P-T conditions of metamorphic stages involving garnet growth and resorption. *European Journal of Mineralogy* 29, 181-199.
- Liu, F., Zhang, L., Li, X., Slabunov, A. I., Wei, C., Bader, T., 2017. The metamorphic evolution of Paleoproterozoic eclogites in Kuru-Vaara, northern Belomorian Province, Russia: Constraints from P-T pseudosections and zircon dating. *Precambrian Research* 298, 31-47.
- Loury, C., Rolland, Y., Cenki-Tok, B., Lanari, P., Guillot, S., 2016. Late Paleozoic evolution of the South Tien Shan: Insights from P – T estimates and allanite geochronology on retrogressed eclogites (Chatkal range, Kyrgyzstan). *Journal of Geodynamics* 96, 62-80.
- Ludwig, K. R., 2003. Isoplot Excell version 3.0. A geochronological toolkit for Microsoft Excel. Berkeley Geochronological Centre Special Publication No. 4, Berkeley, California.
- Luvizotto, G. L., 2003. Caracterização metamórfica das rochas do grupo Araxá na região de São Sebastião do Paraíso, Sudoeste de Minas Gerais. Universidade Estadual Paulista "Júlio de Mesquita Filho", p.187.
- Mantovani, M. S. M., Brito-Neves, B. B., 2005. The Paranapanema lithospheric block: Its importance for Proterozoic (Rodinia, Gondwana) supercontinent theories. *Gondwana Research* 8(3), 303-315.
- McClelland, W.C., Lapen, T.J., 2013. Linking Time to the Pressure–Temperature Path for Ultrahigh-Pressure Rocks. *Elements* 9, 273-279.
- McDonough, W.F., Sun, S.S., 1995. The composition of the earth. *Chemical Geology* 120, 223-254.
- Mészáros, M., Hofmann, B.A., Lanari, P., Korotev, R.L., Gnos, E., Greber, N.D., Greenwood, R.C., Jull, A.J.T., Al-Wagdani, K., Mahjoub, A., Al-Solami, A.A., Habinullah, A.N., 2016. Petrology and geochemistry of feldspathic impact-melt breccia Abar al' Uj 012, the first lunar meteorite from Saudi Arabia. *Meteoritics & Planetary Science* 51(10), 1830-1848.
- Motta, R. G., Moraes, R., 2017. Pseudo- and real-inverted metamorphism caused by superposition and extrusion of a stack of nappes: example of the Southern Brasília Orogen, Brazil. *International Journal of Earth Sciences*. doi: 10.1007/s00531-016-1436-7



- Nasdala, L., Zhang, M., Kempe, U., Panczer, G., Gaft, M., Andrut, M., Plötze, M., 2003. Spectroscopic methods applied to zircon, in: Hanchar, J.M., Hoskin, P.W.O. (Eds.), *Zircon. Reviews in Mineralogy and Geochemistry*, Washington 53, pp. 427-467.
- Parkinson, C.D., Motoki, A., Onishi, C.T., Maruyama, S., 2001. Ultrahigh-pressure pyrope-kyanite granulites and associated eclogites in Neoproterozoic Nappes of Southeast Brazil. UHPM Workshop, Waseda University, pp. 87-90.
- Powell, R., Holland, T.J.B., 2008. On thermobarometry. *Journal of Metamorphic Geology* 26(2), 155-179.
- Reno, B.L., Brown, M., Kobayashi, K., Nakamura, E., Piccoli, P.M., Trouw, R.A.J., 2009. Eclogite-high-pressure granulite metamorphism records early collision in West Gondwana: new data from the Southern Brasilia Belt, Brazil. *Journal of the Geological Society* 166, 1013-1032.
- Ribeiro, A., Nascimento, D., Bongioiolo, E., Trouw, R., Polo, H., Tavares, F., Nepomuceno, F., 2011. *Geologia da Folha Pouso Alegre 1:100.000*. Programa Geologia do Brasil, CPRM-UFRJ, Rio de Janeiro, Brazil.
- Robyr, M., Darbellay, B., Baumgartner, L.P., 2014. Matrix-dependent garnet growth in polymetamorphic rocks of the Sesia zone, Italian Alps. *Journal of Metamorphic Geology* 32(1), 3-24.
- Rocha, B. C., Moraes, R., Möller, A., Cioffi, C. R., Jercinovic, M.J., 2016. Timing of anatexis and melt crystallization in the Socorro-Guaxupé Nappe, SE Brazil: insights from trace element composition of zircon, monazite and garnet coupled to U-Pb geochronology. *Lithos* 277, 337-355.
- Rubatto, D., 2002. Zircon trace element geochemistry: distribution coefficients and the link between U–Pb ages and metamorphism. *Chemical Geology* 184, 123-138.
- Rubatto, D., 2017. Zircon: The Metamorphic Mineral, in: Kohn, M.J., Lanari, P., Engi, M. (Eds.) *Petrochronology. Reviews in Mineralogy and Geochemistry*, 83 pp. 261-289.
- Rubatto, D., Hermann, J., 2001. Exhumation as fast as subduction? *Geology* 29(1), 3-6.
- Rubatto, D., Hermann, J., 2003. Zircon formation during fluid circulation in eclogites (Monviso, Western Alps): implications for Zr and Hf budget in subduction zones. *Geochimica et Cosmochimica Acta* 67, 2173-2187.
- Rubatto, D., Hermann, J., Buick, I.S., 2006. Temperature and bulk composition control on the growth of monazite and zircon during low-pressure anatexis (Mount Stafford, central Australia). *Journal of Petrology* 47, 1973-1996.
- Santos, M.M., Lana, C., Scholz, R., Buick, I., Schmitz, M.D., Kamo, S.L., Gerdes, A., Corfu, F., Tapster, S., Lancaster, P., Storey, C.D., Basei, M.A.S., Tohver, E., Alkmim, A., Nalini H., Krambrock, K., Fantini, C., 2017. A new appraisal of Sri Lankan zircons as reference material for in

- situ U–Pb geochronology, REE analyses and Lu–Hf isotope tracing. *Geostandards and Geoanalytical Research Journal* 41(3), 335–358.
- Sawyer, E.W., 2008. The Atlas of migmatites. The Canadian Mineralogist, Special Publication 9. NRC Research Press, Ottawa, p. 371.
- Schlunegger, F., Willett, S.D., 1999. Spatial and temporal variations in exhumation of the central Swiss Alps and implications for exhumation mechanisms, in: Ring, U., Brandon, M.T., Lister, G.S., Willett, S.D. (Eds.), *Exhumation Processes: Normal Faulting, Ductile Flow and Erosion*. Geological Society, London, Special Publications 154, pp. 157-179.
- Singh, P., Pant, N. C., Saikia, A., Kundu, A., 2013. The role of amphiboles in the metamorphic evolution of the UHP rocks: a case study from the Tso Moriri Complex, northwest Himalayas. *International Journal of Earth Sciences (Geoloische Rundsch)* 102, 2137-2152.
- Sizova, E., Gerya, T., Brown, M., 2014. Contrasting styles of Phanerozoic and Precambrian continental collision. *Gondwana Research* 25, 522-545.
- Slama, J., Kosler, J., Condon, D.J., Crowley, J.L., Gerdes, A., Hanchar, J.M., Horstwood, M.S.A., Morris, G.A., Nasdala, L., Norberg, N., Schaltegger, U., Schoene, B., Tubrett, M.N., Whitehouse, M.J., 2008. Plesovice zircon - A new natural reference material for U-Pb and Hf isotopic microanalysis. *Chemical Geology* 249, 1-35.
- Stacey, J.S., Kramers, J.D., 1975. Approximation of Terrestrial Lead Isotope Evolution by a 2 Stage Model. *Earth and Planetary Science Letters* 26(2), 207-221.
- Steiger, R.H., Jäger, E., 1977. Subcommittee on geochronology - Convention on use of decay constants in geochronology and cosmochronology. *Earth and Planetary Science Letters* 36, 359-362.
- Tindle, A.G., Webb, P.C., 1994. PROBE-AMPH a spreadsheet program to classify microprobe-derived amphibole analyses. *Computers and Geosciences*, 20, 1201-1228.
- Tinkham, D.K., Zuluaga, C.A., Stowell, H.H., 2001. Metapelite phase equilibria modeling in MnNCKFMASH: The effect of variable Al<sub>2</sub>O<sub>3</sub> and MgO/(MgO+FeO) on mineral stability. *Geological Materials Research* 3(1), 1-42.
- Tomkins, H.S., Powell, R., Ellis, D.J., 2007. The pressure dependence of the zirconium-in-rutile thermometer. *Journal of Metamorphic Geology* 25, 703-713.
- Trouw, C. C., 2008, Mapeamento da Folha Virgínia –MG, Geocronologia U-Pb (SHRIMP) em zircões e interpretação geotectônica. PhD Thesis, Universidade do Rio de Janeiro, p.127.
- Trouw, R. A. J., Heilbron, M., Ribeiro, A., Paciullo, F. V. P., Valeriano, C. M., Almeida, J. C. H., Tupinambá, M., Andreis, R. R., 2000. The central segmento of the Ribeira Belt, in: Cordani, U. G.;

- Milani, E. J.; Thomaz Filho, A.; Campos, D. A. (Eds.), Tectonic Evolution of South America. 31 International Geological Congress, Rio de Janeiro, pp. 335-365.
- Trouw, R.A.J., Peternel, R., Ribeiro, A., Heilbron, M., Vinagre, R., Duffles, P., Trouw, C.C., Fontainha, M., Kussama, H.H., 2013. A new interpretation for the interference zone between the southern Brasília belt and the central Ribeira belt, SE Brazil. *Journal of South American Earth Sciences* 48, 43-57.
- Valeriano, C., 2017. The Southern Brasília Belt, in: Heilbron, M., Cordani, U.G., Alkmim, F.F. (Eds), São Francisco Craton, Eastern Brazil. Springer International Publishing, Switzerland, 326 p.
- Vermeesch, P., 2012. On the visualisation of detrital age distributions. *Chemical Geology* 312-313, 190-194.
- Waters, D., 2003. P-T path from Cpx-Hbl-Pl symplectites, [www.earth.ox.ac.uk/~davewa/index.html](http://www.earth.ox.ac.uk/~davewa/index.html).
- Watson, E.B., Wark, D.A., Thomas, J.B., 2006. Crystallization thermometers for zircon and rutile. *Contribution to Mineralogy and Petrology* 151, 413-433.
- Watson, E.B., Wark, D.A., Thomas, J.B., 2006. Crystallization thermometers for zircon and rutile. *Contributions to Mineralogy Petrology* 151, 413-433.
- Weller, O.M., St-Onge, M.R., 2017. Record of modern-style plate tectonics in the Palaeoproterozoic Trans-Hudson orogeny. *Nature Geoscience* 10, 305-311.
- Westin, A., Campos Neto, M.C., Hawkesworth, C.J., Cawood, P.A., Dhuime, B., Delavault, H., 2016. A Paleoproterozoic intra-arc basin associated with a juvenile source in the Southern Brasilia Orogen: Application of U–Pb and Hf–Nd isotopic analyses to provenance studies of complex areas. *Precambrian Research* 276, 178-193.
- White, R. W., Powell, R., Clarke, G. L., 2002. The interpretation of reaction textures in Fe-rich metapelitic granulites of the Musgrave Block, central Australia: constraints from mineral equilibria calculations in the system  $K_2O$ -FeO-MgO-Al<sub>2</sub>O<sub>3</sub>-SiO<sub>2</sub>-H<sub>2</sub>O-TiO<sub>2</sub>-Fe<sub>2</sub>O<sub>3</sub>. *Journal of Metamorphic Geology* 20, 41–55.
- White, R. W., Powell, R., Holland, T. J. B., 2007. Progress relating to calculation of partial melting equilibria for metapelites. *Journal of Metamorphic Geology* 25, 511–527.
- White, R.W., Powell, R., Baldwin, J.A., 2008. Calculated phase equilibria involving chemical potentials to investigate the textural evolution of metamorphic rocks. *Journal of Metamorphic Geology* 26, 181-198.
- Whitehouse, M., Kemp, A.I.S., 2010. On the difficulty of assigning crustal residence, magmatic protolith and metamorphic ages to Lewisian granulites: constraints from combined in situ U–Pb and Lu–Hf isotopes. Geological Society, London, Special Publications 335, 81-101.

Whitney, D.L., Evans, B.W., 2010. Abbreviations for names of rock-forming minerals. *American Mineralogist* 95, 185-187.

Wiedenbeck, M., Alle, P., Corfu, F., Griffin, W.L., Meier, M., Oberli, F., Von Quadt, A., Roddick, J.C., Spiegel, W., 1995. 3 natural zircon standards for U-Th-Pb, Lu-Hf, trace-element and REE analyses. *Geostandards Newsletter* 19, 1-23.

Wilson, M., 1989. *Igneous petrogenesis: A global tectonic approach*, first ed. Harper Collins Academic, New York.

Zack, T., Moraes, R., Kronz, A., 2004. Temperature dependence of Zr in rutile: empirical calibration of a rutile thermometer. *Contributions to Mineralogy and Petrology* 148, 471-48

## 5 Regional discussions

### 5.1 The basement of the southern portion of the Brasília orogen

The origin of the basement of the southernmost portion of the Brasília orogen has recently been revealed by studies focussing on rocks located in the structural window between the nappe systems, in the Ouro Fino Shear Zone (Campos Neto et al., 2011; Cioffi et al., 2016a, b). These rocks have further been related to the São Francisco craton based on similar chronological and isotopic signatures.

Little is known about basement of the active margin that was involved in the Brasília orogeny though, the so called Paranapanema Block. So far, the only basement rocks potentially associated with the active margin are the ca. 2.1 Ga gneisses of the Socorro nappe (Trouw, 2008). This author, however, highlights that these gneisses could also be part of the São Francisco craton basement. After the discovery of the proximal (ca. 2.1 Ga old) gneisses from the Pouso Alegre, the origin of the Paleoproterozoic gneisses in the Socorro nappe became even more intriguing.

In this work, two types of rocks are similar to the basement. The first corresponds to the country rocks hosting the high-pressure clinopyroxene-garnet amphibolite (MT-13). The age of ca. 2.07 Ga (MT-17 =  $2065 \pm 2$  Ma, MT-19 =  $2076 \pm 3$  Ma and MT-20 =  $2076 \pm 4$  Ma) is compatible with the younger crust generation event of the Pouso Alegre complex (Cioffi et al., 2016a). Lithogeochemical signatures and proximity with the rocks studied by Cioffi et al. (2016a) allows a correlation with the Pouso Alegre complex, which in turn is interpreted as part of the São Francisco craton (Cioffi et al., 2016a).

The Neoproterozoic gneiss (C-833-A) sampled in the Guaxupé nappe, in contrast, more likely points towards an exotic terrane accretion to the São Francisco craton. An age of  $2559 \pm 66$  Ma coupled with a juvenile Hf isotope signature ( $\epsilon\text{Hf}_{(2550)}$  between +2.7 and +10.0) constitutes the first record of rocks with such characteristics in Southern Brazil. In addition, it preserves an uncommon  $2405 \pm 10$  Ma metamorphic age despite having undergone UHT metamorphism during the Brasiliano orogeny. No metamorphic event of this age has been described in the São Francisco craton yet. All together, these findings suggest that this is the first known occurrence of the Paranapanema block in the Guaxupé nappe. A correlation with the São Francisco craton cannot be fully discarded, however, since the reworked margin of São Francisco craton contains igneous rocks crystallized at 2.4 Ga (i.e., Mineiro Belt; Teixeira and Alkmim, 2017). The first identification of basement rocks from the active margin has significant implications on the understanding of the related arc magmatism (see section 5.3). In this respect, it bears potential for improving

paleogeographic reconstructions in which the Paranapanema block has been largely neglected and for new constraints on the paleogeographic position based on associated Neoproterozoic orogens (e.g. Merdith et al., 2017).

## 5.2 Timing and source of the arc magmatism in the Guaxupé nappe

The use of coupled U-Pb and Lu-Hf isotope systems allowed the magmatic protolith crystallization ages of the Guaxupé nappe gneisses to be assessed. Three different protoliths have been identified based on the bulk rock compositions and their zircon U-Pb and Lu-Hf signatures: (i) the Opdalite (C-838-2) registers a magmatic event age of  $786 \pm 10$  Ma and crustal  $\epsilon_{\text{Hf}}$  (-12.6 to -13.4); (ii) Banded mafic granulite (C-838-A) yielded a magmatic crystallization age of  $691 \pm 3$  Ma and  $\epsilon_{\text{Hf}}$  signature between -8.2 and -12.6; and (iii) mafic granulite enclave (C-716-B), the youngest magmatic rock in this area, which crystallized at  $664 \pm 9$  Ma exhibits a gabbroic composition and has the most juvenile Hf isotope signature ( $\epsilon_{\text{Hf}} = -5.9$  to -11.4) among the Neoproterozoic rocks.

In the Hf evolution diagram, the line of average crustal evolution is subparallel to a line linking the Neoproterozoic juvenile basement (C-833-A) and the magmatic Neoproterozoic rocks, suggesting that the composition of the latter could result from melting of the former. This is in agreement with model ages ( $\text{Nd } T_{\text{DM}}$ ) between ca. 1.6 Ga and 2.0 Ga that indicate melting of lower crust material (Janasi, 1999; Rocha, 2006). Rocha (2016) argues, however, that the process of contamination-assimilation is unlikely to explain the crustal signatures. This interpretation is mainly based on the argument that geochronological inheritance from a Paleoproterozoic basement has not been reported, while 700–800 Ma grains that are considered as inherited are preserved. In this study, the ca. 700–800 Ma grains were demonstrated to reflect the crystallization age of the rock. Furthermore, a juvenile Neoproterozoic basement has been described for the first time in this region. The absence of inherited grains could be the result of high Zr solubility in mafic melts (Boehnke et al., 2013). The presence of gabbroic rocks (e.g., mafic enclave C-716-B) indicates that a mantle source contributed to the formation of these rocks. This, together with the crustal signatures, points towards the mixing of metasomatic mantle melts as proposed by Rocha (2016) and assimilation-contamination by the local basement. The lithochemical signatures of the Neoproterozoic rocks are compatible with a volcanic-arc environment. The  $\epsilon_{\text{Hf}}$  signatures and lithochemistry, together with the opdalite as the oldest rock and the gabbroic rock the youngest, suggest that the magmatic activity became more juvenile with time.

### 5.3 Metamorphic evolution of the banded mafic granulites from the Guaxupénappe

Thermometry on cores of clinopyroxene and orthopyroxene from the banded mafic granulite (C-838-A) yielded peak conditions of  $998 \pm 23$  °C, and  $916 \pm 19$  °C recorded by the rims. In amphibole and biotite, a temperature of ca. 740 °C is recorded. Amp-Pl pairs further provided pressure conditions of ca. 6 kbar. A more robust link between these conditions and the timing of evolution of the Southern Brasília orogen requires the interpretation of these data in the light of other studies in the region.

Thermometry based on orthopyroxene and clinopyroxene in the banded mafic granulite should be considered with caution, since obtained temperatures could actually represent the igneous stage or mixes between metamorphic and igneous conditions due to partial re-equilibration (e.g., Kelsey et al., 2008). The temperatures obtained in this study are overlapping within errors with temperatures estimated by garnet and orthopyroxene thermometry on paraderived gneisses, thus indicating metamorphic conditions ( $1030 \pm 110$  °C; Rocha et al., 2017), corroborating its metamorphic texture. Zircon dating revealed that the protoliths of the banded mafic granulites are older than the UHT metamorphism, hence supporting the interpretation that pyroxenes records metamorphic temperatures. Furthermore, the post-peak conditions recorded in the pyroxene rims are the same as in orthopyroxene and garnet rims from the paragneiss ( $865 \pm 38$  °C). In conclusion, the pyroxene-exchange thermometer is considered to indicate metamorphic peak-conditions of the granulite.

The combined evaluation of metamorphic zircon rims from different samples allowed the identification of a long-lasting metamorphic event with duration of at least 80 m.y., including three main periods of zircon growth at (i) 670–650 Ma, (ii) 640–630 Ma, and (iii) 615–600 Ma. The first period is related to subduction metamorphism, while the other two record collision and subsequent decompression metamorphism accompanied by widespread anatexis during which zircon crystallization was more prominent.

The emplacement of gabbroic magma at  $664 \pm 9$  Ma similar to the age of anatexis is herewith suggested to have triggered the UHT metamorphism. Two grains crystallized at ca. 660 Ma record temperatures higher than 900 °C and could indicate first sub-solidus recrystallization of zircon before widespread migmatization. An onset of the UHT conditions before 630 Ma is further suggested by the monazite-garnet textures in X-ray maps from Rocha et al. (2017). The monazite crystals recording ca. 630 Ma are associated with post-peak garnet rims and thus more likely record high temperatures during the collisional stage (see above). Furthermore, reaching such high temperatures (as recorded in the garnet and orthopyroxene cores  $> 900$  °C) in only 5 m.y. during

continental collision as proposed by Rocha (2016) appears unlikely. A long-lived mountain plateau with high internal concentrations of heat-producing elements and low erosion rates is the most likely setting for producing extreme conditions (Clark et al., 2011; Harley, 2016). Although it is still intensely debated whether or not mafic magmas can trigger ultra-high temperature, they have been interpreted to be the cause of many high temperature metamorphic events (e.g. Ivrea Zone, Ewing et al, 2013; Val Malenco, Hermann et al., 1997) including arc-related settings (Harley, 2016 and references therein).

## 5.4 Origin and evolution of the “retro-eclogites” from Pouso Alegre

The protolith of the Pouso Alegre clinopyroxene-garnet amphibolite has a minimum crystallization age of  $1513 \pm 17$  Ma in agreement with  $1504 \pm 29$  Ma obtained by Coelho et al. (2017). Its lithochemical signature resembling N-MORB to E-MORB together with an interval of 900 M.y. that separates their formation from the Brasília metamorphism, and its position in a crustal section suggest a rift origin for this rock. Chronocorrelation link their formation to the Calymmian (1.6–1.4 Ga) events registered in the region (e.g., Fonte Boa et al., 2017; Heilbron et al., 2017). Alternatively, these mafic rocks could represent volcanic rocks that intruded into the Paranapanema block as proposed by Coelho et al. (2017). This however requires that the Pouso Alegre complex, the host of the mafic rocks, is part of the Paranapanema block.

The detailed systematic investigation of these rocks revealed that it records two metamorphic stages, the peak metamorphism and the retrogression. The peak conditions of  $13.5 \pm 3.0$  kbar and  $720 \pm 30$  °C were obtained from thermodynamic modelling based on bulk rock and garnet compositions, and Zr-in-rutile thermometry. The local composition of the reintegrated symplectite was used to estimate the composition of the original pyroxene (i.e., before the symplectite formation). The jadeite content of this pyroxene, an important geobarometer, confirms maximum pressure conditions of ca. 13 kbar obtained by the modelling. Mass balance modelling validated the use of the reintegrated composition of the symplectite for this purpose, and further revealed that corona and symplectite formations were coupled reactions. Two metamorphic ages were obtained from CL-bright domains on zircon rims, one of ca. 630 Ma, which corroborates the ca. 625 Ma from Coelho et al. (2017), and another of ca. 600 Ma, which was constrained from the majority of zircon rims in this sample. The ca. 630 Ma age is attributed to the peak-conditions based on trace elements abundances in zircon (flat pattern – type 1) and garnet, and the presence of secondary inclusions with the same reconstructed jadeite composition in the core of zircon. The retrograde stage, related to the symplectite and corona formation, is dated at  $603 \pm 7$  Ma. It records zircon crystallization with incorporation of HREEs that were released from garnet dissolution during decompression.



Similar metamorphic peak conditions and ages (ca. 630 Ma) are recorded in the basement rocks. Monazite from the sillimanite-garnet gneiss dates to  $637 \pm 7$  Ma, which is in agreement with ages from the whole sequence that is thus interpreted to have evolved together. The age of the aluminous gneiss is tentatively attributed to an earlier stage of metamorphism around  $672 \pm 4$  Ma or older, maybe related to the garnet core formation. This age is not recorded by any other rocks in the region.

The maximum *P-T* conditions recorded by this sample correspond to a geothermal gradient of  $\sim 50$  °C/kbar that is comparable with what is commonly observed in collisional belts (Brown, 2007; Sizova et al., 2014). *HP* and *UHP* rocks related to subduction evolve along cooler geotherms of 35 °C/kbar or less (Brown, 2007, 2009; Weller and St-Onge, 2017). The Pouso Alegre *HP* metabasites, which previously have been referred to as “retro-eclogites”, thus more likely represent *HP* metamorphic products of mafic intrusions in a continental setting that were metamorphosed in the deep root of the Ediacaran continent-continent collisional zone. Decompression with an exhumation rate of 1 mm/y is compatible with erosion-driven exhumation (Burbank, 2002; Schlunegger and Willett, 1999). However, the limited cooling during exhumation suggests a tectonic process during which rock units move upwards crossing different geothermal gradients.

## 5.5 Other regional implications

### 5.5.1 Arc magmatism in the Southern Brasília orogen

The first documentation of an igneous rock of around 800 Ma (opdalite C-838-2) constrains the chronological relations between the Guaxupé nappe in the southernmost portion, and the northern part of the Brasília Orogen. It is furthermore necessary to identify the tectonic setting in which these rocks were emplaced.

Igneous rocks of ca. 800 Ma as part of a magmatic arc have been described in the northern portion of the Brasília orogen. In contrast to the crustal isotopic signatures of the Guaxupé nappe magmatites, these rocks exhibit juvenile to slightly negative  $\epsilon_{Nd}$  (Pimentel and Fuck 1992; Laux et al., 2005; Pimentel et al., 2016). The youngest Neoproterozoic magmatic event reported for the Northern Brasília orogen proceeded between 670 and 630 Ma, synchronous with the generation of the magmatic arc hosted by the Guaxupé nappe.

### 5.5.2 The 790 Ma source for the metasedimentary rocks

The first record of a ca. 790 Ma igneous rock (opdalite, sample C-838-2) has important implications for the southernmost portion of the Brasília orogen. This age has been recognized in inherited zircon cores of metasedimentary gneisses in the Guaxupé nappe (Rocha et al., 2017) and in zircon grains metasedimentary rocks in the Andrelândia nappe system (e.g., Belém et al., 2011; Westin et al., 2016).

The migmatitic sillimanite-garnet gneiss (MT-22A), mainly based on a narrow age range distribution and zircon typology, is suggested to represent a metamorphosed volcanic acidic rock. A more robust interpretation requires confirmation by a similar approach applied to rocks from Guaxupé nappe (e.g., U-Pb coupled to Lu-Hf analysis) however, and thus the presented hypothesis is not ultimately conclusive (i.e. single source derived sedimentary rocks). In case the 790 Ma-source is only represented by rocks of the Guaxupé nappe, that constrains the metasedimentary rocks containing 800 Ma zircon dates to an active margin or as collisional sediments (e.g. flysch basins). Otherwise, the aluminous rock (migmatitic sillimanite-garnet gneiss) likely had an acid volcanic protolith hosted by the Pouso Alegre complex and the ca. 790 Ma age does not discriminate a straightforward provenance. Similarly, zircons from the arc dating to ca. 690 Ma could also help to trace the provenance.

An important notion for the provenance studies is that most of the grains from the nappes that experienced UHT metamorphism or even high temperatures may potentially have lost Pb (Fig. 3.7 and 3.8). This process is more difficult to identify in metasedimentary rocks and can lead to misinterpretation of the sources involved in the sedimentation, as well as result in a younger maximum sedimentation age.

### 5.5.3 Metamorphic evolution of the Southern Brasília orogen

The present work contributes to the understanding of the complex nappe framework of the Southern Brasília orogen. Among the Guaxupé nappe, the orthopyroxene-clinopyroxene-bearing rocks were interpreted as part of the metamorphosed magmatic arc (Figueiredo and Campos-Neto, 1995). Bulk-rock compositions remained one of the arguments supporting this interpretation, as metamorphic ages of ca. 620 Ma were identified in other nappes (e.g. Reno et al., 2012). Crustal isotopic signatures (Lu-Hf and Sm-Nd) are conspicuous and remain unexplained however, especially due to the presence of contrasting juvenile rock signatures in the magmatic arc of the northern part of the Brasília orogen (Pimentel, 2016 and references therein) and the lack of basement rocks within the Guaxupé nappe. The identification of mafic to intermediate rocks that were metamorphosed shortly after their formation, i.e., within 20 m.y. starting at 680 Ma that marks

a much older event than the largely recognized metamorphic age of 630 Ma, is an important argument towards a magmatic arc origin of the Guaxupé nappe. Such older ages have been already recognized in monazites from the metasediments of the Andrelândia nappe system (Reno et al., 2012) and were suggested to maybe represent subduction metamorphism (Coelho et al., 2017). Thus, a common metamorphic event is indicated for the arc rocks and for the metasedimentary rocks. The subduction-related metamorphism however does not allow us to constrain whether these metasediments derive from passive or active margins, since they can potentially be affected by both kind of metamorphism.

The migmatitic sillimanite-garnet gneiss also records a metamorphic age  $672 \pm 4$  Ma that can be related the subduction stage. An explanation why this rock, by contrast to the other rocks of the sequence, records the pre-collisional stage could be related to its more hydrated composition compared to the granitic basement and the mafic rocks. A potential geodynamic setting exhibiting such pre-peak conditions is the trench or the accretionary wedge.

The collisional stage at ca. 630 Ma is recorded by monazite in the migmatitic sillimanite-garnet gneiss, and zircon in the clinopyroxene-garnet amphibolite and the basement in the region of Pouso Alegre. In the Guaxupé nappe context, monazite formation in the paraderived rocks and zircon growth in the leucosomes are related to this collisional stage. Post-collisional metamorphism (630–600 Ma) related to decompression and induced by fluids is recorded by zircon rims in the clinopyroxene-garnet amphibolite, by the great amount of zircon crystallized, and by monazite in the leucosome in the Guaxupé nappe and in the orogen (Fig 3.12 and 3.13).

## 5.6 References

- Belém, J., Pedrosa-Soares, A.C., Noce, C.M., da Silva, L.C., Armstrong, R., Fleck, A., Gradim, C.T., Queiroga, G.N., 2011. Bacia precursora versus bacias orogênicas: exemplos do Grupo Andrelândia com base em datações U-Pb (LA-ICP-MS) em zircão e análises litoquímicas. *Geonomos* 19, 224–243.
- Boehnke, P., Watson, E.B.B., Trail, D., Harrison, T.M.M., Schmitt, A.K.K., 2013. Zircon Saturation Re-Revisited. *Chemical Geology* 351, 324–334.
- Brown, M., 2007. Metamorphic conditions in orogenic belts: A record of secular change. *International Geology Review* 49, 193-234.
- Brown, M., 2009. Metamorphic patterns in orogenic systems and the geological record. *Geological Society, London, Special Publications* 318, 37-74.
- Burbank, D.W., 2002. Rates of erosion and their implications for exhumation. *Mineralogical Magazine* 66, 25-52.

- Cioffi, C.R., Campos Neto, M.d.C., Möller, A., Rocha, B.C., 2016a. Paleoproterozoic continental crust generation events at 2.15 and 2.08 Ga in the basement of the southern Brasília Orogen, SE Brazil. *Precambrian Research* 275, 176–196.
- Cioffi, C. R.; Campos Neto, M. C., Möller, A., Rocha, B. C. 2016b. Tectonic significance of the Meso- to Neoproterozoic complexes in the basement of the southern Brasília Orogen. *Precambrian Research* 287, 91–107.
- Clark, C., Fitzsimons, I.C. W, Healy, D, Harley, S.L, 2011. How does the continental crust get really hot? *Elements* 7, 235-240.
- Coelho, M.B., Trouw, R.A.J., Ganade, C.E., Vinagre, R., Mendes, J.C., Sato, K., 2017. Constraining timing and P-T conditions of continental collision and late overprinting in the Southern Brasília Orogen (SE-Brazil): U-Pb zircon ages and geothermobarometry of the Andrelândia Nappe System. *Precambrian Research* 292, 194–215.
- Ewing, T., Hermann, J., Rubatto, D., 2013. The robustness of the Zr-in-rutile and Ti-in-zircon thermometers during high-temperature metamorphism (Ivrea-Verbano Zone, northern Italy). *Contributions to Mineralogy and Petrology* 165, 757–779.
- Fonte-Boa, T.M.R., Novo, T.A., Pedrosa-Soares, A.C., Dussin, I., 2017. Registros de eventos tafrogênicos mesoproterozoicos no embasamento do Orógeno Araçuaí, sudeste do Brasil. *Brazilian Journal of Geology* 47(3), 447–466.
- Harley, S.L., 2016. A matter of time: The importance of the duration of UHT metamorphism. *Journal of Mineralogical and Petrological Sciences* 111, 50-72.
- Heilbron, M., Cordani, U., Alkmim, F., (Eds.) 2017. São Francisco Craton, Eastern Brazil. Springer International Publishing, Switzerland, 326 p.
- Hermann, J., Müntener, O., Trommsdorff, V., Hansmann, W., Piccardo, G. B., 1997. Fossil crust-to-mantle transition, Val Malenco (Italian Alps). *Journal of Geophysical Research* 102, 20123–20132.
- Kelsey, D.E., 2008. On ultrahigh-temperature crustal metamorphism. *Gondwana Research* 13, 1-29.
- Janasi, V.A., 1999. Petrogênese de granitos crustais da Nappe de Empurrão Socorro- Guaxupé (SP-MG): uma contribuição da geoquímica elemental e isotópica. Thesis (Livre-Docência)-IGc-USP, p. 304
- Laux, J.H., Pimentel, M.M., Dantas, E.L., Armstrong, R., Junges, S.L. 2005. Two Neoproterozoic crustal accretion events in the Brasília Belt, central Brazil. *Journal of South American Earth Sciences* 18, 183–198.

- Merdith, A.S., Collins, A. S., Williams, S. E., Pisarevsky, S., Foden, J. D., Archibald, D. B., Blades, M.D., Alessio, B. L., Armistead, S., Plavsa, D., Clark, C., Müller, R. D., 2017. A full-plate global reconstruction of the Neoproterozoic. *Gondwana Research* 50, 84–134.
- Pimentel, M.M., 2016. The tectonic evolution of the Neoproterozoic Brasília Belt, central Brazil: a geochronological and isotopic approach. *Brazilian Journal of Geology* 46 (1), 67–82.
- Pimentel, M.M., Fuck R.A., 1992. Neoproterozoic crustal accretion in central Brazil. *Geology* 20, 375-379.
- Reno, B.L., Piccoli, P.M., Brown, M., Trouw, R.A.J., 2012. In situ monazite (U–Th)–Pb ages from the Southern Brasília Belt, Brazil: constraints on the high temperature retrograde evolution of HP granulites. *Journal of Metamorphic Geology* 30 (1), 81–112.
- Rocha, B.C. 2016. Idade, duração e condições P-T do metamorfismo de temperatura ultra-alta, anatexia e cristalização de fundido na nappe Socorro-Guaxupé. PhD thesis, Universidade de São Paulo, p. 229.
- Rocha, B. C., Moraes, R., Möller, A., Cioffi, C. R., Jercinovic, M.J., 2017. Timing of anatexis and melt crystallization in the Socorro-Guaxupé Nappe, SE Brazil: insights from trace element composition of zircon, monazite and garnet coupled to U-Pb geochronology. *Lithos* 277, 337–355.
- Schlunegger, F., Willett, S.D., 1999. Spatial and temporal variations in exhumation of the central Swiss Alps and implications for exhumation mechanisms, in: Ring, U., Brandon, M.T., Lister, G.S., Willett, S.D. (Eds.), *Exhumation Processes: Normal Faulting, Ductile Flow and Erosion*. Geological Society, London, Special Publications 154, pp. 157-179.
- Sizova, E., Gerya, T., Brown, M., 2014. Contrasting styles of Phanerozoic and Precambrian continental collision. *Gondwana Research* 25, 522-545.
- Teixeira, W., Alkmim, F., 2017. The Paleoproterozoic Mineiro Belt and the Quadrilátero Ferrífero. In: Helibron, M., Cordani, U.G., Alkmim, F.F. (Eds.), *São Francisco Craton, Eastern Brazil*. Springer International Publishing, Switzerland, pp. 71–94.
- Trouw, C. C., 2008. Mapeamento da Folha Virgínia–MG, Geocronologia U-Pb (SHRIMP) em zircões e interpretação geotectônica. PhD Thesis, Universidade do Rio de Janeiro, p.127.
- Weller, O.M., St-Onge, M.R., 2017. Record of modern-style plate tectonics in the Palaeoproterozoic Trans-Hudson orogeny. *Nature Geoscience* 10, 305-311.
- Westin, A., Campos Neto, M.C., Hawkesworth, C.J., Cawood, P.A., Dhuime, B., Delavault, H., 2016. A Paleoproterozoic intra-arc basin associated with a juvenile source in the southern Brasilia Orogen: application of U–Pb and Hf–Nd isotopic analyses to provenance studies of complex areas. *Precambrian Research* 276,

## 6 General conclusions and outlook

The combination of field information and petrochronology allowed constraining a series of rock formation and metamorphic events in the evolution of the southernmost portion of the Brasília orogen. The studied area comprised rocks that enabled a better understanding the history of the SBO, from Neoproterozoic and Paleoproterozoic basement formation to the late metamorphic stages. The most important findings are summarized, and an outlook for future studies in this area is given (Fig. 6.1).

- A fragment of the basement of the Guaxupé nappe has been identified for the first time. It is a Neoproterozoic, juvenile ( $\epsilon\text{Hf}_{(2550)}$  between +2.7 and +10.0) banded mafic granulite displaying a very similar mineral assemblage and bulk-rock composition compared to the Neoproterozoic granulites. Two metamorphic stages are recorded in these rocks, an older at  $2405 \pm 10$  Ma and the Neoproterozoic stage that is registered in all other rocks from the nappe.
- Igneous protoliths dated at  $786 \pm 10$  Ma,  $691 \pm 3$  Ma and  $664 \pm 9$  Ma were identified in the Guaxupé nappe. This indicates that magmatic activity is older than previously considered. It is indeed partially synchronous with the magmatic arc activity recorded in the Northern Brasília orogeny. Thus, the older zircon grains in the granulites are protolith grains and not inheritance (i.e. contamination). Further investigation is required to clarify the tectonic setting of the ca. 790 Ma opdalite, which is probably the product of partial melting in the lower crust. The other rocks formed in a magmatic arc setting as a product of the interaction between metasomatic mantle and assimilation-contamination in the Neoproterozoic juvenile basement.
- The rocks from the Guaxupé nappe record a long-lasting metamorphic event with a duration of at least 80 m.y., including three main episodes of zircon growth recorded at (i) 670–650 Ma, (ii) 640–630 Ma, and (iii) 615–600 Ma. The first is related to a subduction stage and the latter two to collision to decompression stages, respectively.
- Anatexis in the Guaxupé nappe was driven by different processes with evidence for incongruent *in situ* melting as well as allochthonous melt intrusion possibly derived from a crustal metasedimentary source. Both, *in situ* partial melting with or without external melt contribution are found in the same outcrop.
- UHT peak metamorphic temperatures of  $998 \pm 23$  °C recorded in the banded mafic granulite were possibly triggered by the emplacement of gabbroic magmas at ca. 660 Ma in

a magmatic arc related setting. In a next step, dating of the zoned garnet crystals in the paraderived orthopyroxene-garnet gneiss could help to further constrain the age of the UHT event.

- The Pouso Alegre rock assemblage is composed of intermediate to felsic rocks that formed at ca. 2.07 Ga (Pouso Alegre complex) and were intruded by gabbros at ca. 1.5 Ga. This igneous complex was overlain by an aluminous volcanoclastic igneous body or immature metasedimentary rocks at around 800 Ma.
- Peak collisional metamorphic conditions of  $13.5 \pm 3.0$  kbar and  $701 \pm 16$  °C were dated to 630 Ma. The surrounding migmatitic garnet-amphibole gneisses record similar *P-T* conditions. The peak metamorphic age was obtained from zircon rims in the country rock gneisses, monazite in the aluminous gneiss, and zircon rims in the clinopyroxene-garnet amphibolite.
- Reconstruction of local domains allowed the determination of *P-T* conditions of late stage symplectite and corona formation to  $4.8 \pm 1.5$  kbar and  $595\text{--}600 \pm 26$  °C. The symplectite containing  $\text{Cpx}_2 + \text{Amp}_2 + \text{Pl} \pm \text{Qz}$ , as well as coronas of plagioclase and amphibole around garnet formed in coupled reactions involving Na exchange at around  $603 \pm 7$  Ma.
- The high geothermal gradient recorded in the clinopyroxene-garnet amphibolite is not compatible with a subduction gradient and rather indicates metamorphism related to continent-continent collision tectonics. Thus, the Pouso Alegre mafic rocks do not support an extension of the UHP belt of the West Gondwana orogen to the Southern Brasília orogen. Nevertheless, the clinopyroxene-garnet amphibolite appears to be related to a relatively high-*P* metamorphism in the root of the Ediacaran continent-continent collisional zone that may link those two orogens. Further dedicated studies on the other “retro-eclogites” could help to elucidate their origin.
- The calculated low maximum exhumation rate of  $1 \text{ mm.y}^{-1}$  for the clinopyroxene-garnet amphibolite and high geothermal gradient for the symplectite and corona formation stage indicate that exhumation was tectonic-driven.
- The metamorphic history of the rocks from Pouso Alegre, comprising collisional peak to decompression metamorphism from ca. 630 Ma to 600 Ma, is in agreement with the evolution registered in the Guaxupé nappe.

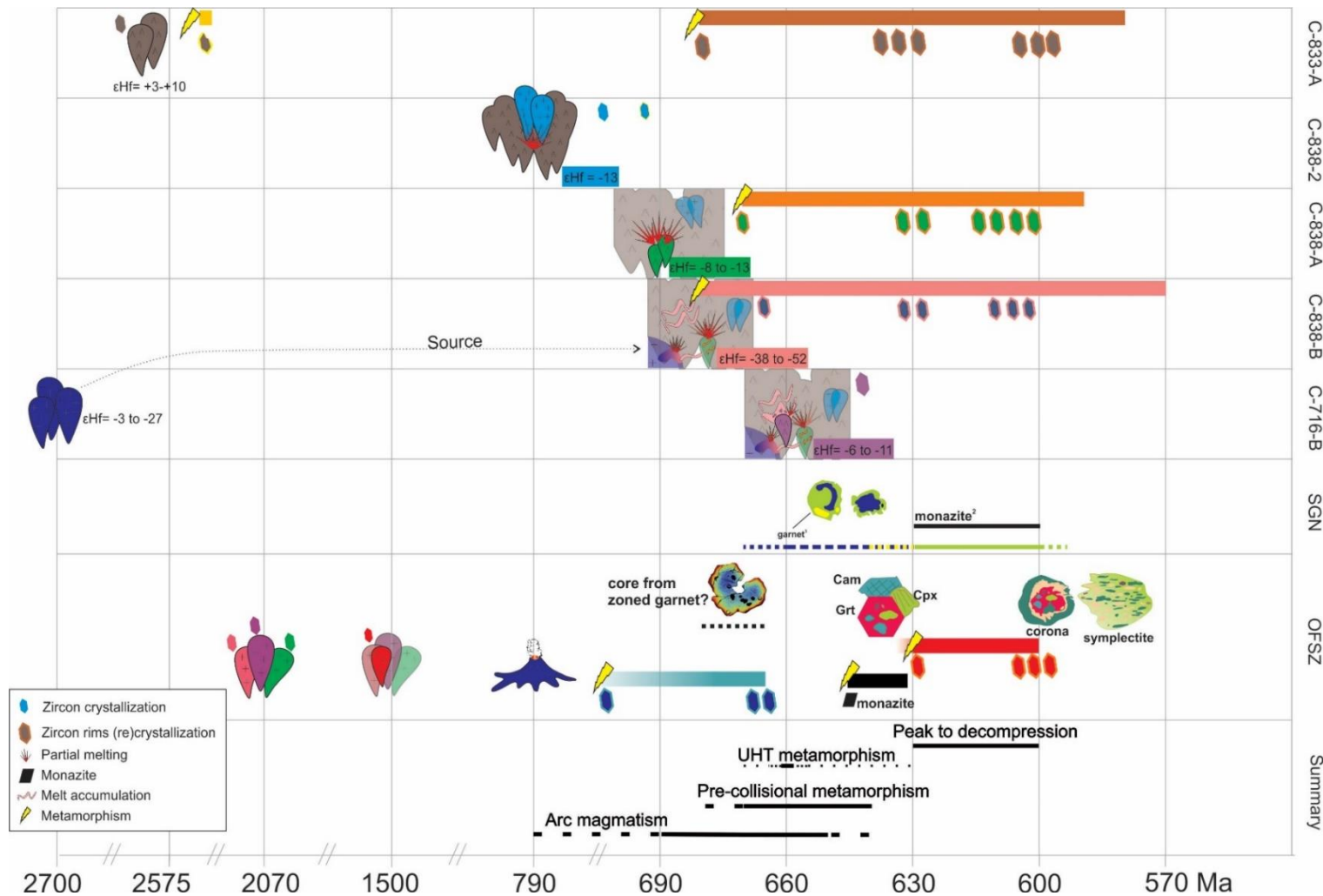


**Figure 6.1:** Summary of the geological evolution of the Guaxupé nappe and Pouso Alegre section with emphasis on the temporal distribution, Hf signatures and P-T constraints of igneous and metamorphic events of the studied samples. Data from (1) Tedeschi et al. (2017); (2 and 3) Rocha et al. (2017). Transparency applied to elements that constitute previous events, bright colors correspond to new events. The distribution of zircon grains represented along the metamorphism bars indicate relative amount of zircon crystallization. SGN – Socorro-Guaxupé nappe; OFSZ – Ouro Fino Shear Zone



## 7 Conference abstracts

### 7.1 Mapeamento geológico 1:100.000 das folhas Caldas e Poços de Caldas (SF-23-V-DIV) e Poços de Caldas (SF-23-V-C-VI), Sudoeste de Minas Gerais. In: 47º Congresso Brasileiro de Geologia, 2014, Salvador. 47º Congresso Brasileiro de Geologia.

Tedeschi, M. <sup>1,2</sup>; Novo, T. <sup>1</sup>; Pedrosa-Soares, A.C.<sup>1</sup>; Azevedo, R.A.<sup>1</sup>; Salim, L.F.<sup>1</sup>; Vieira, P.L.N.C<sup>1</sup>; Evaristo, A.<sup>1</sup>

<sup>1</sup>Universidade Federal de Minas Gerais; <sup>2</sup>Companhia de Pesquisa de Recursos Minerais

RESUMO: A região englobada pelas folhas Caldas e Poços de Caldas, mapeada no Projeto Fronteiras de Minas Gerais (contrato CODEMIG-FUNDEP-UFMG), localiza-se no lobo setentrional da nappe Socorro-Guaxupé. Esta constitui uma pilha alóctone interpretada como representante do arco magmático Paranapanema, compondo parte do sistema de nappes do Orógeno Brasília Meridional cavalgado sobre o Cráton do São Francisco durante a Orogenia Brasileira. A base da nappe é composta por granulitos, aflorantes apenas na porção norte da área em uma faixa E-W. O núcleo da nappe é composto por (gm)-(anf)-bt gnaisses migmatíticos, graníticos a granodiorticos, do Complexo São João da Mata, localmente contendo intercalações de rocha máfica, metamorfisados em fácies anfíbolito, com a quantidade de granada crescente de leste para oeste. Ocorrem, de forma descontínua dentro desta unidade, afloramentos de paragnaisse caracterizados pela presença de aluminossilicatos e abundantes granada e biotita. Intrudindo estes gnaisses são encontrados ortopiroxênio granitoides que gradam da cor verde, quando frescos, a branca quando alterados, isotrópicos a fortemente foliados. Estas rochas chamockitóides ocorrem em duas regiões, no nordeste das folhas, onde encontram-se dobradas em um sistema de anticlinais e sinclinais cisalhados em sua porção meridional, e ao longo de uma faixa na porção central da folha Caldas, na Surte São Pedro de Caldas (ca. 625 Ma\*), cuja terminação ocidental é truncada pela intrusão alcalina Poços de Caldas. Estas rochas são consideradas produto da fusão dos gnaisses granulíticos da base da nappe. No sul da área aflora o batólito Pinhal Ipuíuna, sinorogênico, composto na região por anf-bt monzodioritos a granitos, porfíricos, que variam de foliados ductilmente a orientados por fluxo magmático. Rochas granitoides dos estágios sina tardicolisionais, texturalmente heterogêneas, essencialmente (anf)-bt granitos a granodioritos, são encontradas em meio ao gnaisse, gradando a partir de rochas muito migmatizadas, constituindo muitas vezes, nebulitos, variando de isotrópicos a foliados. Estes granitos ocorrem em vários pontos da folha Caldas, em corpos irregulares, orientados preferencialmente na direção leste-oeste. O final do evento magmático neoproterozóico na região,

de ca. 610 Ma\*, é representado pelo Sienito Capituva, na porção central, um maciço elíptico zonado concentricamente composto por sienitos e melasienitos, e pelo Sienito Pedra Branca, no sudoeste da folha Caldas, também zonado, composto por rochas homônimas. O Maciço Poços de Caldas representa o magmatismo cretácico na região, possui aproximadamente 800 km<sup>2</sup> e ocupa a porção sudoeste das folhas. i: composto principalmente por fonólitos intrusivos e nefelina sienitos, com lavas fonolíticas e rochas piroclásticas subordinadas. A região registra três fases deformacionais (D1, D2 e D3), sendo D1 e D2 progressivas, com D3 tardia truncando e defletindo estruturas pretéritas. A estrutura principal é a foliação Sn (sub)paralela a flancos de dobras isoclinais a fechadas, tem direção variando de E-W a NW-SE com mergulhos médios a altos para sul ou sudoeste. Em resposta à progressão de D1, tem-se D2 retratada por zonas de cisalhamento paralelas à foliação e dobras abertas de eixo aproximadamente N-S. Por fim, D3 gera zona de cisalhamento quilométrica na porção oeste da área, de orientação NE-SW e movimento transpressivo sinistral de topo para NW.

\*Dados da literatura.

**PALAVRAS-CHAVE:** MAPEAMENTO GEOLÓGICO, NAPPE SOCORRO-GUAXUPÉ. ORÓGENO BRASÍLIA MERIDIONAL

## **7.2 Reconstruction of high-pressure metamorphic conditions from symplectites: insights from Pouso Alegre mafic rocks (Brasília Belt, Brazil) In: 14th Swiss Geoscience Meeting, 2016, Geneva. Abstract Volume 14th Swiss Geoscience Meeting.**

Mahyra Tedeschi<sup>1,2,3</sup>, Pierre Lanari<sup>1</sup>, Daniela Rubatto<sup>1</sup>, Jörg Hermann<sup>1</sup>, Antônio Pedrosa-Soares<sup>2</sup>, Ivo Dussin<sup>4</sup>, Marco Aurélio P. Pinheiro<sup>3</sup>

<sup>1</sup> Institute of Geological Sciences, University of Bern, Baltzerstrasse 1+3, Bern, Switzerland (mahyratedeschi@gmail.com)

<sup>2</sup> Programa de Pós-Graduação em Geologia, Universidade Federal de Minas Gerais, Av. Antônio Carlos 6627, Belo Horizonte, Brazil

<sup>3</sup> Geological Survey of Brazil, Avenida Brasil 1731, Belo Horizonte, MG, Brazil

<sup>4</sup> Multilab, Universidade do Estado do Rio de Janeiro, R. São Francisco Xavier 524, Rio de Janeiro, Brazil

Mafic rocks within crustal sections that underwent polycyclic tectono-metamorphic evolutions may be used as markers for suture zones, particularly if they preserve relict of high-pressure metamorphism. Reconstructing the metamorphic history of such mafic rocks is challenging because they are commonly retrogressed and are scarce in supercrustal sequences. The mafic rocks from Pouso Alegre in the Meridional Brasília Orogen (SW-Brazil), outcrop as rare lenses within (Ky)-Sil-Grt gneiss, Amp-Grt orthogneiss and Bt granite and are heavily weathered. It has been previously suggested that the Pouso Alegre garnet amphibolites are “retro-eclogites”, based on a characteristic symplectite texture and mineralogical observations, and thus they have been interpreted to mark the suture zone between the Paranapanema and São Francisco cratons. However, no quantitative estimates of the pressure is available to support this conclusion. In this study we investigated in detail these samples to refine their P-T-t history. The Grt-Cpx amphibolite from Pouso Alegre shows symplectite and corona textures overprinting a former Grt-Cpx1 paragenesis, as commonly observed in retrogressed eclogites. Bulk rock chemistry indicates a tholeiitic gabbroic composition, with a MORB-like signature. The bulk-rock composition was used for P-T modelling with THERIAK-DOMINO (De Capitani & Petrakakis 2010). The Grt-Cpx1 assemblage is stable at 700°C and 14 kbar. The symplectite is developed from the reaction  $\text{Omp} + \text{Qz} + \text{H}_2\text{O} \rightarrow \text{Cpx} + \text{Amp} + \text{Pl} + \text{Qz}$ . Local compositions of the symplectite domains were used to retrieve the jadeite content of Cpx1. This value is in line with the predictions of the model and confirms a maximum pressure of 14 kbar. The P-T conditions for the formation of the symplectite are between 600-750°C and less than 7kbar as estimated using XMapTools (Lanari et al. 2014) and BINGO-ANTIDOTE (Lanari & Duesterhoeft 2016). This program compares the metamorphic assemblage, mineral modes and composition observed in a given domain of the rock to those predicted by the thermodynamic models. Rutile is a good candidate to preserve relict metamorphic stages that have been completely obliterated in the matrix. Zr-in-rutile thermometry (Tomkins et al. 2007) indicates that rutile forms at temperature of ca. 715°C. The Zr-in-rutile data are consistent with the T from modelling, without evidence of a preceding, higher grade stage. The inclusions trapped in the garnet porphyroblast, rutile and in zircon were systematically analyzed to search for relicts of a metamorphic stage predating the Grt-Cpx1 assemblage. Inclusions of Cpx, Amp, Grt, Ttn, Zrn and Bt are similar in composition to the matrix minerals, supporting the results of the thermodynamic models with a

maximal pressure of 14 kbar. We thus conclude that this sample equilibrated at lower crustal conditions. U-Pb zircon age (LA-ICP-MS) of zircon cores spread along concordia from ca. 1.7 to 1.0 Ga with a significant cluster at  $1518 \pm 9$  Ma (MSDW = 1.3), which is interpreted as the protolith crystallization age. Zircon rim ages in the interval 660-590 Ma are correlated to the metamorphic event based on CL imaging and Th/U ratios. U-Pb geochronology of the samples provide a crystallization age for the orthogneiss and granite of ca. 2.1 Ga, a maximum sedimentation age of the (Ky)-Sil-Grt gneiss at  $794 \pm 4$  Ma and metamorphism in the orthogneiss rocks at  $626 \pm 5$  Ma. In the mafic rocks, the significant time span between protolith crystallization and metamorphism (ca. 800 Ma), the lack of evidence of a collision in this period and the bulk-rock chemistry indicate a continental basalt/gabbro origin. The mafic magma intruded the granitic country rocks at ca. 1.5 Ga, and sediments deposited on this basement by 800 Ma. The sequence was involved in the collision at ca. 630 Ma, when it reached the peak metamorphic conditions.

## REFERENCES

- de Capitani, C. & Petrakakis, K. 2010: The computation of equilibrium assemblage diagrams with Theriak/Domino software. *Am. Mineral.* 95, 1006–1016.
- Lanari, P. & Duysterhoeft, E. 2016: Thermodynamic modeling using Bingo-Antidote: A new strategy to investigate Symposium 2: Mineralogy, Petrology, Geochemistry Platform Geosciences, Swiss Academy of Science, SCNAT Swiss Geoscience Meeting 2016 metamorphic rocks. EGU-2016-11363.
- Lanari, P., Vidal, O., De Andrade, V., Dubacq, B., Lewin, E., Grosch, E. G. & Schwartz, S. 2014: XMapTools: a MATLAB®-based program for electron microprobe X-ray image processing and geothermobarometry. *Comput. Geosci.* 62, 227–240.
- Tomkins, H.S., Powell, R. & Ellis, D.J., 2007: The pressure dependence of the zirconium-in-rutile thermometer, *Journal of Metamorphic Geology*, 25, 703–713.

### **7.3 Reconstruction of P-T-t metamorphic conditions from symplectites: insights from Pouso Alegre mafic rocks (Brasília Belt, Brazil) In: European Geoscience Union 2017, 2017, Vienna. European Geoscience Union 2017.**

Mahyra Tedeschi <sup>(1,2,3)</sup>, Pierre Lanari <sup>(1)</sup>, Daniela Rubatto <sup>(1,5)</sup>, Jörg Hermann <sup>(1)</sup>, Antônio Carlos Pedrosa-Soares <sup>(2)</sup>, Ivo Dussin <sup>(4)</sup>, Marco Aurélio Pinheiro <sup>(3)</sup>, Anne-Sophie Bouvier <sup>(5)</sup>, and Lukas Baumgartner <sup>(5)</sup>

<sup>(1)</sup> Institute of Geological Sciences, University of Bern, Baltzerstrasse1+3, Bern, Switzerland (mahyratedeschi@gmail.com), <sup>(2)</sup> Programa de Pos-Graduação em Geologia, Universidade Federal de Minas Gerais, Av. Antônio Carlos 6627, Belo Horizonte, Brazil, <sup>(3)</sup> Geological Survey of Brazil, Avenida Brasil 1731, Belo Horizonte, MG, Brazil, <sup>(4)</sup> Multilab, Universidade do Estado do Rio de Janeiro, R. São Francisco Xavier 524, Rio de Janeiro, Brazil, <sup>(5)</sup> Institut des sciences de la Terre, University of Lausanne, CH-1015 Lausanne, Switzerland

Reconstructing the metamorphic history of polycyclic tectono-metamorphic mafic rocks that preserve potential relicts of high-pressure metamorphism is challenging because such rocks are commonly retrogressed and rare in supercrustal sequences. However, pressure-temperature-time (P-T-t) information is required to obtain the paleo-geothermal gradients and thus to define those units as markers for suture zones. The mafic rocks from Pouso Alegre in the Meridional Brasília Orogen (SW-Brazil) outcrop as rare lenses within Sil-Grt gneisses, Amp-Grt orthogneisses and Bt granites. They are heavily weathered. They have previously been defined as “retro-eclogites”, based on the characteristic symplectite texture and some mineralogical observations. They have been interpreted to mark the suture zone between the Paranapanema and São Francisco cratons, although no quantitative estimates of the pressure is available to support this conclusion. In this study we investigated in detail these samples to refine their P-T-t history. As commonly observed in retrogressed eclogites, the studied mafic rock shows symplectite and corona textures overprinting the former paragenesis of Garnet (Grt) - Clinopyroxene (Cpx) 1 - Amphibole (Amp) 1 – Rutile (Rt). Phase equilibrium modelling shows that this assemblage is stable at 690 °C and 13.5 kbar, in line with Zr-in-rutile thermometry ( $720 \pm 30^\circ \text{C}$ ). Local compositions of the symplectite domains were used to retrieve the jadeite content of Cpx1. This low-Jd cpx is in line with the predictions of the model and confirms a maximum pressure of ~14 kbar. The symplectite formed from the reaction  $\text{Cpx1} + \text{Qz} + \text{H}_2\text{O} \rightarrow \text{Cpx2} + \text{Amp} + \text{Pl} + \text{Qz}$  taking place at conditions of 600-750 °C and <7 kbar. Zircon and monazite U-Th-Pb geochronology was performed for the mafic and surrounding rocks. Zircon core dates from the mafic rock spread along concordia from ca. 1.7 to 1.0 Ga with a cluster at  $1520 \pm 17 \text{ Ma}$ , which is interpreted as the protolith crystallization age. Zircon rim dates are in the interval 660-590 Ma, with a weighted average of  $603.5 \pm 6.8 \text{ Ma}$  for the

youngest cluster. Monazite and metamorphic zircon ages from the host rocks are older at ca. 630 Ma. Zircon rims REE patterns as well as clinopyroxene and amphibole inclusions indicate that the age of the metamorphism of  $603.5 \pm 6.8$  Ma is related to the decompression event. The significant time span between protolith crystallization and metamorphism (ca. 800 Ma), the lack of evidence of a collision in this period, and the bulk-rock chemistry (typical MORB) suggest a continental basalt/gabbro origin. The mafic magma intruded the 2.1 Ga granitic country rocks at ca. 1.5 Ga, and volcanoclastic sediments were deposited on this basement by 800 Ma. The sequence was involved in a collision and reached the pressure peak conditions at ca. 630 Ma. The geothermal gradient reconstructed from the Grt-Cpx amphibolite does not necessarily indicate subduction, and therefore the Pouso Alegre should not be used as suture marker.

## **7.4 Reconstrução dos múltiplos estágios P-T-t de rochas máficas retrometamorfisadas: subducção versus colisão no orógeno Brasília Meridional (SE Brasil) In: Geosudeste 2017, 2017, Diamantina. Anais Geosudeste 2017.**

Mahyra Tedeschi<sup>1,2,3\*</sup>, Pierre Lanari, Daniela Rubatto, Antônio Pedrosa-Soares, Jörg Hermann, Ivo Dussin, Marco Aurélio P. Pinheiro, Anne-Sophie Bouvier, Lukas Baumgartner

<sup>1</sup> Programa de Pós-Graduação em Geologia, Universidade Federal de Minas Gerais, Belo Horizonte, Brasil; mahyratedeschi@gmail.com

<sup>2</sup> Institute of Geological Sciences, Universität Bern, Bern, Suíça

<sup>3</sup> Companhia de Pesquisa de Recursos Minerais, Belo Horizonte, MG, Brasil

A identificação de marcadores de zonas de subducção tais como rochas máficas metamorfisadas em cinturões orogênicos requer que os gradientes paleo-geotermiais sejam obtidos ao longo de estimativas pressão-temperatura-tempo (P-T-t). Entretanto, por serem elementos subordinados em sequências supracrustais, principalmente em orógenos precambrianos fortemente deformados, metamorfisados e erodidos, tornam desafiadora a reconstrução geodinâmica desses ambientes tectônicos, principalmente, diante da escassez de fases indicativas da sua condição de alta pressão. Na região de Pouso Alegre, na porção meridional do Orógeno Brasília, rochas metamáficas afloram como lentes e boudins entre unidades crustais gnaissificadas. Um desses metamafitos, previamente considerado um eclogito retrometamorfisado (retroeclogitos), principalmente em função de sua característica composicional, com granada e clinopiroxênio, e texturais, com reações retrometamórficas definidas por corona de plagioclásio ao redor de granada e simplectita formada a partir da quebra de clinopiroxênio onfacítico ( $\text{Omp} + \text{Qz} + \text{H}_2\text{O} \rightarrow \text{Cpx} + \text{Amp} + \text{Pl} + \text{Qz}$ ), foi investigado. A paragênese de pico metamórfico, a partir de modelagem termodinâmica com THERIAK-DOMINO e química mineral em granada e onfacita ( $\text{Jd}_{20}$ ), pela composição reconstituída a partir dos mapas composicionais, utilizando XMapTools, e termometria Zr em rutilo registram condições de  $690 \pm 35$  °C e  $13,5 \pm 3,0$  kbar. A retrogressão para simplectita e corona foi estimada em  $595 \pm 25$  °C e  $4,8 \pm 1,5$  kbar e o balanço de massa aponta que as reações foram sincrônicas. Análises U-Pb em zircão (LA-ICPMS e SIMS) forneceram uma idade de ca. 1,5 Ga para a cristalização e ca. 600 Ma, correlacionada ao estágio de retrogressão. Idades de metamorfismo em ca. 630 Ma foram obtidas nas rochas encaixantes riacianas (LA-ICP-MS em zircão), no sil-grt gnaisse (U-Th-Pb em monazita), e em parte dos grãos de zircão da rocha metamáfica, e são associadas ao pico de pressão. Os valores máximos de pressão em torno de 14 kbar e o alto gradiente geotermal ( $\sim 500$  °C/GPa), não necessariamente indicam um metamorfismo relacionado à subducção, mas, provavelmente, condições de metamorfismo relacionadas a colisão continental.

## **7.5 Crosta juvenil arqueana no embasamento (Paranapanema) do orógeno Brasília Meridional: primeiros dados U-Pb e Lu-Hf (LA-ICPMS) em zircão de ortogranulito In: Geosudeste 2017, 2017, Diamantina. Anais Geosudeste 2017.**

Mahyra Tedeschi\*, Antônio Pedrosa-Soares, Ivo Dussin, Marco Aurélio P. Pinheiro, Cristiano Lana

\*Programa de Pós-Graduação em Geologia, Universidade Federal de Minas Gerais, Belo Horizonte, Brasil; mahyratedeschi@gmail.com; Companhia de Pesquisa de Recursos Minerais, Belo Horizonte, MG, Brasil

O reconhecimento de blocos continentais antigos é imprescindível para a reconstrução paleogeográfica e o entendimento dos processos geodinâmicos edificadores de crosta no tempo e espaço. Na porção sul da Província Tocantins, o Orógeno Brasília Meridional (OBM), tem sua edificação atribuída à colisão dos blocos Paranapanema e São Francisco, resultando numa pilha de

nappes durante o Neoproterozoico. Neste cenário, o bloco Paranapanema, delimitado a partir de estudos gravimétricos, permanece com sua infraestrutura obscurecida pelas unidades da Bacia do Paraná e pelo metamorfismo granulítico de alta temperatura (UHT) da Nappe Socorro-Guaxupé. Esta nappe incluiria um arco magmático neoproterozoico do Orógeno Brasília Meridional. Nos arredores de Botelhos foi coletado um ortognaisse migmatítico para investigação petrocronológica. Suas bandas máficas são constituídas por cpx + opx + hbl + pl ± bt, foliado, com trama nematoblástica fina a média. As bandas félsicas exibem tons verdes e composição charnoquítica. Análises U-Pb (LA-ICP-MS) em zircão forneceram dados com espalhamento ao longo da Concórdia, feição comum a rochas submetidas a metamorfismo UHT. O espalhamento contínuo mais antigo é registrado entre ca. 2,6 Ga até ca. 1,9 Ga, seguido por um intervalo sem registro de idade sucedido por novo agrupamento expressivo entre 700 Ma e 600 Ma. Os núcleos dos zircões do agrupamento mais antigo fornecem uma idade  $^{207}\text{Pb}/^{206}\text{Pb}$  de média ponderada de  $2559 \pm 18$  Ma (n=4), interpretada como a idade de cristalização do protólito magmático, corroborado pelos valores das razões iniciais  $^{176}\text{Hf}/^{177}\text{Hf}(t)$  para grãos distribuídos ao longo do conjunto. Os valores de  $\epsilon\text{Hf}$  (2550 Ma) variam entre +11,15 e +5,78, indicando uma origem juvenil para o protólito. As análises de sobrecrescimentos e de cristais metamórficos neoformados indicam a presença de dois grupos: o primeiro, mais abundante, com idades entre 600- 700 Ma, relacionado ao metamorfismo brasileiro, e o segundo, envolvendo 15 % dos grãos, registra idades entre ca. 2,4 Ga e 2,3 Ga para um evento metamórfico sideriano. Esses dados evidenciam a presença de crosta juvenil neoarqueana (2,55 Ga) e um evento metamórfico sideriano anteriormente desconhecidos na Nappe Guaxupé, revelando exposição do bloco Paranapanema.



## 8 Appendices

# **Appendix I**

## **Bulk rock chemistry**

Table 1: Bulk rock chemistry – chapter 3

Sample ID		C-716-B	C-833-B	C-838-A	C-716-1	C-838-1	C-833-A	C-838-2	C-716-2	C-833-2	C-838-B	C-833-3	C-838-4	C-1013-2	C-1013-B	C-716
Rock type	Unit	mafic enclave	mafic layer	Banded mafic granulite	Banded mafic granulite	Banded mafic granulite	Banded mafic granulite	(opx)- (cpx)-hbl-bt leucosome	(opx)- (cpx)-hbl-bt leucosome	(opx)- (cpx)-hbl-bt leucosome	hbl-bt leucosome	hbl-bt leucosome	hbl-bt leucosome	hbl-bt leucosome	bt-ms leucosome	hbl-bt leucosome
SiO <sub>2</sub>	(wt%)	47.9	46.8	49.8	57.1	68.4	64.0	62.8	68.0	70.5	71.8	72.9	74.5	66.8	70.5	68.8
Al <sub>2</sub> O <sub>3</sub>	(wt%)	10.3	16.3	15.7	16.9	12.0	15.1	17.7	16.2	15.7	14.7	14.1	13.4	16.1	15.1	15.3
Fe <sub>2</sub> O <sub>3t</sub>	(wt%)	12.0	13.3	11.6	8.6	8.0	5.6	4.3	11.7	2.5	1.5	1.7	2.3	3.9	3.0	3.8
FeO <sub>t</sub>	(wt%)	10.8	12.0	10.4	7.7	7.2	5.1	3.8	1.6	2.3	1.3	1.5	2.1	3.5	2.7	3.5
CaO	(wt%)	12.0	9.4	7.8	7.5	3.2	3.5	4.3	2.8	3.3	1.9	1.5	2.8	2.9	1.8	2.5
MgO	(wt%)	12.9	6.8	5.4	2.9	3.3	2.8	2.0	0.9	1.3	0.6	0.6	1.2	1.1	0.7	0.7
TiO <sub>2</sub>	(wt%)	1.2	2.5	1.9	1.3	0.9	0.6	0.8	0.3	0.2	0.2	0.3	0.3	0.6	0.5	0.5
P <sub>2</sub> O <sub>5</sub>	(wt%)	0.1	0.4	0.8	0.3	0.2	0.1	0.6	0.2	0.1	0.1	0.0	0.1	0.2	0.1	0.1
Na <sub>2</sub> O	(wt%)	1.8	3.4	3.6	3.9	3.0	3.9	4.4	3.2	4.1	3.2	2.8	3.8	3.3	3.0	3.0
K <sub>2</sub> O	(wt%)	1.3	1.3	2.0	1.0	1.3	2.1	3.0	5.1	2.3	4.9	5.5	1.3	4.5	4.9	4.8
MnO	(wt%)	0.2	0.2	0.2	0.2	0.1	0.1	0.1	0.0	0.0	0.0	0.0	0.0	0.0	0.0	0.0
Total	(wt%)	99.6	100.4	98.7	99.7	100.4	97.9	99.9	98.5	100.0	99.0	99.4	99.7	99.5	99.6	99.6
LOI		1.1	0.5	0.9	1.1	0.2	0.6	0.9	0.8	0.9	0.6	0.6	0.6	0.6	0.7	0.6
Ba	ppm	194.0	283.0	994.0	173.0	533.0	697.0	988.0	1928.0	694.0	1488.0	2185.0	401.0	1369.0	2031.0	1393.0
Ce	ppm	39.0	45.7	122.0	118.2	76.1	58.1	193.5	39.7	43.3	38.2	29.9	82.6	46.2	59.2	135.6
Co	ppm	71.1	51.1	67.1	76.9	102.8	108.0	48.1	102.1	115.3	161.6	155.9	134.2	89.4	164.0	115.8
Cs	ppm	0.8	<0.05	0.1	0.4	0.1	0.6	0.2	1.3	0.8	0.2	0.3	0.3	0.6	1.1	1.1
Cu	ppm	106.0	81.0	44.0	134.0	36.0	70.0	6.0	14.0	22.0	6.0	<5	8.0	13.0	19.0	19.0
Dy	ppm	4.4	6.0	7.1	10.6	6.1	1.4	3.3	1.0	0.8	0.5	0.6	1.0	1.3	1.1	1.4
Er	ppm	2.2	3.3	3.6	5.6	3.4	0.8	1.4	0.5	0.4	0.2	0.4	0.5	0.7	0.6	0.7
Eu	ppm	1.5	2.3	2.8	1.7	1.7	1.0	2.0	1.2	1.0	1.1	1.1	1.4	1.3	1.5	1.3
Ga	ppm	14.8	21.6	21.7	24.7	17.0	20.5	23.5	17.7	18.5	17.3	15.4	17.1	18.9	18.1	20.1
Gd	ppm	5.3	6.7	9.7	12.1	7.2	2.5	6.9	1.7	1.4	1.2	0.9	2.1	2.3	1.8	3.3
Hf	ppm	2.0	4.8	6.4	4.8	11.7	4.6	5.3	3.2	2.7	2.5	5.9	5.3	6.2	4.8	8.4
Ho	ppm	0.8	1.2	1.3	2.0	1.2	0.3	0.6	0.2	0.1	0.1	0.1	0.2	0.2	0.2	0.2
La	ppm	8.7	11.5	52.7	44.2	33.7	29.8	102.3	16.1	20.5	22.0	13.7	42.5	18.0	41.6	80.5
Lu	ppm	0.3	0.4	0.5	0.7	0.4	0.1	0.1	<0.05	0.1	<0.05	0.1	0.1	0.1	0.1	0.1
Mo	ppm	<2	2.0	<2	4.0	3.0	3.0	2.0	3.0	3.0	3.0	4.0	4.0	3.0	4.0	3.0
Nb	ppm	5.6	10.4	17.3	29.7	16.1	6.1	12.5	5.5	4.9	<0.05	7.4	5.8	8.3	6.8	5.8
Nd	ppm	23.3	26.5	57.8	59.3	35.5	20.4	68.2	13.9	12.7	12.5	8.7	25.3	17.6	18.2	38.6
Ni	ppm	197.0	53.0	97.0	24.0	73.0	107.0	15.0	18.0	23.0	17.0	11.0	23.0	8.0	13.0	17.0
P	ppm	423.3	1662.7	3334.1	1422.7	855.3	632.8	2679.5	990.6	349.1	497.5	192.0	305.5	877.2	549.9	580.4
Pr	ppm	5.2	5.9	14.7	14.7	8.8	5.9	19.7	4.0	4.0	3.7	2.7	7.9	4.9	5.7	12.5
Rb	ppm	39.9	10.1	38.5	12.9	22.5	94.8	62.5	135.9	52.8	119.0	128.9	37.1	120.3	139.2	141.3
Sm	ppm	5.1	6.2	10.5	12.6	7.0	3.0	8.9	2.2	1.6	1.6	1.2	2.9	2.8	2.4	4.4
Sn	ppm	2.0	2.3	<0.3	5.8	1.5	<0.3	1.2	0.6	0.7	<0.3	0.9	0.5	1.0	<0.3	<0.3
Sr	ppm	294.0	461.0	647.0	521.0	311.0	501.0	555.0	531.0	507.0	591.0	461.0	348.0	431.0	512.0	408.0
Ta	ppm	0.1	0.6	<0.05	1.4	0.8	<0.05	0.4	0.5	0.8	<0.05	1.2	0.7	0.5	<0.05	<0.05
Tb	ppm	0.8	1.0	1.4	1.9	1.1	0.3	0.8	0.2	0.2	0.1	0.1	0.2	0.3	0.2	0.4
Th	ppm	0.9	2.4	2.6	4.9	0.7	1.8	10.0	0.7	1.4	<0.1	1.6	4.8	0.4	7.1	13.8
Ti	ppm	6954.2	15227.3	11270.6	7673.6	5095.8	3537.1	4856.0	1678.6	1259.0	1438.8	1858.5	2038.3	3537.1	2697.8	2937.6
Tm	ppm	0.3	0.4	0.5	0.8	0.5	0.1	0.2	0.1	0.1	<0.05	0.1	0.1	0.1	0.1	0.1
U	ppm	0.2	0.7	0.3	0.7	0.4	0.2	0.3	0.4	2.1	0.1	0.5	0.5	0.3	0.8	0.6
V	ppm	203.0	262.0	184.0	167.0	40.0	63.0	39.0	<5	<5	<5	<5	<5	27.0	54.0	39.0
Zn	ppm	87.0	50.0	114.0	90.0	114.0	49.0	61.0	31.0	12.0	36.0	10.0	17.0	45.0	32.0	39.0
Zr	ppm	29.0	169.0	247.0	123.0	416.0	139.0	189.0	97.0	78.0	33.0	195.0	160.0	232.0	225.0	323.0
W	ppm	48.5	49.2	163.3	350.4	608.9	559.5	263.4	676.0	769.0	1006.0	1103.0	921.5	592.2	1011.0	691.2
Y	ppm	20.4	29.2	36.2	51.3	30.7	7.6	14.9	4.7	3.9	2.2	3.5	4.6	6.2	6.0	6.4
Yb	ppm	1.9	2.8	3.3	5.1	2.7	0.7	1.0	0.3	0.4	0.1	0.5	0.5	0.6	0.5	0.6

Table 2: Bulk rock chemistry – chapter 3

Sample ID		MT-13	MT-17	MT-19	MT-20
Rock type		Cpx-Grt amphibolite	migmatitic Grt- Amp gneiss	Aln-bearing Bt granite	Bt gneiss
<b>SiO2</b>	wt%	50.3	62.5	73.8	67.4
<b>Al2O3</b>	wt%	11.2	14.6	14.9	14.3
<b>Fe2O3</b>	wt%	15.0	9.2	1.4	6.1
<b>CaO</b>	wt%	12.6	4.6	1.6	2.7
<b>MgO</b>	wt%	8.06	0.73	0.41	1.64
<b>TiO2</b>	wt%	1.80	1.36	0.21	0.79
<b>P2O5</b>	wt%	0.154	0.562	0.050	0.218
<b>Na2O</b>	wt%	1.42	2.47	2.93	2.29
<b>K2O</b>	wt%	0.12	3.05	4.56	3.57
<b>MnO</b>	wt%	0.25	0.11	0.01	0.08
<b>Total</b>	wt%	100.90	99.23	99.90	99.12
<b>LOI</b>		0.02	-0.04	0.77	0.94
<b>Ba</b>	ppm	25.0	1643.0	2030.0	750.0
<b>Ce</b>	ppm	14.1	207.3	38.9	107.0
<b>Co</b>	ppm	131.0	104.7	219.4	74.5
<b>Cs</b>	ppm	0.06	2.32	1.11	2.97
<b>Cu</b>	ppm	284	31	5	26
<b>Dy</b>	ppm	6.65	17.16	0.72	6.28
<b>Er</b>	ppm	4.12	9.58	0.34	3.27
<b>Eu</b>	ppm	1.35	3.39	0.82	1.46
<b>Ga</b>	ppm	19.8	30.9	17.6	24.2
<b>Gd</b>	ppm	6.38	20.48	1.44	8.09
<b>Hf</b>	ppm	2.51	20.04	1.8	7.86
<b>Ho</b>	ppm	1.42	3.44	0.12	1.19
<b>K</b>	ppm	996.24	25321.10	37857.12	29638.14
<b>La</b>	ppm	7.0	97.6	17.0	57.5
<b>Lu</b>	ppm	0.49	1.25	<0.05	0.42
<b>Mo</b>	ppm	<2	4	4	3
<b>Nb</b>	ppm	4.15	28.95	1.49	16.12
<b>Nd</b>	ppm	13.5	106.2	15.0	47.5
<b>Ni</b>	ppm	248	12	12	32
<b>P</b>	ppm	672.06	2452.57	218.20	951.35
<b>Pr</b>	ppm	2.66	25.88	4.53	12.35
<b>Rb</b>	ppm	1.2	113.8	85.3	146.4
<b>Sm</b>	ppm	4.0	21.0	2.2	8.7
<b>Sn</b>	ppm	<0.3	<0.3	<0.3	<0.3
<b>Sr</b>	ppm	123	413	709	226
<b>Ta</b>	ppm	<0.05	<0.05	<0.05	<0.05
<b>Tb</b>	ppm	1.03	3.02	0.19	1.2
<b>Th</b>	ppm	0.7	7.9	7.1	10.6
<b>Ti</b>	ppm	10791	8153.2	1258.95	4736.05
<b>Tl</b>	ppm	<0.5	<0.5	<0.5	<0.5
<b>Tm</b>	ppm	0.53	1.31	<0.05	0.43
<b>U</b>	ppm	0.13	1.71	0.93	2.01

**Appendix II**  
**Mineral Chemistry**  
**(EMPA)**

Table 1: Composition of mineral inclusions – Clinopyroxene-garnet amphibolite (MT-13). Mineral abbreviations from Whitney and Evans (2010). – Chapter 4

Mineral	Host mineral	Domain	SiO <sub>2</sub>	TiO <sub>2</sub>	Al <sub>2</sub> O <sub>3</sub>	FeO	MnO	MgO	CaO	Na <sub>2</sub> O	K <sub>2</sub> O	Total	n°
			(wt%)	(wt%)	(wt%)	(wt%)	(wt%)	(wt%)	(wt%)	(wt%)	(wt%)	(wt%)	
Amp	Zrn	white	48.57	0.49	9.36	13.71	0.00	12.74	11.41	1.52	0.58	98.38	51
	Zrn	white	46.17	0.85	9.99	13.11	0.00	12.21	11.39	1.86	0.56	96.14	41
	Zrn	oscillatory	45.22	1.73	12.58	14.75	0.00	9.63	11.13	2.26	0.80	98.10	17
	Rt		45.99	2.80	11.52	10.26	0.09	12.72	11.72	1.79	0.73	97.62	11
	Rt		44.90	3.22	12.85	11.02	0.05	12.24	11.38	2.13	0.89	98.68	13a
	Rt		45.48	2.64	12.16	10.69	0.09	12.88	11.57	1.92	0.93	98.36	19
	Grt		46.31	0.79	10.31	13.72	0.11	12.25	11.28	1.77	0.51	97.05	XM-1
	Grt		46.02	0.98	11.02	13.97	0.11	13.25	10.97	1.83	0.36	98.50	XM-2
	Grt		46.48	0.80	10.10	13.70	0.11	12.35	11.24	1.75	0.51	97.05	XM-3
			47.40	0.74	9.28	13.43	0.11	12.82	11.26	1.65	0.45	97.15	XM-4
Cpx	Zrn	white	51.99	0.13	1.47	9.21	0.15	12.72	22.68	0.40	0.01	98.76	50
	Zrn	white	55.72	0.03	0.67	8.18	0.00	12.33	22.40	0.42	0.02	99.76	45
	Zrn	dark/oscillatory	51.64	0.10	5.03	8.24	0.00	10.95	21.16	1.17	0.01	98.30	49
	Rt		52.57	1.40	2.72	7.89	0.16	12.89	22.64	0.69	0.01	100.96	4
	Rt		51.94	0.81	3.50	8.64	0.12	11.80	22.24	0.68	0.01	99.74	12
	Grt		51.03	0.10	4.71	8.90	0.13	12.35	20.83	0.73	0.01	98.80	XM-5
			52.64	0.10	2.40	8.82	0.14	13.14	22.05	0.51	0.01	99.80	XM-6
Grt	Rt		38.90	0.69	21.28	25.91	1.01	4.72	8.39	0.02	0.01	100.92	5(0)
	Rt		38.74	0.48	21.87	26.27	1.02	4.64	8.36	0.00	0.01	101.39	5(0)
	Rt		39.01	0.06	21.90	25.37	0.93	5.00	9.00	0.04	0.01	101.31	1
	Zrn	white	39.55		21.78	26.44	1.05	4.19	7.05	0.00	0.03	100.09	2
Bt	Rt		37.59	4.63	17.83	13.22	0.02	14.03	0.04	0.35	11.48	99.19	23(3)
	Rt		37.16	4.78	16.73	13.87	0.01	13.67	0.03	0.45	12.09	98.79	23(0)
	Zrn	white	36.96	2.29	15.88	15.30	0.04	13.88	0.02	0.67	11.63	96.67	24(3)
	Zrn	white	36.52	2.26	16.65	15.45	0.05	13.78	0.01	0.68	11.46	96.86	24(0)

Table 2: Representative mineral compositions – Migmatitic sillimanite-garnet gneiss (MT-22A) - Chapter 4. Mineral abbreviations from Whitney and Evans (2010).

Mineral	SiO <sub>2</sub>	TiO <sub>2</sub>	Al <sub>2</sub> O <sub>3</sub>	FeO	MnO	MgO	CaO	Na <sub>2</sub> O	K <sub>2</sub> O	Total	Alm	Sps	Pyr	Gro
	(wt%)	(wt%)	(wt%)	(wt%)	(wt%)	(wt%)	(wt%)	(wt%)	(wt%)	(wt%)				
Grt	37.14	0.02	21.25	39.06	1.73	1.33	1.44	0.04	0.00	102.01	86.7	3.9	5.2	4.1
	37.65	0.00	20.98	38.06	1.73	1.83	1.35	0.02	0.02	101.63	84.9	3.9	7.3	3.9
	37.24	0.00	20.45	37.20	1.71	1.86	1.37	0.00	0.01	99.85	84.5	3.9	7.5	4.0
	37.29	0.00	21.08	38.35	1.55	1.74	1.31	0.00	0.01	101.33	85.8	3.5	7.0	3.7
	37.33	0.04	21.04	38.22	1.73	1.88	1.60	0.05	0.00	101.88	84.2	3.9	7.4	4.5
	37.42	0.00	20.83	38.51	1.90	1.18	1.77	0.02	0.01	101.64	85.9	4.3	4.7	5.1
	37.43	0.00	20.99	37.64	1.75	1.38	1.81	0.00	0.00	101.01	85.2	4.0	5.6	5.3
	37.36	0.03	21.14	39.30	1.69	1.42	1.88	0.01	0.00	102.82	85.5	3.7	5.5	5.2
	37.13	0.01	21.21	38.97	1.70	1.47	1.97	0.00	0.03	102.49	85.0	3.8	5.7	5.5
37.73	0.00	20.82	39.13	1.84	1.40	1.27	0.03	0.00	102.22	86.5	4.2	5.6	3.7	
Ms	45.29	0.15	34.70	1.61	0.02	0.42	0.02	0.29	9.49	91.99				
	45.89	0.34	34.01	1.63	0.03	0.61	0.02	0.45	10.01	92.99				
	46.78	0.25	35.39	1.15	0.00	0.44	0.02	0.42	10.41	94.85				
	47.29	0.14	35.39	1.20	0.03	0.52	0.08	0.41	10.35	95.41				
weathered mineral (PI?)	33.79	0.01	41.54	0.13	0.00	0.04	0.16	0.18	0.46	76.30				
	34.18	0.02	38.58	0.16	0.00	0.05	0.13	0.10	0.42	73.63				
	25.05	0.00	31.12	0.05	0.00	0.00	0.05	0.08	0.09	56.45				
	33.89	0.00	42.86	0.11	0.03	0.01	0.08	0.11	0.14	77.21				
	36.41	0.02	41.46	0.13	0.03	0.03	0.19	0.26	1.65	80.18				
	31.01	0.00	38.74	0.19	0.09	0.02	0.22	0.08	0.30	70.64				
	33.54	0.00	41.41	0.15	0.00	0.02	0.19	0.27	0.19	75.76				
	32.80	0.00	41.26	0.04	0.03	0.00	0.14	0.06	0.26	74.59				
34.68	0.00	42.59	0.16	0.07	0.02	0.12	0.07	0.32	78.02					

Table 3: Representative mineral compositions – Migmatitic sillimanite-garnet gneiss (MT-17) – Chapter 4. Mineral abbreviations are from Whitney and Evans (2010).

Mineral	SiO <sub>2</sub>	TiO <sub>2</sub>	Al <sub>2</sub> O <sub>3</sub>	FeO	MnO	MgO	CaO	Na <sub>2</sub> O	K <sub>2</sub> O	Total
	(wt%)	(wt%)	(wt%)	(wt%)	(wt%)	(wt%)	(wt%)	(wt%)	(wt%)	(wt%)
Amp	38.55	1.86	12.04	28.07	0.09	3.11	11.05	1.41	1.72	97.90
	39.63	1.97	12.25	25.65	0.11	3.69	10.95	1.46	1.80	97.52
	39.83	1.76	12.31	26.01	0.06	3.65	11.07	1.36	1.72	97.76
	40.13	1.86	12.07	25.57	0.09	3.88	10.96	1.27	1.72	97.55
	39.86	1.74	12.98	25.41	0.06	3.75	11.32	1.45	1.70	98.24
	40.47	1.77	12.27	25.19	0.07	3.87	11.22	1.16	1.73	97.74
	41.10	1.61	13.42	25.12	0.06	3.58	11.11	0.98	1.78	98.75
	41.33	1.61	13.57	25.24	0.07	2.80	10.88	0.80	1.73	98.03
	39.91	2.07	12.14	25.54	0.11	3.74	10.98	1.31	1.76	97.57
	39.77	2.02	12.28	25.68	0.12	4.01	11.02	1.21	1.80	97.91
	39.75	2.09	11.98	25.09	0.09	3.85	11.31	1.31	1.78	97.26
	39.84	2.00	12.62	25.74	0.09	3.88	10.98	1.44	1.79	98.38
	39.93	2.02	11.97	25.29	0.15	3.80	11.16	1.21	1.81	97.34
	39.39	2.01	12.25	25.44	0.07	3.66	10.95	1.56	1.78	97.10
	39.40	1.91	12.52	25.83	0.21	3.69	11.06	1.31	1.79	97.72
	39.77	1.81	12.17	26.26	0.08	3.77	10.97	1.40	1.73	97.96
	39.88	1.87	12.35	25.48	0.20	3.85	11.00	1.44	1.74	97.80
	39.17	1.92	12.88	25.52	0.08	3.42	11.14	1.24	1.93	97.30
	39.77	1.97	12.30	26.35	0.04	3.47	11.16	1.30	1.76	98.11
	Bt	35.04	3.73	15.96	28.43	0.07	4.82	0.02	0.12	8.87
34.81		3.73	15.98	27.06	0.03	4.90	0.05	0.14	8.83	95.52
34.82		3.80	15.36	28.02	0.00	5.06	0.05	0.15	8.70	95.96
34.68		3.91	15.30	28.56	0.08	5.11	0.03	0.08	8.73	96.47
34.66		4.70	14.52	28.46	0.06	4.45	0.03	0.13	8.60	95.61
35.06		4.51	14.89	27.02	0.14	4.63	0.04	0.01	8.81	95.09
35.19		4.35	15.20	27.62	0.00	4.94	0.00	0.12	8.80	96.21
34.52		4.36	15.49	27.69	0.06	4.89	0.03	0.10	9.05	96.18
35.28		4.20	15.42	27.00	0.01	4.90	0.06	0.06	8.86	95.79
35.41		4.34	15.36	28.12	0.00	4.88	0.04	0.15	8.64	96.94
33.79		4.27	14.66	28.21	0.10	4.96	0.08	0.05	8.53	94.64
34.86		3.93	14.67	27.00	0.06	5.61	0.05	0.04	8.94	95.15
34.47		3.72	15.66	26.29	0.05	5.36	0.07	0.00	8.82	94.44
34.86		3.84	15.58	26.32	0.11	5.50	0.05	0.02	9.05	95.31
34.93		4.14	14.76	26.66	0.04	5.05	0.02	0.05	8.82	94.47
34.55		3.87	15.60	27.00	0.09	5.25	0.03	0.06	8.84	95.28
34.09		4.07	15.19	27.89	0.09	5.04	0.05	0.05	8.72	95.19



Table 3: Representative mineral compositions. Migmatitic amphibole-garnet gneiss (MT-17) Cont. – Chapter 4

Mineral	SiO <sub>2</sub>	TiO <sub>2</sub>	Al <sub>2</sub> O <sub>3</sub>	FeO	MnO	MgO	CaO	Na <sub>2</sub> O	K <sub>2</sub> O	Total
	(wt%)	(wt%)	(wt%)	(wt%)	(wt%)	(wt%)	(wt%)	(wt%)	(wt%)	(wt%)
Grt	36.52	0.03	21.09	29.47	0.97	1.10	10.69	0.04	0.01	99.92
	37.17	0.07	21.57	29.04	0.81	0.98	10.47	0.06	0.00	100.17
	37.51	0.00	21.09	30.25	1.35	0.65	9.60	0.03	0.05	100.51
	38.01	0.05	20.46	30.01	0.91	0.96	9.90	0.00	0.01	100.30
	38.27	0.04	20.45	28.80	0.71	1.27	10.45	0.07	0.01	100.06
	38.49	0.03	20.59	28.77	0.74	1.10	10.64	0.04	0.02	100.40
	38.10	0.04	20.89	29.38	0.77	1.12	10.09	0.03	0.01	100.43
	37.99	0.09	20.40	27.94	0.62	1.19	11.52	0.03	0.01	99.79
	38.46	0.06	20.53	29.03	1.10	0.92	10.53	0.03	0.00	100.67
	37.98	0.09	20.34	27.86	0.65	1.15	11.20	0.10	0.01	99.37
	37.79	0.15	20.64	29.15	1.11	0.91	10.52	0.05	0.00	100.31
	37.70	0.00	20.44	29.21	0.65	1.13	11.16	0.02	0.00	100.32
Kfs	63.40	0.00	17.91	0.00	0.00	0.00	0.04	0.82	14.23	96.39
	63.36	0.00	17.96	0.01	0.08	0.00	0.03	1.03	14.07	96.54
	63.14	0.00	17.99	0.07	0.02	0.05	0.02	0.72	14.36	96.38
	63.25	0.00	18.16	0.10	0.01	0.00	0.05	0.69	14.61	96.86
	63.33	0.00	18.21	0.00	0.01	0.01	0.02	0.93	14.39	96.90
	63.02	0.00	17.85	0.11	0.00	0.01	0.02	0.82	14.64	96.47
	63.11	0.00	17.72	0.03	0.03	0.02	0.03	1.09	13.96	95.97
	63.14	0.00	17.99	0.04	0.05	0.00	0.00	1.15	13.95	96.31
	63.04	0.00	17.93	0.10	0.00	0.03	0.01	2.41	13.94	97.46
	63.67	0.00	18.00	0.00	0.07	0.00	0.01	0.83	14.65	97.22
	63.82	0.00	17.90	0.00	0.07	0.00	0.04	0.79	14.53	97.15
Pl	61.72	0.01	22.82	0.07	0.03	0.00	5.00	8.67	0.18	98.48
	61.91	0.00	22.92	0.00	0.00	0.01	4.90	9.00	0.22	98.96
	61.22	0.02	23.10	0.01	0.00	0.00	4.87	8.72	0.13	98.06
	62.33	0.04	22.94	0.06	0.04	0.01	4.70	8.73	0.12	98.97
	63.17	0.00	22.47	0.07	0.00	0.00	3.95	9.30	0.19	99.14
	62.39	0.00	22.54	0.01	0.08	0.00	4.33	8.81	0.31	98.47
	62.46	0.04	22.86	0.02	0.01	0.01	4.79	8.99	0.25	99.41
	59.96	0.01	23.85	0.06	0.00	0.00	5.82	7.96	0.17	97.83
	59.25	0.01	24.04	0.06	0.01	0.01	5.75	8.16	0.17	97.45
	62.12	0.01	23.13	0.01	0.00	0.00	4.87	8.96	0.18	99.28
	61.79	0.00	23.31	0.10	0.00	0.00	5.30	8.44	0.17	99.12
	62.03	0.03	22.92	0.03	0.08	0.00	4.70	8.62	0.21	98.62
	62.25	0.01	23.01	0.10	0.01	0.01	4.62	8.77	0.14	98.94

**Appendix III**  
**Mineral trace elements**  
**(LA-ICP-MS)**

Table 1: Zircon trace element results determined by LA-ICP-MS - Banded mafic granulite (C-833-A)

Element	SiO <sub>2</sub> (wt%)	Y	Ti	La	Ce	Pr	Nd	Sm	Eu	Gd	Tb	Dy	Ho	Er	Tm	Yb	Lu
Grain #	Internal standard	ppm	ppm	ppm	ppm	ppm	ppm	ppm	ppm	ppm	ppm	ppm	ppm	ppm	ppm	ppm	ppm
12	32.78	1526.82	14.82	0.70	50.11	-	1.56	4.79	1.03	27.02	11.71	160.13	62.90	276.39	66.05	728.06	98.02
16	32.78	802.28	5.74	2.36	21.33	0.77	3.00	1.96	0.39	11.37	4.21	54.74	21.26	95.95	24.34	275.71	38.02
19	32.78	1330.36	<5.30	0.79	39.25	0.58	4.30	5.45	1.58	23.06	9.60	129.99	48.32	218.20	53.09	587.31	79.58
20	32.78	318.15	8.45	1.01	19.41	0.37	3.05	2.29	0.89	4.45	2.05	22.37	9.08	42.29	10.81	128.96	19.30
23	32.78	357.63	13.26	-	27.68	0.20	2.32	3.78	0.90	12.66	3.34	32.26	10.46	41.96	10.36	107.54	14.14
24	32.78	576.26	<5.20	0.56	33.79	0.36	3.44	4.77	1.53	13.75	4.33	43.24	14.00	58.11	13.33	139.83	19.72
25	32.78	239.36	<5.66	0.53	32.63	-	1.60	2.02	0.62	6.22	1.77	20.74	7.14	30.74	7.35	78.32	11.84
26	32.78	273.63	28.74	-	27.82	0.36	1.78	2.45	0.86	11.36	2.63	22.45	7.70	32.76	8.24	90.14	11.84
27	32.78	337.96	125.56	-	27.89	-	1.86	4.02	0.83	8.98	2.84	31.10	10.53	41.26	9.89	106.95	14.21
28	32.78	823.86	<5.90	0.70	11.18	-	1.45	2.86	0.94	13.73	4.89	56.09	21.84	92.98	22.07	238.69	38.08
39	32.78	192.14	9.56	1.64	19.11	1.39	7.80	2.36	1.40	5.21	1.61	15.92	5.44	22.95	6.17	78.74	13.25
40	32.78	230.08	<4.83	-	10.00	-	0.88	0.66	0.30	3.19	1.29	15.94	5.80	31.67	8.86	113.02	18.10
41	32.78	627.05	7.99	-	24.55	0.23	0.92	1.69	0.42	4.56	2.82	34.85	14.16	66.03	18.55	223.00	29.57
48	32.78	299.50	<5.85	-	21.56	0.31	1.00	0.91	0.18	3.52	2.01	22.07	8.77	37.06	9.63	101.61	15.56
49	32.78	139.89	12.50	-	16.61	-	1.46	2.29	0.37	7.56	1.14	14.16	4.32	13.90	2.72	27.18	3.46
50	32.78	454.77	9.07	0.62	32.24	0.26	4.03	4.40	1.19	11.32	3.85	38.56	13.16	52.15	12.06	128.18	19.18
54	32.78	293.61	<4.58	1.11	11.53	0.54	3.60	2.84	0.78	4.76	1.98	20.49	8.22	43.01	11.65	148.45	24.39
56	32.78	93.54	9.88	-	8.75	-	1.50	2.18	0.98	5.55	1.38	8.74	2.50	10.22	2.75	29.30	4.47
58	32.78	214.75	<5.09	-	30.68	0.22	1.27	2.91	0.59	2.91	1.81	19.40	5.99	26.82	5.95	72.73	10.39
58	32.78	1602.88	8.56	1.72	45.59	1.18	7.65	5.37	2.64	24.67	11.56	153.08	60.52	276.52	64.77	707.00	111.72
59	32.78	869.71	7.82	2.84	16.53	1.32	8.18	4.33	1.56	3.58	3.57	51.53	22.19	119.96	33.35	423.26	67.43
63	32.78	222.91	<5.25	0.40	11.86	0.14	1.57	1.31	0.31	2.01	1.28	17.29	6.03	30.07	8.00	103.20	15.24
71	32.78	1339.25	<5.40	0.34	41.18	-	2.20	4.82	0.82	23.15	10.57	136.56	53.51	243.12	58.77	664.49	87.13
73	32.78	418.65	<5.15	0.40	20.58	0.28	2.01	2.76	0.46	11.04	3.76	42.82	12.51	52.95	10.49	112.15	15.21
74	32.78	52.84	17.91	0.65	14.33	-	1.48	2.72	1.52	4.41	0.79	5.45	1.46	5.35	1.43	19.17	4.31

Table 1: Zircon trace element results determined by LA-ICP-MS - Banded mafic granulite (C-833-A)\_Cont. – Chapter 3

Element	SiO <sub>2</sub> (wt%)	Y	Ti	La	Ce	Pr	Nd	Sm	Eu	Gd	Tb	Dy	Ho	Er	Tm	Yb	Lu
Grain #	Internal standard	ppm	ppm	ppm	ppm	ppm	ppm	ppm	ppm	ppm	ppm	ppm	ppm	ppm	ppm	ppm	ppm
76	32.78	613.38	11.18	0.74	8.92	0.24	2.16	2.42	0.74	5.25	2.19	31.45	13.72	71.39	20.67	263.69	36.82
78	32.78	780.80	6.69	0.74	16.47	0.67	4.53	5.02	1.78	10.05	4.10	47.65	16.47	74.45	18.80	213.81	32.82
80	32.78	536.04	9.89	-	31.08	-	1.32	3.35	0.26	7.68	2.63	36.48	13.79	62.54	15.28	174.15	23.60
81	32.78	241.99	<5.24	0.85	21.41	0.27	3.04	3.49	1.29	7.59	2.55	21.58	6.84	28.58	6.63	79.14	12.71
81.1	32.78	168.01	66.01	-	16.66	0.18	0.99	1.77	0.88	4.32	1.31	14.04	4.18	19.54	4.94	58.63	9.39
82	32.78	296.02	10.37	0.52	23.05	0.12	1.33	2.20	0.33	6.36	2.00	22.26	7.91	39.49	10.77	141.50	20.94
83	32.78	420.05	6.57	0.64	38.89	-	1.73	3.11	0.49	9.31	2.93	31.62	11.80	49.69	12.32	145.12	20.26
87	32.78	729.60	17.13	-	38.58	0.50	4.89	5.69	1.43	15.42	4.89	47.87	15.48	63.13	13.50	145.97	22.01
88	32.78	240.61	15.65	0.32	20.87	-	0.53	1.35	0.36	4.24	1.52	19.98	6.80	30.57	8.21	105.31	15.50
89	32.78	391.96	5.44	2.54	29.01	0.53	4.39	3.63	1.04	10.50	3.54	32.05	9.79	40.25	9.52	117.42	16.84
90	32.78	749.27	<4.66	-	18.79	-	0.99	1.54	0.26	8.20	2.84	36.26	14.92	77.25	20.59	266.82	38.49
91.1	32.78	311.22	<4.82	-	39.92	0.23	1.29	2.08	0.66	4.81	2.57	24.80	9.25	37.92	9.07	100.84	13.82
91.2	32.78	298.90	8.13	0.48	23.72	0.16	0.82	1.06	0.55	5.44	1.97	22.19	8.35	39.36	9.76	118.39	18.78
93	32.78	45.20	15.14	0.69	13.40	-	1.26	1.43	0.63	2.94	0.38	3.50	1.29	5.36	1.52	16.86	3.86
94	32.78	226.61	<4.67	-	7.09	-	0.44	1.20	0.17	2.71	0.93	14.32	5.99	30.59	8.52	125.38	19.99
97	32.78	356.51	<4.81	0.32	29.74	0.15	2.62	3.63	0.80	8.96	2.78	32.08	10.48	43.92	9.83	113.60	15.57
98	32.78	248.23	11.91	0.45	33.23	-	1.51	2.96	0.40	5.40	2.22	20.90	7.28	32.20	7.67	88.10	11.95
99	32.78	460.18	17.27	-	37.94	0.25	2.89	4.70	0.80	13.54	3.39	35.30	12.18	47.60	11.91	132.95	17.50
101.1	32.78	444.58	418.75	0.43	13.61	0.28	1.63	2.22	0.32	5.59	2.49	29.52	12.90	64.22	15.74	198.05	35.46
101.2	32.78	586.51	<5.31	0.55	9.33	-	1.42	1.35	0.54	5.30	2.12	28.86	12.91	66.41	17.47	218.18	35.16
102.1	32.78	72.06	99.54	1.07	10.86	0.53	3.66	3.10	1.23	2.00	1.11	7.69	2.28	8.31	1.99	20.73	2.72
103	32.78	41.69	5.87	0.32	8.05	-	1.00	2.16	0.63	2.62	0.53	4.58	1.12	4.39	0.79	10.63	1.75
104	32.78	29.37	<5.57	-	6.93	-	0.92	1.87	0.31	5.20	0.56	4.34	0.69	3.16	0.51	4.65	0.78

Table 2: Zircon trace element results determined by LA-ICP-MS - Banded mafic granulite (C-838-A) – Chapter 3

Element	SiO <sub>2</sub> (wt%)	Ti	Y	La	Ce	Pr	Nd	Sm	Eu	Gd	Tb	Dy	Ho	Er	Tm	Yb	Lu
Grain #	Internal standard	ppm	ppm	ppm	ppm	ppm	ppm	ppm	ppm	ppm	ppm	ppm	ppm	ppm	ppm	ppm	ppm
14	32.78	9.480	222.112	-	16.711	-	1.081	1.244	0.359	3.446	1.489	17.110	6.280	28.080	7.380	88.485	12.970
15	32.78	14.680	513.782	-	30.054	0.151	1.286	2.073	0.585	7.961	3.214	35.220	12.750	57.610	14.090	165.688	23.670
17	32.78	8.970	737.095	0.878	37.797	0.614	3.335	4.030	1.557	12.406	5.533	61.630	24.896	116.280	29.780	354.271	50.020
18	32.78	24.990	261.447	0.757	17.958	-	0.979	1.094	0.358	7.874	1.758	19.520	7.107	35.220	8.860	107.902	16.110
19	32.78	12.490	1051.339	-	22.759	0.524	6.828	7.738	3.735	25.441	8.349	91.440	31.600	138.860	32.050	377.584	53.920
54	32.78	<6.00	285.800	0.536	12.839	0.436	2.037	1.359	0.624	4.919	1.240	18.970	8.454	38.180	9.180	116.114	19.290
55	32.78	57.280	981.906	1.211	20.943	0.546	4.928	7.634	2.708	14.302	7.302	71.130	26.614	113.800	25.110	286.042	43.120
56	32.78	10.670	201.658	-	5.293	0.331	-	0.806	0.246	-	0.808	12.060	5.240	28.200	7.740	101.510	19.040
57	32.78	10.370	210.871	0.536	15.355	-	0.751	1.531	-	4.988	1.165	13.770	6.121	27.540	7.380	83.109	14.080
96	32.78	9.480	365.794	19.885	48.405	4.036	15.682	3.846	0.639	5.643	2.190	25.280	10.777	50.980	13.860	179.200	29.200
108	32.78	5.810	215.324	0.371	10.652	-	0.629	0.725	0.327	-	1.100	14.530	6.290	29.660	8.160	106.588	16.230
111	32.78	6.828	626.838	0.378	25.239	-	2.653	2.202	0.576	8.730	3.510	40.800	16.334	68.180	15.470	181.763	26.461
113	32.78	10.057	313.815	0.610	20.170	0.187	1.876	1.421	0.663	6.570	1.972	22.040	9.615	39.890	10.580	128.654	19.034
126	32.78	9.990	769.663	18.337	70.753	3.778	17.781	6.536	2.622	14.800	5.781	66.040	27.597	118.310	31.360	399.292	56.807
144	32.78	10.084	653.123	1.846	31.446	1.381	7.914	5.616	2.586	14.980	4.160	50.980	20.695	88.980	22.250	273.775	40.653
145	32.78	6.896	226.537	0.688	6.534	0.318	0.466	2.284	0.222	<1.99	0.966	14.170	6.948	33.530	9.040	120.130	19.222
146	32.78	10.717	233.397	-	16.071	-	0.733	1.666	-	<2.03	1.013	17.590	7.314	30.440	8.570	104.525	14.902
166	32.78	7.306	742.767	25.998	82.609	4.582	21.167	6.408	2.372	21.570	5.492	59.440	24.472	103.190	25.070	314.485	44.371
165	32.78	13.206	234.371	0.516	16.281	0.270	0.688	1.084	0.423	4.650	1.600	14.890	7.749	32.850	8.420	107.696	15.770
163	32.78	6.862	631.026	-	18.790	-	1.077	3.099	1.210	9.940	3.788	40.680	16.368	65.940	15.730	193.799	26.737
19	32.78	-	273.425	-	19.264	-	0.977	2.062	0.428	4.070	1.961	20.770	8.814	36.840	9.390	117.232	16.687
13	32.78	-	173.073	0.438	15.628	0.183	-	1.806	0.204	3.910	1.109	13.460	5.895	23.390	5.190	63.815	9.586
12	32.78	5.241	337.859	1.789	20.254	0.435	2.508	2.202	0.677	9.600	2.013	27.420	10.290	39.700	9.400	114.686	16.322

Table 4: Zircon trace element results determined by LA-ICP-MS - Opdalite (C-838-2) – Chapter 3

Element	SiO <sub>2</sub> (wt%)	Ti	Y	La	Ce	Pr	Nd	Sm	Eu	Gd	Tb	Dy	Ho	Er	Tm	Yb	Lu
Grain #	Internal standard	ppm	ppm	ppm	ppm	ppm	ppm	ppm	ppm	ppm	ppm	ppm	ppm	ppm	ppm	ppm	ppm
10	32.78	11.41	924.31	-	37.53	0.79	7.03	10.63	4.09	27.55	7.77	79.41	28.50	104.90	25.81	301.76	38.05
12	32.78	6.47	1592.74	0.37	138.25	1.66	18.90	25.13	10.48	81.23	22.99	238.35	81.29	291.78	62.85	714.04	83.01
14	32.78	-	928.88	0.83	53.58	0.45	6.19	8.66	3.19	25.07	8.57	87.55	30.21	109.01	25.08	281.91	33.63
20	32.78	6.40	277.50	-	14.76	-	1.74	1.98	0.94	7.65	2.04	23.89	8.94	36.05	8.11	101.92	14.05
19	32.78	-	363.97	0.32	17.22	0.19	3.16	1.96	0.98	8.77	2.47	25.06	9.96	42.13	10.03	130.94	18.50
18	32.78	-	906.77	0.57	39.16	0.57	6.97	7.93	3.21	22.05	6.51	66.54	25.43	88.17	20.32	232.68	29.23
30	32.78	4.13	1064.11	0.63	70.34	0.63	10.06	15.47	6.64	46.93	13.02	132.15	45.71	169.10	38.18	423.14	52.41
59	32.78	6.14	184.40	0.64	8.67	0.34	1.90	1.97	0.72	4.44	1.20	13.14	5.70	23.14	5.53	65.60	11.08
54	32.78	9.47	513.52	0.84	20.03	-	3.36	3.76	1.79	11.50	3.96	38.73	14.14	55.12	13.66	151.46	21.55
55	32.78	5.50	680.87	-	16.54	-	0.78	2.20	0.56	5.31	3.13	37.31	17.36	82.04	20.95	276.84	40.84
56	32.78	7.82	830.12	-	27.27	0.40	7.10	8.67	3.79	25.21	6.36	63.82	23.77	86.72	19.89	220.55	30.98
72	32.78	5.46	612.91	0.53	28.58	-	1.37	2.70	0.83	10.77	3.06	38.02	14.57	60.81	14.55	187.29	26.18
70	32.78	7.90	450.40	-	11.79	-	0.71	-	0.39	6.91	2.01	29.55	13.11	57.50	15.47	210.32	29.07
73	32.78	4.97	1192.88	0.63	108.00	0.80	14.33	23.66	9.25	65.42	17.64	167.72	57.74	202.03	43.82	466.10	54.84
28	32.78	12.29	1431.74	0.93	104.46	1.56	22.34	30.72	12.34	77.18	19.87	203.69	70.06	231.69	50.17	531.16	67.12
29	32.78	5.72	667.60	2.98	34.50	1.79	11.87	8.62	2.41	14.17	4.17	46.72	17.15	73.01	17.59	219.03	30.27
98	32.78	6.18	2172.74	1.12	151.18	2.14	33.56	46.86	20.19	141.59	36.43	344.50	117.39	403.31	86.00	895.31	110.75
92	32.78	9.01	1028.53	-	69.77	0.70	10.61	15.34	5.47	43.42	12.89	129.03	44.69	162.39	34.88	390.33	47.70

Table 5: Zircon trace element results determined by LA-ICP-MS - Mafic enclave (C-716-B) – Chapter 3

Element	SiO <sub>2</sub> (wt%)	Ti	Y	La	Ce	Pr	Nd	Sm	Eu	Gd	Tb	Dy	Ho	Er	Tm	Yb	Lu
Grain #	Internal standard	ppm	ppm	ppm	ppm	ppm	ppm	ppm	ppm	ppm	ppm	ppm	ppm	ppm	ppm	ppm	ppm
1	32.78	7.34	218.07	-	7.73	-	0.46	1.72	0.26	-	0.97	14.38	5.83	27.55	6.38	80.23	13.73
3	32.78	<7.85	1288.36	-	30.75	-	1.60	3.54	0.57	17.98	6.21	93.91	35.58	152.03	34.85	388.74	59.24
5	32.78	<7.11	1305.61	0.48	33.08	0.18	2.01	3.50	0.37	16.20	5.26	85.08	31.24	137.96	32.02	352.13	53.69
6	32.78	9.65	951.99	0.63	36.75	0.29	1.81	1.77	0.40	14.45	4.41	56.42	22.17	94.79	21.59	249.08	39.86
7	32.78	14.82	1137.44	-	12.20	0.26	4.15	4.48	2.28	18.52	5.95	73.96	26.43	102.69	21.84	235.34	39.07
8	32.78	113.08	650.39	2.47	11.29	0.38	3.02	4.52	1.80	11.51	3.75	59.99	20.12	83.73	18.26	199.76	29.84
12	32.78	<7.57	1177.84	0.69	11.90	0.51	3.68	6.11	2.87	23.42	6.05	75.18	25.70	106.85	22.41	245.79	38.25
13	32.78	<7.87	87.96	-	2.98	-	-	-	-	-	0.43	4.19	2.55	11.59	2.68	36.11	7.04
17.2	32.78	11.17	556.78	-	10.04	-	1.12	2.63	1.00	7.21	2.66	37.04	16.50	72.74	17.91	192.80	34.53
17.1	32.78	12.02	127.44	0.41	5.44	0.35	-	1.34	-	4.77	0.69	9.19	3.31	16.63	4.20	55.04	9.84
20	32.78	<7.13	686.56	-	10.39	0.49	1.85	1.43	2.17	11.77	3.99	52.09	17.98	75.13	15.07	163.26	27.41
43	32.78	<6.85	616.01	-	8.64	0.34	3.40	4.62	1.86	11.67	3.88	50.73	16.28	69.74	13.05	148.90	23.74
39	32.78	<7.40	1277.96	-	32.29	0.22	2.21	2.96	0.80	23.39	7.68	105.71	40.38	167.57	36.37	393.46	61.21
35	32.78	8.92	937.90	-	10.86	-	1.56	1.70	1.35	12.99	3.77	58.56	22.79	96.34	20.97	234.55	39.32
36	32.78	20.44	689.06	-	9.32	0.35	2.54	3.15	2.22	11.12	3.86	48.86	18.13	72.00	15.19	163.54	27.03
32	32.78	7.74	1373.81	-	17.94	0.38	6.46	8.13	4.60	29.42	8.55	111.10	38.49	150.29	30.71	333.14	50.83
34	32.78	17.17	1060.51	-	17.30	0.34	5.82	6.72	3.86	27.74	9.18	107.64	37.00	144.70	30.14	336.99	49.27
27	32.78	17.16	1089.12	-	11.61	0.34	3.01	4.95	2.84	23.39	5.91	80.46	28.23	114.10	23.65	260.41	40.08
46	32.78	7.01	251.86	0.57	4.74	-	1.11	0.86	0.96	9.53	1.43	21.90	7.44	31.50	6.48	75.14	12.67
49	32.78	10.80	323.40	0.55	6.62	-	0.46	1.34	0.70	3.80	1.55	24.80	8.91	41.34	9.69	113.45	20.45
53	32.78	<7.63	1092.75	-	36.87	-	1.59	2.03	0.35	7.54	4.46	62.32	24.36	111.56	24.88	292.00	45.24
63	32.78	11.64	1046.41	-	11.79	0.39	4.28	4.57	3.24	19.76	5.63	70.16	25.79	101.83	22.09	243.21	38.30
62	32.78	<7.48	1247.15	-	30.89	0.35	2.37	5.63	1.17	20.10	6.66	91.35	32.34	138.88	30.32	336.07	52.93
61	32.78	13.52	778.74	1.13	11.21	-	4.07	4.35	2.25	16.47	4.85	58.54	20.37	81.89	17.11	191.97	29.82
60	32.78	<7.32	1120.32	0.89	29.47	0.42	2.02	2.58	0.88	18.42	6.15	81.56	30.47	132.06	29.74	332.94	48.39
58	32.78	8.24	698.72	-	8.68	-	1.70	1.96	0.84	8.66	3.02	43.45	17.84	81.70	17.68	206.24	34.41
57	32.78	<7.80	1171.35	0.41	13.08	-	1.87	3.17	1.38	11.36	4.12	65.48	26.85	116.78	26.81	289.73	45.24
55	32.78	12.01	577.14	0.84	9.15	0.32	3.04	4.21	2.29	11.32	3.40	47.68	16.61	70.00	14.05	169.13	26.36

Table 6: Zircon trace element results determined by LA-ICP-MS - Clinopyroxene-garnet amphibolite (MT-13) – Chapter 4

Element	SiO <sub>2</sub> (wt%)	Ti	Y	La	Ce	Pr	Nd	Sm	Eu	Gd	Tb	Ho	Er	Tm	Lu
Spot	Internal standard	ppm	ppm	ppm	ppm	ppm	ppm	ppm	ppm	ppm	ppm	ppm	ppm	ppm	ppm
C1	32.45	7.777	1281.113	0.093	3.112	0.143	3.039	5.630	2.364	27.686	9.268	39.161	183.230	37.648	80.761
C2	32.45	13.211	3344.052	0.085	30.709	1.304	19.060	23.834	11.015	92.957	26.854	102.670	474.486	97.433	189.841
C3	32.45	7.172	1170.319	<0.047	7.116	0.228	4.807	6.658	2.741	28.881	8.575	36.337	170.292	39.131	93.579
C4	32.45	21.074	2128.325	114.100	31.231	98.179	521.881	200.084	62.535	214.677	40.583	66.771	228.426	42.434	86.382
C5	32.45	14.400	2048.416	15.819	19.834	4.960	33.449	17.868	7.254	56.639	14.518	58.566	276.200	62.932	149.493
C6	32.45	8.698	1649.165	<0.131	13.564	0.543	6.839	6.959	4.477	29.965	10.640	47.107	224.586	50.549	129.492
C7	32.45	5.156	789.163	<0.069	5.393	0.215	3.389	4.475	1.841	15.533	5.285	21.391	110.683	25.566	61.850
C8	32.45	15.880	2395.090	12.648	18.320	9.105	56.806	32.208	11.584	69.450	19.027	69.418	333.255	73.439	155.115
C9	32.45	9.789	2050.573	0.122	6.073	0.214	4.344	8.971	3.768	47.038	15.465	68.398	321.678	66.809	132.164
C10	32.45	10.097	1380.142	0.640	4.535	0.207	2.884	4.941	2.198	26.516	8.536	41.963	211.221	46.923	102.293
C11	32.45	6.620	1320.351	5.185	9.115	4.243	27.395	16.111	6.299	39.452	10.547	38.043	182.965	41.549	93.668
C12	32.45	8.857	1277.776	0.425	6.826	0.435	5.635	6.567	2.717	25.400	7.738	34.455	173.593	39.694	92.513
CR3	32.45	7.934	1625.933	27.858	14.630	18.235	113.793	41.939	14.452	80.110	11.359	20.235	51.359	5.680	3.869
R1	32.45	<2.567	33.767	<0.065	0.915	<0.050	<0.128	0.614	0.460	2.696	0.594	0.846	2.365	0.413	0.426
R2	32.45	<2.263	17.889	<0.053	0.857	<0.066	<0.142	0.538	0.295	1.050	0.249	0.285	1.012	0.105	0.270
R3	32.45	<3.285	36.295	<0.083	0.830	<0.082	<0.463	0.456	0.632	4.002	0.743	0.826	3.101	0.451	0.426
R4	32.45	4.859	776.547	0.990	5.273	0.698	5.799	4.392	2.093	16.742	5.038	22.110	106.342	25.184	55.947
R5	32.45	6.747	474.180	26.886	4.537	23.392	124.023	50.858	12.622	44.618	8.930	18.001	71.108	17.172	45.540
R6	32.45	<2.557	638.733	0.753	6.858	0.564	4.226	3.808	2.403	17.283	4.532	19.550	91.916	20.492	47.171
R7	32.45	13.172	395.818	1.421	2.253	1.015	5.930	2.647	1.254	7.518	2.035	10.977	69.764	18.905	55.943
R8	32.45	<2.879	33.125	<0.0834	0.350	<0.060	<0.470	0.257	0.222	1.463	0.259	0.832	2.347	0.459	0.680
R9	32.45	1.835	61.445	<0.075	0.621	<0.053	0.210	0.496	0.225	2.054	0.509	1.622	7.108	1.578	5.389
R10	32.45	17.853	737.723	25.332	10.641	14.434	86.810	32.869	12.002	50.663	8.624	14.682	42.508	5.549	7.490
R11	32.45	2.003	30.240	<0.044	0.689	<0.048	0.128	0.503	0.413	2.215	0.437	0.695	2.117	0.290	0.516
R12	32.45	<2.849	36.568	<0.061	0.786	<0.057	<0.137	0.614	0.678	3.937	0.777	0.959	2.601	0.452	0.607
R13	32.45	<2.657	42.182	<0.069	0.957	<0.058	<0.162	0.991	0.452	3.513	0.791	1.168	3.285	0.453	0.696
R14	32.45	<3.526	60.025	<0.117	1.112	<0.034	<0.192	0.420	0.393	3.526	0.755	1.693	7.021	1.754	3.593
R15	32.45	2.335	134.407	<0.070	0.358	<0.058	<0.138	<0.163	<0.106	0.758	0.375	2.986	22.134	6.493	27.875
R16	32.45	<2.271	82.955	<0.047	0.686	<0.052	0.186	0.736	0.505	4.722	1.078	2.363	9.370	2.205	4.567
R17	32.45	<2.444	31.420	<0.024	0.977	<0.062	<0.302	0.788	0.537	3.288	0.530	0.628	2.323	0.314	0.514
R18	32.45	1.479	39.707	<0.0227	0.756	<0.021	0.093	0.567	0.628	4.040	0.711	1.048	3.168	0.517	0.649
R19	32.45	40.773	2299.583	48.555	57.709	29.524	175.868	71.179	33.927	109.121	22.827	55.860	231.216	45.276	99.518
R20	32.45	1.652	43.904	0.081	0.736	0.030	0.306	0.516	0.619	4.398	0.773	1.060	3.854	0.652	1.018
R21	32.45	2.034	105.189	0.270	1.365	0.282	1.408	0.938	0.912	5.747	1.106	3.061	14.856	3.515	8.874
R22	32.45	1.581	29.524	<0.027	0.673	<0.025	<0.173	0.608	0.427	2.755	0.477	0.632	2.277	0.362	0.588
R23	32.45	<2.308	27.897	<0.069	0.700	<0.049	<0.099	0.489	0.340	2.433	0.345	0.746	2.590	0.350	0.690
R24	32.45	<1.315	33.284	0.418	0.315	0.116	0.601	0.363	0.236	1.013	0.247	0.752	3.888	1.137	5.119
RC1	32.45	<3.446	104.355	<0.046	0.275	<0.072	<0.481	0.368	<0.130	0.727	0.438	2.697	17.276	4.141	15.027
RC2	32.45	8.016	912.024	<0.15123	9.079	0.292	6.924	4.865	3.156	23.796	8.601	29.766	130.437	27.971	52.292
RC4	32.45	10.450	849.406	80.105	8.897	70.063	352.938	133.288	38.908	128.334	24.527	35.498	114.343	20.667	41.284
RC6	32.45	<3.095	353.923	1.489	3.202	1.249	6.167	2.372	1.217	6.742	2.003	9.476	53.023	12.930	36.772
RC7	32.45	<5.957	492.260	<0.161	3.186	<0.146	2.002	1.990	1.183	10.790	3.991	14.352	78.202	17.798	45.033
RR19	32.45	41.712	1107.936	55.236	24.469	41.824	249.509	103.927	40.594	131.242	22.210	30.147	92.927	12.364	12.178
RR21	32.45	<2.379	29.624	<0.0455	0.560	<0.026	<0.141	<0.321	0.359	3.802	0.613	0.576	2.134	0.280	0.590



Table 7: Garnet trace element concentrations determined by LA-ICP-MS - Clinopyroxene-garnet amphibolite (MT-13) – Chapter 4

Element	SiO <sub>2</sub> (wt%)	Ti	Y	Ce	Pr	Nd	Sm	Eu	Gd	Tb	Dy	Ho	Er	Tm	Lu	Hf	Zr	Yb
Spot	Internal standard	ppm	ppm	ppm	ppm	ppm	ppm	ppm	ppm	ppm	ppm	ppm	ppm	ppm	ppm	ppm	ppm	ppm
C4	39.0	266.72	49.04	0.18	0.05	0.52	1.04	0.56	4.44	1.10	8.59	1.92	5.10	0.70	0.70	0.03	1.63	4.85
C9	39.0	391.13	36.39	0.40	0.13	1.39	1.45	0.62	3.99	0.87	6.25	1.34	3.83	0.53	0.59	5.17	180.40	3.55
C10	39.0	369.51	49.36	0.35	0.08	1.00	1.69	0.75	5.23	1.10	7.48	1.60	4.86	0.68	0.70	0.04	2.52	4.57
C14	39.0	229.79	81.17	<0.01	<0.01	0.14	0.67	0.78	9.43	2.30	16.76	3.22	7.91	0.95	0.85	<0.02	0.71	6.10
C15	39.0	382.73	41.43	0.11	0.03	0.26	0.62	0.37	3.52	0.85	6.42	1.60	5.02	0.80	1.02	0.14	3.69	5.76
C17	39.0	242.20	40.89	0.06	0.02	0.17	0.68	0.43	3.54	0.88	6.45	1.45	4.12	0.65	0.64	0.02	1.09	4.46
P16	39.0	257.13	64.13	<0.01	0.01	0.13	0.65	0.47	4.30	1.31	10.91	2.57	7.65	1.08	1.12	0.02	1.00	7.67
P19	39.0	408.20	32.56	0.04	0.17	0.82	0.80	0.45	3.16	0.78	5.34	1.22	3.08	0.46	0.51	0.03	2.24	3.26
R1	39.0	206.68	42.79	0.04	0.01	0.26	0.79	0.55	4.20	0.99	7.19	1.60	4.38	0.59	0.55	0.04	1.21	3.62
R2	39.0	211.37	48.67	0.05	0.02	0.34	0.98	0.63	5.03	1.20	8.70	1.86	5.07	0.70	0.71	0.02	1.27	4.49
R3	39.0	391.90	40.48	0.03	0.01	0.28	1.03	0.65	4.45	1.09	6.93	1.46	3.95	0.52	0.49	0.06	2.30	3.55
R5	39.0	270.18	51.43	0.04	0.02	0.30	0.86	0.63	4.95	1.16	8.55	1.89	5.48	0.76	0.75	0.03	1.56	5.20
R6	39.0	247.18	50.26	0.18	0.16	0.91	0.96	0.53	4.28	1.09	8.15	1.77	4.95	0.67	0.63	0.26	8.43	4.30
R7	39.0	311.03	148.34	0.01	0.01	0.17	0.83	0.71	7.89	2.74	24.71	5.79	16.56	2.28	2.09	0.03	1.62	15.27
R8	39.0	360.70	53.19	0.02	0.01	0.23	0.65	0.39	3.81	0.94	7.79	1.94	5.74	0.79	0.95	0.03	1.83	5.86
R11	39.0	578.78	36.86	0.07	0.03	0.51	1.14	0.65	3.96	0.82	6.08	1.38	4.14	0.63	0.68	0.07	3.78	4.08
R12	39.0	358.72	48.81	0.03	<0.00	0.22	0.74	0.41	3.67	0.90	7.14	1.74	5.20	0.74	0.63	0.02	1.48	4.71
R18	39.0	303.25	28.64	0.08	0.03	0.18	0.69	0.43	2.75	0.64	4.70	0.99	2.79	0.41	0.42	0.03	1.44	2.67

Table 8: Rutile trace element concentrations determined by LA-ICP-MS - Clinopyroxene-garnet amphibolite (MT-13) – Chapter 4

Element	Ti49 (ppm)	Al	Si	P	V	Cr	Mn	Fe	Ni	Zn	Y	Zr	Nb	Mo	Yb	Hf	Ta	W	Pb	U
Unit	Internal standard	ppm	ppm	ppm	ppm	ppm	ppm	ppm	ppm	ppm	ppm	ppm	ppm	ppm	ppm	ppm	ppm	ppm	ppm	ppm
7	593133	148.44	790.26	1.74	1186.17	588.78	1.23	956.78	10.49	1.83	1.30	604.51	612.00	20.88	0.04	19.44	28.93	20.49	0.25	0.57
8	593133	161.96	1275.59	<0.83	1005.19	548.80	0.53	1447.38	28.36	2.52	0.39	569.39	701.50	61.04	<0.02	17.25	23.40	17.21	0.33	1.08
9	593133	174.29	2248.73	<0.95	1277.90	798.36	4.26	2460.25	32.41	5.67	0.39	566.81	429.36	23.65	<0.03	15.80	19.50	5.01	0.52	1.53
10	593133	105.83	552.63	2.07	1186.89	805.73	<0.43	910.74	40.59	2.74	0.49	465.83	591.21	18.23	0.05	14.58	24.85	6.37	0.44	1.29
11	593133	122.64	715.37	2.53	1391.98	465.35	6.65	4401.65	26.16	3.20	0.54	440.69	493.63	20.75	0.02	14.26	19.49	14.28	0.45	1.33
12	593133	75.27	874.00	2.90	1146.72	803.70	0.63	871.34	18.46	4.46	4.15	500.50	470.75	19.39	0.35	16.00	18.45	8.46	0.54	1.00
13	593133	171.90	470.38	1.55	1626.20	721.75	<0.22	345.37	13.37	0.98	0.36	691.04	361.19	14.55	<0.03	23.81	17.27	6.04	0.25	0.67
14	593133	133.05	1117.25	1.67	1199.81	610.15	<0.18	1343.77	14.69	1.34	0.34	493.37	522.50	38.82	<0.02	15.25	23.45	10.57	0.35	1.12
16	593133	194.94	593.09	<2.58	1742.08	785.60	<0.77	507.79	10.13	<1.35	0.39	532.32	322.02	10.20	<0.10	14.94	23.61	10.47	0.49	1.17
17	593133	89.06	374.35	1.57	1636.57	509.44	<0.190	575.32	17.17	1.29	0.36	477.42	450.99	19.40	<0.02	16.21	22.23	5.87	0.39	1.22
18	593133	188.03	154.75	1.15	960.12	680.18	13.34	2170.82	10.48	2.52	0.38	763.48	472.06	18.19	<0.02	28.45	24.29	7.88	0.55	2.13
19	593133	147.29	88.30	1.40	975.62	576.86	<0.08	1910.46	10.15	0.74	0.37	770.22	633.98	34.11	<0.01	26.64	27.57	11.49	0.25	0.96
20	593133	158.84	365.72	1.51	941.71	815.73	104.47	13196.70	14.93	15.60	0.39	608.55	429.60	18.26	0.01	18.95	20.16	8.91	0.30	0.92
21	593133	235.71	1918.24	1.72	1384.59	837.81	<0.33	594.41	29.63	2.33	0.37	468.86	454.13	18.35	<0.02	13.96	16.00	5.63	0.41	1.26
22	593133	106.11	<71.47	1.19	1534.26	503.05	0.13	918.34	12.75	1.02	0.34	563.63	554.88	23.37	<0.03	18.55	22.29	8.30	0.14	0.61
23	593133	187.46	341.80	1.62	1349.29	684.03	<0.17	568.93	32.50	2.66	0.36	390.85	375.86	13.78	<0.02	14.01	24.88	5.08	0.41	1.38
24	593133	162.34	<100.58	1.98	1002.47	461.89	<0.17	1659.51	15.53	1.28	0.37	598.56	550.26	26.12	<0.01	17.79	22.08	7.70	0.49	1.58
25	593133	278.54	<50.03	1.22	1258.58	929.66	<0.08	653.12	12.36	0.77	0.37	509.30	422.03	10.01	<0.01	15.30	17.09	6.19	0.29	1.15

Table 9: Garnet trace element concentrations determined by LA-ICP-MS – Migmatitic sillimanite-garnet gneiss (MT-22A) – Chapter 4

Element	SiO <sup>2</sup> (ppm)	Y89	Nb93	La139	Ce140	Pr141	Nd146	Sm149	Eu151	Gd157	Tb159	Dy162	Ho165	Er167	Tm169	Yb172	Lu175
Unit	internal standard	ppm	ppm	ppm	ppm	ppm	ppm	ppm	ppm	ppm	ppm	ppm	ppm	ppm	ppm	ppm	ppm
C2	172962.22	438.85	<0.01	<0.01	0.01	0.00	0.09	0.44	0.01	4.23	3.56	54.35	16.88	62.21	10.93	75.99	9.45
C5	172962.22	328.82	<0.01	<0.01	0.01	0.01	0.16	0.75	<0.016	7.71	5.39	62.61	12.90	27.45	3.15	15.49	1.37
C6	172962.22	389.70	<0.01	<0.01	0.01	0.01	0.14	0.83	0.01	7.36	4.66	57.53	12.77	34.01	4.31	21.85	1.85
C10	172962.22	931.11	0.01	<0.01	0.01	0.00	0.07	0.59	<0.01	7.45	7.07	111.93	31.44	98.19	12.84	60.86	5.09
C15?	172962.22	633.49	0.01	0.41	1.63	0.29	1.23	0.97	0.01	4.48	3.84	65.09	23.13	102.86	20.50	155.47	20.52
C17	172962.22	316.68	<0.01	<0.01	<0.010	<0.01	0.07	0.49	<0.01	3.30	2.49	36.18	10.06	33.36	4.75	24.98	2.10
C19	172962.22	471.67	0.01	<0.01	0.00	0.00	0.07	0.39	<0.01	2.97	2.74	46.18	16.46	76.14	14.31	100.97	11.88
R1	172962.22	367.30	<0.01	<0.01	0.01	0.01	0.08	0.50	0.01	4.72	3.66	48.69	13.27	40.25	6.45	44.70	5.03
R3	172962.22	439.95	<0.02	0.03	0.11	0.02	0.16	0.49	<0.02	4.60	3.50	52.79	14.99	53.77	9.26	67.54	8.26
R4	172962.22	310.98	<0.02	<0.012	<0.012	<0.01	0.08	0.58	0.01	4.98	3.97	50.22	12.08	28.28	3.36	16.93	1.64
R7	172962.22	344.02	0.01	<0.01	0.04	0.01	0.09	0.68	0.01	4.55	3.17	38.99	9.61	29.81	4.28	23.92	2.24
R8	172962.22	301.63	<0.01	<0.01	0.00	<0.01	0.09	0.53	0.01	4.23	3.17	41.20	10.62	29.93	3.86	20.88	2.18
R9	172962.22	689.24	0.00	<0.01	0.02	0.01	0.10	0.77	<0.01	7.43	6.12	89.58	23.99	71.97	9.10	42.06	3.57
R11	172962.22	609.91	0.01	<0.01	0.01	0.01	0.09	0.74	<0.01	7.18	5.65	80.76	21.61	63.51	7.72	35.69	2.99
R12	172962.22	307.45	<0.01	<0.01	<0.006	0.00	0.09	0.50	<0.01	3.53	2.61	37.89	9.86	31.12	4.27	21.56	1.86
R13	172962.22	574.32	0.01	0.00	<0.009	0.00	0.06	0.43	<0.01	3.83	3.59	58.92	19.82	87.86	17.02	129.57	16.81
R14	172962.22	460.35	0.01	<0.01	<0.007	0.00	0.07	0.54	<0.01	4.58	3.80	56.42	15.86	53.09	7.56	41.16	3.95
R16	172962.22	231.11	<0.01	<0.01	0.00	<0.01	0.07	0.46	<0.01	2.39	1.97	27.58	7.56	24.25	3.14	16.25	1.43
R18	172962.22	336.91	0.01	<0.01	0.02	<0.01	0.10	0.61	<0.01	3.57	2.59	37.90	10.60	36.49	5.15	28.14	2.45
R20	172962.22	307.90	<0.01	<0.01	0.01	0.00	0.06	0.45	<0.01	3.27	2.58	35.65	10.05	33.15	4.63	24.42	2.15

Table 10: Monazite trace element concentrations determined by LA-ICP-MS – Migmatitic sillimanite-garnet gneiss (MT-22A) – Chapter 4

Element	P <sub>2</sub> O <sub>5</sub> (ppm)	Y	La	Ce	Pr	Nd	Sm	Eu	Gd	Tb	Ho	Er	Tm	Lu	Th
Unit	internal standard	ppm	ppm	ppm	ppm	ppm	ppm	ppm	ppm	ppm	ppm	ppm	ppm	ppm	ppm
1	128941.67	18744.13	119728.52	296065.38	33501.00	103560.44	24352.87	101.61	14977.91	2065.07	691.69	841.83	56.78	10.94	3122.54
2	128941.67	23452.19	92474.61	271191.78	33794.12	111713.69	28294.63	121.55	18424.67	2568.09	907.61	1136.79	74.86	13.76	185.32
3	128941.67	19276.56	119816.91	285509.87	32152.72	99216.41	23554.68	100.10	14953.38	2097.38	722.06	870.46	55.36	8.52	11483.49
4	128941.67	17761.86	117985.61	272882.91	31294.27	99895.67	22942.04	161.31	13630.14	1829.91	687.12	930.83	66.74	14.47	11791.29
5	128941.67	19378.08	111581.20	267767.63	30196.01	92877.12	21681.05	91.04	14041.78	1985.71	717.47	908.10	61.73	10.98	69404.24
6	128941.67	22047.10	127469.91	301625.94	34184.78	106828.45	24521.16	105.21	15691.98	2238.82	850.05	1139.30	80.13	17.34	18947.68
7	128941.67	21923.90	111915.48	257225.96	29518.40	95111.20	22313.11	99.86	14928.63	2131.91	848.44	1129.23	78.58	15.63	10377.84
8	128941.67	22232.54	100340.33	269885.44	32934.11	108562.38	26991.14	116.41	17400.21	2461.32	842.34	1039.72	66.72	11.41	3037.51
9	128941.67	21776.82	97500.92	234377.82	28883.04	104102.80	23594.36	155.83	18023.50	2357.05	885.71	1021.45	56.68	9.66	111941.43
10	128941.67	14412.78	118712.63	300395.81	33594.80	98632.82	22636.47	86.21	12755.83	1788.36	552.88	658.57	40.13	6.42	629.58
11	128941.67	14642.97	120331.82	290802.62	32314.07	92587.26	20690.15	80.67	11638.57	1670.73	549.58	689.89	45.15	8.58	5389.88
12	128941.67	18361.11	116844.27	271065.31	31506.53	99165.85	23278.09	101.16	14337.05	2028.10	698.34	858.82	54.01	9.32	8274.66
13	128941.67	26221.84	103504.19	297781.54	36838.54	115808.99	31316.50	143.70	19853.34	3034.12	1032.79	1243.47	79.43	14.62	55.21
14	128941.67	22982.79	106774.08	252877.86	29966.22	99124.79	23571.60	244.84	15944.95	2317.67	920.17	1237.03	82.52	16.61	54194.28
15	128941.67	20055.67	111401.20	268117.56	31649.73	102425.46	24058.04	102.13	15449.40	2211.16	776.72	982.69	61.81	10.24	3826.13
16	128941.67	22183.14	105345.44	263480.24	31916.07	106221.58	24827.61	111.91	16156.97	2288.40	886.44	1188.93	81.89	16.96	8525.18

**Appendix IV**  
**SIMS**  
**U-Th-Pb dating**

Table 1: Zircon SIMS U-Pb data – Clinopyroxene-garnet amphibolite (MT-13) – Chapter 4

Sample/ spot #	[U] ppm	[Th] ppm	[Pb] ppm	f <sub>206</sub> %	Isotope ratios					Ages (Ma)						Disc. % conv.
					<sup>207</sup> Pb	±s	<sup>206</sup> Pb	±s	r	<sup>207</sup> Pb	±s	<sup>207</sup> Pb	±s	<sup>206</sup> Pb	±s	
					<sup>235</sup> U	%	<sup>238</sup> U	%		<sup>206</sup> Pb	<sup>235</sup> U	<sup>238</sup> U				
MT88C@3	568	11814	201	1.32	2.5741	2	0.2159	1.27	0.6359	1349	30	1293	15	1260	15	-7.3
Mt88C@4	383	2669	165	0.54	3.1596	1.58	0.2444	1.27	0.8048	1503	18	1447	12	1410	16	-6.9
Mt88C@5	542	16536	201	1.78	2.7048	2.31	0.233	1.27	0.5515	1297	37	1330	17	1350	16	4.5
Mt88C@6	273	5127	135	2.57	2.9754	2.35	0.2477	1.29	0.5473	1363	37	1401	18	1427	16	5.2
Mt88C@7	312	3231	122	4.68	2.1376	3.45	0.1877	1.28	0.3696	1260	61	1161	24	1109	13	-13.1
Mt88C@8	381	7800	157	1.36	2.6113	2.01	0.2164	1.27	0.6320	1372	30	1304	15	1263	15	-8.7
Mt88C@9	547	15143	210	1.24	3.2829	1.59	0.2537	1.27	0.7987	1505	18	1477	12	1457	17	-3.6
Mt88C@10	235	5444	127	2.41	3.0499	3.32	0.2462	1.27	0.3827	1422	58	1420	26	1419	16	-0.2
Mt88C@11	559	13246	197	1.72	2.3921	2.09	0.2055	1.28	0.6106	1303	32	1240	15	1205	14	-8.2
Mt88C@12	274	3403	105	1.28	1.9757	2.69	0.1756	1.32	0.4921	1236	45	1107	18	1043	13	-16.9
Mt88C@13	284	6327	97	13.85	0.7504	18.81	0.1417	1.71	0.0911	-457	434	568	85	854	14	306.9
Mt88C@14	1482	62576	485	0.74	3.4333	1.7	0.2618	1.29	0.7612	1530	21	1512	13	1499	17	-2.3
Mt88C@15	211	3137	103	5.01	1.5965	11.42	0.1606	1.61	0.1413	988	214	969	74	960	14	-3
Mt88C@16	341	4402	150	0.17	2.2653	1.60	0.1918	1.50	0.9382	1331	11	1202	11	1131	16	-16.4
Mt88C@17	843	26073	320	0.06	3.4800	1.58	0.2681	1.55	0.9847	1511	5	1523	13	1531	21	1.5
Mt88C@18	554	18874	175	6.36	2.3607	15.01	0.2036	1.65	0.1096	1295	266	1231	113	1195	18	-8.5
Mt88C@19	751	23188	278	0.14	3.4084	1.83	0.2644	1.50	0.8197	1498	20	1506	15	1513	20	1.1
Mt88C@20	797	39200	309	0.06	3.5350	1.52	0.2702	1.50	0.9845	1526	5	1535	12	1542	21	1.2
MT88C@21	670	28104	275	0.04	3.4854	1.54	0.2706	1.50	0.9778	1496	6	1524	12	1544	21	3.6
Mt88R@16	96	101	126	0.35	0.7866	2.93	0.0980	1.55	0.5283	539	54	589	13	603	9	12.4
Mt88R@17	542	7322	199	0.08	2.2746	1.64	0.1895	1.53	0.9345	1362	11	1204	12	1119	16	-19.4
Mt88R@18	67	76	128	0.12	0.8155	3.54	0.0990	1.60	0.4535	594	67	606	16	609	9	2.7
Mt88R@19	174	2926	142	0.09	1.9681	1.72	0.1700	1.55	0.8989	1291	15	1105	12	1012	15	-23.3
Mt88R@20	122	1336	126	0.30	2.1199	1.98	0.1763	1.52	0.7647	1365	24	1155	14	1047	15	-25.2
Mt88R@21	61	57	131	0.15	0.7423	2.91	0.0969	1.57	0.5372	435	54	564	13	596	9	38.9
Mt88R@22	19	89	142	5.80	0.9367	15.86	0.0969	1.58	0.0993	932	294	671	81	596	9	-37.7
Mt88R@23	32	43	117	0.29	0.8109	4.24	0.1019	1.54	0.3632	519	84	603	20	625	9	21.4
Mt88R@24	76	464	127	* 0.00	1.0456	3.25	0.1133	1.80	0.5541	835	55	727	17	692	12	-18.0
Mt88R@25	99	100	131	0.95	0.7564	4.73	0.0929	1.57	0.3322	569	94	572	21	573	9	0.7

Table 1: Zircon SIMS U-Pb data – Clinopyroxene-garnet amphibolite (MT-13) – Chapter 4\_Cont.

Sample/ spot #	[U] ppm	[Th] ppm	[Pb] ppm	f <sub>206</sub> %	Isotope ratios					Ages (Ma)						Disc. % conv.
					<sup>207</sup> Pb	±s	<sup>206</sup> Pb	±s	r	<sup>207</sup> Pb	±s	<sup>207</sup> Pb	±s	<sup>206</sup> Pb	±s	
					<sup>235</sup> U	%	<sup>238</sup> U	%		<sup>206</sup> Pb	<sup>235</sup> U	<sup>235</sup> U	<sup>238</sup> U	<sup>238</sup> U		
Mt88R @26	34	145	110	0.29	0.8621	4.21	0.1053	1.87	0.4432	581	80	631	20	646	12	11.7
Mt88R @27	220	3677	104	0.17	1.8598	1.78	0.1625	1.50	0.8432	1269	19	1067	12	971	14	-25.3
Mt88R @28	129	93	131	* 0.00	0.7791	2.54	0.0994	1.87	0.7388	485	37	585	11	611	11	27.1
Mt88R @29	825	32259	334	0.12	3.4691	1.56	0.2670	1.52	0.9717	1513	7	1520	12	1526	21	1.0
Mt88R @30	96	552	129	0.76	1.3077	3.39	0.1397	2.38	0.7018	866	49	849	20	843	19	-2.8
Mt88R @31	114	203	126	* 0.00	0.7949	2.37	0.0956	1.66	0.7012	614	36	594	11	589	9	-4.4
Mt88R @32	122	69	129	0.21	0.7630	2.52	0.0980	1.57	0.6225	471	43	576	11	603	9	20.0
Mt88R @33	88	51	127	0.13	0.7841	3.76	0.0952	1.82	0.4853	594	70	588	17	586	10	-1.4
Mt88R @34	100	55	126	* 0.00	0.7503	2.26	0.0971	1.53	0.6777	453	37	568	10	598	9	33.4

Table 2: Monazite SIMS U-Th-Pb data – Migmatitic sillimanite-garnet gneiss (MT-22A) – Chapter 4

Sample/ spot #	[U] ppm	[Th] ppm	[Pb] ppm	Th/U calc	Th/U meas	f <sub>206</sub> %	Isotopes ratios						Ages							
							<sup>207</sup> Pb	±s	<sup>206</sup> Pb	±s	r	<sup>207</sup> Pb	±s	<sup>207</sup> Pb	±s	<sup>206</sup> Pb	±s	Disc. %		
							<sup>235</sup> U	%	<sup>238</sup> U	%		<sup>206</sup> Pb	%	<sup>206</sup> Pb	<sup>235</sup> U	<sup>238</sup> U	conv.			
MT1	14680	1929	1719	0.149	0.131	0.02	0.87859	1.14	0.1062	1.13	0.99078	0.06016	0.15	603.9	3.3	640.2	5.4	650.6	7.0	8.1
MT2	14174	40661	3226	4.170	2.869	0.07	0.83174	1.14	0.1020	1.13	0.99312	0.05967	0.12	571.4	2.9	614.6	5.3	626.4	6.8	10.1
MT4	3792	34	416	0.004	0.009	0.08	0.84222	1.19	0.1036	1.16	0.97621	0.05956	0.23	566.0	5.6	620.4	5.5	635.4	7.0	12.9
MT5	12672	21146	2204	2.243	1.669	0.06	0.84001	1.16	0.1027	1.15	0.99149	0.05978	0.14	578.2	3.3	619.2	5.4	630.4	6.9	9.5
MT6	11435	31210	2546	3.949	2.729	0.07	0.83291	1.17	0.1018	1.13	0.96686	0.05988	0.29	578.9	6.5	615.2	5.4	625.2	6.7	8.4
MT7	17307	15056	2327	0.833	0.870	0.02	0.85093	1.16	0.1043	1.15	0.99211	0.05936	0.14	573.3	3.2	625.2	5.4	639.6	7.0	12.2
MT8	18798	2925	2149	0.147	0.156	0.04	0.82958	1.68	0.1045	1.17	0.69907	0.05787	1.19	513.2	26.2	613.4	7.8	640.9	7.2	26.1
MT9	12171	6907	1507	0.434	0.567	0.03	0.85509	1.15	0.1054	1.13	0.98279	0.05905	0.21	561.4	4.6	627.4	5.4	645.9	7.0	15.8
MT10	11985	5739	1462	0.361	0.479	0.03	0.86130	1.18	0.1052	1.14	0.96836	0.05961	0.29	581.2	6.4	630.8	5.5	644.8	7.0	11.5
MT12	13137	5975	1601	0.387	0.455	0.03	0.85145	1.16	0.1047	1.15	0.99037	0.05921	0.15	565.6	3.5	625.4	5.4	642.1	7.0	14.2
MT13	13583	36825	2611	2.971	2.711	0.10	0.83446	1.16	0.1030	1.15	0.98761	0.05954	0.15	558.1	4.0	616.1	5.4	632.0	6.9	13.9
MT14	16250	5783	1940	0.259	0.356	0.03	0.86453	1.16	0.1055	1.14	0.97873	0.05962	0.23	582.8	5.2	632.6	5.5	646.6	7.0	11.5
MT15	11057	3322	1296	0.218	0.300	0.04	0.86385	1.15	0.1043	1.14	0.98894	0.06042	0.16	606.5	3.7	632.2	5.4	639.4	6.9	5.7
MT16	5957	3063	724	0.469	0.514	0.22	0.82819	1.17	0.1027	1.13	0.96767	0.06019	0.23	548.7	6.4	612.6	5.4	630.0	6.8	15.6
MT17	4048	320	419	0.052	0.079	0.07	0.78929	1.23	0.0962	1.19	0.96659	0.06002	0.29	585.3	6.8	590.8	5.5	592.2	6.7	1.2
MT18	11273	17782	1611	1.213	1.577	0.04	0.83418	1.22	0.1032	1.21	0.98692	0.05890	0.18	552.8	4.3	615.9	5.7	633.2	7.3	15.3
MT19	15350	1664	1727	0.079	0.108	0.02	0.85389	1.16	0.1040	1.13	0.97819	0.05973	0.24	587.3	5.2	626.8	5.4	637.8	6.9	9.0
MT20	10340	8540	1298	0.579	0.826	0.05	0.83870	1.16	0.1026	1.14	0.98549	0.05962	0.19	576.7	4.3	618.4	5.4	629.9	6.9	9.7
MT21	790	31	80	0.205	0.039	4.62	0.71606	3.88	0.0907	1.33	0.34279	0.09322	1.20	501.3	78.4	548.3	16.6	559.7	7.1	12.2
MT22	15372	14397	2098	0.888	0.937	0.04	0.85429	1.14	0.1046	1.13	0.99261	0.05951	0.13	574.7	3.0	627.0	5.3	641.6	6.9	12.2
MT23	15735	21929	2090	0.796	1.394	0.04	0.84763	1.16	0.1032	1.14	0.98057	0.05988	0.22	587.6	4.9	623.3	5.4	633.2	6.9	8.2
MT24	13761	26223	2077	1.393	1.906	0.04	0.85210	1.16	0.1040	1.13	0.97669	0.05975	0.24	582.3	5.4	625.8	5.4	637.9	6.9	10.0
MT25	14529	28279	2271	1.649	1.946	0.04	0.83768	1.15	0.1025	1.14	0.99005	0.05960	0.15	576.2	3.5	617.9	5.3	629.3	6.8	9.7
MT26	7165	6251	848	0.283	0.872	0.08	0.85154	1.25	0.1038	1.23	0.97868	0.06012	0.22	584.9	5.6	625.5	5.9	636.8	7.4	9.3
MT27	12419	33204	1573	0.718	2.674	1.33	0.81209	1.20	0.1022	1.13	0.93919	0.06797	0.15	516.2	9.0	603.6	5.5	627.2	6.7	22.6
MT28	9386	85875	3656	8.972	9.150	0.14	0.85462	1.15	0.1024	1.13	0.98156	0.06164	0.17	623.2	4.8	627.2	5.4	628.3	6.8	0.9
MT29	14611	5961	1720	0.251	0.408	0.06	0.85890	1.16	0.1039	1.14	0.98711	0.06037	0.16	601.5	4.0	629.5	5.4	637.4	6.9	6.3

**Appendix V**  
**LA-ICP-MS**  
**U-Pb zircon dating**



Table 1: Zircon LA-ICP-MS U-Pb data – Banded mafic granulite (C-833-A) – Chapter 3

Spot number	$f_{206}^a$	Pb ppm	Th ppm	U ppm	Th/U <sup>b</sup>	Isotope ratios <sup>c</sup>						Ages (Ma)						% Disc.	
						<sup>207</sup> Pb/ <sup>235</sup> U		<sup>206</sup> Pb/ <sup>238</sup> U		Rho <sup>d</sup>	<sup>207</sup> Pb/ <sup>206</sup> Pb <sup>e</sup>		<sup>206</sup> Pb/ <sup>238</sup> U		<sup>207</sup> Pb/ <sup>235</sup> U		<sup>206</sup> Pb/ <sup>238</sup> U		
						1 s	[%]	1 s	[%]		1 s	[%]	1 s	abs	1 s	abs	1 s		abs
C-833A 1.1	0.0014	35	82	145	0.56	4.12411	2.55	0.29397	0.53	0.21	0.10175	2.49	1661	9	1659	42	1656	41	0
C-833A 2.1	0.0057	4	44	32	1.39	0.80743	3.24	0.09799	2.13	0.66	0.05976	2.44	603	13	601	19	595	14	-1
C-833A 3.1	0.0023	18	166	141	1.18	0.85024	1.46	0.10286	0.63	0.43	0.05995	1.32	631	4	625	9	602	8	-5
C-833A 4.1	0.0006	59	108	132	0.82	7.95062	1.44	0.41012	0.83	0.57	0.14060	1.18	2215	18	2225	32	2235	26	1
C-833A 5.1(4.2)	0.0039	11	116	88	1.32	0.80303	1.83	0.09712	1.15	0.63	0.05997	1.42	597	7	599	11	602	9	1
C-833A 6.1	0.0005	89	32	244	0.13	5.92560	1.46	0.35596	1.33	0.91	0.12073	0.59	1963	26	1965	29	1967	12	0
C-833A 7.1	0.0032	75	91	668	0.14	0.90270	1.34	0.10676	0.88	0.65	0.06133	1.02	654	6	653	9	651	7	0
C-833A 8.1	0.0065	6	69	42	1.63	0.75009	3.95	0.09213	3.25	0.82	0.05905	2.23	568	18	568	22	569	13	0
C-833A 9.1	0.0050	6	62	51	1.20	0.78675	2.34	0.09581	1.54	0.66	0.05956	1.77	590	9	589	14	587	10	0
C-833A 10.1	0.0033	11	73	88	0.82	0.81405	1.94	0.09845	1.46	0.75	0.05997	1.29	605	9	605	12	602	8	0
C-833A 11.1(10.2)	0.0042	73	75	320	0.23	5.28301	2.87	0.33610	2.42	0.84	0.11400	1.56	1868	45	1866	54	1864	29	0
C-833A 12.1	0.0003	83	391	654	0.60	0.86702	1.76	0.10313	1.45	0.83	0.06097	0.98	633	9	634	11	638	6	1
C-833A 13.1	0.0011	75	29	676	0.04	0.86817	1.52	0.10321	1.18	0.78	0.06101	0.96	633	7	635	10	640	6	1
C-833A 14.1	0.0005	65	133	132	1.00	9.04279	1.59	0.43517	0.68	0.43	0.15071	1.44	2329	16	2342	37	2354	34	1
C-833A 15.1(14.2)	0.0026	7	60	54	1.12	0.80323	1.99	0.09749	0.81	0.41	0.05975	1.82	600	5	599	12	595	11	-1
C-833A 16.1	0.0033	118	127	241	0.52	10.30320	2.02	0.46653	1.76	0.87	0.16018	0.99	2468	43	2462	50	2458	24	0
C-833A 17.1	0.0049	18	64	146	0.44	0.88543	2.00	0.10502	1.58	0.79	0.06115	1.24	644	10	644	13	644	8	0
C-833A 18.1	0.0011	106	519	844	0.61	0.87458	1.58	0.10399	0.99	0.63	0.06100	1.23	638	6	638	10	639	8	0
C-833A 19.1	0.0036	80	458	595	0.77	0.89940	3.38	0.10605	3.23	0.96	0.06151	0.98	650	21	651	22	657	6	1
C-833A 20.1(19.2)	0.0005	79	104	717	0.15	0.85926	2.02	0.10268	1.76	0.87	0.06069	1.00	630	11	630	13	628	6	0
C-833A 21.1	0.0060	7	75	54	1.40	0.83284	1.93	0.10017	0.80	0.42	0.06030	1.75	615	5	615	12	614	11	0
C-833A 22.1	0.0006	53	99	161	0.62	5.38332	2.93	0.33848	2.80	0.96	0.11535	0.86	1879	53	1882	55	1885	16	0
C-833A 23.1	0.0002	98	220	178	1.23	9.87817	3.59	0.45194	3.49	0.97	0.15852	0.83	2404	84	2423	87	2440	20	1
C-833A 24.1	0.0022	34	95	99	0.97	7.21683	2.61	0.39191	2.23	0.85	0.13356	1.36	2132	48	2139	56	2145	29	1
C-833A 25.1(24.2)	0.0026	110	177	224	0.79	9.61438	1.29	0.44805	0.91	0.71	0.15563	0.91	2387	22	2399	31	2409	22	1
C-833A 26.1	0.0004	72	149	149	1.00	10.45138	2.24	0.46824	1.66	0.74	0.16189	1.50	2476	41	2476	55	2475	37	0
C-833A 27.1	0.0005	59	97	111	0.87	10.38370	2.06	0.46690	1.82	0.88	0.16130	0.98	2470	45	2470	51	2469	24	0
C-833A 28.1	0.0005	72	74	158	0.47	9.98519	2.32	0.45995	2.16	0.93	0.15745	0.83	2439	53	2433	56	2428	20	0
C-833A 29.1(28.2)	0.0024	4	41	29	1.43	0.89115	2.74	0.10558	1.56	0.57	0.06122	2.26	647	10	647	18	647	15	0
C-833A 30.1	0.0011	31	82	104	0.79	5.31388	2.19	0.33441	1.42	0.65	0.11525	1.67	1860	26	1871	41	1884	31	1
C-833A 31.1	0.0027	51	60	475	0.13	0.92516	2.65	0.10880	2.28	0.86	0.06167	1.34	666	15	665	18	663	9	0
C-833A 32.1(31.2)	0.0041	13	129	83	1.56	0.90910	2.49	0.10711	1.86	0.75	0.06156	1.65	656	12	657	16	659	11	0
C-833A 33.1	0.0007	57	70	131	0.54	8.27495	1.56	0.41905	1.30	0.83	0.14322	0.86	2256	29	2262	35	2266	20	0
C-833A 34.1	0.0010	73	160	160	1.00	8.90033	1.99	0.42911	1.73	0.87	0.15043	0.98	2302	40	2328	46	2351	23	2
C-833A 35.1	0.0003	97	149	201	0.74	9.75800	2.43	0.45287	1.56	0.64	0.15628	1.87	2408	38	2412	59	2416	45	0
C-833A 36.1	0.0004	69	59	151	0.39	9.96976	4.29	0.45804	4.00	0.93	0.15786	1.56	2431	97	2432	104	2433	38	0
C-833A 37.1	0.0031	10	73	78	0.94	0.93303	3.70	0.10945	2.31	0.62	0.06183	2.89	670	15	669	25	668	19	0
C-833A 38.1	0.0008	90	55	288	0.19	6.65085	2.88	0.37673	2.45	0.85	0.12804	1.52	2061	51	2066	60	2071	31	0
C-833A 39.1	0.0018	78	79	250	0.32	8.74171	4.23	0.43195	3.96	0.94	0.14678	1.49	2314	92	2311	98	2309	34	0
C-833A 40.1	0.0004	78	200	689	0.29	0.88651	1.44	0.10622	1.06	0.74	0.06053	0.97	651	7	644	9	623	6	-5

Table 1: Zircon LA-ICP-MS U-Pb data – Banded mafic granulite (C-833-A) – Chapter 3\_Cont.

Spot #	$f_{206}^a$	Pb ppm	Th ppm	U ppm	Th/U <sup>b</sup>	Isotope ratios <sup>c</sup>						Ages (Ma)						% Disc.	
						<sup>207</sup> Pb/ <sup>235</sup> U	1 s	<sup>206</sup> Pb/ <sup>238</sup> U	1 s	Rho <sup>d</sup>	<sup>207</sup> Pb/ <sup>206</sup> Pb <sup>e</sup>	1 s	<sup>206</sup> Pb/ <sup>238</sup> U	1 s	<sup>207</sup> Pb/ <sup>235</sup> U	1 s	<sup>207</sup> Pb/ <sup>206</sup> Pb		1 s
C-833A 41.1	0.0037	13	76	110	0.69	0.83562	2.20	0.10033	1.39	0.63	0.06041	1.70	616	9	617	14	618	11	0
C-833A 42.1(41.2)	0.0044	9	84	63	1.34	0.82149	2.84	0.09898	2.09	0.74	0.06020	1.92	608	13	609	17	611	12	0
C-833A 43.1	0.0014	48	109	126	0.86	6.69287	1.24	0.37710	0.96	0.78	0.12872	0.78	2063	20	2072	26	2081	16	1
C-833A 44.1	0.0010	7	68	51	1.35	0.82381	2.77	0.09921	1.52	0.55	0.06023	2.31	610	9	610	17	612	14	0
C-833A 45.1	0.0005	98	128	217	0.59	10.40959	2.89	0.46997	2.79	0.96	0.16064	0.77	2483	69	2472	71	2462	19	-1
C-833A 46.1	0.0026	94	79	194	0.41	9.91882	0.93	0.46042	0.82	0.88	0.15624	0.44	2441	20	2427	23	2415	11	-1
C-833A 47.1	0.0003	146	355	274	1.30	9.85547	4.03	0.45402	4.02	1.00	0.15743	0.34	2413	97	2421	98	2428	8	1
C-833A 48.1	0.0037	11	104	82	1.26	0.83532	2.38	0.10054	1.62	0.68	0.06026	1.74	618	10	617	15	613	11	-1
C-833A 49.1(48.2)	0.0012	35	78	130	0.60	4.23413	3.17	0.29758	2.54	0.80	0.10319	1.88	1679	43	1681	53	1682	32	0
C-833A 50.1	0.0009	59	99	124	0.80	9.41462	3.02	0.44467	2.90	0.96	0.15355	0.83	2372	69	2379	72	2386	20	1
C-833A 51.1	0.0012	37	88	104	0.85	6.09270	0.73	0.36188	0.40	0.55	0.12211	0.61	1991	8	1989	15	1987	12	0
C-833A 52.1(51.2)	0.0005	97	110	862	0.13	0.87450	2.05	0.10397	1.86	0.91	0.06100	0.85	638	12	638	13	639	5	0
C-833A 53.1	0.0037	8	97	55	1.75	0.82400	2.61	0.09931	1.37	0.53	0.06018	2.22	610	8	610	16	610	14	0
C-833A 54.1	0.0005	45	32	420	0.08	0.85389	1.37	0.10213	0.92	0.67	0.06064	1.01	627	6	627	9	626	6	0
C-833A 55.1	0.0038	15	154	122	1.27	0.79884	2.15	0.09664	1.32	0.61	0.05995	1.70	595	8	596	13	602	10	1
C-833A 56.1	0.0011	94	115	347	0.33	5.39652	2.72	0.33984	2.40	0.88	0.11517	1.28	1886	45	1884	51	1883	24	0
C-833A 57.1	0.0006	118	198	240	0.82	10.51952	2.09	0.47019	1.48	0.71	0.16226	1.47	2484	37	2482	52	2479	37	0
C-833A 58.1	0.0031	74	82	668	0.12	0.95998	1.62	0.11142	1.09	0.67	0.06249	1.20	681	7	683	11	691	8	1
C-833A 59.1(58.2)	0.0011	62	132	339	0.39	0.87354	4.76	0.10353	4.60	0.97	0.06119	1.25	635	29	637	30	646	8	2
C-833A 60.1	0.0035	18	45	102	0.44	3.14877	2.26	0.25163	1.68	0.74	0.09076	1.51	1447	24	1445	33	1441	22	0
C-833A 61.1(60.2)	0.0028	37	231	315	0.73	0.83209	1.89	0.09982	0.99	0.53	0.06046	1.61	613	6	615	12	620	10	1
C-833A 62.1	0.0019	163	234	336	0.70	9.93751	2.24	0.45858	1.31	0.59	0.15717	1.81	2433	32	2429	54	2425	44	0
C-833A 63.1	0.0030	24	88	203	0.43	0.83569	3.20	0.10042	2.75	0.86	0.06036	1.63	617	17	617	20	616	10	0
C-833A 64.1	0.0006	65	112	132	0.85	10.57130	5.01	0.46991	4.22	0.84	0.16316	2.69	2483	105	2486	124	2489	67	0
C-833A 65.1	0.0018	44	89	139	0.64	5.23910	1.89	0.33481	0.98	0.52	0.11349	1.62	1862	18	1859	35	1856	30	0
C-833A 66.1	0.0006	83	185	185	1.00	8.39931	2.35	0.41981	1.93	0.82	0.14511	1.35	2260	44	2275	54	2289	31	1
C-833A 67.1	0.0005	124	258	239	1.08	10.11917	0.81	0.46568	0.51	0.63	0.15760	0.62	2465	13	2446	20	2430	15	-1
C-833A 68.1	0.0002	101	77	279	0.27	9.55426	1.48	0.44776	1.43	0.97	0.15476	0.39	2385	34	2393	35	2399	9	1
C-833A 69.1	0.0024	14	139	111	1.25	0.82299	2.05	0.09939	1.50	0.73	0.06006	1.40	611	9	610	13	606	9	-1
C-833A 70.1(69.2)	0.0018	11	100	88	1.13	0.81906	2.00	0.09907	0.87	0.43	0.05996	1.81	609	5	608	12	602	11	-1
C-833A 71.1	0.0011	101	134	935	0.14	0.86857	2.87	0.10345	2.64	0.92	0.06090	1.12	635	17	635	18	636	7	0
C-833A 72.1	0.0047	9	84	76	1.11	0.85715	2.67	0.10221	1.69	0.63	0.06082	2.07	627	11	629	17	633	13	1
C-833A 73.1(72.2)	0.0011	64	119	192	0.62	5.54841	3.13	0.34263	2.98	0.95	0.11745	0.96	1899	57	1908	60	1918	18	1
C-833A 74.1	0.0009	95	175	175	1.00	10.19490	1.37	0.45888	1.14	0.83	0.16113	0.77	2435	28	2453	34	2468	19	1
C-833A 75.1	0.0011	79	173	174	0.99	8.30538	2.79	0.41829	2.07	0.74	0.14401	1.86	2253	47	2265	63	2276	42	1
C-833A 76.1	0.0005	123	275	215	1.28	10.42589	1.18	0.46775	1.09	0.93	0.16166	0.44	2474	27	2473	29	2473	11	0
C-833A 77.1	0.0047	8	74	64	1.16	0.81326	2.57	0.09828	1.47	0.57	0.06001	2.11	604	9	604	16	604	13	0
C-833A 78.1	0.0012	141	287	273	1.05	10.53947	1.02	0.47078	0.47	0.46	0.16237	0.91	2487	12	2483	25	2480	23	0
C-833A 79.1	0.0010	68	83	123	0.67	10.21636	2.87	0.46144	2.51	0.88	0.16057	1.38	2446	61	2455	70	2462	34	1
C-833A 80.1	0.0018	9	84	67	1.25	0.87198	2.35	0.10407	1.19	0.51	0.06077	2.02	638	8	637	15	631	13	-1

Table 1: Zircon LA-ICP-MS U-Pb data – Banded mafic granulite (C-833-A) – Chapter 3\_Cont.

Spot #	$f_{206}^a$	Pb ppm	Th ppm	U ppm	Th/U <sup>b</sup>	Isotope ratios <sup>c</sup>						Ages (Ma)						% Disc.	
						<sup>207</sup> Pb/ <sup>235</sup> U	1 s [%]	<sup>206</sup> Pb/ <sup>238</sup> U	1 s [%]	Rho <sup>d</sup>	<sup>207</sup> Pb/ <sup>206</sup> Pb <sup>e</sup>	1 s [%]	<sup>206</sup> Pb/ <sup>238</sup> U	1 s abs	<sup>207</sup> Pb/ <sup>235</sup> U	1 s abs	<sup>207</sup> Pb/ <sup>206</sup> Pb		1 s abs
C-833A 81.1	0.0024	8	81	59	1.37	0.90977	1.79	0.10686	0.93	0.52	0.06175	1.53	654	6	657	12	665	10	2
C-833A 82.1(81.2)	0.0009	88	69	219	0.32	7.94815	4.19	0.41177	3.92	0.94	0.14000	1.47	2223	87	2225	93	2227	33	0
C-833A 83.1	0.0008	92	189	175	1.08	10.66090	3.10	0.46971	2.78	0.90	0.16461	1.37	2482	69	2494	77	2504	34	1
C-833A 84.1(83.2)	0.0038	8	83	63	1.32	0.96380	3.02	0.11159	1.77	0.59	0.06264	2.44	682	12	685	21	696	17	2
C-833A 85.1	0.0023	47	64	430	0.15	0.86499	1.34	0.10302	0.83	0.62	0.06090	1.05	632	5	633	8	636	7	1
C-833A 86.1(85.2)	0.0011	105	147	200	0.73	10.82654	0.85	0.47384	0.51	0.60	0.16571	0.68	2500	13	2508	21	2515	17	1
C-833A 87.1	0.0107	5	55	42	1.32	0.82001	3.88	0.09877	2.26	0.58	0.06021	3.15	607	14	608	24	611	19	1
C-833A 88.1(87.2)	0.0014	75	119	133	0.89	11.22018	4.49	0.48376	4.15	0.92	0.16822	1.72	2544	106	2542	114	2540	44	0
C-833A 89.1	0.0017	99	167	168	1.00	11.27000	4.10	0.48029	3.90	0.95	0.17018	1.28	2529	99	2546	104	2559	33	1
C-833A 90.1	0.0047	15	121	116	1.04	0.83598	3.09	0.10042	2.30	0.75	0.06038	2.06	617	14	617	19	617	13	0
C-833A 91.1	0.0024	27	65	67	0.97	7.07973	3.80	0.38922	3.36	0.88	0.13192	1.78	2119	71	2121	81	2124	38	0
C-833A 92.1	0.0020	20	40	50	0.81	9.27594	2.94	0.44364	2.53	0.86	0.15164	1.50	2367	60	2366	70	2365	35	0
C-833A 93.1	0.0016	33	43	332	0.13	0.86733	3.41	0.10284	3.25	0.95	0.06117	1.03	631	21	634	22	645	7	2
C-833A 94.1(93.2)	0.0018	21	41	41	1.01	10.37739	3.89	0.46548	3.86	0.99	0.16169	0.53	2464	95	2469	96	2473	13	0
C-833A 95.1	0.0018	22	44	59	0.75	7.48849	2.23	0.39925	1.53	0.68	0.13604	1.63	2166	33	2172	48	2177	35	1
C-833A 96.1	0.0043	4	10	39	0.25	0.84230	3.67	0.10103	2.58	0.70	0.06047	2.60	620	16	620	23	620	16	0
C-833A 97.1	0.0010	50	112	88	1.27	10.45539	1.48	0.46742	1.28	0.87	0.16223	0.74	2472	32	2476	37	2479	18	0
C-833A 98.1	0.0038	23	41	42	0.99	11.20740	2.14	0.48159	1.17	0.55	0.16878	1.79	2534	30	2541	54	2546	46	0
C-833A 99.1	0.0025	15	25	29	0.89	10.43929	4.25	0.46905	3.24	0.76	0.16142	2.76	2479	80	2475	105	2471	68	0
C-833A 100.1	0.0008	75	130	117	1.11	11.60726	2.42	0.49013	2.05	0.85	0.17176	1.28	2571	53	2573	62	2575	33	0
C-833A 101.1	0.0020	24	56	217	0.26	0.90660	3.04	0.10675	2.87	0.94	0.06160	1.02	654	19	655	20	660	7	1
C-833A 102.1(101.2)	0.0019	22	40	78	0.51	5.27138	2.23	0.33310	2.15	0.96	0.11478	0.59	1853	40	1864	42	1876	11	1
C-833A 103.1	0.0016	32	71	99	0.72	5.49715	2.46	0.34280	2.04	0.83	0.11630	1.38	1900	39	1900	47	1900	26	0
C-833A 104.1(103.2)	0.0007	74	22	216	0.10	5.87612	2.25	0.35516	1.62	0.72	0.12000	1.56	1959	32	1958	44	1956	31	0
C-833A 105.1	0.0017	8	51	71	0.72	0.87401	2.16	0.10388	1.32	0.61	0.06102	1.70	637	8	638	14	640	11	0
C-833A 106.1(105.2)	0.0019	25	61	126	0.49	4.16824	1.28	0.28008	0.39	0.31	0.10794	1.22	1592	6	1668	21	1765	22	10
C-833A 107.1	0.0014	84	171	356	0.48	6.09885	3.31	0.35746	2.77	0.84	0.12374	1.82	1970	55	1990	66	2011	37	2
C-833A 108.1	0.0005	74	64	271	0.24	5.27496	1.94	0.33431	1.59	0.82	0.11444	1.11	1859	30	1865	36	1871	21	1

<sup>a</sup>Fraction of the non-radiogenic <sup>206</sup>Pb in the analyzed zircon spot. where  $f_{206} = \frac{[^{206}\text{Pb}/^{204}\text{Pb}]_c - [^{206}\text{Pb}/^{204}\text{Pb}]_s}{[^{206}\text{Pb}/^{204}\text{Pb}]_c}$  (c=common; s=sample);

<sup>b</sup>Th/U ratios and amount of Pb, Th and U (in ppm) are calculated relative to 91500 reference zircon

<sup>c</sup>Corrected for background and within-run Pb/U fractionation and normalised to reference zircon GJ-1 (ID-TIMS values/measured value); <sup>207</sup>Pb/<sup>235</sup>U calculated using  $(^{207}\text{Pb}/^{206}\text{Pb}) / (^{238}\text{U}/^{206}\text{Pb} * 1/137.88)$

<sup>d</sup>Rho is the error correlation defined as the quotient of the propagated errors of the <sup>206</sup>Pb/<sup>238</sup>U and the <sup>207</sup>/<sup>235</sup>U ratio

<sup>e</sup>Corrected for mass-bias by normalising to GJ-1 reference zircon and common Pb using the model Pb composition of Stacey and Kramers (1975)

<sup>f</sup>Degree of concordance =  $(^{206}\text{Pb}/^{238}\text{U} \text{ age} * 100 / ^{207}\text{Pb}/^{206}\text{U} \text{ age})$

Table 2: Zircon LA-ICP-MS U–Pb data – Banded mafic granulite (C-838-A) – Chapter 3

Grain #						Isotope ratios						Ages (Ma)						Disc. (%)	
	<sup>207</sup> Pb <sup>a</sup>	U <sup>b</sup>	Pb <sup>b</sup>	Th <sup>b</sup>	<sup>206</sup> Pb <sup>c</sup>	<sup>207</sup> Pb <sup>d</sup> / <sub>235</sub> U	±2s	<sup>206</sup> Pb <sup>d</sup> / <sub>238</sub> U	±2s	rhoe	<sup>207</sup> Pb <sup>d</sup> / <sub>206</sub> Pb	±2s	<sup>206</sup> Pb/ <sub>238</sub> U	±2s	<sup>207</sup> Pb/ <sub>235</sub> U	±2s	<sup>207</sup> Pb/ <sub>206</sub> Pb		±2s
	(cps)	(ppm)	(ppm)	U	(%)	(%)	(%)	(%)	(%)	(%)	(%)	(%)	(Ma)	(Ma)	(Ma)	(Ma)	(Ma)		(Ma)
C-838A_10	2632	85.02	11.63	1.27	0.8605	0.814835	1.56	0.098363	0.72	0.46	0.060081	1.39	605	4	605	7	606	30	0
C-838A_11	1070	32.84	4.07	0.84	0.1178	0.837878	2.18	0.100593	1.42	0.65	0.060410	1.66	618	8	618	10	618	36	0
C-838A_12	5456	32.21	9.74	0.57	0.0098	0.845002	1.29	0.152151	1.03	0.79	0.110595	0.79	1450	13	1602	10	1809	14	20
C-838A_13	3657	108.15	14.27	0.98	0.0501	0.822928	1.05	0.099157	0.57	0.55	0.060192	0.87	609	3	610	5	610	19	0
C-838A_14	1141	35.14	3.71	0.35	0.1070	0.829525	1.74	0.099758	0.82	0.47	0.060309	1.54	613	5	613	8	615	33	0
C-838A_15	2800	87.41	11.32	0.63	0.0000	0.973786	0.96	0.113130	0.52	0.54	0.062429	0.80	691	3	690	5	689	17	0
C-838A_16	1475	49.38	6.66	0.99	0.0000	0.918104	1.90	0.108126	0.99	0.52	0.061583	1.62	662	6	661	9	660	35	0
C-838A_17	4678	151.72	19.46	1.02	0.8969	0.824061	1.64	0.099180	0.72	0.44	0.060261	1.48	610	4	610	8	613	32	1
C-838A_18	2390	69.44	8.74	0.71	0.5229	0.870112	1.64	0.103214	0.89	0.54	0.061141	1.38	633	5	636	8	644	30	2
C-838A_19	1723	51.95	6.66	0.75	0.1049	0.916701	1.56	0.107883	0.70	0.45	0.061627	1.39	660	4	661	8	661	30	0
C-838A_29	970	29.58	3.88	0.97	1.3891	0.874743	2.42	0.104045	0.81	0.34	0.060976	2.28	638	5	638	12	638	49	0
C-838A_30	1031	31.95	3.83	0.78	0.2364	0.818437	1.61	0.098719	0.75	0.47	0.060129	1.42	607	4	607	7	608	31	0
C-838A_31	1627	47.11	5.33	0.35	0.1301	0.913565	1.49	0.107562	0.81	0.54	0.061600	1.25	659	5	659	7	660	27	0
C-838A_32	16415	455.61	105.97	3.34	0.7704	0.811587	7.11	0.098005	7.01	0.99	0.060060	1.18	603	40	603	33	606	26	1
C-838A_34	1675	48.50	5.08	0.13	0.0000	0.920136	1.43	0.108307	0.74	0.52	0.061616	1.22	663	5	662	7	661	26	0
C-838A_35	3248	102.02	10.97	0.46	0.0000	0.817206	1.13	0.098600	0.78	0.69	0.060111	0.81	606	5	606	5	608	18	0
C-838A_36	1614	49.32	5.91	0.57	0.1499	0.900286	1.43	0.106439	1.05	0.73	0.061345	0.98	652	6	652	7	651	21	0
C-838A_37	3816	112.25	15.14	0.82	0.0000	0.971099	1.32	0.112906	0.95	0.72	0.062380	0.91	690	6	689	7	687	19	0
C-838A_38	11134	325.27	49.28	1.62	0.4663	0.804826	1.93	0.097318	1.74	0.90	0.059980	0.84	599	10	600	9	603	18	1
C-838A_48	2705	68.65	10.52	1.20	1.1992	0.966540	2.37	0.112433	1.30	0.55	0.062348	1.98	687	9	687	12	686	42	0
C-838A_49	1284	36.99	4.22	0.42	0.4785	0.897064	1.66	0.106159	1.08	0.65	0.061287	1.26	650	7	650	8	649	27	0
C-838A_50	2069	63.42	6.39	0.26	0.0000	0.818846	1.54	0.098674	1.20	0.78	0.060187	0.96	607	7	607	7	610	21	1
C-838A_51	578	17.48	2.22	0.91	0.0000	0.821948	2.15	0.099070	1.61	0.75	0.060173	1.43	609	9	609	10	610	31	0
C-838A_52	1706	50.61	6.64	0.68	0.0000	0.959521	1.27	0.111747	0.80	0.63	0.062275	0.99	683	5	683	6	684	21	0
C-838A_53	16392	427.37	48.84	0.30	0.0000	0.946572	4.20	0.110619	4.16	0.99	0.062061	0.56	676	27	676	21	676	12	0
C-838A_54	333	10.00	1.25	0.92	0.3545	0.786624	3.35	0.095601	2.11	0.63	0.059677	2.60	589	12	589	15	592	56	1
C-838A_55	5143	151.28	22.39	1.53	0.0000	0.810728	1.64	0.097753	1.21	0.74	0.060151	1.10	601	7	603	7	609	24	1
C-838A_56	5202	159.12	15.20	0.11	0.0513	0.823041	0.89	0.099175	0.61	0.69	0.060189	0.64	610	4	610	4	610	14	0
C-838A_57	923	29.21	3.73	1.00	0.0827	0.816108	2.09	0.098548	1.15	0.55	0.060062	1.74	606	7	606	10	606	38	0
C-838A_58	1349	41.40	4.79	0.61	0.0000	0.831112	1.72	0.099932	1.01	0.58	0.060319	1.40	614	6	614	8	615	30	0
C-838A_68	2748	84.50	10.15	0.77	0.0974	0.821718	1.02	0.099036	0.64	0.63	0.060177	0.80	609	4	609	5	610	17	0
C-838A_69	20874	173.74	21.54	0.48	4.4213	0.840214	4.12	0.097113	1.85	0.45	0.062750	3.68	597	11	619	19	700	78	15
C-838A_70	4336	136.04	13.59	0.24	0.8240	0.820156	1.43	0.098907	0.55	0.39	0.060141	1.32	608	3	608	7	609	29	0

Table 2: Zircon LA-ICP-MS U-Pb data – Banded mafic granulite (C-838-A) – Chapter 3\_Cont.

Grain #						Isotope ratios						Ages (Ma)					Disc. (%)		
	<sup>207</sup> Pb <sup>a</sup>	U <sup>b</sup>	Pb <sup>b</sup>	Th <sup>b</sup>	<sup>206</sup> Pbc <sup>c</sup>	<sup>207</sup> Pb <sup>d</sup> / <sub><sup>235</sup>U</sub>	±2s	<sup>206</sup> Pb <sup>d</sup> / <sub><sup>238</sup>U</sub>	±2s	rhoe	<sup>207</sup> Pb <sup>d</sup> / <sub><sup>206</sup>Pb</sub>	±2s	<sup>206</sup> Pb/ <sub><sup>238</sup>U</sub>	±2s	<sup>207</sup> Pb/ <sub><sup>235</sup>U</sub>	±2s		<sup>207</sup> Pb/ <sub><sup>206</sup>Pb</sub>	±2s
	(cps)	(ppm)	(ppm)	U	(%)	(%)	(%)	(%)	(%)	(%)	(%)	(%)	(Ma)	(Ma)	(Ma)	(Ma)		(Ma)	(Ma)
C-838A_71	2615	79.62	8.91	0.47	0.0000	0.860524	1.06	0.102673	0.56	0.53	0.060787	0.90	630	3	630	5	632	19	0
C-838A_72	2838	84.60	9.40	0.54	0.0000	0.808215	1.01	0.097729	0.66	0.66	0.059979	0.76	601	4	601	5	603	16	0
C-838A_73	13270	393.37	57.27	1.22	0.0000	0.912855	0.72	0.107595	0.52	0.72	0.061533	0.50	659	3	659	4	658	11	0
C-838A_74	4968	151.39	17.58	0.69	0.4433	0.820667	1.07	0.098958	0.49	0.46	0.060147	0.95	608	3	608	5	609	21	0
C-838A_75	5228	158.81	18.80	0.55	0.0000	0.916694	1.19	0.107980	0.97	0.82	0.061572	0.68	661	6	661	6	659	15	0
C-838A_76	4914	143.95	15.24	0.38	0.2399	0.813513	0.99	0.098133	0.66	0.67	0.060124	0.74	603	4	604	5	608	16	1
C-838A_77	1953	58.05	5.89	0.19	0.1587	0.854820	1.13	0.102103	0.58	0.52	0.060721	0.96	627	3	627	5	629	21	0
C-838A_87	3630	106.75	11.82	0.51	0.4261	0.809898	1.42	0.097875	0.94	0.66	0.060015	1.06	602	5	602	6	604	23	0
C-838A_88	4577	140.44	16.69	0.66	0.9633	0.853227	1.59	0.102011	0.58	0.36	0.060662	1.49	626	3	626	7	627	32	0
C-838A_89	1875	59.49	7.06	0.77	0.0000	0.818534	1.23	0.098716	0.70	0.57	0.060138	1.01	607	4	607	6	609	22	0
C-838A_90	6817	204.24	25.55	0.89	0.2444	0.827999	1.09	0.099554	0.55	0.50	0.060321	0.94	612	3	613	5	615	20	1
C-838A_91	3506	113.31	10.97	0.16	0.0726	0.821267	0.98	0.098993	0.46	0.47	0.060170	0.86	609	3	609	4	610	19	0
C-838A_92	1549	49.05	5.32	0.50	0.0000	0.807036	1.33	0.097606	0.78	0.59	0.059968	1.08	600	4	601	6	602	23	0
C-838A_93	6093	176.96	17.80	0.26	2.5432	0.819301	3.64	0.098721	0.66	0.18	0.060191	3.58	607	4	608	17	610	77	1
C-838A_94	3806	115.65	15.51	1.09	0.0619	0.835049	1.05	0.100282	0.59	0.56	0.060393	0.87	616	3	616	5	618	19	0
C-838A_95	368	11.58	1.37	1.02	0.1484	0.712074	3.57	0.087719	2.40	0.67	0.058875	2.65	542	12	546	15	562	58	4
C-838A_96	3643	106.31	11.33	0.46	2.6995	0.809057	3.93	0.097774	0.74	0.19	0.060015	3.86	601	4	602	18	604	83	0
C-838A_107	4112	127.29	13.65	0.36	0.0000	0.852101	1.36	0.101950	0.34	0.25	0.060618	1.31	626	2	626	6	626	28	0
C-838A_108	785	23.59	2.95	0.66	0.3269	0.930134	2.72	0.109233	1.14	0.42	0.061757	2.47	668	7	668	13	666	53	0
C-838A_109	5132	40.48	3.85	0.12	0.0653	0.818111	1.31	0.098688	0.54	0.41	0.060124	1.19	607	3	607	6	608	26	0
C-838A_110	2513	18.79	1.89	0.25	0.3565	0.817124	1.73	0.098575	0.58	0.33	0.060120	1.63	606	3	606	8	608	35	0
C-838A_111	3511	27.71	3.56	0.96	0.3524	0.849013	1.52	0.101645	0.47	0.31	0.060580	1.45	624	3	624	7	624	31	0
C-838A_112	3191	21.28	2.76	1.02	1.2736	0.817914	2.90	0.098207	1.05	0.36	0.060404	2.70	604	6	607	13	618	58	2
C-838A_113	2900	20.75	3.35	1.53	0.3981	0.961255	2.84	0.115728	2.34	0.82	0.060242	1.61	706	16	684	14	612	35	-15
C-838A_114	2918	21.89	2.73	0.76	0.1905	0.829604	1.77	0.099816	0.93	0.53	0.060279	1.50	613	5	613	8	614	32	0
C-838A_115	2793	21.05	2.16	0.29	0.2959	0.830985	1.56	0.099852	0.50	0.32	0.060358	1.48	614	3	614	7	616	32	0
C-838A_125	1053	31.74	3.74	0.69	0.2621	0.845941	1.63	0.101139	0.76	0.46	0.060663	1.45	621	4	622	8	627	31	1
C-838A_126	4571	133.30	15.17	0.49	0.2911	0.861876	1.09	0.102617	0.69	0.63	0.060915	0.84	630	4	631	5	636	18	1
C-838A_127	5563	162.79	27.24	2.08	0.2394	0.814744	0.82	0.098182	0.42	0.51	0.060185	0.70	604	2	605	4	610	15	1
C-838A_128	3011	81.72	12.09	0.86	2.3717	1.107500	3.70	0.124638	1.18	0.32	0.064445	3.51	757	8	757	20	756	74	0
C-838A_129	1332	38.89	4.67	0.83	0.3997	0.800160	1.50	0.096721	0.64	0.43	0.060000	1.36	595	4	597	7	604	29	1
C-838A_130	2339	61.36	7.09	0.34	0.6933	0.949097	2.31	0.110382	0.73	0.32	0.062361	2.19	675	5	678	11	686	47	2
C-838A_131	13054	158.18	21.85	0.43	2.7451	0.987229	3.17	0.111845	1.59	0.50	0.064017	2.74	683	10	697	16	742	58	8

Table 2: Zircon LA-ICP-MS U-Pb data – Banded mafic granulite (C-838-A) – Chapter 3\_Cont.

Grain #						Isotope ratios							Ages (Ma)					Disc. (%)	
	<sup>207</sup> Pb <sup>a</sup>	U <sup>b</sup>	Pb <sup>b</sup>	Th <sup>b</sup>	<sup>206</sup> Pb <sup>c</sup>	<sup>207</sup> Pb <sup>d</sup> / <sub><sup>235</sup>U</sub>	±2s	<sup>206</sup> Pb <sup>d</sup> / <sub><sup>238</sup>U</sub>	±2s	rhoe	<sup>207</sup> Pb <sup>d</sup> / <sub><sup>206</sup>Pb</sub>	±2s	<sup>206</sup> Pb/ <sub><sup>238</sup>U</sub>	±2s	<sup>207</sup> Pb/ <sub><sup>235</sup>U</sub>	±2s	<sup>207</sup> Pb/ <sub><sup>206</sup>Pb</sub>		±2s
	(cps)	(ppm)	(ppm)	U	(%)	(%)	(%)	(%)	(%)	(%)	(%)	(%)	(Ma)	(Ma)	(Ma)	(Ma)	(Ma)		(Ma)
C-838A_132	3007	87.56	8.17	0.22	0.5168	0.751567	1.77	0.091946	1.13	0.64	0.059283	1.36	567	6	569	8	578	30	2
C-838A_133	1306	40.35	5.34	1.10	0.1816	0.848418	1.53	0.101378	0.57	0.38	0.060697	1.42	622	3	624	7	629	31	1
C-838A_134	3718	98.18	13.24	0.86	1.5825	0.904548	2.80	0.106631	1.54	0.55	0.061524	2.34	653	10	654	14	658	50	1
C-838A_144	4992	140.04	19.02	1.17	0.4853	0.824674	1.48	0.098984	1.03	0.69	0.060425	1.06	608	6	611	7	619	23	2
C-838A_145	11296	73.50	21.09	0.82	3.1961	2.802376	2.60	0.229709	0.77	0.30	0.088480	2.48	1333	9	1356	20	1393	48	4
C-838A_146	626	18.46	2.38	0.97	0.7018	0.847214	2.34	0.101296	1.13	0.49	0.060660	2.04	622	7	623	11	627	44	1
C-838A_147	2804	82.51	9.07	0.52	0.5350	0.804455	1.43	0.097176	0.81	0.57	0.060040	1.18	598	5	599	6	605	26	1
C-838A_148	1678	50.45	6.29	0.94	0.4584	0.830201	1.45	0.099727	0.58	0.40	0.060377	1.33	613	3	614	7	617	29	1
C-838A_149	4463	125.48	14.39	0.40	0.0000	0.910445	0.81	0.107181	0.58	0.71	0.061607	0.57	656	4	657	4	661	12	1
C-838A_150	4953	138.24	19.30	1.18	0.3818	0.814225	1.63	0.098095	1.31	0.80	0.060200	0.97	603	8	605	7	611	21	1
C-838A_151	3223	93.44	10.51	0.63	1.4010	0.799016	2.26	0.096615	0.77	0.34	0.059980	2.12	595	4	596	10	603	46	1
C-838A_152	13340	33.11	15.21	0.85	7.4313	6.149658	3.81	0.349737	1.23	0.32	0.127529	3.60	1933	21	1997	34	2064	63	6
C-838A_153	8351	249.11	24.39	0.21	1.4538	0.816221	2.20	0.098322	0.55	0.25	0.060208	2.13	605	3	606	10	611	46	1
C-838A_163	3220	95.21	11.37	0.79	1.0124	0.823804	1.69	0.099101	0.52	0.31	0.060290	1.60	609	3	610	8	614	35	1
C-838A_164	6074	167.79	30.32	2.21	3.2215	0.888006	4.89	0.105090	1.74	0.36	0.061285	4.57	644	11	645	24	649	98	1
C-838A_165	5466	148.47	21.44	1.27	1.1200	0.858493	1.89	0.102302	0.76	0.40	0.060863	1.73	628	5	629	9	634	37	1
C-838A_166	556	15.78	1.95	0.91	1.0751	0.794486	2.58	0.096060	1.13	0.44	0.059985	2.32	591	6	594	12	603	50	2
C-838A_167	2255	66.20	7.72	0.58	1.3233	0.858859	2.27	0.102420	0.67	0.30	0.060818	2.17	629	4	629	11	633	47	1
C-838A_168	4505	123.70	15.75	0.90	0.3387	0.830186	1.12	0.099609	0.63	0.57	0.060447	0.92	612	4	614	5	620	20	1
C-838A_169	1499	41.05	5.18	0.87	0.4421	0.837344	1.30	0.100093	0.75	0.57	0.060674	1.07	615	4	618	6	628	23	2
C-838A_170	3875	114.78	12.00	0.28	0.3377	0.854875	1.03	0.101943	0.69	0.67	0.060820	0.76	626	4	627	5	633	16	1
C-838A_171	2512	71.57	9.44	0.95	0.1743	0.867027	1.51	0.103157	1.25	0.83	0.060958	0.85	633	8	634	7	638	18	1
C-838A_172	2957	83.11	11.07	0.94	0.2709	0.881938	1.13	0.104510	0.71	0.63	0.061204	0.88	641	4	642	5	646	19	1
C-838A_10	10949	305.93	44.12	1.29	0.7717	0.882201	1.69	0.104467	1.17	0.70	0.061247	1.21	641	7	642	8	648	26	1
C-838A_11	1833	54.89	7.36	1.16	0.0000	0.815420	1.38	0.098175	0.93	0.68	0.060239	1.02	604	5	605	6	612	22	1
C-838A_12	2006	60.36	6.94	0.62	0.3650	0.833568	1.21	0.099845	0.66	0.55	0.060550	1.01	613	4	616	6	623	22	2
C-838A_13	1861	54.69	5.94	0.50	0.0000	0.810465	1.29	0.097623	0.77	0.59	0.060211	1.04	600	4	603	6	611	23	2
C-838A_14	841	24.25	2.49	0.23	0.6355	0.854240	1.83	0.101729	0.98	0.54	0.060902	1.55	625	6	627	9	636	33	2
C-838A_15	2572	76.28	8.59	0.46	0.0222	0.866477	1.21	0.102981	0.83	0.69	0.061024	0.88	632	5	634	6	640	19	1
C-838A_16	2078	62.06	7.39	0.68	0.1806	0.854281	1.06	0.101890	0.64	0.61	0.060809	0.84	625	4	627	5	632	18	1
C-838A_17	2917	85.73	11.08	1.41	5.8809	0.694771	8.68	0.086263	2.58	0.30	0.058414	8.29	533	13	536	37	545	181	2
C-838A_18	1559	44.29	4.35	0.29	0.3852	0.759195	1.69	0.092702	1.32	0.78	0.059397	1.06	571	7	574	7	582	23	2
C-838A_19	1883	56.90	6.82	0.74	0.3882	0.845541	1.44	0.101057	0.85	0.59	0.060683	1.16	621	5	622	7	628	25	1
C-838A_20	2791	80.73	9.01	0.54	1.0517	0.810850	1.96	0.097663	0.82	0.42	0.060216	1.78	601	5	603	9	611	38	2

Table 3: Zircon LA-ICP-MS U–Pb data – Opdalite (C-838-2) – Chapter 3

Grain #						Isotope ratios							Ages (Ma)						Disc. (%)
	<sup>207</sup> Pb <sup>a</sup>	U <sup>b</sup>	Pb <sup>b</sup>	Th <sup>b</sup>	<sup>206</sup> Pb/c <sup>c</sup>	<sup>207</sup> Pb <sup>d</sup> / <sup>235</sup> U	±2s	<sup>206</sup> Pb <sup>d</sup> / <sup>238</sup> U	±2s	rhoe	<sup>207</sup> Pb <sup>d</sup> / <sup>206</sup> Pb	±2s	<sup>206</sup> Pb/ <sup>238</sup> U	±2s	<sup>207</sup> Pb/ <sup>235</sup> U	±2s	<sup>207</sup> Pb/ <sup>206</sup> Pb	±2s	
	(cps)	(ppm)	(ppm)	U	(%)	(%)	(%)	(%)	(%)	(%)	(%)	(%)	(Ma)	(Ma)	(Ma)	(Ma)	(Ma)	(Ma)	
C-838-2_10	3560	101.14	15.71	1.35	0.91	0.94775	1.82	0.11053	0.73	0.40	0.06219	1.66	676	5	677	9	681	36	1
C-838-2_11	14226	415.26	66.87	1.46	0.00	0.92453	0.95	0.10866	0.81	0.85	0.06171	0.50	665	5	665	5	664	11	0
C-838-2_12	7239	224.01	34.96	1.20	0.00	1.03120	1.05	0.11822	0.83	0.80	0.06327	0.63	720	6	720	5	717	13	0
C-838-2_13	3209	98.14	14.37	0.78	0.00	1.11980	1.17	0.12594	0.87	0.75	0.06449	0.78	765	6	763	6	758	16	-1
C-838-2_14	3293	96.88	14.90	0.89	0.35	1.13099	1.40	0.12688	0.76	0.55	0.06465	1.17	770	6	768	8	763	25	-1
C-838-2_15	8760	290.10	33.61	0.24	0.00	1.00397	1.45	0.11600	0.78	0.54	0.06277	1.22	707	5	706	7	700	26	-1
C-838-2_16	7283	236.75	26.19	0.23	0.00	0.94676	0.94	0.11075	0.72	0.77	0.06200	0.60	677	5	676	5	674	13	0
C-838-2_17	5546	174.97	23.73	0.95	2.67	0.91362	3.87	0.10764	0.89	0.23	0.06156	3.76	659	6	659	19	659	81	0
C-838-2_18	3827	119.53	18.46	1.31	0.37	0.95347	1.13	0.11135	0.75	0.66	0.06210	0.85	681	5	680	6	678	18	0
C-838-2_19	2019	61.96	7.07	0.30	0.00	0.94284	1.49	0.11025	0.81	0.54	0.06203	1.26	674	5	674	7	675	27	0
C-838-2_20	5215	166.06	19.89	0.32	0.00	1.01965	1.30	0.11722	1.08	0.83	0.06309	0.72	715	7	714	7	711	15	0
C-838-2_30	5407	167.82	29.31	1.56	0.00	1.11318	0.98	0.12536	0.77	0.79	0.06440	0.61	761	6	760	5	755	13	-1
C-838-2_31	4245	126.57	17.64	0.64	0.21	1.08531	1.19	0.12295	0.84	0.70	0.06402	0.85	748	6	746	6	742	18	-1
C-838-2_32	4033	128.77	15.12	0.18	0.00	1.04987	0.99	0.11992	0.76	0.76	0.06349	0.64	730	5	729	5	725	14	-1
C-838-2_33	6313	195.89	35.07	1.85	0.00	1.02121	0.89	0.11736	0.70	0.78	0.06311	0.56	715	5	715	5	712	12	0
C-838-2_34	2851	86.25	14.23	1.32	0.00	1.07604	1.14	0.12216	0.74	0.64	0.06389	0.87	743	5	742	6	738	18	-1
C-838-2_35	7642	240.83	27.46	0.15	0.00	1.02165	0.92	0.11747	0.70	0.77	0.06308	0.59	716	5	715	5	711	13	-1
C-838-2_36	2702	81.63	9.17	0.11	0.47	1.01796	1.46	0.11700	0.82	0.56	0.06310	1.21	713	6	713	8	712	26	0
C-838-2_37	12057	382.90	44.92	0.17	0.00	1.05344	0.97	0.12022	0.83	0.85	0.06355	0.51	732	6	731	5	727	11	-1
C-838-2_38	3774	118.36	17.55	1.00	0.00	1.04054	1.02	0.11909	0.75	0.73	0.06337	0.70	725	5	724	5	721	15	-1
C-838-2_39	6970	215.85	37.56	1.66	0.00	1.03256	0.98	0.11839	0.78	0.80	0.06325	0.59	721	5	720	5	717	12	-1
C-838-2_40	8480	248.56	44.89	1.56	0.00	1.11371	1.10	0.12522	0.79	0.72	0.06450	0.77	761	6	760	6	758	16	0
C-838-2_50	3455	95.39	15.57	1.34	0.00	1.00605	1.91	0.11593	1.56	0.82	0.06294	1.09	707	10	707	10	706	23	0
C-838-2_51	8684	259.73	28.32	0.17	0.00	0.94997	1.01	0.11101	0.89	0.88	0.06206	0.48	679	6	678	5	676	10	0
C-838-2_52	5454	161.85	17.00	0.24	0.02	0.87106	1.18	0.10372	1.00	0.85	0.06091	0.62	636	6	636	6	636	13	0
C-838-2_53	2888	85.64	13.61	1.29	0.00	1.03096	1.38	0.11825	0.98	0.71	0.06323	0.96	720	7	719	7	716	20	-1
C-838-2_54	7208	218.35	24.26	0.41	0.01	0.87382	1.07	0.10394	0.89	0.84	0.06097	0.58	637	5	638	5	638	13	0
C-838-2_55	11686	362.14	41.21	0.31	0.00	0.94764	0.88	0.11085	0.74	0.84	0.06200	0.48	678	5	677	4	674	10	-1
C-838-2_56	2407	73.88	7.96	0.18	0.00	0.93395	1.42	0.10961	1.02	0.72	0.06179	0.98	671	6	670	7	667	21	-1
C-838-2_57	3810	104.22	17.29	1.11	0.00	1.14210	1.14	0.12784	0.94	0.83	0.06480	0.64	776	7	774	6	768	13	-1

Table 3: Zircon LA-ICP-MS U-Pb data – Opdalite (C-838-2) – Chapter 3\_Cont.

Grain #						Isotope ratios							Ages (Ma)					Disc. (%)	
	<sup>207</sup> Pb <sup>a</sup>	U <sup>b</sup>	Pb <sup>b</sup>	Th <sup>b</sup>	<sup>206</sup> Pbc <sup>c</sup>	<sup>207</sup> Pbd	±2s	<sup>206</sup> Pbd	±2s	rhoe	<sup>207</sup> Pb <sup>d</sup>	±2s	<sup>206</sup> Pb	±2s	<sup>207</sup> Pb	±2s	<sup>207</sup> Pb		±2s
	(cps)	(ppm)	(ppm)	U	(%)	<sup>235</sup> U	(%)	<sup>238</sup> U	(%)		<sup>206</sup> Pb	(%)	<sup>238</sup> U	(Ma)	<sup>235</sup> U	(Ma)	<sup>206</sup> Pb		(Ma)
C-838-2_58	7758	231.73	42.20	1.90	0.00	1.01528	0.97	0.11681	0.77	0.80	0.06304	0.59	712	5	712	5	709	12	0
C-838-2_59	4743	130.12	16.18	0.66	0.37	0.89792	1.63	0.10617	1.45	0.89	0.06134	0.75	650	9	651	8	651	16	0
C-838-2_60	7260	196.42	35.10	1.74	0.00	0.95832	1.22	0.11172	1.08	0.89	0.06221	0.56	683	7	682	6	681	12	0
C-838-2_70	7059	209.08	21.68	0.14	0.00	0.90262	1.09	0.10669	0.92	0.85	0.06136	0.58	654	6	653	5	652	12	0
C-838-2_71	2724	75.38	10.30	0.83	3.50	0.97273	6.09	0.11313	3.44	0.57	0.06236	5.02	691	23	690	31	686	107	-1
C-838-2_72	10380	315.51	34.36	0.15	0.49	0.95785	1.31	0.11176	0.81	0.62	0.06216	1.03	683	5	682	7	680	22	-1
C-838-2_73	9767	297.91	49.37	1.54	0.00	0.96762	0.99	0.11258	0.81	0.82	0.06234	0.57	688	5	687	5	686	12	0
C-838-2_74	5090	151.48	23.03	1.32	0.00	0.89244	1.02	0.10569	0.78	0.76	0.06124	0.66	648	5	648	5	648	14	0
C-838-2_75	7090	227.37	27.50	0.75	0.02	0.84300	1.46	0.10105	1.29	0.89	0.06050	0.68	621	8	621	7	622	15	0
C-838-2_76	13173	400.21	71.84	1.56	0.00	1.16390	1.44	0.12968	1.32	0.92	0.06510	0.58	786	10	784	8	777	12	-1
C-838-2_77	7770	250.36	28.25	0.20	0.00	0.98474	1.74	0.11416	1.54	0.88	0.06256	0.82	697	10	696	9	693	17	0
C-838-2_78	7672	225.95	44.30	2.01	0.00	1.09564	0.92	0.12382	0.71	0.77	0.06418	0.58	752	5	751	5	748	12	-1
C-838-2_79	9995	311.22	37.19	0.29	2.60	1.02620	3.81	0.11783	0.82	0.22	0.06317	3.72	718	6	717	20	714	79	-1
C-838-2_89	7368	211.48	22.37	0.15	0.23	0.97039	1.98	0.10787	1.87	0.95	0.06524	0.64	660	12	689	10	782	14	16
C-838-2_90	5627	156.34	18.70	0.21	0.00	1.10726	1.13	0.11945	0.91	0.81	0.06723	0.67	727	6	757	6	845	14	14
C-838-2_91	2771	75.36	10.18	0.94	0.55	0.92903	2.00	0.10416	1.66	0.83	0.06469	1.12	639	10	667	10	764	24	16
C-838-2_92	3702	97.66	16.07	1.19	0.00	1.06765	1.53	0.11614	1.31	0.85	0.06667	0.79	708	9	738	8	827	17	14
C-838-2_93	2464	72.48	11.67	1.32	0.00	1.08754	1.12	0.11782	0.80	0.72	0.06695	0.78	718	5	747	6	836	16	14
C-838-2_96	3427	104.00	13.74	0.80	0.00	0.93138	1.77	0.10927	1.05	0.59	0.06182	1.43	669	7	668	9	668	31	0
C-838-2_97	4360	129.05	19.01	1.08	0.54	0.94423	2.16	0.11049	1.62	0.75	0.06198	1.43	676	10	675	11	673	31	0
C-838-2_98	10019	270.27	55.76	2.30	0.20	1.013117	1.16	0.116655	0.71	0.61	0.062988	0.92	711	5	710	6	708	20	0
C-838-2_108	4783	135.55	15.07	0.09	0.00	1.011595	1.57	0.116384	0.99	0.63	0.063040	1.22	710	7	710	8	710	26	0
C-838-2_109	2142	62.15	6.98	0.38	0.14	0.878777	1.96	0.104626	0.81	0.42	0.060917	1.78	641	5	640	9	636	38	-1
C-838-2_110	3737	122.52	16.29	0.88	0.00	0.924094	1.50	0.108747	0.70	0.47	0.061631	1.33	665	4	665	7	661	28	-1
C-838-2_111	7138	225.94	24.23	0.27	0.00	0.885195	1.19	0.105134	0.69	0.58	0.061066	0.97	644	4	644	6	642	21	0
C-838-2_112	10105	310.82	45.74	1.14	0.00	0.977640	1.21	0.113448	0.86	0.71	0.062500	0.85	693	6	692	6	691	18	0
C-838-2_113	2193	66.94	8.35	0.48	0.00	0.981192	1.97	0.113796	0.77	0.39	0.062535	1.81	695	5	694	10	692	39	0
C-838-2_114	7936	245.44	23.86	0.12	0.00	0.839932	1.43	0.100817	1.06	0.74	0.060424	0.96	619	6	619	7	619	21	0
C-838-2_115	10215	306.90	32.47	0.26	0.00	0.869773	1.20	0.103647	0.81	0.68	0.060862	0.89	636	5	635	6	634	19	0
C-838-2_116	9142	268.96	50.54	2.14	0.00	0.950724	1.18	0.111054	0.76	0.65	0.062090	0.90	679	5	678	6	677	19	0
C-838-2_117	11256	353.78	33.34	0.02	0.00	0.853749	1.09	0.102015	0.69	0.64	0.060696	0.84	626	4	627	5	628	18	0



Table 3: Zircon LA-ICP-MS U-Pb data – Opdalite (C-838-2) – Chapter 3\_Cont.

Grain #	<sup>207</sup> Pb <sup>a</sup> (cps)	U <sup>b</sup> (ppm)	Pb <sup>b</sup> (ppm)	Th <sup>b</sup> U	<sup>206</sup> Pb/c <sup>c</sup> (%)	Isotope ratios						Ages (Ma)						Disc. (%)	
						<sup>207</sup> Pb/d	±2s	<sup>206</sup> Pb/d	±2s	rhoe	<sup>207</sup> Pb <sup>d</sup>	±2s	<sup>206</sup> Pb	±2s	<sup>207</sup> Pb	±2s	<sup>207</sup> Pb		±2s
						<sup>235</sup> U (%)	(%)	<sup>238</sup> U (%)	(%)		<sup>206</sup> Pb (%)	(%)	<sup>238</sup> U (Ma)	(Ma)	<sup>235</sup> U (Ma)	(Ma)	<sup>206</sup> Pb (Ma)		(Ma)
C-838-2_127	11059	147916.40	16159.28	501.49	0.00	0.897660	0.65	0.106217	0.35	0.55	0.061294	0.54	651	2	650	3	650	12	0
C-838-2_128	762	10392.83	2582.78	6780.53	0.11	0.870123	2.20	0.103543	0.83	0.38	0.060948	2.04	635	5	636	10	637	44	0
C-838-2_129	12713	164151.19	#####	704.44	0.00	0.965500	0.82	0.112404	0.67	0.82	0.062298	0.47	687	4	686	4	684	10	0
C-838-2_130	3554	43481.47	4798.74	340.18	0.86	0.915686	1.57	0.107837	0.63	0.40	0.061586	1.44	660	4	660	8	660	31	0
C-838-2_131	11812	146887.50	#####	1946.95	0.00	0.910771	0.77	0.107381	0.59	0.77	0.061515	0.49	658	4	657	4	657	11	0
C-838-2_132	4582	56757.31	8685.28	2258.41	0.31	0.899238	0.94	0.106352	0.47	0.50	0.061324	0.82	652	3	651	5	651	18	0
C-838-2_133	8436	104935.73	#####	2723.79	0.05	0.896382	0.73	0.106018	0.42	0.57	0.061322	0.59	650	3	650	3	651	13	0
C-838-2_134	2117	25215.33	3276.82	1404.23	1.28	0.880206	2.53	0.104393	1.03	0.41	0.061152	2.31	640	6	641	12	645	50	1
C-838-2_135	4461	51142.76	5317.18	251.29	0.31	0.892530	1.19	0.105718	0.91	0.77	0.061231	0.77	648	6	648	6	647	16	0
C-838-2_136	9894	119360.39	12116.93	117.59	0.00	0.906571	1.11	0.106993	0.97	0.88	0.061453	0.52	655	6	655	5	655	11	0
C-838-2_146	3426	43078.87	4993.42	798.53	0.44	0.871743	1.18	0.103862	0.74	0.63	0.060874	0.92	637	5	637	6	635	20	0
C-838-2_147	1769	21640.62	2275.54	339.76	0.83	0.882208	1.91	0.105068	0.64	0.33	0.060898	1.80	644	4	642	9	636	39	-1
C-838-2_148	6521	86871.67	7598.50	311.76	0.22	0.700465	1.48	0.087040	1.25	0.84	0.058367	0.79	538	6	539	6	544	17	1
C-838-2_149	2856	32943.91	4820.00	1862.02	0.00	0.892035	2.11	0.105354	1.01	0.48	0.061409	1.85	646	6	647	10	654	40	1
C-838-2_150	5002	62716.79	6483.66	266.47	0.00	0.885899	1.35	0.104898	0.59	0.44	0.061252	1.21	643	4	644	6	648	26	1
C-838-2_151	2489	32176.54	3903.28	843.18	0.00	0.945528	0.88	0.110573	0.43	0.49	0.062019	0.77	676	3	676	4	675	16	0
C-838-2_152	2965	30079.45	4176.60	1550.60	1.87	0.929180	6.89	0.107233	0.91	0.13	0.062845	6.83	657	6	667	34	703	145	7
C-838-2_153	3896	1346.59	1000.67	3659.19	58.91	2.849133	10.21	0.130326	7.05	0.69	0.158555	7.39	790	53	1369	80	2440	125	68
C-838-2_154	2504	34963.97	3916.58	768.75	0.08	0.874448	1.07	0.104124	0.56	0.53	0.060909	0.91	639	3	638	5	636	20	0
C-838-2_155	7080	97789.38	10190.91	286.56	0.00	0.896214	0.84	0.106070	0.60	0.72	0.061280	0.59	650	4	650	4	649	13	0
C-838-2_165	3832	35761.15	4489.22	737.85	2.24	0.969439	2.60	0.111299	0.50	0.19	0.063173	2.55	680	3	688	13	714	54	5
C-838-2_166	4451	54745.61	5692.74	231.63	0.00	0.893238	0.89	0.105802	0.63	0.70	0.061231	0.64	648	4	648	4	647	14	0
C-838-2_167	3198	39756.35	4410.29	514.91	0.02	0.878842	1.44	0.104480	1.23	0.85	0.061006	0.75	641	7	640	7	639	16	0
C-838-2_168	12395	146681.48	16291.81	457.11	0.08	0.916612	0.96	0.107863	0.71	0.73	0.061633	0.66	660	4	661	5	661	14	0
C-838-2_169	4146	44233.78	5883.48	1442.86	1.54	0.861995	2.39	0.102813	0.81	0.34	0.060807	2.25	631	5	631	11	632	48	0
C-838-2_170	7736	84984.81	11460.27	1217.91	0.00	0.970790	1.28	0.112803	1.11	0.86	0.062417	0.65	689	7	689	6	688	14	0
C-838-2_171	3178	39248.37	5317.80	1536.77	0.18	0.892315	1.13	0.105669	0.78	0.70	0.061245	0.81	648	5	648	5	648	17	0
C-838-2_172	8603	103193.74	11406.12	354.16	0.17	0.942204	1.07	0.110248	0.90	0.84	0.061983	0.58	674	6	674	5	674	12	0
C-838-2_173	5391	61788.10	11245.17	3088.03	0.41	0.937461	1.30	0.109834	0.83	0.64	0.061903	1.00	672	5	672	6	671	21	0
C-838-2_174	5048	57740.10	8524.87	1991.41	0.69	0.874621	1.82	0.103981	1.38	0.76	0.061005	1.18	638	8	638	9	639	25	0

Table 4: Zircon LA-ICP-MS U-Pb data – Granitic (hornblende)-biotite leucosome (C-838-B) – Chapter 3

Grain #	Isotope ratios										Ages (Ma)						Disc.		
	<sup>207</sup> Pb <sup>a</sup>	U <sup>b</sup>	Pb <sup>b</sup>	Th/ U <sup>b</sup>	<sup>206</sup> Pbc <sup>c</sup>	<sup>207</sup> Pb/ <sup>235</sup> U <sup>d</sup>	±2s	<sup>206</sup> Pb/ <sup>238</sup> U <sup>d</sup>	±2s	rhoe	<sup>207</sup> Pb/ <sup>206</sup> Pb <sup>d</sup>	±2s	<sup>206</sup> Pb/ <sup>238</sup> U	±2s	<sup>207</sup> Pb/ <sup>235</sup> U	±2s		<sup>207</sup> Pb/ <sup>206</sup> Pb	±2s
	(cps)	(ppm)	(ppm)		(%)	(%)	(%)	(%)	(%)	(%)	(%)	(%)	(Ma)	(Ma)	(Ma)	(Ma)		(Ma)	(Ma)
C-838B_1	4072	49944	6211	0.81	0.00	0.87044	0.97	0.10382	0.76	0.78	0.06081	0.61	637	5	636	5	632	13	-1
C-838B_2	6906	66249	7474	0.22	1.72	0.94931	2.90	0.10980	1.04	0.36	0.06271	2.70	672	7	678	14	698	58	4
C-838B_3	43921	113011	31843	0.26	1.60	3.67266	1.49	0.27232	0.76	0.51	0.09781	1.27	1553	11	1565	12	1583	24	2
C-838B_4	39458	95280	30483	0.54	1.39	3.94716	1.41	0.28403	0.84	0.59	0.10079	1.14	1612	12	1623	12	1639	21	2
C-838B_5	51358	179399	42417	0.04	1.48	3.09768	1.61	0.24677	0.73	0.45	0.09104	1.44	1422	9	1432	12	1447	27	2
C-838B_6	3439	41714	5714	1.12	0.00	0.88380	1.10	0.10500	0.78	0.71	0.06105	0.78	644	5	643	5	641	17	0
C-838B_7	59223	12818	3665	0.21	1.63	3.85911	1.47	0.27994	0.75	0.51	0.09998	1.27	1591	11	1605	12	1624	24	2
C-838B_8	73859	9509	3730	0.35	4.64	6.40092	2.58	0.36186	0.86	0.33	0.12829	2.44	1991	15	2032	23	2075	43	4
C-838B_9	3190	3653	505	1.03	0.00	0.92356	1.06	0.10881	0.81	0.77	0.06156	0.68	666	5	664	5	659	15	-1
C-838B_10	9670	8594	908	0.13	1.26	0.90192	2.03	0.10551	0.81	0.40	0.06199	1.86	647	5	653	10	674	40	4
C-838B_20	12066	145876	16319	0.33	0.00	0.92369	1.04	0.10884	0.90	0.86	0.06155	0.53	666	6	664	5	659	11	-1
C-838B_21	83848	75852	40903	0.53	3.60	10.55516	1.84	0.46312	0.87	0.47	0.16530	1.63	2453	18	2485	17	2511	27	2
C-838B_22	47369	113694	31789	0.31	1.89	3.52025	1.64	0.26526	0.76	0.46	0.09625	1.45	1517	10	1532	13	1553	27	2
C-838B_23	55769	131481	40765	0.20	0.81	4.44175	1.05	0.30438	0.74	0.70	0.10584	0.74	1713	11	1720	9	1729	14	1
C-838B_24	84183	164121	58456	0.18	0.00	5.66260	0.83	0.34828	0.72	0.86	0.11792	0.42	1926	12	1926	7	1925	8	0
C-838B_25	2364	28887	4298	1.39	0.00	0.91122	1.26	0.10759	0.81	0.64	0.06142	0.97	659	5	658	6	654	21	-1
C-838B_26	41338	145000	30519	0.28	2.27	2.29700	2.03	0.20371	0.76	0.38	0.08178	1.88	1195	8	1211	14	1240	37	4
C-838B_27	5817	70189	10400	1.29	0.00	0.95582	0.99	0.11174	0.71	0.72	0.06204	0.69	683	5	681	5	675	15	-1
C-838B_28	27536	61345	14669	0.30	4.16	2.70413	3.20	0.22484	0.93	0.29	0.08723	3.06	1307	11	1330	24	1365	59	4
C-838B_29	494	5937	1066	2.35	0.00	0.87353	3.81	0.10273	1.07	0.28	0.06167	3.66	630	6	637	18	663	78	5
C-838B_39	71754	164074	49799	0.32	1.52	4.01979	1.39	0.28684	0.76	0.55	0.10164	1.17	1626	11	1638	11	1654	22	2
C-838B_40	14097	164632	17725	0.20	0.04	0.92668	1.02	0.10895	0.79	0.78	0.06169	0.65	667	5	666	5	663	14	0
C-838B_41	32147	75352	23106	0.36	1.26	4.02733	1.31	0.28743	0.78	0.60	0.10162	1.05	1629	11	1640	11	1654	19	2
C-838B_42	353	4133	1061	4.36	0.00	0.88866	4.63	0.10542	1.11	0.24	0.06114	4.49	646	7	646	22	644	97	0
C-838B_43	16932	70082	12242	0.06	2.44	1.95865	2.30	0.18373	0.85	0.37	0.07732	2.14	1087	9	1101	16	1129	43	4
C-838B_44	81479	177442	55352	0.33	1.40	4.17687	1.30	0.29319	0.71	0.55	0.10333	1.09	1657	10	1669	11	1685	20	2
C-838B_45	84613	58007	37004	0.72	2.73	13.00139	1.41	0.50842	0.77	0.55	0.18547	1.18	2650	17	2680	13	2702	19	2
C-838B_46	25178	75282	19332	0.30	1.69	3.09198	1.56	0.24595	0.71	0.46	0.09118	1.39	1418	9	1431	12	1450	26	2
C-838B_47	1140	14103	2769	2.86	0.00	0.85908	1.46	0.10266	0.92	0.63	0.06069	1.14	630	6	630	7	628	24	0
C-838B_48	36566	83797	24630	0.37	1.96	3.68640	1.71	0.27259	0.81	0.48	0.09808	1.50	1554	11	1568	14	1588	28	2
C-838B_58	5008	4116	394	0.10	2.05	0.82753	2.99	0.09971	0.50	0.17	0.06019	2.95	613	3	612	14	611	64	0
C-838B_59	31388	11934	1270	0.12	2.68	0.95576	2.85	0.10902	0.89	0.31	0.06359	2.70	667	6	681	14	728	57	8
C-838B_60	119653	22330	4354	0.39	3.62	1.81306	4.23	0.17248	3.10	0.73	0.07624	2.87	1026	29	1050	28	1101	57	7
C-838B_61	15684	14169	1398	0.25	0.00	0.80805	0.85	0.09778	0.70	0.82	0.05994	0.49	601	4	601	4	601	11	0
C-838B_62	47402	7487	2058	0.28	3.05	3.38083	2.39	0.25687	0.54	0.23	0.09546	2.33	1474	7	1500	19	1537	44	4
C-838B_63	69361	209713	35374	0.04	2.95	1.83909	2.57	0.17528	0.64	0.25	0.07610	2.49	1041	6	1060	17	1098	50	5
C-838B_64	524	3536	631	2.80	0.96	0.69417	8.48	0.08620	1.72	0.20	0.05841	8.31	533	9	535	36	545	182	2
C-838B_65	24830	74202	14272	0.26	2.17	2.03062	1.93	0.18806	0.50	0.26	0.07831	1.86	1111	5	1126	13	1155	37	4
C-838B_66	151706	241953	86188	0.05	2.49	6.20634	1.59	0.36017	0.39	0.25	0.12498	1.54	1983	7	2005	14	2028	27	2
C-838B_67	10695	84512	10283	0.19	0.15	1.11076	1.66	0.12475	0.59	0.35	0.06457	1.56	758	4	759	9	761	33	0
C-838B_77	5132	49199	5535	0.58	0.00	0.82614	0.81	0.09963	0.48	0.59	0.06014	0.65	612	3	611	4	609	14	-1
C-838B_78	54510	112177	29446	0.28	2.49	3.18930	2.13	0.24987	0.99	0.47	0.09257	1.88	1438	13	1455	17	1479	36	3
C-838B_79	1506	14791.49	2415.12	2.29	0.87	0.75417	2.26	0.09257	0.55	0.25	0.05909	2.19	571	3	571	10	570	48	0
C-838B_80	3134	29962.37	5393.39	2.56	0.87	0.79155	1.63	0.09621	0.59	0.37	0.05967	1.51	592	3	592	7	592	33	0

Table 4: Zircon LA-ICP-MS U-Pb data – Granitic (hornblende)-biotite leucosome (C-838-B) – Chapter 3 Cont.

Grain #						Isotope ratios							Ages (Ma)						Disc. (%)
	<sup>207</sup> Pb <sup>a</sup>	U <sup>b</sup>	Pb <sup>b</sup>	Th/ U <sup>b</sup>	<sup>206</sup> Pbc <sup>c</sup>	<sup>207</sup> Pb/ <sup>235</sup> U <sup>d</sup>	±2s	<sup>206</sup> Pb/ <sup>238</sup> U <sup>d</sup>	±2s	rhoe	<sup>207</sup> Pb/ <sup>206</sup> Pb <sup>d</sup>	±2s	<sup>206</sup> Pb/ <sup>238</sup> U	±2s	<sup>207</sup> Pb/ <sup>235</sup> U	±2s	<sup>207</sup> Pb/ <sup>206</sup> Pb	±2s	
	(cps)	(ppm)	(ppm)		(%)	(%)	(%)	(%)	(%)	(%)	(%)	(%)	(Ma)	(Ma)	(Ma)	(Ma)	(Ma)	(Ma)	
C-838B_81	54993	105868	27105	0.52	2.83	2.64880	2.19	0.22216	0.49	0.22	0.08647	2.14	1293	6	1314	16	1349	41	4
C-838B_82	3203	29721	4145	1.34	0.00	0.82319	0.89	0.09924	0.54	0.61	0.06016	0.71	610	3	610	4	609	15	0
C-838B_83	4127	38998	4849	0.88	0.06	0.85380	0.84	0.10224	0.43	0.51	0.06056	0.73	628	3	627	4	624	16	-1
C-838B_84	79811	55300	32821	0.33	0.00	13.83439	1.41	0.53347	0.78	0.55	0.18808	1.18	2756	17	2738	13	2725	19	-1
C-838B_85	44535	76435	22013	0.33	2.23	3.63464	1.81	0.27000	0.73	0.40	0.09763	1.66	1541	10	1557	15	1579	31	2
C-838B_86	6555	62366	6337	0.50	0.00	0.73754	0.78	0.09087	0.50	0.65	0.05887	0.59	561	3	561	3	562	13	0
C-838B_96	69507	110372	26088	0.22	3.05	2.75825	2.31	0.22746	0.62	0.27	0.08795	2.23	1321	7	1344	17	1381	43	4
C-838B_97	1322	10840	1630	1.40	3.54	0.90409	5.23	0.10682	1.36	0.26	0.06138	5.05	654	8	654	26	653	108	0
C-838B_98	50836	80768	26486	0.31	0.90	4.59658	0.95	0.31021	0.50	0.52	0.10747	0.82	1742	8	1749	8	1757	15	1
C-838B_99	3878	35064	2999	0.23	0.16	0.66690	1.30	0.08365	1.00	0.77	0.05782	0.83	518	5	519	5	523	18	1
C-838B_100	9652	34610	2351	0.37	3.32	0.43156	7.02	0.05642	2.95	0.42	0.05548	6.37	354	10	364	22	431	142	18
C-838B_101	85974	139157	35352	0.20	2.63	3.14978	2.01	0.24740	0.56	0.28	0.09234	1.94	1425	7	1445	16	1474	37	3
C-838B_102	24451	96173	9727	0.13	2.65	0.88184	4.08	0.10269	1.67	0.41	0.06228	3.72	630	10	642	20	684	79	8
C-838B_103	72374	204503	27031	0.14	4.03	1.16110	3.26	0.12513	0.75	0.23	0.06730	3.17	760	5	782	18	847	66	10
C-838B_104	119705	24432	17378	1.00	59.67	1.19362	13.47	0.05900	10.88	0.81	0.14674	7.94	370	39	798	77	2308	136	84
C-838B_105	3529	29575	3072	0.21	0.00	0.86817	1.36	0.10366	0.57	0.42	0.06074	1.24	636	3	635	6	630	27	-1
C-838B_115	30916	19472	7144	0.40	9.35	5.34874	4.20	0.32141	1.16	0.28	0.12069	4.03	1797	18	1877	37	1967	72	9
C-838B_116	35637	56954	20873	0.68	1.03	4.61315	1.34	0.31064	0.98	0.73	0.10771	0.92	1744	15	1752	11	1761	17	1
C-838B_117	71341	63479	19296	0.45	8.87	3.63863	4.36	0.25931	1.01	0.23	0.10177	4.24	1486	13	1558	35	1657	78	10
C-838B_118	3358	2892	1016	3.14	31.69	1.43872	8.11	0.11442	4.05	0.50	0.09119	7.02	698	27	905	50	1451	134	52
C-838B_119	3298	29223	5559	2.43	0.00	0.90004	1.42	0.10659	1.08	0.76	0.06124	0.92	653	7	652	7	648	20	-1
C-838B_120	2670	23381	2590	0.76	0.20	0.71571	1.75	0.08858	1.26	0.72	0.05860	1.21	547	7	548	7	552	26	1
C-838B_121	89908	163159	51701	0.08	0.11	4.87775	1.03	0.32197	0.37	0.36	0.10987	0.96	1799	6	1798	9	1797	18	0
C-838B_131	84593	108963	40386	0.47	0.95	5.05412	0.88	0.32630	0.42	0.48	0.11234	0.77	1820	7	1828	7	1838	14	1
C-838B_132	902	7491	1545	3.04	0.86	0.83418	2.32	0.10017	1.01	0.44	0.06039	2.09	615	6	616	11	618	45	0
C-838B_133	42934	56516	18452	0.31	1.60	4.44026	1.43	0.30301	0.80	0.56	0.10628	1.19	1706	12	1720	12	1737	22	2
C-838B_134	3338	26491	3203	0.53	0.00	0.94057	1.32	0.11023	0.70	0.53	0.06188	1.12	674	4	673	7	670	24	-1
C-838B_135	3320	29398	5314	2.36	0.00	0.83575	1.12	0.10045	0.85	0.76	0.06034	0.72	617	5	617	5	616	16	0
C-838B_136	4575	38096	4649	0.88	0.09	0.78095	1.03	0.09509	0.68	0.67	0.05956	0.76	586	4	586	5	588	17	0
C-838B_137	2055	16926	1703	0.34	0.82	0.77179	1.82	0.09422	0.87	0.48	0.05941	1.60	580	5	581	8	582	35	0
C-838B_138	2248	18882	2962	1.78	0.29	0.80368	1.41	0.09735	0.57	0.41	0.05988	1.29	599	3	599	6	599	28	0
C-838B_139	85645	84338	30299	0.41	6.00	5.05149	3.18	0.31711	0.90	0.28	0.11553	3.05	1776	14	1828	27	1888	55	6
C-838B_140	53401	82654	23109	0.51	2.86	3.00678	2.30	0.24005	1.01	0.44	0.09084	2.07	1387	13	1409	18	1443	39	4
C-838B_150	29278	54064	12926	0.38	2.90	2.56285	2.36	0.21751	0.77	0.33	0.08546	2.23	1269	9	1290	17	1326	43	4
C-838B_151	19197	88	21	21.58	2.37	2.46358	2.54	0.21221	1.67	0.66	0.08420	1.92	1241	19	1261	19	1297	37	4
C-838B_152	43915	71136	21848	0.60	1.88	3.39378	1.62	0.25927	0.65	0.40	0.09494	1.49	1486	9	1503	13	1527	28	3
C-838B_153	866	15	3	125.23	0.36	0.74724	2.79	0.09150	1.58	0.57	0.05923	2.29	564	9	567	12	576	50	2
C-838B_154	4435	80	8	11.04	0.00	0.83866	1.65	0.10057	1.49	0.90	0.06048	0.70	618	9	618	8	621	15	0
C-838B_155	48134	153	45	9.18	3.33	4.05728	2.97	0.28764	1.67	0.56	0.10230	2.46	1630	24	1646	25	1666	45	2
C-838B_156	894	13	2	67.51	0.34	0.87667	3.19	0.10413	1.92	0.60	0.06106	2.54	639	12	639	15	641	55	0
C-838B_157	39694	114	35	9.44	1.69	4.13121	1.86	0.29010	1.37	0.73	0.10328	1.26	1642	20	1660	15	1684	23	2
C-838B_158	45931	182	42	9.00	3.09	2.75714	2.75	0.22735	1.47	0.54	0.08796	2.33	1321	18	1344	21	1382	45	4
C-838B_159	15262	276	29	0.68	0.00	0.94648	2.74	0.11040	1.85	0.68	0.06218	2.02	675	12	676	14	680	43	1
C-838B_169	2971	52	8	75.77	0.00	0.83208	1.84	0.09974	1.43	0.78	0.06051	1.16	613	8	615	9	622	25	1

Table 4: Zircon LA-ICP-MS U–Pb data – Granitic (hornblende)-biotite leucosome (C-838-B) – Chapter 3\_Cont.

Grain #						Isotope ratios						Ages (Ma)						Disc. (%)	
	<sup>207</sup> Pb <sup>a</sup>	U <sup>b</sup>	Pb <sup>b</sup>	Th/ U <sup>b</sup>	<sup>206</sup> Pb <sup>c</sup>	<sup>207</sup> Pb/ <sup>235</sup> U <sup>d</sup>	±2s	<sup>206</sup> Pb/ <sup>238</sup> U <sup>d</sup>	±2s	rhoe	<sup>207</sup> Pb/ <sup>206</sup> Pb <sup>d</sup>	±2s	<sup>206</sup> Pb/ <sup>238</sup> U	±2s	<sup>207</sup> Pb/ <sup>235</sup> U	±2s	<sup>207</sup> Pb/ <sup>206</sup> Pb		±2s
	(cps)	(ppm)	(ppm)		(%)		(%)		(%)			(%)	(Ma)	(Ma)	(Ma)	(Ma)	(Ma)		(Ma)
C-838B_171	32096	137	33	11.34	2.54	2.84072	2.51	0.23247	1.52	0.61	0.08863	1.99	1347	19	1366	19	1396	38	3
C-838B_172	32352	115	39	12.03	0.00	5.00723	1.63	0.32521	1.51	0.93	0.11167	0.62	1815	24	1821	14	1827	11	1
C-838B_173	12277	167	19	9.49	0.00	0.92237	4.06	0.10755	1.35	0.33	0.06220	3.83	658	8	664	20	681	82	3
C-838B_174	110449	425	99	1.86	4.59	3.00064	3.43	0.23634	1.70	0.50	0.09208	2.98	1368	21	1408	26	1469	56	7
C-838B_175	6055	102	13	17.59	0.00	1.08694	1.57	0.12311	1.43	0.91	0.06403	0.66	748	10	747	8	743	14	-1
C-838B_176	1865	34	4	49.33	0.00	0.70310	2.17	0.08716	1.96	0.91	0.05851	0.92	539	10	541	9	549	20	2
C-838B_177	40412	144	78	27.23	0.00	10.06600	1.63	0.46968	1.48	0.90	0.15544	0.70	2482	31	2441	15	2407	12	-3
C-838B_178	77967	343	85	4.49	0.88	3.27649	2.36	0.25413	2.21	0.94	0.09351	0.83	1460	29	1475	19	1498	16	3

Valid f for samples C-838-A, C-838-2 and C-838-B

<sup>a</sup> Within run background-corrected mean <sup>207</sup>Pb signal in cps (counts per second).

<sup>b</sup> U and Pb content and Th/U ratio were calculated relative to GJ-1 reference zircon.

<sup>c</sup> percentage of the common Pb on the <sup>206</sup>Pb. b.d. = below detection limit.

<sup>d</sup> corrected for background. within-run Pb/U fractionation (in case of <sup>206</sup>Pb/<sup>238</sup>U) and common Pb using Stacy and Kramers (1975) model Pb composition and subsequently normalized to GJ-1 (ID-TIMS value/mean)

<sup>e</sup> rho is the <sup>206</sup>Pb/<sup>238</sup>U/<sup>207</sup>Pb/<sup>235</sup>U error correlation coefficient.

<sup>f</sup> degree of concordance = <sup>206</sup>Pb/<sup>238</sup>U age / <sup>207</sup>Pb/<sup>206</sup>Pb age x 100

<sup>g</sup> Accuracy and reproducibility was checked by repeated analyses (n = 7) of reference zircon Plesovice. Felix and 91500; data given as mean with 2 standard deviation uncertainties

Table 5: Zircon LA-ICP-MS U-Pb data – Mafic enclave (C-716-B) – Chapter 3

Spot number	$f_{206}^a$	Pb ppm	Th ppm	U ppm	Th/ U <sup>b</sup>	Isotope ratios <sup>c</sup>						Ages (Ma)						% Disc <sup>f</sup>		
						<sup>207</sup> Pb/ <sup>235</sup> U		<sup>206</sup> Pb/ <sup>238</sup> U		Rho <sup>d</sup>		<sup>207</sup> Pb/ <sup>206</sup> Pb <sup>e</sup>		<sup>206</sup> Pb/ <sup>238</sup> U		<sup>207</sup> Pb/ <sup>235</sup> U			<sup>206</sup> Pb/ <sup>206</sup> Pb	
						1 s [%]	1 s [%]	1 s [%]	1 s [%]	1 s abs	1 s abs	1 s abs	1 s abs	1 s abs	1 s abs					
C_716B_1.1	0.0035	10	29	82	0.35	0.9047	2.91	0.1069	2.15	0.74	0.0614	1.97	655	14	654	19	652	13	0	
C_716B_2.1	0.0051	7	55	49	1.12	0.9194	5.50	0.1083	4.32	0.79	0.0616	3.41	663	29	662	36	660	22	0	
C_716B_3.1	0.0033	17	119	129	0.93	0.8854	2.34	0.1050	1.45	0.62	0.0612	1.83	644	9	644	15	645	12	0	
C_716B_4.1	0.0038	23	237	151	1.57	0.9191	1.71	0.1084	0.68	0.40	0.0615	1.56	664	5	662	11	656	10	-1	
C_716B_5.1	0.0021	31	220	242	0.91	0.8784	1.62	0.1047	0.65	0.40	0.0609	1.48	642	4	640	10	635	9	-1	
C_716B_6.1	0.0026	24	261	162	1.61	0.8678	2.19	0.1035	1.42	0.65	0.0608	1.66	635	9	634	14	632	10	0	
C_716B_7.1	0.0026	22	219	152	1.44	0.8721	2.73	0.1038	2.09	0.77	0.0609	1.75	637	13	637	17	636	11	0	
C_716B_8.1	0.0028	15	105	111	0.95	0.8759	2.89	0.1041	2.30	0.79	0.0610	1.76	638	15	639	18	641	11	0	
C_716B_9.1	0.0026	25	286	166	1.73	0.8770	2.61	0.1043	2.06	0.79	0.0610	1.59	639	13	639	17	639	10	0	
C_716B_10.1	0.0068	10	48	85	0.57	0.8430	4.07	0.1011	3.08	0.76	0.0605	2.65	621	19	621	25	622	16	0	
C_716B_11.1	0.0035	20	124	155	0.80	0.8538	4.04	0.1020	3.53	0.87	0.0607	1.98	626	22	627	25	628	12	0	
C_716B_12.1	0.0044	16	148	111	1.33	0.8595	3.59	0.1026	2.96	0.83	0.0608	2.02	630	19	630	23	630	13	0	
C_716B_13.1	0.0034	9	67	65	1.04	0.8710	4.88	0.1036	3.85	0.79	0.0610	2.99	636	24	636	31	638	19	0	
C_716B_14.1	0.0040	11	92	84	1.10	0.8458	3.67	0.1013	3.00	0.82	0.0605	2.13	622	19	622	23	623	13	0	
C_716B_15.1	0.0037	17	126	135	0.94	0.7888	3.30	0.0958	2.78	0.84	0.0597	1.77	590	16	590	19	593	11	1	
C_716B_16.1	0.0080	7	55	48	1.13	0.8082	4.83	0.0977	4.10	0.85	0.0600	2.55	601	25	601	29	603	15	0	
C_716B_17.1	0.0028	17	87	130	0.67	0.9045	2.61	0.1071	1.88	0.72	0.0613	1.80	656	12	654	17	649	12	-1	
C_716B_18.1	0.0032	15	96	118	0.82	0.8587	2.51	0.1027	1.85	0.74	0.0607	1.70	630	12	629	16	627	11	0	
C_716B_19.1	0.0043	5	28	42	0.67	0.7537	7.27	0.0927	6.53	0.90	0.0590	3.21	571	37	570	41	567	18	-1	
C_716B_20.1	0.0037	9	39	78	0.50	0.8507	3.18	0.1018	1.84	0.58	0.0606	2.60	625	11	625	20	624	16	0	
C_716B_21.1	0.0046	6	31	48	0.65	0.7954	4.47	0.0965	3.24	0.72	0.0598	3.08	594	19	594	27	595	18	0	
C_716B_22.1	0.0037	11	92	81	1.15	0.8122	4.08	0.0981	3.61	0.88	0.0600	1.91	603	22	604	25	605	12	0	
C_716B_23.1	0.0047	6	48	44	1.09	0.8054	4.39	0.0976	3.05	0.70	0.0599	3.16	600	18	600	26	598	19	0	
C_716B_24.1	0.0040	10	81	70	1.17	0.8066	4.28	0.0974	3.06	0.72	0.0600	2.99	599	18	601	26	605	18	1	
C_716B_25.1	0.0030	16	130	127	1.03	0.7800	3.55	0.0951	3.09	0.87	0.0595	1.75	585	18	585	21	586	10	0	
C_716B_26.1	0.0027	17	161	104	1.55	0.8296	3.42	0.0999	2.53	0.74	0.0602	2.30	614	16	613	21	612	14	0	
C_716B_27.1	0.0028	20	220	127	1.73	0.8244	4.13	0.0992	3.67	0.89	0.0603	1.90	610	22	611	25	614	12	1	
C_716B_28.1	0.0022	22	140	159	0.88	0.8883	3.43	0.1053	2.92	0.85	0.0612	1.80	645	19	645	22	646	12	0	
C_716B_29.1	0.0027	20	163	141	1.15	0.8674	2.96	0.1033	2.27	0.77	0.0609	1.91	634	14	634	19	636	12	0	
C_716B_30.1	0.0019	28	312	191	1.64	0.8086	3.60	0.0977	3.09	0.86	0.0600	1.85	601	19	602	22	604	11	0	
C_716B_31.1	0.0041	13	86	89	0.97	0.8931	3.73	0.1057	3.20	0.86	0.0613	1.92	648	21	648	24	648	12	0	
C_716B_32.1	0.0036	16	117	114	1.03	0.8291	3.43	0.0995	2.68	0.78	0.0604	2.14	612	16	613	21	619	13	1	
C_716B_33.1	0.0026	20	205	134	1.53	0.8302	4.01	0.0999	3.39	0.85	0.0603	2.13	614	21	614	25	613	13	0	
C_716B_34.1	0.0019	25	253	158	1.60	0.8496	4.40	0.1016	3.82	0.87	0.0606	2.18	624	24	624	27	627	14	0	
C_716B_35.1	0.0030	12	86	86	1.00	0.8597	3.56	0.1028	2.36	0.66	0.0607	2.66	631	15	630	22	628	17	0	
C_716B_36.1	0.0050	8	64	57	1.12	0.8347	5.47	0.1004	4.51	0.82	0.0603	3.09	617	28	616	34	614	19	0	
C_716B_37.1	0.0084	7	38	58	0.65	0.8512	4.92	0.1018	4.11	0.84	0.0606	2.70	625	26	625	31	626	17	0	
C_716B_38.1	0.0017	42	342	304	1.12	0.8127	2.54	0.0982	2.05	0.81	0.0600	1.51	604	12	604	15	604	9	0	
C_716B_39.1	0.0034	17	122	121	1.01	0.8554	4.52	0.1022	3.68	0.81	0.0607	2.63	627	23	628	28	629	17	0	
C_716B_40.1	0.0054	8	46	59	0.79	0.8744	4.22	0.1041	3.18	0.75	0.0609	2.78	638	20	638	27	637	18	0	
C_716B_41.1	0.0098	8	56	57	0.98	0.8661	5.19	0.1032	4.30	0.83	0.0609	2.92	633	27	633	33	634	19	0	
C_716B_42.1	0.0022	22	152	155	0.98	0.8851	3.67	0.1050	3.28	0.89	0.0611	1.66	644	21	644	24	644	11	0	
C_716B_43.1	0.0035	12	40	105	0.38	0.8515	3.26	0.1020	2.29	0.70	0.0606	2.33	626	14	625	20	623	15	0	
C_716B_44.1	0.0025	35	365	226	1.61	0.8610	2.98	0.1029	2.37	0.80	0.0607	1.80	631	15	631	19	629	11	0	
C_716B_45.1	0.0031	15	106	104	1.02	0.8791	5.37	0.1046	4.93	0.92	0.0610	2.13	641	32	640	34	638	14	0	
C_716B_46.1	0.0037	15	133	100	1.33	0.8655	2.76	0.1032	2.06	0.75	0.0608	1.84	633	13	633	17	632	12	0	
C_716B_47.1	0.0063	10	96	66	1.44	0.8526	4.97	0.1019	4.46	0.90	0.0607	2.20	625	28	626	31	628	14	0	
C_716B_48.1	0.0023	5	39	37	1.06	0.8988	3.79	0.1060	1.56	0.41	0.0615	3.46	649	10	651	25	657	23	1	
C_716B_49.1	0.0042	7	53	55	0.96	0.8700	4.08	0.1037	3.10	0.76	0.0608	2.65	636	20	636	26	633	17	0	
C_716B_50.1	0.0029	21	220	133	1.66	0.8627	2.66	0.1029	2.15	0.81	0.0608	1.58	631	14	632	17	633	10	0	

Table 5: Zircon LA-ICP-MS U-Pb data – Mafic enclave (C-716-B) – Chapter 3\_Cont.

Spot number	$f_{206}^a$	Pb ppm	Th ppm	U ppm	Th/ U <sup>b</sup>	Isotope ratios <sup>c</sup>						Ages (Ma)						% Disc <sup>f</sup>	
						<sup>207</sup> Pb/ <sup>235</sup> U	1 s [%]	<sup>206</sup> Pb/ <sup>238</sup> U	1 s [%]	Rho <sup>d</sup>	<sup>207</sup> Pb/ <sup>206</sup> Pb <sup>e</sup>	1 s [%]	<sup>206</sup> Pb/ <sup>238</sup> U	1 s abs	<sup>207</sup> Pb/ <sup>235</sup> U	1 s abs	<sup>207</sup> Pb/ <sup>206</sup> Pb		1 s abs
C_716B_51.1	0.0095	7	48	44	1.09	0.9332	5.93	0.1094	4.75	0.80	0.0619	3.55	669	32	669	40	670	24	0
C_716B_52.1	0.0043	8	50	60	0.83	0.8255	4.54	0.0991	3.16	0.70	0.0604	3.25	609	19	611	28	618	20	1
C_716B_53.1	0.0019	21	188	139	1.35	0.8476	2.90	0.1016	1.92	0.66	0.0605	2.17	624	12	623	18	621	13	0
C_716B_54.1	0.0030	18	154	120	1.29	0.8669	2.74	0.1033	1.92	0.70	0.0609	1.95	634	12	634	17	635	12	0
C_716B_55.1	0.0032	11	73	79	0.92	0.8614	3.67	0.1028	2.56	0.70	0.0608	2.63	631	16	631	23	632	17	0
C_716B_56.1	0.0033	15	130	102	1.28	0.8752	3.40	0.1041	2.59	0.76	0.0610	2.20	638	17	638	22	639	14	0
C_716B_57.1	0.0065	9	70	62	1.13	0.8697	5.13	0.1037	3.91	0.76	0.0608	3.31	636	25	635	33	633	21	0
C_716B_58.1	0.0032	9	70	67	1.05	0.8656	3.00	0.1033	2.19	0.73	0.0608	2.05	633	14	633	19	632	13	0
C_716B_59.1	0.0014	5	74	37	2.02	0.8828	4.00	0.1048	3.70	0.92	0.0611	1.54	642	24	642	26	643	10	0
C_716B_60.1	0.0033	14	90	103	0.88	0.8809	2.66	0.1046	1.85	0.70	0.0611	1.91	641	12	641	17	641	12	0
C_716B_61.1	0.0046	12	108	84	1.28	0.8546	6.23	0.1023	5.51	0.88	0.0606	2.90	628	35	627	39	625	18	0
C_716B_62.1	0.0026	26	219	191	1.15	0.8828	3.63	0.1047	3.14	0.86	0.0612	1.82	642	20	642	23	645	12	0
C_716B_63.1	0.0043	6	42	40	1.05	0.8277	4.48	0.0996	3.24	0.72	0.0603	3.10	612	20	612	27	614	19	0

<sup>a</sup>Fraction of the non-radiogenic <sup>206</sup>Pb in the analyzed zircon spot. where  $f_{206} = \frac{^{206}\text{Pb}/^{204}\text{Pb}}{c/^{206}\text{Pb}/^{204}\text{Pb}} - 1$  (c=common; s=sample);

<sup>b</sup>Th/U ratios and amount of Pb, Th and U (in ppm) are calculated relative to 91500 reference zircon

<sup>c</sup>Corrected for background and within-run Pb/U fractionation and normalized to reference zircon GJ-1 (ID-TIMS v values/measured v value); <sup>207</sup>Pb/<sup>235</sup>U calculated using  $(^{207}\text{Pb}/^{206}\text{Pb}) / (^{238}\text{U}/^{206}\text{Pb} * 1/137.88)$

<sup>d</sup>Rho is the error correlation defined as the quotient of the propagated errors of the <sup>206</sup>Pb/<sup>238</sup>U and the <sup>207</sup>/<sup>235</sup>U ratio

<sup>e</sup>Corrected for mass-bias by normalizing to GJ-1 reference zircon and common Pb using the model Pb composition of Stacey and Kramers (1975)

<sup>f</sup>Degree of concordance =  $(^{206}\text{Pb}/^{238}\text{U} \text{ age} * 100 / ^{207}\text{Pb}/^{206}\text{Pb} \text{ age})$

Table 6: Zircon LA-ICP-MS U–Pb data – Clinopyroxene-garnet amphibolite (MT-13) – Chapter 4

Spot #						Isotope ratios <sup>c</sup>						Ages (Ma)					Disc. <sup>f</sup> (%)		
	<sup>207</sup> Pb <sup>a</sup> (cps)	U <sup>b</sup> (ppm)	Pb <sup>b</sup> (ppm)	Th <sup>b</sup> U	<sup>206</sup> Pb <sup>c</sup> (%)	<sup>207</sup> Pb/ <sup>235</sup> U <sup>d</sup>	±2s (%)	<sup>206</sup> Pb/ <sup>238</sup> U <sup>d</sup>	±2s (%)	rho <sup>e</sup>	<sup>207</sup> Pb/ <sup>206</sup> Pb <sup>d</sup>	±2s (%)	<sup>206</sup> Pb/ <sup>238</sup> U	±2s (Ma)	<sup>207</sup> Pb <sup>235</sup> U	±2s (Ma)		±2s (Ma)	
MT-13_16	15934	120	33	0.24	2.47	2.9624	3.39	0.2387	0.59	0.17	0.0900	3.34	1380	7	1398	26	1426	64	3
MT-13_17	5060	5	3	1.04	62.90	2.6174	10.66	0.1111	7.79	0.73	0.1709	7.27	679	50	1306	81	2566	122	74
MT-13_18	47223	539	122	0.28	1.92	2.1780	1.77	0.2037	0.43	0.24	0.0775	1.72	1195	5	1174	12	1135	34	-5
MT-13_19	41990	432	88	0.20	1.45	1.9990	1.50	0.1870	0.64	0.43	0.0775	1.35	1105	7	1115	10	1135	27	3
MT-13_20	45273	523	116	0.28	0.63	2.1955	0.81	0.1994	0.35	0.43	0.0799	0.73	1172	4	1180	6	1194	14	2
MT-13_21	26721	231	62	0.29	0.78	2.7911	0.90	0.2332	0.39	0.44	0.0868	0.81	1351	5	1353	7	1357	16	0
MT-13_22	5349	12	5	1.66	44.09	1.6317	8.46	0.1089	4.67	0.55	0.1087	7.06	666	30	983	55	1778	129	63
MT-13_23	8016	77	16	0.20	3.85	1.9467	3.86	0.1815	0.70	0.18	0.0778	3.80	1075	7	1097	26	1142	76	6
MT-13_24	1283	48	4	0.01	0.00	0.8399	1.05	0.1008	0.54	0.51	0.0604	0.90	619	3	619	5	618	19	0
MT-13_25	1967	71	6	0.01	0.00	0.8148	1.01	0.0985	0.69	0.68	0.0600	0.75	606	4	605	5	603	16	0
MT_13_32	42931	365	96	0.09	0.19	3.3757	0.69	0.2620	0.51	0.74	0.0934	0.46	1500	7	1499	5	1497	9	0
MT_13_33	4696	9	3	0.66	49.23	0.8584	10.07	0.0556	7.11	0.71	0.1120	7.13	349	24	629	48	1832	129	81
MT_13_34	730	22	2	0.03	0.00	0.8829	1.60	0.1049	0.93	0.58	0.0611	1.30	643	6	643	8	641	28	0
MT_13_35	4001	4	3	0.63	58.55	3.0431	9.94	0.1365	6.71	0.68	0.1617	7.33	825	52	1418	79	2473	124	67
MT_13_36	79906	688	178	0.32	1.05	2.5278	1.13	0.2181	0.56	0.49	0.0841	0.99	1272	6	1280	8	1294	19	2
MT_13_37	42701	371	112	0.50	0.65	2.9034	0.75	0.2383	0.31	0.41	0.0884	0.69	1378	4	1383	6	1391	13	1
MT_13_38	2280	83	8	0.01	0.00	0.8208	1.10	0.0993	0.49	0.45	0.0600	0.99	610	3	609	5	602	21	-1
MT_13_39	2019	71	6	0.01	0.00	0.7983	0.93	0.0969	0.44	0.47	0.0597	0.82	596	3	596	4	594	18	0
MT_13_40	2123	76	7	0.01	0.00	0.8094	1.10	0.0981	0.53	0.49	0.0599	0.96	603	3	602	5	599	21	-1
MT_13_41	2196	74	7	0.01	1.70	0.7869	2.46	0.0957	0.69	0.28	0.0596	2.36	589	4	589	11	590	51	0
MT-13_48	23710	204	58	0.20	0.03	3.4486	0.88	0.2648	0.55	0.62	0.0945	0.69	1514	7	1516	7	1517	13	0
MT-13_49	85686	1091	224	0.12	0.76	2.2414	1.00	0.2029	0.55	0.55	0.0801	0.83	1191	6	1194	7	1200	16	1
MT-13_50	65503	518	151	0.28	1.09	3.3446	1.21	0.2599	0.50	0.41	0.0933	1.10	1490	7	1492	9	1494	21	0
MT-13_51	47530	302	49	0.56	3.42	0.7059	29.04	0.0853	28.82	0.99	0.0600	3.54	528	148	542	130	604	76	13
MT-13_52	3155	110	10	0.01	0.00	0.8527	0.91	0.1021	0.47	0.52	0.0605	0.78	627	3	626	4	623	17	-1
MT-13_53	17056	134	40	0.25	0.50	3.4657	0.87	0.2651	0.38	0.43	0.0948	0.78	1516	5	1519	7	1525	15	1
MT-13_54	7451	97	18	0.18	0.98	1.8344	1.49	0.1764	0.61	0.41	0.0754	1.36	1047	6	1058	10	1080	27	3
MT-13_55	10746	115	33	0.21	5.31	3.4118	4.94	0.2648	0.87	0.18	0.0935	4.86	1514	12	1507	40	1497	92	-1
MT-13_56	2431	83	8	0.01	0.00	0.8410	1.08	0.1009	0.55	0.51	0.0604	0.93	620	3	620	5	619	20	0
MT-13_57	2254	75	7	0.01	0.08	0.8659	1.02	0.1031	0.50	0.48	0.0609	0.89	633	3	633	5	636	19	1
MT-13_64	36456	270	88	0.33	0.00	3.7954	0.65	0.2807	0.37	0.57	0.0981	0.53	1595	5	1592	5	1587	10	0
MT-13_65	3736	115	14	0.29	0.00	1.5273	2.70	0.1185	2.26	0.84	0.0935	1.47	722	15	941	17	1498	28	52
MT-13_66	2904	42	-2	0.05	5.79	-0.3820	14.65	-0.0702	13.51	0.92	0.0395	5.67	-469	-65	-489	-88	-384	147	-22
MT-13_67	956	45	4	0.01	0.00	0.7676	2.94	0.0955	0.93	0.32	0.0583	2.79	588	5	578	13	542	61	-8
MT-13_68	43522	344	87	0.08	0.75	3.1582	0.95	0.2515	0.56	0.59	0.0911	0.77	1446	7	1447	7	1448	15	0
MT-13_69	6610	64	14	0.15	2.09	2.1527	2.08	0.1961	0.79	0.38	0.0796	1.92	1154	8	1166	14	1188	38	3
MT-13_70	388	9	1	0.02	0.00	1.3112	3.94	0.1424	2.42	0.62	0.0668	3.10	858	20	851	23	831	65	-3
MT-13_71	64201	470	139	0.34	1.53	3.0382	1.38	0.2446	0.38	0.28	0.0901	1.33	1411	5	1417	11	1427	25	1
MT-13_72	2837	88	8	0.01	0.00	0.8639	0.96	0.1032	0.54	0.56	0.0607	0.79	633	3	632	5	629	17	-1
MT-13_73	25388	192	56	0.21	0.00	3.4812	0.80	0.2669	0.63	0.79	0.0946	0.49	1525	9	1523	6	1520	9	0
MT-13_83	44826	406	88	0.21	3.73	2.1331	4.98	0.1907	0.66	0.13	0.0811	4.94	1125	7	1160	35	1225	97	8
MT-13_84	1258	44	4	0.00	0.00	0.7007	1.66	0.0869	0.95	0.57	0.0585	1.36	537	5	539	7	548	30	2
MT-13_85	1867	66	6	0.01	0.00	0.8434	0.98	0.1012	0.54	0.55	0.0604	0.82	622	3	621	5	619	18	0
MT-13_86	2504	83	7	0.01	0.50	0.7857	1.84	0.0952	0.47	0.25	0.0599	1.78	586	3	589	8	599	39	2
MT-13_87	13493	160	35	0.21	1.04	2.3289	1.30	0.2074	0.43	0.33	0.0814	1.23	1215	5	1221	9	1232	24	1
MT-13_88	2537	87	8	0.01	0.18	0.8114	0.91	0.0979	0.44	0.48	0.0601	0.79	602	3	603	4	609	17	1
MT-13_89	20173	176	40	0.26	1.84	2.2216	1.73	0.1986	0.43	0.25	0.0811	1.67	1168	5	1188	12	1224	33	5
MT-13_90	34722	285	74	0.22	0.95	3.0380	0.99	0.2445	0.39	0.39	0.0901	0.91	1410	5	1417	8	1428	17	1
MT-13_91	20745	170	47	0.31	2.13	3.0575	1.90	0.2455	0.38	0.20	0.0903	1.86	1415	5	1422	15	1433	35	1
MT-13_92	68708	525	146	0.27	0.95	3.1623	0.98	0.2503	0.42	0.43	0.0916	0.89	1440	5	1448	8	1459	17	1
MT-13-99	64830	544	163	0.26	0.00	3.6058	0.63	0.2724	0.45	0.73	0.0960	0.43	1553	6	1551	5	1548	8	0

Table 6: Zircon LA-ICP-MS U-Pb data – Clinopyroxene-garnet amphibolite (MT-13) – Chapter 4 Cont.

Spot #						Isotope ratios <sup>c</sup>							Ages (Ma)					Disc. <sup>f</sup>	
	207Pb <sup>a</sup> (cps)	U <sup>b</sup> (ppm)	Pb <sup>b</sup> (ppm)	Th <sup>b</sup> U	<sup>206</sup> Pb/c <sup>c</sup> (%)	<sup>207</sup> Pb/ <sup>235</sup> U <sup>d</sup>	±2s (%)	<sup>206</sup> Pb/ <sup>238</sup> U <sup>d</sup>	±2s (%)	rho <sup>e</sup>	<sup>207</sup> Pb/ <sup>206</sup> Pb <sup>d</sup>	±2s (%)	<sup>206</sup> Pb/ <sup>238</sup> U	±2s (Ma)	<sup>207</sup> Pb <sup>235</sup> U	±2s (Ma)	<sup>207</sup> Pb <sup>206</sup> Pb		±2s (Ma)
MT-13-100	2277	90	8	0.01	0.00	0.7772	1.11	0.0952	0.47	0.42	0.0592	1.00	586	3	584	5	575	22	-2
MT-13_101	2411	79	7	0.01	0.48	0.7505	1.73	0.0920	0.48	0.28	0.0592	1.66	567	3	569	8	573	36	1
MT-13_102	8564	87	11	0.17	3.42	0.9421	4.30	0.1073	0.73	0.17	0.0637	4.24	657	5	674	21	731	90	10
MT-13-103	393	10	1	0.05	0.49	1.0703	3.31	0.1212	2.38	0.72	0.0640	2.30	738	17	739	18	743	49	1
MT-13_104	36346	254	76	0.21	0.19	3.6759	0.86	0.2751	0.60	0.69	0.0969	0.62	1567	8	1566	7	1565	12	0
MT-13-105	9930	159	29	0.16	0.06	1.8051	1.31	0.1751	0.77	0.59	0.0748	1.06	1040	7	1047	9	1062	21	2
MT-13-106	25072	225	58	0.08	0.47	3.3444	0.90	0.2593	0.66	0.73	0.0935	0.61	1486	9	1491	7	1499	12	1
MT-13_107	1929	67	5	0.01	0.00	0.7196	1.92	0.0892	0.68	0.36	0.0585	1.79	551	4	550	8	548	39	-1
MT-13-108	26318	248	69	0.13	0.43	3.6268	1.51	0.2724	0.97	0.65	0.0965	1.15	1553	13	1555	12	1558	22	0
MT-13_115	22091	193	57	0.26	0.47	3.4782	0.88	0.2664	0.41	0.47	0.0947	0.78	1522	6	1522	7	1522	15	0
MT-13-116	26645	316	48	0.16	3.99	1.3073	3.23	0.1356	0.86	0.27	0.0699	3.11	820	7	849	19	927	64	12
MT-13-117	20196	176	41	0.17	2.11	2.5263	1.96	0.2189	0.58	0.30	0.0837	1.87	1276	7	1280	14	1285	36	1
MT-13_118	29760	250	82	0.32	0.09	3.8491	0.96	0.2824	0.65	0.68	0.0989	0.70	1603	9	1603	8	1603	13	0
MT-13_119	11698	101	24	0.22	2.28	2.3874	2.20	0.2088	0.74	0.33	0.0829	2.07	1222	8	1239	16	1267	40	4
MT-13-120	45824	381	127	0.40	0.26	3.7939	0.69	0.2816	0.47	0.68	0.0977	0.50	1599	7	1591	6	1581	9	-1
MT-13-121	1968	76	7	0.01	0.00	0.8454	1.23	0.1018	0.68	0.55	0.0602	1.03	625	4	622	6	612	22	-2
MT-13-122	13433	175	39	0.26	1.13	2.2696	1.26	0.2054	0.48	0.39	0.0801	1.16	1204	5	1203	9	1200	23	0
MT-13-123	1872	73	7	0.01	0.00	0.8309	1.39	0.1002	0.61	0.44	0.0601	1.25	616	4	614	6	608	27	-1
MT-13-124	9800	131	22	0.11	1.53	1.6713	1.70	0.1666	0.68	0.40	0.0728	1.56	993	6	998	11	1008	32	1
MT-13_7	1501	47	6	0.01	1.04	1.2472	3.77	0.1353	0.90	0.24	0.0668	3.66	818	7	822	21	833	76	2
MT-13_8	1398	75	7	0.01	0.00	0.8219	1.45	0.0999	0.62	0.43	0.0597	1.31	614	4	609	7	591	28	-4
MT-13_9	1227	85	8	0.01	0.00	0.8435	2.35	0.1031	0.65	0.28	0.0594	2.26	632	4	621	11	580	49	-9
MT-13_10	6159	83	17	0.15	1.48	2.1048	1.71	0.1935	0.93	0.54	0.0789	1.44	1140	10	1150	12	1169	28	2
MT-13_11	1609	81	8	0.01	0.00	0.8259	1.93	0.1000	0.50	0.26	0.0599	1.86	614	3	611	9	601	40	-2
MT-13_12	3261	4	3	0.93	55.34	3.5201	10.14	0.1626	7.00	0.69	0.1570	7.34	971	63	1532	84	2424	124	60
MT-13_13	54729	516	79	0.21	2.94	1.0521	3.19	0.1172	1.92	0.60	0.0651	2.55	714	13	730	17	778	54	8
MT-13_14	1666	88	8	0.03	0.00	0.8041	1.33	0.0982	0.61	0.46	0.0594	1.19	604	4	599	6	581	26	-4
MT-13_15	178	18	2	0.01	0.00	0.8966	6.44	0.1093	1.41	0.22	0.0595	6.29	669	9	650	31	585	136	-14
MT-13_16(2)	-486	5	1	0.04	0.00	2.5454	7.04	0.2585	5.83	0.83	0.0714	3.95	1482	78	1285	53	969	81	-53
MT-13_23(2)	9595	138	33	0.20	0.05	2.6567	0.81	0.2267	0.57	0.70	0.0850	0.58	1317	7	1316	6	1315	11	0
MT-13_24(2)	1173	59	6	0.01	0.00	0.9620	3.35	0.1134	0.64	0.19	0.0615	3.29	692	4	684	17	658	71	-5
MT-13_25(2)	1013	55	6	0.02	0.00	0.9651	1.85	0.1138	0.72	0.39	0.0615	1.71	695	5	686	9	657	37	-6
MT-13_26	21086	204	70	0.24	0.00	4.5344	0.91	0.3123	0.49	0.54	0.1053	0.76	1752	8	1737	8	1719	14	-2
MT-13_27	45833	509	153	0.23	0.28	3.6436	0.64	0.2733	0.32	0.50	0.0967	0.55	1557	4	1559	5	1561	10	0
MT-13_28	55037	475	145	0.36	4.86	2.9939	2.97	0.2413	0.82	0.28	0.0900	2.85	1394	10	1406	23	1425	55	2
MT-13_29	4530	119	12	0.08	1.16	0.8991	1.94	0.1053	0.87	0.45	0.0619	1.73	646	5	651	9	671	37	4
MT-13_30	14377	230	46	0.20	0.86	1.9714	1.33	0.1859	0.67	0.50	0.0769	1.15	1099	7	1106	9	1119	23	2
MT-13_31	2274	48	14	0.13	0.00	3.5273	3.66	0.2747	0.59	0.16	0.0931	3.61	1564	8	1533	29	1491	68	-5
MT-13_32(2)	5567	99	17	0.20	2.11	1.5640	2.42	0.1591	0.63	0.26	0.0713	2.33	952	6	956	15	966	48	1

<sup>a</sup> Within run background-corrected mean <sup>207</sup>Pb signal in cps (counts per second).

<sup>b</sup> U and Pb content and Th/U ratio were calculated relative to GJ-1 reference zircon.

<sup>c</sup> percentage of the common Pb on the <sup>206</sup>Pb. b. d. = below detection limit.

<sup>d</sup> corrected for background. within-run Pb/U fractionation (in case of <sup>206</sup>Pb/<sup>238</sup>U) and common Pb using Stacy and Kramers (1975) model Pb composition and subsequently normalized to GJ-1 (ID-TIMS v value/measured v value); <sup>207</sup>Pb/<sup>235</sup>U calculated using <sup>207</sup>Pb/<sup>206</sup>Pb/(<sup>238</sup>U/<sup>235</sup>U\*1/137.88)

<sup>e</sup> rho is the <sup>206</sup>Pb/<sup>238</sup>U/<sup>207</sup>Pb/<sup>235</sup>U error correlation coefficient.

<sup>f</sup> degree of concordance = <sup>206</sup>Pb/<sup>238</sup>U age / <sup>207</sup>Pb/<sup>235</sup>U age x 100

<sup>g</sup> Accuracy and reproducibility was checked by repeated analyses (n = 7) of reference zircon Plesovice. Felix and 91500; data given as mean with 2 standard deviation uncertainties



Table 7: Zircon LA-ICP-MS U-Pb data – Migmatitic sillimanite-garnet gneiss (MT-22A) – Chapter

Spot number	$f_{206}^a$	Pb ppm	Th ppm	U ppm	Th/ U <sup>b</sup>	Isotope ratios <sup>c</sup>						Ages (Ma)						% Disc.	
						<sup>207</sup> Pb/ <sup>235</sup> U	1 s	<sup>206</sup> Pb/ <sup>238</sup> U	1 s	Rho <sup>d</sup>	<sup>207</sup> Pb/ <sup>206</sup> Pb <sup>e</sup>	1 s	<sup>206</sup> Pb/ <sup>238</sup> U	1 s	<sup>207</sup> Pb/ <sup>235</sup> U	1 s	<sup>207</sup> Pb/ <sup>206</sup> Pb		1 s
						[%]	[%]	[%]	[%]	abs	abs	abs	abs	abs	abs	abs	abs		
MT-22A 1.1	0.0026	24	163	136	1.20	1.1646	3.41	0.1292	2.76	0.81	0.0654	2.00	783	22	784	27	786	16	0
MT-22A 2.1(1.2)	0.0013	62	38	755	0.05	1.1242	1.99	0.1253	1.18	0.59	0.0651	1.61	761	9	765	15	776	12	2
MT-22A 3.1	0.0010	157	182	1805	0.10	1.5261	3.34	0.1566	2.71	0.81	0.0707	1.95	938	25	941	31	948	18	1
MT-22A 4.1	0.0023	40	203	270	0.75	1.2918	1.36	0.1417	0.73	0.54	0.0661	1.15	854	6	842	11	811	9	-5
MT-22A 5.1(4.2)	0.0020	93	31	966	0.03	1.0176	3.22	0.1168	2.94	0.91	0.0632	1.31	712	21	713	23	714	9	0
MT-22A 6.1	0.0047	20	50	165	0.31	1.1736	3.30	0.1296	1.96	0.59	0.0657	2.66	786	15	788	26	796	21	1
MT-22A 7.1	0.0011	58	74	404	0.18	1.2013	2.86	0.1324	2.63	0.92	0.0658	1.12	802	21	801	23	800	9	0
MT-22A 8.1	0.0034	128	23	1765	0.01	1.0258	2.09	0.1164	1.33	0.64	0.0639	1.61	710	9	717	15	739	12	4
MT-22A 9.1(8.2)	0.0014	49	34	342	0.10	1.2049	1.73	0.1325	1.30	0.75	0.0659	1.14	802	10	803	14	804	9	0
MT-22A 10.1	0.0018	58	45	631	0.07	1.3029	4.00	0.1405	3.82	0.95	0.0673	1.21	847	32	847	34	846	10	0
MT-22A 11.1	0.0010	97	123	3457	0.04	0.7413	2.24	0.0893	1.79	0.80	0.0602	1.34	551	10	563	13	611	8	10
MT-22A 12.1	0.0026	20	34	160	0.21	1.2170	2.52	0.1336	1.65	0.65	0.0661	1.90	808	13	808	20	808	15	0
MT-22A 13.1(12.2)	0.0022	22	39	151	0.26	1.1959	3.30	0.1319	2.98	0.90	0.0658	1.41	799	24	799	26	799	11	0
MT-22A 14.1	0.0055	137	64	2144	0.03	1.3906	1.50	0.1457	0.79	0.53	0.0692	1.27	877	7	885	13	906	11	3
MT-22A 15.1	0.0034	115	52	2252	0.02	1.3058	2.59	0.1404	2.17	0.84	0.0675	1.41	847	18	848	22	852	12	1
MT-22A 16.1	0.0026	44	58	563	0.10	1.2567	2.01	0.1373	1.20	0.60	0.0664	1.61	829	10	826	17	819	13	-1
MT-22A 17.1	0.0044	72	124	3200	0.04	1.2978	2.49	0.1361	1.50	0.60	0.0691	1.98	823	12	845	21	903	18	9
MT-22A 18.1	0.0049	15	2	59	0.03	0.8447	6.58	0.1011	6.23	0.95	0.0606	2.12	621	39	622	41	626	13	1
MT-22A 19.1	0.0007	122	44	844	0.05	1.1968	1.71	0.1319	1.04	0.61	0.0658	1.35	799	8	799	14	800	11	0
MT-22A 20.1	0.0021	37	43	291	0.15	1.0231	1.91	0.1179	1.67	0.87	0.0629	0.93	719	12	715	14	706	7	-2
MT-22A 21.1(20.2)	0.0049	113	96	503	0.19	2.3821	3.43	0.2113	3.30	0.96	0.0818	0.92	1236	41	1237	42	1240	11	0
MT-22A 22.1	0.0029	102	56	2051	0.03	0.9508	3.58	0.1112	3.43	0.96	0.0620	1.03	680	23	679	24	675	7	-1
MT-22A 23.1	0.0004	90	54	549	0.10	1.1609	1.68	0.1288	1.43	0.85	0.0654	0.87	781	11	782	13	786	7	1
MT-22A 24.1(23.2)	0.0031	69	12	615	0.02	0.8664	1.50	0.1031	1.16	0.77	0.0609	0.94	633	7	634	9	637	6	1
MT-22A 25.1	0.0039	105	16	993	0.02	0.9083	3.97	0.1068	3.72	0.94	0.0617	1.38	654	24	656	26	663	9	1
MT-22A 26.1	0.0004	62	203	243	0.84	2.2392	1.39	0.2035	1.05	0.75	0.0798	0.92	1194	13	1193	17	1192	11	0
MT-22A 27.1	0.0006	120	41	1364	0.03	0.9622	1.92	0.1118	1.64	0.85	0.0624	1.01	683	11	684	13	688	7	1
MT-22A 28.1	0.0026	92	71	654	0.11	1.2336	3.65	0.1348	3.55	0.97	0.0664	0.83	815	29	816	30	817	7	0
MT-22A 29.1	0.0007	61	141	379	0.37	1.1788	1.99	0.1305	1.76	0.89	0.0655	0.92	791	14	791	16	791	7	0
MT-22A 30.1	0.0009	61	78	531	0.15	1.1583	3.66	0.1287	3.46	0.95	0.0653	1.18	781	27	781	29	783	9	0
MT-22A 31.1	0.0026	23	11	359	0.03	0.9091	2.79	0.1072	2.47	0.89	0.0615	1.29	657	16	657	18	657	8	0
MT-22A 32.1	0.0020	42	40	288	0.14	1.4096	4.78	0.1481	3.36	0.70	0.0690	3.40	890	30	893	43	900	31	1

Table 7: Zircon LA-ICP-MS U-Pb data – Migmatitic sillimanite-garnet gneiss (MT-22A) – Chapter 4

Spot number	$f_{206}^a$	Pb ppm	Th ppm	U ppm	Th/ U <sup>b</sup>	Isotope ratios <sup>c</sup>						Ages (Ma)						% Disc.	
						<sup>207</sup> Pb/ <sup>235</sup> U	1 s [%]	<sup>206</sup> Pb/ <sup>238</sup> U	1 s [%]	Rho <sup>d</sup>	<sup>207</sup> Pb/ <sup>206</sup> Pb <sup>e</sup>	1 s [%]	<sup>206</sup> Pb/ <sup>238</sup> U	1 s abs	<sup>207</sup> Pb/ <sup>235</sup> U	1 s abs	<sup>207</sup> Pb/ <sup>206</sup> Pb		1 s abs
MT-22A 33.1	0,0018	28	27	205	0,13	1,1778	3,71	0,1304	3,60	0,97	0,0655	0,89	790	28	790	29	791	7	0
MT-22A 34.1	0,0013	45	60	321	0,19	1,1980	2,54	0,1321	2,36	0,93	0,0658	0,94	800	19	800	20	800	8	0
MT-22A 35.1	0,0018	50	151	349	0,43	1,2481	2,29	0,1362	1,89	0,83	0,0665	1,28	823	16	823	19	821	11	0
MT-22A 36.1	0,0022	80	28	696	0,04	0,9517	3,06	0,1113	2,59	0,84	0,0620	1,64	680	18	679	21	675	11	-1
MT-22A 37.1	0,0009	96	34	819	0,04	1,1067	2,52	0,1247	1,92	0,76	0,0644	1,62	758	15	757	19	754	12	0
MT-22A 38.1	0,0034	70	79	579	0,14	1,4291	3,17	0,1494	2,44	0,77	0,0694	2,03	898	22	901	29	910	19	1
MT-22A 39.1	0,0012	81	15	1018	0,02	0,8880	2,02	0,1050	1,59	0,79	0,0613	1,25	644	10	645	13	650	8	1
MT-22A 40.1	0,0016	83	35	1526	0,02	0,9667	1,92	0,1128	1,40	0,73	0,0622	1,31	689	10	687	13	680	9	-1
MT-22A 41.1	0,0017	34	34	259	0,13	1,2973	2,54	0,1402	2,12	0,84	0,0671	1,39	846	18	845	21	842	12	0
MT-22A 42.1	0,0022	97	32	1417	0,02	0,9647	2,05	0,1121	1,73	0,85	0,0624	1,09	685	12	686	14	687	8	0
MT-22A 43.1	0,0033	45	133	255	0,52	3,2822	2,97	0,2580	2,35	0,79	0,0923	1,81	1480	35	1477	44	1473	27	0
MT-22A 44.1	0,0047	92	49	1463	0,03	1,5274	3,32	0,1573	2,18	0,66	0,0704	2,51	942	21	941	31	941	24	0
MT-22A 45.1	0,0002	113	19	1328	0,01	0,9154	2,66	0,1079	2,43	0,91	0,0615	1,10	660	16	660	18	658	7	0

<sup>a</sup>Fraction of the non-radiogenic <sup>206</sup>Pb in the analyzed zircon spot, where  $f_{206} = \frac{[^{206}\text{Pb}/^{204}\text{Pb}]_c}{[^{206}\text{Pb}/^{204}\text{Pb}]_s}$  (c=common; s=sample);

<sup>b</sup>Th/U ratios and amount of Pb, Th and U (in ppm) are calculated relative to 91500 reference zircon

<sup>c</sup>Corrected for background and within-run Pb/U fractionation and normalized to reference zircon GJ-1 (ID-TIMS values/measured value); <sup>207</sup>Pb/<sup>235</sup>U calculated using  $(^{207}\text{Pb}/^{206}\text{Pb}) / (^{238}\text{U}/^{206}\text{Pb} * 1/137.88)$

<sup>d</sup>Rho is the error correlation defined as the quotient of the propagated errors of the <sup>206</sup>Pb/<sup>238</sup>U and the <sup>207</sup>/<sup>235</sup>U ratio

<sup>e</sup>Corrected for mass-bias by normalizing to GJ-1 reference zircon and common Pb using the model Pb composition of Stacey and Kramers (1975)

<sup>f</sup>Degree of concordance =  $(^{206}\text{Pb}/^{238}\text{U} \text{ age} * 100 / ^{207}\text{Pb}/^{206}\text{Pb} \text{ age})$

Table 8: Zircon LA-ICP-MS U–Pb data – Migmatitic amphibole-garnet gneiss (MT-17) – Chapter 4

Spot number	$f_{206}^a$	Pb ppm	Th ppm	U ppm	Th/U <sup>b</sup>	Isotope ratios <sup>c</sup>						Ages (Ma)						% Disc.	
						$^{207}\text{Pb}/$ $^{235}\text{U}$	1 s [%]	$^{206}\text{Pb}/$ $^{238}\text{U}$	1 s [%]	Rho <sup>d</sup>	$^{207}\text{Pb}/$ $^{206}\text{Pb}^e$	1 s [%]	$^{206}\text{Pb}/$ $^{238}\text{U}$	1 s abs	$^{207}\text{Pb}/$ $^{235}\text{U}$	1 s abs	$^{206}\text{Pb}/$ $^{238}\text{U}$		1 s abs
MT-17 1.1	0.0017	21	24	47	0.50	6.6816	2.02	0.3781	1.83	0.91	0.1282	0.84	2067	38	2070	42	2073	18	0
MT-17 2.1	0.0008	23	27	53	0.50	6.6641	1.97	0.3786	1.79	0.91	0.1277	0.82	2070	37	2068	41	2066	17	0
MT-17 3.1	0.0005	69	79	162	0.48	6.6070	1.92	0.3775	1.76	0.91	0.1269	0.79	2065	36	2060	40	2056	16	0
MT-17 4.1	0.0009	30	52	71	0.73	6.4485	2.10	0.3728	1.92	0.91	0.1255	0.86	2042	39	2039	43	2035	17	0
MT-17 5.1	0.0015	18	23	48	0.48	6.4201	1.85	0.3707	1.38	0.75	0.1256	1.24	2033	28	2035	38	2037	25	0
MT-17 6.1	0.0007	51	55	119	0.46	6.5573	1.10	0.3726	0.89	0.82	0.1276	0.63	2042	18	2054	23	2066	13	1
MT-17 7.1	0.0008	40	66	115	0.58	6.5920	1.19	0.3766	0.92	0.77	0.1269	0.76	2061	19	2058	25	2056	16	0
MT-17 8.1	0.0013	23	32	52	0.61	6.6890	1.73	0.3782	1.53	0.89	0.1283	0.80	2068	32	2071	36	2075	17	0
MT-17 9.1	0.0062	19	29	47	0.61	6.7406	0.78	0.3805	0.40	0.52	0.1285	0.66	2079	8	2078	16	2077	14	0
MT-17 10.1	0.0020	16	20	37	0.53	6.6940	3.66	0.3783	3.59	0.98	0.1284	0.72	2068	74	2072	76	2076	15	0
MT-17 11.1	0.0014	21	27	48	0.56	6.6964	2.82	0.3800	2.68	0.95	0.1278	0.87	2076	56	2072	58	2068	18	0
MT-17 12.1	0.0015	23	38	52	0.74	6.7483	3.11	0.3812	3.01	0.97	0.1284	0.79	2082	63	2079	65	2076	16	0
MT-17 13.1	0.0014	21	25	50	0.51	6.6546	3.11	0.3782	2.99	0.96	0.1276	0.86	2068	62	2067	64	2065	18	0
MT-17 14.1	0.0008	39	38	90	0.42	6.6709	1.62	0.3780	1.51	0.93	0.1280	0.60	2067	31	2069	34	2071	12	0
MT-17 15.1	0.0012	31	49	65	0.74	6.7106	3.09	0.3789	3.02	0.98	0.1285	0.66	2071	62	2074	64	2077	14	0
MT-17 16.1	0.0013	14	15	27	0.54	6.6387	3.52	0.3783	3.34	0.95	0.1273	1.10	2068	69	2065	73	2061	23	0
MT-17 17.1	0.0008	30	41	69	0.59	6.5826	0.96	0.3748	0.68	0.71	0.1274	0.67	2052	14	2057	20	2062	14	0
MT-17 18.1	0.0019	17	22	37	0.58	6.7910	2.93	0.3820	2.82	0.96	0.1289	0.80	2086	59	2085	61	2083	17	0
MT-17 19.1	0.0012	39	46	92	0.50	6.6792	2.17	0.3783	2.10	0.97	0.1280	0.56	2068	43	2070	45	2071	12	0
MT-17 20.1	0.0027	15	20	37	0.54	6.4140	3.87	0.3687	3.62	0.94	0.1262	1.36	2023	73	2034	79	2045	28	1
MT-17 21.1	0.0006	48	61	113	0.54	6.6911	2.05	0.3797	1.89	0.92	0.1278	0.78	2075	39	2071	42	2068	16	0
MT-17 22.1	0.0013	31	35	71	0.49	6.6997	1.98	0.3794	1.81	0.91	0.1281	0.81	2073	37	2073	41	2072	17	0
MT-17 23.1	0.0013	32	34	73	0.46	6.6729	1.58	0.3769	1.43	0.91	0.1284	0.66	2062	30	2069	33	2076	14	1
MT-17 24.1	0.0006	63	92	180	0.51	5.9984	1.24	0.3545	1.09	0.88	0.1227	0.60	1956	21	1976	25	1996	12	2
MT-17 25.1(24.2)	0.0008	70	61	194	0.31	6.3418	1.87	0.3677	1.73	0.92	0.1251	0.72	2019	35	2024	38	2030	15	1
MT-17 26.1	0.0006	57	47	139	0.34	6.5604	2.01	0.3750	1.91	0.95	0.1269	0.64	2053	39	2054	41	2055	13	0
MT-17 27.1	0.0011	52	66	129	0.51	6.5674	1.27	0.3759	0.94	0.74	0.1267	0.85	2057	19	2055	26	2053	18	0
MT-17 28.1	0.0008	62	86	170	0.50	6.2198	0.99	0.3624	0.67	0.68	0.1245	0.73	1994	13	2007	20	2021	15	1
MT-17 29.1(28.2)	0.0016	22	27	52	0.52	6.7299	2.21	0.3796	2.04	0.93	0.1286	0.84	2075	42	2077	46	2079	17	0
MT-17 30.1	0.0012	26	26	60	0.43	6.4724	1.65	0.3720	1.51	0.91	0.1262	0.67	2039	31	2042	34	2046	14	0
MT-17 31.1	0.0029	28	33	65	0.50	6.6933	1.81	0.3789	1.65	0.91	0.1281	0.74	2071	34	2072	37	2072	15	0
MT-17 32.1	0.0025	43	58	172	0.34	5.9436	1.85	0.3558	0.38	0.20	0.1212	1.81	1962	7	1968	36	1973	36	1
MT-17 33.1	0.0030	20	24	47	0.52	6.6692	0.87	0.3778	0.44	0.51	0.1280	0.75	2066	9	2069	18	2071	16	0
MT-17 34.1	0.0021	23	24	56	0.43	6.6338	2.58	0.3773	2.41	0.93	0.1275	0.92	2064	50	2064	53	2064	19	0
MT-17 35.1	0.0008	61	66	141	0.47	6.7267	1.60	0.3799	1.48	0.93	0.1284	0.60	2076	31	2076	33	2076	12	0
MT-17 36.1	0.0020	26	28	59	0.48	6.7401	2.98	0.3807	2.85	0.96	0.1284	0.87	2080	59	2078	62	2076	18	0
MT-17 37.1	0.0007	43	48	99	0.49	6.6623	1.31	0.3775	1.15	0.88	0.1280	0.62	2064	24	2068	27	2071	13	0
MT-17 38.1	0.0020	26	26	61	0.43	6.6929	1.54	0.3791	1.31	0.85	0.1280	0.80	2072	27	2072	32	2071	17	0
MT-17 39.1	0.0039	15	14	35	0.40	6.5433	3.02	0.3739	2.74	0.91	0.1269	1.28	2048	56	2052	62	2056	26	0
MT-17 40.1	0.0010	43	44	107	0.41	6.6877	1.17	0.3789	0.95	0.81	0.1280	0.69	2071	20	2071	24	2071	14	0
MT-17 41.1	0.0028	16	17	38	0.45	6.7063	2.58	0.3787	2.34	0.91	0.1284	1.09	2070	48	2073	53	2077	23	0
MT-17 42.1	0.0018	20	29	44	0.67	6.7398	1.03	0.3798	0.55	0.53	0.1287	0.87	2075	11	2078	21	2077	18	0
MT-17 43.1	0.0014	34	42	80	0.52	6.6291	0.86	0.3753	0.54	0.63	0.1281	0.67	2054	11	2063	18	2072	14	1
MT-17 44.1	0.0026	11	12	25	0.47	6.6862	2.16	0.3792	1.88	0.87	0.1279	1.06	2073	39	2071	45	2069	22	0
MT-17 45.1	0.0030	17	27	38	0.70	6.6616	1.82	0.3779	1.50	0.82	0.1279	1.04	2066	31	2068	38	2069	21	0
MT-17 46.1	0.0033	8	9	18	0.52	6.7557	2.88	0.3763	2.22	0.77	0.1302	1.83	2059	46	2080	60	2101	38	2
MT-17 47.1	0.0021	14	14	32	0.43	6.6900	2.51	0.3788	2.28	0.91	0.1281	1.06	2071	47	2071	52	2072	22	0

Table 9: Zircon LA-ICP-MS U-Pb data – Allanite-bearing biotite granite (MT-19) – Chapter 4

Spot number	$f_{206}^a$	Pb ppm	Th ppm	U ppm	Th/U <sup>b</sup>	Isotope ratios <sup>c</sup>					Ages (Ma)					% Disc.			
						<sup>207</sup> Pb/ <sup>235</sup> U	1 s [%]	<sup>206</sup> Pb/ <sup>238</sup> U	1 s [%]	Rho <sup>d</sup>	<sup>207</sup> Pb/ <sup>206</sup> Pb <sup>e</sup>	1 s [%]	<sup>206</sup> Pb/ <sup>238</sup> U	1 s abs	<sup>207</sup> Pb/ <sup>235</sup> U		1 s abs	<sup>207</sup> Pb/ <sup>206</sup> Pb	1 s abs
MT-19 1.1	0.0010	138	38	394	0.10	6.8078	1.82	0.3809	0.77	0.42	0.1296	1.65	2081	16	2087	38	2093	35	1
MT-19 2.1	0.0045	23	16	94	0.17	6.7361	3.25	0.3781	2.01	0.62	0.1292	2.56	2067	42	2077	68	2087	53	1
MT-19 3.1	0.0034	145	284	924	0.31	7.0180	1.85	0.3867	1.01	0.55	0.1316	1.55	2107	21	2114	39	2120	33	1
MT-19 4.1	0.0031	153	82	426	0.19	6.7666	3.26	0.3805	3.21	0.98	0.1290	0.60	2079	67	2081	68	2084	13	0
MT-19 5.1	0.0009	128	81	388	0.21	6.3180	5.60	0.3681	5.52	0.98	0.1245	0.98	2021	111	2021	113	2021	20	0
MT-19 6.1	0.0069	7	4	77	0.05	0.9215	2.27	0.1080	1.08	0.47	0.0619	2.00	661	7	663	15	670	13	1
MT-19 7.1	0.0012	125	69	389	0.18	5.9741	2.70	0.3555	2.60	0.96	0.1219	0.72	1961	51	1972	53	1984	14	1
MT-19 8.1	0.0016	89	56	325	0.17	5.7808	3.16	0.3395	2.95	0.93	0.1235	1.13	1884	56	1944	61	2007	23	6
MT-19 9.1	0.0036	103	6	960	0.01	0.8577	3.36	0.1025	3.19	0.95	0.0607	1.04	629	20	629	21	629	7	0
MT-19 10.1(9.2)	0.0049	77	41	293	0.14	5.9348	3.08	0.3575	2.98	0.97	0.1204	0.79	1970	59	1966	61	1962	15	0
MT-19 11.1	0.0028	119	62	337	0.18	6.1286	1.58	0.3600	1.19	0.75	0.1235	1.05	1982	24	1994	32	2007	21	1
MT-19 12.1	0.0035	98	58	292	0.20	6.1266	2.46	0.3630	2.28	0.93	0.1224	0.90	1996	46	1994	49	1992	18	0
MT-19 13.1	0.0029	142	66	478	0.14	6.5832	2.41	0.3773	2.23	0.93	0.1265	0.90	2064	46	2057	49	2051	18	-1
MT-19 14.1	0.0009	112	59	358	0.17	6.4763	4.82	0.3723	4.43	0.92	0.1262	1.89	2040	90	2043	98	2045	39	0
MT-19 15.1	0.0016	37	2	350	0.01	0.8435	3.73	0.1012	3.48	0.93	0.0605	1.35	621	22	621	23	620	8	0
MT-19 16.1(15.2)	0.0047	86	32	334	0.10	6.3124	4.53	0.3681	2.79	0.62	0.1244	3.57	2021	56	2020	92	2020	72	0
MT-19 17.1	0.0007	33	17	342	0.05	0.8848	2.64	0.1049	2.23	0.85	0.0612	1.40	643	14	644	17	645	9	0
MT-19 18.1(17.2)	0.0026	68	57	300	0.19	5.9094	4.49	0.3568	3.81	0.85	0.1201	2.38	1967	75	1963	88	1958	47	0
MT-19 19.1	0.0009	113	40	312	0.13	6.5036	2.42	0.3739	1.87	0.77	0.1262	1.54	2048	38	2046	50	2045	32	0
MT-19 20.1	0.0006	145	61	589	0.10	5.7096	1.22	0.3468	0.60	0.49	0.1194	1.07	1919	12	1933	24	1947	21	1
MT-19 21.1(20.2)	0.0007	120	71	333	0.21	6.4468	3.03	0.3638	2.44	0.80	0.1285	1.80	2000	49	2039	62	2078	37	4
MT-19 22.1	0.0027	120	75	455	0.17	6.0112	4.49	0.3571	4.36	0.97	0.1221	1.09	1968	86	1977	89	1987	22	1
MT-19 23.1	0.0004	117	101	285	0.35	6.7696	4.94	0.3800	4.82	0.98	0.1292	1.05	2076	100	2082	103	2087	22	1
MT-19 24.1	0.0013	130	44	517	0.08	5.8503	4.10	0.3544	2.89	0.71	0.1197	2.90	1956	57	1954	80	1952	57	0
MT-19 25.1(24.2)	0.0006	134	77	399	0.19	6.1208	2.05	0.3570	0.90	0.44	0.1243	1.84	1968	18	1993	41	2020	37	3
MT-19 26.1	0.0019	87	42	243	0.17	6.6073	2.31	0.3768	1.84	0.80	0.1272	1.40	2061	38	2060	48	2059	29	0
MT-19 27.1	0.0076	25	2	260	0.01	0.8359	2.54	0.1004	2.14	0.84	0.0604	1.37	617	13	617	16	617	8	0
MT-19 28.1(27.2)	0.0038	97	60	302	0.20	6.5006	4.20	0.3753	3.29	0.78	0.1256	2.62	2054	68	2046	86	2038	53	-1
MT-19 29.1	0.0043	13	0	124	0.00	0.8543	2.80	0.1022	2.01	0.72	0.0606	1.95	627	13	627	18	625	12	0
MT-19 30.1	0.0034	83	25	192	0.13	6.8397	1.45	0.3818	1.12	0.77	0.1299	0.92	2085	23	2091	30	2097	19	1
MT-19 31.1	0.0046	84	34	232	0.15	6.5648	3.60	0.3728	3.20	0.89	0.1277	1.64	2043	65	2055	74	2067	34	1
MT-19 32.1	0.0035	12	0	117	0.00	0.8419	2.89	0.1010	2.42	0.84	0.0604	1.58	620	15	620	18	619	10	0
MT-19 33.1	0.0008	121	52	337	0.15	6.7937	2.60	0.3823	2.46	0.95	0.1289	0.84	2087	51	2085	54	2083	18	0
MT-19 34.1	0.0030	81	38	212	0.18	6.5200	2.62	0.3744	1.72	0.66	0.1263	1.98	2050	35	2049	54	2047	40	0
MT-19 35.1	0.0014	68	27	290	0.09	5.9577	1.79	0.3578	1.16	0.65	0.1208	1.37	1972	23	1970	35	1967	27	0
MT-19 36.1	0.0016	87	55	211	0.26	7.0610	3.39	0.3889	3.31	0.98	0.1317	0.69	2118	70	2119	72	2121	15	0
MT-19 37.1	0.0017	33	2	272	0.01	0.9516	4.39	0.1110	4.15	0.95	0.0622	1.43	678	28	679	30	681	10	0
MT-19 38.1	0.0014	108	42	302	0.14	6.6705	2.15	0.3751	2.04	0.95	0.1290	0.66	2053	42	2069	44	2084	14	1
MT-19 39.1	0.0016	98	42	382	0.11	6.0429	3.83	0.3586	3.62	0.95	0.1222	1.23	1976	72	1982	76	1989	25	1
MT-19 40.1	0.0020	122	40	369	0.11	6.9049	1.55	0.3852	1.19	0.76	0.1300	1.00	2100	25	2099	33	2098	21	0
MT-19 41.1	0.0008	89	53	247	0.21	6.8354	2.70	0.3830	2.41	0.89	0.1294	1.21	2090	50	2090	56	2090	25	0
MT-19 42.1	0.0017	92	65	430	0.15	5.3105	1.57	0.3318	1.07	0.68	0.1161	1.15	1847	20	1871	29	1896	22	3
MT-19 43.1	0.0002	76	30	266	0.11	6.1014	2.79	0.3616	2.45	0.88	0.1224	1.32	1990	49	1990	55	1991	26	0
MT-19 44.1	0.0029	84	84	326	0.26	6.7963	3.66	0.3813	2.19	0.60	0.1293	2.92	2082	46	2085	76	2088	61	0
MT-19 45.1	0.0038	93	41	268	0.15	6.7206	3.00	0.3785	2.38	0.79	0.1288	1.83	2069	49	2075	62	2081	38	1
MT-19 46.1	0.0018	109	45	402	0.11	6.0329	1.38	0.3598	1.11	0.80	0.1216	0.83	1981	22	1981	27	1980	16	0
MT-19 47.1	0.0002	100	72	361	0.20	6.0745	2.29	0.3588	2.05	0.89	0.1228	1.03	1976	41	1987	46	1997	21	1
MT-19 48.1	0.0027	80	39	255	0.15	6.6217	3.50	0.3719	3.03	0.87	0.1291	1.76	2039	62	2062	72	2086	37	2
MT-19 49.1	0.0007	114	43	372	0.12	6.4075	4.40	0.3693	3.40	0.77	0.1258	2.80	2026	69	2033	89	2041	57	1
MT-19 50.1	0.0028	102	33	290	0.11	6.9455	3.19	0.3865	2.95	0.92	0.1303	1.22	2106	62	2104	67	2103	26	0

Table 9: Zircon LA-ICP-MS U-Pb data – Allanite-bearing biotite granite (MT-19) – Chapter 4. Cont.

Spot number	$f_{206}^a$	Pb ppm	Th ppm	U ppm	Th/U <sup>b</sup>	Isotope ratios <sup>c</sup>						Ages (Ma)						% Disc.	
						<sup>207</sup> Pb/ <sup>235</sup> U	1 s [%]	<sup>206</sup> Pb/ <sup>238</sup> U	1 s [%]	Rho <sup>d</sup>	<sup>207</sup> Pb/ <sup>206</sup> Pb <sup>e</sup>	1 s [%]	<sup>206</sup> Pb/ <sup>238</sup> U	1 s abs	<sup>207</sup> Pb/ <sup>235</sup> U	1 s abs	<sup>207</sup> Pb/ <sup>206</sup> Pb		1 s abs
MT-19 51.1	0.0023	96	43	321	0.13	6.3544	5.56	0.3683	5.41	0.97	0.1251	1.27	2022	109	2026	113	2030	26	0
MT-19 52.1	0.0025	99	32	284	0.11	6.7945	1.85	0.3803	1.36	0.73	0.1296	1.26	2078	28	2085	39	2092	26	1
MT-19 53.1	0.0023	90	18	278	0.07	6.1128	2.44	0.3599	1.97	0.81	0.1232	1.44	1982	39	1992	49	2003	29	1
MT-19 54.1	0.0006	114	62	337	0.18	6.6483	3.06	0.3748	3.01	0.98	0.1287	0.55	2052	62	2066	63	2080	11	1
MT-19 55.1	0.0012	111	38	327	0.12	6.6841	1.87	0.3740	1.68	0.90	0.1296	0.82	2048	34	2071	39	2093	17	2
MT-19 56.1	0.0012	85	15	248	0.06	6.7407	2.81	0.3779	1.99	0.71	0.1294	1.98	2066	41	2078	58	2090	41	1
MT-19 57.1	0.0018	100	38	330	0.12	6.7679	2.85	0.3777	2.62	0.92	0.1299	1.10	2066	54	2082	59	2097	23	1
MT-19 58.1	0.0096	58	40	187	0.21	6.7802	2.11	0.3810	2.00	0.94	0.1291	0.69	2081	42	2083	44	2085	14	0
MT-19 59.1	0.0009	122	74	399	0.19	6.6275	3.53	0.3780	3.06	0.87	0.1272	1.75	2067	63	2063	73	2059	36	0
MT-19 60.1	0.0020	79	13	574	0.02	6.5703	5.17	0.3765	5.05	0.98	0.1266	1.13	2060	104	2055	106	2051	23	0
MT-19 61.1	0.0034	87	37	247	0.15	6.8126	1.95	0.3835	1.71	0.88	0.1288	0.94	2093	36	2087	41	2082	20	0
MT-19 62.1	0.0033	25	10	88	0.11	6.5743	3.17	0.3730	3.03	0.96	0.1278	0.94	2044	62	2056	65	2068	19	1
MT-19 63.1	0.0025	101	34	370	0.09	6.0184	3.90	0.3609	3.51	0.90	0.1209	1.71	1986	70	1979	77	1970	34	-1
MT-19 64.1	0.0036	79	35	203	0.17	6.8058	3.12	0.3815	2.95	0.95	0.1294	1.00	2083	62	2086	65	2090	21	0
MT-19 65.1	0.0016	70	39	192	0.20	6.9202	2.56	0.3858	2.46	0.96	0.1301	0.72	2104	52	2101	54	2099	15	0
MT-19 66.1	0.0029	75	33	277	0.12	6.4046	2.17	0.3680	1.78	0.82	0.1262	1.25	2020	36	2033	44	2046	26	1
MT-19 67.1	0.0019	70	32	225	0.14	6.4680	2.77	0.3727	2.62	0.95	0.1259	0.90	2042	53	2042	56	2041	18	0
MT-19 68.1	0.0799	4	14	28	0.48	3.5188	6.44	0.1656	3.36	0.52	0.1541	5.50	988	33	1531	99	2392	131	59
MT-19 69.1	0.0035	66	25	203	0.12	6.6171	2.71	0.3764	2.50	0.92	0.1275	1.04	2059	51	2062	56	2064	22	0
MT-19 70.1	0.0015	65	45	222	0.20	6.5301	4.24	0.3725	3.99	0.94	0.1272	1.42	2041	81	2050	87	2059	29	1
MT-19 71.1	0.0034	46	20	176	0.11	6.6850	3.58	0.3776	3.04	0.85	0.1284	1.88	2065	63	2071	74	2076	39	1
MT-19 72.1	0.0017	59	32	179	0.18	6.7496	3.17	0.3815	3.03	0.95	0.1283	0.94	2083	63	2079	66	2075	20	0

Valid for MT-17 and MT-19

<sup>a</sup>Fraction of the non-radiogenic <sup>206</sup>Pb in the analyzed zircon spot. where  $f_{206} = \frac{^{206}\text{Pb}/^{204}\text{Pb}}{^{206}\text{Pb}/^{204}\text{Pb}}_c / \frac{^{206}\text{Pb}/^{204}\text{Pb}}{^{206}\text{Pb}/^{204}\text{Pb}}_s$  (c=common; s=sample);

<sup>b</sup>Th/U ratios and amount of Pb, Th and U (in ppm) are calculated relative to 91500 reference zircon

<sup>c</sup>Corrected for background and within-run Pb/U fractionation and normalized to reference zircon GJ-1 (ID-TIMS values/measured value); <sup>207</sup>Pb/<sup>235</sup>U calculated using  $(^{207}\text{Pb}/^{206}\text{Pb}) / (^{238}\text{U}/^{206}\text{Pb} * 1/137.88)$

<sup>d</sup>Rho is the error correlation defined as the quotient of the propagated errors of the <sup>206</sup>Pb/<sup>238</sup>U and the <sup>207</sup>/<sup>235</sup>U ratio

<sup>e</sup>Corrected for mass-bias by normalizing to GJ-1 reference zircon and common Pb using the model Pb composition of Stacey and Kramers (1975)

<sup>f</sup>Degree of concordance =  $(^{206}\text{Pb}/^{238}\text{U} \text{ age} * 100 / ^{207}\text{Pb}/^{206}\text{Pb} \text{ age})$

Table 10: Zircon LA-ICP-MS U-Pb data – Biotite gneiss (MT-20) – Chapter 4

Spot number	$f_{206}^a$	Pb ppm	Th ppm	U ppm	Th/U <sup>b</sup>	Isotope ratios <sup>c</sup>					Ages (Ma)					% Disc.			
						$^{207}\text{Pb}/^{235}\text{U}$ [ $\%$ ]	$^{206}\text{Pb}/^{238}\text{U}$ [ $\%$ ]	1 s Rho <sup>d</sup>	$^{207}\text{Pb}/^{206}\text{Pb}$ [ $\%$ ]	1 s	$^{206}\text{Pb}/^{238}\text{U}$ abs	1 s	$^{207}\text{Pb}/^{235}\text{U}$ abs	1 s	$^{207}\text{Pb}/^{206}\text{Pb}$ abs		1 s		
MT-20 1.1	0.0009	35	60	71	0.84	6.6680	4.64	0.3772	4.56	0.98	0.1282	0.88	2063	94	2068	96	2074	18	0
MT-20 2.1	0.0016	20	2	195	0.01	0.8243	5.10	0.0994	4.85	0.95	0.0601	1.56	611	30	610	31	608	9	0
MT-20 3.1(2.2)	0.0008	75	85	237	0.36	6.1099	0.99	0.3624	0.72	0.73	0.1223	0.67	1994	14	1992	20	1990	13	0
MT-20 4.1	0.0005	77	77	189	0.41	6.4659	0.92	0.3710	0.71	0.77	0.1264	0.59	2034	14	2041	19	2048	12	1
MT-20 5.1	0.0030	34	45	90	0.50	6.5128	1.22	0.3754	0.76	0.62	0.1258	0.96	2055	16	2048	25	2040	20	-1
MT-20 6.1	0.0008	71	63	167	0.38	6.7023	3.12	0.3783	3.07	0.99	0.1285	0.54	2069	64	2073	65	2077	11	0
MT-20 7.1	0.0062	17	3	177	0.02	0.8227	3.08	0.0992	2.65	0.86	0.0602	1.58	610	16	610	19	609	10	0
MT-20 8.1	0.0004	56	54	139	0.39	6.5952	4.05	0.3772	3.99	0.99	0.1268	0.69	2063	82	2059	83	2054	14	0
MT-20 9.1	0.0013	18	20	38	0.54	6.7912	4.70	0.3809	4.60	0.98	0.1293	0.97	2081	96	2085	98	2089	20	0
MT-20 10.1	0.0042	10	6	91	0.06	0.8226	4.28	0.0990	3.90	0.91	0.0602	1.76	609	24	610	26	612	11	1
MT-20 11.1(10.2)	0.0006	99	175	302	0.58	6.2382	2.94	0.3660	2.78	0.94	0.1236	0.97	2011	56	2010	59	2009	19	0
MT-20 12.1	0.0007	42	37	139	0.27	6.3281	2.58	0.3695	1.90	0.74	0.1242	1.75	2027	39	2022	52	2018	35	0
MT-20 13.1	0.0005	82	93	239	0.39	6.1383	1.21	0.3635	0.88	0.73	0.1225	0.83	1999	18	1996	24	1993	17	0
MT-20 14.1	0.0018	61	20	600	0.03	0.8593	3.23	0.1028	3.07	0.95	0.0606	0.98	631	19	630	20	626	6	-1
MT-20 15.1(14.2)	0.0013	51	51	118	0.44	6.6381	3.26	0.3754	3.13	0.96	0.1283	0.90	2055	64	2064	67	2074	19	1
MT-20 16.1	0.0004	83	114	169	0.67	6.7010	1.87	0.3764	1.69	0.90	0.1291	0.80	2060	35	2073	39	2086	17	1
MT-20 17.1	0.0048	10	0	81	0.01	0.8527	4.67	0.1021	4.16	0.89	0.0606	2.13	627	26	626	29	624	13	0
MT-20 18.1	0.0009	41	42	86	0.49	6.5975	2.87	0.3734	2.75	0.96	0.1281	0.80	2045	56	2059	59	2073	17	1
MT-20 19.1	0.0008	47	57	121	0.47	6.5523	2.97	0.3755	2.91	0.98	0.1265	0.59	2055	60	2053	61	2050	12	0
MT-20 20.1	0.0010	53	59	135	0.44	6.5688	2.95	0.3757	2.69	0.91	0.1268	1.22	2056	55	2055	61	2054	25	0
MT-20 21.1	0.0012	58	97	201	0.48	6.0333	2.13	0.3616	1.94	0.91	0.1210	0.88	1990	39	1981	42	1971	17	-1
MT-20 22.1	0.0004	40	49	120	0.41	6.3760	2.33	0.3707	1.92	0.82	0.1247	1.32	2033	39	2029	47	2025	27	0
MT-20 23.1	0.0011	45	102	156	0.65	5.3590	2.66	0.3362	1.53	0.58	0.1156	2.17	1868	29	1878	50	1889	41	1
MT-20 24.1	0.0020	39	34	104	0.32	6.6728	2.85	0.3778	2.73	0.96	0.1281	0.82	2066	56	2069	59	2072	17	0
MT-20 25.1	0.0009	40	38	99	0.38	6.6847	4.18	0.3789	4.09	0.98	0.1280	0.87	2071	85	2071	87	2070	18	0
MT-20 26.1	0.0013	29	24	70	0.34	6.7672	3.68	0.3810	3.57	0.97	0.1288	0.89	2081	74	2081	77	2082	19	0
MT-20 27.1	0.0035	16	1	163	0.01	0.8414	5.92	0.1009	5.79	0.98	0.0605	1.24	620	36	620	37	620	8	0
MT-20 28.1(27.2)	0.0016	29	39	74	0.53	6.5073	3.85	0.3727	3.76	0.98	0.1266	0.85	2042	77	2047	79	2052	18	0
MT-20 29.1	0.0011	42	3	470	0.01	0.8395	4.55	0.1006	4.38	0.96	0.0605	1.22	618	27	619	28	621	8	0
MT-20 30.1	0.0006	81	34	214	0.16	6.7584	3.16	0.3808	3.08	0.97	0.1287	0.70	2080	64	2080	66	2081	15	0
MT-20 31.1	0.0006	70	77	182	0.42	6.5289	2.40	0.3742	2.27	0.95	0.1266	0.78	2049	46	2050	49	2051	16	0
MT-20 32.1	0.0003	116	87	283	0.31	6.7734	3.54	0.3797	3.48	0.98	0.1294	0.62	2075	72	2082	74	2089	13	1
MT-20 33.1	0.0027	19	25	145	0.17	1.1985	3.81	0.1320	3.50	0.92	0.0658	1.52	799	28	800	30	801	12	0
MT-20 34.1(33.2)	0.0012	26	36	113	0.32	2.3448	2.55	0.2085	2.35	0.92	0.0816	1.01	1221	29	1226	31	1235	12	1
MT-20 35.1	0.0047	112	59	2179	0.03	0.8645	4.33	0.1020	4.15	0.96	0.0615	1.24	626	26	633	27	656	8	5
MT-20 36.1(35.2)	0.0016	34	49	263	0.19	1.1911	3.59	0.1313	3.39	0.94	0.0658	1.20	795	27	796	29	800	10	1
MT-20 37.1	0.0027	23	35	66	0.53	6.2041	4.04	0.3630	3.81	0.94	0.1240	1.35	1996	76	2005	81	2014	27	1
MT-20 38.1	0.0012	59	52	144	0.36	6.3913	4.06	0.3693	3.99	0.98	0.1255	0.75	2026	81	2031	83	2036	15	0
MT-20 39.1	0.0015	35	39	88	0.44	6.5931	1.36	0.3756	0.72	0.53	0.1273	1.15	2055	15	2058	28	2061	24	0
MT-20 40.1	0.0039	13	2	125	0.02	0.8904	2.99	0.1056	2.43	0.81	0.0612	1.74	647	16	647	19	645	11	0
MT-20 41.1(40.2)	0.0019	30	30	74	0.41	6.5409	0.88	0.3733	0.58	0.66	0.1271	0.66	2045	12	2051	18	2058	14	1
MT-20 42.1	0.0015	30	5	289	0.02	0.8363	2.18	0.1005	1.81	0.83	0.0604	1.21	617	11	617	13	616	7	0
MT-20 43.1(42.2)	0.0016	39	70	84	0.83	6.6840	3.11	0.3791	2.94	0.94	0.1279	1.02	2072	61	2071	64	2069	21	0
MT-20 44.1	0.0026	19	19	168	0.11	0.8889	4.15	0.1054	3.80	0.92	0.0612	1.67	646	25	646	27	646	11	0
MT-20 45.1	0.0017	37	45	265	0.17	1.1572	1.95	0.1286	1.56	0.80	0.0653	1.17	780	12	781	15	783	9	0
MT-20 46.1	0.0020	26	3	248	0.01	0.8842	1.95	0.1048	1.49	0.76	0.0612	1.27	643	10	643	13	645	8	0
MT-20 47.1	0.0045	11	1	108	0.01	0.8526	2.92	0.1020	2.31	0.79	0.0606	1.78	626	14	626	18	625	11	0
MT-20 48.1(47.2)	0.0008	77	131	169	0.77	6.6733	1.62	0.3777	1.46	0.90	0.1282	0.71	2065	30	2069	34	2073	15	0
MT-20 49.1	0.0016	43	46	104	0.44	6.5382	1.07	0.3716	0.50	0.46	0.1276	0.95	2037	10	2051	22	2065	20	1
MT-20 50.1	0.0017	41	4	426	0.01	0.8432	1.87	0.1012	1.47	0.79	0.0604	1.15	621	9	621	12	619	7	0

Table 10: Zircon LA-ICP-MS U-Pb data – Biotite gneiss (MT-20) – Chapter 4\_Cont.

Spot number	$f_{206}^a$	Pb ppm	Th ppm	U ppm	Th/U <sup>b</sup>	Isotope ratios <sup>c</sup>						Ages (Ma)						% Disc.	
						<sup>207</sup> Pb/ <sup>235</sup> U	1 s [%]	<sup>206</sup> Pb/ <sup>238</sup> U	1 s [%]	Rho <sup>d</sup>	<sup>207</sup> Pb/ <sup>206</sup> Pb <sup>e</sup>	1 s [%]	<sup>206</sup> Pb/ <sup>238</sup> U	1 s abs	<sup>207</sup> Pb/ <sup>235</sup> U	1 s abs	<sup>207</sup> Pb/ <sup>206</sup> Pb		1 s abs
MT-20 51.1(50.2)	0.0009	24	24	59	0.41	6.6903	2.47	0.3792	2.17	0.88	0.1280	1.17	2072	45	2071	51	2070	24	0
MT-20 52.1	0.0042	59	6	576	0.01	0.8195	2.82	0.0988	2.57	0.91	0.0602	1.17	607	16	608	17	610	7	0
MT-20 53.1	0.0022	23	2	236	0.01	0.8473	1.88	0.1015	1.38	0.73	0.0605	1.28	623	9	623	12	623	8	0
MT-20 54.1(53.2)	0.0014	34	35	81	0.44	6.5825	1.99	0.3759	1.68	0.84	0.1270	1.06	2057	35	2057	41	2057	22	0
MT-20 55.1	0.0010	45	51	344	0.15	1.1784	2.16	0.1306	1.85	0.86	0.0655	1.11	791	15	791	17	789	9	0
MT-20 56.1	0.0012	26	41	59	0.69	6.7008	2.21	0.3789	2.01	0.91	0.1283	0.92	2071	42	2073	46	2074	19	0
MT-20 57.1	0.0040	10	1	102	0.01	0.8471	3.40	0.1015	2.93	0.86	0.0605	1.74	623	18	623	21	622	11	0
MT-20 58.1(57.2)	0.0009	55	53	163	0.32	6.5055	3.10	0.3740	3.03	0.98	0.1261	0.68	2048	62	2047	64	2045	14	0
MT-20 59.1	0.0034	13	1	133	0.00	0.8406	1.82	0.1006	0.97	0.53	0.0606	1.54	618	6	619	11	624	10	1
MT-20 60.1	0.0017	27	23	275	0.08	0.8540	1.82	0.1022	1.34	0.73	0.0606	1.24	627	8	627	11	626	8	0
MT-20 61.1	0.0047	9	1	95	0.01	0.8507	3.17	0.1019	2.29	0.72	0.0606	2.19	625	14	625	20	624	14	0
MT-20 62.1(61.2)	0.0009	46	55	143	0.38	6.1620	4.46	0.3631	4.25	0.95	0.1231	1.36	1997	85	1999	89	2001	27	0
MT-20 63.1	0.0037	11	25	23	1.08	6.4105	2.76	0.3701	2.46	0.89	0.1256	1.24	2030	50	2034	56	2038	25	0
MT-20 64.1	0.0040	8	2	83	0.02	0.8381	3.36	0.1005	2.71	0.81	0.0605	1.99	617	17	618	21	621	12	1
MT-20 65.1(64.2)	0.0005	41	45	103	0.44	6.7117	2.89	0.3799	2.74	0.94	0.1281	0.95	2076	57	2074	60	2072	20	0
MT-20 66.1	0.0027	14	10	138	0.07	0.8552	3.75	0.1023	3.47	0.93	0.0606	1.42	628	22	628	24	626	9	0
MT-20 67.1	0.0006	39	14	330	0.04	0.9152	2.90	0.1078	2.71	0.93	0.0616	1.03	660	18	660	19	659	7	0
MT-20 68.1	0.0010	23	2	244	0.01	0.8229	3.56	0.0992	3.37	0.95	0.0602	1.15	610	21	610	22	610	7	0
MT-20 69.1(68.2)	0.0003	42	50	121	0.41	6.3222	1.36	0.3671	1.05	0.77	0.1249	0.87	2016	21	2022	27	2027	18	1
MT-20 70.1	0.0008	28	2	304	0.01	0.8256	3.86	0.0994	3.73	0.96	0.0602	1.02	611	23	611	24	612	6	0
MT-20 71.1(70.2)	0.0008	34	60	89	0.68	6.3394	2.15	0.3679	1.63	0.76	0.1250	1.40	2020	33	2024	43	2028	28	0
MT-20 72.1	0.0013	27	107	194	0.55	1.1895	3.60	0.1314	3.39	0.94	0.0657	1.20	796	27	796	29	796	10	0
MT-20 73.1(72.2)	0.0025	25	4	270	0.01	0.8455	3.69	0.1012	3.30	0.89	0.0606	1.65	622	20	622	23	624	10	0

<sup>a</sup>Fraction of the non-radiogenic <sup>206</sup>Pb in the analyzed zircon spot. where  $f_{206} = \frac{^{206}\text{Pb}/^{204}\text{Pb}}{c/^{206}\text{Pb}/^{204}\text{Pb}}$  (c=common; s=sample);

<sup>b</sup>Th/U ratios and amount of Pb, Th and U (in ppm) are calculated relative to 91500 reference zircon

<sup>c</sup>Corrected for background and within-run Pb/U fractionation and normalised to reference zircon GJ-1 (ID-TIMS values/measured value); <sup>207</sup>Pb/<sup>235</sup>U calculated using  $(^{207}\text{Pb}/^{206}\text{Pb}) / (^{238}\text{U}/^{206}\text{Pb} * 1/137.88)$

<sup>d</sup>Rho is the error correlation defined as the quotient of the propagated errors of the <sup>206</sup>Pb/<sup>238</sup>U and the <sup>207</sup>/<sup>235</sup>U ratio

<sup>e</sup>Corrected for mass-bias by normalising to GJ-1 reference zircon and common Pb using the model Pb composition of Stacey and Kramers (1975)

<sup>f</sup>Degree of concordance =  $(^{206}\text{Pb}/^{238}\text{U} \text{ age} * 100 / ^{207}\text{Pb}/^{206}\text{Pb} \text{ age})$

**Appendix VI**  
**Lu-Hf isotopes in zircon**  
**(LA-ICP-MS)**



Tabela 1: Hf isotopes results determined by LA-ICP-MS – Banded mafic granulite (C-833-A)

Grain#	$\frac{^{176}\text{Yb}}{^{177}\text{Hf}}$ <sup>a</sup>	$\pm 2s$	$\frac{^{176}\text{Lu}}{^{177}\text{Hf}}$ <sup>a</sup>	$\pm 2s$	$\frac{^{178}\text{Hf}}{^{177}\text{Hf}}$	$\frac{^{180}\text{Hf}}{^{177}\text{Hf}}$	Sig <sub>Hf</sub> <sup>b</sup> (V)	$\frac{^{176}\text{Hf}}{^{177}\text{Hf}}$	$\pm 2s$ <sup>c</sup>	age <sup>f</sup>					age <sup>f</sup>			
										(Ma)	$\pm 2s$	$\frac{^{176}\text{Hf}}{^{177}\text{Hf}}$ <sup>d</sup>	eHf(t) <sup>d</sup>	$\pm 2s$ <sup>c</sup>	(Ma)	$\pm 2s$	eHf(t) <sup>d</sup>	$\pm 2s$ <sup>c</sup>
										(measured)					(pref./min.)			
28	0.017719	17.103178	0.000527	3.926757	1.467224	1.886892	19.075689	0.281327	224.185306	2428	40	0.281303	2.72	0.66	2550	20	5.52	0.66
51	0.006386	5.111385	0.000212	1.274019	1.467201	1.886812	18.270217	0.281730	19.456447	1987	24	0.281722	7.34	0.64	2550	66	20.37	0.64
49	0.003753	3.004850	0.000131	0.788751	1.467210	1.886890	13.742640	0.281397	19.455045	1682	63	0.281393	-11.36	0.64	2550	66	8.68	0.64
48	0.006467	5.174199	0.000203	1.219577	1.467201	1.886880	16.870181	0.281574	17.829718	618	20	0.281572	-29.16	0.64	618	10	-29.16	0.64
72	0.010656	8.879155	0.000341	2.184917	1.467238	1.886877	23.723742	0.281872	20.267393	627	21	0.281868	-18.45	0.65	627	11	-18.45	0.65
74	0.007719	6.793491	0.000281	1.944239	1.467221	1.886813	20.002028	0.281338	14.336049	2468	18	0.281325	4.41	0.64	2550	66	6.33	0.64
79	0.004279	3.434495	0.000134	0.807246	1.467157	1.886894	22.766532	0.281296	19.326231	2462	68	0.281290	3.03	0.64	2550	66	5.08	0.64
78	0.015935	12.778249	0.000531	3.186631	1.467214	1.886854	20.534031	0.281454	22.680065	2480	45	0.281428	8.39	0.65	2550	66	10.00	0.65
82	0.003327	2.663692	0.000116	0.698210	1.467225	1.886864	19.147965	0.281413	23.301356	2227	65	0.281408	1.75	0.64	2550	66	9.26	0.64
81	0.006335	5.069847	0.000208	1.246334	1.467179	1.886789	19.267194	0.281632	20.203317	654	12	0.281630	-26.29	0.64	654	6	-26.29	0.64
80	0.010661	8.534325	0.000320	1.918676	1.467195	1.886884	23.409000	0.281797	28.128160	638	15	0.281793	-20.86	0.65	638	8	-20.86	0.65
83	0.007885	6.317313	0.000267	1.605461	1.467240	1.886870	17.484114	0.281587	21.921813	2504	69	0.281574	14.12	0.64	2550	66	15.20	0.65
89	0.006533	5.234416	0.000225	1.352198	1.467179	1.886844	19.922448	0.281335	17.703559	2559	65	0.281324	6.52	0.64	2550	66	6.30	0.64
87	0.006667	5.345234	0.000212	1.275189	1.467179	1.886754	19.721181	0.281591	23.022783	607	27	0.281588	-28.81	0.64	607	14	-28.81	0.64
90	0.016592	13.374023	0.000633	3.838013	1.467226	1.886859	16.268803	0.281706	19.136830	617	28	0.281699	-24.67	0.65	617	14	-24.67	0.65
91	0.007536	6.036808	0.000226	1.362598	1.467197	1.886825	18.680402	0.281306	19.162536	2124	76	0.281297	-4.60	0.64	2550	66	5.26	0.64
54	0.007684	6.150058	0.000227	1.363250	1.467195	1.886919	18.610402	0.281323	17.886006	627	12	0.281321	-37.85	0.64	627	6	-37.85	0.64
98	0.011586	10.262489	0.000347	2.440850	1.467170	1.886805	17.410331	0.281358	23.060941	2546	91	0.281341	6.83	0.65	2550	66	6.93	0.65
97	0.007522	6.054121	0.000228	1.382849	1.467250	1.886947	17.671764	0.281344	21.614795	2479	37	0.281333	4.98	0.64	2550	66	6.63	0.64
102	0.005149	4.145014	0.000165	1.000795	1.467189	1.886846	21.529611	0.281384	18.930114	1876	22	0.281378	-7.42	0.64	2550	66	8.16	0.64
104	0.001031	0.826527	0.000036	0.219404	1.467208	1.886902	23.500181	0.281321	23.234678	1956	61	0.281320	-7.64	0.64	637	8	-37.61	0.64
105	0.010110	8.173345	0.000349	2.133816	1.467192	1.886878	18.736510	0.281407	19.754864	637	17	0.281403	-34.70	0.64	2550	66	8.66	0.65
106	0.014516	11.696493	0.000436	2.644066	1.467186	1.886742	22.990878	0.281244	20.051113	1765	43	0.281229	-15.28	0.65	2550	66	2.69	0.65
102.2	0.006258	5.290045	0.000188	1.231769	1.467224	1.886784	20.924992	0.281313	18.297719	1876	22	0.281306	-9.98	0.64	654	19	-37.60	0.64
102.1	0.006498	6.809454	0.000191	1.667255	1.467182	1.886656	18.988952	0.281312	19.554091	654	38	0.281309	-37.64	0.64	2550	66	5.54	0.64
107	0.001312	1.062728	0.000041	0.249807	1.467228	1.886739	27.381613	0.281325	20.123247	2011	73	0.281324	-6.25	0.64	2550	66	6.28	0.64

Tabela 2: Hf isotopes results determined by LA-ICP-MS – Banded mafic granulite (C-838-A)

Grain #	$^{176}\text{Yb}/^{177}\text{Hf}^a$	$\pm 2\sigma$	$^{176}\text{Lu}/^{177}\text{Hf}^a$	$\pm 2\sigma$	$^{178}\text{Hf}/^{177}\text{Hf}$	$^{180}\text{Hf}/^{177}\text{Hf}$	Sig <sub>Hf</sub> <sup>b</sup> (V)	$^{176}\text{Hf}/^{177}\text{Hf}$	$\pm 2\sigma^c$	age <sup>f</sup> (Ma)	$\pm 2\sigma$	$^{176}\text{Hf}/^{177}\text{Hf}_{(t)}^d$			age <sup>f</sup> (Ma)	$\pm 2\sigma$	$\delta\text{Hf}(t)^d$	
												(measured)	$\pm 2\sigma^c$	(pref./min.)			$\pm 2\sigma^c$	
14	0.007444	7.064548	0.000317	2.093637	1.467198	1.886909	12.980371	0.282038	12.012825	613	5	0.282033892	-12.9	0.6				
15	0.013021	12.510864	0.000535	4.260271	1.467190	1.886857	12.550071	0.282063	11.700906	691	3	0.282055619	-10.4	0.7	691	3	-10.4	0.7
19	0.031171	24.946673	0.001227	7.361276	1.467200	1.886742	11.161768	0.282068	16.132240	660	4	0.28205249	-11.2	0.7	691	3	-10.5	0.7
17	0.023828	19.067194	0.000930	5.577970	1.467171	1.886831	12.739275	0.282029	18.933275	610	4	0.282018507	-13.5	0.7	691	3	-11.7	0.7
18	0.026941	21.557505	0.001062	6.371792	1.467190	1.886829	13.107339	0.282042	23.454764	633	5	0.282029626	-12.6	0.7				
30	0.006316	5.053808	0.000266	1.597554	1.467206	1.886808	12.862061	0.282006	17.462236	607	4	0.282003326	-14.1	0.6				
48	0.026328	21.068991	0.001050	6.300496	1.467220	1.886663	7.519845	0.282079	18.802128	687	9	0.282065126	-10.1	0.7	691	3	-10.0	0.7
56	0.005871	4.728228	0.000254	1.543050	1.467183	1.886870	11.773767	0.282038	14.872045	610	4	0.282035106	-12.9	0.6	691	3	-11.1	0.6
55	0.016863	13.535221	0.000687	4.143741	1.467240	1.886863	11.197011	0.282072	18.315253	601	7	0.282063867	-12.1	0.7	691	3	-10.1	0.7
54	0.006976	5.589082	0.000299	1.796744	1.467196	1.886732	12.646761	0.282051	15.437261	589	12	0.282047817	-13.0	0.6				
52	0.011751	9.438947	0.000498	3.014952	1.467174	1.886823	12.948048	0.282089	15.643175	683	5	0.282082713	-9.6	0.6	691	3	-9.4	0.6
49	0.011644	9.710640	0.000497	3.187017	1.467213	1.886707	12.761453	0.282126	14.837233	650	7	0.282119555	-9.0	0.6				
50	0.012959	10.793115	0.000541	3.465208	1.467194	1.886834	13.895866	0.281998	15.227777	607	7	0.28199225	-14.5	0.6	691	3	-12.7	0.6
96	0.019045	15.248311	0.000769	4.615463	1.467166	1.886777	15.271307	0.282001	14.111508	601	4	0.281992567	-14.6	0.7	691	3	-12.7	0.7
94	0.034042	27.311912	0.001357	8.142779	1.467205	1.886857	9.757694	0.282066	20.783162	616	3	0.282050587	-12.2	0.7				
89	0.004000	3.208552	0.000173	1.040238	1.467217	1.886949	12.802895	0.282027	15.023585	607	4	0.28202539	-13.3	0.6	691	3	-11.5	0.6
88	0.008909	7.154790	0.000372	2.233898	1.467216	1.886741	12.985465	0.282055	17.194423	626	3	0.282050847	-12.0	0.6	691	3	-10.6	0.6
87	0.008814	7.083155	0.000378	2.266774	1.467180	1.886915	12.101821	0.282000	13.911733	602	5	0.281995771	-14.5	0.6	691	3	-12.5	0.6
75	0.011286	9.273740	0.000479	2.937253	1.467224	1.886863	13.550058	0.282045	13.933650	661	6	0.282038885	-11.6	0.6	691	3	-11.0	0.6
73	0.014105	11.462408	0.000575	3.463957	1.467159	1.886762	8.263707	0.282083	13.830244	659	3	0.282075517	-10.4	0.7	691	3	-9.7	0.7
113	0.008176	6.652681	0.000338	2.041901	1.467164	1.886816	13.367254	0.282025	17.687534	706	16	0.282020292	-11.3	0.6				
111	0.010851	8.835422	0.000473	2.863024	1.467207	1.886735	14.460541	0.282065	14.098062	624	3	0.282059163	-11.8	0.6	691	3	-10.3	0.6
114	0.013616	11.509112	0.000560	3.799198	1.467208	1.886788	12.038613	0.282033	12.021907	613	5	0.282026901	-13.1	0.7	691	3	-11.4	0.7
127	0.015223	12.438320	0.000647	3.913510	1.467210	1.886815	12.375987	0.282053	15.246561	604	2	0.282045849	-12.7	0.7	691	3	-10.8	0.7
126	0.014515	12.027158	0.000586	3.636822	1.467183	1.886762	14.116148	0.282011	19.834082	630	4	0.282003645	-13.6	0.7	691	3	-12.2	0.7
130	0.020632	16.551964	0.000842	5.054216	1.467246	1.886798	13.487401	0.282004	14.992740	675	5	0.281993434	-12.9	0.7	691	3	-12.6	0.7
145	0.008317	6.676521	0.000389	2.334070	1.467168	1.886865	15.419124	0.281998	18.119259	1393	48	0.281987671	3.1	0.6				
146	0.005510	4.421130	0.000223	1.341039	1.467204	1.886847	14.704503	0.281326	14.721138	622	7	0.28132339	-37.9	0.6				
150	0.012406	10.074727	0.000507	3.067021	1.467185	1.886888	11.356779	0.282037	15.129740	603	8	0.28203079	-13.2	0.6	691	3	-11.3	0.6
163	0.009126	7.341931	0.000368	2.249652	1.467200	1.886871	13.157235	0.282028	13.655502	609	3	0.282023404	-13.4	0.6	691	3	-11.5	0.6
165	0.006439	5.172849	0.000275	1.674954	1.467213	1.886828	11.618346	0.282058	15.542951	628	5	0.282055248	-11.8	0.6	691	3	-10.4	0.6
166	0.033242	26.700556	0.001300	7.805312	1.467153	1.886831	10.284595	0.282034	21.157491	591	6	0.282019974	-13.9	0.7				
19	0.006104	4.902105	0.000261	1.567691	1.467228	1.886819	7.750800	0.282010	16.701725	621	5	0.282006966	-13.7	0.6	691	3	-12.1	0.6
13	0.006053	4.868996	0.000243	1.458383	1.467222	1.886873	11.809468	0.282024	16.544819	600	4	0.282021218	-13.6	0.6	691	3	-11.6	0.6
12	0.004742	3.907693	0.000192	1.261523	1.467152	1.886862	11.422384	0.282038	14.850635	613	4	0.282035475	-12.8	0.6	691	3	-11.1	0.6
10	0.025311	20.293006	0.001017	6.105564	1.467263	1.886786	10.386917	0.282002	15.101119	641	7	0.281989907	-13.8	0.7				

Tabela 3: Hf isotopes results determined by LA-ICP-MS - Opdalite (C-838-2)

Grain#	$^{176}\text{Yb}/^{177}\text{Hf}$ <sup>a</sup>		$^{176}\text{Lu}/^{177}\text{Hf}$ <sup>a</sup>		$^{178}\text{Hf}/^{177}\text{Hf}$	$^{180}\text{Hf}/^{177}\text{Hf}$	$\text{Sig}_{\text{Hf}}$ <sup>b</sup>			$\text{age}$ <sup>f</sup>					$\text{age}$ <sup>f</sup>				
	$\pm 2\text{s}$	$\pm 2\text{s}$	$\pm 2\text{s}$	$\pm 2\text{s}$			(V)	$^{176}\text{Hf}/^{177}\text{Hf}$	$\pm 2\text{s}$ <sup>c</sup>	(Ma)	$\pm 2\text{s}$	$^{176}\text{Hf}/^{177}\text{Hf}_{(t)}$ <sup>d</sup>	$\text{eHf}(t)$ <sup>d</sup>	$\pm 2\text{s}$ <sup>c</sup>	(Ma)	$\pm 2\text{s}$	$\text{eHf}(t)$ <sup>d</sup>	$\pm 2\text{s}$ <sup>c</sup>	
											(measured)					(pref./min.)			
12	0.014412	11.821887	0.000522	3.191866	1.465531	1.886344	0.651392	0.282109	15.868479	720	6	0.282102	-8.1	0.7	786	10	-6.6	0.7	
14	0.024532	19.742957	0.000885	5.470872	1.467181	1.886809	16.791989	0.281953	13.698005	770	6	0.281940	-12.7	0.7	786	10	-12.4	0.7	
20	0.008290	6.657029	0.000329	1.988855	1.467209	1.886883	12.662685	0.281974	15.277030	715	7	0.281970	-12.9	0.6	786	10	-11.3	0.6	
19	0.005801	4.656202	0.000265	1.591095	1.467165	1.886835	12.848560	0.281979	21.413222	674	5	0.281975	-13.6	0.6	786	10	-11.1	0.6	
18	0.017877	14.341833	0.000676	4.058830	1.467183	1.886848	11.202638	0.281994	18.653246	681	5	0.281986	-13.1	0.7	786	10	-10.8	0.7	
17	0.011802	9.483636	0.000485	2.910870	1.467198	1.886907	13.643171	0.281968	17.879437	659	6	0.281962	-14.4	0.6	786	10	-11.6	0.6	
33	0.042583	34.296462	0.001567	9.407428	1.467252	1.886726	11.323069	0.281961	13.924912	715	5	0.281940	-13.9	0.7	786	10	-12.4	0.7	
32	0.003576	2.869126	0.000180	1.083151	1.467168	1.886822	13.054907	0.281994	14.598347	730	5	0.281991	-11.8	0.6	786	10	-10.5	0.6	
31	0.018789	15.099224	0.000707	4.305586	1.467168	1.886841	12.913427	0.281971	12.773080	748	6	0.281961	-12.5	0.7	786	10	-11.6	0.7	
30	0.018557	20.534318	0.000703	6.823750	1.467151	1.886852	13.296805	0.281943	22.444506	761	6	0.281933	-13.1	0.7	786	10	-12.6	0.7	
36	0.006403	8.942490	0.000256	3.070896	1.467225	1.886823	15.465130	0.281990	18.205739	713	6	0.281987	-12.3	0.6	786	10	-10.7	0.6	
34	0.035686	33.781821	0.001326	10.548908	1.467197	1.886901	11.642772	0.281938	14.126271	743	5	0.281920	-14.0	0.7	786	10	-13.1	0.7	
59	0.003994	5.625863	0.000194	2.527655	1.467203	1.886903	12.409486	0.281988	20.260311	650	9	0.281986	-13.8	0.6	786	10	-10.7	0.6	
54	0.012394	10.982795	0.000489	3.119696	1.467194	1.887030	10.646125	0.281982	17.974075	637	5	0.281976	-14.4	0.6	786	10	-11.1	0.6	
55	0.010193	9.449908	0.000432	3.440167	1.467185	1.886766	13.720842	0.281916	19.291907	678	5	0.281911	-15.8	0.6					
57	0.029724	31.890582	0.001118	10.629455	1.467171	1.886839	10.063925	0.281986	24.499838	776	7	0.281970	-11.5	0.7	786	10	-11.3	0.7	
51	0.005851	7.121611	0.000253	2.771570	1.467181	1.886865	14.092338	0.281941	18.252469	679	6	0.281938	-14.8	0.6	786	10	-12.4	0.6	
50	0.015082	12.695320	0.000579	3.917489	1.467215	1.886812	11.784249	0.281964	13.075741	707	10	0.281956	-13.5	0.7	786	10	-11.8	0.7	
39	0.019478	15.657231	0.000761	4.628831	1.467161	1.886891	11.447902	0.281971	14.481603	721	5	0.281960	-13.1	0.7	786	10	-11.6	0.7	
38	0.028955	23.362332	0.001094	6.720978	1.467204	1.886710	10.985476	0.281956	13.072079	725	5	0.281941	-13.7	0.7	786	10	-12.3	0.7	
71	0.009677	8.477461	0.000381	2.652509	1.467175	1.886744	14.121947	0.281974	14.488865	691	23	0.281969	-13.5	0.6	786	10	-11.3	0.6	
70	0.011823	9.507634	0.000501	3.024856	1.467214	1.886866	15.043107	0.281931	13.837297	654	6	0.281925	-15.8	0.6			-30.2	0.6	
72	0.012297	9.858062	0.000512	3.107368	1.467212	1.886901	13.956880	0.281966	12.849712	683	5	0.281959	-14.0	0.6	786	10	-11.7	0.6	
76	0.025669	20.594045	0.000929	5.575014	1.467152	1.886808	12.311592	0.281943	20.783162	786	10	0.281930	-12.7	0.7	786	10	-12.7	0.7	
98	0.034753	27.881245	0.001277	7.664271	1.467258	1.886876	11.926751	0.281955	17.891999	711	5	0.281938	-14.1	0.7	786	10	-12.5	0.7	
97	0.014029	11.256782	0.000541	3.250904	1.467222	1.886880	13.982600	0.281977	17.699806	676	10	0.281970	-13.8	0.6	786	10	-11.3	0.7	
96	0.022571	18.090066	0.000847	5.092075	1.467194	1.886897	13.244563	0.281966	11.162087	669	7	0.281955	-14.4	0.7	786	10	-11.9	0.7	
90	0.024899	19.939835	0.000973	5.847333	1.467173	1.886865	10.328856	0.281983	11.799278	727	6	0.281970	-12.6	0.7	786	10	-11.3	0.7	
110	0.009551	7.739243	0.000403	2.426244	1.467181	1.886804	18.292205	0.281922	13.512171	665	4	0.281917	-15.8	0.6	786	10	-13.2	0.6	
113	0.022805	25.952742	0.000831	8.728000	1.467178	1.886791	14.186221	0.281959	16.582024	695	5	0.281948	-14.1	0.7	786	10	-12.1	0.7	
115	0.013555	10.866596	0.000541	3.256099	1.467156	1.886803	14.311312	0.281941	16.868590	636	5	0.281935	-15.9	0.6			-29.8	0.6	

Tabela 4:Hf isotopes results determined by LA-ICP-MS - Granitic (hornblende)-biotite leucosome (C-838-B)

Grain#	$\frac{^{176}\text{Yb}}{^{177}\text{Hf}}$ <sup>a</sup>	$\pm 2s$	$\frac{^{176}\text{Lu}}{^{177}\text{Hf}}$ <sup>a</sup>	$\pm 2s$	$\frac{^{178}\text{Hf}}{^{177}\text{Hf}}$	$\frac{^{180}\text{Hf}}{^{177}\text{Hf}}$	Sig <sub>Hf</sub> <sup>b</sup> (V)	$\frac{^{176}\text{Hf}}{^{177}\text{Hf}}$	$\pm 2s$ <sup>c</sup>	age <sup>f</sup> (Ma)	$\pm 2s$	$\frac{^{176}\text{Hf}}{^{177}\text{Hf}}_{(t)}$ <sup>d</sup>	eHf(t) <sup>d</sup>	$\pm 2s$ <sup>c</sup>
27	0.008990	9.927428	0.000372	3.442861	1.467116	1.886834	14.805365	0.281552	17.762929	683	5	0.281547	-28.6	0.8
29	0.006492	5.238173	0.000259	1.576507	1.467140	1.886878	14.899442	0.281220	13.490189	630	6	0.281217	-41.4	0.7
28	0.014816	12.060225	0.000582	3.577667	1.467161	1.886766	14.970909	0.281187	19.525790	1365	59	0.281172	-26.5	0.8
25	0.005595	5.418700	0.000219	1.701016	1.467153	1.886710	14.372188	0.281216	19.497177	659	5	0.281213	-40.9	0.7
24	0.011872	9.589260	0.000459	2.795651	1.467195	1.886814	17.697859	0.281039	26.663680	1926	12	0.281023	-18.9	0.8
20	0.009879	7.986589	0.000419	2.525649	1.467177	1.886727	15.118475	0.281780	21.347640	666	6	0.281775	-20.9	0.8
10	0.015426	13.360785	0.000644	4.185167	1.467190	1.886739	18.096749	0.281332	14.875169	647	5	0.281324	-37.3	0.8
9	0.008131	9.404161	0.000340	3.414347	1.467183	1.886793	15.206083	0.281216	19.712488	666	5	0.281212	-40.8	0.8
8	0.017800	25.684078	0.000660	8.805144	1.467174	1.886673	12.016729	0.280972	189.454299	2075	43	0.280946	-18.2	0.8
47	0.006912	5.571781	0.000276	1.653967	1.467188	1.886842	14.339065	0.281203	17.701594	630	6	0.281200	-42.0	0.7
79	0.004486	3.591711	0.000184	1.102877	1.467160	1.886775	13.382198	0.281244	19.802343	571	3	0.281242	-41.9	0.7
78	0.015301	12.246247	0.000642	3.855354	1.467201	1.886921	16.109990	0.281123	21.874960	1479	36	0.281105	-26.2	0.8
77	0.011330	9.078644	0.000476	2.857650	1.467152	1.886660	17.041357	0.281322	17.477502	612	3	0.281317	-38.3	0.8
99	0.001038	0.831136	0.000038	0.228918	1.467173	1.886860	20.282565	0.280987	20.252718	518	5	0.280987	-52.1	0.7
61	0.015207	13.957276	0.000580	4.085738	1.467181	1.886878	19.293933	0.281124	15.340961	601	4	0.281118	-45.6	0.8
84	0.018879	16.390473	0.000731	4.632342	1.467197	1.886825	15.472464	0.280966	15.986155	2725	19	0.280928	-3.7	0.8

Tabela 5: Hf isotopes results determined by LA-ICP-MS - Mafic enclave (C-716-B)

Grain#	$^{176}\text{Yb}/^{177}\text{Hf}$ <sup>a</sup>	$\pm 2s$	$^{176}\text{Lu}/^{177}\text{Hf}$ <sup>a</sup>	$\pm 2s$	$^{178}\text{Hf}/^{177}\text{Hf}$	$^{180}\text{Hf}/^{177}\text{Hf}$	Sig <sub>Hf</sub> <sup>b</sup> (V)	$^{176}\text{Hf}/^{177}\text{Hf}$	$\pm 2s$ <sup>c</sup>	age <sup>f</sup> (Ma)	$\pm 2s$	$^{176}\text{Hf}/^{177}\text{Hf}$ <sup>d</sup>			age <sup>f</sup> (Ma)			
												eHf(t) <sup>d</sup>	$\pm 2s$ <sup>c</sup>	(measured)	(pref./min.)	$\pm 2s$	eHf(t) <sup>d</sup>	$\pm 2s$ <sup>c</sup>
4	0.027042	21.649524	0.000794	4.771531	1.467223	1.886876	21.363529	0.282178	16.246440	664	5	0.282168	-7.03	0.68	664	9	-7.02	0.68
1	0.006343	5.080041	0.000203	1.219353	1.467202	1.886795	23.750689	0.282201	16.711675	655	14	0.282199	-6.13	0.64	664	9	-5.93	0.64
8	0.042423	33.947026	0.001272	7.641317	1.467184	1.886795	14.316663	0.282144	14.519733	638	15	0.282129	-8.96	0.72	664	9	-8.40	0.72
7	0.034488	27.780412	0.001005	6.075624	1.467244	1.886953	15.341702	0.282157	16.607797	637	13	0.282145	-8.44	0.70	664	9	-7.85	0.70
6	0.017368	13.917273	0.000533	3.212692	1.467196	1.886766	22.214593	0.282098	17.689930	635	9	0.282092	-10.36	0.66	664	9	-9.72	0.66
5	0.020684	17.683033	0.000619	4.147075	1.467178	1.886802	21.264575	0.281931	24.065766	642	4	0.281923	-16.17	0.66	664	9	-15.68	0.66
13	0.016974	15.683688	0.000513	3.853574	1.467208	1.887027	15.445089	0.282157	13.687128	636	24	0.282151	-8.24	0.66	664	9	-7.62	0.66
12	0.027145	38.657993	0.000830	10.751280	1.467221	1.886807	15.947669	0.282174	15.739751	630	19	0.282164	-7.91	0.75	664	9	-7.16	0.75
17	0.013494	10.909729	0.000438	2.659524	1.467200	1.886818	17.706334	0.282189	14.323327	656	12	0.282184	-6.63	0.65	664	9	-6.45	0.65
20	0.009699	7.803402	0.000310	1.868607	1.467232	1.886869	18.071895	0.282195	19.679752	625	11	0.282191	-7.07	0.65	664	9	-6.20	0.65
27	0.034500	27.640618	0.001003	6.030270	1.467263	1.886943	13.244183	0.282166	15.394390	610	22	0.282155	-8.69	0.70	664	9	-7.51	0.70
32	0.034750	28.137319	0.001029	6.270769	1.467195	1.886810	14.811072	0.282166	15.506444	612	16	0.282154	-8.67	0.70	664	9	-7.53	0.70
36	0.014470	13.728310	0.000459	3.366675	1.467208	1.886919	16.508834	0.282192	12.163430	617	28	0.282186	-7.42	0.66	664	9	-6.38	0.66
35	0.015105	13.092435	0.000468	3.151787	1.467219	1.886846	14.951901	0.282181	16.454065	631	15	0.282175	-7.50	0.65	664	9	-6.75	0.65
39	0.032876	27.791910	0.000964	6.303439	1.467201	1.886839	21.899797	0.282215	18.297719	627	23	0.282203	-6.59	0.70	664	9	-5.79	0.70
43	0.025051	20.047956	0.000723	4.340650	1.467212	1.886862	13.741447	0.282166	21.020825	626	14	0.282158	-8.23	0.67	664	9	-7.39	0.67
46	0.009667	7.736227	0.000299	1.797350	1.467146	1.886821	14.933159	0.282165	21.448519	633	13	0.282161	-7.94	0.65	664	9	-7.26	0.65
49	0.013894	11.119983	0.000448	2.689307	1.467170	1.886790	15.898043	0.282175	20.397617	636	20	0.282169	-7.58	0.65	664	9	-6.97	0.65
62	0.017681	14.151275	0.000539	3.234591	1.467210	1.886780	23.059403	0.282052	18.147312	642	20	0.282046	-11.84	0.66	664	9	-11.35	0.66
63	0.024385	19.513640	0.000740	4.441331	1.467179	1.886753	15.006190	0.282150	21.517990	612	20	0.282141	-9.12	0.67	664	9	-7.98	0.67
61	0.026074	21.253924	0.000766	4.713533	1.467183	1.886887	13.191101	0.282148	19.828605	628	35	0.282139	-8.85	0.67	664	9	-8.05	0.67
60	0.025963	21.369886	0.000769	4.782501	1.467216	1.886828	18.832630	0.282177	17.148138	641	12	0.282168	-7.52	0.68	664	9	-7.02	0.68
58	0.026215	21.027704	0.000831	4.997138	1.467225	1.886899	12.908684	0.282153	16.324219	633	14	0.282143	-8.57	0.67	664	9	-7.90	0.67
55	0.036096	44.785079	0.001068	10.703404	1.467206	1.886737	12.116143	0.282146	22.450724	631	16	0.282134	-8.97	0.78	664	9	-8.24	0.78

**Appendix VII**  
**Reactions figure 4.6**

## Complementary data Fig. 6

### Symplectite:

15) Pl Cpx Opx Amp Qz

17) Pl Cpx Opx Qz

### Corona:

3) Pl (3)Amp

4) Ol Pl (2) Amp

5) Pl (2) Amp

8) Ol Pl Cpx Opx Amp

10) Ol Pl Cpx Opx

11) Pl (2) Amp

18) Pl Chl (2) Amp Zo Qz

20) Pl Amp Zo Qz

21) Pl Amp Qz

23) Pl Cpx Opx Amp

27) Pl (2) Amp Zo Pg

29) Pl Cpx Amp Zo Qz

33) Chl (2) Amp Zo

35) (3) Amp Zo Qz

38) Cpx (2) Amp Zo Qz

39) Cpx Amp Zo Qz

41) Grt Chl (2) Amp Zo

42) Grt Chl (2) Amp Zo

43) Grt (2) Amp Zo

44) Grt (2) Amp Zo Qz

48) Grt Chl (2) Amp Zo Qz

50) Grt Cpx Chl (2) Amp Lws

51) Grt Cpx (2) Amp Lws

52) Grt Cpx (2) Amp Lws Qz

56) Grt Cpx Amp Ky Pg Qz

62) Grt Cpx Ky Qz  
66) Ol Pl Cpx Amp Pg  
73) Pl Chl (2) Amp Zo Pg  
75) Chl (2) Amp Zo Pg  
76) Chl (2) Amp Zo Qz  
77) Cpx Chl (2) Amp Zo  
78) Cpx Chl Amp Zo Qz  
79) Grt Cpx Chl Amp Zo Qz  
80) Grt Cpx Chl Amp Lws Qz  
97) Pl (2) Amp Qz  
103) Grt (3) Amp Zo Qz  
110) Pl Grt Amp  
111) Grt Cpx Amp Ky Zo Qz  
117) Pl Grt Cpx Qz  
119) Ol Pl Cpx Opx Amp  
120) Pl Grt Cpx Opx Amp  
121) Grt Cpx Qz  
135) Pl Chl (2) Amp Qz  
138) Pl Grt Amp Qz  
140) (3) Amp Zo Pg Qz  
149) (2) Amp Zo Qz  
153) Grt Chl (2) Amp Zo Qz  
154) Grt Cpx Chl (2) Amp Zo